UNIVERSITÁ DEGLI STUDI DI NAPOLI
FEDERICO II

UNIVERSITÁ DEGLI STUDI DI NAPOLI
PARTHENOPE

DOTTORATO DI RICERCA REGIONALE
IN
INGEGNERIA GEOTECNICA XXVI CICLO

Centrifuge Modelling of Flexible Retaining Walls in Saturated Sand under Seismic Actions

Michele Tricarico

Tutor: Prof. Ing. Stefano Aversa

Marzo 2015

Acknowledgements

I would like to acknowledge Professor Stefano Aversa for his guide and advices indispensable for the organization of the research and for the understanding and interpretation of the results and Professor Gopal Madabhushi of University of Cambridge for his guidance in the performing of the centrifuge tests at the Schofield Centre. I am thankful to Dr. Luca De Sanctis and Dr. Riccardo Conti for their precious advices and suggestions in the tests design and data interpretation. I am grateful to Mark Stringer and Charles Heron of Cambridge University to have worked intensely for the realization of the tests. Thanks to their help and expertise the tests have been carried out obtaining the best results in the shortest time possible. Special acknowledgments are for those people and colleagues that have represented a support during all the period of the PhD.: researchers, PhD. students, students and technicians in Federico II University, in Parthenope University and at the Schofield Centre of the University of Cambridge.

List of Tables

2.1 Scaling factors for centrifuge modeling linking physical quantities from model to prototype scale. 52
2.2 Basic properties of the sand. 62
2.3 Technical specifications of the CDAQS acquisition module. . . 68
2.4 Calibration factors of strain gauges for tests CWU1 and PWU1. 84
2.5 Calibration factors of strain gauges for test CWU2. 84
2.6 Calibration factors of strain gauges for test PWU2. 84
2.7 Calibration factors of strain gauges for test CWU3, PWU3 and CWU4 85

3.1 Chronological Sequence of the tests and their preparation and execution. 109
3.2 Geometrical properties of the tests at the model scale and at the prototype scale. 109
3.3 Test CWU1: characteristics of the input earthquakes. 114
3.4 Test CWU1: list of instruments that did not work properly. . 115
3.5 Test PWU1: characteristics of the input earthquakes. 115
3.6 Test PWU1: list of instruments that did not work properly. . 116
3.7 Test CWU2: characteristics of the input earthquakes. 117
3.8 Test CWU2: list of instruments that did not work properly. . 118
3.9 Test PWU2: characteristics of the input earthquakes. 119
3.10 Test PWU2: list of instruments that did not work properly. . 120
3.11 Test CWU3: characteristics of the input earthquakes. 121
3.12 Test CWU3: list of instruments that did not work properly. . 122
3.13 Test PWU3: characteristics of the input earthquakes. 123
3.14 Test CWU4: characteristics of the input earthquakes. 126
3.15 Test CWU4: list of instruments did not work properly. 127
3.16 Relative density Before and After the tests. 149
3.17 CWU1: values of r_u coefficient at the end of the earthquakes. 167

3.18 PWU1: values of r_u coefficient at the end of the earthquakes. 187
3.19 CWU2: values of r_u coefficient at the end of the earthquakes. 208
3.20 PWU2: values of r_u coefficient at the end of the earthquakes. 227
3.21 Bending moment at pre-earthquakes, maximum, short term residual and long term residual for the tests CWU1, PWU1, CWU2 and PWU2. 259

4.1 Comparison between the tests in saturated sand and the tests in dry sand (Conti, 2010) of the accumulated displacement at the top of the cantilever walls and at the bottom of the propped walls. 301

5.1 Parameters of Dafalias and Manzari model. 335
5.2 List of the tests performed by Visone (2008). 338

B.1 Strain gauges positions from the top of the walls at the model scale. 400
B.2 Instrument position before and after test CWU1. 402
B.3 Instrument position before and after test PWU1. 404
B.4 Instrument position before and after test CWU2. 406
B.5 Instrument position before and after test PWU2. 408
B.6 Instrument position before and after test CWU3. 410
B.7 Instrument position before and after test PWU3. 412
B.8 Instrument position before and after test CWU4. 414

C.1 Applied suction and suction increments for the determination of the water retention curve of the Leighton Buzzard sand. . 421
C.2 Basic physical properties of the Leighton Buzzard sand. . . . 422
C.3 Van Genuchten parameters for Loose Sample and Dense Sample. 424

List of Figures

1.1 Initial problem geometry (from Lancellotta 2007). 34
1.2 Transformed problem geometry (from Lancellotta 2007). . . . 35
1.3 Stress discontinuities (from Lancellotta 2007). 35
1.4 Schematic of Newmark method. (a)base acceleration and block acceleration before the sliding; (b)block inertial force and shear force at the contact surface; (c)block inertial force and shear force at the contact surface during the sliding; (d)base acceleration and block acceleration comparison with time during sliding. 37
1.5 Scheme of the rotational failure of a cantilever wall. 38
1.6 Limit equilibrium condition for a cantilever retaining wall: seismic active and passive pressures on a cantilever retaining wall. 39
1.7 Richards Elms (1992). Passive failure on walls with an anchor at the top: forces, accelerations and displacements. 40
1.8 Hydrodynamic pressures on a quay wall. 44

2.1 Model and prototype stress distributions along the vertical. . 54
2.2 Effect of the radial acceleration on the curvature of the fluid surface. 56
2.3 Schofield Center Beam Centrifuge 57
2.4 Figure Taken from Madabhushi, S. P. G., Schofield, A. N. Lesley, S. (1998): schematic diagram showing the planar view of Stored Angolar Momentum (SAM) shaker. 58
2.5 Model container: a) Aluminium rectangular rings and cylindrical bearings. b) Laminar box built. 60
2.6 Particle size distribution of Leighton Buzzard sand 100/170 (modified from Tan 1990). 61

2.7 Dry unit weight with relative density of LB sand (Visone, Santucci de Magistris, 2009) 62
2.8 Evolution of elastic properties of Leighton Buzzard Sand with p'. a) Initial shear modulus G_0, b) initial damping ratio D_0, c) Shear wave velocity (after Visone, Santucci de Magistris 2009). 63
2.9 Peak strength of Leighton Buzzard Sand in Drained Tests on dense samples (D_r= 60-80%): a) in (q, p') plane, b) in (e, lnp') plane (Visone & Santucci de Magistris, 2009). 64
2.10 Aluminium Wall 65
2.11 Hydroxypropyl methylcellulose powder dissolving into water. 66
2.12 Data Acquisition System. 68
2.13 Hopper for sand pouring (from Zhao et al., 2006). 69
2.14 a) Muzzle at the base of the hopper with the nozzle at the top, b) Sieve at the bottom of the muzzle. 70
2.15 Sand pouring. a) Hopper calibration; b) Pouring sand into the model. 71
2.16 Path of the hopper. a) first cycle path, b) second cycle path 71
2.17 a) Measuring the height of sand poured into the container during the hopper calibration; b) procedure of flattening the sand surface. 72
2.18 Piezoelectric accelerometer. 73
2.19 Frequency response of piezoelectric accelerometers. 73
2.20 Piezoelectric Accelerometers Calibrator. 74
2.21 Calibration factors of the piezoelectric accelerometers of test PWU3. 75
2.22 MEMS accelerometer on the top of the wall. 76
2.23 Calibration factors of MEMS of test PWU3. 77
2.24 MEMS accelerometer on the top of the wall. 77
2.25 Pore Pressure Transducer; a) photography, b) schematic of the PPT. 78
2.26 Calibration station of the PPTs. 78
2.27 Schematic of the calibration station of the PPTs. 79
2.28 Calibration data of pore pressure transducers of test PWU3. . 80
2.29 Covering strain gauges with epoxy resin. 81
2.30 Electrical scheme of a Wheatstone bridge. 82
2.31 Calibration data of the strain gauges of left wall of test PWU3. 83
2.32 Calibration of left wall clumping at the base and loading from the top. 83

2.33 LVDTs measuring horizontal displacements of the walls and the vertical settlements of the soil in the model of test CWU1. 86
2.34 Calibration of an LVDT 86
2.35 Calibration results of the LVDTs relative to test PWU3. . . . 87
2.36 Wire Potentiometer 87
2.37 Test PWU1. a) and b) positioning the potentiometer on the support; c) linking the potentiometer cable to the top of the wall. 88
2.38 Calibration data of potentiometer of test PWU3. 88
2.39 Load cell F250 from Novatech. a) schematic, b) photo of the instrument. 89
2.40 Load cells on the props of test PWU1. 89
2.41 Calibration of Load Cells of test PWU3. 89
2.42 Geometrical characteristics of the pressure sensor. 90
2.43 Typical sensor performance (taken from Tekscan Inc. web site). 91
2.44 Electrical schematic of the data acquisition system 92
2.45 Calibration of the sensor pressure. 92
2.46 PWU3 layout. All the distances in millimeters. 93
2.47 ACC2 and PPT1 placed at the same depth and shifted along the depth of the laminar box. 94
2.48 a) accelerometer positioning, b) wall positioning. 96
2.49 Fans that prevent sand transit from active side to passive side glued on the sides of the wall. 96
2.50 LVDT support. 97
2.51 Scheme of pressure sensor installation on the wall for tests CWU3 and PWU3 (frontal view). 97
2.52 Scheme of pressure sensor installation on the wall for tests CWU3 and PWU3 (lateral view). 98
2.53 CAM-sat system used for saturating models developed at the Schofield Centre. 99
2.54 Area A_{AFGBD} occupied by the HPCM during the flight (not drawn to scale). 100
2.55 Area A_{EFGH} (not drawn to scale). 101
2.56 Area A_{AEDHB} (not drawn to scale). 102
2.57 Area A_{ADBC} (not drawn to scale). 103
2.58 Area A_{AEHB} (not drawn to scale). 104

3.1 Test PWU3 layout, vertical alignment of accelerometers and pore pressure transducers at the back of the left wall. 110

3.2 Scheme of the LVDT support connected to the base plate of the laminar box: vertical and planar view. 111
3.3 Scheme of the models and principal geometric characteristics: (a) CWU tests on cantilevered walls and (b) PWU tests on propped walls. 113
3.4 Test CWU1: model layout. 114
3.5 Test PWU1: model layout 116
3.6 Test CWU2: model layout 118
3.7 Test PWU2: model layout 120
3.8 Test CWU3: model layout 122
3.9 Test PWU3: model layout 124
3.10 Test CWU4: model layout 126
3.11 Scheme of the LVDT support connected to the base plate of the laminar box: vertical and planar view. 130
3.12 Model CWU1 in the centrifuge, the support of the LVDTs is visible (figure already reported in Chapter 2). 132
3.13 Interpretation of LVDT measurements of horizontal displacements of the walls. (a) measured displacements, (b) displacements of the laminar box rings, (c) displacements of the walls relative to the soil. 133
3.14 Test CWU1 EQ1: LVDTs time history with its time trend compared with the symmetrical time trend with the superimposition of the dynamic part of the measured displacement for a) LVDT3 (top left wall, b) LVDT4 (bottom left wall), c) LVDT5 (top right wall), d) LVDT6 (bottom right wall). . . . 136
3.15 Test CWU1 - EQ1: Symmetrical time trend during EQ1 for a) the top LVDTs (LVDT3 and LVDT5) and b) the bottom LVDTs (LVDT4 and LVDT6) compared with the original time histories. 137
3.16 Test CWU1 EQ1: average of the top LVDTs (original signal) compared with the smoothed signal. 140
3.17 Test CWU1: post seismic time trend of the horizontal displacements of the walls measured with the LVDTs. 142
3.18 Test CWU1: post seismic time trend of pore pressures. 143
3.19 Test CWU1: post seismic time trend of the bending moment. 144
3.20 Test CWU1: long term residual values reported at the end of the dynamic time trend of the measured displacements. . . . 145
3.21 Typical time history of a physical quantity measured during the applied earthquake and adopted terminology. 146

3.22 Test PWU3, earthquake EQ1: maximum bending moment during EQ1 and the strain gauge where it is attained. The Maximum Left wall time instant is common for all the other physical quantities of the test. 148
3.23 CWU1: acceleration time histories at the back of the left wall during EQ1 and EQ2. 151
3.24 CWU1: acceleration time histories between the walls during EQ1 and EQ2. 152
3.25 Test CWU1: amplification factor with the depth at the back of the left wall for EQ1. Starting from the bottom, at each circled marker correspond respectively Acc1, Acc2, Acc3, Acc4 and Acc5. 153
3.26 Test CWU1: amplification factor with the depth at the back of the left wall for EQ2. Starting from the bottom, at each circled marker correspond respectively Acc1, Acc2, Acc3, Acc4 and Acc5. 154
3.27 Test CWU1: amplification factor with the depth at the excavated side for EQ1. Starting from the bottom, at each circled marker correspond respectively Acc1, Acc6 and Acc7. 154
3.28 Test CWU1: amplification factor with the depth at the excavated side for EQ2. Starting from the bottom, at each circled marker correspond respectively Acc1, Acc6 and Acc7. 155
3.29 CWU1- EQ1: phase difference computed in the time domain. 156
3.30 CWU1 EQ2: phase difference computed in the time domain. 157
3.31 CWU1: walls horizontal displacement time histories during EQ1 and EQ2. 159
3.32 CWU1: walls symmetrical displacements time histories during EQ1 and EQ2. 160
3.33 Test CWU1 EQ1: Rotation of the walls computed from the signals of the LVDTs (symmetrical). 161
3.34 Test CWU1 EQ2: Rotation computed from the signals of the LVDTs (symmetrical). 161
3.35 CWU1: displacement space distribution. (a) EQ1 and PS1 measured displacements, (b) EQ1 and PS1 symmetrical displacements. 163
3.36 CWU1: pore pressures time histories during EQ1 and EQ2. 166
3.37 CWU1: time history of the pore pressure coefficient r_u. . . . 167
3.38 Test CWU1: pore pressure space distribution during EQ1 and EQ2. (a) EQ1 and PS1, (b) EQ2 and PS2. 168
3.39 CWU1: bending moment time histories during EQ1 and EQ2. 169

3.40 CWU1: bending moment space distribution during EQ1 and EQ2. (a) EQ1 and PS1, (b)EQ2 and PS2. 170
3.41 PWU1: acceleration time histories at the back of the left wall during EQ1 and EQ2. 172
3.42 PWU1: acceleration time histories between the walls during EQ1 and EQ2. 173
3.43 Test PWU1: amplification factor with the depth at the back of the left wall for EQ1. Starting from the bottom, at each circled marker correspond respectively Acc1, Acc2, Acc3, Acc4 and Acc5. 174
3.44 Test PWU1: amplification factor with the depth at the back of the left wall for EQ2. Starting from the bottom, at each circled marker correspond respectively Acc1, Acc2, Acc3, Acc4 and Acc5. 175
3.45 Test PWU1: amplification factor with the depth at the excavated side for EQ1. Starting from the bottom, at each circled marker correspond respectively Acc1, Acc2, Acc3, Acc4 and Acc5. 175
3.46 Test PWU1: amplification factor with the depth at the excavated side for EQ2. Starting from the bottom, at each circled marker correspond respectively Acc1, Acc2, Acc3, Acc4 and Acc5. 176
3.47 Test PWU1 EQ1: phase difference computed in the time domain. 177
3.48 PWU1 EQ2: phase difference computed in the time domain. 178
3.49 PWU1: walls horizontal displacement time histories during EQ1 and EQ2. 179
3.50 PWU1: walls horizontal symmetrical displacement time histories during EQ1 and EQ2. 180
3.51 Test PWU1 EQ1: Rotation of the walls computed from the symmetrical displacements. 181
3.52 PWU1 EQ2: Rotation of the walls computed from the symmetrical displacements. 182
3.53 PWU1: displacement space distribution. (a) EQ1 and PS1 measured displacements, (b) EQ1 and PS1 symmetrical displacements, (c) EQ2 and PS2 measured displacements, (d) EQ2 and PS2 symmetrical displacements. 183
3.54 PWU1: pore pressures time histories during EQ1 and EQ2. . 185
3.55 Test PWU1: r_u time history during EQ1 and EQ2. 186

3.56 PWU1: pore pressure space distribution during EQ1 and EQ2. (a) EQ1 and PS1, (b) EQ2 and PS2. 187
3.57 Model of Test PWU1: sand boils observed at the sand surface at the excavated side immediately after the test. 188
3.58 Test PWU1: bending moment time histories during EQ1 and EQ2. 189
3.59 Test PWU1: bending moment space distribution during EQ1 and EQ2. (a) EQ1 and PS1, (b)EQ2 and PS2. 189
3.60 Test PWU1: axial force in the front prop during EQ1 and EQ2. 190
3.61 Test CWU2: acceleration time history at the back of the left wall during EQ1, EQ2 and EQ3. 192
3.62 Test CWU2: acceleration time histories between the walls during EQ1, EQ2 and EQ3. 193
3.63 Test CWU2: acceleration at the top of the wall measured by the MEMS accelerometer. 193
3.64 Test CWU2: amplification factor with the depth at the back of the left wall for EQ1. Starting from the bottom, at each circled marker correspond respectively Acc1, Acc2, Acc3 and Acc4 194
3.65 Test CWU2: amplification factor with the depth at the back of the left wall for EQ2. Starting from the bottom, at each circled marker correspond respectively Acc1, Acc2, Acc3 and Acc4 195
3.66 Test CWU2: amplification factor with the depth at the back of the left wall for EQ3. Starting from the bottom, at each circled marker correspond respectively Acc1, Acc2, Acc3 and Acc4 195
3.67 Test CWU2: amplification factor with the depth at the excavated side for EQ1. Starting from the bottom, at each circled marker correspond respectively Acc1, Acc5 and Acc6. 196
3.68 Test CWU2: amplification factor with the depth at the excavated side for EQ1. Starting from the bottom, at each circled marker correspond respectively Acc1, Acc5 and Acc6. 196
3.69 Test CWU2: amplification factor with the depth at the excavated side for EQ3. Starting from the bottom, at each circled marker correspond respectively Acc1, Acc5 and Acc6. 197
3.70 Test CWU2 - EQ1: phase difference computed in the time domain. 198

3.71 Test CWU2 EQ2: phase difference computed in the time domain . . . 198
3.72 Test CWU2 EQ3: phase difference computed in the time domain. . . . 199
3.73 Test CWU2: walls horizontal displacement time histories during EQ1, EQ2 and EQ3. . . . 200
3.74 Test CWU2: walls horizontal symmetrical displacement time histories during EQ1 and EQ2. . . . 200
3.75 Test CWU2 EQ1: comparison between the rotation computed from LVDTs (symmetrical case) and the rotation given from the MEMS accelerometer placed on the top of the left wall. . . . 202
3.76 Test CWU2 EQ2: comparison between the rotation computed from LVDTs (symmetrical case) and the rotation given from the MEMS accelerometer placed on the top of the left wall. . . . 203
3.77 Test CWU2 EQ3: comparison between the rotation computed from LVDTs (symmetrical case) and the rotation given from the MEMS accelerometer placed on the top of the left wall. . . . 203
3.78 Test CWU2: displacement space distribution. (a) EQ1 and PS1 measured, (b) EQ1 and PS1 symmetrical, (c) EQ2 and PS2 measured, (d) EQ2 and PS2 symmetrical, (e) EQ3 and PS3 measured, (f) EQ3 and PS3 symmetrical. . . . 205
3.79 Test CWU2: pore pressures time histories during EQ1, EQ2 and EQ3. . . . 207
3.80 Test CWU2: r_u time history during EQ1, EQ2 and EQ3. . . . 208
3.81 Test CWU2: pore pressure space distribution during EQ1, EQ2 and EQ3. (a) EQ1 and PS1, (b) EQ2 and PS2, (c) EQ3 and PS3. . . . 209
3.82 Test CWU2: bending moment time histories during EQ1 and EQ2. . . . 211
3.83 Test CWU2: bending moment space distribution. (a) EQ1 and PS1, (b) EQ2 and PS2, (c) EQ3 and PS3. . . . 212
3.84 Test PWU2: acceleration time history at the back of the left wall during EQ1, EQ2 and EQ3. . . . 214
3.85 Test PWU2: acceleration time histories between the walls during EQ1, EQ2 and EQ3. . . . 215
3.86 Test PWU2: acceleration time history recorded by the MEMS placed on the top of the left wall. . . . 215

3.87 Test PWU2: amplification factor with the depth at the back of the left wall for EQ1. Starting from the bottom, at each circled marker correspond respectively Acc1, Acc2, Acc3, Acc4, Acc5 and Acc6. 216
3.88 Test PWU2: amplification factor with the depth at the back of the left wall for EQ2. Starting from the bottom, at each circled marker correspond respectively Acc1, Acc2, Acc3, Acc4, Acc5 and Acc6. 216
3.89 Test PWU2: amplification factor with the depth at the back of the left wall for EQ3. Starting from the bottom, at each circled marker correspond respectively Acc1, Acc2, Acc3, Acc4, Acc5 and Acc6. 217
3.90 Test PWU2: amplification factor with the depth at the excavated side for EQ1. Starting from the bottom, at each circled marker correspond respectively Acc1, Acc7 and Acc8. 217
3.91 Test PWU2: amplification factor with the depth at the excavated side for EQ2. Starting from the bottom, at each circled marker correspond respectively Acc1, Acc7 and Acc8. 218
3.92 Test PWU2: amplification factor with the depth at the excavated side for EQ3. Starting from the bottom, at each circled marker correspond respectively Acc1, Acc7 and Acc8. 218
3.93 PWU2 - EQ1: phase difference computed in the time domain. 219
3.94 PWU2 - EQ2: phase difference computed in the time domain. 219
3.95 PWU2 EQ3: phase difference computed in the time domain. 220
3.96 Test PWU2: walls horizontal displacement time histories during EQ1, EQ2 and EQ3. 222
3.97 Test PWU2: walls horizontal symmetrical displacement time histories during EQ1 and EQ2. 222
3.98 Test PWU2 EQ1: Rotation of the walls computed from the signals of the LVDTs (symmetrical) 223
3.99 Test PWU2 EQ2: Rotation of the walls computed from the signals of the LVDTs (symmetrical) 223
3.100 Test PWU2 EQ3: Rotation of the walls computed from the signals of the LVDTs (symmetrical). 224
3.101 Test PWU2: displacement space distribution. (a) EQ1 and PS1 non-symmetrical, (b) EQ1 and PS1 symmetrical , (c) EQ2 and PS2 non-symmetrical, (d) EQ2 and PS2 symmetrical, (e) EQ3 and PS3 non-symmetrical, (f) EQ3 and PS3 symmetrical. 225

3.102Test PWU2: pore pressure time histories during EQ1, EQ2 and EQ3. 226
3.103Test PWU2: r_u time history during EQ1, EQ2 and EQ3. . . 227
3.104Test PWU2: pore pressure space distribution during EQ1, EQ2 and EQ3. 228
3.105Test PWU2: bending moment displacement time histories during EQ1, EQ2 and EQ3. 230
3.106Test PWU2: bending moment space distribution: (a) EQ1 and PS1, (b) EQ2 and PS2, (c) EQ3 and PS3. 231
3.107Test PWU2: axial force in the props time histories during EQ1, EQ2 and EQ3. 232
3.108Test CWU3: modality of placement of the Tekscan pressure film, a) lateral view and b) frontal view 233
3.109Test PWU3: modality of placement of the Tekscan pressure film, a) lateral view and b) frontal view. 233
3.1102D Tekscan data from Test PWU3 before EQ3. 234
3.1113D visualization of the Tekscan data for test CWU3 before EQ1. 236
3.1123D visualization of the Tekscan data for test CWU3 before EQ1: pressures acting at the active side. 237
3.1133D visualization of the Tekscan data for test CWU3 before EQ1: pressure acting at the passive side. 237
3.114Test CWU3: vertical distribution of the total horizontal pressure before EQ1 computed as the average of the Tekscan measured pressure along the depth of the wall. 238
3.1153D visualization of the Tekscan data for test CWU3 before EQ2. 239
3.1163D visualization of the Tekscan data for test CWU3 before EQ2: pressures acting at the active side. 239
3.1173D visualization of the Tekscan data for Test CWU3 before EQ2: pressure acting at the passive side. 240
3.118Test CWU3: vertical distribution of the total horizontal pressure before EQ2 computed as the average of the Tekscan measured pressure along the depth of the wall. 241
3.1193D visualization of the Tekscan data for test CWU3 before EQ3. 241
3.1203D visualization of the Tekscan data for test CWU3 before EQ3: pressures acting at the active side. 242
3.1213D visualization of the Tekscan data for test CWU3 before EQ3: pressure acting at the passive side. 242

3.122Test CWU3: vertical distribution of the total horizontal pressure before EQ3 computed as the average of the Tekscan measured pressure along the depth of the wall. 243
3.123Test CWU3: comparison between the vertical distribution of the horizontal pressure in EQ1, EQ2 and EQ3; EQ1-circled marker, EQ2-tricangular marker, EQ3-squared marker. 244
3.1243D visualization of the Tekscan data for test PWU3 before EQ1. 244
3.1253D visualization of the Tekscan data for test PWU3 before EQ1: pressures acting at the active side. 245
3.1263D visualization of the Tekscan data for test PWU3 before EQ1: pressure acting at the passive side. 245
3.127Test PWU3: vertical distribution of the total horizontal pressure before EQ1 computed as the average of the Tekscan measured pressure along the depth of the wall. 246
3.1283D visualization of the Tekscan data for test PWU3 before EQ2. 246
3.1293D visualization of the Tekscan data for Test PWU3 before EQ3: pressures acting at the active side. 247
3.1303D visualization of the Tekscan data for Test PWU3 before EQ3: pressure acting at the passive side. 247
3.131Test PWU3: vertical distribution of the total horizontal pressure before EQ3 computed as the average of the Tekscan measured pressure along the depth of the wall. 248
3.1323D visualization of the Tekscan data for Test PWU3 before EQ3. 248
3.1333D visualization of the Tekscan data for Test PWU3 before EQ3: pressures acting at the active side. 249
3.1343D visualization of the Tekscan data for Test PWU3 before EQ3: pressure acting at the passive side. 249
3.135Test PWU3: vertical distribution of the total horizontal pressure before EQ3 computed as the average of the Tekscan measured pressure along the depth of the wall. 250
3.136Test PWU3: comparison between the vertical distribution of the total horizontal pressure in EQ1, EQ2 and EQ3; EQ1 circles marker, EQ2 triangular marker, EQ3 squared marker. 251
3.137Test PWU3: comparison between the vertical distribution of the total horizontal pressure in EQ1, EQ2 and EQ3; EQ1 circles marker, EQ2 triangular marker, EQ3 squared marker. 252
3.138Test PWU3: model before the test. 253

3.139Test CWU3: walls measured displacements (a,d,g), symmetrical displacements (b,e,h) and corrected displacements (c,f,i). 254
3.140Test PWU3: walls measured displacements (a,d,g), symmetrical displacements (b,e,h) and corrected displacements (c,f,i). 255

4.1 Displacement space distribution, comparison between CWU2 and CWU3. Time instants: a) static, b) Pre-EQ3, c) Pre-EQ3, d) Maximum EQ1 (left wall), e) Maximum EQ2 (left wall) , f) Maximum EQ3 (left wall), g) Short term residual EQ1, h) Short term residual EQ2, i) Short term residual EQ3, l) Long term residual EQ1, m) Long term residual EQ2, n) Long term residual EQ3. 263
4.2 Pore pressure space distribution, comparison between CWU2 and CWU3. Time instants: a) static, b) Pre-EQ3, c) Pre-EQ3, d) Maximum EQ1 (left wall), e) Maximum EQ2 (left wall) , f) Maximum EQ3 (left wall), g) Short term residual EQ1, h) Short term residual EQ2, i) Short term residual EQ3, l) Long term residual EQ1, m) Long term residual EQ2, n) Long term residual EQ3. 264
4.3 Bending moment space distribution, comparison between CWU2 and CWU3. Time instants: a) static, b) Pre-EQ3, c) Pre-EQ3, d) Maximum EQ1 (left wall), e) Maximum EQ2 (left wall) , f) Maximum EQ3 (left wall), g) Short term residual EQ1, h) Short term residual EQ2, i) Short term residual EQ3, l) Long term residual EQ1, m) Long term residual EQ2, n) Long term residual EQ3. 265
4.4 Displacement space distribution, comparison between PWU2 and PWU3. Time instants: a) static, b) Pre-EQ3, c) Pre-EQ3, d) Maximum EQ1 (left wall), e) Maximum EQ2 (left wall) , f) Maximum EQ3 (left wall), g) Short term residual EQ1, h) Short term residual EQ2, i) Short term residual EQ3, l) Long term residual EQ1, m) Long term residual EQ2, n) Long term residual EQ3. 267
4.5 Pore pressure space distribution, comparison between PWU2 and PWU3. Time instants: a) static, b) Pre-EQ3, c) Pre-EQ3, d) Maximum EQ1 (left wall), e) Maximum EQ2 (left wall) , f) Maximum EQ3 (left wall), g) Short term residual EQ1, h) Short term residual EQ2, i) Short term residual EQ3, l) Long term residual EQ1, m) Long term residual EQ2, n) Long term residual EQ3. 268

4.6 Bending moment space distribution, comparison between PWU2 and PWU3. Time instants: a) static, b) Pre-EQ3, c) Pre-EQ3, d) Maximum EQ1 (left wall), e) Maximum EQ2 (left wall) , f) Maximum EQ3 (left wall), g) Short term residual EQ1, h) Short term residual EQ2, i) Short term residual EQ3, l) Long term residual EQ1, m) Long term residual EQ2, n) Long term residual EQ3. 269
4.7 Comparison between the maximum input acceleration and the maximum top acceleration during the applied earthquakes of all the tests: a) test CWU1, b) PWU1 test, c) CWU2 test, d) PWU2 test, e) CWU3 test, f)PWU3 test, CWU4 test (EQ1, EQ2 and EQ3), h) CWU4 test (EQ4, EQ5, EQ6 and EQ7). 272
4.8 Comparison between the maximum input acceleration ad the maximum top acceleration a) for all the saturated tests and b) for the tests in saturated sand and those in dry sand (Conti, 2010). 273
4.9 Comparison between the Arias intensity of the input acceleration and the Arias intensity of the maximum top acceleration during the applied earthquakes of all the tests: a) test CWU1, b) PWU1 test, c) CWU2 test, d) PWU2 test, e) CWU3 test, f)PWU3 test, CWU4 test (EQ1, EQ2 and EQ3), h) CWU4 test (EQ4, EQ5, EQ6 and EQ7). 274
4.10 Comparison between the Arias intensity of the input acceleration and the Arias intensity for a) all the saturated tests and b) for the tests in saturated sand and those in dry sand (Conti, 2010); in c) an enlarged view of the figure in b) is proposed. 275
4.11 Example of the computation of the phase difference of two accelerometers during the shaking. PWU2 test, a) superposition of the accelerometers Acc1 (reference acceleration) and Acc4, b) zoom between 7.2s and 8.4s: individuation of the peaks of the reference acceleration and of the peak of the second acceleration time history. 277
4.12 Peaks relative to Acc1 and Acc3 of test PWU2. 279
4.13 Example of non selectable peaks in the above presented acceleration time histories. 279
4.14 Example of normalized Cross Power Spectrum. 281

4.15 PWU1 test EQ2: example of double peak response of the second acceleration time history (Acc3), with the blue marker the selected peaks of the reference acceleration and of the second acceleration time history are highlighted with the blue marker. 282
4.16 PWU1 test EQ2: resulting plot of the phase difference of Acc3 during the earthquake. 283
4.17 PWU1 test EQ1: double peak response of Acc5, highlight on the first part of the earthquake. 283
4.18 PWU1 test EQ1: double peak response of Acc5, highlight on the second part of the earthquake. 284
4.19 PWU1 test - EQ1: phase difference of Acc5 computed in time domain, jump on the computed phase difference due to the double peak response of Acc5. 284
4.20 Test CWU2 EQ1: phase difference of Acc5 during EQ3, jump of the time trend. 287
4.21 Test CWU2 EQ3: phase difference of Acc5 during EQ3, jump of the time trend. 287
4.22 Test CWU3 EQ1: phase difference in the time domain. . . . 288
4.23 Test CWU3 EQ2: phase difference in the time domain. . . . 288
4.24 Test CWU3 EQ3: phase difference in the time domain. . . . 289
4.25 Test PWU2 EQ1: phase difference computed in time domain. 290
4.26 Test PWU2 EQ2: phase difference computed in time domain. 290
4.27 Test PWU2 EQ3: phase difference computed in time domain. 291
4.28 Test CWU1 EQ1 active side: phase difference computed in the frequency domain. 293
4.29 Test CWU1 EQ1 passive side: phase difference computed in the frequency domain. 293
4.30 Test CWU1 - EQ1: phase difference computed in time domain.294
4.31 Test CWU3 - EQ1 active side: phase difference computed in frequency domain. 294
4.32 Test CWU3 - EQ1 passive side: phase difference computed in frequency domain. 295
4.33 Test CWU3 - EQ1: phase difference computed in time domain.295
4.34 Layout of test CW1 relative to the tests performed in dry sand (Conti, 2010). 296
4.35 Acceleration time histories of accelerometers A4, A5 and A6 of test CW1 (Conti, 2010). 297
4.36 Layout of test PW1 relative to the tests in dry sand (Conti, 2010). 297

4.37 Acceleration time histories relative to the accelerometers A4, A5 and A6 of test PW1. 298
4.38 Layout of test dry CW1 (Conti. 2010). 299
4.39 Test CW1: horizontal displacements of the left wall from the end of the swing up to EQ5 (Conti, 2010). 300
4.40 Layout of dry test PW2 (Conti, 2010). 300
4.41 Test PW2: horizontal displacements of the right wall from the end of the swing up to EQ5 (Conti, 2010). 301
4.42 CWU1 test: the rise of the capillary suction up to the soil surface can be observed from the top view of the model before the beginning of the test. 303
4.43 Leighton Buzzard sand water retention curve for loose sample and interpolation with the Van Genuchten model. 304
4.44 Leighton Buzzard sand water retention curve for dense sample and interpolation with the Van Genuchten model. 304
4.45 Earth pressure distribution used in the first method with linear distribution of active and passive side to predict the bending moment distribution for the cantilevered tests. 306
4.46 Earth pressure distribution used in the second method to compute the bending moment distribution along the wall. At the active side a linear distribution of the contact stress in considered. At the passive side a bilinear distribution of the passive resistance is supposed. 308
4.47 Test CWU1: comparison between the measured bending moment before EQ1 (static) and EQ2 and its prevision through limit equilibrium analysis (LE) with different horizontal earth pressure distributions. 311
4.48 Test CWU2: comparison between the measured bending moment before EQ1 (static), EQ2 and EQ3 and prevision through limit equilibrium analysis with different horizontal earth pressure distributions. 311
4.49 Test CWU3: comparison between the measured bending moment before EQ1 (static), EQ2 and EQ3 and its prevision through limit equilibrium analysis with different horizontal earth pressure distributions. 312
4.50 Test PWU1: comparison between the measured bending moment before EQ1 (static) and EQ2 and its prevision through limit equilibrium analysis (LE) with different horizontal earth pressure distributions. 312

4.51 Test PWU2: comparison between the measure bending moment before EQ1 (static), EQ2 and EQ3 and the prevision through limit equilibrium analysis with different horizontal earth pressure distributions. 313
4.52 Test PWU3: comparison between the measured bending moment before EQ1 (static), EQ2 and EQ3 and its prevision through limit equilibrium analysis with different horizontal earth pressure distributions. 313
4.53 Test CWU1: comparison between the maximum measured bending moment during EQ1 and EQ2 and its prevision through limit equilibrium analysis with two different contact stress distribution. 315
4.54 Test PWU1: comparison between the maximum measured bending moment during EQ1 and EQ2 and its prevision through limit equilibrium analysis with two different horizontal earth pressure distributions. 316
4.55 Test CWU2: comparison between the maximum measured bending moment during EQ1, EQ2 and EQ3 and prevision through limit equilibrium analysis with two different horizontal earth pressure distributions. 316
4.56 Test CWU3: comparison between the maximum measured bending moment during EQ1, EQ2 and EQ3 and its prevision through limit equilibrium analysis with two different horizontal earth pressure distributions. 317
4.57 Test PWU2: comparison between the measure bending moment before EQ1 (static), EQ2 and EQ3 and the prevision through limit equilibrium analysis with different horizontal earth pressure distributions. 317
4.58 Test PWU3: comparison between the maximum measured bending moment during EQ1, EQ2 and EQ3 and its prevision through limit equilibrium analysis with two different horizontal earth pressure distributions. 318

5.1 Yield surface and bounding surfaces of the model of Manzari and Dafalias model (from Manzari and Dafalias, 2004). 325

5.2 Initial state of Manzari and Dafalias model. Calibration of the model for a Drained Triaxial Test at 100kPa of pressure of consolidation. Example used to show how the model performs in the case of a simple calculation. In position N-W there is the $p' - q$ plane, in position N-E there is the ϵ_a,$_v$ plane, in position S-W there is the $\epsilon_a q$ plane, in position S-E there is the $p' - e$ plane. 328
5.3 Example from the calibration of the Manzari and Dafalias model - state of the model before the peak of the $\epsilon_a - q$ plane. 329
5.4 Example from the calibration of the Manzari and Dafalias model - state of the model at the peak of the $\epsilon_a - q$ plane. . . 330
5.5 Example from the calibration of the Manzari and Dafalias model - state of the model at $\epsilon_a = 0.1$. 331
5.6 Example from the calibration of the Manzari and Dafalias model, state of the model at $\epsilon_a = 0.2$. 332
5.7 Dafalias and Manzari model in predicting the undrained response of the sand under cyclic loading without taking into account the fabric change in the macroscopic behavior (from Dafalias and Manzari, 2004). 333
5.8 Multiaxial generalization of the Yielp surface, the Bounding surface, the Critical surface and the Dilatancy surface: projection on the π plane (from Dafalias and Manzari (2004). . . 336
5.9 Multiaxial generalization of the Yield surface, the Bounding surface, the Critical surface and the Dilatancy surface: projection on the π plane (from Dafalias and Manzari (2004). . . 340
5.10 DTC100: axial deformation vs deviator comparison between numerical simulation and experiment. 341
5.11 DTC100: axial strain vs volumetric strain comparison between numerical simulations and experiment. 342
5.12 DTC200: axial strain vs deviator comparison between numerical simulation and experiments. 342
5.13 DTC200: axial strain vs volumetric strain comparison between numerical simulation and experiment. 343
5.14 DTE100: axial strain vs deviator comparison between numerical simulation and experiment. 343
5.15 DTE100: axial strain vs volumetric strain comparison between numerical simulation and experiment. 344
5.16 DTE200: axial strain vs volumetric strain comparison between numerical simulation and experiment. 344

5.17 DTE200: axial strain vs volumetric strain comparison between numerical simulation and experiment. 345
5.18 Axial strain vs deviator: comparison between numerical simulation and experiment. 345
5.19 UTC200: axial deformation vs excess pore pressure comparison between numerical simulation and experiment. 346
5.20 UTC400: axial strain vs deviator comparison between numerical simulation and experiment. 346
5.21 UTC400: axial strain vs excess pore pressure comparison between numerical simulation and experiment. 347
5.22 UTE200: axial deformation vs deviator comparison between numerical simulation and experiment. 347
5.23 UTE200: axial deformation vs excess pore pressure comparison between numerical simulation and experiment. 348
5.24 UTE400: axial strain vs deviator comparison between numerical simulation and experiment. 348
5.25 UTE400: axial strain vs excess pore pressure comparison between numerical simulation and experiment. 349

A.1 Piezoelectric accelerometers calibration for test CWU1. . . . 355
A.2 LVDTs calibration for test CWU1. 356
A.3 Pore pressure transducers calibration for test CWU1. 357
A.4 Left wall strain gauges calibration for test CWU1. 358
A.5 Right wall strain gauges calibration for test CWU1. 359
A.6 Piezoelectric accelerometers calibration for test PWU1. . . . 360
A.7 LVDT calibration for test PWU1. 361
A.8 Potentiometer calibration for test PWU1. 361
A.9 Pore pressure transducers calibration for test PWU1. 362
A.10 Left wall strain gauges calibration for test PWU1. 363
A.11 Right wall strain gauges calibration for test PWU1. 364
A.12 Load cells calibration for test PWU1. 365
A.13 Piezoelectric accelerometers calibration for test CWU2. . . . 366
A.14 MEMS accelerometers calibration for test CWU2. 367
A.15 LVDT calibration for test CWU2. 367
A.16 Potentiometer calibration for test CWU2. 368
A.17 Pore pressure transducers calibration for test CWU2. 369
A.18 Left wall strain gauges calibration for test CWU2. 370
A.19 Right wall strain gauges calibration for test CWU2. 371
A.20 Piezoelectric accelerometers calibration for test PWU2. . . . 372
A.21 MEMS accelerometer calibration for test PWU2. 373

A.22 LVDT calibration for test PWU2. 374
A.23 Pore pressure transducers calibration for test PWU2. 375
A.24 Left wall strain gauges calibration for test PWU2. 376
A.25 Right wall strain gauges calibration for test PWU2. 377
A.26 Load cells calibration for test PWU2. 378
A.27 Piezoelectric accelerometers calibration for test CWU3. . . . 379
A.28 MEMS accelerometer calibration for test CWU3. 380
A.29 LVDT calibration for test CWU3. 381
A.30 Potentiometer calibration for test CWU3. 382
A.31 Pore pressure transducers calibration for test CWU3. 383
A.32 Left wall strain gauges calibration for test CWU3. 384
A.33 Right wall strain gauges calibration for test CWU3. 385
A.34 Piezoelectric accelerometers calibration for test PWU3. . . . 386
A.35 MEMS accelerometers calibration for test PWU3. 387
A.36 LVDTs calibration for test PWU3. 388
A.37 Potentiometer calibration for the test PWU3. 389
A.38 Pore pressure transducers calibration for test PWU3. 390
A.39 Left wall strain gauges calibration for the test PWU3. 391
A.40 Right wall strain gauges calibration for test PWU3. 392
A.41 Load cells calibration for test PWU3. 393
A.42 Piezoelectric accelerometers transducers calibration for test CWU4. 394
A.43 MEMS accelerometers transducers calibration for test CWU4. 395
A.44 Pore pressure transducers calibration for test CWU4. 396
A.45 Left wall strain gauges calibration for the test CWU4. 397
A.46 Right wall strain gauges calibration for the test CWU4. . . . 398

B.1 Right wall strain gauges calibration for the test CWU4. . . . 400
B.2 CWU1: layout and coordinate reference system for the position of the instruments. 401
B.3 PWU1: layout and coordinate reference system for the position of the instruments. 403
B.4 CWU2: layout and coordinate reference system for the position of the instruments. 405
B.5 PWU2: layout and coordinate reference system for the position of the instruments. 407
B.6 CWU3: layout and coordinate reference system for the position of the instruments. 409
B.7 PWU3: layout and coordinate reference system for the position of the instruments. 411

B.8 CWU4: layout and coordinate reference system for the position of the instruments. 413

C.1 Example of soil water retention curve (Vanapalli et al., 1996). 417
C.2 Tempe Cell schematic. 419
C.3 System to apply the suction decreasing the water pressure. At the left bottom there is the water tank used to impose the suction. At the right top the Tempe Cells can be seen. 419
C.4 Leighton Buzzard Sand;: water retention curve for dense sand and interpolation with the van Genuchten model. 423
C.5 Leighton Buzzard Sand: water retention curve for loose sand and interpolation with the van Genuchten model. 423

Contents

1 Introduction **28**
- 1.1 Scope of the research . . . 28
- 1.2 Structure of the Thesis . . . 28
- 1.3 Problem Generalities . . . 29
- 1.4 Dynamic earth pressure with pseudo-static method . . . 31
- 1.5 Permanent displacements computed with Newmark method . 36
- 1.6 Physical modeling and numerical analyses . . . 41
- 1.7 Presence of water . . . 42
  - 1.7.1 Hydrodynamic pressure . . . 43
  - 1.7.2 Dynamic earth pressure in saturated backfill . . . 44
- 1.8 Summary . . . 45

2 Centrifuge Modelling **46**
- 2.1 Principles of Physical Modelling and Centrifuge Modelling . . 47
- 2.2 Dimensional Analysis . . . 48
  - 2.2.1 Dimensional Analysis Applied to Physical Modeling . 49
- 2.3 Experimental Equipment . . . 57
  - 2.3.1 Materials . . . 61
  - 2.3.2 Instrumentation and Calibration . . . 66
- 2.4 Model Preparation . . . 92
  - 2.4.1 Sand Pouring, Instruments placement, Walls placement. 93
  - 2.4.2 Saturation . . . 98
- 2.5 Centrifuge Preparation . . . 105
  - 2.5.1 Balance Calculation . . . 105
  - 2.5.2 Pre-flight operations . . . 105
- 2.6 Test Procedures . . . 105
- 2.7 Summary . . . 106

3 Test Data - Part I **107**
3.1 Geometry of the Models . . . 112
3.1.1 CWU1 . . . 113
3.1.2 PWU1 . . . 115
3.1.3 CWU2 . . . 117
3.1.4 PWU2 . . . 119
3.1.5 CWU3 . . . 121
3.1.6 PWU3 . . . 123
3.1.7 CWU4 . . . 124
3.2 Data . . . 127
3.3 Test CWU1 Data . . . 149
3.4 Test PWU1 Data . . . 170
3.5 Test CWU2 Data . . . 190
3.6 Test PWU2 Data . . . 212
3.7 Tests CWU3 and PWU3 Data . . . 232
3.8 Tests CWU3 and PWU3 Tekscan Data . . . 235
3.9 CWU3 and PWU3 Laminar Box Displacements . . . 251
3.10 Summary . . . 255

4 Test Data - Part II **261**
4.1 Comparison between similar Tests . . . 262
4.1.1 Comparison between CWU2 and CWU3 . . . 262
4.1.2 Comparison between PWU2 and PWU3 . . . 266
4.2 Amplification . . . 270
4.3 Soil Acceleration Phase Difference . . . 275
4.3.1 Computation of Phase Difference in Time Domain . . . 276
4.3.2 Computation of the phase difference in the frequency domain . . . 280
4.3.3 Comments on the computation of the phase difference in the time domain . . . 281
4.3.4 Comparison between the computation of the phase difference in the time domain and in the frequency domain 291
4.3.5 Comparison of phase difference with test in dry sand (Conti, 2010). . . . 296
4.4 Displacements: Comparison with Tests in Dry Sand . . . 298
4.5 Bending Moments: Comparison with Limit Equilibrium Analysis . . . 302
4.6 Bending Moment - Comparison with Tests in Dry Sand . . . 318
4.7 Summary . . . 319

5 Calibration of Constitutive Model **322**
5.1 Numerical Model for the mechanical Behaviour of the Sand: Dafalias and Manzari Model. 322
5.2 Tochnog Finite Element Code. 337
5.3 Calibration of Dafalias and Manzari model. 338
5.3.1 Calibration of Dafalias and Manzari model. Test DTC100 341
5.3.2 Calibration of Dafalias and Manzari model. Test DTC200.342
5.3.3 Calibration of Dafalias and Manzari model. Test DTE100.343
5.3.4 Calibration of Dafalias and Manzari model. Test DTE200.344
5.3.5 Calibration of Dafalias and Manzari model. Test UTC 200. 345
5.3.6 Calibration of Dafalias and Manzari model.Test UTC400.346
5.3.7 Calibration of Dafalias and Manzari model. Test UTE200.347
5.3.8 Calibration of Dafalias and Manzari model. Test UTE400. 348
5.4 Summary 349

6 Conclusions **350**

Appendix A Calibration Factors **354**

Appendix B Position of Instruments **399**

Appendix C Soil Water Retention Curve **415**

References **425**

Chapter 1

Introduction

1.1 Scope of the research

This work represents a contribution for understanding the dynamic behavior of flexible retaining walls embedded in saturated sand.

An experimental campaign consisting of seven dynamic centrifuge tests has been carried out at the Schofield Centre of the University of Cambridge (UK) with the aim to study the dynamic response of these structures.

The tests have been performed on reduced scale models of pairs of retaining walls, both cantilevered and with one level of support near the top.

The main objective of this work is to shed some light on the main mechanisms affecting the dynamic behaviour of embedded retaining walls in the presence of water. The behaviour of the soil-structure system has been studied in terms of acceleration in the soil, displacement of the walls, pore pressures in the soil, structural bending moment and, in case of tests with one level of prop, axial force in the prop.

The first four tests have been performed under the SERIES project 2007-2014 and the other three tests have been performed under the ReLuis project 2009-2013.

1.2 Structure of the Thesis

In the first chapter the problem to be studied is presented and the relative major findings already present in literature are reported. Specifically, the simplified solutions for the computation of the earth pressure in seismic condition are described; then the dynamic simplified analysis for the computation of the permanent displacement is illustrated besides the main results

regarding the experimental studies on physical models and the numerical analyses. Finally the factors related to the presence of the water influencing the seismic behaviour of the flexible retaining walls are highlighted.

In the second chapter the principles of centrifuge modelling are illustrated and the experimental equipment and the model preparation of a centrifuge test at the Schofield Centre of the University of Cambridge are described.

The third chapter is dedicated to the description of the phenomena characterizing the behaviour of the models through a detailed analysis of the test data at the scale of the single test. For each test monitored physical quantities are plotted both with respect to time and space.

The fourth chapter is dedicated to the comparison of the results across the tests in order to individuate similarities and differences among them; also, the results of the tests are compared with similar tests realized in dry sand with the same centrifuge and similar flexible walls (Conti, 2010). Thus the repeatability of the centrifuge tests is investigated, the amplification phenomena, the accumulated displacements and the bending moment are compared among all the tests and with respect to those in dry sand; moreover, as regards the bending moment, the possibility to predict the bending moment using the limit equilibrium analysis is investigated considering different aspects influencing the static and maximum bending moment distribution.

The fifth chapter is dedicated to the calibration of a constitutive model for the behaviour of the sand to be used for the numerical simulation of the tests.

1.3 Problem Generalities

Earth retaining structures are used in civil engineering to support soil, similar materials or water at an inclination higher than the inclination they would assume without the presence of the structure (EN 1997-1:2004). The retaining structures are, for example, useful in urban areas for building underground stations, at the water front in port areas, for the stabilization of slopes and for roads protection. In case of gravity walls, the self weight of the structure guarantees the stability with respect the earth pressures, while for flexible retaining walls the stability of the soil-structure system comes from the resistance of the structure and the mobilization of the passive shear resistance downstream the wall. Flexible retaining walls are usually realized with different kinds of materials, like reinforced concrete, and with one or

more levels of constraint.

The study and the monitoring of real structures (Bureau of Ports and Harbors 1989; Iai and Kameoko 1993; Kamon et al. 1996) and of physical models in centrifuge simulations (Zeng and Steedman 1993; Zeng 1998; Dewoolkar et al. 2001) have shown the vulnerability of these structures during a seismic event. The collapses have been observed to be related to both the failure of the structure and the shear strength mobilization within the soil or the occurrence of liquefaction in the case of the presence of saturated soil.

A complete prediction of the behaviour of these structures is practically impossible to achieve due to the complex interaction mechanisms between the soil and the structure and to the difficulty to predict the seismic action. The soil structure interaction in fact is a complex phenomenon whose prediction requires the knowledge of the complete stress-strain behaviour of the material of the structure and of the soil.

The difficulty regarding the prediction of the response to the seismic loading requires to refer to simplified approaches for the design. To this aim the limit equilibrium analysis, applying horizontal pseudo-static forces whose intensity is computed on the basis of the technical codes, directed to the determination a safety factor has been widely used in common practice but it has been proved to be unsatisfactory. Since the soil is described as rigid-plastic and the seismic action is considered as pseudo-static, the limit equilibrium approach does not actually describe the progressive accumulation of permanent displacements during the earthquake due to both the mechanical behaviour of the soil, which can accumulate displacement before achieving the failure condition, and the temporarily mobilization of soil strength within the soil. In the limit equilibrium analysis the distance from the activation of a collapse mechanism is quantified through the computation of the safety factor and no additional information about the performance of the structure during the seismic event are given.

A Performance Based Design approach instead represents an improvement of the design approach, being based on the idea to select a plastic mechanism activated within a selected element of the system during the earthquake and to study the behaviour of the soil-structure system once the plastic mechanism is activated. The objective within a Performance Based Design is then to compute the accumulated displacements due to the activation of the plastic mechanism and also the earth pressure acting on the structure.

The prediction of the permanent displacement can be based both on simplified approaches and on numerical analyses. In fact different attempts to extend the Newmark method to the retaining structures, specifically for

gravity retaining walls (Richards & Elms, 1979; Whitman, 1990; Zeng & Steedman, 2000) and for flexible retaining walls, have been carried out, generally based on the computation of the action exchanged between the structure and the soil through a limit equilibrium analyses and the integration of the expected acceleration time history with respect a critical acceleration defined as the acceleration requested to activate the plastic mechanism. While for the gravity retaining walls, for which the plastic mechanism is represented by a translation of the wall over the base, the extension of the Newmark approach is straightforward, in the case of the flexible retaining walls, being the plastic mechanism related with the increase of the active force and the decrease of the passive resistance as the inertial acceleration increases, is less immediate and presents some issues from the kinematical viewpoint and consequently for the integration technique. On the other hand the numerical analyses strongly depend on the reliability of the constitutive model adopted for the description of the mechanical response of the soil.

The actions on the structure can be evaluated using mathematical formulations based on the Limit Equilibrium Analysis or Limit Analysis. Such approaches can be verified through experiments, such as physical models and real scale structures, and also with numerical analyses that allow to implement more complex constitutive law that more correctly describe the mechanical soil behaviour.

Another important factor that strongly influences the seismic response of the retaining structures is the presence of the water. It affects the response mainly for three reasons; firstly the unit weight of the soil decreases due to the buoyancy force, secondly hydrodynamic pressures can alter the action on the structure and finally pore pressures increase due to the tendency of the soil to experience volume changes. This last aspect can determine the occurrence of liquefaction which, besides the structural failure and the mobilization of shear strength is another relevant cause of collapse of retaining structures.

1.4 Dynamic earth pressure with pseudo-static method

As regards the computation of the pressure acting on the structures, with the works of Okabe (1926) and Mononobe and Matsuo (1929) the Coulomb theory for active and passive earth thrust calculation has been extended to the seismic case introducing pseudo static forces to take into account the

earthquake effect. The wall is supposed to translate along the horizontal direction or to rotate completely activating the shearing resistance along a slip surface that causes the formation of a sliding wedge.

The inclination of the slip surface with respect to horizontal α is considered as an unknown. With the following hypotheses:

1. The soil is dry, homogeneous, isotropic, with no coesion and with a rigid-plastic behaviour and a Mohr-Coulomb failure criterion;
2. The wall is long enough to reach the plane strain condition;
3. The contact surface between the wall and the soil is planar and eventually inclined with respect to vertical, it presents contact friction;
4. The soil surface is planar, eventually inclined with respect to horizontal;
5. The seismic acceleration is supposed to be constant in all the point belonging to the soil wedge, its horizontal and vertical components respectively are $a_h = k_h \cdot g$ and $a_v = k_v \cdot g$, where k_h is the horizontal seismic coefficient, k_v is the vertical seismic coefficient and g is the gravity acceleration.

it is possible to write the translational equilibrium equations of the soil wedge subjected to the action of its weight W and the forces $k_h \cdot W$ and $k_v \cdot W$. The active seismic force S_{ae} acting on the wall is obtained searching for its maximum value with respect to inclination α of the slip surface with respect to horizontal.

The expression of the seismic active S_{ae} force is:

$$S_{ae} = \frac{1}{2} \cdot K_{ae} \cdot \gamma \cdot H^2 \cdot (1 - k_v) \tag{1.1}$$

where γ is the unit weight of the soil, H is the height of the soil, K_{ae} is the seismic active coefficient. The expression of K_{ae} is:

$$K_{ae} = \frac{\cos^2(\varphi' - \theta - \beta)}{\cos\theta \cdot \cos^2\beta \cdot \cos(\delta + \beta + \theta) \cdot \left[1 + \frac{\sqrt{\sin(\varphi' + \delta) \cdot sin(\varphi' - \theta - i)}}{\cos(\delta + \beta + \theta) \cdot (i - \beta)}\right]^2} \tag{1.2}$$

where:

1. $\theta = \arctan\left(\frac{k_h}{1 - k_v}\right)$;

2. φ' is the angle of shearing resistance;

3. δ is the friction between the wall and the soil;

4. β is the inclination with respect to vertical of the wall;

5. i is the angle of the soil surface with respect to horizontal.

Similarly, the passive resistance can be determined searching for its minimum value with respect to inclination of the slip surface with respect to horizontal. The expression of the seismic passive force S_{pe} is:

$$S_{pe} = \frac{1}{2} \cdot K_{pe} \cdot \gamma \cdot H^2 \cdot (1 - k_v) \tag{1.3}$$

and the expression of the seismic passive coefficient K_{pe} is:

$$K_{pe} = \frac{\cos^2(\varphi' - \theta + \beta)}{\cos\theta \cdot \cos^2\beta \cdot \cos(\delta - \beta + \theta) \cdot \left[1 - \frac{\sqrt{\sin(\varphi'+\delta) \cdot sin(\varphi'-\theta+i)}}{\cos(\delta-\beta+\theta)\cdot(i-\beta)}\right]^2} \tag{1.4}$$

This method does not give any indication on the position of the earth pressure since the determination of the seismic active and passive forces comes from the translational equilibrium while the rotational equilibrium is not considered.

The seismic earth pressure can be seen as the sum between its static component S_a and its dynamic component ΔS_{ae}. Whitman (1970) proved that the position of ΔS_{ae} depends on the value of the displacement that the structure experiences and on the characteristics of the failure mechanism; generally, for the design of the structure, Whitman recommends to assume the position of ΔS_{ae} at $0.6H$ from the bottom of the wall. With the works of Ishibashi and Fang (1987) and of Richards et al. (1999) it has been shown that the position of S_{ae} is at $H/3$ from the bottom of the wall if the wall rotates around the bottom, while it is at $0.45H$ when the wall translates and it is at $0.5H$ when the wall rotates around the top.

As regards the point of application of the passive resistance Richards and Elms (1992) have shown that S_{pe} can be considered applied at about the 20% of the embedded length of the wall, while Chang and Chen (1990) show that S_{pe} can be considered applied between 28% and 40% of the height of the wall, depending on the failure mechanism.

Anyway, it is well known that the presence of the wall friction implies a curvature of the failure surface, and the solutions derived from the works

of Okabe and Matsuo do not correctly consider it; this results in a strong dependency of the coefficient of passive resistance on the friction between soil and wall. Thus, particularly regarding the passive resistance, several solutions obtained on the basis of the upper bound theorem of plasticity with a curved failure surface have been proposed in literature (Caquot & Kerisel, 1948; Chang, 1981; Morrison & Ebeling 1995; Soubra, 2000; Kerisel & Absi, 1990). Those solutions are not conservative since they are based on the upper bound theorem of limit analysis.

Lancellotta (2007) proposed an analytical solution for the seismic passive earth resistance based on the lower bound theorem of plasticity. More precisely Lancellotta initially considers a problem where a soil surface inclined of an angle i is subjected to its self weight γ' and to the horizontal body force $k_h \cdot \gamma'$ (Figure 1.1) and then a rotation of the problem geometry of an angle $\Psi = \arctan(k_h)$ is performed (Figure 1.2) so that the problem is transformed into a determination of the passive resistance acting on a rough wall that is inclined of an angle Ψ and the soil surface is inclined of an angle $\beta = i - \Psi$.

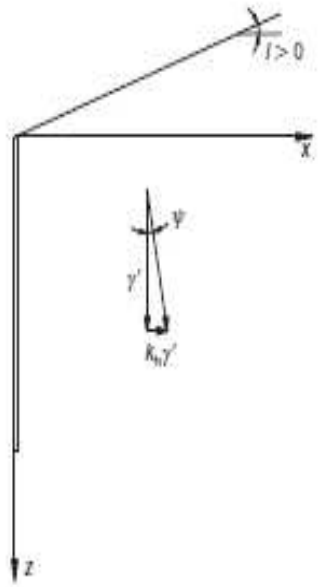

Figure 1.1: Initial problem geometry (from Lancellotta 2007).

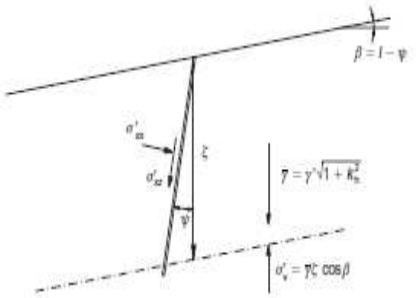

Figure 1.2: Transformed problem geometry (from Lancellotta 2007).

As shown in Figure 1.3 two passive zones are identified, the first one is close to the wall and it is affected by the presence of the friction between the soil and the wall, and the second one is far from the wall and it is indicated as conventional passive zone where the stress state is known. Between the two passive zones there is a transition zone where the principal stresses rotate of a finite angle Θ.

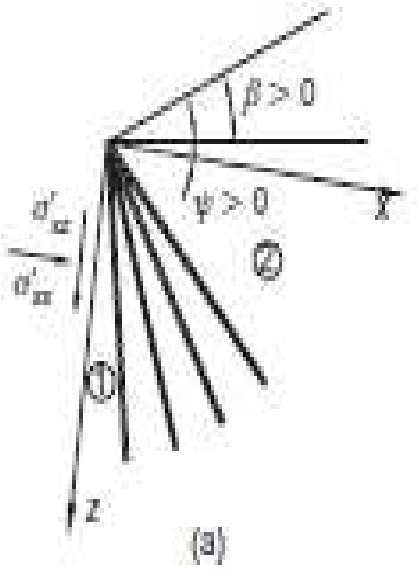

Figure 1.3: Stress discontinuities (from Lancellotta 2007).

On the basis of the local equilibrium the value of the passive seismic coefficient is determined and its expression is reported hereinafter:

$$K_{pe} = \left[\frac{\cos\delta}{\cos(i-\Psi) - \sqrt{\sin^2(1-\Psi)}} \cdot \left(\cos\delta + \sqrt{\sin^2\phi' - \sin^2\delta} \right) \cdot e^{2\theta \tan\phi'} \right] \tag{1.5}$$

with

$$2\Theta = \arcsin\left(\frac{\sin\delta}{\sin\phi'}\right) + \arcsin\left[\frac{sin(i-\Psi)}{sin\phi'}\right] + \delta + (i-\Psi) + 2\Psi \tag{1.6}$$

1.5 Permanent displacements computed with Newmark method

It has been said that a part of the performance based design of flexible retaining walls consists in the prevision of the permanent displacement accumulated after the activation of the plastic mechanism. The Newmark sliding block method, originally elaborated for dams (Newmark, 1965), is a dynamic simplified method for the computation of accumulated displacements during earthquake, and it has been used also for slopes and for gravity and flexible retaining walls. It allows to have a more accurate description of the seismic behavior respect the simple pseudo-static approach.

Schematically, the Newmark method describes the permanent displacement accumulation process of a rigid block of mass m base restin on a base subjected to an acceleration $a_b(t)$ through a rigid-plastic interface with a Mohr-Coulomb failure criterion. A critical acceleration ac can be defined: it is the acceleration for which the failure along the contact surface is reached. When the critical acceleration is achieved the block continues to move with an acceleration that is equal to a_c and the relative permanent displacement can be computed integrating over the time the difference between the acceleration of the base a_c and the acceleration of the block a_c (Figure 1.4).

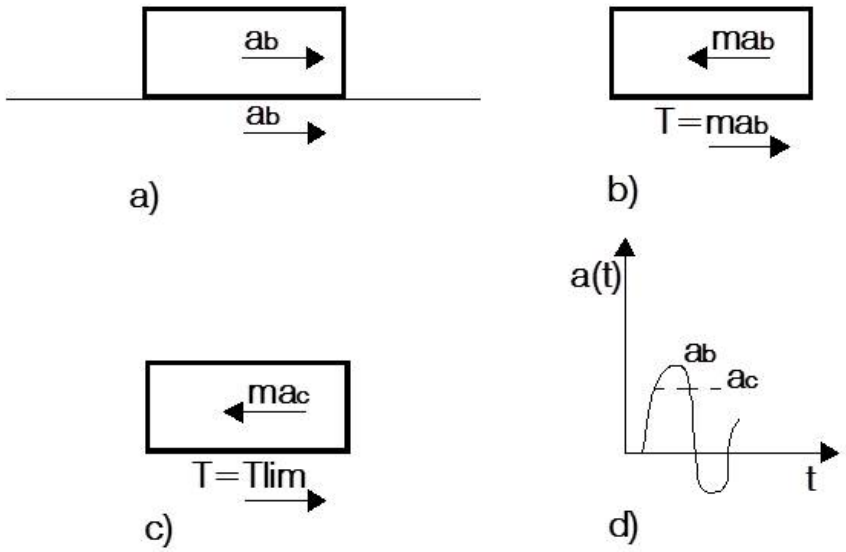

Figure 1.4: Schematic of Newmark method. (a)base acceleration and block acceleration before the sliding; (b)block inertial force and shear force at the contact surface; (c)block inertial force and shear force at the contact surface during the sliding; (d)base acceleration and block acceleration comparison with time during sliding.

In this simple scheme, the failure along the contact surface is reached because the inertial force of the upper block ma_b reaches the shear resistance T_{lim}. The permanent displacement derives from the computation of the integral $\int\int(a_b - a_c)dt$ up to the time instant when the relative velocity is zero.

As already said, the Newmark method has been applied in literature for the gravity walls. In this case, a contact surface similar to the one defined in the original method still can be identified, and it is the surface that separates the wall with the soil at foundation level. A sliding mechanism can be still clearly recognized and the critical acceleration has a clear kinematic meaning; it is in fact the acceleration of the wall during the sliding whilst the underlying soil continues to move as the input signal. The accumulation of permanent displacements is due to the activation of the sliding mechanism that depends on the mechanical strength of the contact surface, on the inertial force of the wall, and on the earth pressure due to the interaction of the structure with the backfill is to be considered.

Richard & Elms (1979) proposed an extension of the Newmarks method to the retaining walls. But it overestimates the accumulated displacements because it does not consider the vertical acceleration of the soil wedge. An enrichment of the Richards & Elms model has been proposed by Zarrabi Kashani (1979) where the vertical slip motion of the soil wedge has been included in the method. Further developments of the method can be found in recent works of Conti et al. (2013).

For the flexible retaining walls, a definitive assessment of a simplified dynamic design methodology is very difficult to achieve due to the complexity of the mechanisms of soil resistances mobilization, especially downstream the wall, and of the formation of the collapse mechanism. The collapse mechanism is generically a rotation; what schematically happens is that an active wedge and a passive wedge translate along an inclined failure surface that pass for the bottom of the wall (Figure 1.5).

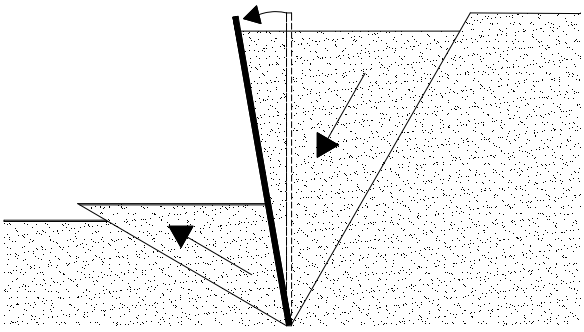

Figure 1.5: Scheme of the rotational failure of a cantilever wall.

Particularly regarding the possibility to apply the Newmark method, the critical acceleration is usually defined as the solution of the equilibrium equation in the pseudo-static ultimate condition. For instance, in Figure 1.6 the limit rotational equilibrium of a cantilever wall method is shown, and the critical acceleration a_c is the value of the acceleration such that the safety factor $SF = \frac{S_{ae} \cdot h_a}{S_{pe} \cdot h_p} = 1$, so it represents the theoretical value of the acceleration that triggers the collapse. Theoretically, after the time instant

when SF is equal to one, the rotational collapse occurs.

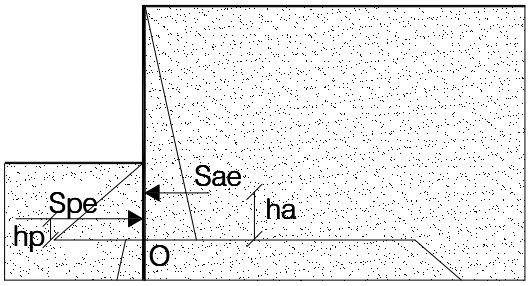

Figure 1.6: Limit equilibrium condition for a cantilever retaining wall: seismic active and passive pressures on a cantilever retaining wall.

Similarly, the critical acceleration for single or propped retaining wall can be computed assuming a plastic mechanism and then performing a limit equilibrium analysis. For instance Towhata and Islam (1987) assume a translation mechanism of a soil-structure system constituted by the wall and the anchor, while Neelakantan et al. (1992) consider a rotation mechanism around the anchor.

Once the critical acceleration has been evaluated, the peculiar plastic mechanism of the flexible cantilever walls makes difficult the choice of an integration scheme. The collapse mechanism is a rotation, so the critical acceleration vectors direction and the sliding direction are no more parallel. Two possible choices could be identified: i) considering the actual wedges sliding direction and perform the integration along a direction belonging to the analysis plane; ii) perform a rotational integration.

Conti et al. (2012) have shown that a Newmark type integration based on a calculation of the critical acceleration with the Blum method predicts accumulated displacements that are much smaller than those actually experimentally observed in centrifuge dynamic test because a part of the energy is dissipated for the mobilization of the passive resistance and the collapse occurs only afterwards.

Richards & Elms (1992) performed three tests where passive failure has been induced on a wall with an anchor at the top. In each test the wall has been subjected to a train of pulses. In Figure 1.7 the forces, accelerations and displacements of the wall relative to the final pulse of the second tests are shown. In the acceleration time history a plateau in the acceleration wall

response can be observed indicating that the sliding of the wall is occurring after that a critical acceleration is achieved and that the acceleration during the sliding is constant. The value of the acceleration at the beginning of the sliding is constant during the movement. This is the evidence of a process of the accumulation of displacements that can be described through the Newmark method.

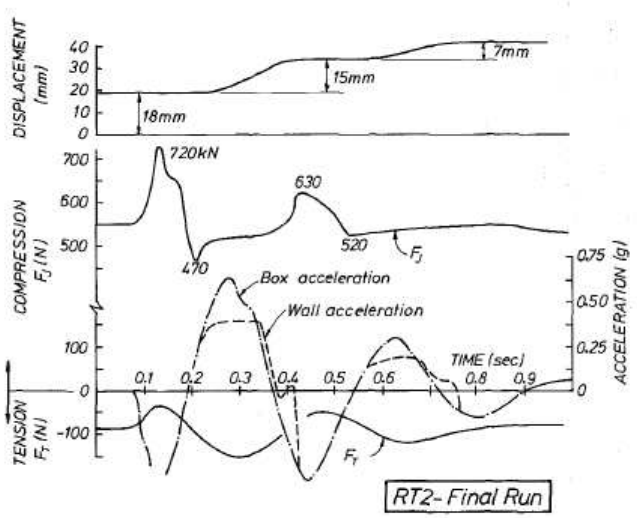

Figure 1.7: Richards Elms (1992). Passive failure on walls with an anchor at the top: forces, accelerations and displacements.

Such clear distinction between the walls response before the sliding and after the sliding trigger is not always observable.

In fact, the works of Callisto & Soccodato (2007) and of Psarropoulos and Paolucci (2007), where the results of the dynamic simplified analysis is compared with the results of a numerical analysis are compared, show that the flexible retaining walls accumulate permanent displacement before that

the critical acceleration is attained; moreover, also in the centrifuge tests presented in the works from Zeng (1990) and Zeng & Steedman (1993) it is shown that the wall accumulate permanent displacements before reaching the critical acceleration.

Consequently, it is apparently difficult to apply the Newmark method for the prevision of seismic induced displacements of flexible retaining walls because, on one hand the logic-mathematical model required for the prevision needs several levels of assumption, on the other hand the phenomenon itself is not always clearly observable and repeatable.

1.6 Physical modeling and numerical analyses

Conti (2010) has performed several dynamic centrifuge tests on pair of cantilever or propped flexible retaining walls embedded in dry sand. The models have been subjected to a train of quasi-sinusoidal earthquakes and accelerations, bending moments, displacements and forces in the props have been monitored. The major findings about the response of the physical modeling can be summarized with the following points:

1. An increment of the transient and residual bending moments has been observed and it depends on the maximum acceleration recorded at the top of the soil deposit; moreover the prediction of the pseudo-static method of the increment of the bending moment is correct for the single propped walls while is overestimated in the case of the cantilever scheme;

2. The accumulation of the permanent displacements does not depend only on the current earthquakes intensity but more on the entire dynamic loading history; The Newmark method cannot be directly applied for the prediction of the permanent displacements.

These findings are in agreement with the already mentioned works of Zeng (1990) and Zeng and Steedman (1993) where the accumulation of permanent displacements has been observed both before reaching the limit equilibrium condition, where contemporarily an accumulation of the bending moment is observed, and after the critical acceleration is attained.

In Conti (2010) also dynamic numerical analyses, where an advanced constitutive model for the soil behaviour has been used, have been performed. The major findings after the comparison between the experimental evidences and the numerical investigation are essentially the following:

1. Experimental and numerical analysis are substantially in agreement in the description of the soil-structure behavior and the amplification phenomena within the soil deposit;

2. With special regards to the cantilever walls, the passive resistance progressively increases during the seismic shaking and contemporarily the bending moment increases;

3. When the passive resistance is fully mobilized a plastic mechanism can eventually be activated;

4. The critical acceleration, defined as the value of the acceleration that induces the collapse as with a pseudo-static limit equilibrium analysis changes during the tests, and this can be explained considering the change of the distribution of the contact stresses down the wall.

The use of the numerical analysis as tool allowing the detailed study of the flexible retaining walls can be found in Callisto and Soccodato (2007) and Callisto et al. (2008). Also in these study the progressive mobilization of the passive resistance and the contemporary accumulation of the bending moment of the structure is highlighted.

1.7 Presence of water

The most part of the recent research works have been devoted to the flexible walls embedded in dry soils, and relatively few experimental works have considered the presence of water in the backfill (Zeng & Steedman, 1993; Dewoolkar et al., 2001; Lee et al., 2005; Towhata et al., 2009), and most of them were devoted to the seismic behaviour of caisson and gravity retaining walls.

As already mentioned, the structures behavior is affected by the saturation mainly for three reasons: the change of the unit weight of the soil due to the buoyancy force, the development of the hydrodynamic pressure on the wall and pore pressure increases in the ground. While for the first two factors some simplified solutions can be used, like the generalized apparent angle of seismic coefficient (Matsusawa, 1984) and the Westergaard solution (1933), the calculation of the pore pressure build up during the shaking is related to the material response to the dynamic and cyclic loading; thus it needs an appropriate constitutive law. The pore pressure change during earthquake depends on several factors, summarizing time and space (Madabhushi, 2007), and it is very difficult to find theoretical or simplified

solutions able to reproduce the pore pressure acting in the ground. Presently the numerical analyses appear to be only way to approach the problem.

In the case of saturated soil the collapse can also be induced by the loss of resistance of the soil due to the pore pressure increase and consequently to the reducing of the effective stress toward zero, that is when liquefaction occurs.

1.7.1 Hydrodynamic pressure

The first detailed study regarding the hydrodynamic pressures on vertical rigid dams were carried out by Westergaard (1933). With the following hypotheses:

1. The liquid is perfect, homogeneous and non compressible;
2. Waves are not present at the liquid surface;
3. The basin in indefinitely extended.

The hydrodynamic pressure distribution, whose trend is approximately represented by a parabola with a vertical axis, has the following equation:

$$P(y) = 7k_h \cdot \gamma_w \frac{(H_w \cdot y)^{\frac{1}{2}}}{8} \tag{1.7}$$

where H_w is the height of the dam below the water level, γ_w is the unit weight of the water and y is ordinate from the water level.

Brants and Heilbron (1933) removed the Westergaards hypotheses 1) and 3), since they studied the influence of the compressibility of the water and of the length of the basin, reaching the conclusion that the compressibility of the water has not an important effect except the case of dam with a significant height. As regard the influence of the flexibility of the dams structure on the hydrodynamic pressure, Brants and Heilbron concluded that considering the typical high stiffness of the dams and the normal frequencies of the earthquakes the effect of the flexibility of the dams structure can be neglected for the determination of the hydrodynamic pressure.

This means that the hypotheses at the basis of the Westergaards theory are not excessively restrictive for the computation of the hydrodynamic pressures on the dams.

In case of quay wall in Figure 1.8, three main differences with respect to the dam case can be identified. Firstly the height of a quay wall is lower than the height of a dam, so the water compressibility can be neglected; secondly

the quay walls are significantly more flexible then the dams, so their natural frequency of vibration can be comparable with the typical frequencies of the earthquakes, which can determine an increment of the hydrodynamic pressure with respect the Westergaards solution; finally the hydrodynamic pressures at the backfill side need to be evaluated. This last aspect is faced in the following paragraph. Seed and Whitman (1970) have proposed to follow the same approach of the Westergaards solution for the computation of the hydrodynamic pressure, so it can be computed as follows:

$$\Delta P_w = 7k_h \cdot \gamma_w \frac{H^2}{12} \tag{1.8}$$

The same authors also assume the position h_w of the resulting force $_w$ to be:

$$h_w = 0.4H_w \tag{1.9}$$

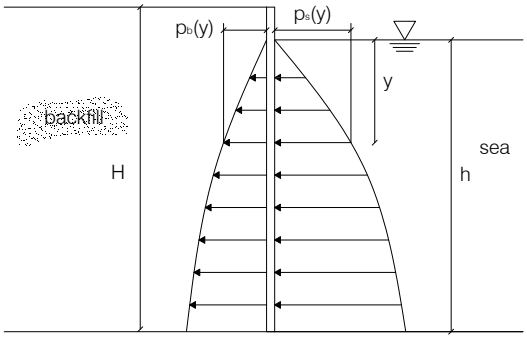

Figure 1.8: Hydrodynamic pressures on a quay wall.

1.7.2 Dynamic earth pressure in saturated backfill

The computation of the hydrodynamic pressure at the backfill side is made difficult due to the interaction between water and the soil. The water movement through the pores depends on the soil permeability. Both in case of soils with high and low permeability the Matsuzawa method gives the possibility to use the Mononobe and Okabe expression changing the dry unit weight with the unit weight of the submerged soil, altering the angle of seis-

mic coefficient and adding the hydrodynamic pressure of the water to its static pressure.

If the backfill is constituted by a highly permeable soil, assuming that the water can move freely in the voids, Matsuzawa proposed to consider as apparent angle of seismic coefficient Θ' :

$$\tan\Theta' = \frac{G_s \cdot \tan\Theta}{G_s - 1} \tag{1.10}$$

where $\tan\Theta$ is the true angle of the seismic coefficient that is defined as $\tan\Theta = \frac{k_h}{1 \pm k_v}$ with k_h and k_v the coefficients of the vertical and horizontal seismic acceleration, $G_s = \frac{\gamma_s}{\gamma_w}$ and γ_s is the unit weight of the soil grains.

In case of backfill with low permeable soil, assuming that the soil and the water move together, the expression of the apparent angle of seismic coefficient proposed by Matsuzawa is the following:

$$\tan\Theta'' = \frac{(G_s + e) \cdot \tan\Theta}{G_s - 1} \tag{1.11}$$

where e is the void index.

1.8 Summary

In this Chapter the scope of the research has been illustrated and the background useful for the introduction to the problem has been depicted; it regards the computation of the dynamic earth pressure, the computation of the permanent displacement through the Newmark block method, the use of the physical modeling and the numerical analyses in order to study the problem and the simplified solutions to take into account the influence of the water on the earth pressure of saturated backfill against a retaining structure.

Chapter 2

Centrifuge Modelling

The monitoring of the structure behavior during the seismic shaking is important for research purposes and to identify rational design criteria. Three possible complementary experimental methodologies can be chosen. Each of them highlights some aspects of the behavior and presents positive and negative points. They are:

1. Field Tests;
2. 1 g tests on small scale models;
3. Centrifuge tests on small scale models.

Field tests allow to monitor the seismic response of a real structure and thus to consider the effect of the heterogeneity of the soil and the effect of real earthquakes. Of course one issue regarding this type of research methodology is that one has to wait a real earthquake that, also, has its peculiar amplitude, frequency content, duration and energy content and hence is not chosen by the researcher. Moreover the results cannot be generalized due to the peculiarity of the structure and ground conditions.

The study of the behavior of the structure can be carried out on small scale models instead than on real scale ones. The 1g tests give the possibility to examine the dependency of the structure interacting with a selected soil, so it is possible to monitor the interaction of the structure with that specific soil. This kind of experimental methodology does not replicate the stress state in the field and consequently the stress strain path in the model is not the same as in the reality. The centrifuge tests overcome this problem virtually increasing the gravity field using the centrifugal acceleration at the end of a rotating beam.

In a centrifuge test, more precisely, the small scale model is collocated at the end of a rotating beam so that the centrifugal acceleration increases the stress state within the model simulating the increase of the gravity field. Generally speaking, the increase of the stress state within the model makes the model equivalent to a real scale whose dimension can be calculated through the use of the dimensional analysis (see paragraph 2.2).

Knowing the scaling laws that express the equivalence between the model and the real scale one, which is called prototype, the small scale model observed behavior can be transferred to the real scale. More precisely, such scaling laws actually establish the ratio between the value of a given physical quantity of the problem at the real scale and its value at the model scale. The most important requirement to individuate the scaling laws is that the model stress state and the prototype stress state have to be equal.

The first centrifuge tests took place around the 1930 in URSS and USA, but the geotechnical centrifuge modeling actually grew up in the Sixties mainly with the works of Andrew Schofield in UK. Nowadays more than one hundreds geotechnical centrifuges exist in the world among which the 60% is in Asia and the remaining is in North America and Europe (Bilotta & Taylor, 2005). The tests described in this thesis have been carried out at the Schofield Center of the Engineering Department of Cambridge (UK).

The geometry of the models and the test data are described in Chapter 3; in here it is just recalled the identification names of the tests because they are sometimes used in this chapter. The tests on cantilever walls are CWU1, CWU2, CWU3 and CWU4 while the tests on propped walls are PWU1, PWU2 and PWU3.

In this chapter the principles of the centrifuge physical modeling will be firstly illustrated, then the facilities useful for the present work, the instrumentation, the soil mechanical properties and the model preparation will be shown. After that the geometry of the models tests will be described.

2.1 Principles of Physical Modelling and Centrifuge Modelling

The idea at the basis of physical modeling is to test the behavior of a small scale model instead of a real scale structure. The test of a real scale structure is expensive and, especially in the case of a field test, is affected by the heterogeneity of the soil. The advantages of working with a physical model are various:

1. The model is simpler to prepare with respect a real scale structure;

2. It is easier to perform a parametric study of the model to check the dependency from certain physical quantities. For example, in the case of a dynamic test, the effect of the frequency can be studied performing several tests changing the frequency content of the earthquake input with the other things being equal;

3. It is quite easy to control some physical quantities or state parameters, like the relative density of granular soil;

4. The influence of some parameters can be isolated in order not to consider the effect of less important parameters.

In the following section the principal scaling laws to pass from the model to the prototype scale will be derived.

2.2 Dimensional Analysis

As already explained in the introduction of this Chapter, the data resulting from the monitoring of the small scale model can be expressed at the scale of the prototype using the scaling laws. This means that the model and the prototype are similar from the mechanical behaviour viewpoint. Generally, the relation between all the physical quantities of the model and the prototype like time, acceleration, velocity, displacement, stress etc , has to be identified. Such relations can be found using the dimensional analysis, whose related techniques are well known in engineering.

The Buckingam (1914) theorem states:

For a given problem described by a set of equations that involve n variables $\{V\}$ *and m dimensions, the original set of equations is equivalent to a set of equations involving* $N = n - m$ *dimensionless parameters* π_i.

So, the Buckingam theorem provides a method to compute the dimensionless parameters needed to describe the problem, but it does not provide the way to find the most appropriate between all the possible that can be defined.

Besides the Buckingam theorem, two conditions have to be considered in order to choose the most representative dimensionless parameters of the problem

The first one is the Bridgman (1931) condition that states: *The set of the dimensions* $\{D\}$ *has to be composed of the minimum number* D_{min} *of dimensions needed to define all the variables* $\{V\}$.

The second one is the Van Diest (1946) condition that regards the choice of the dimensionless parameters π_i. Since the set of variables $\{V\}$ can be

subdivided into N isolated variables and into $m = n - N$ repeated variables, the Van Diest condition states: *The repeated variables has to be chosen in order not to form dimensionless parameters. In this way, the dimensionless groups π_i are independent.*

2.2.1 Dimensional Analysis Applied to Physical Modeling

Since the Newtons laws of motion have to be satisfied within the prototype and the model, the following dimensionless equation has to be verified (Bilotta &Taylor, 2005):

$$\widetilde{F} = \widetilde{m} \cdot \widetilde{a} \tag{2.1}$$

where $\widetilde{F} = \frac{F_m}{F_p}$, $\widetilde{m} = \frac{m_m}{m_p}$ and $\widetilde{a} = \frac{a_m}{a_p}$ are the scaling factors relative to the forces, masses and accelerations, and the physical quantities relative to the model are indicated with the subscript m while the physical quantities relative to the prototype are indicated with the subscript p.

The equation 2.1 shows the existence of the dimensionless parameter $\frac{F}{m \cdot a}$ and it assumes the same value in the model and in the prototype. This relation can be transformed as follows:

$$\widetilde{\sigma} = \widetilde{\rho} \cdot \widetilde{a} \cdot \widetilde{L} \tag{2.2}$$

where $\widetilde{\rho} = \frac{\rho_m}{\rho_p}$ and $\widetilde{L} = \frac{L_m}{L_p}$ are the scaling factors relative to the material density and to the length.

Besides the equation 2.1 the following equation holds:

$$\widetilde{\sigma} = \frac{\sigma_m}{\sigma_p} = 1 \tag{2.3}$$

because the mechanical behavior of the granular materials depends on the stress state.

Combining the equations 2.1 and 2.2 we obtain:

$$\rho_m \cdot m \cdot L_m = \rho_p \cdot p \cdot L_p \tag{2.4}$$

If $\rho_m = \rho_p$, and we consider the case when $a_p = g$ the relation 2.4can be written as:

$$\frac{L_p}{L_m} = \frac{a_m}{g} \tag{2.5}$$

that represents the basic scaling law in centrifuge modeling establishing the mechanical equivalence between the model and the prototype in the gravitational field.

Scaling Factors for Static Problems

Considering a model subjected to a centrifuge acceleration N times bigger than the gravity acceleration, the stress within the model at the depth h_m is:

$$\sigma_{vm} = \rho N g h_m \tag{2.6}$$

and the stress relative to the prototype is:

$$\sigma_{vp} = \rho g h_p \tag{2.7}$$

Considering the equation 2.3, the equation 2.7 becomes:

$$_m = \frac{h_p}{N} \tag{2.8}$$

that represents the scaling factor for the length.

The scaling factor for the area and the volume are directly derived from equation 2.8:

$$A_m = \frac{A_p}{N^2} \tag{2.9}$$

where A_m and A_p are the surface at the model scale and the surface at the prototype scale respectively.

$$V_m = \frac{V_p}{N^3} \tag{2.10}$$

where V_m and V_p are the volume at the model scale and the volume at the prototype scale respectively.

The scaling factor for the displacements can be derived from equation 2.8 noticing that the geometry of the model is a linear representation of the prototype, this implies that the scaling factor for the displacements is $1 : N$ as for the length.

Since there is a linear relation between the displacements of the model and the displacements in the prototype, the scaling factor for the strain is $1 : 1$.

The scaling factor for the time related to the pore pressure dissipation can be determined from the dimensionless time factor:

$$T_v = \frac{c_v \cdot T}{H^2} \tag{2.11}$$

where c_v is coefficient of consolidation.

For a given degree of consolidation, T_v relative to the model is equal to T_v relative to the prototype. Thus:

$$\frac{c_{vm}t_m}{H_m^2} = \frac{c_{vp}t_p}{H_p^2}. \tag{2.12}$$

From equation 2.8

$$t_m = \frac{1}{N^2}\frac{c_{vp}}{c_{vm}}t_p. \tag{2.13}$$

This means that if $c_{vp}/c_{vm} = 1$, which happens when the soil used in the model is the same of the one used in the prototype,

$$t_m = \frac{t_p}{N^2}. \tag{2.14}$$

The scaling factor for the time related to seepage phenomena is calculated as follows:

$$t_m = \frac{L_m}{\nu_m}. \tag{2.15}$$

where ν_m is the seepage velocity at the model scale.
Bilotta and Taylor (2005) have shown that:

$$\nu_m = N \tag{2.16}$$

where ν_p is the seepage velocity at the prototype scale, so the equation 2.13 becomes:

$$t_m = \left(\frac{L_p}{N}\right)\left(\frac{1}{N\nu_p}\right) = \frac{t_p}{N^2} \tag{2.17}$$

that shows that the scaling factor related to the seepage phenomena is $1 : N^2$, the same as for the pore pressure dissipation.

Scaling Factors for Dynamic Problems

The scaling factor for the time related to the inertial effects can be determined directly from the dimensional analysis. In fact, knowing that:

$$\frac{a_m}{a_p} = N \tag{2.18}$$

and considering the dimension of the acceleration $[L/s^2]$, it follows that:

Physical Quantity	*Scaling Factor*
Length $[m]$	$1:N$
Area $[m^2]$	$1:N^2$
Volume $[m^3]$	$1:N^3$
Stress $[kPa]$	1
Strain $[-]$	1
Density $[kg/m3]$	1
H Displacement $[m]$	$1:N$
Force $[N]$	$1:N^2$
Bending Moment $[Nm]$	$1:N^3$
Permeability $[m/s]$	1
Time (Diffusion, Consolidation, Seepage) $[s]$	$1:N^2$
Time (Inertial effects) (s)	$1:N$
Acceleration $[m/s2]$	N
Velocity $[m/s]$	1

Table 2.1: Scaling factors for centrifuge modeling linking physical quantities from model to prototype scale.

$$\frac{a_m}{a_p} = \frac{\frac{L_m}{t_m^2}}{\frac{L_p}{t_p^2}} = \frac{1}{N}\left(\frac{t_p}{t_m}\right)^2 \tag{2.19}$$

and combining 2.18 with 2.19

$$N = \frac{1}{N}\left(\frac{t_p}{t_m}\right)^2 \Longrightarrow \frac{t_p}{t_m} = \sqrt{N^2} = N \tag{2.20}$$

From the equation 2.20 the scaling factor for the frequencies related to inertial effects can be derived:

$$\frac{t_p}{t_m} = \frac{f_m}{f_p} = N \tag{2.21}$$

The scaling factors for both static and dynamic problems are listed in Table 2.1.

Viscous Pore Fluid in Centrifuge Modeling

IAs shown before, there is no match between the scaling factor for the time related to the inertial effect $(1/N)$ and the scaling factor related to the pore pressure dissipation $(1/N^2)$.

In order to achieve such matching, the permeability of the soil is decreased increasing the viscosity of the porous fluid. For the tests of this work, where $N = 40$, the hydroxypropyl methylcellulose dissolved into water with a viscosity of 40 cSt has been used.

In paragraph 2.3.1 the details regarding the preparation of the pore fluid are shown and the saturation process is illustrated.

Error due to the non-uniformity of the acceleration field in centrifuge modeling

The centrifuge acceleration within the model is ωr^2. So it is not constant since it depends on the distance of the point belonging to the model from the centre of rotation of the centrifuge. At the same time the acceleration field of the prototype is constant since the gravity field for the typical civil engineering problems is uniform. Following Bilotta &Taylor (2005) it is shown how to minimize the error due to the non-uniformity of the acceleration field within the model.

Let us consider three equations that allow to determine the matching point between the stress within the model and the stress within the prototype.

The vertical stress within the prototype at the depth $h_p = Nh_m$, where h_m is the height of the model, is:

$$\sigma_{vp} = \rho g h_p = \rho g N h_m \tag{2.22}$$

At the distance R_e from the centre of rotation, called effective radius, the following equality holds:

$$Ng = \omega^2 R_e \tag{2.23}$$

Considering R_t the distance of the top of the model from the centre of rotation, the vertical stress within the model at depth z can be calculated as follows:

$$\sigma_{vm} = \int_0^z \rho\omega^2(R_t + z)dz = \rho\omega^2 z(R_t + \frac{z}{2}) \tag{2.24}$$

So, for a given $z = h_i$ we can set $\sigma_{vm} = \sigma_{vp}$ and considering the equations 2.22, 2.23 and 2.24 it follows that:

$$R_e = R_t + 0.5h_i \tag{2.25}$$

The equation 2.25 means that the centrifuge acceleration Ng is achieved within the model at a distance equal to $0.5h_i$ from the top of the model.

Now let us consider Figure 2.1 where the model and prototype stress distributions are illustrated. r_0 and r_u are the maximum and minimum errors due to the non-linearity of the centrifuge acceleration within the model.

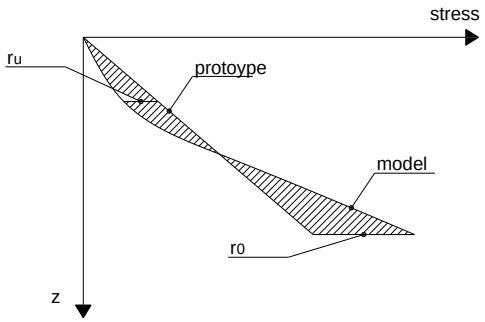

Figure 2.1: Model and prototype stress distributions along the vertical.

r_0 and r_u can be computed as follows:

$$r_u = \frac{0.5h_i\rho gN - 0.5h_i\rho\omega^2\left(R_t + \frac{0.5h_i}{2}\right)}{0.5h_i\rho gN} \tag{2.26}$$

that, considering equations 2.23 and 2.25, becomes:

$$r_u = \frac{h_i}{4R_e} \tag{2.27}$$

$$r_0 = \frac{h_m\rho gN - 0.5h_m\rho\omega^2\left(R_t + \frac{h_m}{2}\right)}{h_m\rho gN} \tag{2.28}$$

$$r_u = \frac{h_m - h_i}{2R_e}. \tag{2.29}$$

If we would like to get $r_0 = r_u$ we obtain:

$$r_u = \frac{2}{3} h_m \tag{2.30}$$

$$r_u = r_0 = \frac{h_m}{6R_e} \tag{2.31}$$

and considering the equation 2.25

$$R_e = R_t + \frac{h_m}{3} \tag{2.32}$$

So the matching between the stress of the model and the stress of the prototype is achieved at $z = 2/3h_m$ and the point where the centrifuge acceleration Ng is achieved is collocated at $1/3$ of the height h_m of the model from the top of the model.

The error 2.31 is usually small even for centrifuges whose effective radius R_e is small (1.5m) and elatively bid models ($h_m = 0.3m$) (Bilotta & Taylor, 2005).

Besides the error due to the non-uniformity of the acceleration field in the vertical direction, another error in the geotechnical modelling is introduced by the presence of a horizontal component of the acceleration for points far from the beam of the centrifuge due to the fact that the acceleration is directed through the centre of rotation.

For a point of the model far 0.2m from the beam of the centrifuge, and for a model with an effective radius of 1.6m, the horizontal component of the acceleration is about 0.125 smaller that the vertical acceleration.

The presence of the horizontal component of the acceleration makes the fluid surface curved. Such curvature is taken into account when computing the mass of the porous fluid to saturate the model; the quantity of the mass needed is usually small (see paragraph 2.4.2).

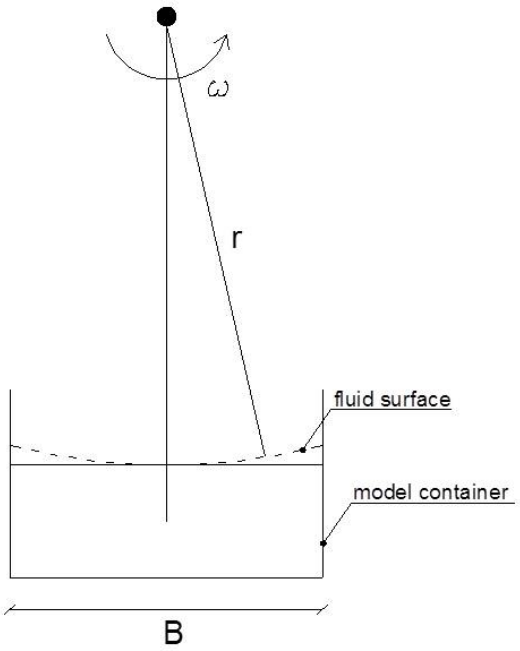

Figure 2.2: Effect of the radial acceleration on the curvature of the fluid surface.

Scale effect due to the particle size

The soil used for the model is the same as the prototype, this means that the particles size, which could be identified with a representative length d, is N times bigger within the prototype than within the model according with the scaling law for the length. The use of gravel for instance would imply too big particles with respect the model dimensions and it would alter the results because the stress-strain path would be different than the actual one within the prototype. Ovesen (1979, 1985) performed a series of experiments regarding the behavior of circular foundations on sand changing the centrifuge acceleration such that they would correspond to the same prototype. Ovesen suggested that the error due to the scaling of the particle size is negligible if the ratio between the size of the foundation and the dimension of the grains is lower than 15.

2.3 Experimental Equipment

In this paragraph the basic characteristics of the centrifuge at the Schofield Centre are illustrated. After the general description the experimental equipment regarding the model preparation is described, such as the model container, the materials used (sand, walls, pore fluid) and the instrumentation used to monitor model behavior. The operating principle of the instruments is illustrated and their calibration as well. The calibration data are also reported with reference to the calibration made for one specific test, namely the PWU3 test, which has been taken as an example. The calibration data of all the other tests are reported in (Appendix A).

Philip Turner Centrifuge

Dynamic centrifuge tests at Schofield Centre are carried out in a 10m beam centrifuge, named after the engineer P.W. Turner, who designed it in the early 1970s (Schofield, 1980).

The centrifuge consists of a beam-like structure, which rotates around a central vertical axis (Figure 2.3). Models can be carried at both the ends of the arm. In the tests performed in this thesis only one model is placed at one end while the other one carries a counterweight attached to the beam. The swinging platform carrying the model and the actuator is installed on the Blue End of the beam and the required counterweight on the Red End.

Figure 2.3: Schofield Center Beam Centrifuge

SAM actuator

The model earthquakes in the centrifuge tests are generated by the Stored Angular Momentum (SAM), an actuator developed at Cambridge University (Madabhushi et al., 1998). The SAM actuator is a powerful tool and allows to apply strong earthquakes at high g level. The SAM actuator can apply successive earthquakes at different amplitudes, frequencies and durations.

Very high levels of energy can be stored in a fly-wheel spinning at high angular velocities. The energy stored in the fly-wheel may be used to subject a centrifuge model to earthquakes. The angular velocity of the fly-wheel determines the frequency of the motion transmitted to the base of the model. The motion is transmitted through a shaft via a fast acting clutch which starts and interrupts the earthquake 2.4. The intensity of the earthquake can be controlled by altering the pivot point of the lever.

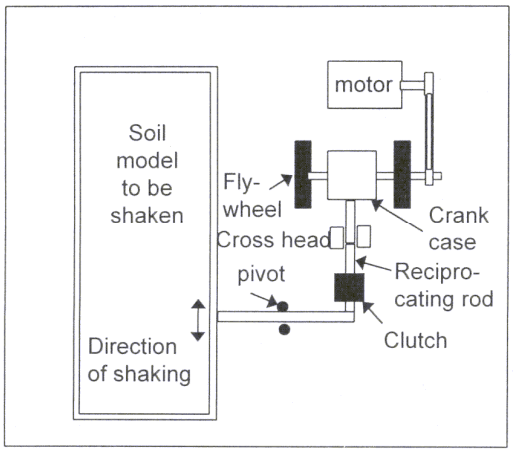

Figure 2.4: Figure Taken from Madabhushi, S. P. G., Schofield, A. N. Lesley, S. (1998): schematic diagram showing the planar view of Stored Angolar Momentum (SAM) shaker.

Laminar box container

It is important the choice of the container due to the small size of the model and the necessity to avoid any disturbance of the container on the response. Thus the principal characteristic of the model container is to deform with the same shear stiffness of the soil.

A first possible choice for the container is the Equivalent Shear Beam box (ESB box) whose behavior is described by Zeng and Schofield (1996). It consists of an alternation of aluminium rectangular rings separated by a rubber layer. This container presents a constant value of the shear stiffness, that has to be matched with that one of the soil. This means that if the soil stiffness is different from the stiffness of the container P-waves can be generated during the test.

Besides the ESB box, the Laminar Box container can be used at the Schofield Center. It is consists of an alternation of aluminum rectangular frames and cylindrical bearings (Figure 2.5). The Laminar Box has been designed in order to have negligible inertia, while being sufficiently stiff in order not to deform under high centrifugal accelerations (Brennan et al., 2006).

The laminar boxs mass is about 40 kg and the internal dimensions are 500x250x300 mm^3. A plate is placed at the base of the box to connect the container with the SAM actuator and fire the earthquake on the model. The mass of the plate is 37kg. The internal part of the laminar box is covered by a flexible rubber sheet to avoid the transition of sand or pore fluid through the rings.

The presence of the roller bearings between the aluminium frames allows to reach a very low shear stiffness of the container, this means that the disturbance of the container on the soil is much less important than that in the ESB box container. Anyway the non negligible mass of the rectangular frames can introduce some boundary effects.

The laminar box deforms with the same stiffness of the soil also when the soil changes its stiffness during the tests, that happens during a dynamic centrifuge tests, due to the decrease of the soil stiffness with the shear strain amplitude and due to the possible occurrence of liquefaction, that determines a very strong loss of shear stiffness.

The models of the present work have been realized within the laminar box container.

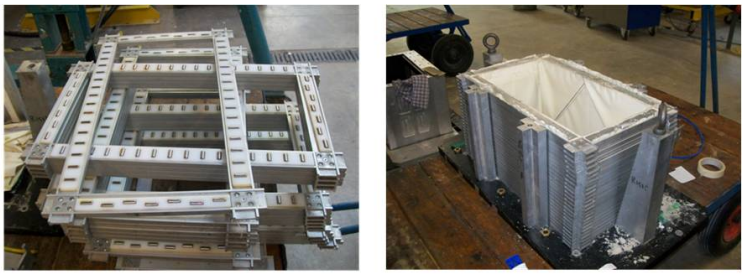

Figure 2.5: Model container: a) Aluminium rectangular rings and cylindrical bearings. b) Laminar box built.

2.3.1 Materials

Leighton Buzzard Sand

The Leighton Buzzard silica sand with grain size 100/70, Fraction E fine has been chosen as sand for the models. The sand contains rounded and sub-angular particles. The specific gravity G_s of the sand particles is 2.65. A wide literature is available about the physical properties and the mechanical behavior of Leighton Buzzard 100/170 sand determined by means of laboratory tests (Jeyatharan, 1991, Tan, 1990). In this work, the tests performed by Visone and Santucci de Magistris (2009) have been the principal reference regarding the behavior of the Leighton Buzzard sand.

It is light brown with nominal grain size , D_{50}, of 0.14mm. Its particle size distribution is shown in Figure 2.6.

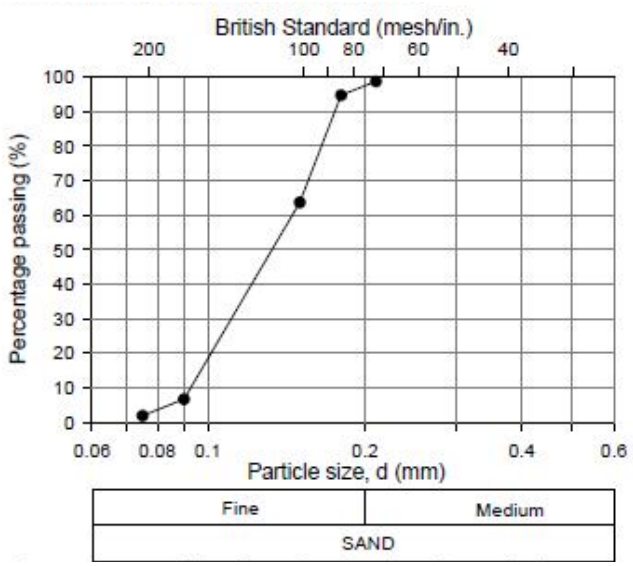

Figure 2.6: Particle size distribution of Leighton Buzzard sand 100/170 (modified from Tan 1990).

Physical Quantity	
D_{50} [mm]	0.14
$D_{10}[mm]$	0.095
G_s	2.65
e_{min}	0.613
e_{max}	1.014

Table 2.2: Basic properties of the sand.

Other physical properties of the sand are reported in Tab.2.2, while in Figure 2.7 the variation of the dry unit weight with the relative density is shown. The dry maximum and minimum values unit weight are 12.90 and 16.05 kN/m^3 and the saturated unit weight maximum and minimum values are 17.84 and 19.90 kN/m^3 corresponding respectively to the maximum void ratio and the minimum void ratio

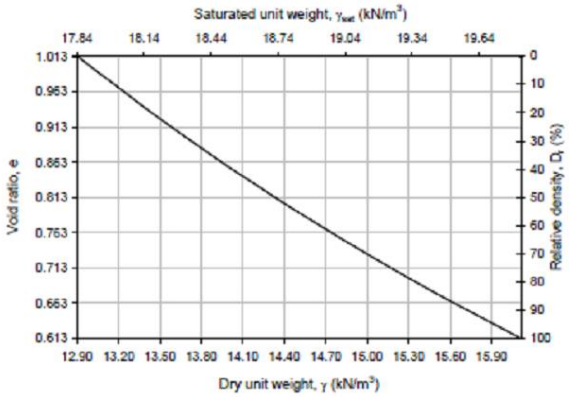

Figure 2.7: Dry unit weight with relative density of LB sand (Visone, Santucci de Magistris, 2009)

The evolution of the elastic properties with the mean effective stress p', expressed in terms of initial shear modulus G_0 and the shear wave velocity V_s, the evolution of the initial damping ratio ξ with p' and the strength of the sand have also been studied and they are highlighted in Figure 2.8 and in Figure 2.9.

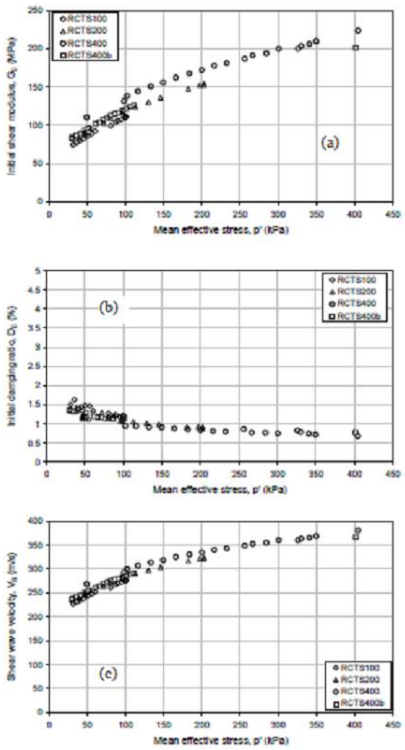

Figure 2.8: Evolution of elastic properties of Leighton Buzzard Sand with p'. a) Initial shear modulus G_0, b) initial damping ratio D_0, c) Shear wave velocity (after Visone, Santucci de Magistris 2009).

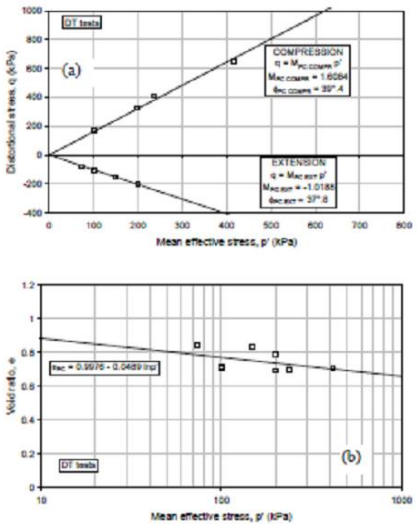

Figure 2.9: Peak strength of Leighton Buzzard Sand in Drained Tests on dense samples (D_r= 60-80%): a) in (q, p') plane, b) in (e, lnp') plane (Visone & Santucci de Magistris, 2009).

Aluminium

The retaining walls are made of a solid aluminium plates. The density of aluminium is 2770 kg/m^3 and the thickness of the walls is 6.36mm (Figure 2.10). At the center of the walls and on both sides of them a series of six strain gauges is positioned. They have been built at the Schofield Center and they allow to measure the strain of the walls and then to compute the bending moment at a certain depth.

For propped walls, two square aluminium rods with an axial stiffness of about 1x106 kN/m at prototype scale, connected to the walls by cylindrical hinges allowing rotation in the vertical plane, have been located at a distance of 195 mm from each other that corresponds to about 8m at the prototype scale.

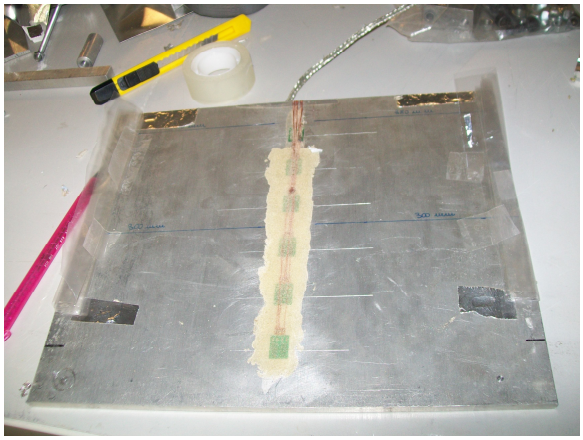

Figure 2.10: Aluminium Wall

Hydroxypropyl methylcellulose

A high viscosity pore fluid has been used for the tests in order to match the time scaling factor related to inertial effect and the time scaling factor related to diffusion phenomena (see paragraph 2.2).

The hydroxypropyl methylcellulose (HPCM) powder is commonly used to fulfill a variety of functions such as thickening and binding in a wide range of industries, including food processing. Methocel products are water-soluble polymers derived from cellulose, and a number of different molecular weights and purities are available. After several viscosity tests on the methylcellulose the relation between the viscosity and the concentration is expressed as the percentage of the methylcellulose of the entire solution by mass (Stewart et al., 1998):

$$\nu_{20} = 6.95 \cdot C^{2.54} \tag{2.33}$$

where ν_{20} is the viscosity of the solution at 20 °C and C is the concentration of HPCM solution in percent. This relation has been used for the preparation of the pore fluid in order to get the desired viscosity 2.11

Figure 2.11: Hydroxypropyl methylcellulose powder dissolving into water.

The ratio between the unit weight of a solution of HPCM dissolved into water with a concentration lower than 5% and the unit weight of the water is lower than 1% (Stewart et al., 1998).

2.3.2 Instrumentation and Calibration

The model preparation has been carried out pouring the sand inside the laminar box and positioning the instruments and the walls at the chosen depths. The sand has been poured through a sand hopper previously calibrated in order to reach the desired relative density for the sand.

Different kinds of instruments have been used for monitoring physical quantities useful for the observation of the seismic behavior of the models during the tests. Those physical quantities are:

1. Acceleration of the soil and the walls;
2. Displacements of the walls and of the soil;
3. Pore pressures;
4. Bending moments on the walls;
5. Axial force in the load cells (for the tests on propped wall);

The instruments used for their monitoring respectively are:

1. Piezoelectric and Micro-Electric-Mechanical accelerometers (MEMs accelerometers) the accelerations;

2. Linear Variable Differential Transformers (LVDTs) for the displacements;

3. Pore Pressure Transducers (PPTs) for the pore pressures;

4. Strain Gauges for the bending moment;

5. Load Cells for the axial load on the props.

The instruments must provide a high strength and precision with minimum interference in a small device as they are used under high g - level (40g). The instruments must also be able to operate at high frequencies under dynamic condition (50Hz). The instruments have been calibrated before the tests and after the tests.

Data Acquisition System

The analogue data generated during the calibration or the test are amplified and after the analog-to-digital conversion they are acquired through the Centrifuge Data AcQuisition System (CDAQS) as illustrated in Figure 2.12. The CDAQS acquisition system consists of a PC running a terminal program connected to an Interface Module in the laboratory. The technical specifications of the CDAQS data acquisition module are reported in 2.3. Data can be acquired at up to 5000 samples per second simultaneously on 32 channels or 48 channels, and is stored in memory for upload at the end of the test.The sample resolution is 16 bit. For the first four tests, namely CWU1, PWU1, CWU2 and PWU2, 32 channels have been used, while for tests CWU3 and PWU3 48 channels have been available, and among them 37 have been used for the instruments of the models.

$Numberofchannels$	32
$Simultaneoussamplingrate$	$1to500samples s^{-1}$
$Sampleresolution$	$16bits$
$Inputsensitivity$	$\pm 10V$
$Databuffercapacity(samples)$	1000000
$Communications$	$DuplexRS485$
$Commsrate$	$19200baud$
$Powerrequired$	$\pm 15V$
$Powerconsumption(max)$	$50W$
$Triggersource$	$5Vpulseorviakeyboard$
$Slipringrequirements$	8
$Size$	$120mmx225mmx100mm$
$Weight$	$2.4kg$
$Rating$	$IP65$

Table 2.3: Technical specifications of the CDAQS acquisition module.

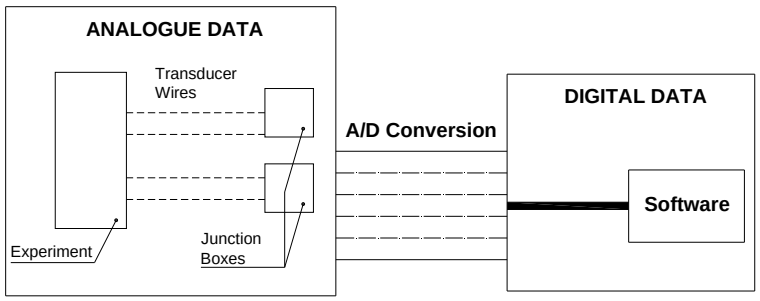

Figure 2.12: Data Acquisition System.

Sand pouring - Calibration of the sand hopper

The sand pouring has been carried out through a hopper that is loaded up with the sand (Figure 2.13). The hopper has been designed at the Schofield Center (Zhao et al., 2006, Madabhushi et al., 2006), and it is inserted within a frame so that its position can be controlled and it can translate in x, y and z direction.

The relative density of the sand poured into the model is controlled by the height of the hopper, the diameter of the orifice plate at the top of muzzle (Figure 2.14) and eventually a sieve or more sieves (usually no more than two) at the bottom of the muzzle. The height of the hopper is the less important parameter controlling the density of the soil, that is more importantly controlled by the flow rate of the sand that in turn is determined by the diameter of the orifice plate inserted at the top of the muzzle, and the presence of the sieves at the bottom of the muzzle. The loose density of the sand (38%) has been obtained combining a muzzle with 5mm diameter orifice plate, no sieves at the bottom and an height of fall of 500mm, while the dense configuration (88%) has been obtained combining a 6mm nozzle, two sieves at the bottom and an height of drop of 600mm.

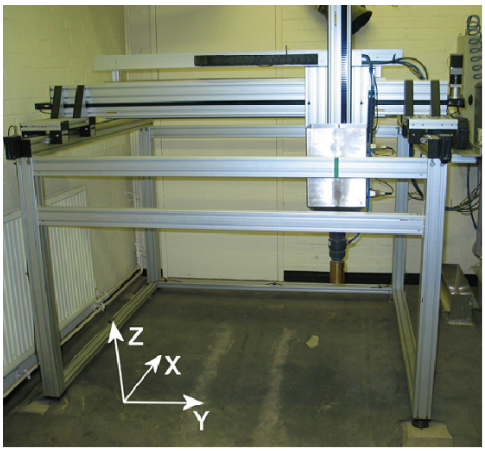

Figure 2.13: Hopper for sand pouring (from Zhao et al., 2006).

Figure 2.14: a) Muzzle at the base of the hopper with the nozzle at the top, b) Sieve at the bottom of the muzzle.

The calibration of the sand hopper has been carried out choosing a combination of muzzle diameter, height of fall and eventual presence of sieves, filling a container with a known volume (Figure 2.15).

The hopper can move either following a circular shaped pattern either a rectangular one. For the tests of the present work, both calibration and model preparation have been carried out following the rectangular pattern. Before the sand pouring the corners of rectangular pattern are properly set in order to cover the area of the container to be filled. As shown in Figure 2.16, for a given height of fall, firstly the hopper pours going from point 1 to point 2; secondly it pours going from point 3 to point 4. In each of these cycles the hopper moves following an S-shaped path where the distance between each line-path is 20 mm. After two cycles the position of the hopper returns at the point 1 and the height of fall is increased with respect the z axis and the cycles are carried out again.

Figure 2.15: Sand pouring. a) Hopper calibration; b) Pouring sand into the model.

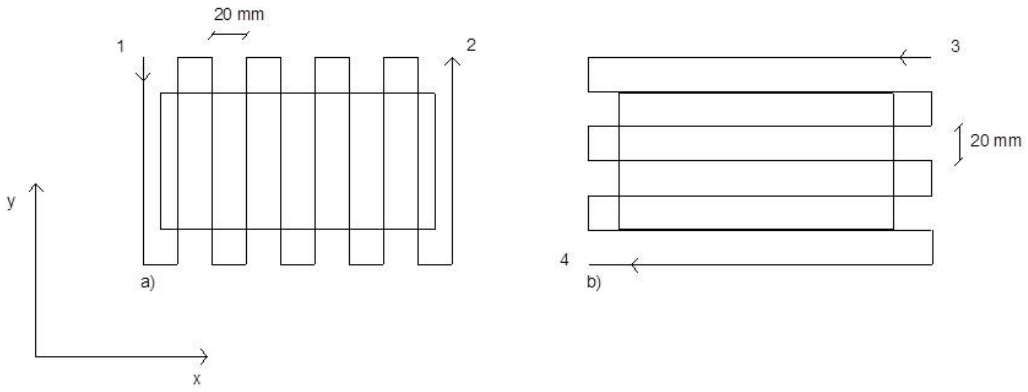

Figure 2.16: Path of the hopper. a) first cycle path, b) second cycle path

In order to keep the height of fall constant, the vertical position of the hopper has been increased of a quantity Δz equal to the thickness of the sand layer deposited after the two cycles. Δz depends on the settings of the hopper (muzzle diameter, presence of sieves and height of fall) and it has been measured during the calibration of the sand pouring.

The container used for the calibration is a small cylinder of 203mm of diameter and 200mm of height. Typically the calibration starts considering a first estimation of Δz and, after that the sand layers thickness actually poured every two cycles is measured and Δz it is eventually updated (Figure 2.17).

Figure 2.17: a) Measuring the height of sand poured into the container during the hopper calibration; b) procedure of flattening the sand surface.

When the cylinder is completely filled, the sands surface is carefully flattened, the container is weighted and the relative density calculated.

The Δz value is used also for the sand pouring of the model.

Piezoelectric accelerometers.

D.J. Birchall type A/23 miniature accelerometers are used to measure the acceleration in the soil, the acceleration at the base plate of the laminar box (that is considered the input acceleration history) and the acceleration of the support of the LVDT. They are approximately 20 mm in length and 10 mm in diameter (Figure 2.18) and their mass is of 5 grams. They have a flat frequency response ranging from 20 Hz to 2000 Hz that includes the frequency of the input acceleration of 50Hz (at the model scale) used for all the tests. The device has a resonant frequency of about 50 kHz and maximum error of 5% (Figure 2.19).

Figure 2.18: Piezoelectric accelerometer.

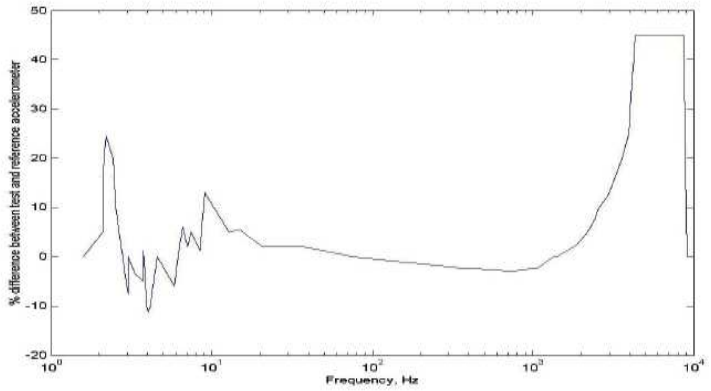

Figure 2.19: Frequency response of piezoelectric accelerometers.

The response of the accelerometers is less satisfactory for frequencies lower than 25 Hz, this means that the signal recorded by piezoelectric accelerometers are not suitable to be integrated to evaluate displacements.

On the other hand Brennan (2005) suggests a procedure to obtain dynamic displacement through the double integration of the signal recorded by the accelerometers with both low pass filter and high pass filter. Anyway this procedure is suitable when there are not significant accumulated displacement during the shaking.

Accelerometers have been calibrated using a calibrator, which excites the

instruments with a sinusoidal input having acceleration amplitude of +/- 1g (Figure 2.20). A constant calibration factor is obtained assuming a linear response for the relevant acceleration range; usually it is included between 6 and 10 g/V (Figure 2.21).

Figure 2.20: Piezoelectric Accelerometers Calibrator.

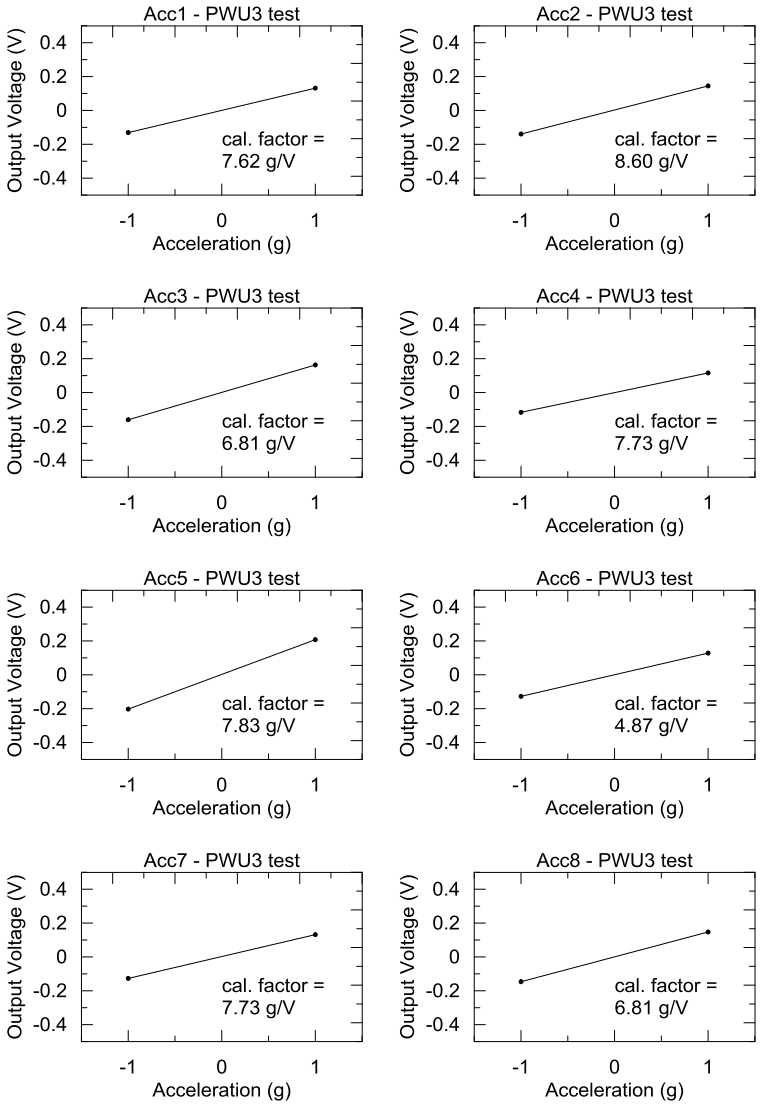

Figure 2.21: Calibration factors of the piezoelectric accelerometers of test PWU3.

MEMS accelerometers

High-g MEMS accelerometers manufactured by Analog Devices have been used to measure the accelerations of the top of the walls (Figure 2.22). The device dimensions are 5mm x 5mm x 2mm, its g-range is 120g, its resonance frequency is 24 kHz and its linear range reaches even low frequencies ($f \approx 0.1Hz$), thus they can measure both dynamic acceleration and static or centrifuge acceleration.

Calibration factors have been calculated exciting the MEMS accelerometer with a constant acceleration of $+/-1g$. A constant calibration factor has been obtained assuming a linear response for the acceleration range (Figure 2.23.

The signal of the MEMS accelerometers can be used to determine the rotation of the wall. If ϑ is the rotation of the wall, a is the g-component measured by the MEMS accelerometer placed on the top of the wall and Ng is the g-field generated by the centrifuge acceleration (Figure 2.24), ϑ can be easily calculated as follows:

$$\vartheta = \arcsin \frac{a}{Ng} \tag{2.34}$$

where a is expressed with the same unit of g. If the acceleration a is divided by g and it is multiplied times N, which normally happens when the acceleration is expressed at the prototype scale, then the expression 2.34 becomes:

$$\vartheta = \arcsin a \tag{2.35}$$

Figure 2.22: MEMS accelerometer on the top of the wall.

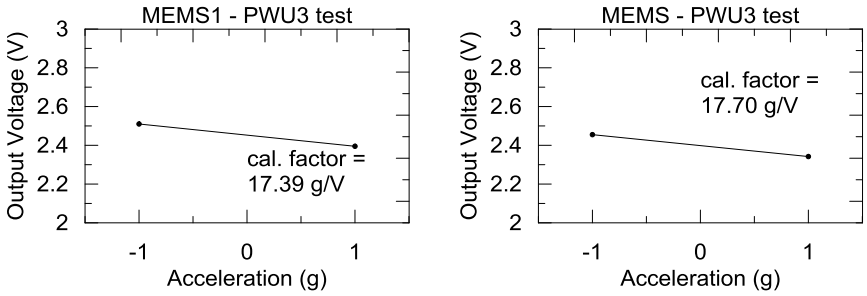

Figure 2.23: Calibration factors of MEMS of test PWU3.

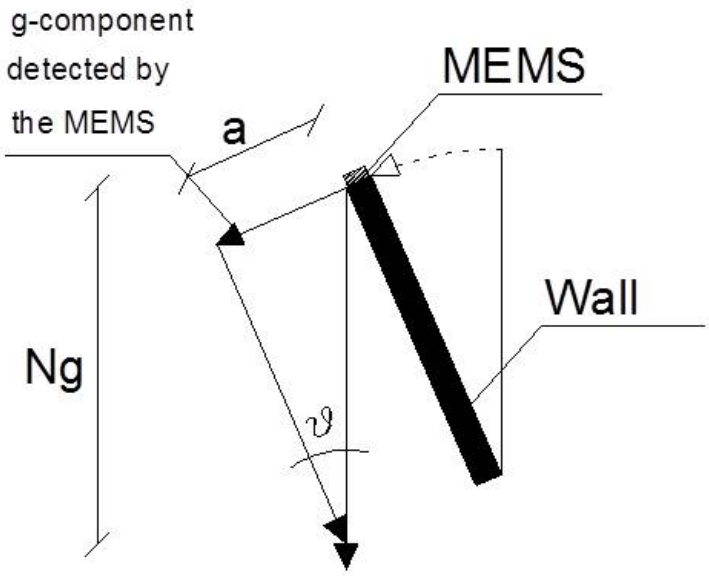

Figure 2.24: MEMS accelerometer on the top of the wall.

Pore Pressure Transducers

Pore Pressure Transducers (PPT) have been used to measure the pore pressure within the soil mass. The main component of a PPT is the head which contains the Diaphragm with 4 strain gauges attached in full bridge configuration. This diaphragm is protected with a Porous Stone (Figure 2.25). The

PPTs have been calibrated in the calibration station (Figure 2.26 and Figure 2.27) where they have been put within a silicon cone filled with de-aired water and then they are completely saturated. The water pressure have been controlled through the compressed air regulator and the air-water interface (see schematic of calibration system illustrated in Figure 2.27) and it has been increased by steps of $20 - 30kPa$ up to about the expected maximum pore water pressure within the model in flight and then it is decreases up to the atmospheric pressure. The output voltage is recorded for each step and the calibration factor corresponds to the slope of the regression line of the acquired data.

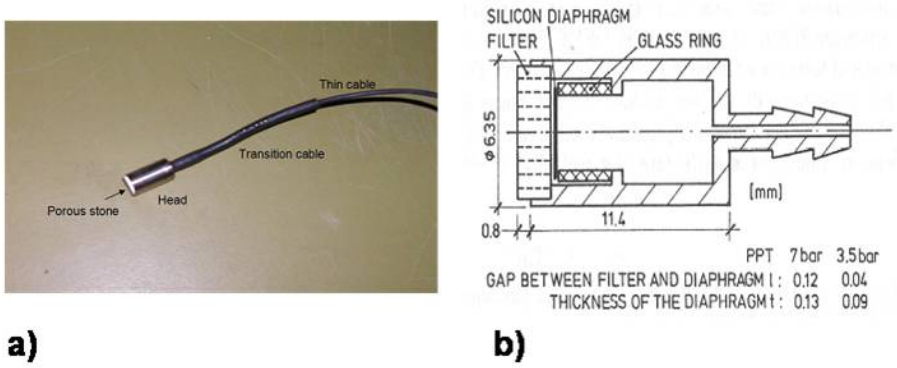

Figure 2.25: Pore Pressure Transducer; a) photography, b) schematic of the PPT.

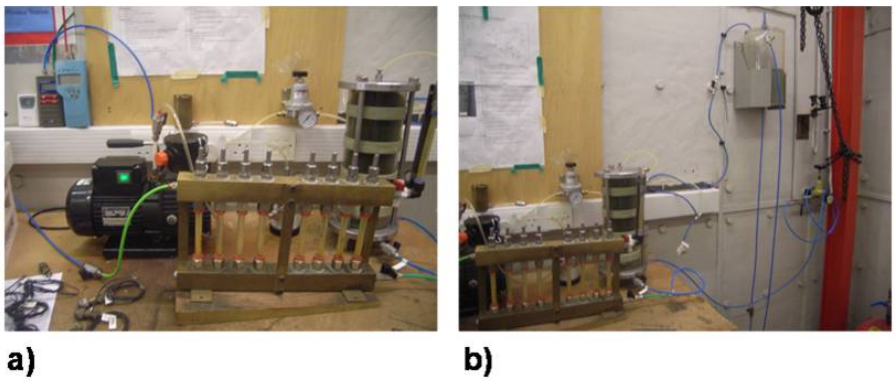

Figure 2.26: Calibration station of the PPTs.

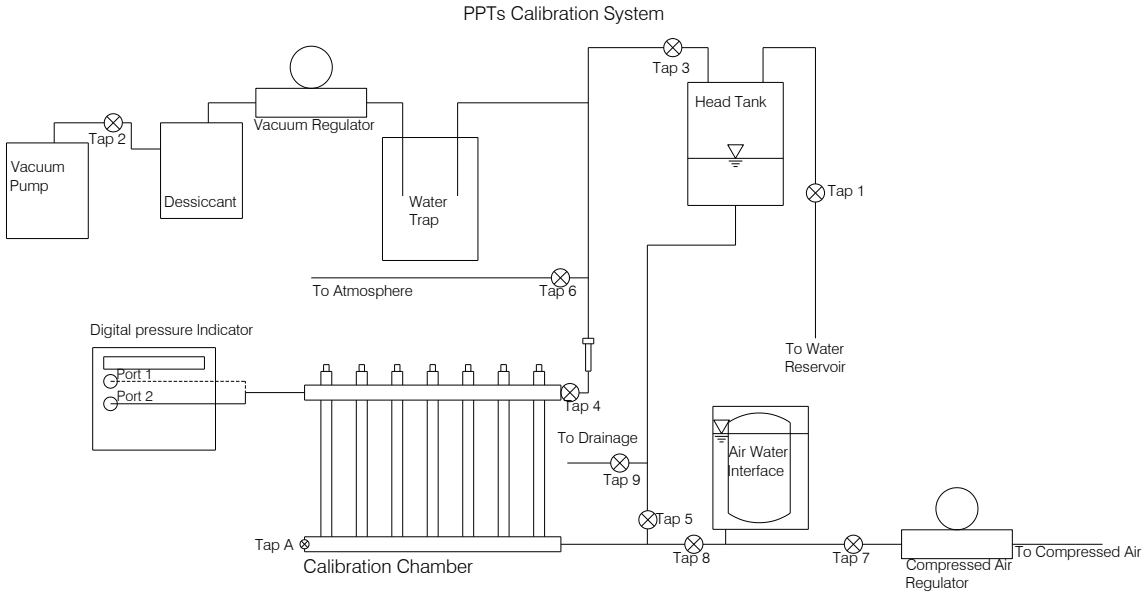

Figure 2.27: Schematic of the calibration station of the PPTs.

In Figure 2.28 the data acquired during the calibration of the PPTs of test PWU3 can be found. The regression line and the calibration factor are reported.

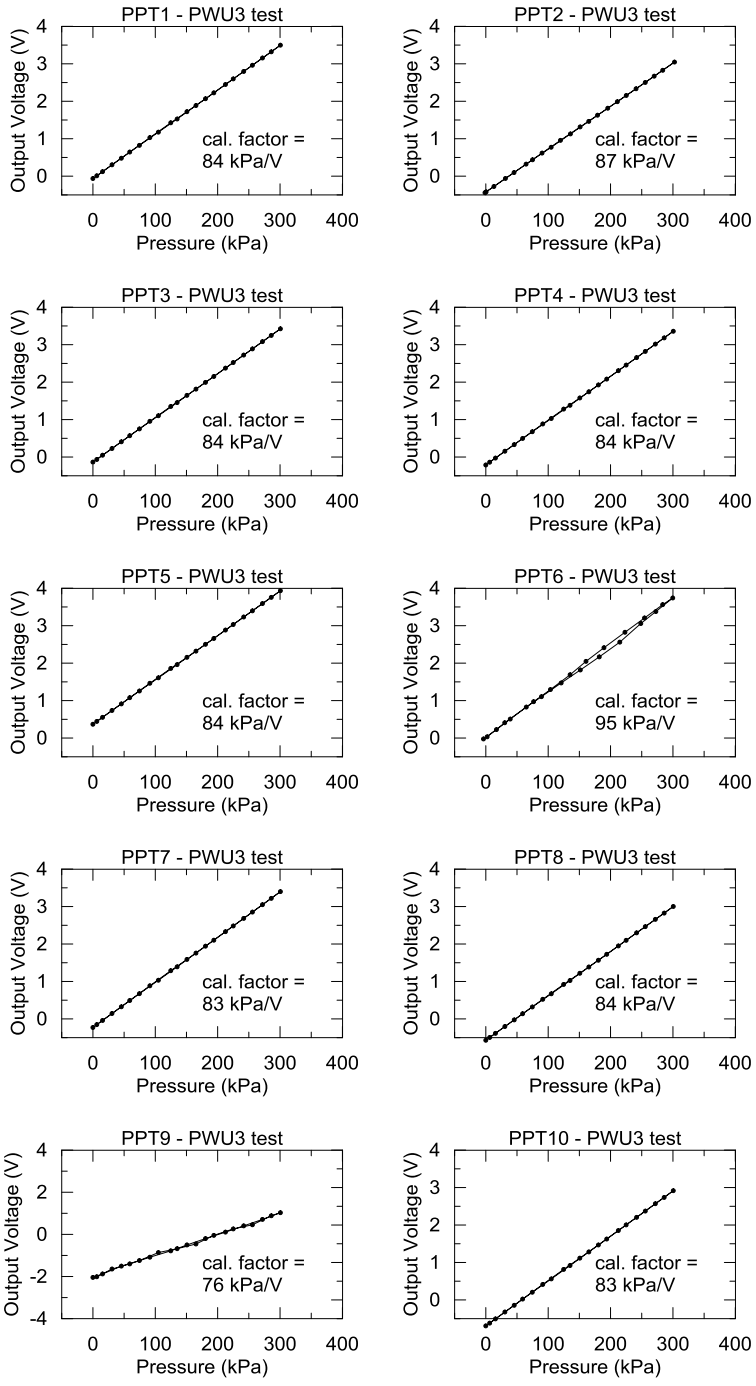

Figure 2.28: Calibration data of pore pressure transducers of test PWU3.

Strain gauges

Strain gauges have been placed in the aluminium plate to measure the bending moments along the central section of the walls. Before the calibration, the strain gauges are covered by epoxy resin in order not to come into contact with the pore fluid (Figure 2.29). The resistance of the strain gauges is proportional to the strain and they are assembled in a Wheatstone bridge so that the change in resistance is changed into a change in voltage (Figure 2.30).

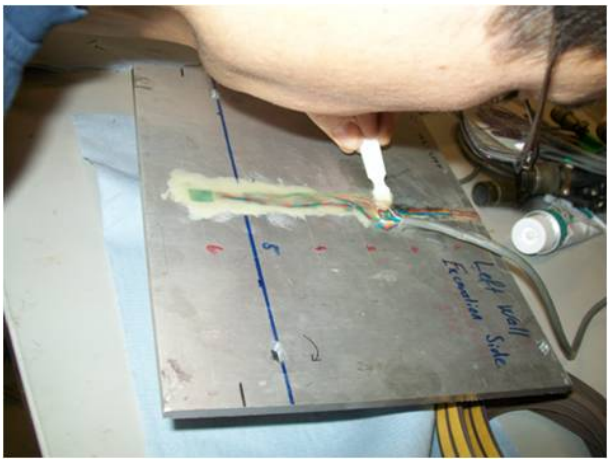

Figure 2.29: Covering strain gauges with epoxy resin.

The strain gauges have been calibrated clumping the wall at the top or at the bottom and applying a known load at the free extremity. The procedure has been repeated two times, the first with the load applied from the soil side and the second one with the load applied from the retained side. The resulting relation is typically linear for each strain gauge and the variation of the output voltage against the variation of a known applied load represents the calibration factor. The readings and the corresponding applied bending moments are plot together in Figure 2.31 where also the calibration factors are reported as well.

The calibration factor is quite sensitive to the procedure of calibration. In fact the applied bending moment has been calculated assuming a uniform distribution of the load along the wall, which is true in case of a perfectly fixed rotation along the entire edge of the wall at the bottom (respectively top) and a uniform distribution of the load at the top (respectively bottom). The first condition is feasible correctly using the clumps (Figure 2.32). Usu-

ally three clumps, with one of them exactly placed at the center of the wall, have been used. The second condition is less easily feasible due to the defections of the walls surface and of the bar used to apply the load. A significant percent variation (about 30%) of the calibration factor has been observed for the strain gauges close to the clump when it is not properly realized, while stable values have been obtained when the above-mentioned clumps configuration has been adopted for the calibration.

The rotation can be reasonably considered fixed when the clumps are properly used, the uniform distribution of the load is harder to obtain. In fact the calibration factor of the strain gauges close to the load can vary significantly. The calibration factors of the strain gauges for all the test are summarized in Tab.2.3, in Tab.2.4, in Tab.2.5 and in Tab.2.6.

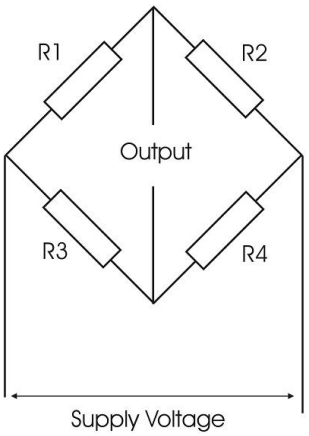

Figure 2.30: Electrical scheme of a Wheatstone bridge.

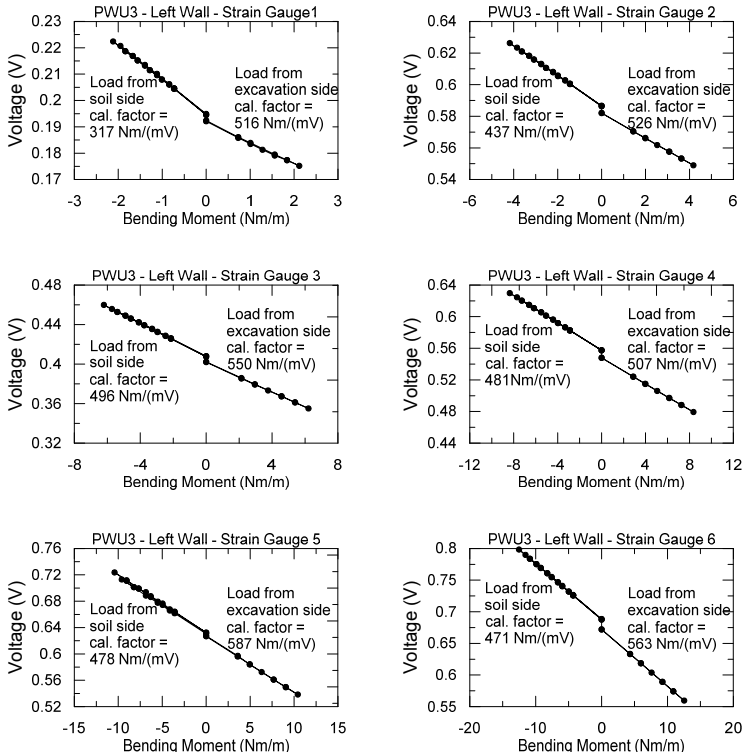

Figure 2.31: Calibration data of the strain gauges of left wall of test PWU3.

Figure 2.32: Calibration of left wall clumping at the base and loading from the top.

It can be noticed that:

1. there is a significant variation of the calibration factor of the strain

Tests CWU1 and PWU1	Left Wall Load from Excavation Side	Left Wall Load from Soil Side	Right Wall Load from Excavation Side	Right Wall Load from Soil Side
SG2	583	539	421	421
SG3	584	551	446	455
SG4	545	511	481	482
SG5	533	494	553	503

Table 2.4: Calibration factors of strain gauges for tests CWU1 and PWU1.

Test CWU2	Left Wall Load from Excavation Side	Left Wall Load from Soil Side	Right Wall Load from Excavation Side	Right Wall Load from Soil Side
SG2	613	577	682	618
SG3	613	585	658	634
SG4	553	536	678	644
SG5	537	526	668	639
SG6	535	517	611	659

Table 2.5: Calibration factors of strain gauges for test CWU2.

Test PWU2	Left Wall Load from Excavation Side	Left Wall Load from Soil Side	Right Wall Load from Excavation Side	Right Wall Load from Soil Side
SG2	501	532	480	454
SG3	600	610	520	501
SG4	553	554	560	539
SG5	537	536	554	531
SG6	535	486	540	506

Table 2.6: Calibration factors of strain gauges for test PWU2.

Tests CWU3, PWU3 and CWU4	Left Wall Load from Excavation Side	Left Wall Load from Soil Side	Right Wall Load from Excavation Side	Right Wall Load from Soil Side
SG1	516	317	772	369
SG2	526	437	583	441
SG3	550	496	540	480
SG4	507	481	512	486
SG5	487	478	523	479
SG6	463	471	524	484

Table 2.7: Calibration factors of strain gauges for test CWU3, PWU3 and CWU4

gauges even if, since the structural characteristic are basically the same from one strain gauge to the other, this is not expected;

2. the slope of the regression line, for a given strain gauge, changes if the load is applied from the soil side or from the excavation side.

LVDTs

The DC15 LVDTs have been used to measure the horizontal displacements of the walls and the settlements of the soil surface, as it is illustrated in Figure 2.33. The LVDTs tend to suffer from high frequency noise (Kutter & Balakrishnan, 1998), thus the output signals are not suitable to obtain the dynamic component of the displacement, while the displacements related to low frequencies are considered reliable.

Calibration of LVDTs has been performed by creating a data base of readings versus distances measured with a digital calliper over the full measuring range of the instrument, with about 5mm steps and maximum displacement of 40mm (Figure 2.34). The $x - y$ graph obtained is always remarkably linear in every case. As an example, calibration factor and R^2 value for LVDT1 of test CWU1 are presented in Figure 2.35

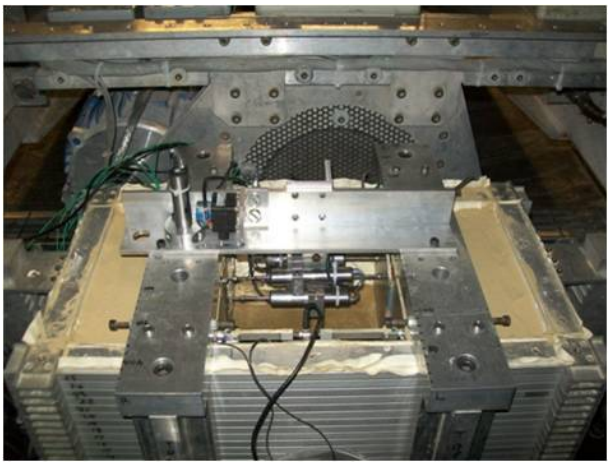

Figure 2.33: LVDTs measuring horizontal displacements of the walls and the vertical settlements of the soil in the model of test CWU1.

Figure 2.34: Calibration of an LVDT

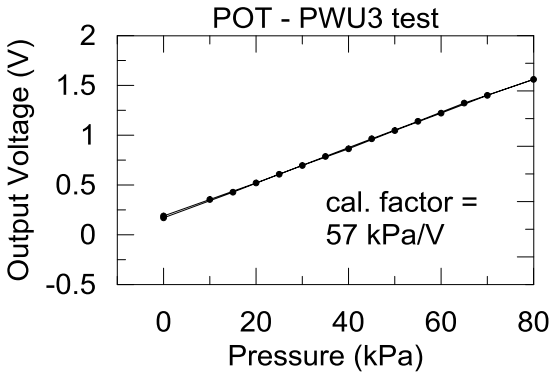

Figure 2.35: Calibration results of the LVDTs relative to test PWU3.

Potentiometer

A wire potentiometer (Figure 2.36) has been used for measuring the settlements of the walls in tests PWU1 and CWU2 (Figure 2.37). The wire is stuck on the top of the wall through a screw, thus the wire measures the walls settlement. Its calibration has been carried out progressively extending the wire of known quantities and reading the output voltage (Figure 2.38).

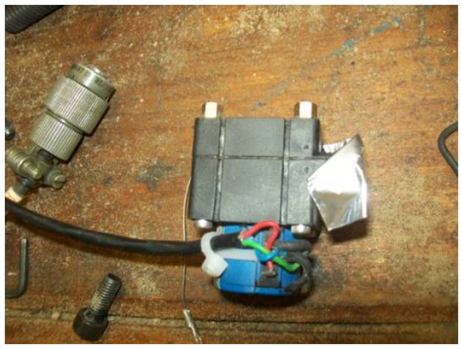

Figure 2.36: Wire Potentiometer

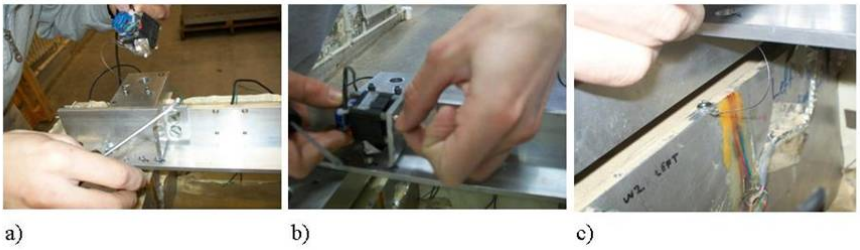

Figure 2.37: Test PWU1. a) and b) positioning the potentiometer on the support; c) linking the potentiometer cable to the top of the wall.

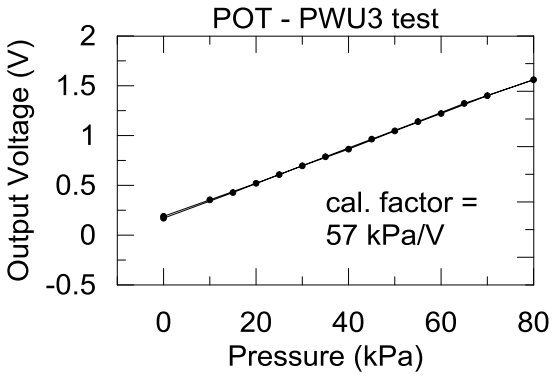

Figure 2.38: Calibration data of potentiometer of test PWU3.

Load Cells

Load cells have been used to measure the axial force in the props. The load cells F250UFROHO (Figure 2.39) are produced by Novatech and they convert a force into a linear electrical signal through the measure of minute movements in a precision metal structure using foil strain gauges bonded to the surface of the metal. They function both in compression and in tension and both in static and dynamic conditions. Their mass is between 8 and 12 grams and the maximum measurable force is 200 N. The load cells are screwed in the middle of the props (Figure 2.40) and they are calibrated applying a known tensile axial force and measuring the output voltage. The calibration factor of the Load Cells in normally about 500 N/V (Figure 2.41).

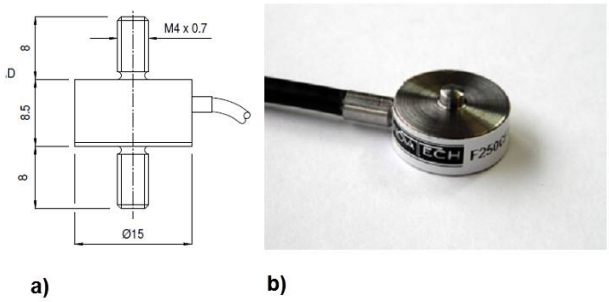

Figure 2.39: Load cell F250 from Novatech. a) schematic, b) photo of the instrument.

Figure 2.40: Load cells on the props of test PWU1.

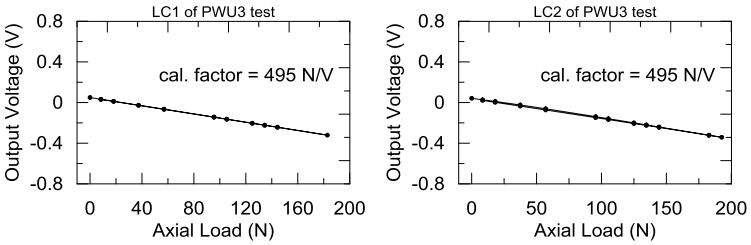

Figure 2.41: Calibration of Load Cells of test PWU3.

Pressure sensor

An ultra thin-film tactile pressure sensor has been used to measure the total normal stress acting on the wall in CWU3 and PWU3 test. It is frequently used in industry, medicine, and dentistry fields. The pressure sensor is 0.1 mm thck and it is produced by Tekscan Inc. It is comprised by numerous individual sensing elements, called sensels (Figure 2.42). It consists of two thin, flexible polyester sheets which have electrically conductive electrodes deposited in varying patterns. The inside surface of one sheet forms a row pattern while the inner surface of the other employs a column pattern. The intersection of these rows and columns creates a sensing cell. The spacing between the rows and columns varies according to sensor application and can be as small as 0.5 mm.

The sensor grid used for tests CWU3 and PWU3 is the 5250 type. It has a rectangular size and a matrix width and a matrix height of 245.9 mm and 245.9 mm respectively. The overall length and the overall width are 622.5 and 358.4 mm respectively (Figure2.42). The grid is composed of 44 rows and 44 columns and the sensel density is of 3.2 sensels/cm^2.

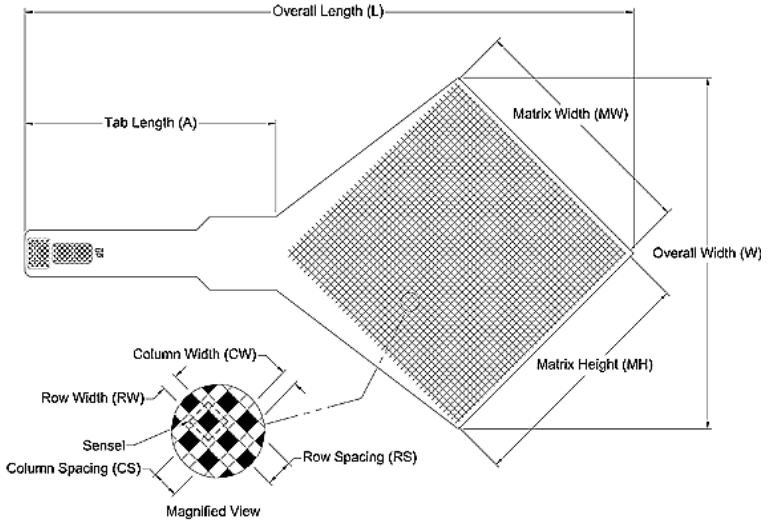

Figure 2.42: Geometrical characteristics of the pressure sensor.

The resistance of the sensing elements (sensels) varies inversely with applied load. The system linearizes sensor output into digital counts, or raw values on a scale from 0-255. Calibration converts raw values into kPa. A typical sensor performance is illustrated in Figure 2.43.

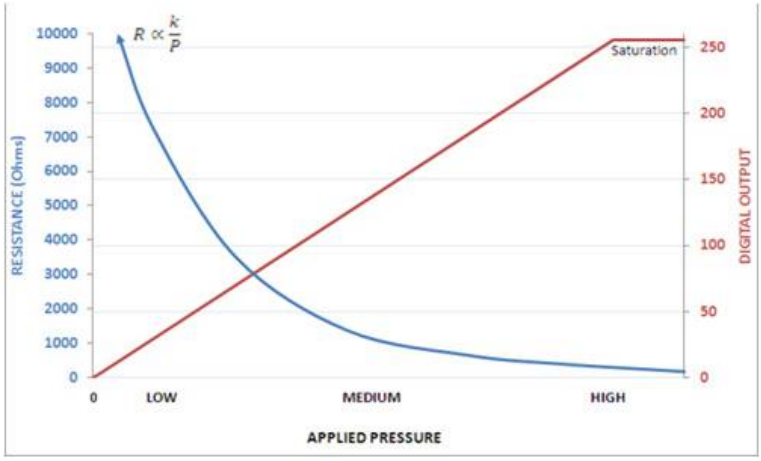

Figure 2.43: Typical sensor performance (taken from Tekscan Inc. web site).

The pressure sensor functions in both static and dynamic condition and the maximum sampling rate is 20 kHz. The data acquisition is carried out through a sophisticated microprocessor based circuitry that controls scanning sequence and frequency, adjusts sensitivity, and optimize the performance of matrix-based sensors. Figure 2.44 illustrates the sensing system and a simplified electrical schematic of the 8 bit electronics that scan the intersecting points of the sensor rows and columns and measure the resistance at each crossing point (sensel). Each sensel is represented by a variable resistor whose value is highest when no force is applied to it. The calibration of the pressure sensor is easily guided by the software that collects the data that are stored into the computer via a USB cable. So the sensor pressure does not affect the available channels for the other instruments in the junction boxes. The calibration is performed increasing the uniformly applied load on the surface of the film (Figure 2.45).

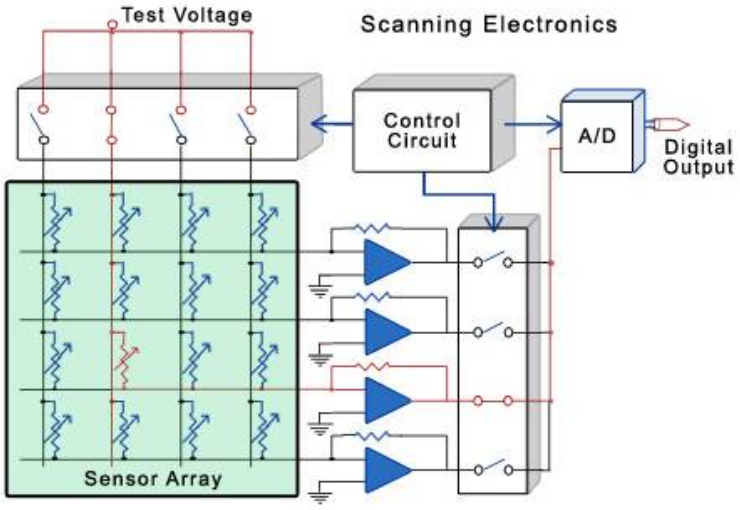

Figure 2.44: Electrical schematic of the data acquisition system

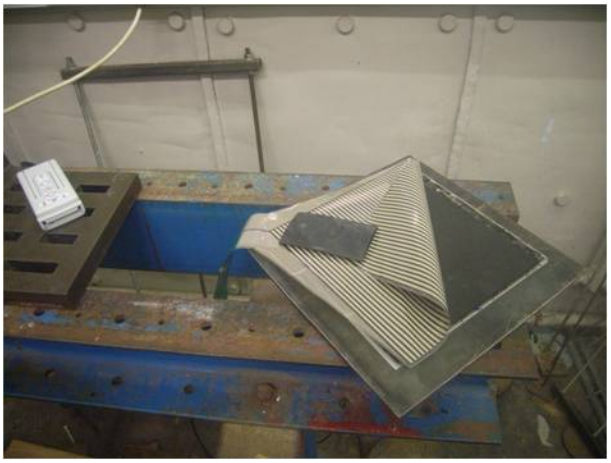

Figure 2.45: Calibration of the sensor pressure.

2.4 Model Preparation

This paragraph describes how the model preparation is made focusing on the common aspects that regard all the models of the present work. They are:

1. Sand pouring;

2. Placement of the instruments;

3. Placement of the wall;

4. Saturation of the model.

To this purpose the model PWU3, whose layout is reported in Figure 2.46, has been considered as an example.

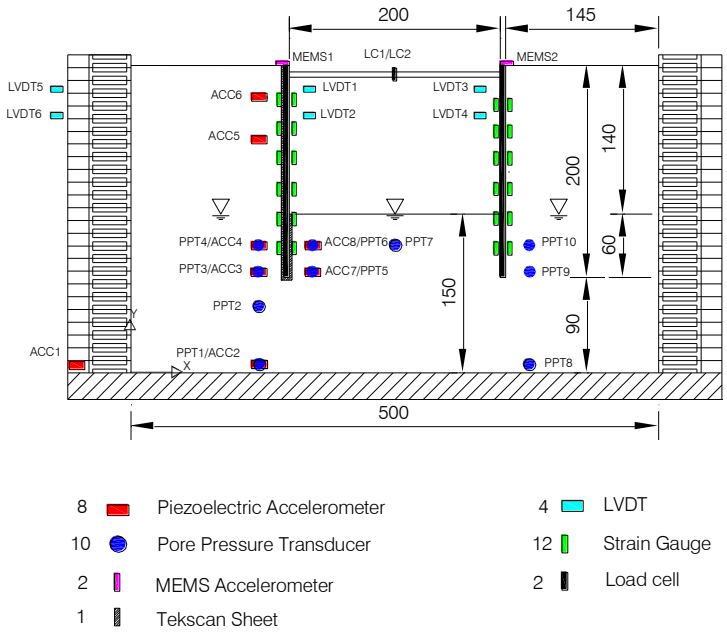

Figure 2.46: PWU3 layout. All the distances in millimeters.

2.4.1 Sand Pouring, Instruments placement, Walls placement.

Considering the layout of the test PWU3 in Figure 2.46, the accelerometer ACC1 has been placed at the bottom of the laminar box and represents the input signal. The other eight accelerometers have been placed along two vertical alignments in order to have the possibility to study the amplification effects of the signal during the earthquake. The first alignment is at the back of the left wall and contains an amount of six accelerometers; four of them are placed below the piezometric head of the porous fluid, and the

remaining two lie above that depth. The accelerometers ACC7 and ACC8 have been placed in the excavated side. Like the accelerometers, the pore pressure transducers have been placed along two different alignments and at the same depths of the accelerometers. At a given depth, the accelerometer and the PPT have been shifted along the depth of the model (Figure 2.47).

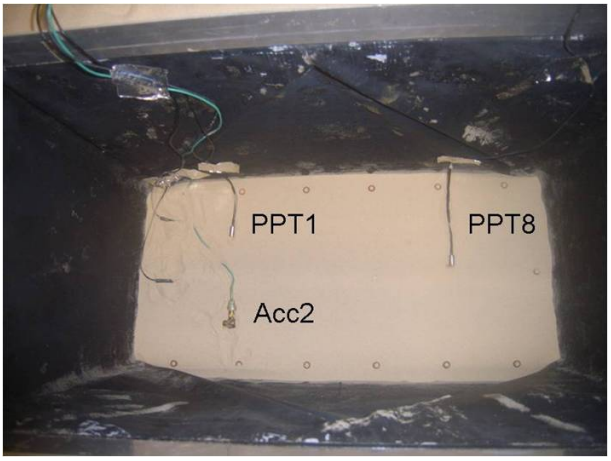

Figure 2.47: ACC2 and PPT1 placed at the same depth and shifted along the depth of the laminar box.

The instruments close to the sand surface or close to the excavation level, like ACC6, PPT6, PPT7 and ACC8 in Figure 2.46, have been placed 3cm below the surface in order to ensure that the instrument actually moves together with the soil. The model is built progressively pouring the sand up to the depths where the instruments have to be placed according to the layout. The piezoelectric accelerometers and PPTs are manually placed at the desired depth. The wire of the instruments is stuck on the internal part of the laminar box leaving the possibility to the instrument to move and follow the displacements of the soil during the test. In Figure 2.48(a) the placing of an accelerometer is illustrated. In case when the instrument depth is higher than the depth of the walls bottom, they have been chosen to be about 25 mm far (model scale) from the wall. Such distance is considered to be large enough in order not to determine a concentrated action against the wall during the test due to the inertia force related to the mass of the instrument, but at the same time it allows to obtain a measurement (acceleration or pore water pressure) that can be approximately considered as acting on the wall. Once the excavation level has been reached, the walls are placed and the sand pouring continues depositing sand only on the back

sides of the walls.

The walls are positioned at the same time by means of two pairs of props and vertical marks on the internal sides of the laminar box in order to achieve the uprightness of the walls (Figure 2.48(b). Moreover, in order to prevent a possible transit of sand from the retained side to the excavation side through the gap between the walls and the laminar box, on the back side of the walls and both on the left and on the right (Figure 2.49) a fan shaped plastic sheet has been glued. One of the fun is glued on the wall, and the other one is glued on the laminar box. In this way, when the wall moves, the fan follows the walls movement extending and remaining attached both to the wall and to laminar box. Attention is paid to leave a slack between the edge of the walls and the internal side of the laminar box in order to preserve the plane strain condition. The wall movement is not prevented by the fan and at the meantime the sand cannot pass through the slack between the wall and the laminar box.

The LVDTs measuring the horizontal displacements of the walls have been placed using a bar parallel to the long side of the laminar box leaning against the cross bars of the laminar box (Figure 2.50(a) and Figure2.50(b).

In the case of tests CWU3 and PWU3 the pressure sensor has been used to measure the total pressure acting on the left wall. The pressure sensor has been waterproofed using a heated laminator, that is passing the pressure sensor film through the laminator and inserting it between two plastic films. Due to the presence of the strain gauges in the middle of the wall, the pressure sensor film has been cut and only 11 columns of sensels have been used.

The pressure sensor film cut and waterproofed has been then placed on the wall as shown in Figure 2.51 and in Figure 2.52. In test CWU3 the pressure sensor covers the entire active side and partially the excavated side, while in test PWU3 it covers the entire active side and passive side. For both tests it covers 11cm over the 24cm of the entire width of the wall; the covering of the whole width of the wall is prevented by the presence of the strain gauges.

Figure 2.48: a) accelerometer positioning, b) wall positioning.

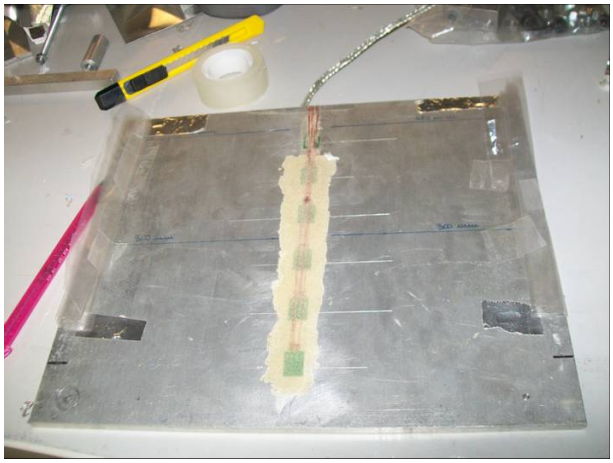

Figure 2.49: Fans that prevent sand transit from active side to passive side glued on the sides of the wall.

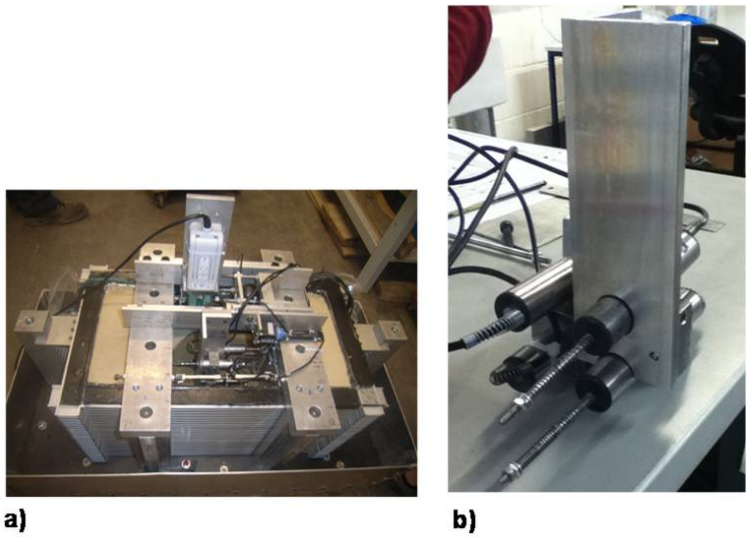

Figure 2.50: LVDT support.

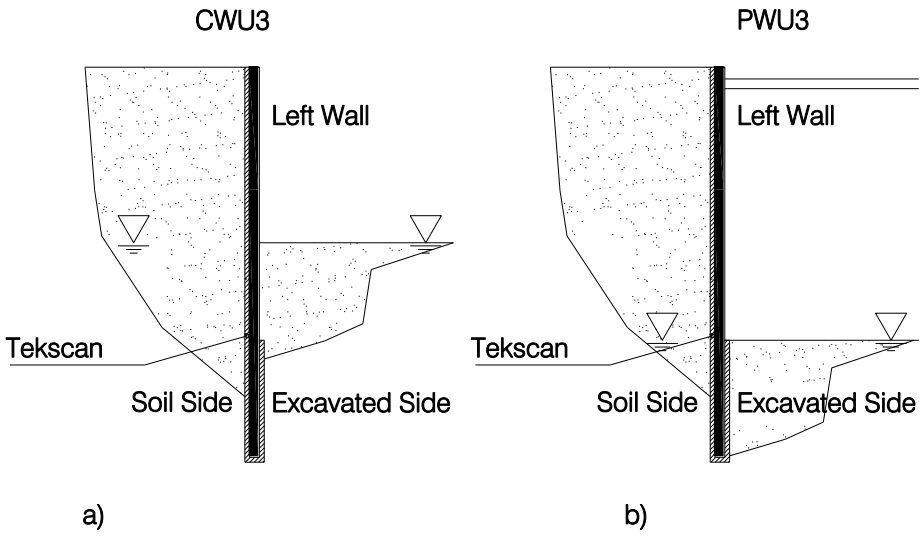

Figure 2.51: Scheme of pressure sensor installation on the wall for tests CWU3 and PWU3 (frontal view).

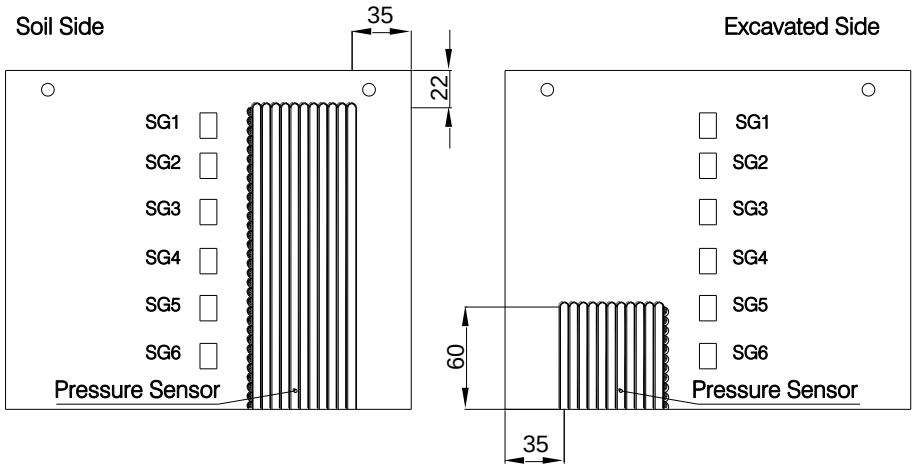

Figure 2.52: Scheme of pressure sensor installation on the wall for tests CWU3 and PWU3 (lateral view).

2.4.2 Saturation

The models were saturated using an experimental set-up developed at Cambridge University (Stringer and Madabhushi, 2009). The CAM-sat (Figure 2.53) is a computer-controlled system which is capable of: (i) monitoring continuously the rate of fluid entering the model; (ii) controlling the mass flow within specified targets; (iii) running for long periods without supervision.

A positive pressure difference drives fluid flow from a tank containing the viscous fluid into the model. The model is placed under vacuum to improve the degree of saturation. The mass flow into the model is measured using a set of digital scales and the rate of saturation controlled by altering the vacuum applied to the reservoir.

Before the saturation, the mass of the methylcellulose needed to fill the pores of the soil up the depth desired is computed. An example of the calculation of the HPCM needed for the saturation of the propped test in dense sand is given hereinafter.

In the schematic Figure 2.54, a propped test in flight is reported and the surface of the HPCM is represented by the arch AB. The surface where the HPCM during the test lies is the circumference having as centre the centre of the centrifuge O; this is due to the presence of the centrifuge force. The mass of HPCM to be computed has to fill the pores the volume relative to

the A_{AFGBD}; it can be computed knowing the relative density D_r of the sand, the density of the HPCM and the following geometrical quantities:

1. the width of the laminar box L and the depth of the model d ;
2. $r_1 = 3.75m$, the distance between the centre of the centrifuge and the base of the laminar box;
3. $l_1 = 0.150m$, the distance from the base of the laminar box and the excavation level;
4. $r_2 = r_1 - l_1 = 3.60m$, the distance between the centre of the centrifuge and the excavation level.

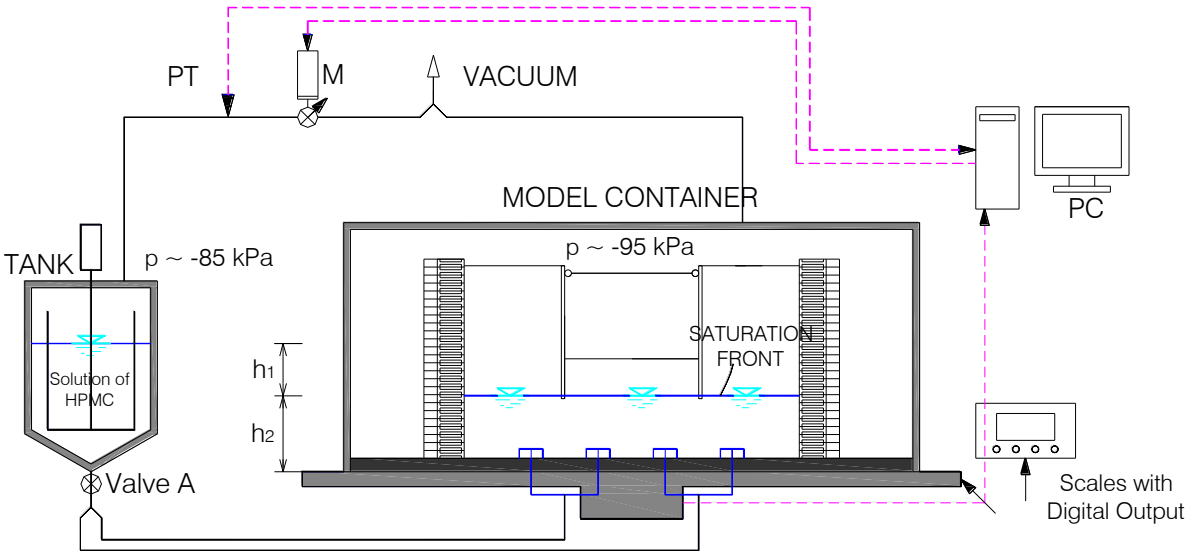

Figure 2.53: CAM-sat system used for saturating models developed at the Schofield Centre.

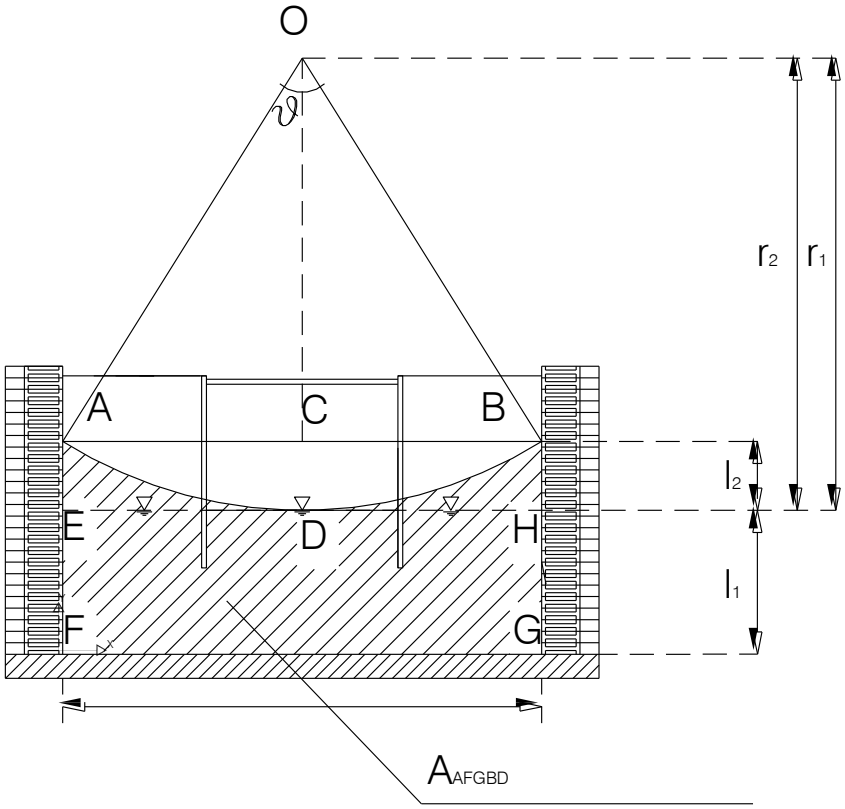

Figure 2.54: Area A_{AFGBD} occupied by the HPCM during the flight (not drawn to scale).

In case of propped test in dense sand the relative density obtained from the calibration of the sand hopper is $D_r = 88\%$, so the void index is:

$$e = e_{max} - D_r(e_{max} - e_{min}) = 1.014 - 0.89(1.014 - 0.613) = 0.657 \quad (2.36)$$

The mass of HPCM needed to fill the pores relative to the volume $V_{EFGH} = A_{EFGH} \cdot d$ (Figure 2.55) is:

$$M_{EFGH} = \frac{V_{EFGH} \cdot e}{1+e} \cdot \rho_{HPCM} = \frac{\bar{EFGH} \cdot d \cdot e}{1+e} \cdot \rho_{HPCM} = \frac{0.15 \cdot 0.5 \cdot 0.25 \cdot 0.65711}{1.65711} \cdot 100 \frac{kg}{m^3} = 7.43l. \quad (2.37)$$

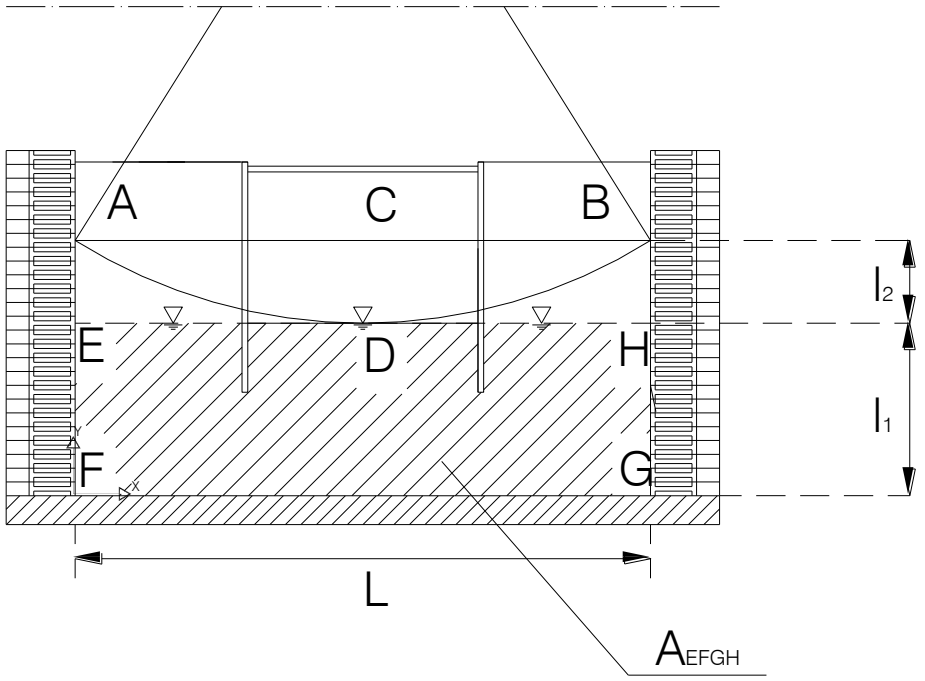

Figure 2.55: Area A_{EFGH} (not drawn to scale).

In addition to M_{EFGH} the mass relative to the volume $V_{AEDHB} = V_{AEDHB} \cdot d$ (Figure 2.56) has to be computed in order to take into account the curvature of the HPCM surface during the test.

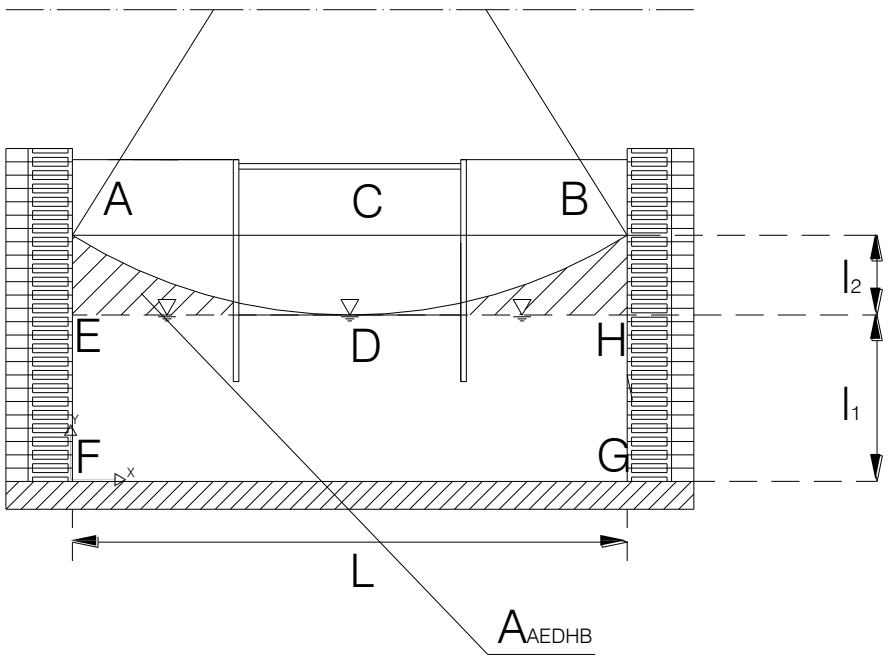

Figure 2.56: Area A_{AEDHB} (not drawn to scale).

To do this, firstly the angle θ is computed as follows:

$$\sin(\frac{\theta}{2}) = \frac{L/2}{r_2} = \frac{0.25m}{3.60m} \Longrightarrow \theta = 2 \cdot \arcsin(\frac{0.25}{3.60}) = 0.13rad. \tag{2.38}$$

So the area A_{ADBC} of the circular segment ADBC (Figure2.57) is:

$$A_{ADBC} = \frac{1}{2}(\theta - \sin\theta)R^2 = 0.5(0.13 - \sin(0.13)) \cdot 3.60^2 m^2 = 0.0008m^2. \tag{2.39}$$

and the relative volume V_{ADBC} is obtained as:

$$V_{ADBC} = A_{ADBC} \cdot d = 0.0008 \cdot 0.25m^3 = 0.0007m^3. \tag{2.40}$$

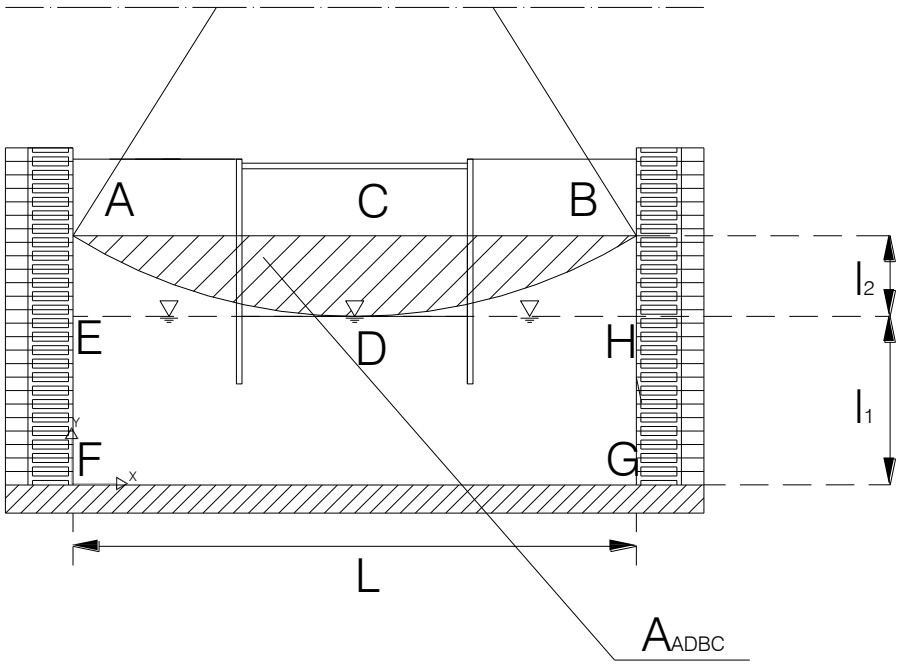

Figure 2.57: Area A_{ADBC} (not drawn to scale).

l_2, the distance between the excavation level and the point of intersection of the arch AB and the vertical edge of the laminar box is:

$$l_2 = r_2 - r_2 \cos\frac{\theta}{2} = 3.6035 - 3.6035 \cos\frac{\theta}{2} = 0.008683m. \tag{2.41}$$

The volume V_{AEHB} (Figure 2.58) is:

$$V_{AEHB} = l_2 \cdot L \cdot d = 0.0086 \cdot 0.5 \cdot 0.25 = 0.0010m^3, \tag{2.42}$$

thus,

$$V_{AEHB} = V_{AEHB} - V_{ADBC} = (0.0010 - 0.0070)m^3 = 0.0003m^3. \tag{2.43}$$

So the corresponding mass $M_{AEHDB} = 0.36kg$. So the to the total mass of HPCM needed is $M_{HPCM} = 7.8kg$.

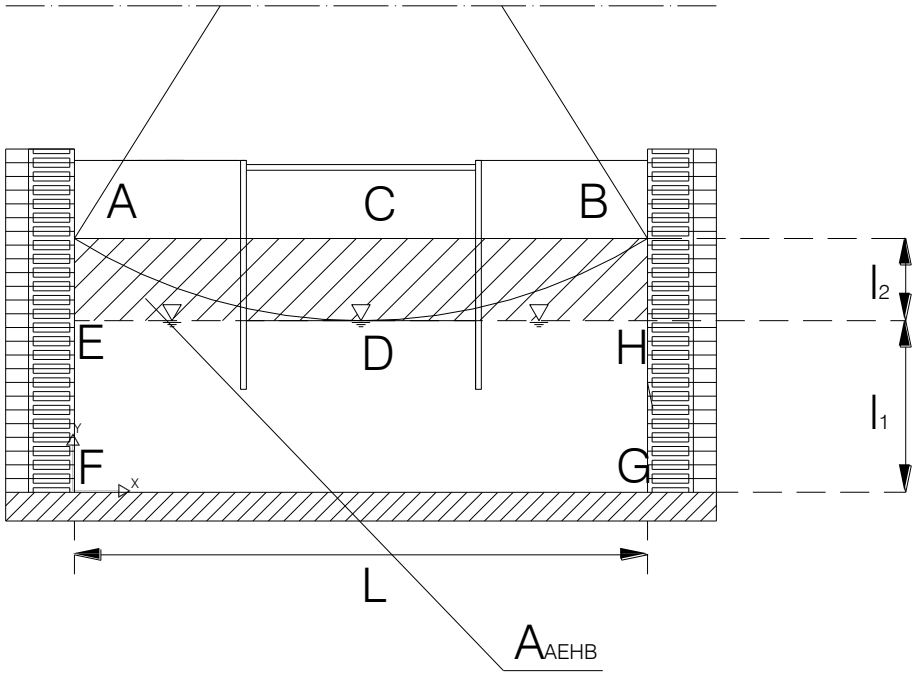

Figure 2.58: Area A_{AEHB} (not drawn to scale).

Before the saturation, the model is hermetically closed inside a tank and then the air into the pores is replaced with CO_2 in order to improve the degree of saturation. When the valve A is open the methylcellulose flows into the model until the saturation is completed. During the saturation, scales measure the current mass of the model, which is converted to the mass flow rate.

The flow rate is kept within thresholds that are set by the user. When the current flow rate is outside the interval set by the thresholds, an adjustment of the vacuum exerted on the tank of the HPCM is needed. So the current vacuum pressure is read and the vacuum regulator is adjusted until the pressure on the HPCM tank is achieved and the flow rate is restored within the thresholds. The upper threshold is calculated imposing that the pressure gradient due to hydraulic gradient must be less than or equal to the buoyant unit weigh at the point where the fluid breaks the surface:

$$\frac{dp}{dz} = \gamma_w \frac{dh}{dz} = \gamma_w \cdot i \leq \left(\frac{G_s + S_r - e}{1 + e} - 1 \right) \tag{2.44}$$

where $\frac{dp}{dz} = \gamma_w \frac{dh}{dz} = \gamma_w \cdot i \leq \left(\frac{G_s+S_r-e}{1+e} - 1\right)$ is the buoyant unit weight of the soil. The corresponding flow rate is computed assuming that one-dimensional flow up-ward occurs during saturation (Stringer and Madabhushi, 2009):

$$Q_{max} = A \cdot Ki_{max} < AK_{water} \frac{\nu_{water}}{\nu_{viscous}} \left(\frac{G_s + S_r - e}{1 + e} - 1\right) \tag{2.45}$$

In the tests of the present work has been equal about to 0.5 kg/h, while the lower threshold has been set equal to 0.15 kg/h.

2.5 Centrifuge Preparation

2.5.1 Balance Calculation

When sand pouring and the saturation are completed, an accurate balance of the centrifuge arm is follows. The computation of the balance includes a list of all the masses and centre of masses for every component of the centrifuge package in order to obtain the necessary counterweight to put in the centrifuge. The tests are only carried out if the total mass of the package, which is checked just before loading, confirms calculations.

2.5.2 Pre-flight operations

The counterweight is loaded onto the centrifuge on its red end and then the SAM actuator without the model was installed on the beam on its blue end. At this point the model is put on the SAM and cables are connected to the Junction boxes, checking the position of all transducers and the tightness of cable connections. Once the model is in the centrifuge, the data acquisition, the triggering system and the pressure in the accumulator required to activate SAM fast-acting clutch are checked before starting the test.

2.6 Test Procedures

All the tests have been carried out at a value of the centrifuge acceleration of 40g. When the test starts the centrifuge is swung up in four steps of 10g up to 40g. At each stage the readings of transducers are taken. After the testing acceleration of 40g is reached at the base of the model the earthquakes are fired. During each test, the model was subjected to a series of

trains of approximately sinusoidal waves with different nominal frequencies, f, amplitudes, a_{max}, and durations, t. For each test, the data acquisition has been performed both during the earthquake and after the earthquake. In fact, during the earthquake, pore pressure build-up is normally observed, and after the earthquake a consolidation phase takes place. The monitoring of the consolidation phase terminates when the pore pressure transducers stabilize indicating the dissipation of the excess pore pressures. Moreover, the models are permanently monitored through a camera installed on the beam. When the test finishes the surface profile of the model is measured and the model container is taken out of the pit.

2.7 Summary

In this Chapter the principles of centrifuge modelling, the instrumentation used for the monitoring of the soil-structure system, the preparation of the model and the test procedure have been illustrated; this represents the basic information for the following Chapters where the results of the experimental campaign are illustrated and the interpretation of the results is carried out.

Chapter 3

Test Data - Part I

This Chapter is dedicated to the description of the test data concentrated at the single test level. In the first part the models are described in terms of geometry, relative density and earthquake characteristics. Then the test data are illustrated and commented. At the summary of the Chapter a first comparison of the tests response is made. A more extended analysis of test data is conducted in Chapter 4.

A total of seven dynamic centrifuge tests on flexible retaining walls embedded in saturated sand have been carried out. Two different types of structure have been chosen: a pair of cantilever walls and a pair of walls with one level of props near the top. The sand has been reconstituted at high and low relative density in order to investigate the effect of the density of the sand on the seismic behaviour of such structures.

The geometrical characteristics of the models have been chosen in order to satisfy as much as possible the correspondence with the geometries relative to the tests performed in dry sand by Conti (2010). This choice allows to isolate the effect of the presence of the water by comparing the results of this experimental campaign with the previous one. In the tests performed by Conti (2010) the ratio between the embedded length d and the retained height H is 0.428 for the propped tests and 1 for the cantilevered tests. For the tests on propped walls, the ratio d/H has been kept 0.428 like in Conti (2010), while for the tests on cantilevered walls the ratio d/H has been chosen to be d/H=1.22. In fact for d/H=1 it would have probably determined the collapse of the walls during the swing up of the model, because the static safety factor correspondent to d/H=1 was lower than 1. On the other hand, for a d/H=1.22 the static safety factor is 1.2.

In all the tests the piezometric head of the porous fluid has been chosen to

be at the dredge level. This choice is imposed by the difficulty to maintain a difference in the piezometric head from the back of the walls and the excavated side during the flight of the centrifuge tests; moreover this choice implies the absence of seepage phenomena during the tests, which would complicate the interpretation of the results.

The tests are reported with respect to chronology in Table 3.1. The tests CWU1 (Cantilevered Walls Undrained number 1), PWU1 (Propped Walls Undrained number 2), CWU2 and PWU2 have been carried out in the period included between January 2012 and July 2012, while tests CWU3, PWU3 and CWU4 have been carried out during the period included between July and August 2013.

The tests CWU1, PWU1 have been performed in loose sand ($D_r = 38\%$) while the remaining tests CWU2, PWU2, CWU3, PWU3 and CWU4 have been performed in dense sand ($D_r = 88\%$). The geometrical characteristics of the tests at the model scale and at the prototype scale are reported in Table 3.2. The relative densities ($D_r = 38\%$) and ($D_r = 88\%$) are intended as the nominal value of the relative density obtained from the calibration of the sand hopper. In paragraph 3.2 the aspect regarding the real value of the relative density obtained with the sand pouring within the model is treated specifically.

As already explained in Chapter 2, accelerometers and pore pressure transducers have been placed within the soil in order to monitor the accelerations and the pore pressures. Accelerometers and pore pressure transducers have been placed in all the models along vertical alignments and at the same depth, both at the back of the walls and in the excavated side; see for instance Figure 3.1 where the vertical alignments of piezoelectric accelerometers and pore pressure transducers at the back of the left wall in test PWU3 are illustrated. The vertical alignment of accelerometers allows also to study the amplification phenomena and to determine the (τ, γ) cyclic response of the soil during the tests.

Test	Period/Date	Procedure
CWU1	09/01/2012 -19/01/2012	Model Preparation
	19/01/2012	Test Execution
PWU1	23/01/2012 - 02/02/2012	Model Preparation
	02/02/2012	Test Execution
CWU2	23/04/2012 - 08/05/2012	Model Preparation
	08/05/2012	Test Execution
PWU2	18/06/2012 - 27/06/2012	Model Preparation
	27/06/2012	Test Execution
CWU3	13/07/2013 - 25/07/2013	Model Preparation
	25/07/2013	Test Execution
CWU4	30/07/2013 - 06/08/2013	Model Preparation
	06/08/2013	Test Execution

Table 3.1: Chronological Sequence of the tests and their preparation and execution.

			Model Scale (mm)					Protoype Scale (mm)				
Test	$D_r(\%)$	N	h	d	s	H	B	h	d	s	H	B
CWU1	38(%)	40	90	110	-	290	200	3.6	4.4	-	10.8	8
PWU1	38(%)	40	140	60	9	290	200	5.6	2.4	0.36	10.8	8
CWU2	88(%)	40	90	110	-	290	200	3.6	4.4	-	10.8	8
PWU2	88(%)	40	140	60	9	290	200	5.6	2.4	0.36	10.8	8
CWU3	88(%)	40	90	110	-	290	200	3.6	4.4	-	10.8	8
PWU3	88(%)	40	140	60	9	290	200	5.6	2.4	0.36	10.8	8
CWU4	88(%)	40	90	110	-	290	200	3.6	4.4	-	10.8	8

Table 3.2: Geometrical properties of the tests at the model scale and at the prototype scale.

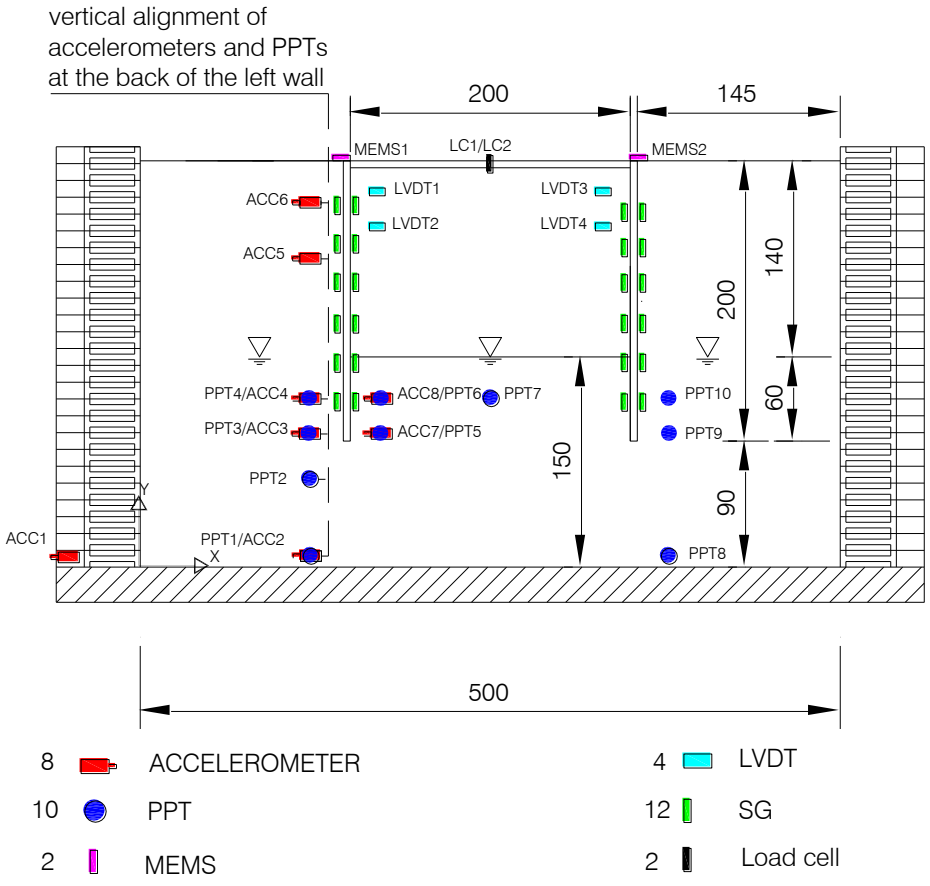

Figure 3.1: Test PWU3 layout, vertical alignment of accelerometers and pore pressure transducers at the back of the left wall.

The walls are monitored using LVDTs for the horizontal displacements, a potentiometer for the settlements and a MEMS accelerometer for the horizontal accelerations at the top of the walls. Besides the LVDTs used to measure the horizontal displacements of the walls, in some tests a single or a pair LVDTs have been used to measure the settlements of the soil surface. LVDTs have also been used to measure laminar box horizontal displacements for tests CWU3 and PWU3. In fact, the support of the LVDTs that measure the horizontal displacements of the walls moves together with the laminar box base plate because it is rigidly connected to the base plate through the

cross bars and the vertical bars of the laminar box (Figure 3.2).The measure of laminar box displacements through LVDTs for tests CWU3 and PWU3 has been carried out at the same depth of the LVDTs measuring the horizontal displacements of the walls in order to have the possibility to deduct the laminar box displacement from the walls displacements. Since the walls displacements contain the laminar box displacement an issue regarding the plot of the displacements has emerged; this aspect is treated specifically in the introduction to test data presented in paragraph 3.2

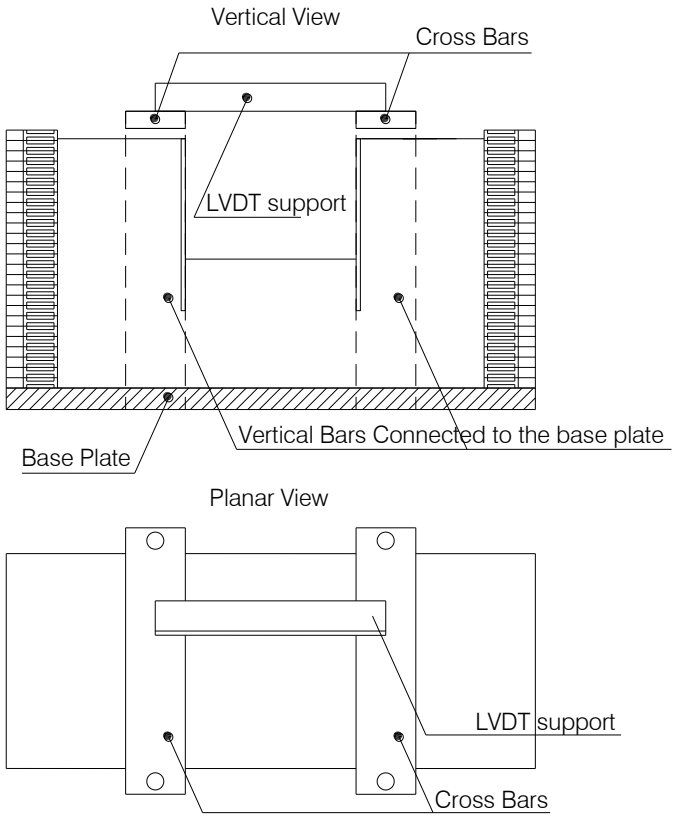

Figure 3.2: Scheme of the LVDT support connected to the base plate of the laminar box: vertical and planar view.

In some tests (i.e. CWU1, CWU2, PWU1 and PWU2) a piezoelectric accelerometer has been placed on the support of the LVDTs because in some

previous dynamic centrifuge tests (Conti, 2010) the LVDTs signals have been seen to be affected by the oscillations of the support. It has been verified through the visualization of the Fourier transform of the signal of the LVDTs that the only significant frequency characterizing the signal coincides with the dominant frequency of the signal. So it has been seen that in these tests the support does not influence the LVDTs signal.

Each model has been subjected to two or three consecutive earthquakes, specifically the tests CWU1 and PWU1 have been subjected to two earthquakes and the tests CWU2, CWU3, PWU2 and PWU3 have been subjected to three earthquakes. The post earthquake behaviour has been monitored as well, because of pore pressure dissipation and the coupled soil response that follows the earthquake. All the earthquakes are a quasi-sinusoidal waves whose peak acceleration increases passing from one earthquake to the following one. For all the tests the frequency of the earthquakes has been approximately 50 Hz at the model scale, corresponding to 1.25 Hz at the prototype scale. The first earthquake has been chosen to have a peak acceleration of about 0.1g, while the second and the third one have been chosen to have an acceleration of about 0.20g and 0.25-0.30g respectively at the prototype scale. The duration of each earthquake has been included between 18s and 33s at prototype scale.

In paragraph 3.1 the geometry of the models and the earthquakes characteristics are described in detail, while in paragraph 3.2 the test data are reported and commented.

3.1 Geometry of the Models

Each model configuration is described in detail hereinafter. All geometric lengths are reported at the model scale and are expressed in millimeters.

In Table 3.2 the geometrical properties of the models that will be described have been shown besides their equivalent length at the prototype scale. The geometrical quantities refer to the scheme illustrated in Figure 3.3. Again, the relative density hereinafter reported are those from the calibration of the sand hopper, namely 38% and 88%. It is reminded that in paragraph 3.2 this aspect is treated specifically.

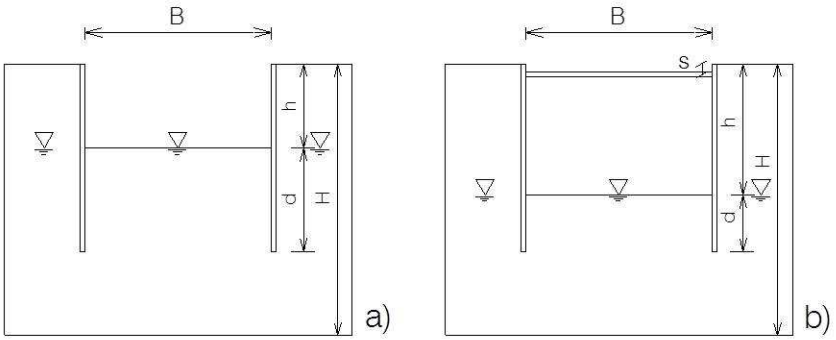

Figure 3.3: Scheme of the models and principal geometric characteristics: (a) CWU tests on cantilevered walls and (b) PWU tests on propped walls.

3.1.1 CWU1

Test CWU1 has been performed on a pair of cantilevered retaining walls with a retained height of 110mm and an embedded length of 90mm. The relative density D_r of the sand is about 38%. The layout of the model is reported in Figure 3.4. The instrumentation consists of:

1. 8 piezoelectric accelerometers: 7 measuring the soil acceleration and 1 measuring the acceleration of the support of the LVDTs;
2. 8 Pore Pressure Transducers;
3. 8 Strain Gauges;
4. 6 LVDTs: two of them measuring the soil surface displacement and four of them measuring the horizontal displacement of the walls.

The main characteristics of the input earthquakes are listed below in Table 3.3.

Test	Earthquake	f(Hz)	$a_{max}(g)$	Duration (s)
CWU1 (Model Scale)	EQ1	50	4.0	0.62
	EQ2	50	8.0	0.62
CWU1 (Prototype Scale)	EQ1	1.25	0.10	25
	EQ2	1.25	0.2	25

Table 3.3: Test CWU1: characteristics of the input earthquakes.

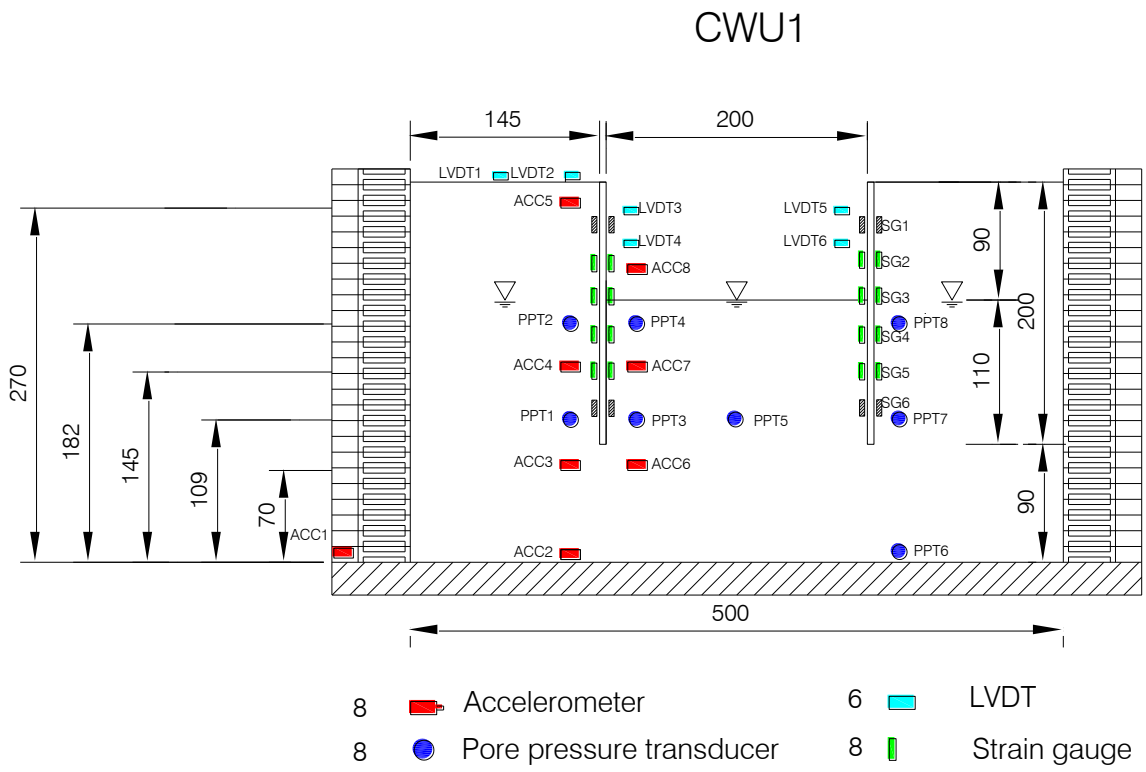

Figure 3.4: Test CWU1: model layout.

The instruments that did not work properly during this test have been reported in Table 3.4.

Test	Instrument did not work properly
CWU1	Strain Gauge 2 of the Left Wall
	Strain Gauge 4 of the Left Wall
	Strain Gauge 2 of the Right Wall during post seismic of EQ2
	PPT2
	PPT8

Table 3.4: Test CWU1: list of instruments that did not work properly.

3.1.2 PWU1

The test PWU1 has been carried out on a pair of retaining walls with one level of prop near the top and a retained height of 140 mm and an embedded length of 60mm. As for test CWU1 the relative density D_r is about 38%. The layout of the model is reported in Figure 3.5. The instrumentation consists of:

1. 8 accelerometers: 7 measuring the soil acceleration and 1 measuring the acceleration of the support of the LVDTs; 8 Pore Pressure Transducers;
2. 8 Strain Gauges;
3. 5 LVDTs;
4. 2 Load Cells measuring the axial force in the props.

In Table 3.5 the characteristic of the input earthquakes are listed.

Test	Earthquake	f(Hz)	$a_{max}(g)$	Duration (s)
PWU1 (Model Scale)	EQ1	50	4.0	0.62
	EQ2	50	8.0	0.62
PWU1 (Prototype Scale)	EQ1	1.25	0.10	25
	EQ2	1.25	0.20	25

Table 3.5: Test PWU1: characteristics of the input earthquakes.

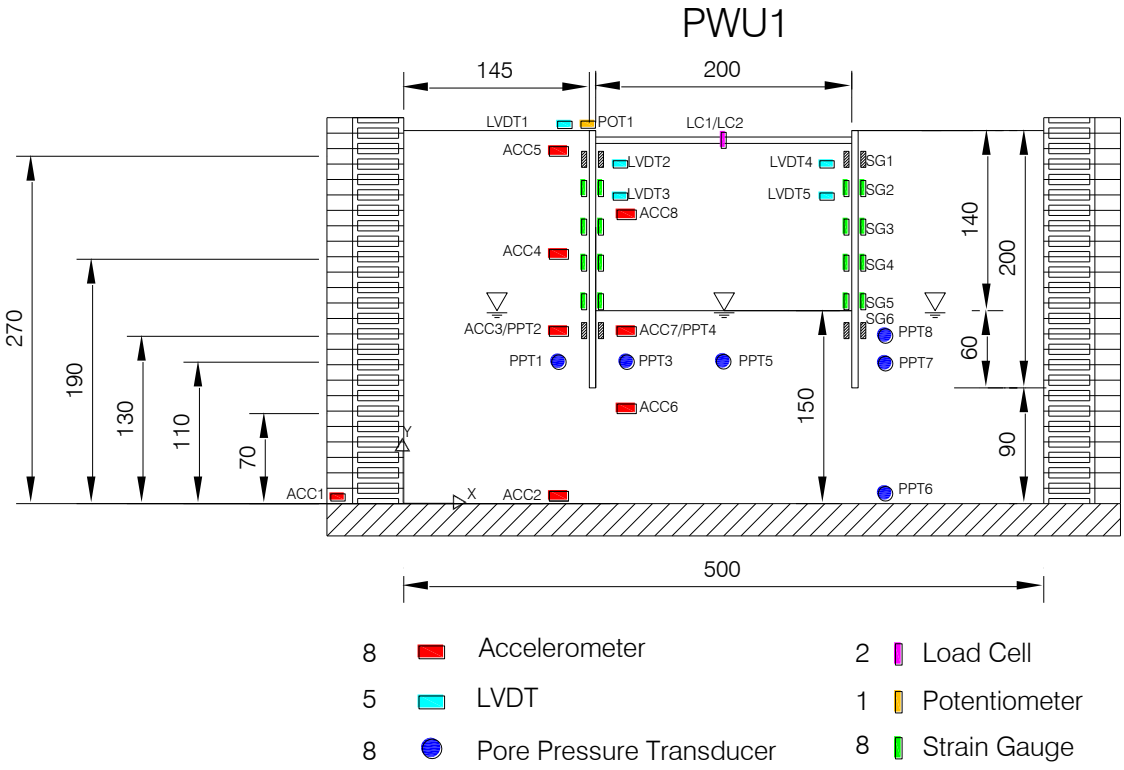

Figure 3.5: Test PWU1: model layout

The instruments that did not work properly during this test have been reported in Table 3.6.

Test	Instrument did not work properly
PWU1	PPT1
	PPT2
	PPT3
	PPT4

Table 3.6: Test PWU1: list of instruments that did not work properly.

3.1.3 CWU2

The test CWU2 has been carried out on a pair of cantilevered retaining walls with a retained height of 110mm and an embedded length of 90mm, so it has the same geometrical features than the test CWU1, while the relative density D_r is higher and it is about 88%. The layout of the model is shown in Figure 3.6.The instrumentation consists of:

1. 8 piezoelectric accelerometers: 7 measuring the soil acceleration and 1 measuring the acceleration of the support of the LVDTs;
2. 8 Pore Pressure Transducers;
3. 10 Strain Gauges;
4. 4 LVDTs measuring the horizontal displacement of the walls;
5. 1 potentiometer measuring the settlements of the left wall;
6. 1 MEMS accelerometer measuring the horizontal accelerometer of the top of the left wall.

In Table 3.7 the characteristic of the input earthquakes are listed.

Test	Earthquake	f(Hz)	$a_{max}(g)$	Duration (s)
CWU2 (Model Scale)	EQ1	50	3.0	0.57
	EQ2	50	4.0	0.65
	EQ3	50	8.0	0.70
CWU2 (Prototype Scale)	EQ1	1.25	0.075	23
	EQ2	1.25	0.10	26
	EQ3	1.25	0.20	28

Table 3.7: Test CWU2: characteristics of the input earthquakes.

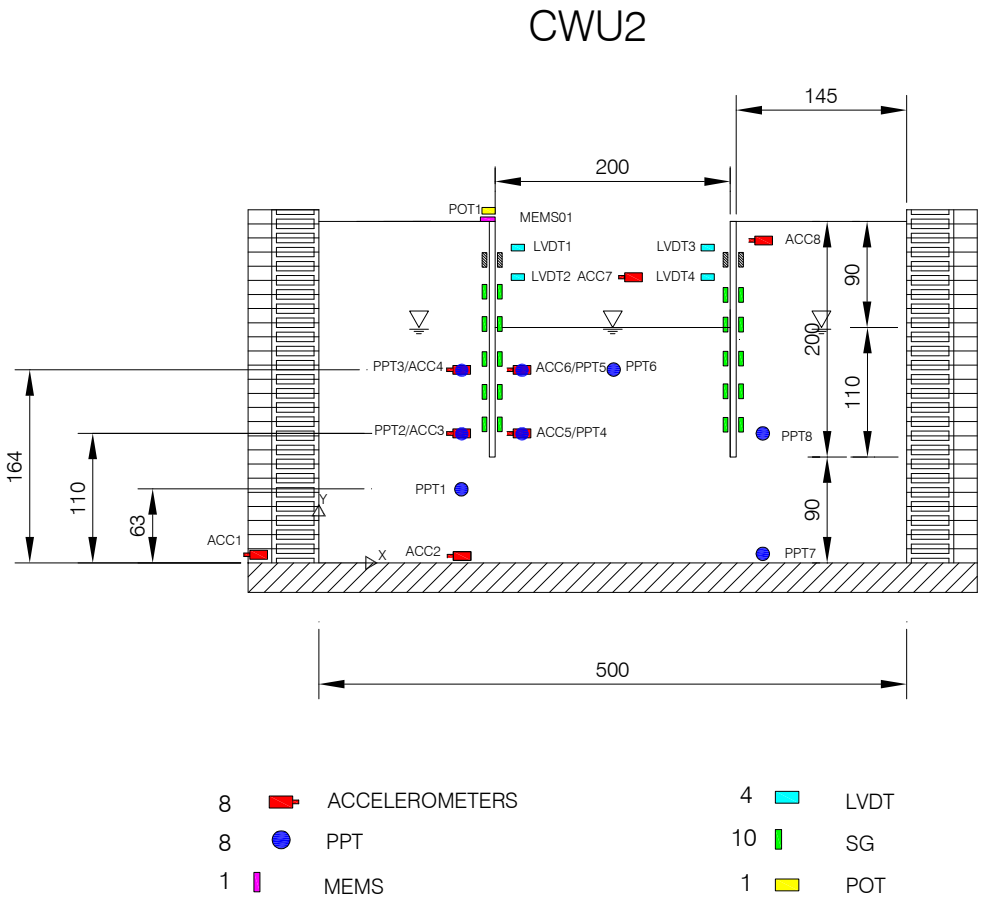

Figure 3.6: Test CWU2: model layout

The instruments that did not work properly during this test have been reported in Table 3.8.

Test	Instrument did not work properly
CWU2	PPT4

Table 3.8: Test CWU2: list of instruments that did not work properly.

3.1.4 PWU2

The Test PWU2 concerns a pair of retaining walls with one level of prop near the top and a retained height of 140mm and an embedded length of 60mm. The relative density D_r is about 88% The layout of the model is reported in Figure 3.7. The instrumentation consists of:

1. 8 accelerometers recording the soil acceleration during the earthquakes;
2. 7 Pore Pressure Transducers;
3. 10 Strain Gauges;
4. 1 MEMS accelerometer measuring the horizontal acceleration with respect the top of the wall;
5. 4 LVDTs measuring the horizontal displacements of the walls;
6. 2 Load cells measuring the axial force acting at the props.

In Table 3.9 the characteristic of the input earthquakes are listed.

Test	Earthquake	f(Hz)	$a_{max}(g)$	Duration (s)
PWU2 (Model Scale)	EQ1	50	4.0	0.50
	EQ2	50	5.2	0.47
	EQ3	50	10.0	0.47
PWU2 (Prototype Scale)	EQ1	1.25	0.10	20
	EQ2	1.25	0.13	19
	EQ3	1.25	0.25	19

Table 3.9: Test PWU2: characteristics of the input earthquakes.

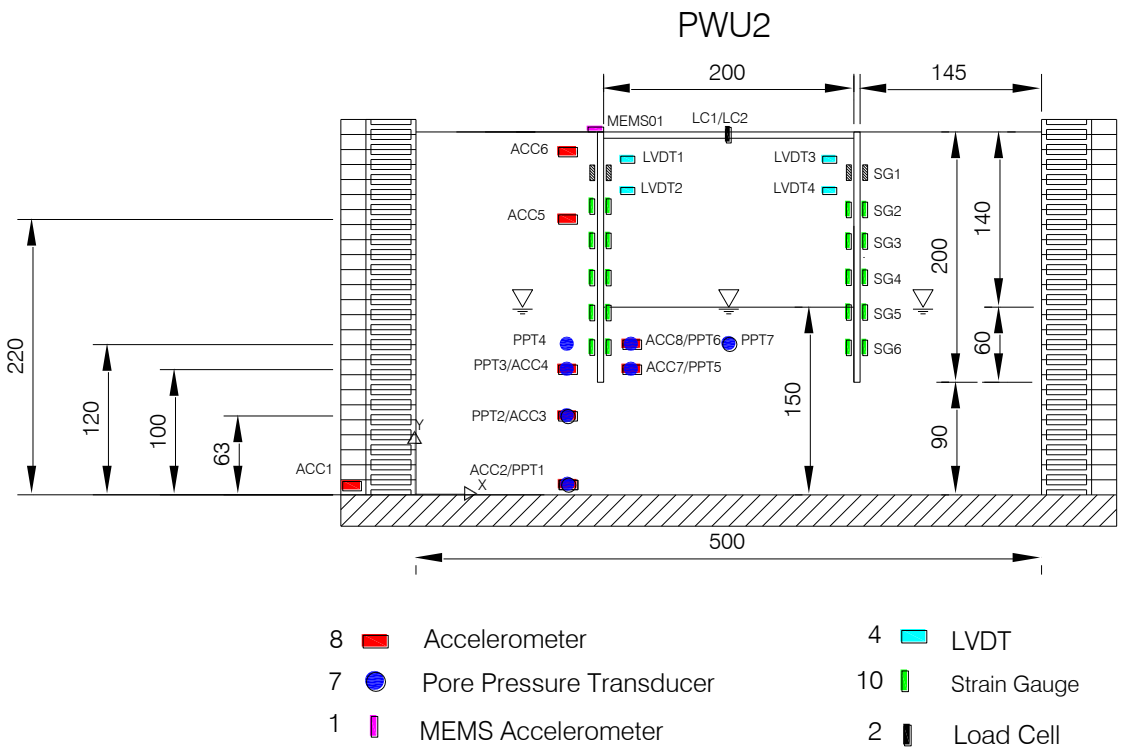

Figure 3.7: Test PWU2: model layout

The instruments that did not work properly during this test have been reported in Table 3.10.

Test	Instrument that did not work properly.
	Strain Gauge 2 of the Left Wall
PWU2	PPT1
	PPT2
	PPT3

Table 3.10: Test PWU2: list of instruments that did not work properly.

3.1.5 CWU3

The geometry of the model of test CWU3 is the same as the geometry of the tests on cantilevered walls CWU1 and CWU2. The relative density is the same as for test CWU2, that is $D_r = 88\%$. In this way a direct comparison between the test CWU2 and the test CWU3 can be done.

In this test the Tekscan pressure sensor has been used to measure the total horizontal pressure acting on the left wall. The layout of the model is shown in Figure 3.8. The instrumentation consists of:

1. 8 accelerometers, among them 5 have been vertically aligned at the back of the left wall and 2 have been placed in the excavated side;
2. 10 Pore Pressure Transducers; 4 of them have been placed at the back of the left wall and at the same depth of the accelerometers, 3 are within the excavated side and 3 are at the back of the right wall;
3. 12 strain gauges;
4. 2 MEMS accelerometers at the top of the walls;
5. 6 LVDTs; 4 of them measure the horizontal displacements of the walls and 2 of them measure the displacements of the laminar box rings;
6. 1 Potentiometer measuring the vertical displacements of the left wall;
7. 1 Tekscan pressure sensor to measure the total horizontal stress on the left wall. A detailed technical scheme of the Tekscan pressure sensor and its placement on the wall have been reported in Chapter 2.

In Table 3.11 the characteristic of the input earthquakes are listed.

Test	Earthquake	f(Hz)	$a_{max}(g)$	Duration (s)
CWU3 (Model Scale)	EQ1	50	4.4	0.45
	EQ2	50	5.2	0.47
	EQ3	50	8.8	0.47
CWU3 (Prototype Scale)	EQ1	1.25	0.11	18
	EQ2	1.25	0.13	19
	EQ3	1.25	0.22	19

Table 3.11: Test CWU3: characteristics of the input earthquakes.

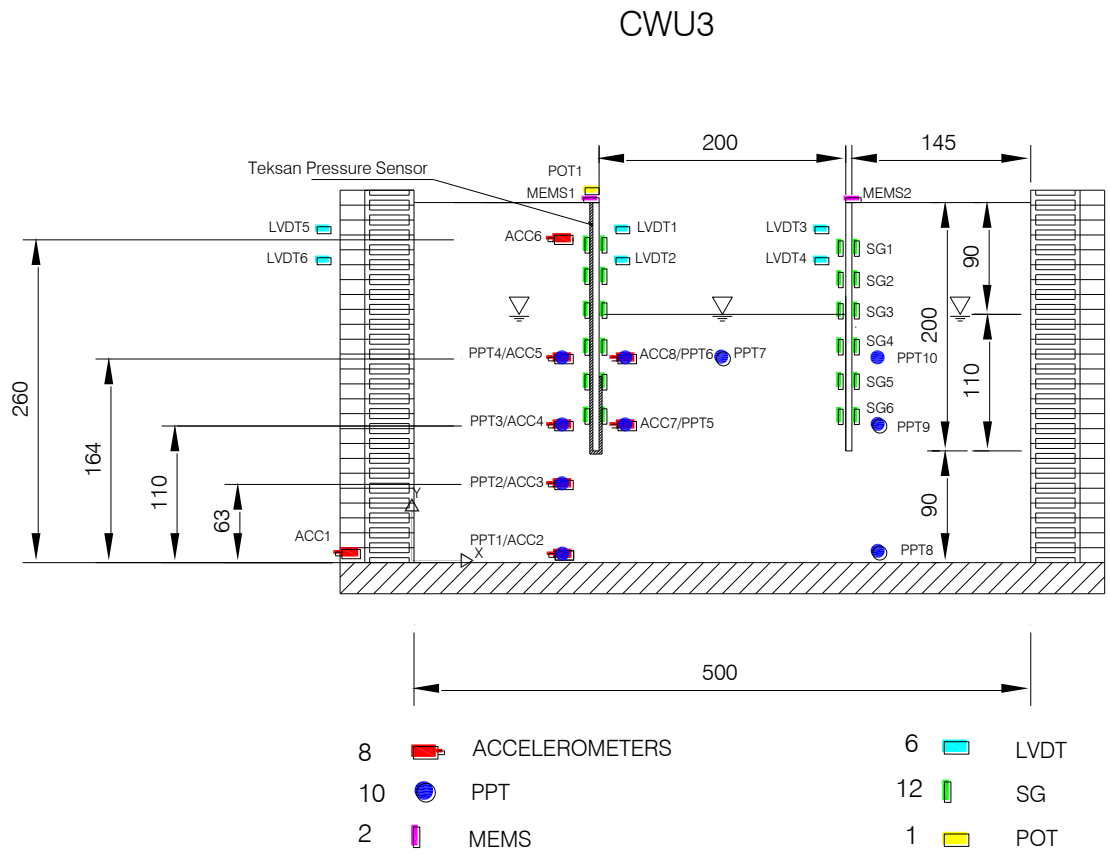

Figure 3.8: Test CWU3: model layout

The instruments that did not work properly during this test have been reported in Table 3.12.

Test	Instrument did not work properly
	Strain Gauge 5 of the Left Wall
CWU3	Strain Gauge 5 of the Right Wall
	Strain Gauge 6 of the Right Wall

Table 3.12: Test CWU3: list of instruments that did not work properly.

3.1.6 PWU3

The geometry of the model of test PWU3 is the same as the geometry of the tests on propped walls PWU1 and PWU2. The relative density is the same as for test PWU2, that is $D_r = 88\%$.

Also in the PWU3 pressure sensor has been used to measure the total horizontal stress acting on the left wall. The layout of the model is shown in Figure 3.9. The instrumentation consists of:

1. 8 accelerometers, among them 5 have been vertically aligned at the back of the left wall and 2 have been placed in the excavated side;
2. 10 Pore Pressure Transducers; 4 of them have been placed at the back of the wall and at the same depth of the accelerometers, 3 are within the excavated side and 3 are at the back of the right wall;
3. 12 strain gauges;
4. 2 MEMS accelerometers at the top of the walls;
5. 6 LVDTs; 4 of them measure the horizontal displacements of the walls and 2 of them measure the displacements of the laminar box rings;
6. 1 Potentiometer measuring the vertical displacements of the left wall;
7. 2 Load Cells measuring the axial force in the props;
8. 1 Pressure Sensor to measure the total horizontal stress on the left wall.

In Table 3.13 the characteristic of the input earthquakes are listed.

Test	Earthquake	f(Hz)	$a_{max}(g)$	Duration (s)
PWU3 (Model Scale)	EQ1	50	4.4	0.45
	EQ2	50	5.6	0.45
	EQ3	50	13.2	0.47
PWU3 (Prototype Scale)	EQ1	1.25	0.11	18
	EQ2	1.25	0.14	18
	EQ3	1.25	0.33	19

Table 3.13: Test PWU3: characteristics of the input earthquakes.

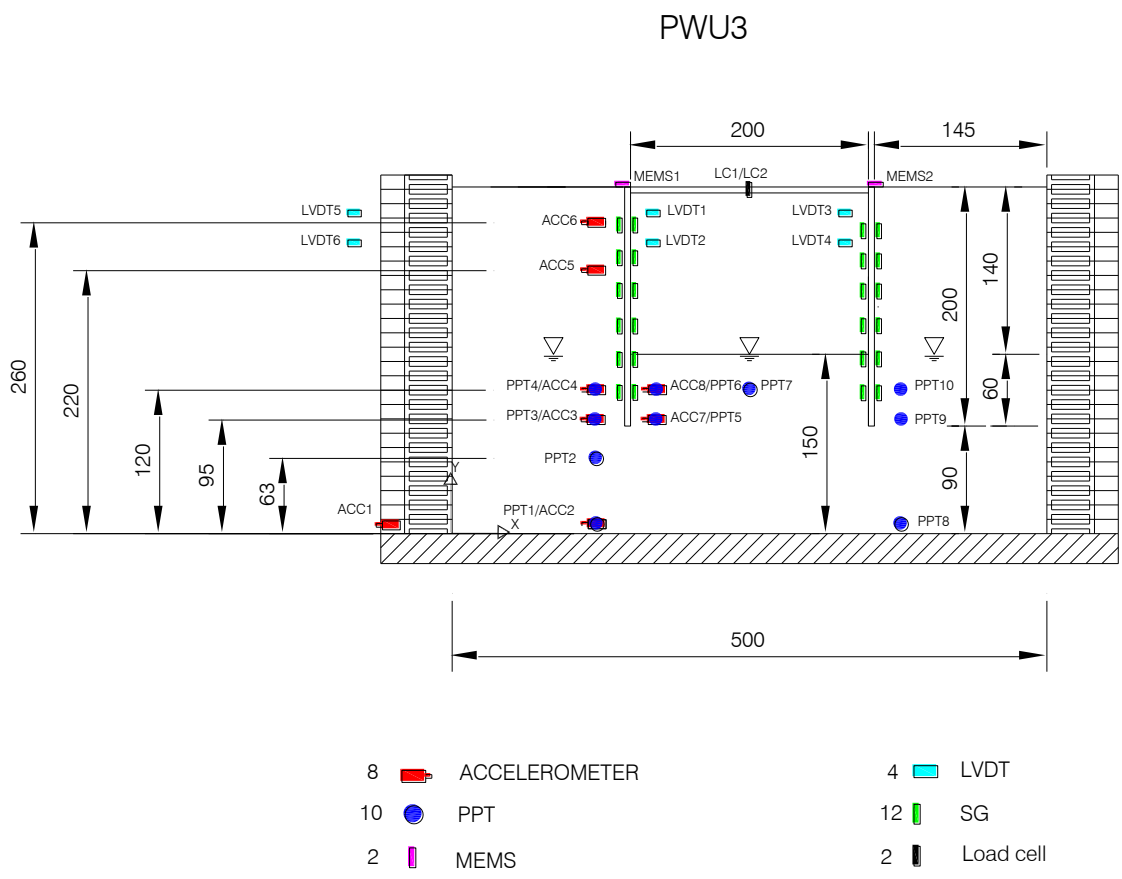

Figure 3.9: Test PWU3: model layout

In this test all instrument have worked correctly.

3.1.7 CWU4

The geometry of the model of test CWU4 is the same as the geometry of the tests CWU2 and CWU3. The relative density is the same as for those tests, that is $D_r = 88\%$.

This test has been the first attempt for the use of the Tekscan pressure sensor.

The layout of the model is shown in Figure 3.10. The instrumentation consists of:

1. 8 accelerometers, among them 5 have been vertically aligned at the

back of the left wall and 2 have been placed in the excavated side;

2. 10 Pore Pressure Transducers; 4 of them have been placed at the back of the wall and at the same depth of the accelerometers, 3 are within the excavated side and 3 are at the back of the right wall;
3. 12 strain gauges;
4. 2 MEMS accelerometers at the top of the walls;
5. 6 LVDTs; 4 of them measure the horizontal displacements of the walls and 2 of them measure the displacements of the laminar box rings;
6. 1 Potentiometer measuring the vertical displacements of the left wall;
7. 2 Load Cells measuring the axial force in the props;
8. 1 Pressure Sensor to measure the total horizontal stress on the left wall. A detailed scheme of the Pressure Sensor has been detailed in Chapter 2.

In Table 3.14 the characteristic of the input earthquakes are listed. This test has been subdivided into two flights, during the first one the earthquakes EQ1, EQ2 and EQ3 have been executed, while during the second one the earthquakes EQ4, EQ5, EQ6 and EQ7 have been executed.

Test	Earthquake	f(Hz)	$a_{max}(g)$	Duration (s)
CWU4 (Model Scale)	EQ1	50	4.4	0.42
	EQ2	50	7.2	0.45
	EQ3	50	13.2	0.45
	EQ4	50	4.4	0.45
	EQ5	50	6.8	0.45
	EQ6	50	11.2	0.45
	EQ7	50	15.2	0.45
CWU4 (Prototype Scale)	EQ1	1.25	0.11	17
	EQ2	1.25	0.18	18
	EQ3	1.25	0.33	18
	EQ4	1.25	0.11	18
	EQ5	1.25	0.17	18
	EQ6	1.25	0.28	18
	EQ7	1.25	0.38	18

Table 3.14: Test CWU4: characteristics of the input earthquakes.

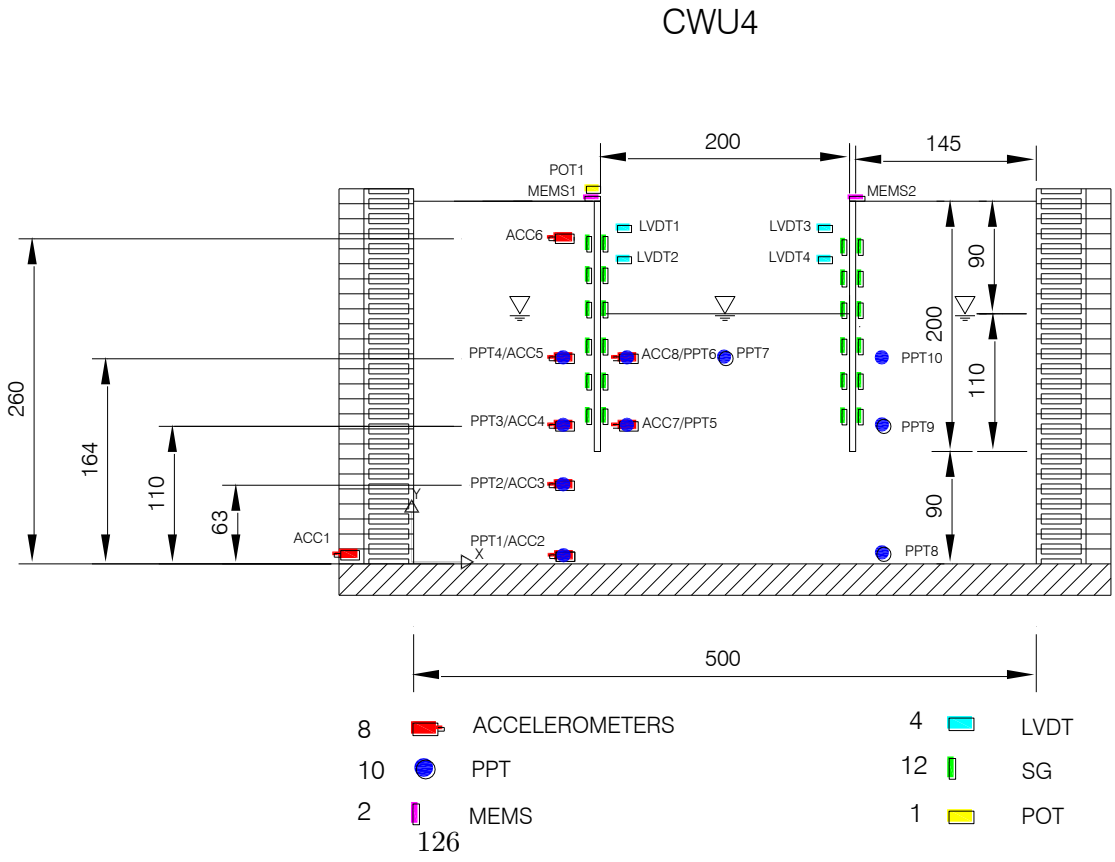

Figure 3.10: Test CWU4: model layout

The instruments that have did not work properly during this test have been reported in Table 3.8.

Test	Instrument that did not work properly
CWU4	Strain Gauge 2 Left Wall
	PPT6

Table 3.15: Test CWU4: list of instruments did not work properly.

3.2 Data

In the present paragraph the data of the tests are reported. The data relative to the swing up and swing down are not presented in order to avoid to report too many data. For each test the data are presented both with respect to time and with respect to their space distribution for a given time instant; particularly the data have been presented as follows:

1. Acceleration time histories along the alignments at the back of the left wall and between the walls;
2. Amplification factor along the vertical alignments of the accelerometers placed at the active side and at the passive side;
3. Phase difference between the acceleration time histories;
4. Walls horizontal displacement time histories;
5. Walls displacement in the space domain;
6. Pore Pressures time histories;
7. Pore Pressures space distribution;
8. Bending Moment time histories;
9. Bending Moment space distribution;
10. Axial force in the props time histories.

Before to report the data plots for each test following the above list it is important to premise and clarify the emerged issues and the used methodologies regarding the data elaboration and the uses of data plots toward the physical interpretation of the soil structure behaviour:

1. In the plots of the acceleration time histories the accelerations recorded with the piezoelectric accelerometers placed within the soil have been reported. In a single plot a number of vertical alignments of acceleration time histories equal to the number of the earthquakes carried out within a single test has been presented. As said before the vertical alignments of accelerometers are those at the back of the left wall or at the excavated side; so, for instance, if test CWU1 is considered, where two earthquakes have been carried out, and the accelerometers placed at the back of the left wall have to be plotted (Acc1, Acc2, Acc3, Acc4 and Acc5), the plot will present two columns of the acceleration time histories Acc1, Acc2, Acc3, Acc4 and Acc5 placed vertically. This plot gives basically information about the amplification of the acceleration by direct comparison of the peak of the acceleration time histories placed along the same vertical alignment. Within each subplot, besides the acceleration time history, the value of the maximum absolute acceleration is reported. It is important to recognize that the input signal usually presents its peak at the beginning of the shaking due to the mechanical behaviour of the SAM actuator, while the remaining part of the input signal is collocated at a nearly constant value of acceleration lower (even if not significantly) than the peak. The computation of the amplification factor, as explained later, has been based on the value of the acceleration at the peak of the beginning of the earthquake; such value of the acceleration has been reported in the subplots;

2. A more complete description of the amplification phenomenon can be achieved through the computation of the amplification factor expressed as the ratio a_{maxs}/a_{maxi} between the maximum acceleration within the soil at a certain depth and the maximum input acceleration. After the plots of the vertical alignments of the acceleration time histories presented at the previous point also the amplification factor is plotted. The amplification factor is plotted along the depth in order to have the profile of the amplification factor along the back of the left wall and along the excavated side. On the basis of what has been seen at the previous point, a_{max} corresponds to the peak of the input acceleration at the beginning of the shaking and this normally happens also for the maximum accelerometers placed within the soil a_{maxs}. This is to underline that a possible different definition of the amplification factor could be individuated, where the maximum acceleration of both the input acceleration and the acceleration within the soil are defined

at a time instant consecutive to the first peak in order to eliminate the influence of the first peak of the value on the amplification factor and, more importantly, to introduce in the computation the values on which the acceleration is for the most part of the duration of the earthquake collocated. With this last approach, which correctly considers the fact that the actual effect of the earthquake on the soil structure response is mainly correlated with the nearly constant value of the acceleration that is lower than the peak acceleration at the beginning of the earthquake, the correct definition of a_{maxs} and a_{max} is lost. So both the possibilities present a strong point and a weak point. Between the two, the first one has been chosen because it gives the possibility to obtain an easier implementation in a Matlab code the computation of the amplification factor and because the correct definition of the maximum acceleration would indicate as maximum value that one that occurs at the beginning of the earthquake; moreover the two different definitions are likely not to determine a diverse interpretation of the amplification phenomenon;

3. Besides the amplification factor, also the phase difference between the acceleration time histories recorded by the piezoelectric accelerometers has been computed. Two different methods for the computation of the phase difference have been tested; with the first one the phase difference is computed in the time domain while in the second one the phase difference is computed in the frequency domain. Here the results obtained only from the first method and regarding each single test are illustrated. The methods are described in detail in Chapter 4, where the comparison of the results relative to all the tests is shown and the performance of the two different methods are compared as well. Here it is just briefly recalled that in case where the time domain is considered, the phase difference is computed through the comparison of the time instants where the peaks of the acceleration take place, while in the case where the frequency domain is considered, the phase difference is computed directly as the difference of the imaginary part of the Cross Power Spectrum of the considered signals. In Figure 3.11, the computation of the phase difference in the time domain between the input acceleration Acc1 and the acceleration Acc4 for the test PWU3 is illustrated. The phase difference $\Delta\phi$ in the time domain is computed as $\Delta\phi = 2\pi f_{inp}\Delta t$, where Δt is the time lag between the peak of Acc4 and the first peak of Acc1 and Δt is the time lag between two consecutive peaks of Acc1 and $f_{inp} = 1/\Delta T$. The computation

of the phase difference in the time domain has been repeated for all the possible configurations distinguishable during the earthquake as that one presented in 3.11 in order to obtain the trend of the phase difference with respect to time;

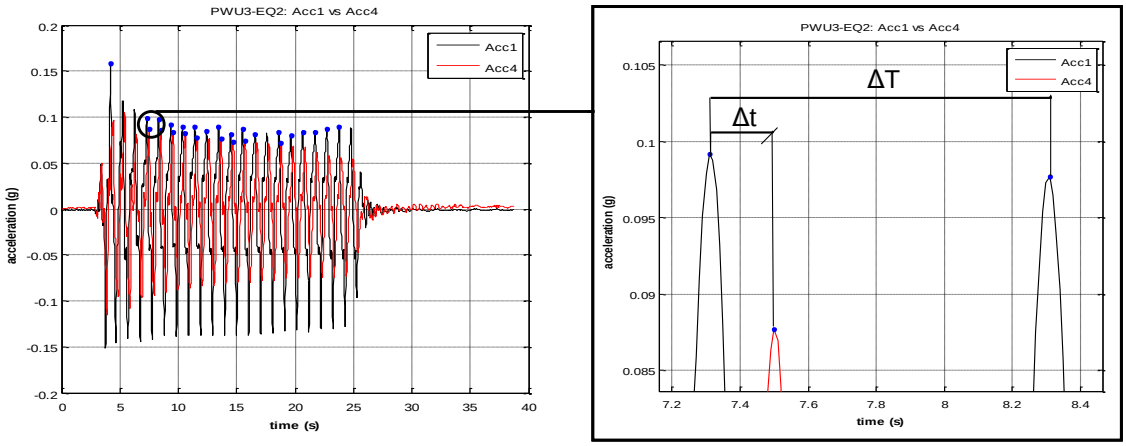

Figure 3.11: Scheme of the LVDT support connected to the base plate of the laminar box: vertical and planar view.

4. The horizontal displacements of the walls measured with the LVDTs give the possibility to study the behaviour of the walls in terms of displacements during the shaking. This interpretation of the behaviour of the walls in terms of displacements can be not immediate because the LVDTs register also the displacements of the rings that compose the laminar box since they are attached, through their support, at the cross bars of the laminar box, at four vertical columns and, finally, at the base plate of the laminar box (Figure 3.12). This means that the measured horizontal displacements contain both the displacements of the walls with respect their un-deformed configuration, which are effectively relevant for the purposes of this study because they can be related to the mobilization of the soil strength and the wall collapse

mechanism, and the displacement of the laminar box rectangular rings of the laminar box with respect the base plate, that are unwanted for this study purposes. In Figure 3.13(a) a possible walls configuration is depicted, where $\bar{u_L}$ and $\bar{u_R}$ are the displacements measured with the LVDTs. Those displacements are the sum of the actual displacements of the walls relative to the soil that interest the study of the soil-structure interaction, indicated in Figure 3.13(c) as u_R and u_L , and the displacement of the box at the depth where the measure of the LVDT is carried out, indicated as u_{BL} and u_{BR} . Since the position of the LVDTs is the same and, at the depth where a pair of LVDTs (top LVDTs or bottom LVDTs) is placed a single ring of the laminar box is individuated, it follows that $u_{BR} = u_{BL} = u_B$. So the measured displacements $\bar{u_L}$ and $\bar{u_R}$ can be expressed as follows (Figure 3.13(a) and Figure 3.13(b)):

$$\bar{u_L} = u_L + u_b \tag{3.1}$$

$$\bar{u_R} = u_R - u_b \tag{3.2}$$

Note that the displacements of the vertical sides of the box are shown as linear in Figure 3.13); in general the sides can reach a non linear configuration, but the assumption of linearity is not relevant for the interpretation of the data because, as said before, at the depth where a pair of LVDT is positioned corresponds only one ring of the laminar box and since along the depth of the walls there are two pairs of LVDTs only a linear configuration of the sides can be individuated. Adding the equations 3.1 and 3.2 the following expression is obtained:

$$\bar{u_L} + \bar{u_R} = u_L + u_R \tag{3.3}$$

that means that at a given depth only the sum is known from the data of the LVDTs. In general the walls do not move symmetrically due to the imperfections of the tests (Figure 3.13(c)), but among all the possible configurations given from all the possible couples of u_R and u_L that satisfy the equation 3.3 it has been chosen to represent that one that assumes the walls to move symmetrically (Figure 3.13(d)):

$$\bar{u_L} = \bar{u_R} = u_{sym} \tag{3.4}$$

$$u_{sym} = \frac{\bar{u_L} + \bar{u_R}}{2} = \frac{u_L + u_R}{2} \tag{3.5}$$

where sym stands for symmetrical.

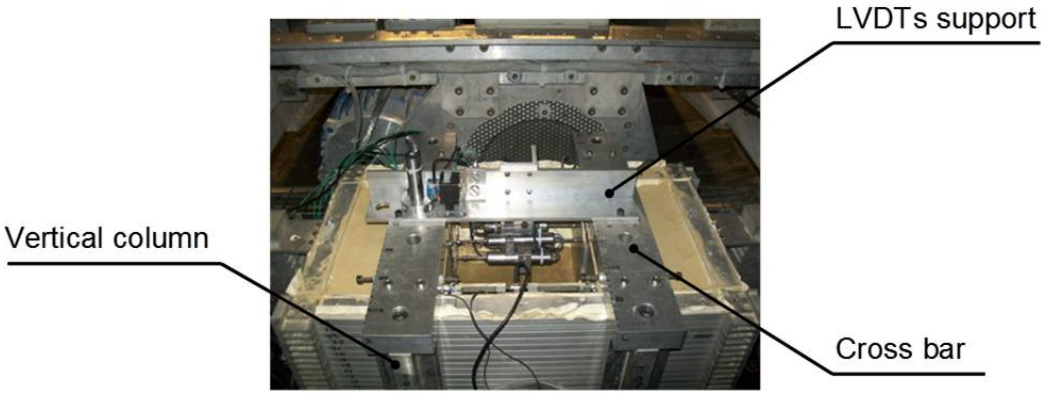

Figure 3.12: Model CWU1 in the centrifuge, the support of the LVDTs is visible (figure already reported in Chapter 2).

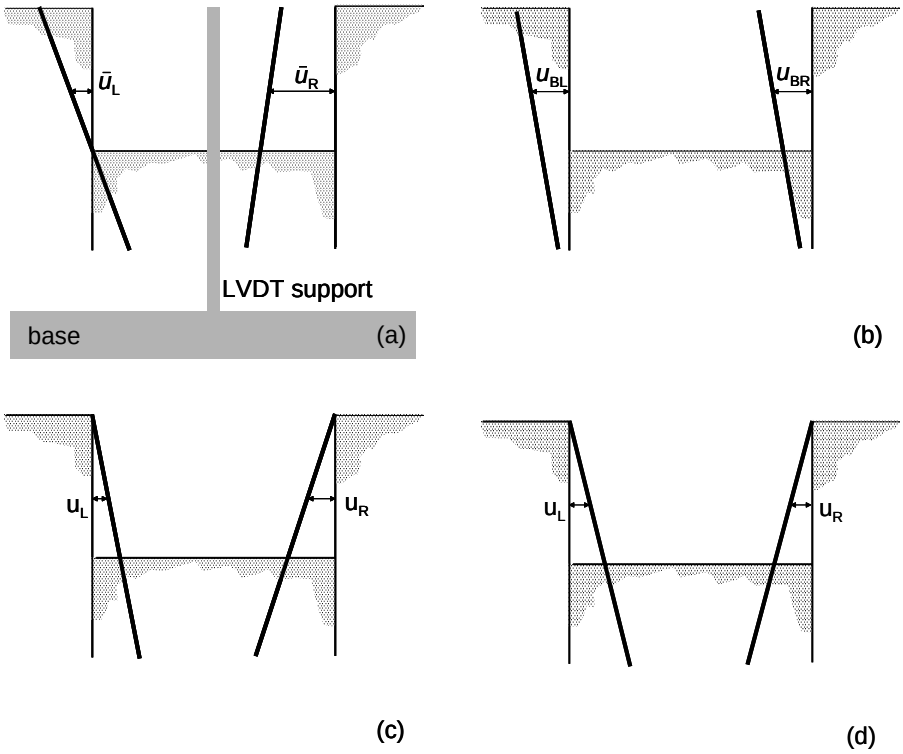

Figure 3.13: Interpretation of LVDT measurements of horizontal displacements of the walls. (a) measured displacements, (b) displacements of the laminar box rings, (c) displacements of the walls relative to the soil.

The use of the sum of the displacements presents the advantage to eliminate the systematic error due to the displacement of the laminar box ring but at the same time it obligates to individuate a criterion of assignation of a fraction of the sum of the displacements to one wall and to assign the remaining part to the other wall. Since there is not an a priori knowledge of the entity of asymmetry of the displacements the only rational choice is represented by the assignation of the average of the sum of the displacements to both the walls. The attribution of the average of the displacements to both the walls is actually acceptable only when the acceleration is zero, that is at the end of the swing up and during the post-seismic phases; but an issue emerges when the average of the walls displacements is attributed at a time instant of the dynamic phase since, during the earthquake, the walls

movement presents an out of phase cyclic component of the motion related with the inertia acceleration determined by the input signal. Indeed the attribution of the average of the displacements to both the walls at a time instant that belongs to the earthquake would imply the attribution of half of the cyclic portion of the movement to both the walls incorrectly non taking into account that such cyclic component is out of phase and non symmetrical. Particularly regarding a time instant belonging to the earthquake, if a rigid body motion is assumed for the walls, the displacements u_R and u_L can be subdivided into a static component and a dynamic component:

$$u_R = u_{RS} + u_{RD} \tag{3.6}$$

$$u_L = u_{LS} + u_{LD} \tag{3.7}$$

where the index S stands for static and the index D stands for dynamic. This subdivision presents the advantage to have the static part of the displacement not correlated with the inertial action on the walls while the latter is directly correlated with the inertial action. Since the static part of the displacement during the earthquake is not correlated with the inertial actions on the walls the assumption of symmetry of the displacement can be done as it has been done for the displacements at the end of the swing up and at the post seismic phase. So, once it is assumed that $u_{LS} = u_{RS} = u_{sym}$, the equation 3.5 becomes:

$$\frac{\bar{u_L} + \bar{u_R}}{2} = \frac{u_{LS} + u_{RS}}{2} + \frac{u_{LD} + u_{RD}}{2} = u_{sym} + \frac{u_{LD} + u_{RD}}{2} \tag{3.8}$$

where u_{sym} is attributable to both the walls while $\frac{u_{LD}+u_{RD}}{2}$ is not attributable symmetrically to the walls. The static part of the displacement (and respectively for the left wall and the right wall) can be seen as the time trend of the displacement time history and can be computed through the application of a moving average algorithm to the time history of the displacement (which is described later), while the dynamic part of the displacement is the difference of the displacement time history with respect the static part. Thus u_{sym} can be seen as the average of the static parts relative to the left wall and the right wall while u_{LD} and u_{RD} are the cyclic parts of the signals. Consequently a possible solution for the plot of the walls position during

the earthquake can be the superposition of the dynamic part on the symmetrical displacement as follows:

$$u_R = u_{sym} + u_{RD} \tag{3.9}$$

$$u_L = u_{sym} + u_{LD} \tag{3.10}$$

The result of this procedure can is highlighted in Figure 3.14 where there is the comparison between the original measured displacement with the LVDTs and its time trend and the symmetrical time trend with the superimposition of the dynamic part of the measured displacement. The latter could substitute the original displacement time history for a given LVDT during the earthquake eliminating the effect of the laminar box displacement and at the same time respecting the non symmetry of the dynamic part of the displacements. Finally in Figure 3.15 there is the comparison between the symmetrical time trend of the top LVDTs and the bottom LVDTs for EQ1 of test CWU1 and the original displacement time histories. It can be seen that the symmetrical time trend is the average of the time trend of the original signals.

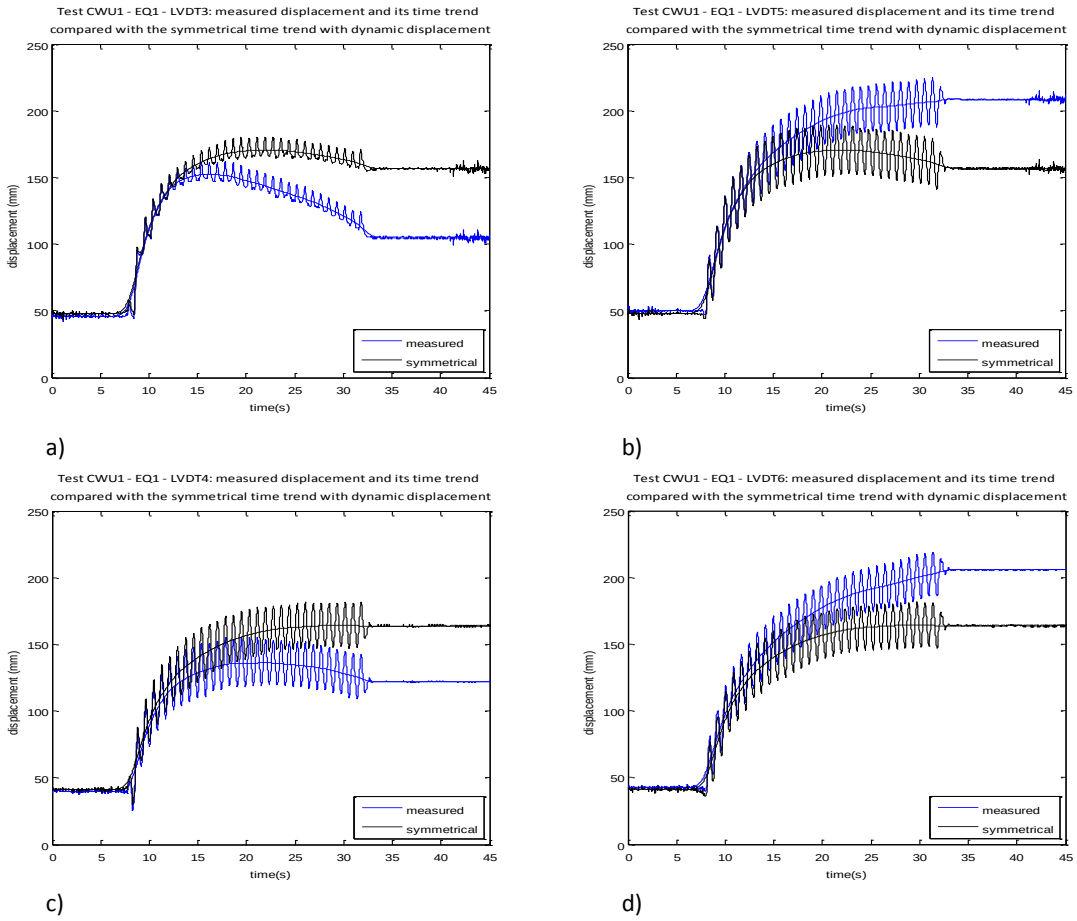

Figure 3.14: Test CWU1 EQ1: LVDTs time history with its time trend compared with the symmetrical time trend with the superimposition of the dynamic part of the measured displacement for a) LVDT3 (top left wall, b) LVDT4 (bottom left wall), c) LVDT5 (top right wall), d) LVDT6 (bottom right wall).

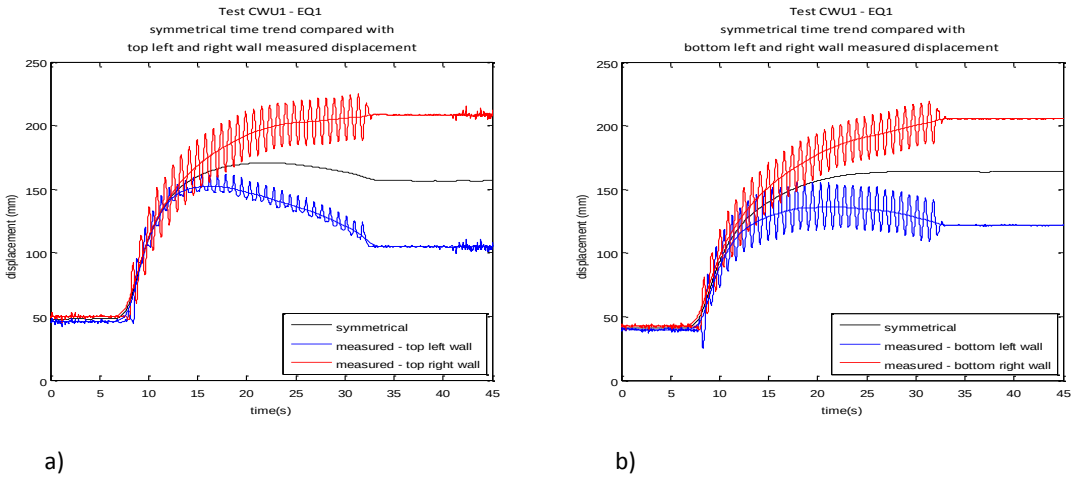

Figure 3.15: Test CWU1 - EQ1: Symmetrical time trend during EQ1 for a) the top LVDTs (LVDT3 and LVDT5) and b) the bottom LVDTs (LVDT4 and LVDT6) compared with the original time histories.

The assumption of symmetry for the end of swing up displacements, the post-seismic displacements and the static part of the earthquake displacements allows to highlight the collapse mechanism of the walls during the seismic phases of the tests because the effect of the laminar box displacement is eliminated. Such assumption presents the limitation of not being applicable for the earthquake displacements, which can be eliminated with the procedure described above. This is why in the following the main observations and deductions about the walls behaviour will be based on plots obtained through the symmetrical components. Anyway the comparison between the non-symmetrical configuration and the assumed symmetrical configuration is important in order to understand how acceptable the assumption of the symmetry of the displacement is; this is why for each test the space distribution of the walls horizontal displacement will be presented both as obtained by direct plot in the space of the measured displacements and as symmetrical displacements. Here it is explicitly underlined that, conventionally, the displacements obtained, as described above, as the average of the measured displacement at a given depth will be called in the text as symmetrical while the displacement obtained as direct measurement of the LVDTs will be called in the text as measured. The

symmetrical displacements are important for the presentation of the test data because they have also been used to compute the rotation of the walls during the shaking. For instance, it will be seen in the following that during the test realized on cantilever walls in loose sand CWU1 a counter-rotation of the walls has been observed; so the representation of the rotation of the walls allows to visualize such response and also to individuate the time instant when the counter-rotation occurs. Also, when a MEMS accelerometer has been used to monitor the acceleration at the top of the walls, the rotation computed using the LVDTs has been compared with the rotation computed using the MEMS accelerometer. Hereinafter the procedure to obtain the rotation of the walls from the symmetrical displacements is illustrated. The signals of the symmetrical displacements have been smoothed by applying a moving average algorithm in order to obtain the general trend of the signal of a given earthquake. The moving average algorithm considers three consecutive values of the displacement and it updates the middle value as a weighted sum of the three values. Considered the time vector $t(i) = [t(1), t(2)...t(k)...t(n)]$ and the displacement vector $d(i) = [d(1), d(2)...d(k)...d(n)]$ where $i = 1, 2...k...n$ whose components represent the value of the displacement d(i) at the time $t(i)$, the moving average algorithm considers three consecutive values of the displacement vector $d(i-1)$, $d(i)$, $d(i+1)$where $i = 2...n-1$ and substitutes to $d(i)$ an updated value computed as follows: $0,25 \cdot d(i-1) + 0.5 \cdot d(i) + 0.25 \cdot d(i+1)$. The algorithm can be applied routinely and as the number of the applications of the algorithm increases the signal is progressively smoothed. In Figure 3.16 the result of the smoothing operation just described can be found. The black line represents the signal to be smoothed, which has been obtained as the average at each time instant of the horizontal displacement given from the top LVDTs, and the blue line represents the smoothed signal. The rotation $\Theta$of the walls at each time instant is computed as:

$$\Theta = \arctan \frac{LVDT_{top} + LVDT_{bot}}{d} \tag{3.11}$$

where $LVDT_{top}$ and $LVDT_{bot}$ are the average horizontal displacement of the top LVDTs and of the bottom LVDTs respectively and d is their vertical distance. So, for a given time instant $t(i)$, $LVDT_{top}$ and $LVDT_{bot}$ have been obtained as:

$$LVDT_{top}(i) = \frac{1}{2}\left(LVDT_{topleft}(i) + LVDT_{topright}(i)\right) \tag{3.12}$$

$$LVDT_{bot}(i) = \frac{1}{2}\left(LVDT_{botleft}(i) + LVDT_{botright}(i)\right) \tag{3.13}$$

where $LVDT_{topleft}$ and $LVDT_{topright}$ are the measured displacements with the top LVDT of the left wall and right wall respectively and $LVDT_{botleft}$ and $LVDT_{botright}$ are the measured displacements with the bottom LVDT of the left wall and the right wall. For the specific case of test CWU1 for instance, where LVDT3, LVDT4, LVDT5 and LVDT6 are respectively the top LVDT of the left wall, the bottom LVDT of the left wall, the top LVDT of the right wall and the bottom LVDT of the right wall, $LVDT_{top}$ and $LVDT_{bot}$ at a given instant $t(i)$ assume the following expressions:

$$LVDT_{top}(i) = \frac{1}{2}\left(LVDT3(i) + LVDT5(i)\right) \tag{3.14}$$

$$LVDT_{bot}(i) = \frac{1}{2}\left(LVDT4(i) + LVDT6(i)\right) \tag{3.15}$$

It is worth to underline that the rotation of the walls with respect to time computed with this procedure cannot give the exact value of the rotation of the walls since $LVDT_{top}$ and $LVDT_{bot}$ are the average displacements at a given time instant of the LVDTs located at the same depth. Thus the absolute value of the rotation does not indicate the actual value of the rotation of the walls, but it is only the average of the rotation of the walls. Anyway its time trend is indicative of the real behaviour of the walls during the earthquakes. The computation of the rotation from the acceleration time history given from the MEMS accelerometers placed on the top of the walls has been carried out applying the smoothing algorithm as well; the resulting rotation time trend has been plotted besides the rotation obtained from the symmetrical displacements;

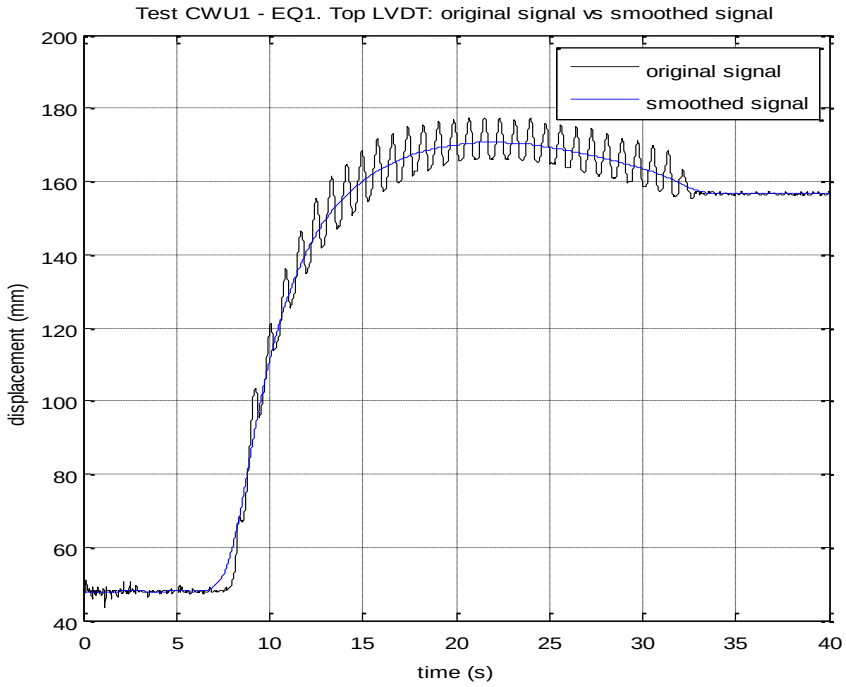

Figure 3.16: Test CWU1 EQ1: average of the top LVDTs (original signal) compared with the smoothed signal.

5. A concluding remark about the plots in time domain of the horizontal displacements of the walls, of the pore pressures and of the bending moment regards the post seismic phase is also necessary. Let us consider the plot in the time domain of the measured horizontal displacements of the walls during the post seismic phase PS1 in Figure 3.17. As it can be seen, the post seismic time trend of the measured horizontal displacements of the walls present a non linear monotonic time trend at the beginning of the post seismic phase, specifically up to about 1000s, and after that time instant it reaches a constant value. This is the typical post seismic time trend that characterizes all the physical quantities involved into the experiments performed, as it can be confirmed considering Figures 3.17, 3.18 and 3.19 where there are the post seismic time trend of the measured displacements, of the pore pressures and of the bending moments. It could be said that three important features of these time trends can be individuated: i) the value at the beginning of the post seismic phase, ii) the time trend itself, iii)

the final value of the physical quantity. The initial value is actually coinciding with the value at the end of the previous earthquake (EQ1 for PS1, EQ2 for PS2 and so on) and it is called short term residual; the final value coincides with the value of the physical quantity at the beginning of the earthquakes that follows the post seismic phase (EQ2 for PS1, EQ3 for PS2 and so on), and it is called long term residual (see the following point of the present list), and finally the time trend would be useful for the study of the consolidation process that takes place after the earthquake. The present Chapter is basically oriented toward the study the model response during the earthquakes, and, in order to do so, among the three most important features of the post seismic response only the initial and the final values are useful. This is the reason why it has been decided to plot only the earthquake time responses and not the post seismic time responses. Indeed the initial and the final value of the post seismic phase are included in the plots as initial and final values of the dynamic responses, as explained before, and the only missing value, that is the final value of the last post seismic phase, is indicated through an arrow in the last time trend of the earthquakes time responses. For instance, in Figure 3.20 the arrow indicating the value at the end of the last post seismic phase is reported at the end of the plots relative to the earthquake EQ2.

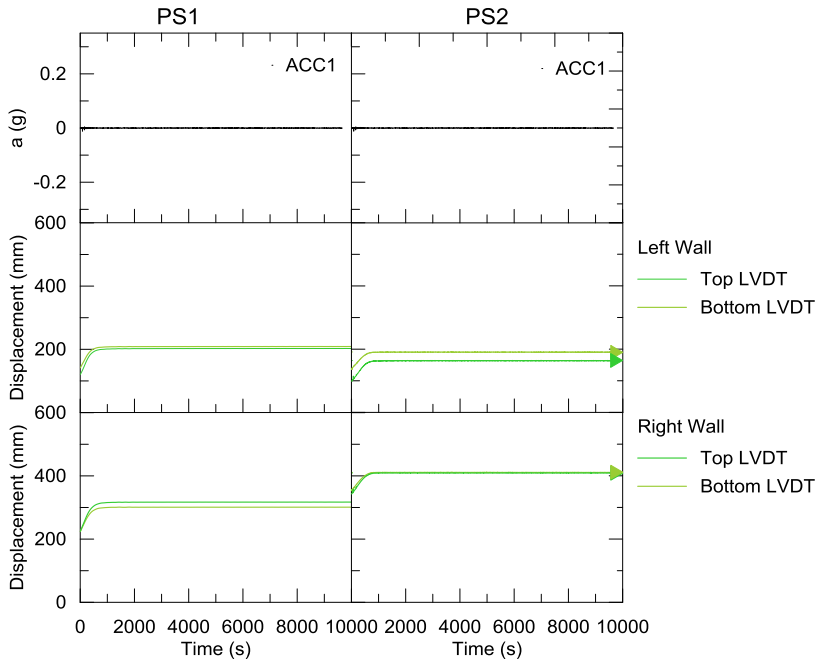

Figure 3.17: Test CWU1: post seismic time trend of the horizontal displacements of the walls measured with the LVDTs.

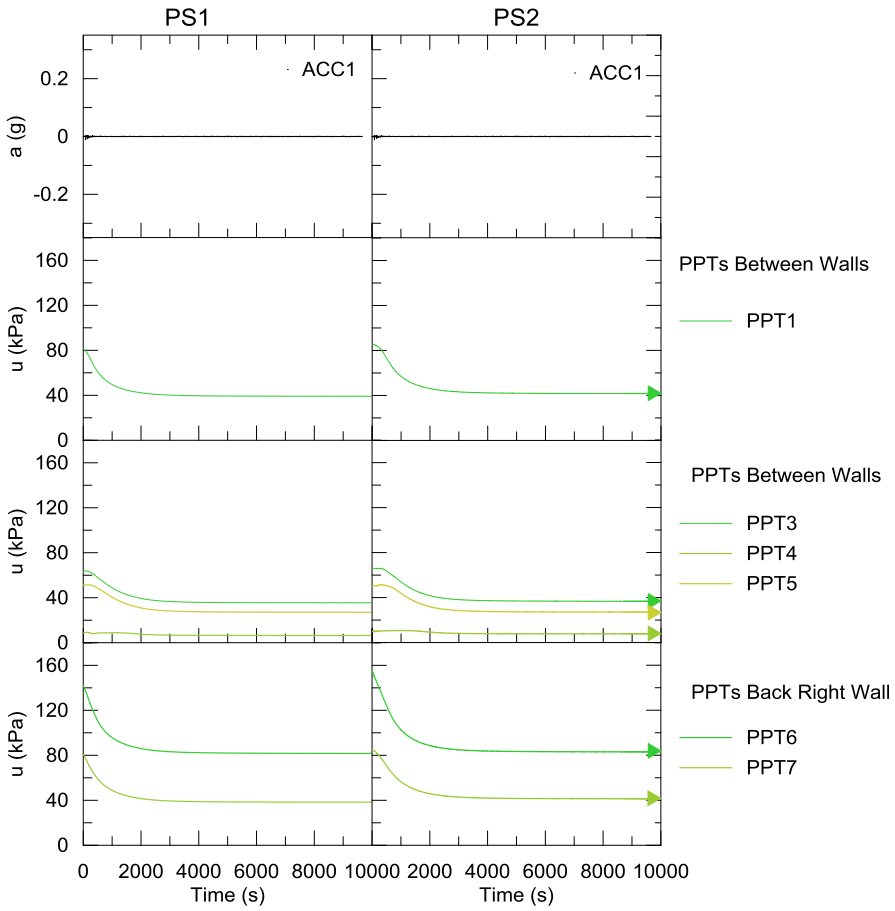

Figure 3.18: Test CWU1: post seismic time trend of pore pressures.

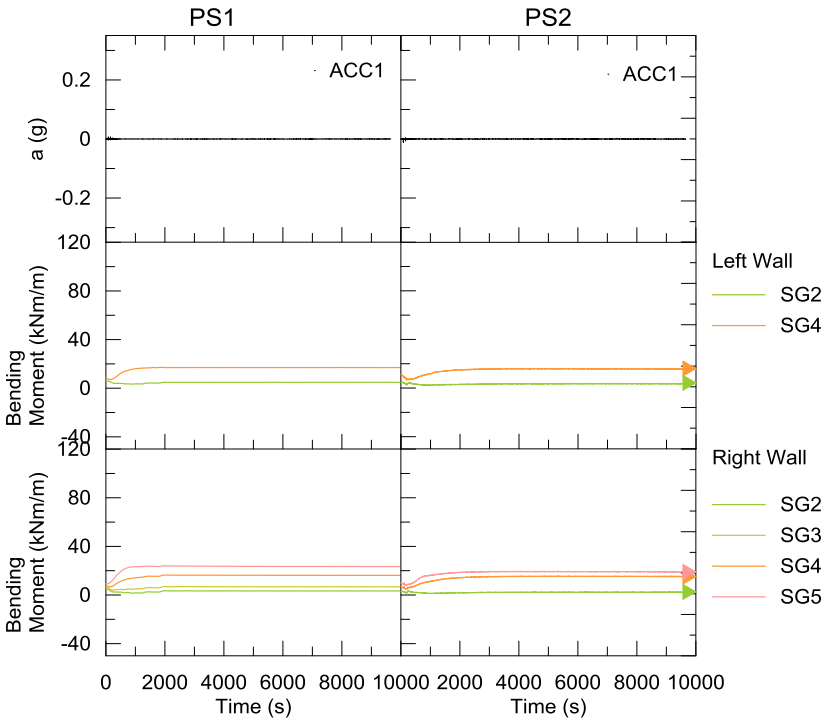

Figure 3.19: Test CWU1: post seismic time trend of the bending moment.

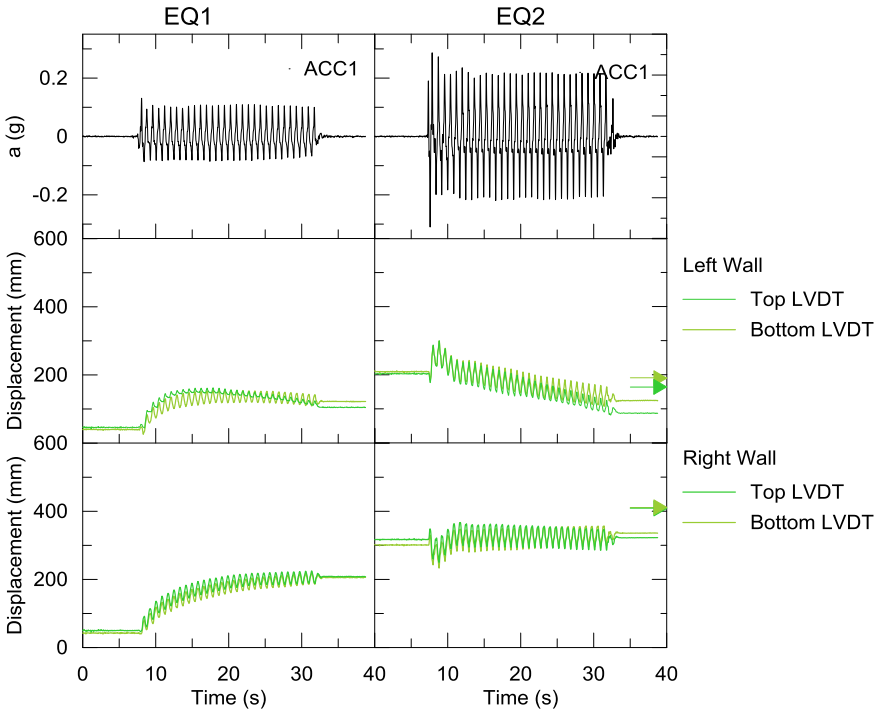

Figure 3.20: Test CWU1: long term residual values reported at the end of the dynamic time trend of the measured displacements.

6. The question regarding the synthetic representation of the post seismic behaviour seen at the previous point results in a more general treatment of the presentation of the results, specifically regarding all the plots in the space domain. In order to understand how the choice of the time instant for the plot of the space distribution of a certain physical quantity is made, let us consider Figure 3.21, where a typical time history of a physical quantity (pore pressure, displacement, bending moment, axial force) measured during the applied earthquake is shown; in this figure the same terminology introduced by Dewoolkar et al. (2001) is adopted. The 'pre-seismic' value is the measurement before the beginning of the seismic event. In the case of the first earthquake, which is called EQ1 for all the tests, the pre-seismic value coincide with the value at the and of the swing up and it is also named static. The maximum and minimum time instants are the maximum and minimum values that the given physical quantity reaches during

the shaking; the term dynamic refers a value of the physical quantity reached during the earthquake and it can be subdivided into dynamic minimum and dynamic maximum; concerning the pore pressure, it coincides with excess pore pressure. The value measured immediately after shaking is defined as short-term residual and, finally, the thick line toward the right side of the plot represents the long-term residual value, recorded after the excess pore pressures are completely dissipated.

The test phase strictly regarding the earthquake is indicated with the abbreviation EQ while the test phase relative to the excess pore pressure dissipation is indicated with the abbreviation PS (i.e. post-seismic).

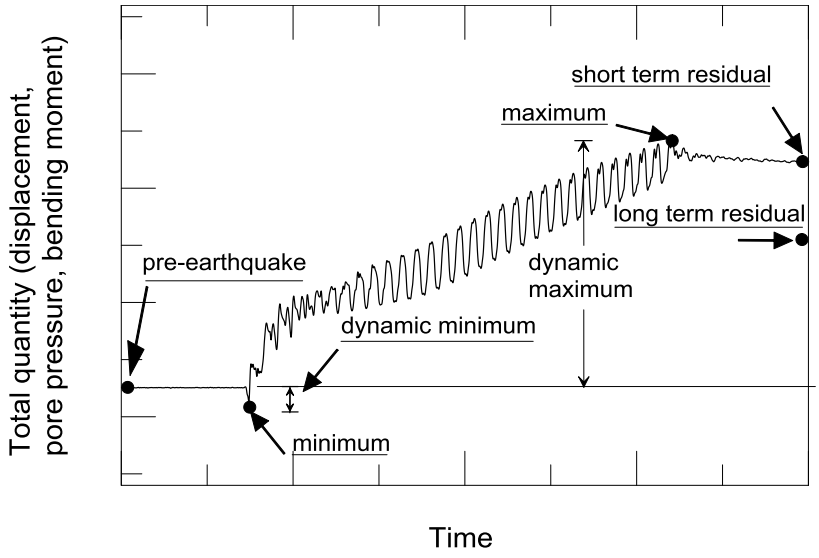

Figure 3.21: Typical time history of a physical quantity measured during the applied earthquake and adopted terminology.

The pre-seismic, the short term residual and the long term residual time instants are the same for all the physical quantities, while this is not true for the maximum or minimum values, which can be attained at different time instants, even for a given physical quantity, if it is measured at different locations in the space. For instance the

pore pressure can attain its maximum value at the beginning of the earthquake for a PPT located near the sand surface in the excavated side and it can reach the maximum value at the end of the earthquake for a PPT located at the bottom of the model. The plot of the space distribution of a given physical quantity requires the choice of a number of consecutive time instants. For the pre-earthquake, the short term residual and the long term residual time instants the choice is already univocal for all the physical quantities, while for the intermediate time instant, that is the time instant when the maximum or the minimum are attained, an arbitrary (of course meaningful for the description of the examined phenomena regarding the given physical quantity) and univocal choice is necessary. In this work the intermediate time instant chosen has been the time instant when the bending moment corresponding to a certain strain gauge of a given wall attains its maximum value during the earthquake. This strain gauge is the one where the bending moment is maximum along the wall in the static phase (Figure 3.22). The maximum bending moment on both left wall and right wall have been considered, but in this chapter only the results regarding the maximum bending moment on the left wall are reported. As it is shown in Figure 3.22, for a given time instant, the space distribution is realized through a line-dot graph where the dots are located in correspondence of the position of the measuring instrument.

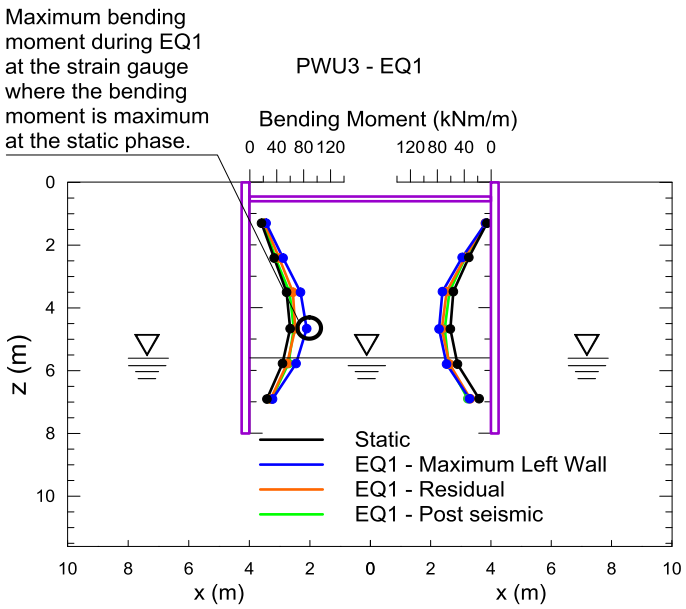

Figure 3.22: Test PWU3, earthquake EQ1: maximum bending moment during EQ1 and the strain gauge where it is attained. The Maximum Left wall time instant is common for all the other physical quantities of the test.

7. Relative density of the sand: in chapter 2 it has been illustrated how the calibration of the sand hopper is carried out in order to obtain the desired relative density of the sand, that is 38% for tests in loose sand and 88% for tests in dense sand. The same configuration as in the calibration of i) diameter of the muzzle, ii) number of sieves and iii) height of fall is kept for the sand pouring of the model, anyway the presence of the boundaries represented by the sides of the laminar box and the walls tend to increase the void index with respect its value supposed to be obtained as in the calibration of the sand hopper. Knowing the mass introduced within the models and the volume that is occupies thanks to the measurements of the soil surface depth and the excavation depth before and after the tests an estimation of the real relative density of the sand of the model has been obtained. For tests in loose sand the relative density has been seen to be lower than 30% before the tests and higher than 30% after the tests while for tests in dense sand the relative density it has been seen to be about 60% before the the tests and to increase up to about 65% after the tests. In Table 3.16 the detailed results of the computation of the relative

Test	Mass	$V_{in}[m^3]$	$V_{fin}[m^3]$	e_{in}	e_{fin}	$D_{rin}(\%)$	$D_{rfin}(\%)$
CWU1	43.4	0.0311	0.0304	0.899	0.856	29	39
PWU1	39.7	0.0288	0.0281	0.920	0.878	23	34
CWU2	46.1	0.038	0.0305	0.768	0.754	61	65
PWU2	43.8	0.0293	0.0290	0.772	0.754	60	64
CWU3	46.7	0.0309	0.0308	0.754	0.749	65	66
PWU3	43.6	0.0293	0.0290	0.784	0.761	57	62
CWU4	46.4	0.0311	0.0389	0.777	0.764	59	62

Table 3.16: Relative density Before and After the tests.

density, knowing the basic physical properties of the sand, before and after the tests has been reported.

8. In the end here it is the sign convention about the physical quantities: the accelerations are positive rightwards; the horizontal displacements of the walls are positive toward the excavated side; the rotation of the walls is positive if the walls rotate approaching the tops (cantilever walls) and it is negative if the walls rotate approaching the toes (propped walls); the bending moment in the case of test on cantilevered walls is positive when the tension side is located at the back of the wall, while in the case of test on propped walls the bending moment is positive when the tension side is located at the excavated side.

3.3 Test CWU1 Data

In Figure 3.23 and in Figure 3.24 the acceleration time histories at the back of the wall and in the excavated side are shown respectively. Both in EQ1 and in EQ2 the accelerations are significantly de-amplified.

The input acceleration (Acc1) and the time history acceleration recorded by the piezoelectric accelerometer (Acc2) placed at the bottom of the laminar box are very similar in EQ1, while in EQ2 the signals are quite different. During the model preparation, the accelerometer Acc2 is placed after a 5mm layer of sand has been poured within the laminar box, so it does not lie directly onto the laminar box base plate. Since the accelerometer is not placed exactly on the base plate, the accelerometer does not move exactly as the laminar box base plate; thus the difference in the time history could be due to the effect of the dynamic response of the soil, which is more important in

EQ2 with respect EQ1 because of the higher level of acceleration reached.

Both in EQ1 and EQ2 the accelerometers below the head of the piezometric fluid and above Acc2, which are Acc3 and Acc4, show a significant de-amplification of the input signal. Also the shape of the time history acceleration is different with respect the input signal, and correspondently the local maximum and minimum values of the signal change with time. The peak acceleration of Acc4 is 0.07g at the beginning of the earthquake, and after that the acceleration remains constantly around the value of 0.03g during EQ1 while the acceleration input is 0.13g. During EQ2 the peak acceleration of Acc4 is 0.09g at the beginning of the earthquake, while during the earthquake it attains values between 0.02g and 0.04g and the corresponding peak acceleration of the input signal is about 0.31g at the first peak of the earthquake and then it is constantly around 0.20g. It is interesting to notice that the acceleration is again amplified above the head of the piezometric fluid. The comparison between Acc4 and Acc5 underlines such amplification both in EQ1 and EQ2. The maximum acceleration relative to Acc4 is 0.07g and 0.09g in EQ1 and EQ2 respectively while, the maximum acceleration of Acc5 is 0.08g and 0.10g; if the intermediate values are considered, for Acc4 the local maxima are about 0.03g and 0.03-0.04g while for Acc5 they are 0.04g and 0.03g respectively for EQ1 and EQ2.

The accelerometers within the excavated side show a de-amplification of the acceleration as well (Figure 3.24). The time histories relative to the accelerometers Acc6 and Acc7 are similar to those of the accelerometers placed at the same depth Acc3 and Acc4. As regards EQ1, the maximum acceleration of Acc6 is 0.11g at the peak of the beginning of the earthquake and then the acceleration is constantly about 0.06g while the acceleration of Acc7 relative to the peak at the beginning of the earthquake is 0.08g and then it is 0.04g. As regards EQ2, the acceleration at the peak of the beginning of the earthquake for Acc6 is 0.18g and then it is about 0.05g, while for Acc7 the acceleration relative to the peak at the beginning of the earthquake is 0.07g and further it is collocated around 0.04g.

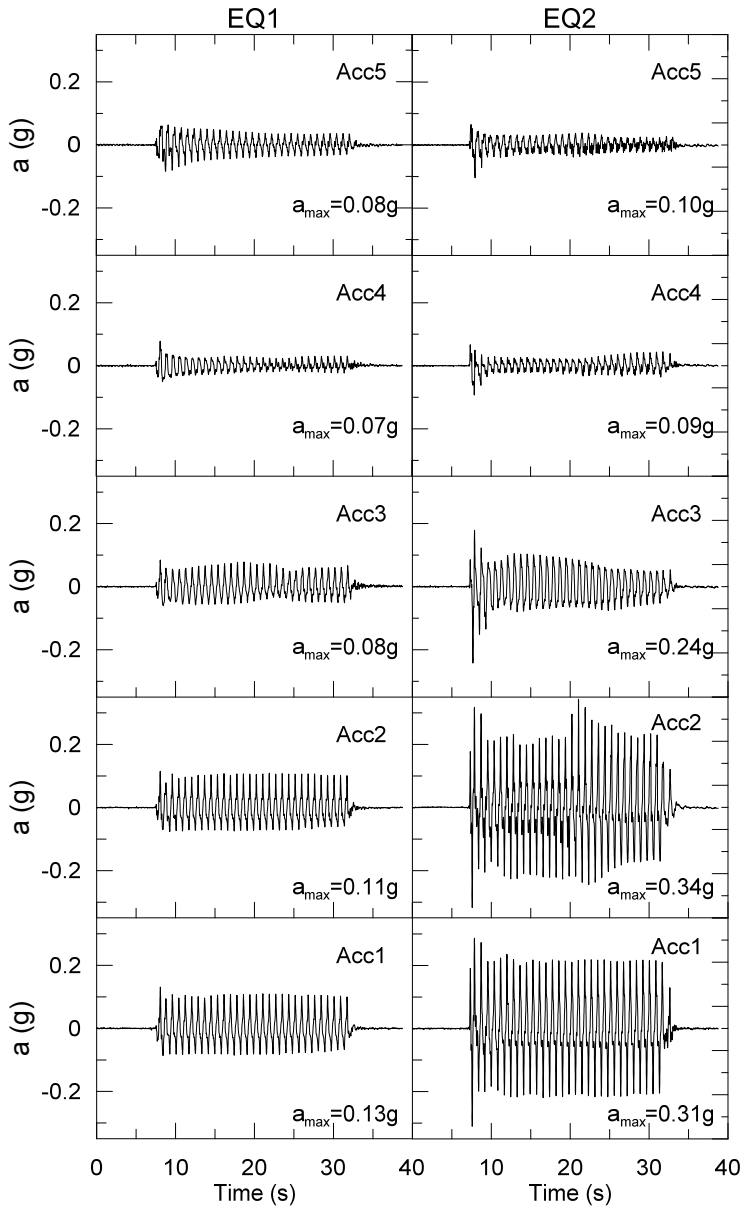

Figure 3.23: CWU1: acceleration time histories at the back of the left wall during EQ1 and EQ2.

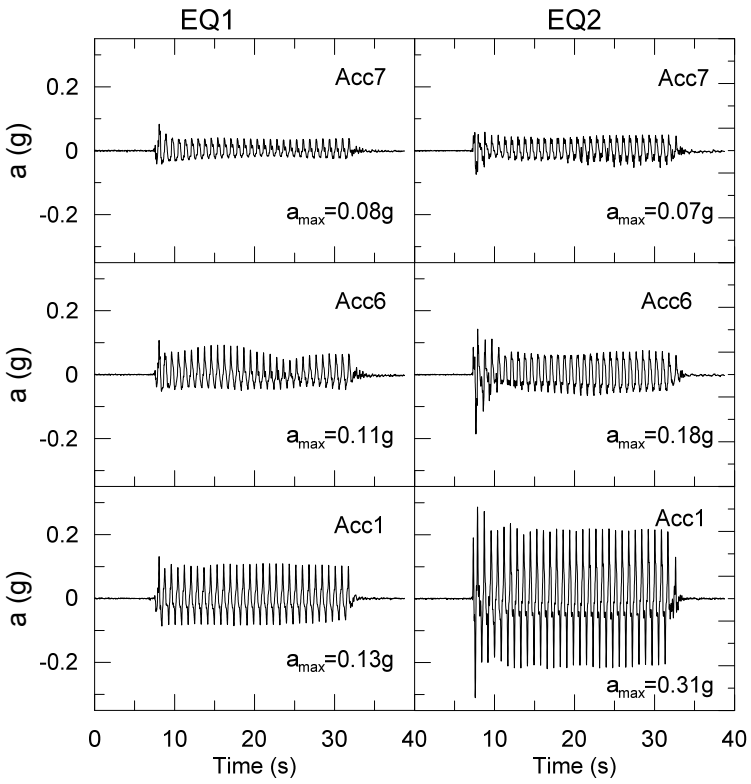

Figure 3.24: CWU1: acceleration time histories between the walls during EQ1 and EQ2.

In Figure 3.25 and in Figure 3.26 the plot representing the amplification factor along the depth is reported. In both the figures it is clear that the amplification factor is less than one along the height of the wall. It is also evident that in EQ1 the amplification factor constantly decreases moving from the bottom to the top of the wall, while in EQ2 it assumes a greater than one value in correspondence with Acc2, then it become less than one

for the following accelerometers. Finally passing from Acc4 to Acc5 the amplification factor start again to increase even if it remains still lower than one.

As well as for the back of the wall, in Figure 3.27 and in Figure 3.28 the trend of the amplification factor with the depth at the excavated side is reported; again it can be observed that it constantly attains a value lower than one.

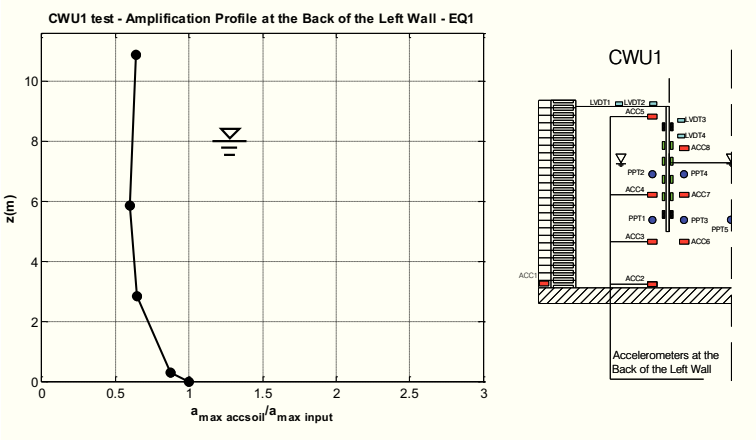

Figure 3.25: Test CWU1: amplification factor with the depth at the back of the left wall for EQ1. Starting from the bottom, at each circled marker correspond respectively Acc1, Acc2, Acc3, Acc4 and Acc5.

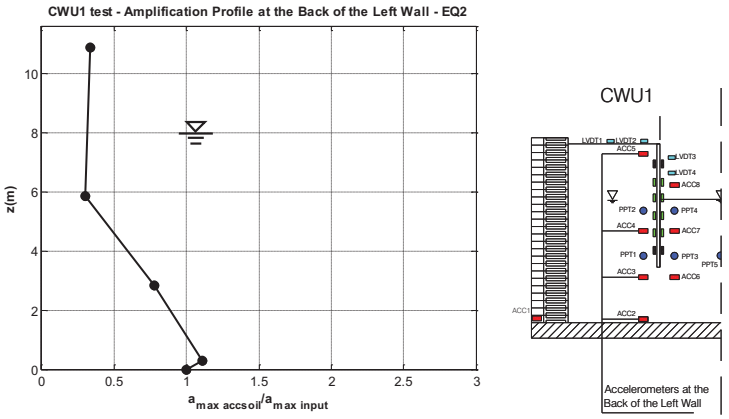

Figure 3.26: Test CWU1: amplification factor with the depth at the back of the left wall for EQ2. Starting from the bottom, at each circled marker correspond respectively Acc1, Acc2, Acc3, Acc4 and Acc5.

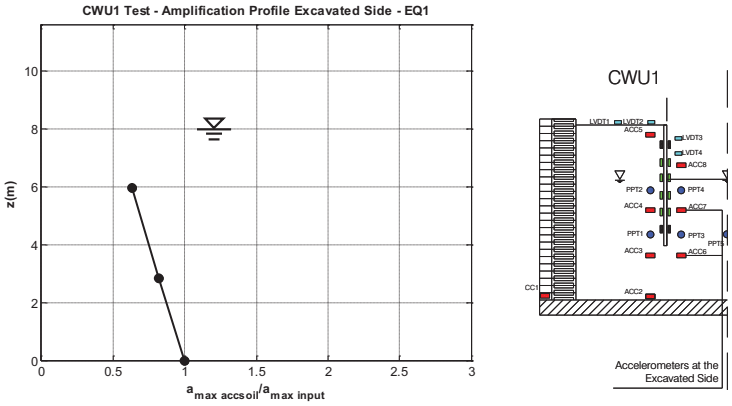

Figure 3.27: Test CWU1: amplification factor with the depth at the excavated side for EQ1. Starting from the bottom, at each circled marker correspond respectively Acc1, Acc6 and Acc7.

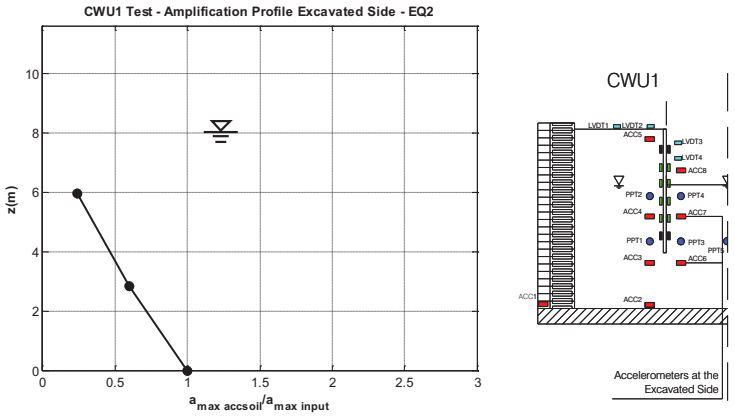

Figure 3.28: Test CWU1: amplification factor with the depth at the excavated side for EQ2. Starting from the bottom, at each circled marker correspond respectively Acc1, Acc6 and Acc7.

In Figure 3.29 and in Figure 3.30 the phase difference between the input accelerometer Acc1 and the accelerometers Acc2, Acc3, Acc4, Acc5, Acc6 and Acc7 are reported respectively for EQ1 and EQ2. For EQ1 (Figure 3.29) the acceleration time history of Acc2 aligned to the input acceleration so that the phase difference is constantly zero during the earthquake and the plot relative to Acc2 does not compare within the figure. As regards the accelerations relative to the accelerometers Acc3, Acc4...Acc7 it can immediately be observed that the phase difference relative to the accelerometers placed below the piezometric head of the porous fluid, namely Acc3, Acc4, Acc6 and Acc7, is constantly lower than 50°, while the phase difference between Acc1 and Acc5 is around 150°. This indicates that the portion of soil included between the base of the laminar box and the excavation level does not significantly differ in phase with respect the input acceleration, while the upper part of the soil, locate above the excavation level, tends to be out of phase with respect the input acceleration.

A similar conclusion can be deduced if EQ2 is considered in Figure 3.30. Here in fact the phase difference between Acc1 and Acc5 is around 150° at the beginning of the earthquake and it increases overcoming 200° as the seismic shaking continues. On the other hand, looking at the remaining acceleration time histories, which are relative to the accelerometers placed

below the excavation level, again it can be observed that their phase difference is around 50°. In this second earthquake also it can be observed that Acc2 is no more aligned in the time domain with Acc1, while its phase difference is zero up to about 20 seconds and, after that time instant, it increases as the shaking continues and it reaches and overcomes 50° at the end of the earthquake.

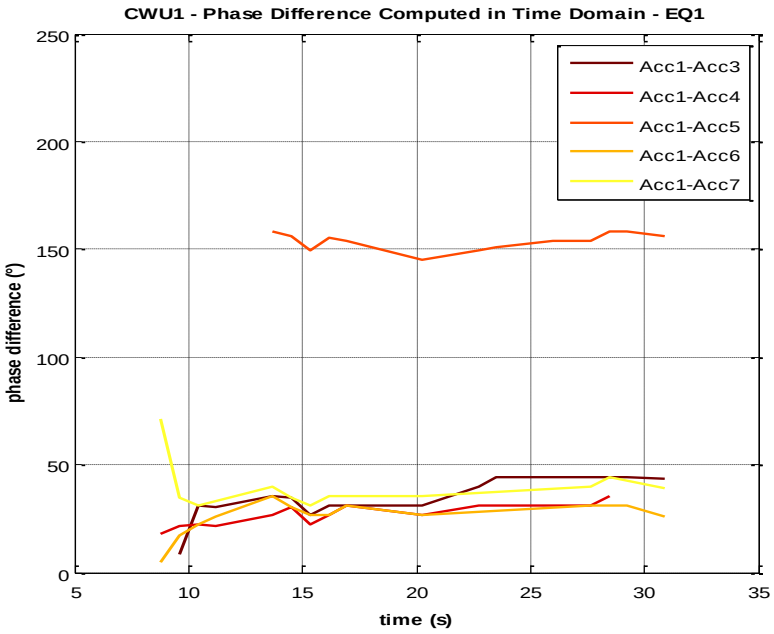

Figure 3.29: CWU1- EQ1: phase difference computed in the time domain.

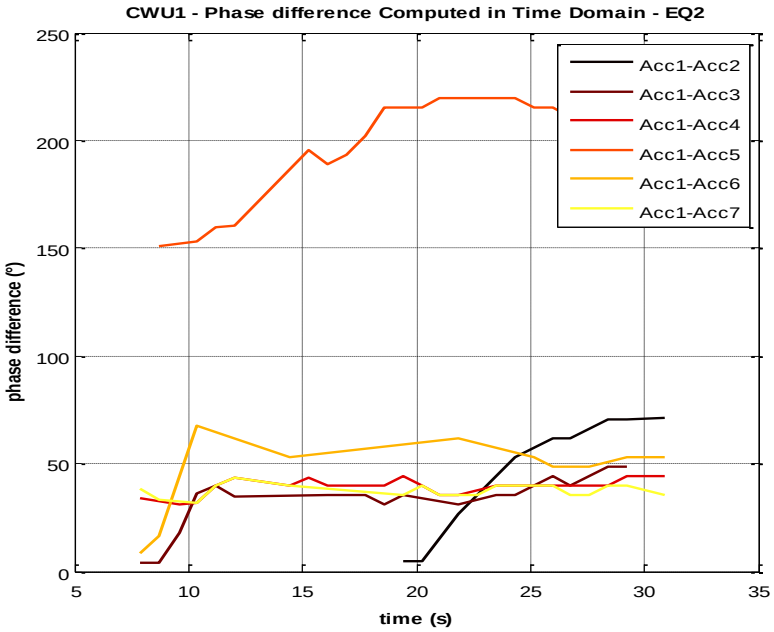

Figure 3.30: CWU1 EQ2: phase difference computed in the time domain.

The horizontal displacements of the walls measured by the LVDTs are reported in Figure 3.31and in Figure 3.32. Considering the measured displacements in Figure 3.31, it can be seen that on both left wall and the wall at the beginning of both EQ1 and EQ2 the displacement at the top is higher than at the bottom, while at the end of the earthquakes the displacement at the bottom is lower than the displacement at the top. At this stage of the test, the laminar box rings displacements do not affect the measurement of the horizontal displacements of the walls since the shaking has not started yet; this implies that the walls have rotated during the swing up approaching the tops as it is expected for a pair of cantilever walls. For the visualization of walls response in the continuation of the test it is necessary to refer to the symmetrical displacements that in Figure 3.32 can be found. Again the top LVDT before the earthquakes EQ1 and EQ2 registers a displacement higher than the displacement of the bottom LVDT. Moreover, considering that at the short term residual time instant, the top LVDT register a displacement lower than the displacement of the bottom LVDT, the walls have counter-rotated during the earthquake. After EQ1 they have

counter-rotated again and have reached a final configuration (that is the configuration pre-EQ2) where again the tops of the walls are closer than the toes. The behaviour observed during EQ1 can be observed during EQ2 as well, where starting from the configuration where the displacement at the top is higher that the displacement at the bottom, the short term residual configuration is achieved where the displacement at the top is lower than the displacement at the bottom. The symmetrical displacements time trend in Figure 3.32 shows between 10s and 15s progressive distancing between the displacement at the top and the displacement at the bottom indicating that the rotation is increasing; after that a maximum distancing is achieved, the displacements tend to approach and then to invert their position indicating that the counter-rotation is occurred. As well as for EQ1 also during EQ2 an initial increase of the rotation can be deduced by the distancing of the top displacement and the bottom displacement at the beginning of the earthquake (at about 8s), and immediately after the displacement tend to approach and to invert their position in the time trend again indicating that a counter rotation is occurring.

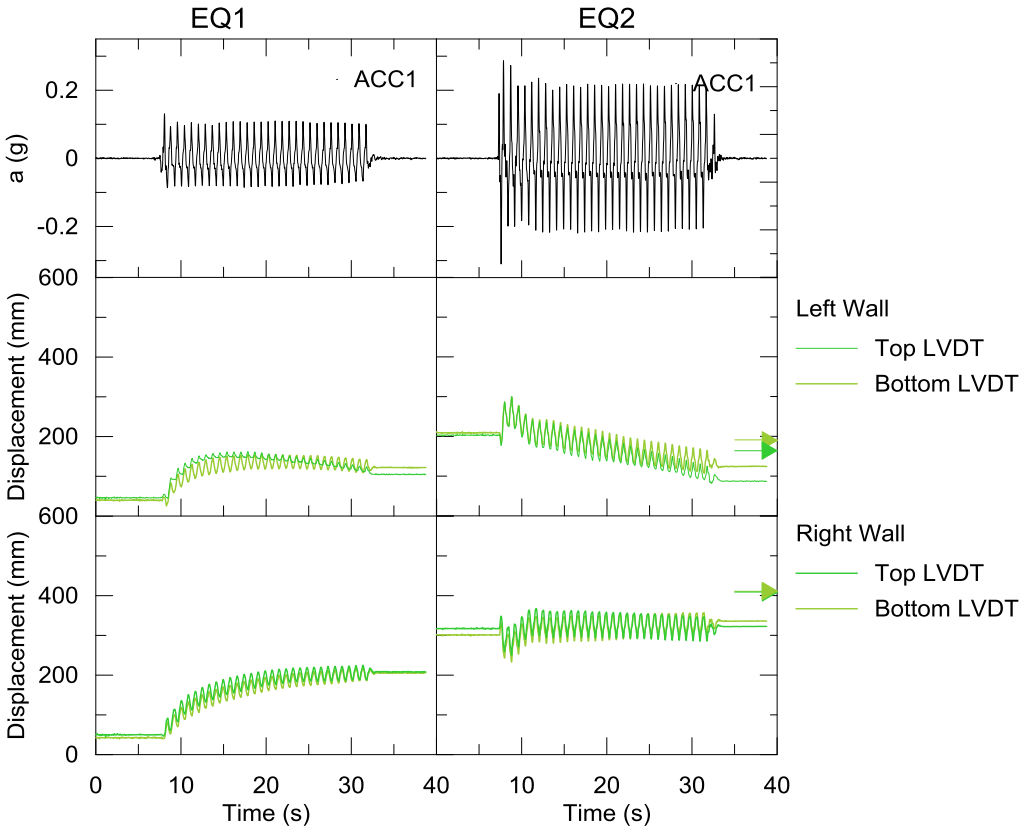

Figure 3.31: CWU1: walls horizontal displacement time histories during EQ1 and EQ2.

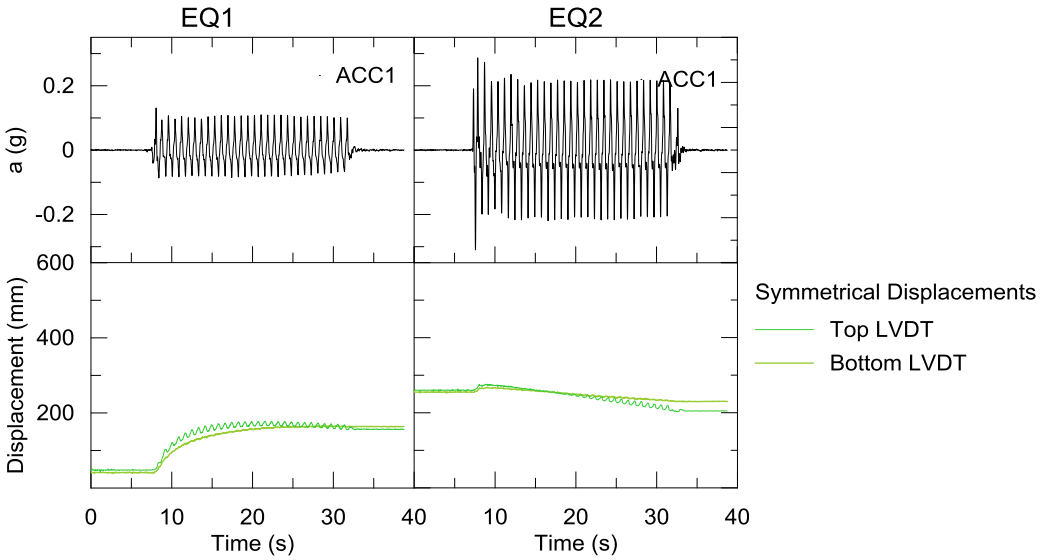

Figure 3.32: CWU1: walls symmetrical displacements time histories during EQ1 and EQ2.

The rotation reported in Figure 3.33 and in Figure 3.34, computed from the symmetrical displacements, clearly highlights what has been asserted above, that is that at the beginning of the earthquakes EQ1 and EQ2 the walls are rotating approaching the tops, then the rotation increases and later they counter-rotate. In fact at $t = 0$, for both EQ1 and EQ2, the rotation is positive, which means, considering the definition of Θ in the expression 3.11 $\Theta = \arctan \frac{LVDT_{top}+LVDT_{bot}}{d}$, that the tops are closer than the bottoms of the walls, and for time instants included between 0 and 13s (EQ1) and 0 and 10s (EQ2) it increases and later it starts to decrease reaching for both the earthquakes negative values indicating that a counter-rotation has occurred and at the end of the earthquakes the toes of the walls are closer than the tops. At the beginning of EQ1 (static) the rotation is 0,3°, then it reaches a maximum value of 0,95° and finally it becomes negative and equal to -0,3° at the end of the earthquake (short term residual); the correspondent values for EQ2 are 0,23°, 0,31° and -1,13°.

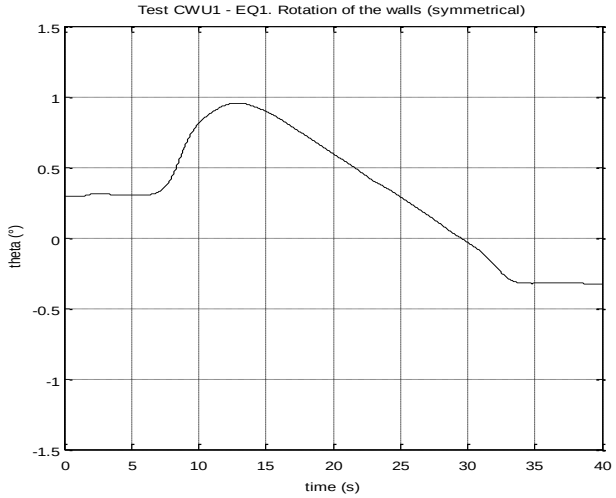

Figure 3.33: Test CWU1 EQ1: Rotation of the walls computed from the signals of the LVDTs (symmetrical).

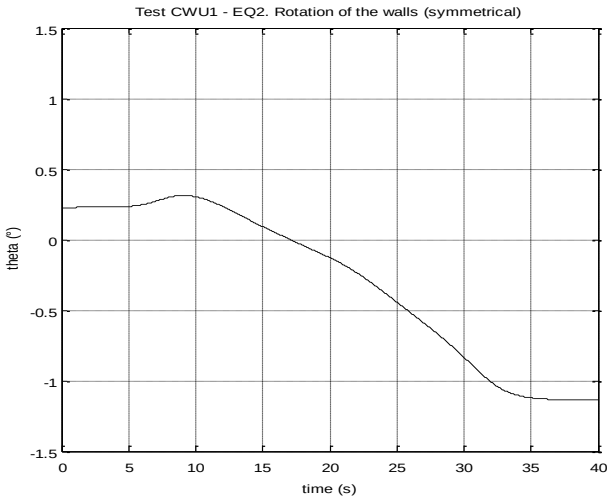

Figure 3.34: Test CWU1 EQ2: Rotation computed from the signals of the LVDTs (symmetrical).

This behaviour of the walls is also highlighted in Figure 3.35 where the

space distribution of the displacements is reported with respect to the consecutive time instants pre-earthquake, maximum, short term residual and long term residual.

In Figure 3.35(a) and in Figure 3.35(c) the measured displacement are shown, while the symmetrical displacements are reported in Figure 3.35(b) and in Figure 3.35(d). The static values of the displacement are 53mm and 6mm respectively for the top and the bottom of the walls. During EQ1 (Figure 3.35(b)), when the maximum time instant is reached, the walls inclination is higher than its static value, confirming what has been seen above, and the displacement at the top of the walls is about 114mm while the displacement at the bottom is about 18mm. At the short term residual the displacement at the top of the walls is about 151mm and at the bottom the displacement is 200mm. Comparing the displacements of the maximum time instant with those of the short term residual, it emerges that the walls have accumulated displacements toward the excavation side of 98mm at the top and 194mm at the bottom; this means that the walls have counter-rotated after the maximum time instant.

The walls space configuration corresponding to the long term residual of EQ1 shows that the displacement at the top is 263mm and that the displacement at the bottom is 229mm indicating that the walls have continued accumulating displacements during the process of dissipation of the pore pressures that follows the short term residual time instant recovering an inclination where the displacement at the top is higher than the displacement at the bottom.

The counter-rotation of the walls, which characterizes their response during EQ1, can be observed also during EQ2. In Figure 3.35(d) it can be seen that the walls have counter-rotated moving from the pre-earthquake configuration, which coincides with the EQ1 long term configuration, to the consecutive maximum, short term residual and long term residual configurations. The displacement at the top of the walls passes in fact from 249mm at the maximum time instant to 186mm and 276mm at the short term residual and long term residual time instant. The corresponding values of the displacements at the bottom are 263mm, 362mm and 374mm, and confirm that the walls have counter-rotated during EQ2. It is worth noting that during the dissipation of the excess pore pressures generated during EQ2, the walls have started to counter-rotate again, as well as during EQ1, reaching a final configuration, which corresponds to the long term residual time instant, where the displacement at the bottom is still higher than the displacement at the top.

This response of the walls in terms of displacements and rotation is likely

due to the strong decrease of the soil resistance at the excavated side related to the increase of the pore pressures during the earthquake; the consequent dissipation of the excess pore pressures generated during the earthquake governs the soil-structure response in terms of displacements during the post-seismic phase. The walls in fact, appear to increase their inclination up to a time instant, which is at about 13s during EQ1 and at about 8s during EQ2, when the equilibrium of the structure is no more guaranteed due to the loss of passive resistance in the excavation side.

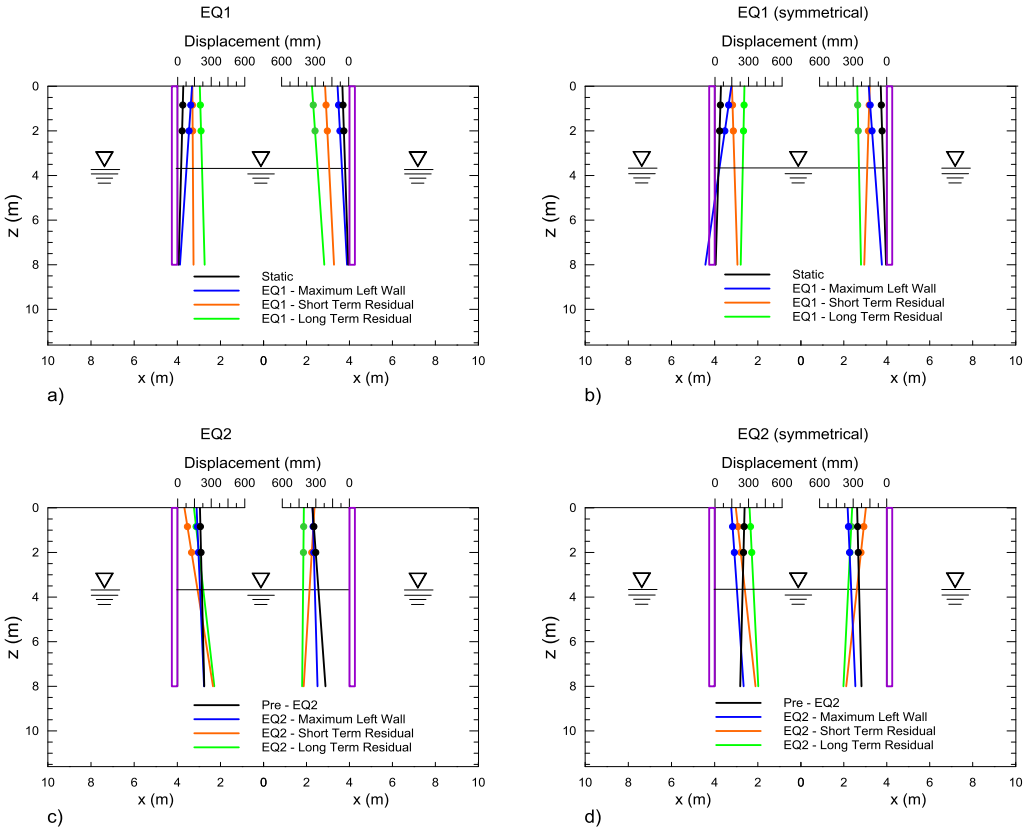

Figure 3.35: CWU1: displacement space distribution. (a) EQ1 and PS1 measured displacements, (b) EQ1 and PS1 symmetrical displacements.

In Figure 3.36 the pore pressure time histories are shown. All the PPTs indicate a significant increase of the pore pressure during the earthquakes. For a given PPT the time response passing from EQ1 to EQ2 is similar, excepted for PPT6 that shows a faster increase of the pore pressure during

the first seconds of EQ2 with respect EQ1. The PPT1 time trend in EQ1 and EQ2 is practically the same apart from a slight increase of the short term residual value of EQ2. In all the time trends of the pore pressures, the cyclic response is not present, excepted for PPT6 that shows a cyclic response during EQ2 and PPT7 that exhibits the cyclic response during both EQ1 and EQ2. Anyway such cyclic response does not appear to be relevant for the interpretation of the global response of the model, that appears to be more importantly governed by the loss of resistance of the soil, that is correlated to the entity of the excess pore pressure rather than to the cyclic response in the time trend. PPT1, PPT3, PPT5 and PPT7 are located about at the same depth but exhibit some differences in the time trend. PPT1 and PPT7 are both at the back of the walls (left wall and right wall respectively) but the first one increases monotonically while the second one exhibit a cyclic response. PPT3 and PPT5 have been placed both in the excavated side. PPT3 is close to the wall while PPT5 is in the middle of the excavated side. The static value of the pressure is the same for both PPT3 and PPT5 while the short term residual of PPT5 is higher than PPT1. The pre-EQ2 pressure of PPT5 is lower than its static value indicating that probably PPT5 has moved toward the top during EQ1 and that PPT5 is closer to the piezometric head of the porous fluid. This is confirmed also by the post test measurements that have indicated that the excavated level has moved toward the top.

In Figure 3.37 the time history of the pore pressure coefficient r_u compared with the unity relative to each PPT is reported. It is clear that liquefaction occurs within the excavated side since r_u becomes higher than 1 during EQ1 and EQ2 for the PPT5, which is placed at the middle of the excavated side. At the same time at the back of the walls r_u is below the unity indicating that liquefaction does not occur. This is due to the self weight of the dry soil above the head of the pore fluid that increases the effective vertical stress which has been calculated. The increment of the pore pressure during the earthquake has a significant effect on the dynamic response of the walls. The counter rotation of the walls during EQ1 and EQ2 is related to the loss of shear resistance within the excavated side caused by the increase of the pore pressure.

It is worth noting that the excess pore pressure increase with depth for a given earthquake (see for instance the r_u time trend of PPT6 and PPT7 in Figure 3.37 where it is clear that the time trend of PPT6 lies above the time trend of PPT7) that it tends to increase passing from EQ1 to EQ2, indeed the final value for EQ1 and EQ2 of the r_u time trend of a given PPT in Figure 3.37 increases passing from EQ1 to EQ2.

It is worth noting also that the r_u time trend of PPT6 and PPT7 (Figure 3.37) indicates that the excess pore pressure increases with depth for a given earthquake, this will be more clear in the following where the spatial distribution of the pore pressure will be described in detail. In Table 3.17 the values of the r_u coefficient at the end of the earthquake are reported. In Figure 3.38 the pore pressure space distribution during EQ1 and EQ2 is reported. The pore pressures do not reach the maximum value simultaneously with the bending moment, but the maximum value is attained at the short term residual time instant during both EQ1 and EQ2. The maximum value reached at the bottom of the laminar box is 142kPa and 168kPa respectively at the short term residual of EQ1 and EQ2. After the short term residual time instant the pore pressures decrease returning at the pre-seismic space distribution.

During EQ2 the pore pressures reach the maximum value at the short term residual time instant as well as in EQ1, but a faster increase during the first seconds of EQ2 can be observed; in fact the pore pressures at the maximum time instant are quite close to their value at the short term residual time instant.

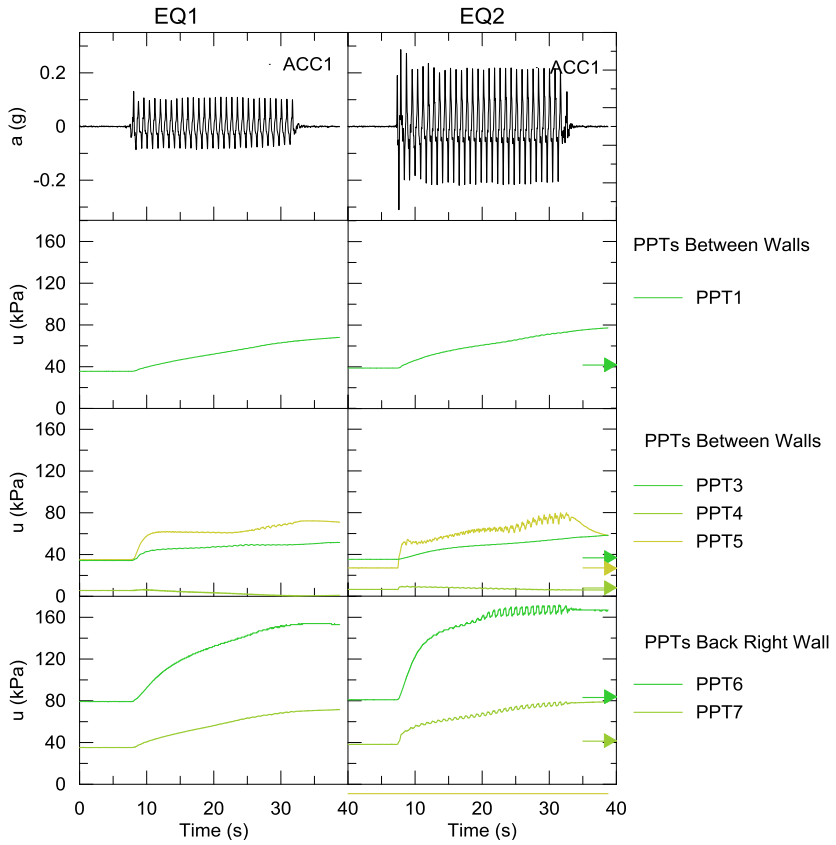

Figure 3.36: CWU1: pore pressures time histories during EQ1 and EQ2.

Test CWU1: values of r_u at the end of the earthquakes		
	$EQ1$	EQ2
PPT1	0.39	0.49
PPT3	0.63	0.88
PPT5	1.36	0.89
PPT6	0.59	0.71
PPT7	0.44	0.52
PPT8	-0.14	0.00

Table 3.17: CWU1: values of r_u coefficient at the end of the earthquakes.

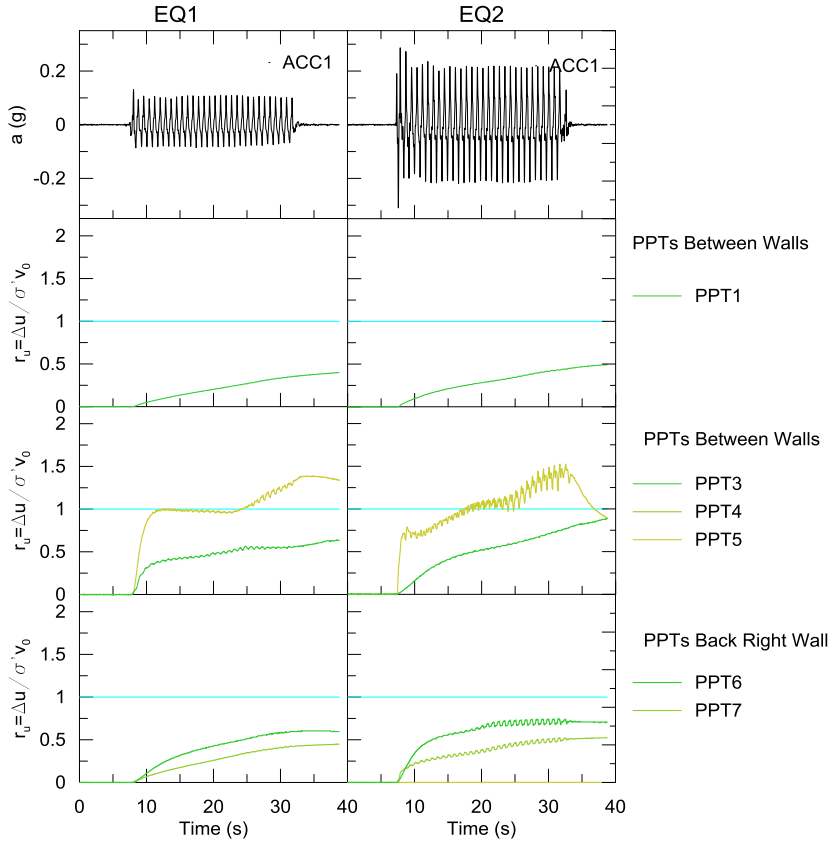

Figure 3.37: CWU1: time history of the pore pressure coefficient r_u.

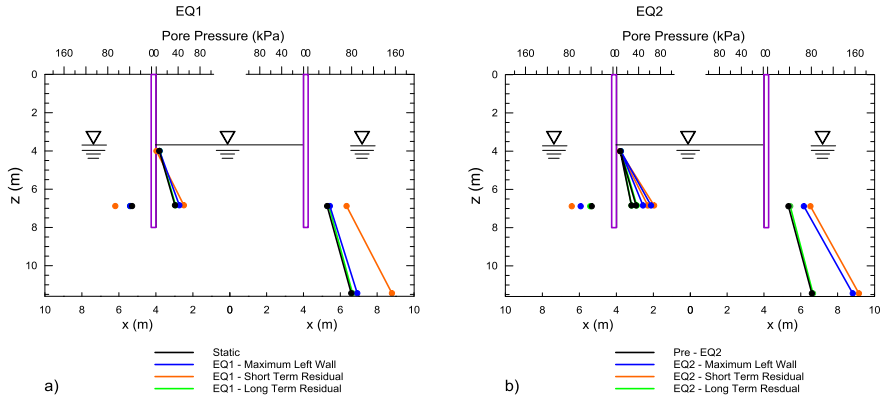

Figure 3.38: Test CWU1: pore pressure space distribution during EQ1 and EQ2. (a) EQ1 and PS1, (b) EQ2 and PS2.

In Figure 3.39 the time histories of the bending moments for both walls are shown. The cyclic response is more evident for the strain gauges closer to the bottom of the wall, and it becomes less significant during the earthquake while the pore pressures increase. Considering the bending moment time histories relative to the strain gauges of the right wall it can be observed that the curves of the time trends intersect during both EQ1 and EQ2; this indicates that the bending moment spatial distribution changes during the seismic shaking. This aspect is highlighted in the following where the spatial bending moment distribution is examined in detail.

In Figure 3.40 the bending moment space distribution is reported. It is worth noting that the strain gauges 3 and 5 of the left wall have not worked during the test, so being the right wall more suitable to understand the structural response of the model, the bending moment distribution obtained considering the maximum bending moment attained at the right wall has been reported. The maximum bending moment during EQ1 on the right wall is attained at the strain gauge 5, which is collocated at 5.79m from the top of the wall, and at the static phase it is 35kNm/m and reaches 44 kNm/m during EQ1, so it increases of about the 25%. At the short term residual it is about 9kNm/m while at the long term residual it is 23 kNm/m. So the first main effect of the earthquake on the bending moment can be highlighted, that is its substantial reduction during the shaking up to the end of the earthquake. Considering EQ2, the pre-earthquake bending moment at strain gauge 5 is 23kNm/m, the maximum value is 34kNm/m, the short term residual value is 10 kNm/m and the long term residual value

is 19 kNm/m. So the maximum static bending moment and the maximum dynamic bending moment are considerably lower than those relative to EQ1, while the short term residual values are similar. So the maximum bending moment does not differ significantly from the pre-earthquake one; this means that the inertia force due to the shaking does not affect considerably the structural response.

Again considering Figure 3.40 it can also be observed that the maximum bending moment distribution is nearly a straight line, while the short term distribution is no more a straight line but it assumes a curved shape that crosses the static bending moment distribution. This implies that the horizontal stress distribution changes during the earthquake.

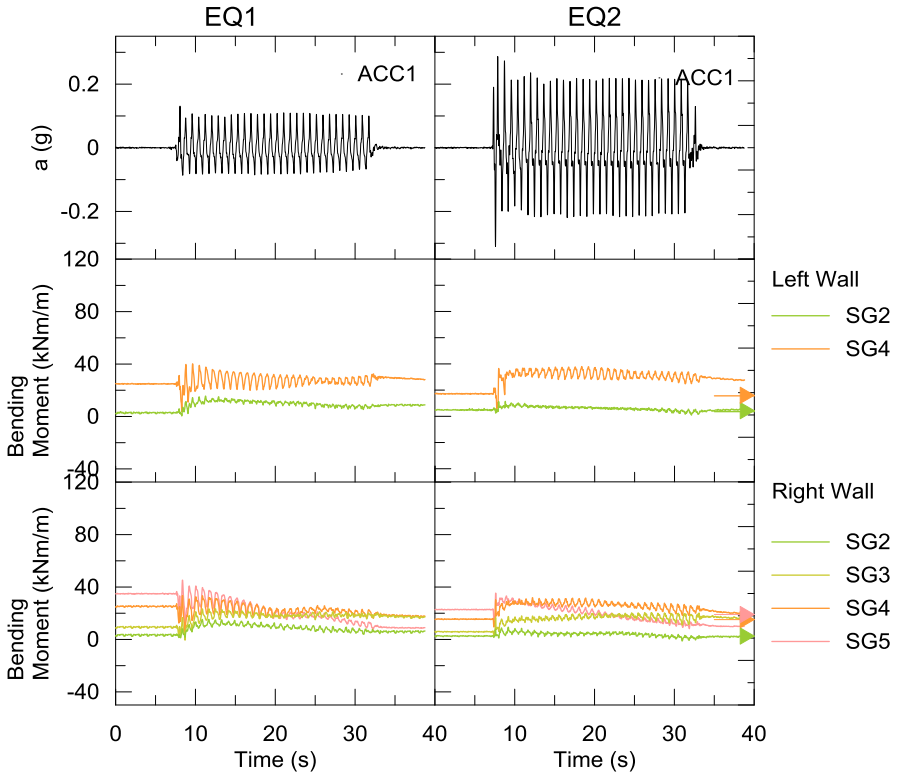

Figure 3.39: CWU1: bending moment time histories during EQ1 and EQ2.

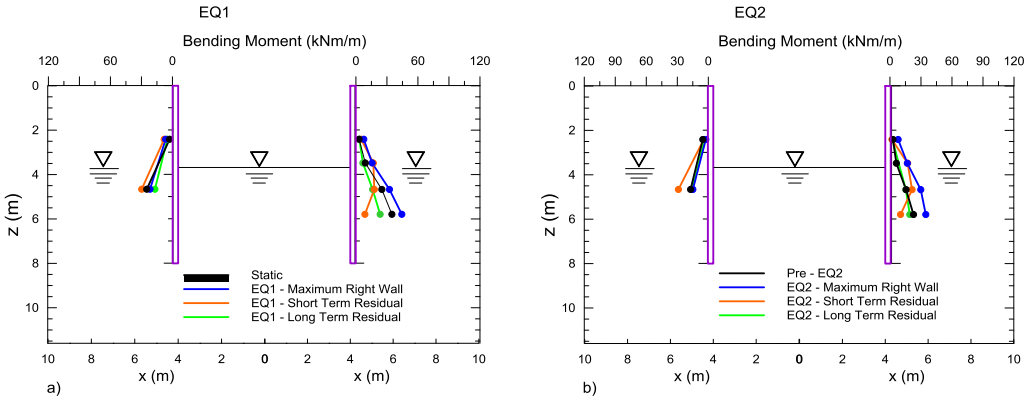

Figure 3.40: CWU1: bending moment space distribution during EQ1 and EQ2. (a) EQ1 and PS1, (b)EQ2 and PS2.

3.4 Test PWU1 Data

In Figure 3.41 and in Figure 3.42 the acceleration time histories at the back of the wall and in the excavated side are shown respectively. As well as in test CWU1 both in EQ1 and in EQ2 the accelerations are significantly de-amplified.

Also in this test, input acceleration (Acc1) and the time history acceleration recorded by the piezoelectric accelerometer (Acc2) located at the bottom of the laminar box are very similar in EQ1, while in EQ2 some differences in the signals can be found. This can be, as in CWU1, attributed to the effect on the input signal of the soil layer included between the base of the laminar box and the Acc2 accelerometer.

In Figure 3.41 the acceleration time histories relative to the accelerometers Acc1, Acc2 and Acc3 clearly show the de-amplification of the acceleration below the water table and the comparison between the acceleration time histories relative to the accelerometers Acc4 and Acc5 shows the amplification of the acceleration above the fluid table. In fact the maximum acceleration relative to EQ1 for the accelerometers Acc1, Acc2 and Acc3 is respectively 0.12g, 0.12g and 0.06g, while for the accelerometers Acc4 and Acc5 it is 0.08g and 0.12g; passing to EQ2, for Acc1, Acc2 and acc3 the maximum acceleration is 0.30g, 0.31g and 0.08g, while for Acc4 and Acc5 it is 0.12g and 0.16g.

The de-amplificaton is evident also in Figure 3.42 comparing the acceleration time histories relative to the accelerometers Acc1, Acc6 and Acc7.

The maximum acceleration of Acc6 and Acc7 is in fact 0.10g and 0.07g for EQ1 and it is 0.09g and 0.06g for EQ2. It is worth noting that the shape of the Acc7 acceleration time history, which is not symmetrical, is probably influenced by the walls movement during the earthquake that probably pushes the accelerometer and consequently determines the non-symmetrical response. Also the Acc6 acceleration time history is probably affected by the walls movement.

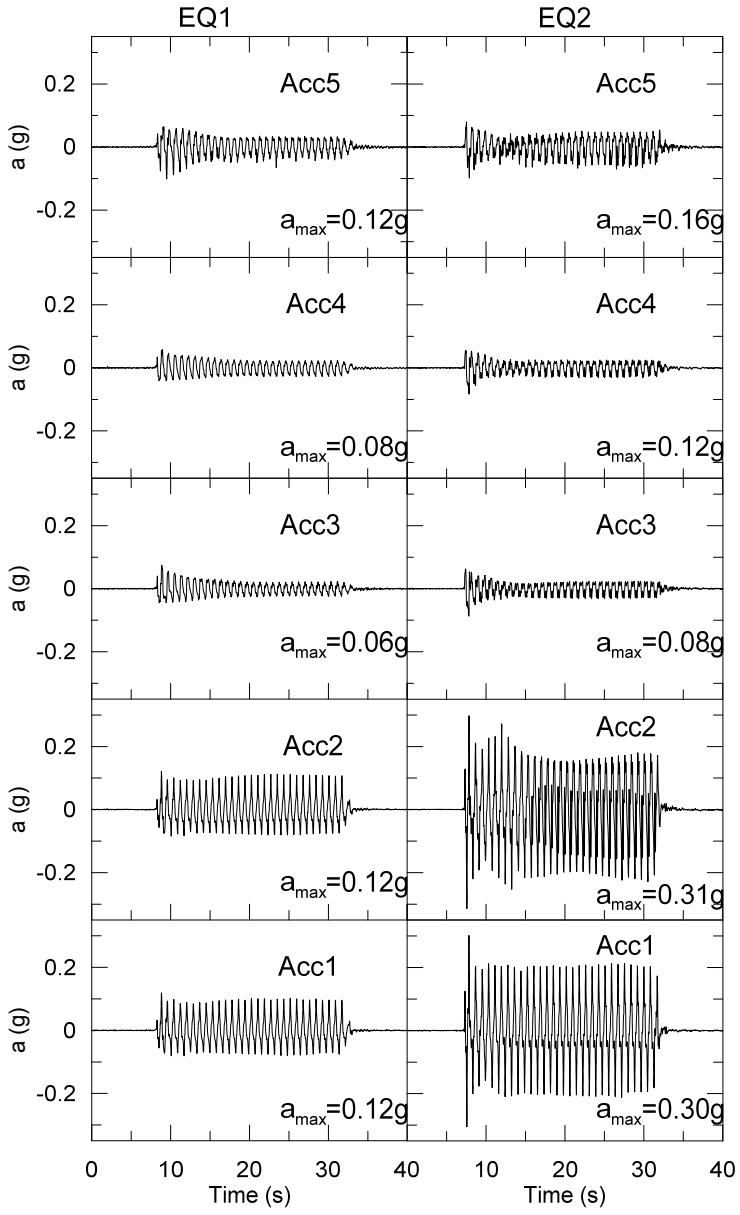

Figure 3.41: PWU1: acceleration time histories at the back of the left wall during EQ1 and EQ2.

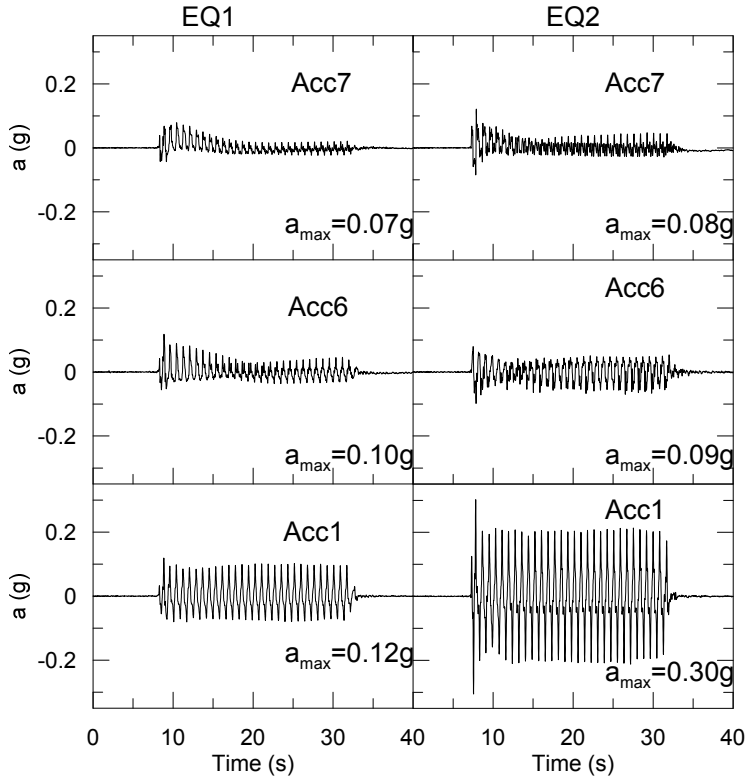

Figure 3.42: PWU1: acceleration time histories between the walls during EQ1 and EQ2.

In Figure 3.43 and in Figure 3.44 the amplification factor trend with respect the depth at the back of the left wall is reported showing the de-amplification of the acceleration with the depth as well as in the test CWU1 happens. In Figure 3.45 and in Figure 3.46 the amplification factor trend with respect to depth at the excavated side is reported indicating, as well as at the back of the wall, the de-amplification of the acceleration. In all

the cases the de-amplification appears to be more marked for the stronger earthquake, EQ2, than for the weaker earthquake, EQ1.

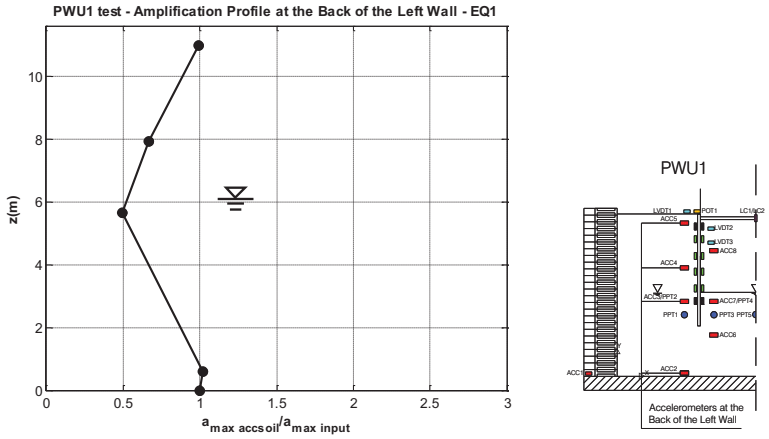

Figure 3.43: Test PWU1: amplification factor with the depth at the back of the left wall for EQ1. Starting from the bottom, at each circled marker correspond respectively Acc1, Acc2, Acc3, Acc4 and Acc5.

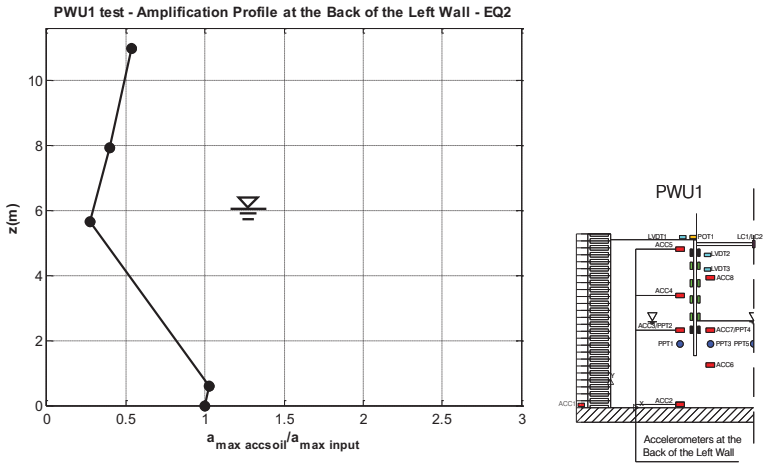

Figure 3.44: Test PWU1: amplification factor with the depth at the back of the left wall for EQ2. Starting from the bottom, at each circled marker correspond respectively Acc1, Acc2, Acc3, Acc4 and Acc5.

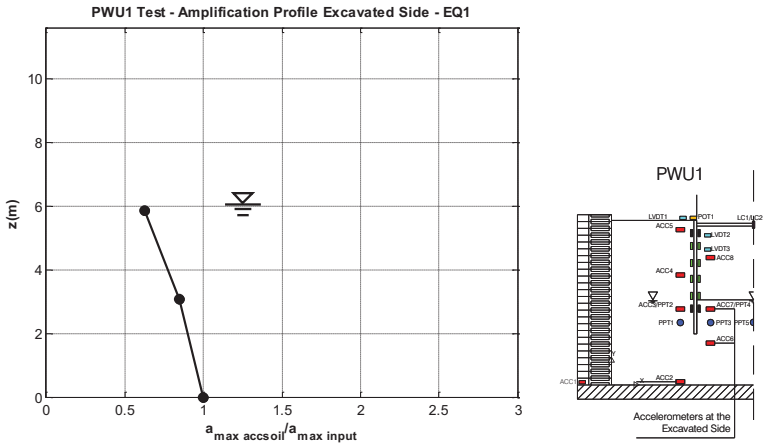

Figure 3.45: Test PWU1: amplification factor with the depth at the excavated side for EQ1. Starting from the bottom, at each circled marker correspond respectively Acc1, Acc2, Acc3, Acc4 and Acc5.

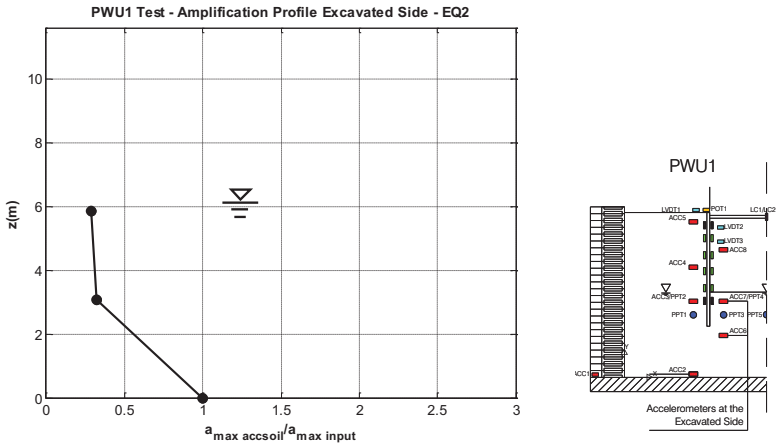

Figure 3.46: Test PWU1: amplification factor with the depth at the excavated side for EQ2. Starting from the bottom, at each circled marker correspond respectively Acc1, Acc2, Acc3, Acc4 and Acc5.

In Figure 3.47, in Figure 3.48 the phase difference computed in the time domain is reported. The interpretation of the phase difference trend in the time domain for this test is less immediate than for the test CWU1. While for the last one in fact, it is clear that the acceleration time histories relative to the accelerometers placed below the excavation level present the phase difference close to the input acceleration and the phase difference of the soil above the excavation level is significantly delayed, it is not the same for the test PWU1. Indeed the acceleration time history relative to Acc3, which is located below the excavation level, during EQ1 is about 50° at the beginning of EQ1, and immediately after it increases reaching about 120°. Moreover accelerometers placed above Acc3 show a phase difference lower than that one of Acc3, which is clearly non admissible from a physical viewpoint. As well as for Acc3, also Acc6 and Acc7 present a phase difference significantly high and of the same order of magnitude as for Acc3, remaining their phase difference lower than the phase difference of the accelerometers placed above the water table. This can be due to the significant effect on the characteristics of the accelerometer signals of the liquefaction or also to a delaying effect on the signals of the accelerometers Acc3, Acc6 and Acc7 of the displacement of the bottom of the wall. This strong modification induced on the characteristics of the signals determines such differences in the phase

difference as those in Figure 3.47 so that, for this test the computation of the phase difference brings to meaningless conclusions. This is the only test where the computation of the phase difference does not give meaningful results. This aspect is treated in detail in Chapter 4. Anyway the results of the computation of the phase difference in the time domain have been reported in Figure 3.47 and in Figure 3.48 for sake of completeness.

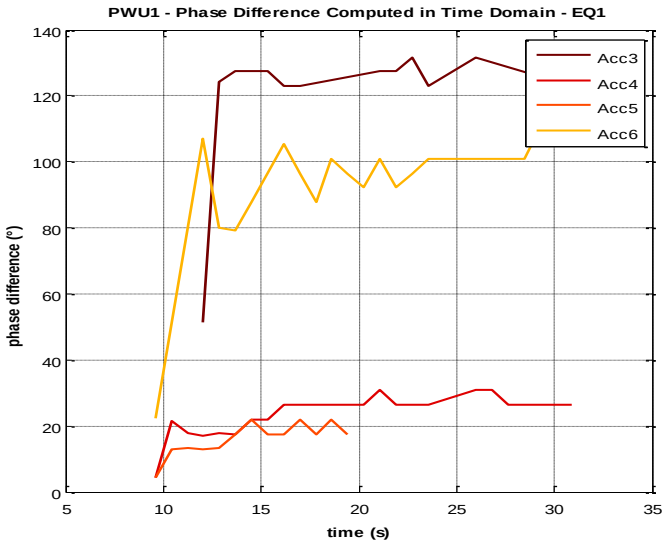

Figure 3.47: Test PWU1 EQ1: phase difference computed in the time domain.

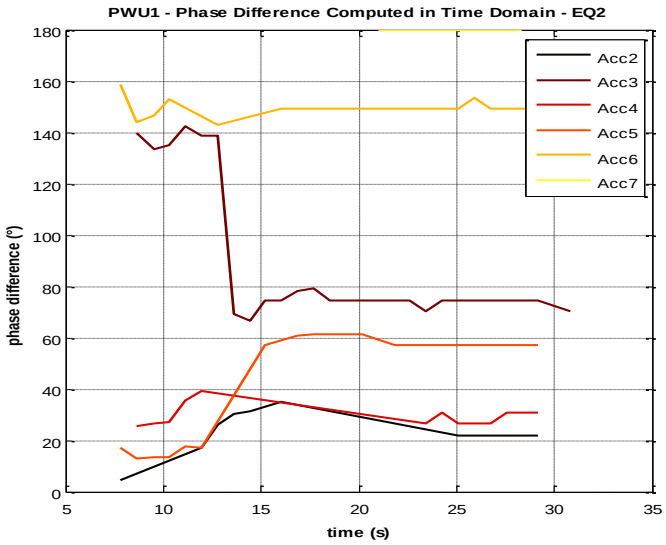

Figure 3.48: PWU1 EQ2: phase difference computed in the time domain.

In Figure 3.49 and in Figure 3.50 the horizontal displacement time histories relative to LVDT1, LVDT2, LVDT3 and LVDT4 are shown respectively for the measured displacements and the symmetrical displacements and for both EQ1 and EQ2. In Figure 3.50 it can be observed that for both EQ1 and EQ2 and for both left wall and right wall the top LVDT constantly record a value of the displacement lower than the value of the displacement recorded by the bottom LVDT. This means that the walls are moving toward each other approaching the toes, which is what typically happens for a pair of propped walls when a collapse mechanism represented by a rotation around the prop is activated.

At the same time, it is worth noting in Figure 3.49 that the time trend relative to the right wall displacements (LVDT4 and LVDT5) is increasing, while the time trend relative to the left wall displacement is decreasing. This means that in addition to the rotation, the left wall and the right wall are also apparently moving toward the left side, this can be explained considering that the LVDT are also measuring the displacements of the laminar box rings.

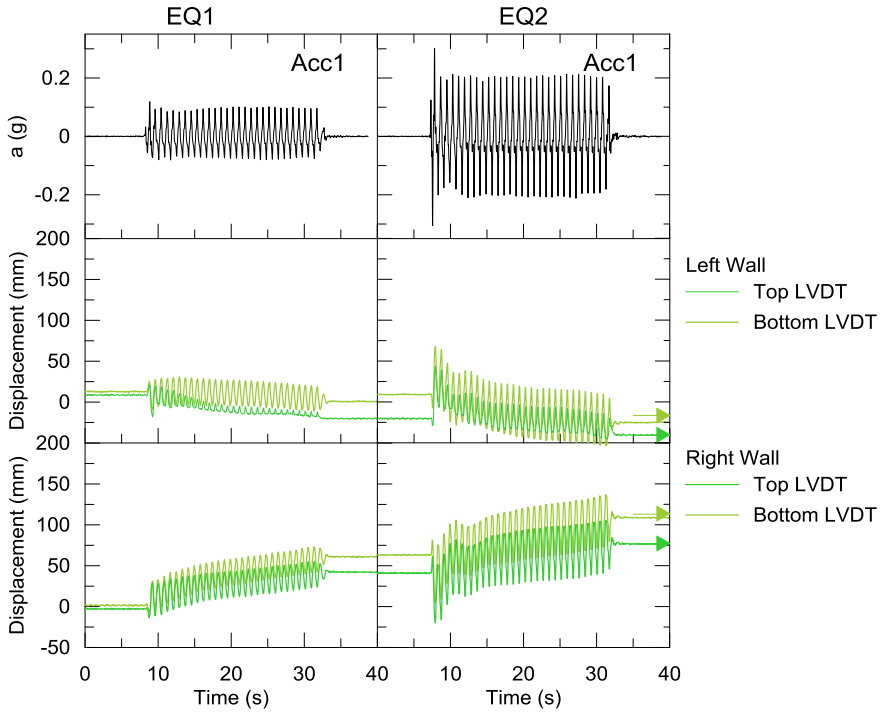

Figure 3.49: PWU1: walls horizontal displacement time histories during EQ1 and EQ2.

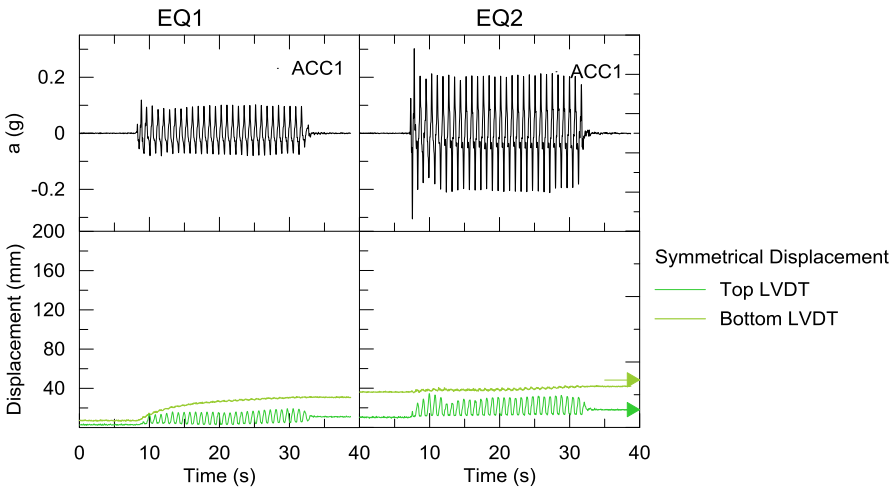

Figure 3.50: PWU1: walls horizontal symmetrical displacement time histories during EQ1 and EQ2.

The rotation of the walls obtained from the symmetrical displacements has been computed also for this test and it has been reported in Figure 3.51 and in Figure 3.52 for EQ1 and EQ2 respectively. Differently with respect to test CWU1 the rotation at the beginning of EQ1 is negative; this means that the toes of the walls are closer than the tops, coherently with the fact that the propped walls rotate around the props when they accumulate displacements. At the end of EQ1 the rotation has increased, meaning that the toes have become closer than at the beginning of the earthquake, and it continues to increase up to the beginning of EQ2. During EQ2 the rotation increases and then it decreases reaching a final value, which is the short term residual value, that is slightly higher that the initial one. At the beginning of EQ1 the rotation is -0.2° and at the end of EQ2 it is -0.95, while at the beginning of EQ2 it is 1.12°, then it decreases up to about -0.86° and finally it reaches a value of -1.2°.

In Figure 3.52 the displacement space distribution is shown both during EQ1, PS1, EQ2 and PS2. In Figure 3.53(a) and in Figure 3.53(c) the measured displacements are reported, and it is possible to notice the effect of the registration of the lateral displacements of the laminar box. In fact in both figures a displacement in correspondence to the prop can be observed toward the right side of the picture, which cannot be physically admissible since it would imply a translation of the right wall toward the soil side. Thus in Figure 3.53(b) and in Figure 3.53(d), the symmetrical displacements are reported; in this case, considering the consecutive maximum, short term

and long term spatial configurations reached by the walls it can be observed that:

1. the displacement in correspondence to the prop is constantly zero;
2. the progressive approach of the walls toes is highlighted.

During EQ1 and PS1 (Figure 3.53(b)) the entity of the accumulated displacements at the bottom are 0.3mm (static configuration), 0.34mm (maximum configuration), 132mm (short term residual configuration) and 169mm (long term residual configuration); while during EQ2 and PS2 the displacement at the bottom are 168mm (pre-EQ2 configuration), 159mm (maximum configuration), 164mm (short term residual configuration) and 206mm (long term residual configuration). It is evident that the accumulated displacements during EQ1 and PS1 are bigger than in EQ2 and PS2, where the maximum and short term residual configurations are very close to the pre-EQ2 configuration, while the long term residual configuration is far from them.

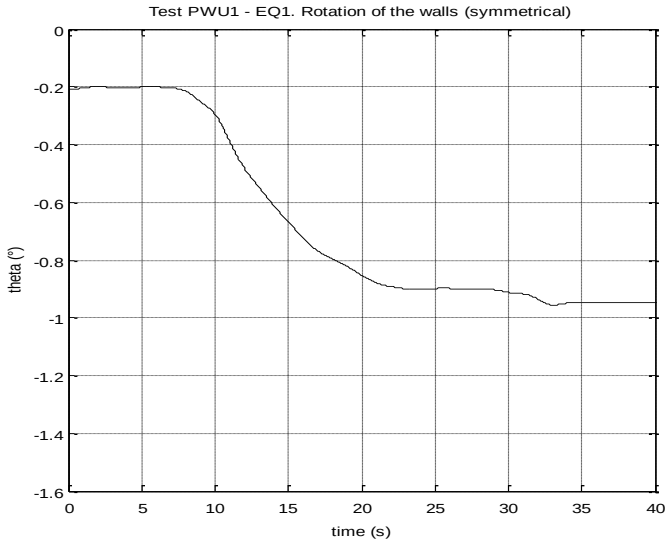

Figure 3.51: Test PWU1 EQ1: Rotation of the walls computed from the symmetrical displacements.

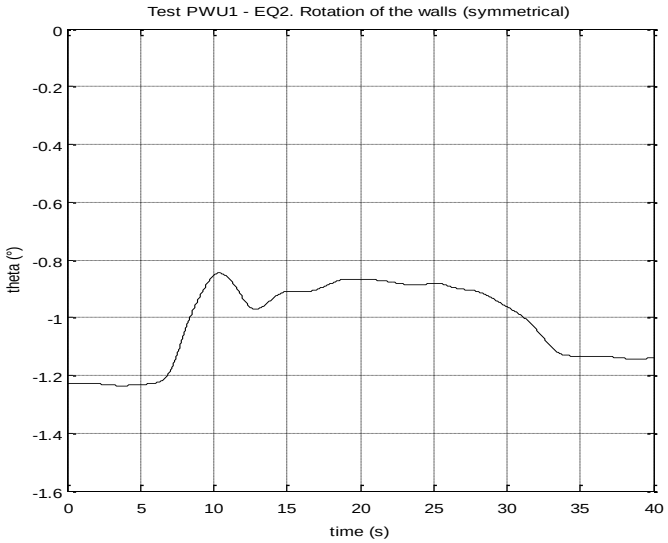

Figure 3.52: PWU1 EQ2: Rotation of the walls computed from the symmetrical displacements.

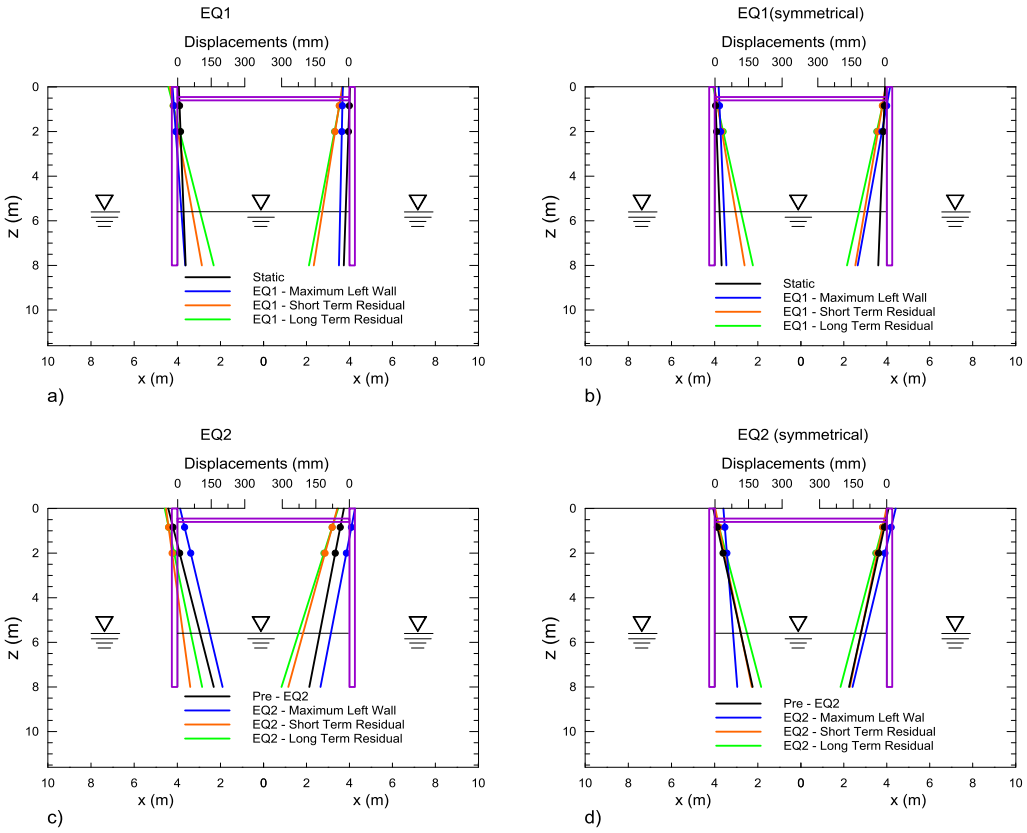

Figure 3.53: PWU1: displacement space distribution. (a) EQ1 and PS1 measured displacements, (b) EQ1 and PS1 symmetrical displacements, (c) EQ2 and PS2 measured displacements, (d) EQ2 and PS2 symmetrical displacements.

In Figure 3.54 the time trend of the pore pressures measured by the PPTs is illustrated. The response of PPT1, PPT2, PPT5 and PPT7, which are placed at the same depth, is very similar, considering both EQ1 and EQ2. The PPT6 shows an important increment of the value of the pore pressure and moreover it shows a cyclic response. Considering EQ1, the pressure measured by PPT6 increases of about 1/2 of the short term residual value during the first seconds of the earthquake and it reaches the short term residual value increasing with a lower velocity during the last seconds of the earthquake. On the other hand, considering the EQ2, the maximum value of the pore pressure of PPT6 is almost reached at the beginning of the earthquake, and this value remains constant up to the end of the earthquake.

In Figure 3.55 the time trend of the pore pressure coefficient r_u is re-

ported. In this case the value of r_u for PPT5 does not clearly intersect the line of the unity during EQ1 and EQ2 indicating that liquefaction has not occurred at the depth of PPT5. This does not necessarily imply that liquefaction has not occurred; it is likely that PPT5 is too close to the sand surface at the excavated side in order to measure a pore pressure value that determines the occurrence of liquefaction. Even if the PPT5 does not directly show the occurrence of liquefaction, sand boils observed at the sand surface at the excavated side appear to indicate that liquefaction as occurred (Figure 3.57). The values of r_u coefficient at the end of the earthquakes are reported in Table 3.18.

In Figure 3.56 the pore pressures space distribution is illustrated. At the back of the right wall the alignment PPT6, PPT7 and PPT8 shows that the maximum values of the pore pressures is reached at the long term residual time instant, while the configuration relative to the intermediate time instant is quite close to the pre-EQ2 configuration. The long term configuration is practically coincident with the pre-EQ2 configuration.

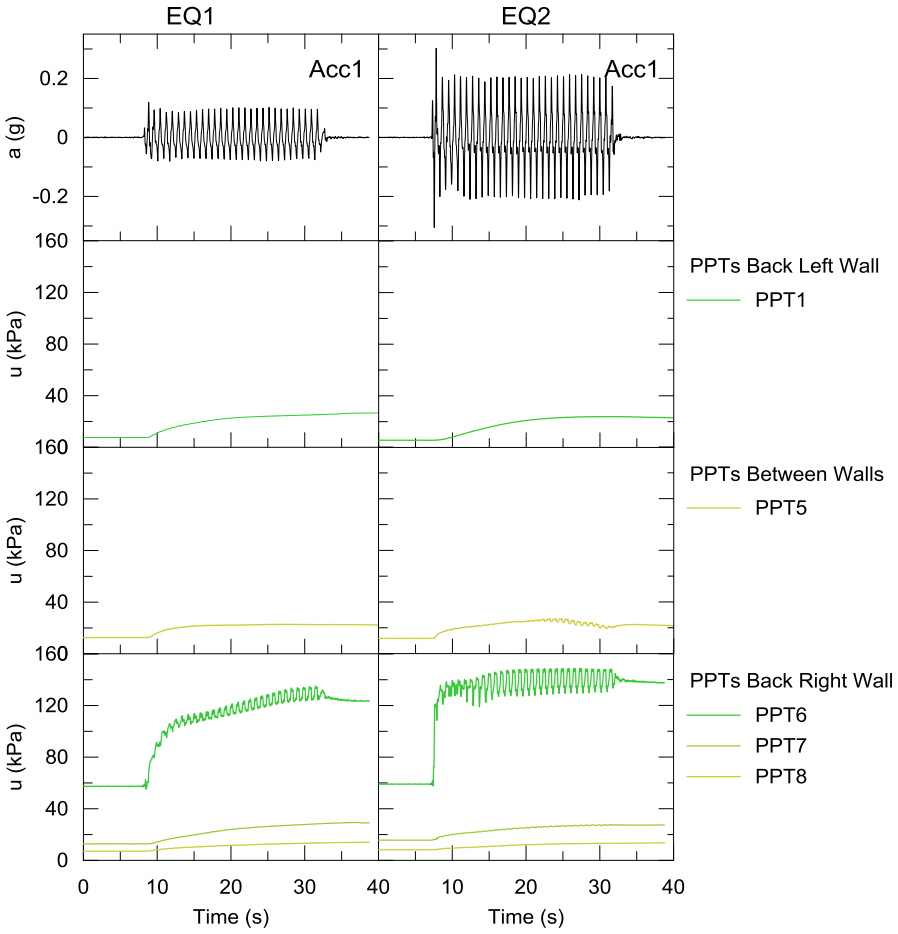

Figure 3.54: PWU1: pore pressures time histories during EQ1 and EQ2.

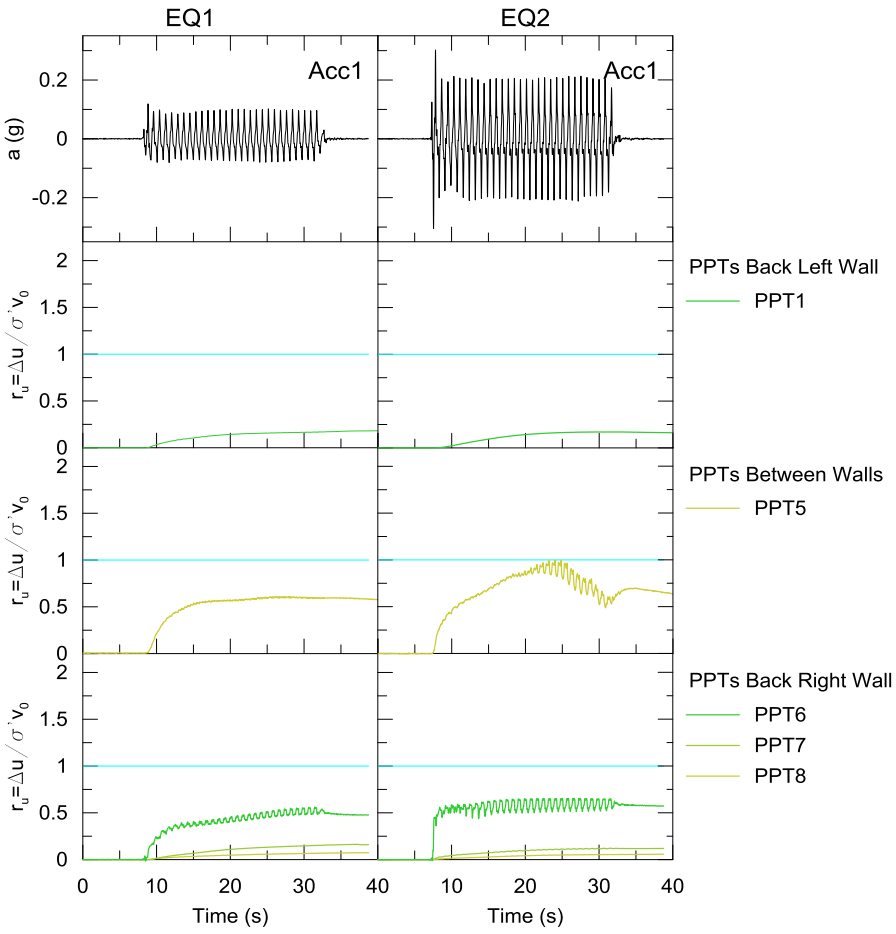

Figure 3.55: Test PWU1: r_u time history during EQ1 and EQ2.

Test PWU1: values of r_u at the end of the earthquakes		
	$EQ1$	EQ2
PPT1	0.18	0.16
PPT5	0.58	0.66
PPT6	0.47	0.57
PPT7	0.16	0.12
PPT8	0.07	0.05

Table 3.18: PWU1: values of r_u coefficient at the end of the earthquakes.

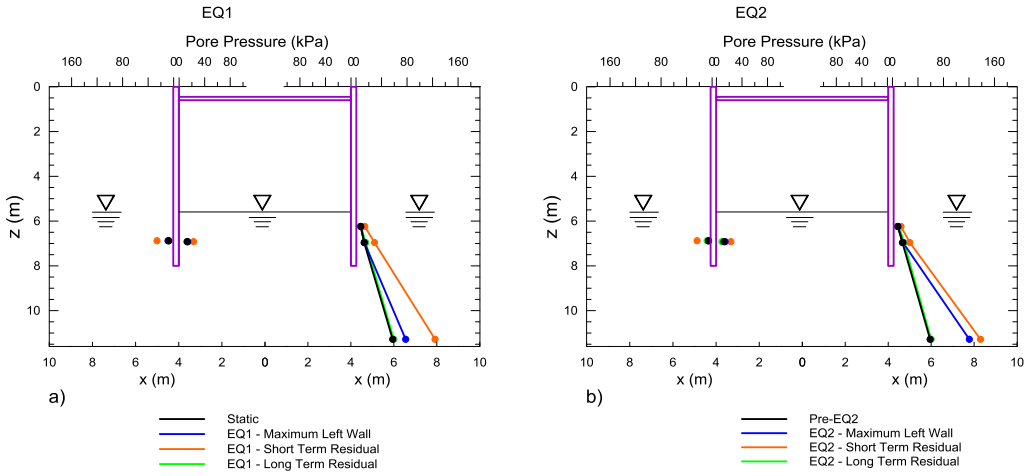

Figure 3.56: PWU1: pore pressure space distribution during EQ1 and EQ2. (a) EQ1 and PS1, (b) EQ2 and PS2.

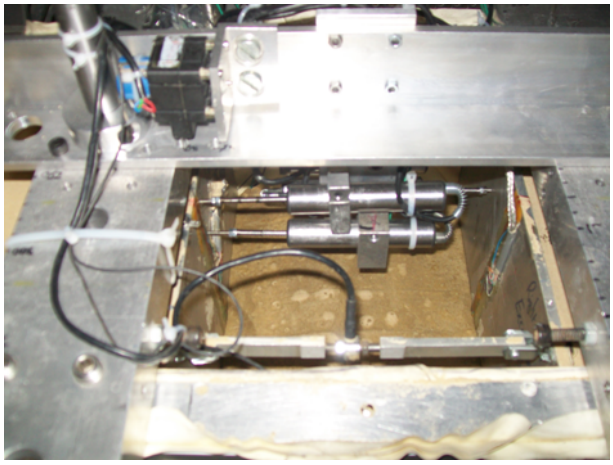

Figure 3.57: Model of Test PWU1: sand boils observed at the sand surface at the excavated side immediately after the test.

The time histories of the bending moment on the walls are shown in Figure 3.58. Two relevant characteristics of the time histories of the bending moment are:

1. the reaching of negative values during both EQ1 and EQ2;
2. as in test CWU1, the signals intersect indicating that the bending moment distribution changes during the earthquakes.

Finally in Figure 3.59 the bending moment space distribution during EQ1 and PS1 (Figure 3.59(a)) and in EQ2 and PS2 (Figure 3.59(b)) are shown. The static bending moment distribution attains its maximum value at the strain gauge 5 of the left wall. The maximum static bending moment, at the same strain gauge, is 76kNm/m on the left wall, then it increases up to 86kNm/m and it decreases on the right wall up to 33 kNm/m at the short term residual, while at the long term residual it is 64 kNm/m. The bending moment at the pre-EQ2 is 65 kNm/m, then it reaches the maximum value 94 kNm/m and at the short term residual it is -16 kNm/m while at the long term residual it is 56 kNm/m. So at the short term configuration of EQ2 negative values of the bending moment are registered.

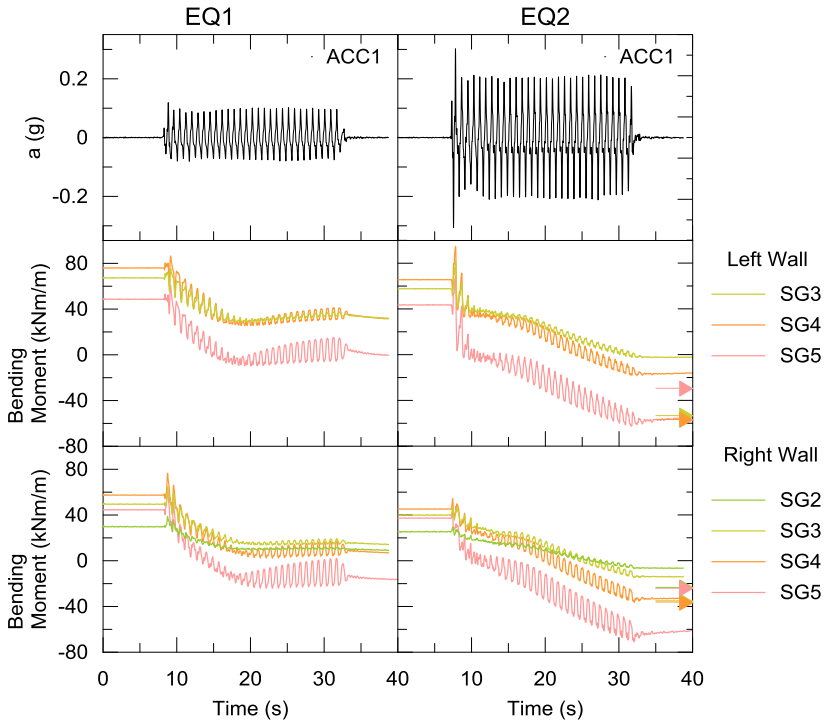

Figure 3.58: Test PWU1: bending moment time histories during EQ1 and EQ2.

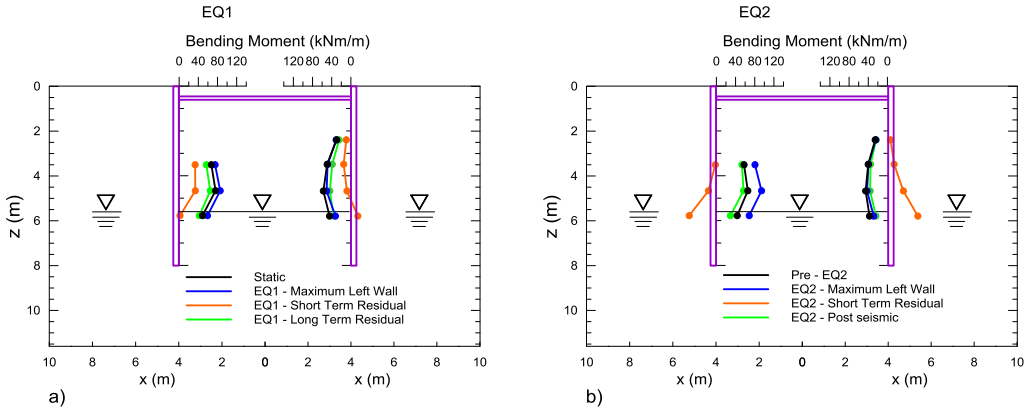

Figure 3.59: Test PWU1: bending moment space distribution during EQ1 and EQ2. (a) EQ1 and PS1, (b)EQ2 and PS2.

A drop of the bending moment is observed in both the earthquakes, and at the same time a drop of the axial force within the props is observed (Figure 3.60). The axial force passes from 140 kN to 100 kN during EQ1 and from 170 kN to 55 kN during EQ2.

These two observations suggest that during the earthquakes a significant change of the total earth pressure distribution acting on the walls is occurring, which is probably due to the increase of the pore pressures, and this determines a re-arrangement of the structural response where the bending moment becomes negative and the axial force decreases significantly. The decrease of the axial force is more important during EQ2 than during EQ1. Its value at the short term residual time instants is 100kN and 56kN respectively for EQ1 and EQ2.

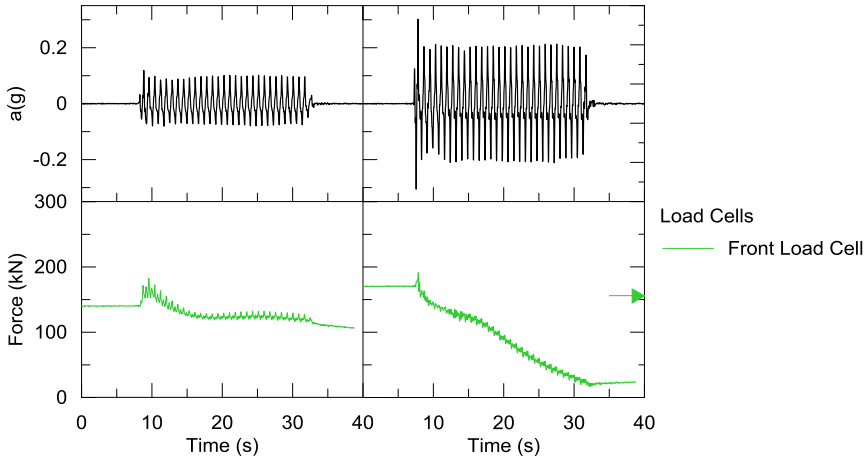

Figure 3.60: Test PWU1: axial force in the front prop during EQ1 and EQ2.

3.5 Test CWU2 Data

The acceleration time histories of the accelerometers at the back of the left wall and placed within the saturate soil layer Acc2, Acc3 and Acc4 are reported in Figure 3.61. The acceleration time trend relative to Acc2 is very similar to the input acceleration for all the earthquakes unlike the tests in loose sand, probably due to the higher relative density of the sand. Moreover there is not a marked de-amplification of the acceleration within the saturated soil layer as it happens for the tests CWU1 and PWU1 realized in

loose sand. The accelerometer Acc3 is likely moving during both EQ2 and EQ3, being its time trend oscillating around a curved line; the movement of the accelerometer shown by the acceleration time trend is due to the interaction of the accelerometer with the left wall that is moving during the earthquakes. In Figure 3.61 also the acceleration Acc8 has been reported. The piezoelectric accelerometer Acc8 is the only one above the head of the piezometric head of the porous fluid among all the accelerometers; it is collocated at the back of the right wall but it has been considered as collocated at the back of the left wall is order to obtain the profile of the amplification factor along the back of the left wall. The maximum acceleration during EQ1 of Acc1, Acc2, Acc4 and Acc8 is respectively 0.10g, 0.08g, 0.07g and 0.10g; during EQ2 they are 0.15g, 0.14g, 0.08g and 0.16g; during EQ3 they are 0.26g, 0.17g, 0.14g and 0.27g. So again a de-amplification, even if no so marked as for the tests in loose sand, is observed along the back of the left wall and the acceleration is again amplified passing from Acc4 to Acc8. As regards the accelerations in the excavated side, in Figure 3.62 the de-amplification of the maximum acceleration can be observed, since it passes from 0.10g to 0.08g and to 0.07g during EQ1, from 0.15g to 0.13g and to 0.08g during EQ2 and from 0.26g, to 0.25g and to 0.14g during EQ3.

In Figure 3.62 the acceleration relative to the excavated side are reported. Also in this figure it is possible to appreciate the amplification of the acceleration, which is less significant as the input acceleration increases.

In Figure 3.63 the response of the MEMS accelerometer placed on the top of the left wall is reported. The asymmetrical response passing from EQ1 to EQ3 can be noticed indicating the accumulation of the rotation of the left wall. The placement of the MEMS accelerometer is such that the acceleration is negative toward the excavated side and it is positive toward the backfill. The thing that the acceleration measured by the MEMS is asymmetrical with respect the x-axis and that the final values of the acceleration, for all the earthquakes, are negative indicate that the left wall is accumulating displacements toward the excavated side.

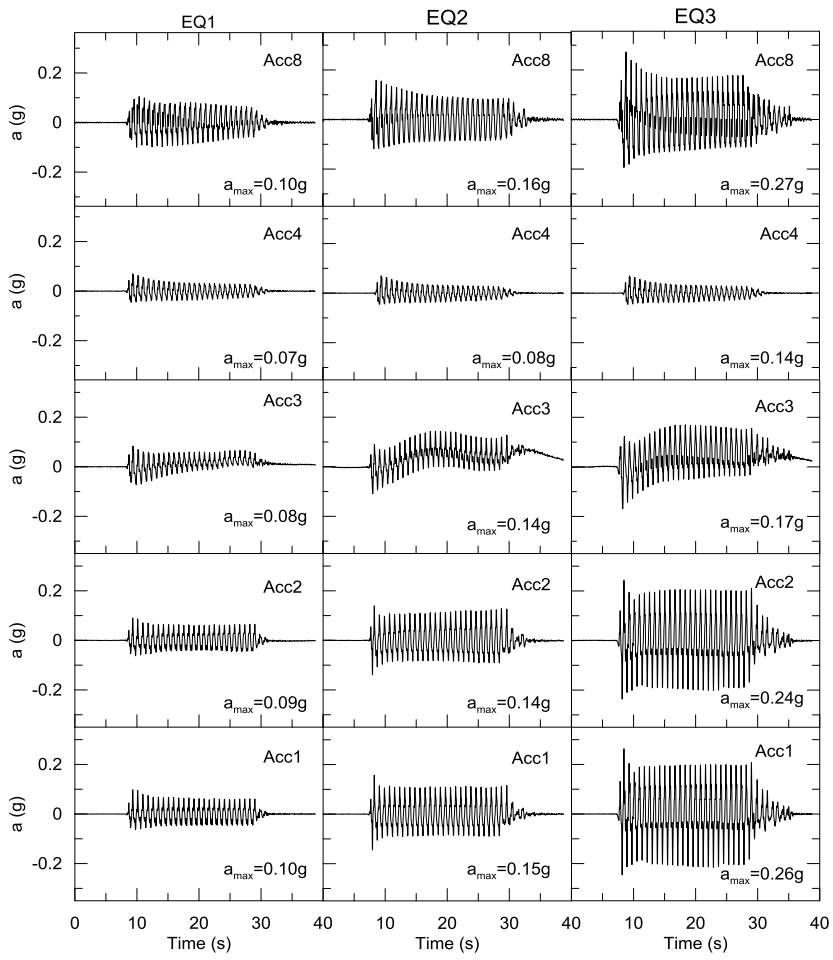

Figure 3.61: Test CWU2: acceleration time history at the back of the left wall during EQ1, EQ2 and EQ3.

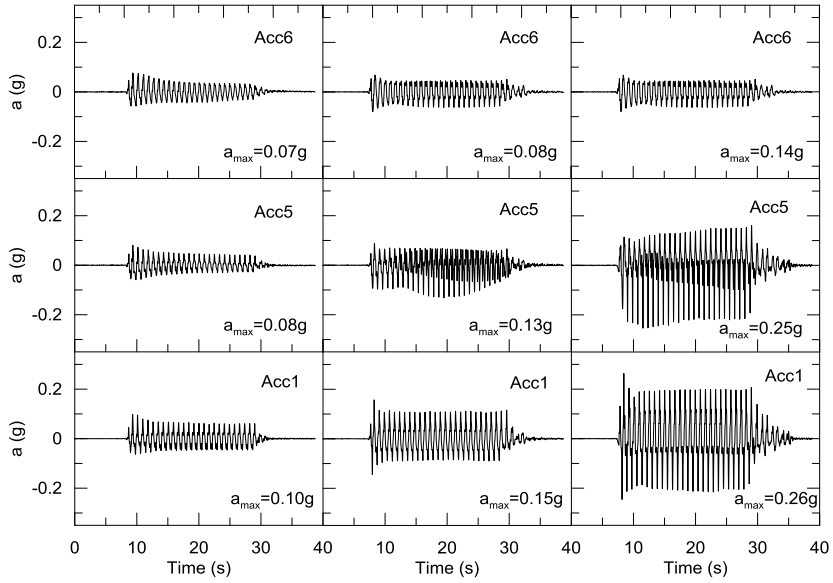

Figure 3.62: Test CWU2: acceleration time histories between the walls during EQ1, EQ2 and EQ3.

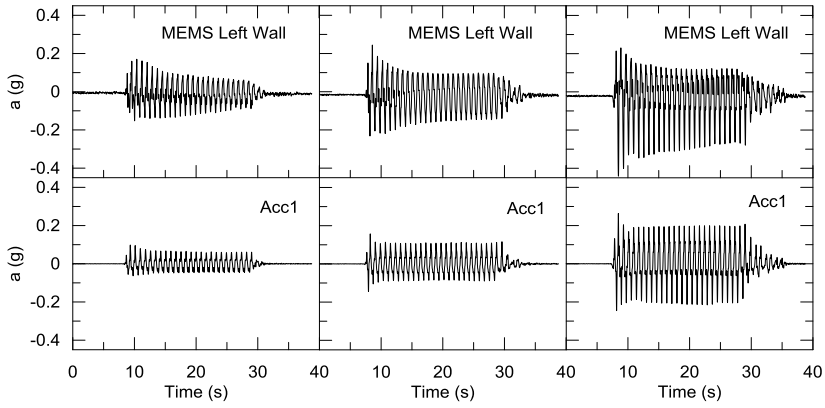

Figure 3.63: Test CWU2: acceleration at the top of the wall measured by the MEMS accelerometer.

In fact in Figure 3.64, in Figure 3.65 and in Figure 3.66 the amplification factor trend along the vertical direction is constantly below the unity

below the water table, but it does not become less than 0.5, a part from its value in correspondence of Acc4 relative to EQ2 and EQ3, indicating that the de-amplification for CWU2 is less significant than for CWU1. Also in Figure 3.67, in Figure 3.68 and in Figure 3.69 it can be observed that the de-amplification is less significant than in CWU1 since the amplification factor remains above 0.5. The amplification factor relative to the accelerometer Acc8, which is collocated above the water table is about equal to one for all the earthquakes, and particularly it is slightly above the unit for EQ1 and EQ3 while it is about equal to one for EQ2.

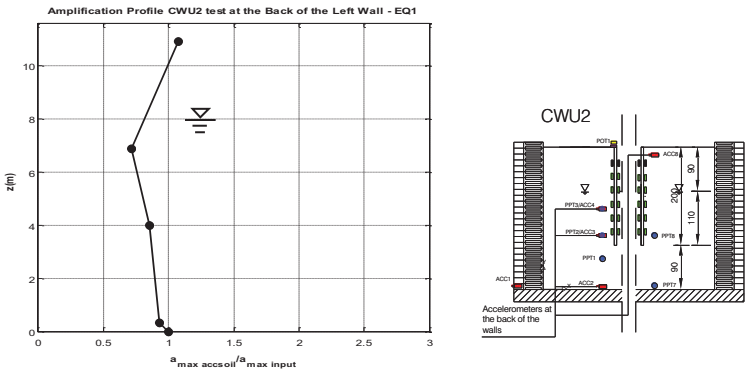

Figure 3.64: Test CWU2: amplification factor with the depth at the back of the left wall for EQ1. Starting from the bottom, at each circled marker correspond respectively Acc1, Acc2, Acc3 and Acc4

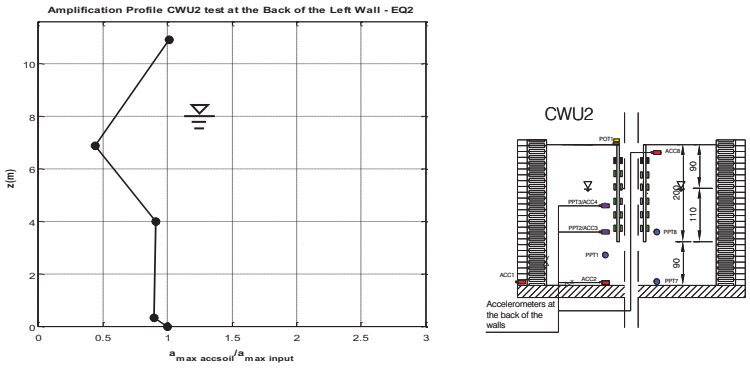

Figure 3.65: Test CWU2: amplification factor with the depth at the back of the left wall for EQ2. Starting from the bottom, at each circled marker correspond respectively Acc1, Acc2, Acc3 and Acc4

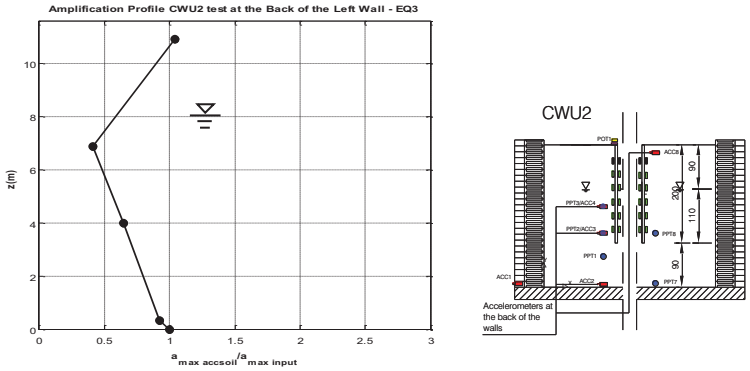

Figure 3.66: Test CWU2: amplification factor with the depth at the back of the left wall for EQ3. Starting from the bottom, at each circled marker correspond respectively Acc1, Acc2, Acc3 and Acc4

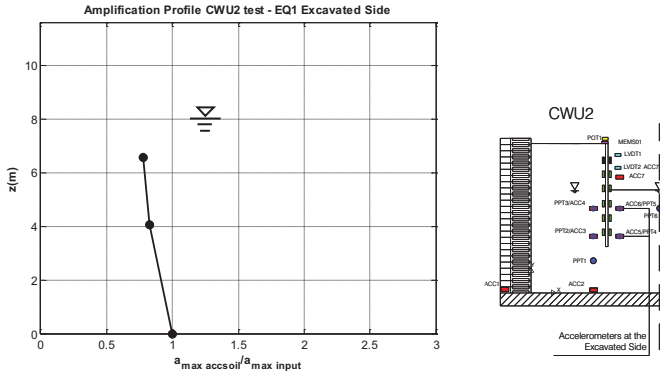

Figure 3.67: Test CWU2: amplification factor with the depth at the excavated side for EQ1. Starting from the bottom, at each circled marker correspond respectively Acc1, Acc5 and Acc6.

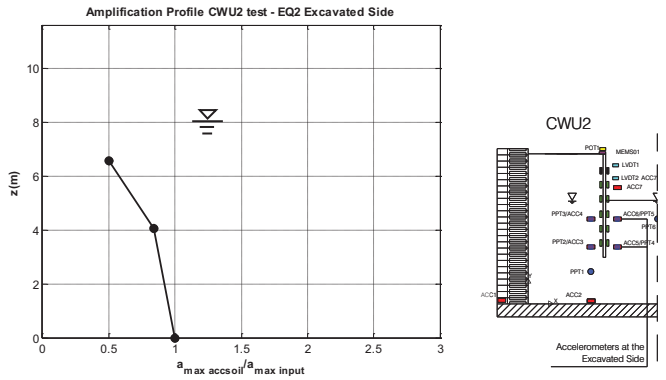

Figure 3.68: Test CWU2: amplification factor with the depth at the excavated side for EQ1. Starting from the bottom, at each circled marker correspond respectively Acc1, Acc5 and Acc6.

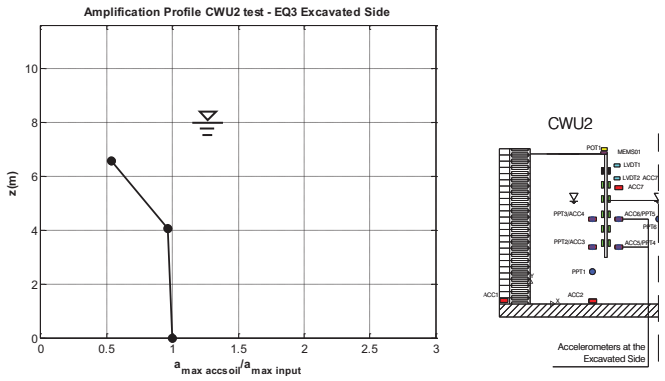

Figure 3.69: Test CWU2: amplification factor with the depth at the excavated side for EQ3. Starting from the bottom, at each circled marker correspond respectively Acc1, Acc5 and Acc6.

In Figure 3.70, Figure 3.71 and in Figure 3.72 the phase difference computed in the time domain is reported. Also for this test, as for the test CWU1, it can be observed that the acceleration time histories relative to Acc2, Acc3, Acc4, Acc5 and Acc6, which are located below the excavation level, present a phase difference about or below 50° for all the earthquakes, excepted for EQ1, where Acc6 during the first half of the earthquake presents a phase difference higher than 50°, and excepted for EQ3, where again Acc6 during the second half of the earthquake presents a phase difference higher that 50°, while the time history relative to Acc8 is essentially constant and equal to 150° for all the earthquakes. The fact that the phase difference for Acc6 during EQ1 and during EQ2 is not constant since it is higher than 50° during the first half of the EQ1 and during the second part of EQ2 is due to the presence of multiple peaks response of the time trend of Acc6 (for this, please read the chapter 4). Apart from this exception, it can be concluded that also for CWU2, as well as for CWU1, the acceleration of the soil below the excavation level is close, with respect to time, to the input acceleration.

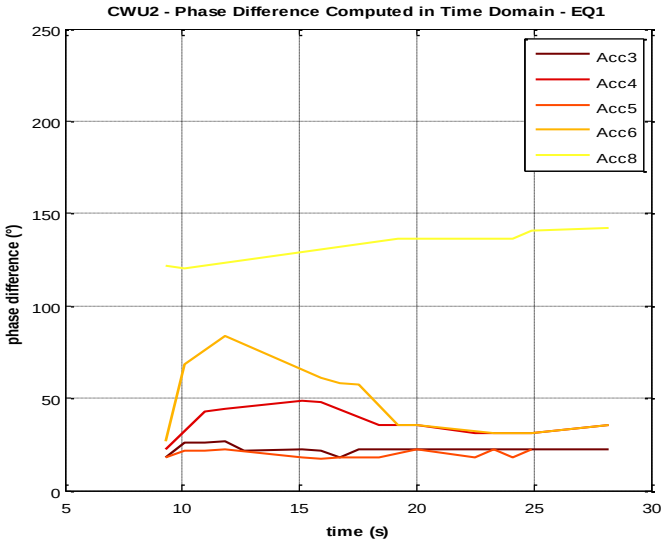

Figure 3.70: Test CWU2 - EQ1: phase difference computed in the time domain.

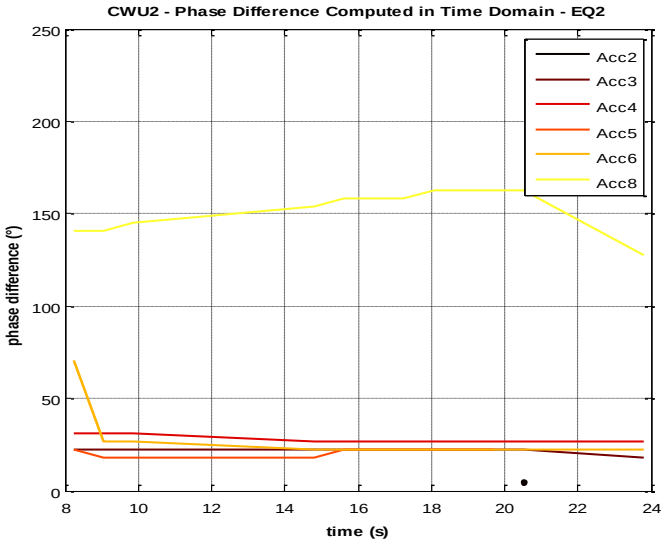

Figure 3.71: Test CWU2 EQ2: phase difference computed in the time domain

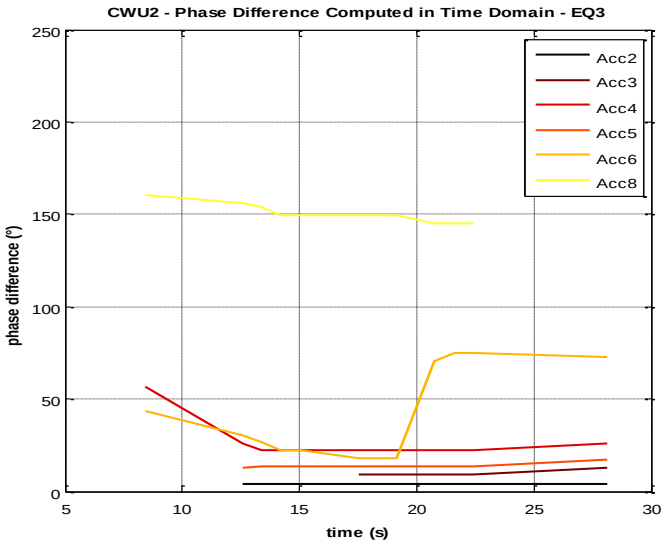

Figure 3.72: Test CWU2 EQ3: phase difference computed in the time domain.

In Figure 3.73 and in Figure 3.74 the horizontal displacement of the walls measured by the LVDTs and the symmetrical displacements are reported respectively. In the first figure, it is evident the non-symmetry of the diagrams of the displacements that can be attributed to the influence of the displacements of the laminar box rings. Indeed the value of the displacement measured by the top LVDT on the left wall is constantly higher that the bottom LVDT during all the earthquakes while on the right wall it is observed the opposite. The symmetrical displacements, on the other hand, allow to catch the response of the walls during the earthquakes, which is actually represented by a rotation of the walls around a point located below the excavation level with the tops approaching as the shaking continues. The response of the walls in this test, which has been performed in dense sand, is essentially different than in test CWU1, where the walls undergo a counter rotation during the earthquakes due to the occurrence of liquefaction within the excavated side.

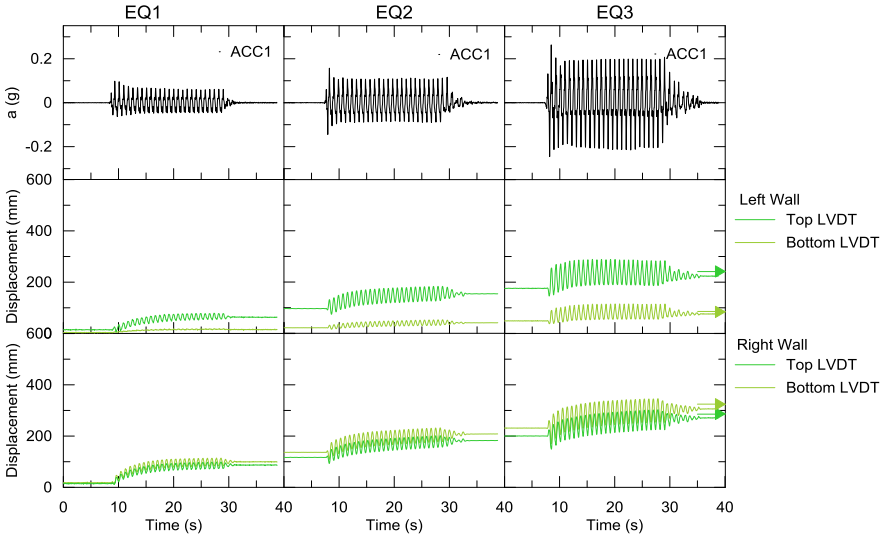

Figure 3.73: Test CWU2: walls horizontal displacement time histories during EQ1, EQ2 and EQ3.

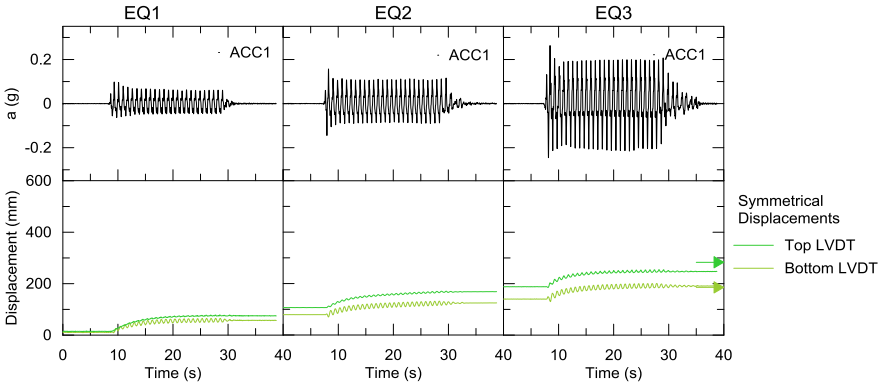

Figure 3.74: Test CWU2: walls horizontal symmetrical displacement time histories during EQ1 and EQ2.

These observations are confirmed considering the trend of the rotation of the walls reported in Figure 3.75, Figure 3.76 and in Figure 3.77. In these figures the rotation computed from the average of the signals of the LVDTs at the same depth, as it has been done for the tests CWU1 and PWU1, has been compared also with the rotation computed from the sig-

nal of the MEMS accelerometer placed at the top of the left wall. As for the signals of the LVDTs, the signal of the MEMS has been smoothed with the moving average algorithm. It has already been seen that the rotation given by the LVDTs does not give a reliable value of the rotation so the direct comparison of the value of the rotation given from the LVDTs and from the MEMS accelerometer is often meaningless. Indeed the rotation computed with the MEMS accelerometer concerns the relative movement of the wall with respect to the soil (and thus it does not contains the displacements of the laminar box rings) since it is attached onto the top of the wall. With regard to this, it is interesting to notice that at the beginning of Figure 3.75 the rotation given from the LVDTs and the rotation computed with the MEMS accelerometer are close and respectively equal to 0.20° and 0.35°. this indicates that when the walls move symmetrically and the laminar box rings do not move significantly affecting the measure of the walls displacements, which reasonably happens during the swing up of the test, the rotation computed in both ways is reasonably equal; otherwise a difference in the computed value can be attributed to i) the effect on the measure of the walls displacements of laminar box rings displacement and to ii) the actual non symmetry of the response of the soil structure system. Further it can be observed that, in all the figures Figure 3.75, Figure 3.76 and Figure 3.77, the time trend of the rotation given by the LVDTs and by the MEMS is similar. Thus, regardless of the values of the rotation (excepted the first value of the rotation during EQ1 as seen above), the time trends are very similar during the earthquakes. This consideration is again important in relation with the reliability of the symmetrical displacements in describing the response of the walls as an alternative to the representation of the displacements directly measured with the LVDTs because, even if the value of the rotation given by the LVDTs can be compared with that one of the MEMS at the end of the swing up, the time trend, which can be related to the walls response in terms of displacements accumulation, is reliable. As it has been concluded above discussing the results in Figure 3.73 and in Figure 3.74, the rotation reported in Figure 3.75, Figure 3.76 and Figure 3.77 given from both the LVDTs and the MEMS accelerometer is always positive and it constantly increases passing from EQ1 to EQ3. A small decrease of the rotation can be observed at the end of EQ3. Specifically the rotation at the beginning of EQ1 is 0,20° for the LVDTs and 0.35° for the MEMS accelerometer, at the end of EQ1 it is 0.91° for the LVDTs and 0.65° for the MEMS accelerometer, at the beginning of EQ2 it is 1.4° and 0.9° for LVDTs and MEMS and at the end of EQ2 it is 2.24° and 1.09°; finally, for EQ3, the rotation is 2.45° and 1.24° for LVDTs and for MEMS while at the

end of EQ3 it is 2.88° and 1.25°.

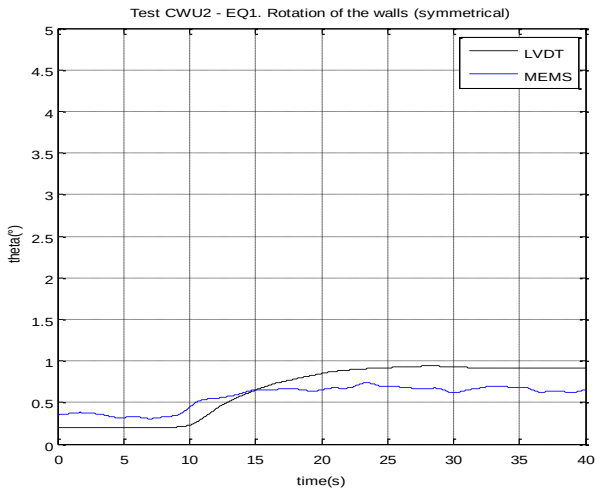

Figure 3.75: Test CWU2 EQ1: comparison between the rotation computed from LVDTs (symmetrical case) and the rotation given from the MEMS accelerometer placed on the top of the left wall.

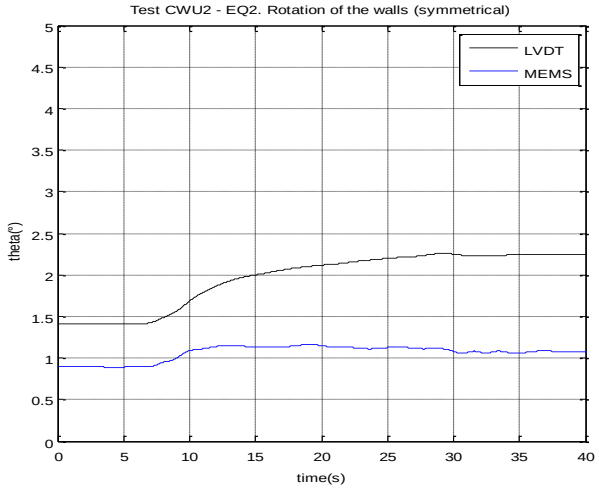

Figure 3.76: Test CWU2 EQ2: comparison between the rotation computed from LVDTs (symmetrical case) and the rotation given from the MEMS accelerometer placed on the top of the left wall.

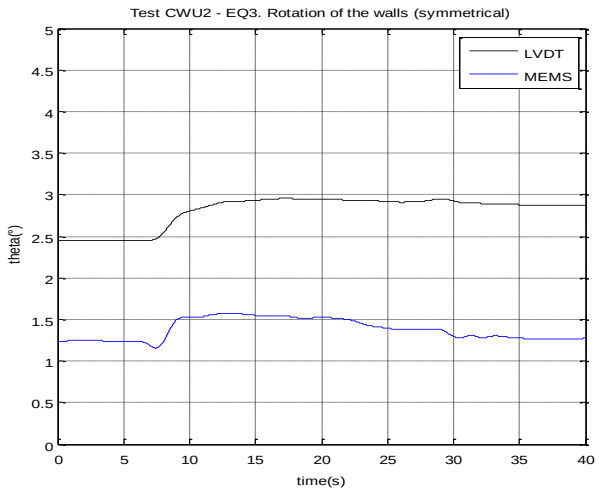

Figure 3.77: Test CWU2 EQ3: comparison between the rotation computed from LVDTs (symmetrical case) and the rotation given from the MEMS accelerometer placed on the top of the left wall.

In Figure 3.78 the spatial distribution of the walls displacements are illustrated. Also in this case the symmetrical displacements allows to appreciate the actual behaviour of the walls during the test. They start from the static configuration and then they accumulate displacements as the earthquakes are applied. For a specific earthquake, the walls accumulate progressively displacements passing through the maximum configuration, the short term configuration and the long term configuration. Regarding EQ1, the displacement at the end of the swing up is 16.59mm at the top and -6.24mm at the bottom, it reaches 35.67mm and -27.26mm at the maximum time instant, 87.41mm and -27.33mm at the short term residual time instant, and finally 147.68mm and -146.30mm at the long term residual time instant.

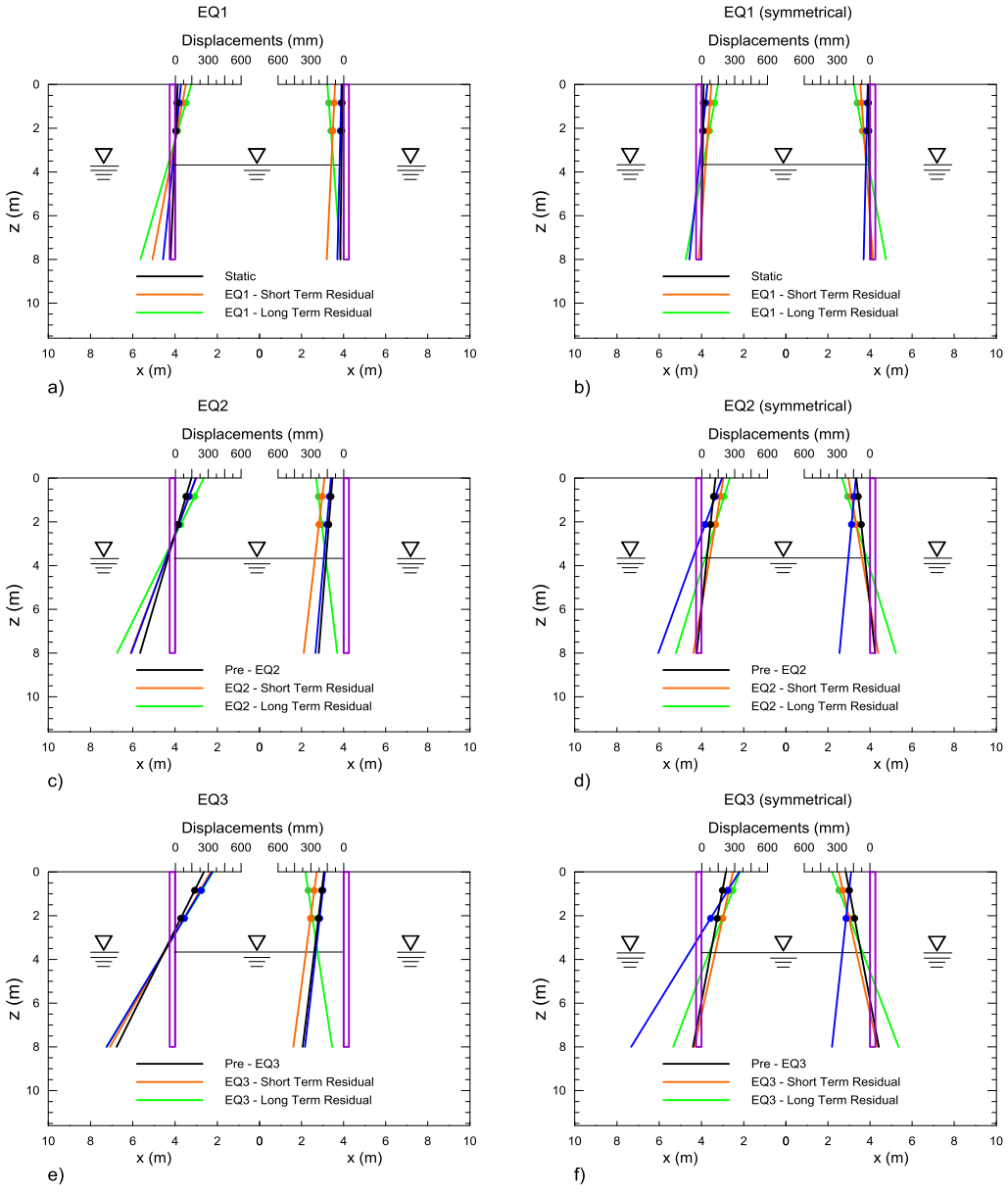

Figure 3.78: Test CWU2: displacement space distribution. (a) EQ1 and PS1 measured, (b) EQ1 and PS1 symmetrical, (c) EQ2 and PS2 measured, (d) EQ2 and PS2 symmetrical, (e) EQ3 and PS3 measured, (f) EQ3 and PS3 symmetrical.

The pore pressure time histories are reported in Figure 3.79. In this test both the increment of the pore pressure during the earthquakes and the cyclic response can be observed. The cyclic response is more significant as the depth of the instrument from the head of the pore fluid increases. In fact the cyclic response is more evident for PPT1 and PPT7, which are placed below the toe of the walls, than for PPT2 and PPT5, which are placed above the toe of the walls.

In Figure 3.80 the time histories relative to the three earthquakes of the pore pressure coefficient r_u are reported. The value of r_u is far for the unit at the back of the walls, while at the excavated side it is below the unit for PPT5 as well and for PPT6 it is close to the unit. Even if the pore pressure coefficient suggests that liquefaction is occurring at the excavated side the walls do not experiment a counter-rotation during the earthquakes, but they continue to accumulate displacements in a different way with respect the test CWU1 performed in loose sand and actually in the same way as if the test was performed in dry sand. In Table 3.19 the values of the coefficient r_u at the end of the earthquake are reported.

In Figure 3.81 the space distribution of the pore pressures is illustrated. As in the tests performed in loose sand the maximum value of the pore pressures is attained in correspondence of the short term residual time instant in all the earthquakes. The long term residual distributions coincide with the distribution before the earthquakes.

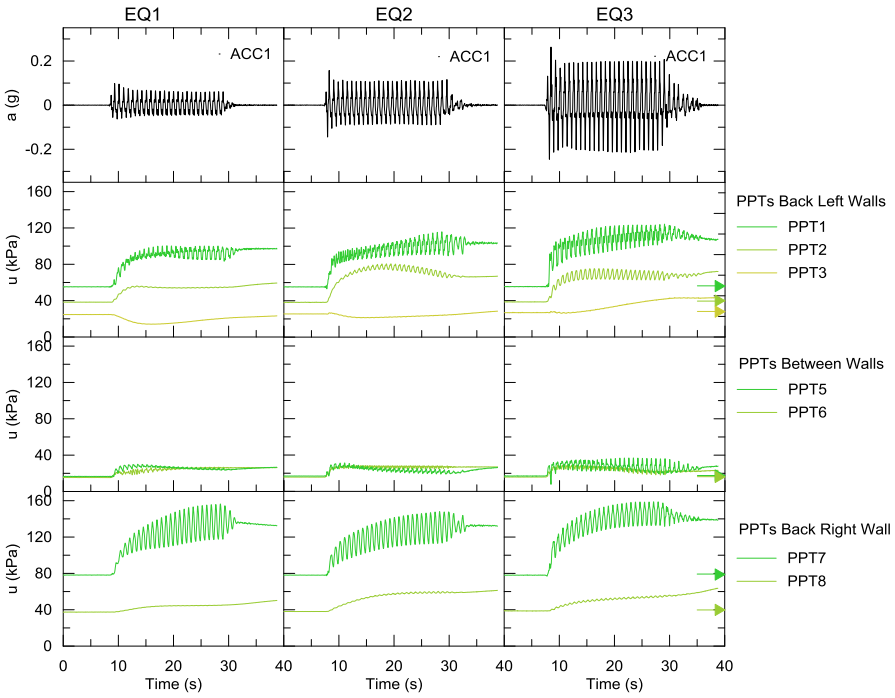

Figure 3.79: Test CWU2: pore pressures time histories during EQ1, EQ2 and EQ3.

Test CWU2: values of r_u at the end of the earthquakes			
	EQ1	EQ2	EQ3
PPT1	0.39	0.45	0.48
PPT2	0.24	0.32	0.37
PPT3	-0.03	0.05	0.32
PPT5	0.07	0.07	0.08
PPT6	0.85	0.91	0.59
PPT7	0.41	0.41	0.46
PPT8	0.14	0.26	0.28

Table 3.19: CWU2: values of r_u coefficient at the end of the earthquakes.

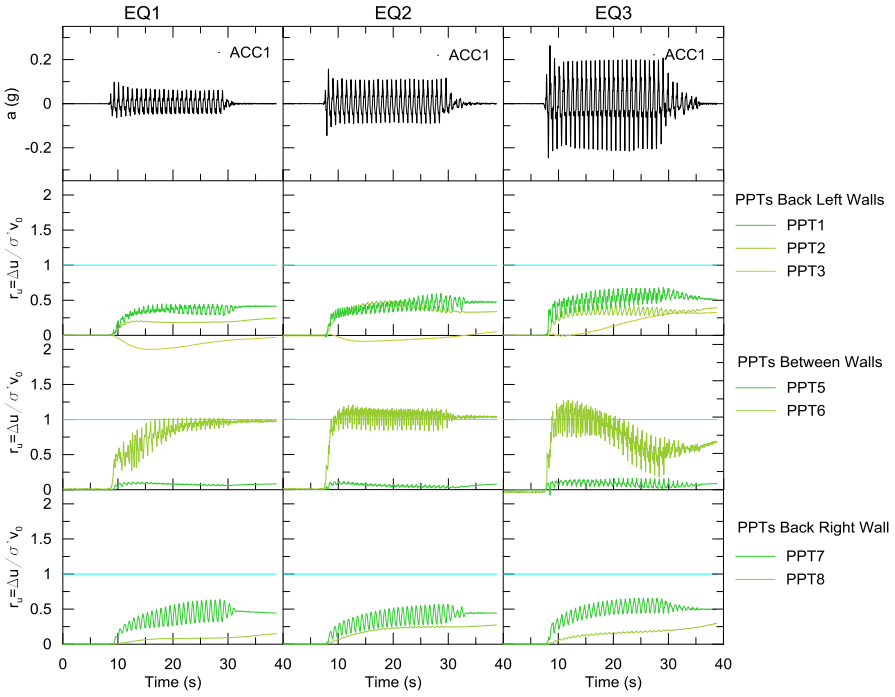

Figure 3.80: Test CWU2: r_u time history during EQ1, EQ2 and EQ3.

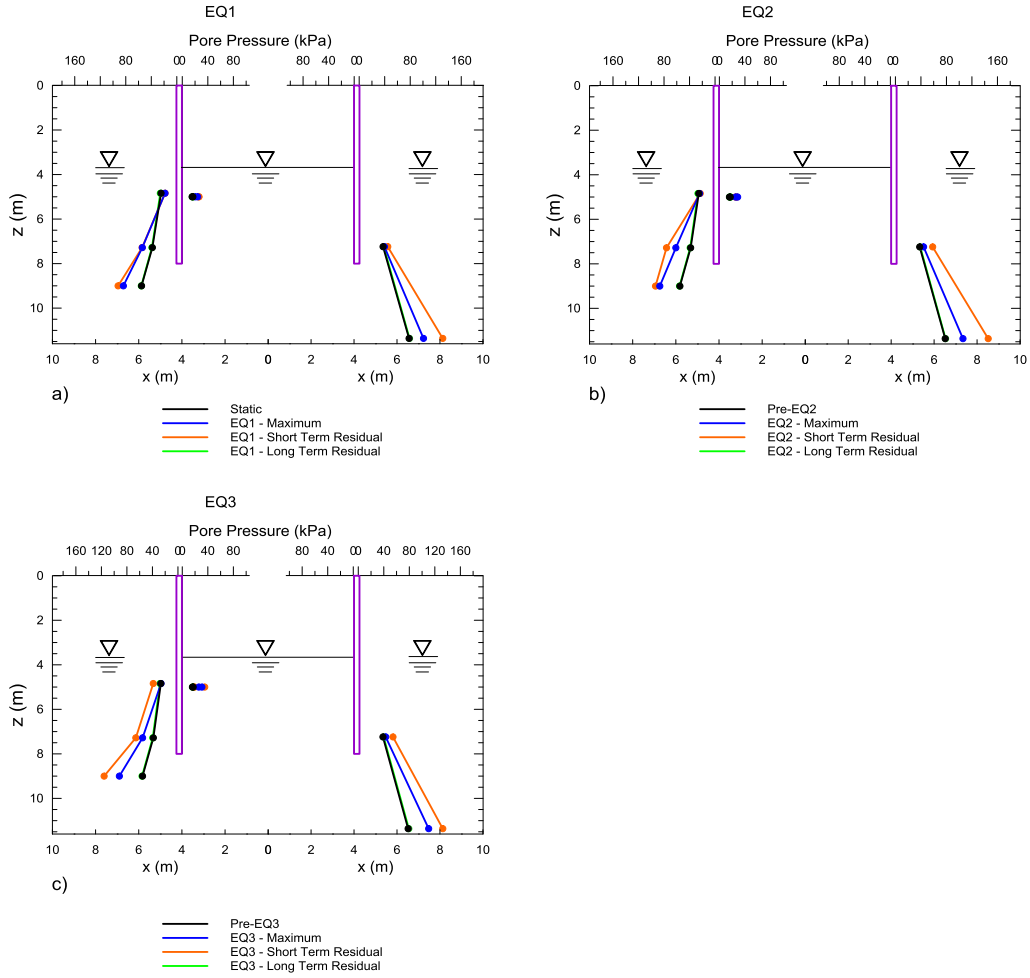

Figure 3.81: Test CWU2: pore pressure space distribution during EQ1, EQ2 and EQ3. (a) EQ1 and PS1, (b) EQ2 and PS2, (c) EQ3 and PS3.

The bending moment time histories are reported in Figure 3.82. The dynamic oscillation of the bending moment is certainly more evident than in the tests CWU1 and PWU1 and moreover, also in this test a redistribution of the bending moment at the end of the earthquakes can be observed. The oscillation of the bending moment increases as the input acceleration increases, in fact it is more evident passing from EQ1 to EQ3. The dynamic oscillation of the bending moment is directly correlated with the inertia force, which actually increases as the input acceleration increases.

In Figure 3.83 the bending moment space distribution is reported. On both the left wall and the right wall the maximum bending moment is reached at the strain gauge 5. Considering the strain gauge 5 on the left wall, the bending moment at the end of the swing up, that is the static bending moment, is 27 kNm/m and then it reaches the maximum value 39 kNm/m at 10.10s; successively it becomes 12 kNm/m at the short term residual relative to EQ1 and finally, it becomes 22 kNm/m at the long term residual. Passing to EQ2, the pre-earthquake bending moment, which is equal to the bending moment at the long term residual of EQ1, is 22 kNm/m, then it reaches its maximum value 39 kNm/m at 10.04s; at the short term residual it is 8 kNm/m and at the long term residual it is 15 kNm/m. This last value is also the pre-earthquake value relative to EQ3. The maximum bending moment relative to EQ3 is 49 kNm/m at 9.45s; then the short term residual value is 4 kNm/m and at the long term residual it is 12 kNm/m. So it can be observed that the pre-earthquake values progressively decreases from 27 kNm/m, to 22 kNm/m and to 15 kNm/m, as well as for the short term residual values, which are respectively 12kNm/m, 8kNm/m and 4 kNm/m, and the long term residual values, which are 22 kNm/m, 15kNm/m and 12 kNm/m. The maximum values are the same for EQ1 and EQ2 and equal to 39 kNm/m, while during EQ3 the maximum value is 49 kNm/m. It is relevant to observe the progressive decrease of the bending moment pre-earthquake, at the short term residual and at the long term residual; this is probably due to the fact that it is not completely recovered during the post seismic phase of every earthquake.

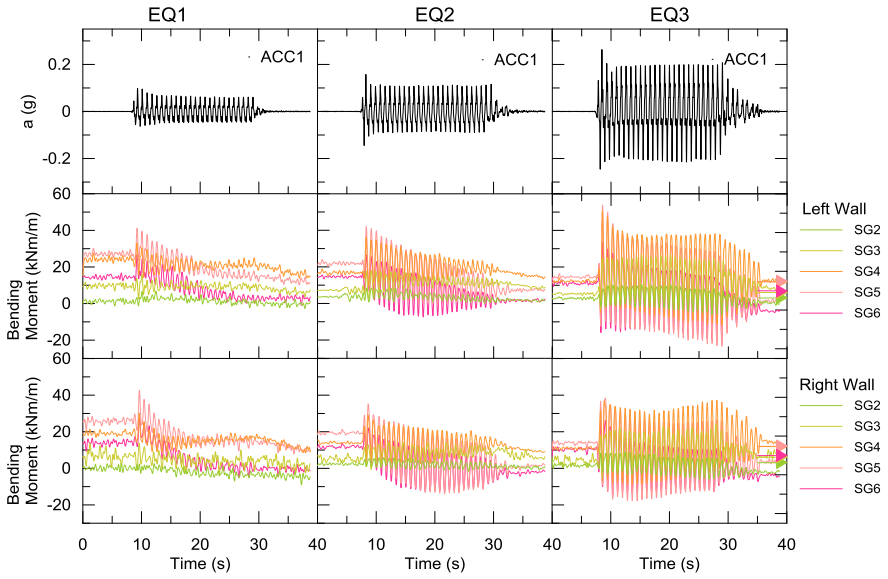

Figure 3.82: Test CWU2: bending moment time histories during EQ1 and EQ2.

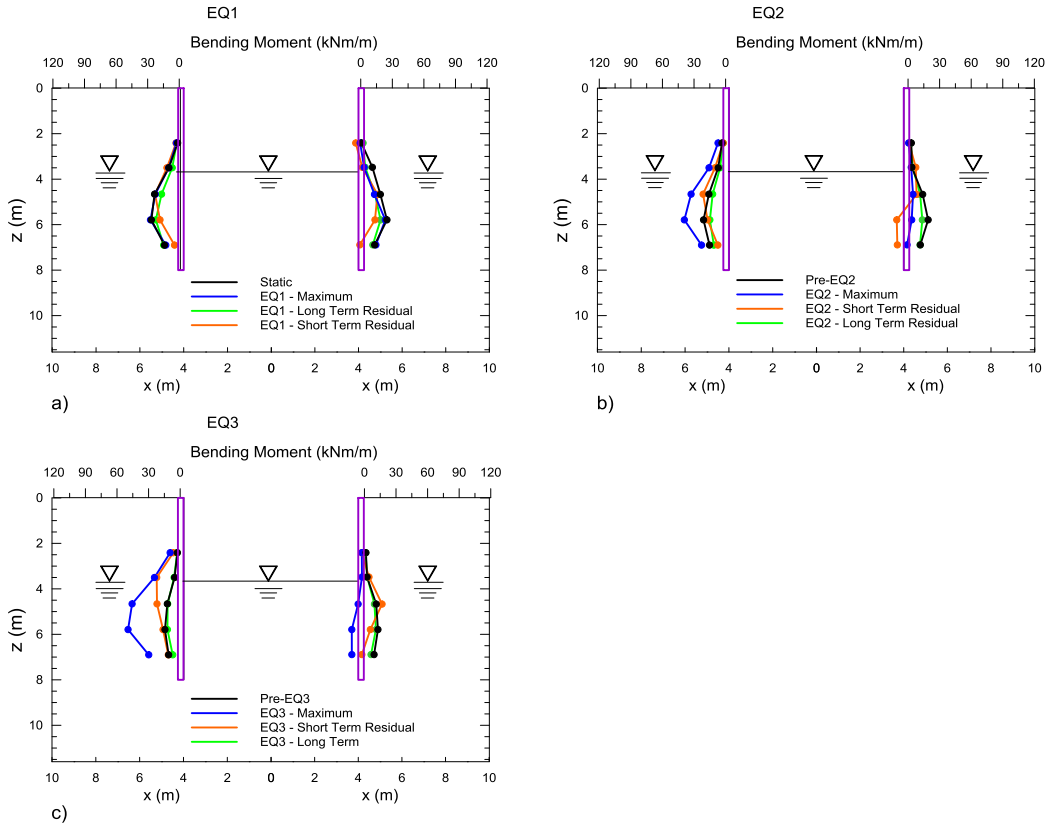

Figure 3.83: Test CWU2: bending moment space distribution. (a) EQ1 and PS1, (b) EQ2 and PS2, (c) EQ3 and PS3.

3.6 Test PWU2 Data

The PWU2 acceleration data are reported in Figure 3.84 and in Figure 3.85 where the acceleration time histories relative to the back of the left wall and the acceleration time histories relative to the excavated side are reported respectively. The maxima of the acceleration for the accelerometers Acc1, Acc2, Acc3, Acc4, Acc5 and Acc6 are 0.11g, 0.10g, 0.10g, 0.09g, 0.08g and 0.10g during EQ1, they are 0.15g, 0.13g, 0.12g, 0.12g, 0.12g and 0.16g during EQ2, and finally they are 0.27g, 0.24g, 0.22g, 0.19g, 0.15g and 0.22 during EQ3. As regards the excavated side, the maxima for the accelerometers Acc1, Acc7 and Acc8 are 0.11g, 0.11g and 0.09g during EQ1, 0.15g, 0.14g and 0.14g during EQ2 and 0.27g, 0.20g and 0.24g during EQ3.

Also in this test, as well as in test CWU2 with respect CWU1, the de-amplification is less important than the correspondent test in loose sand PWU1. In the figures Figure 3.87, Figure 3.88and Figure 3.89 the amplification factor at the back of the wall is shown, and in Figure 3.90, Figure 3.91 and in Figure 3.92, the amplification factor at the excavated side is shown and it can be observed that in all of them the amplification factor is less than one, but it remains constantly above 0.5, confirming that the de-amplification is less significant than in test PWU1.

As regards the phase difference between the acceleration time histories obtained from the piezoelectric accelerometers placed within the soil, in Figure 3.93, Figure 3.94 and in Figure 3.95 the phase difference computed in the time domain for the earthquakes EQ1, EQ2 and EQ3 is reported. Also in this test it can be observed that the acceleration time histories relative to the accelerometers placed above the excavation level (Acc5 and Acc6) present a significant phase difference with respect the input accelerometer while all the acceleration time histories below the excavation are in sync with respect the input accelerometer. The phase difference of Acc5 is in fact included between about 70° (EQ1) and 120° (EQ3) while the phase difference of Acc6 is included between 100° (EQ1) and 150° (EQ3) while the phase difference of the remaining accelerometers, which are Acc3, Acc4, Acc7 and Acc8, is lower than 50°.

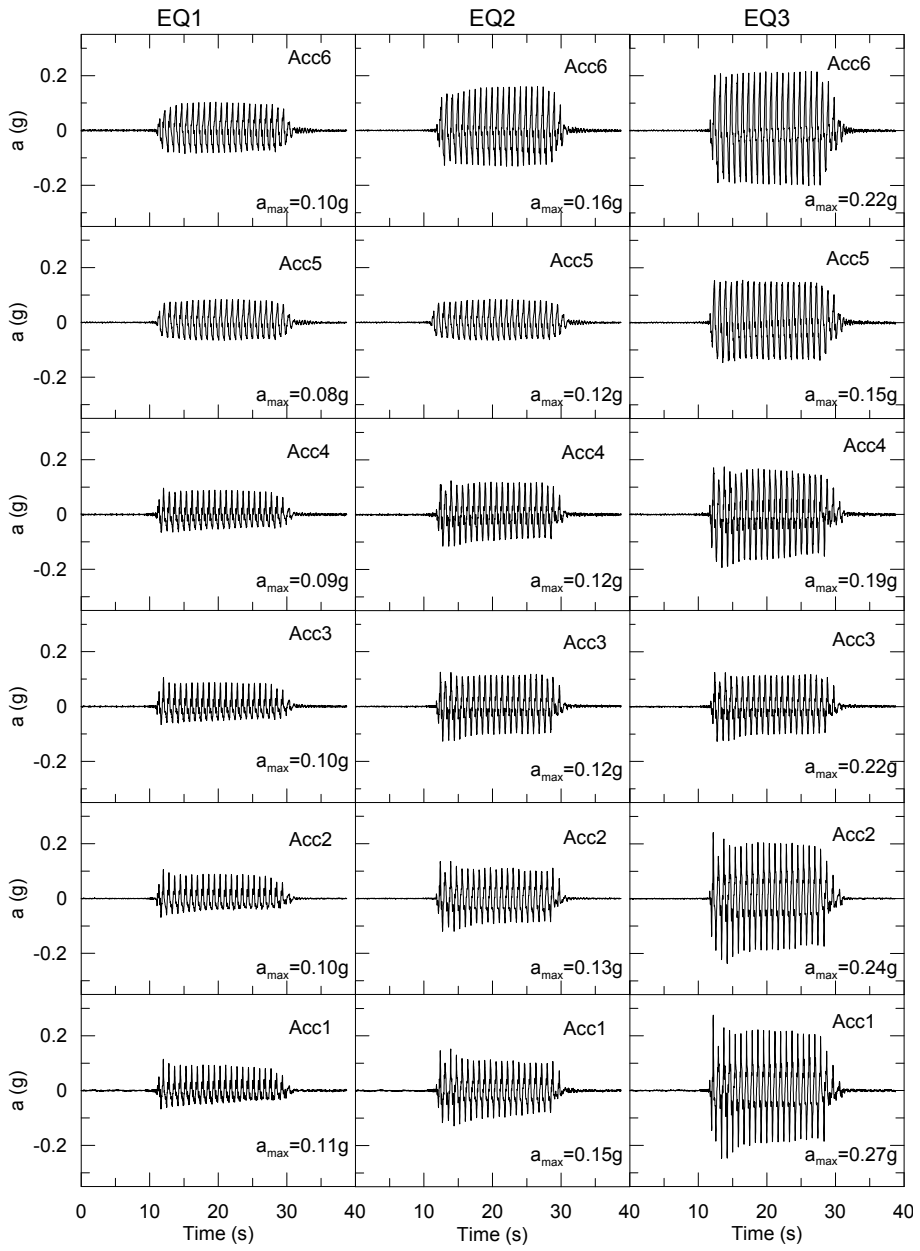

Figure 3.84: Test PWU2: acceleration time history at the back of the left wall during EQ1, EQ2 and EQ3.

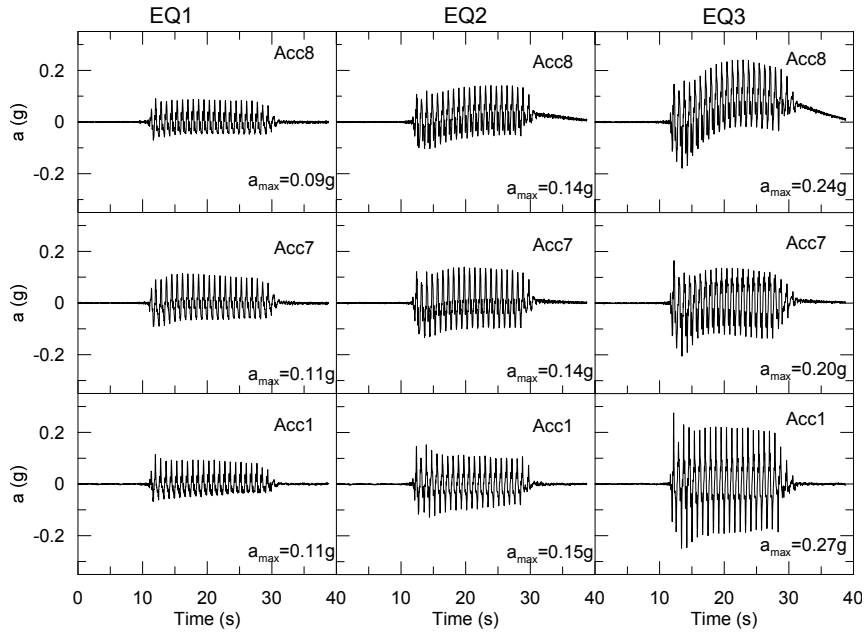

Figure 3.85: Test PWU2: acceleration time histories between the walls during EQ1, EQ2 and EQ3.

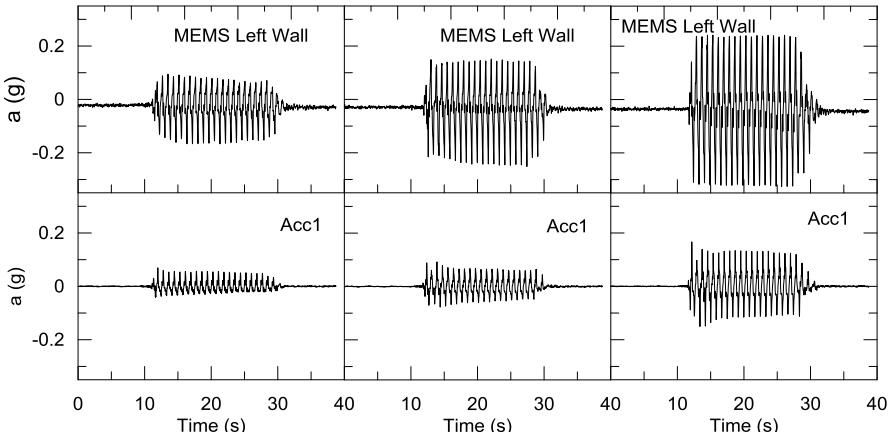

Figure 3.86: Test PWU2: acceleration time history recorded by the MEMS placed on the top of the left wall.

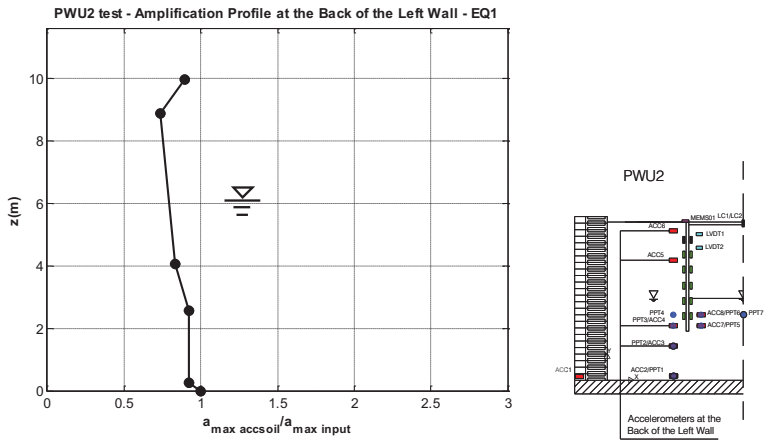

Figure 3.87: Test PWU2: amplification factor with the depth at the back of the left wall for EQ1. Starting from the bottom, at each circled marker correspond respectively Acc1, Acc2, Acc3, Acc4, Acc5 and Acc6.

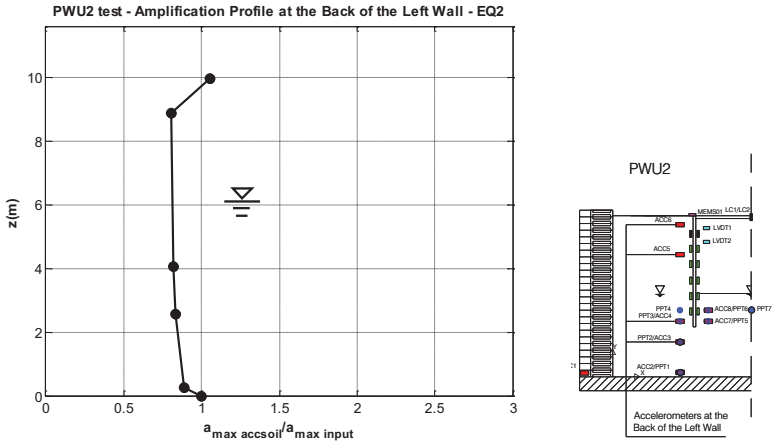

Figure 3.88: Test PWU2: amplification factor with the depth at the back of the left wall for EQ2. Starting from the bottom, at each circled marker correspond respectively Acc1, Acc2, Acc3, Acc4, Acc5 and Acc6.

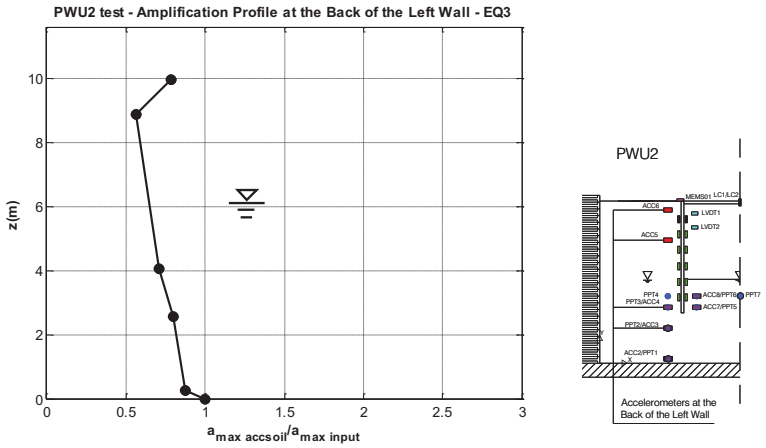

Figure 3.89: Test PWU2: amplification factor with the depth at the back of the left wall for EQ3. Starting from the bottom, at each circled marker correspond respectively Acc1, Acc2, Acc3, Acc4, Acc5 and Acc6.

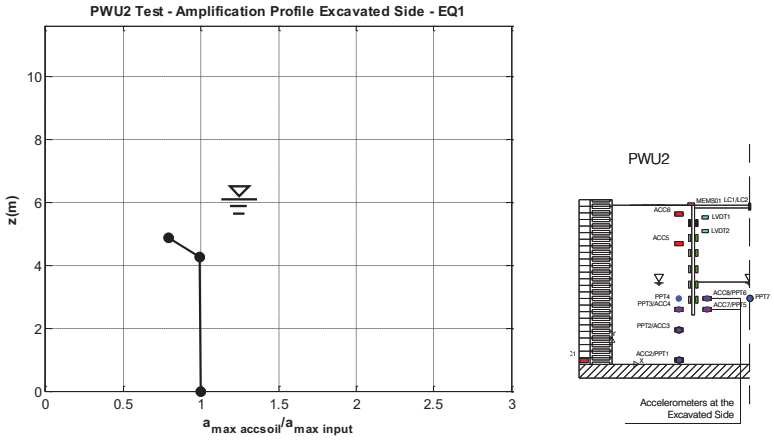

Figure 3.90: Test PWU2: amplification factor with the depth at the excavated side for EQ1. Starting from the bottom, at each circled marker correspond respectively Acc1, Acc7 and Acc8.

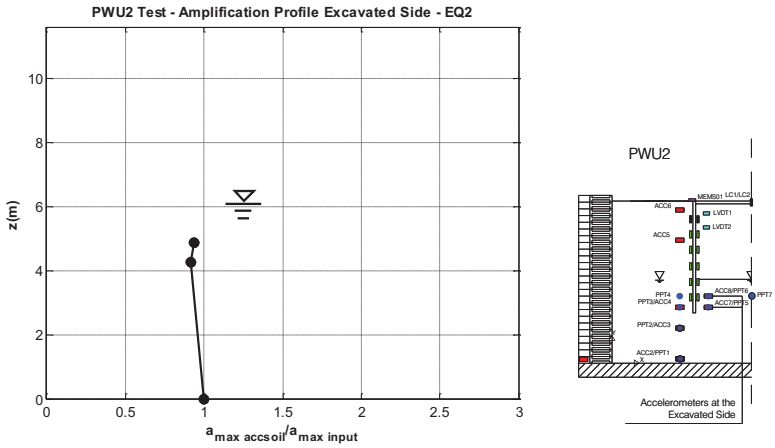

Figure 3.91: Test PWU2: amplification factor with the depth at the excavated side for EQ2. Starting from the bottom, at each circled marker correspond respectively Acc1, Acc7 and Acc8.

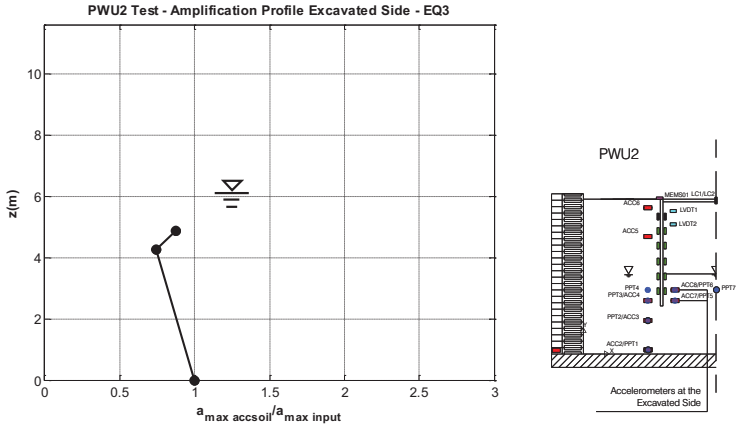

Figure 3.92: Test PWU2: amplification factor with the depth at the excavated side for EQ3. Starting from the bottom, at each circled marker correspond respectively Acc1, Acc7 and Acc8.

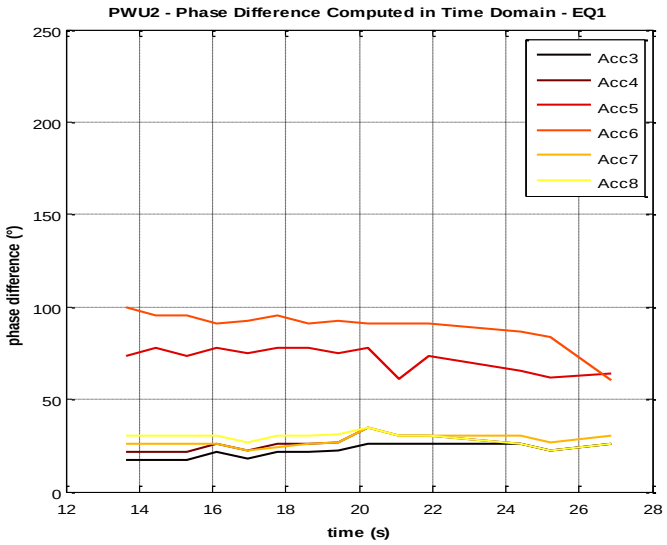

Figure 3.93: PWU2 - EQ1: phase difference computed in the time domain.

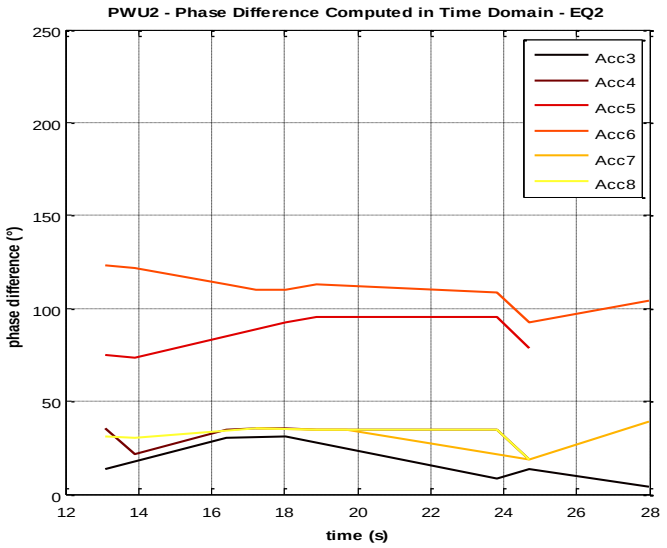

Figure 3.94: PWU2 - EQ2: phase difference computed in the time domain.

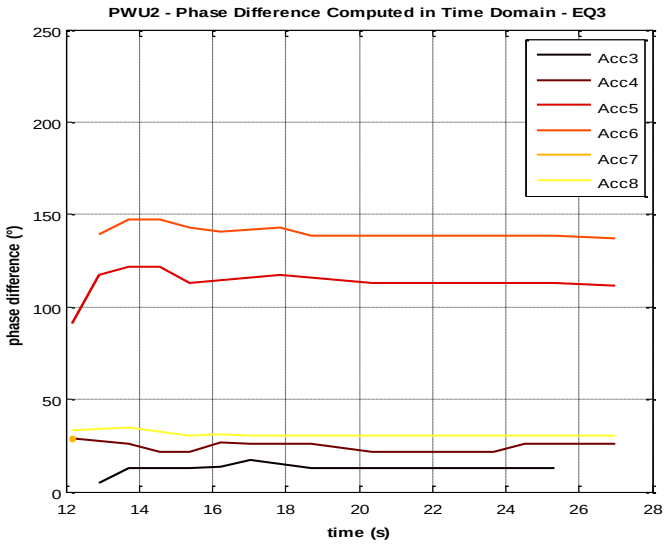

Figure 3.95: PWU2 EQ3: phase difference computed in the time domain.

In Figure 3.96 the walls horizontal displacement time histories during EQ1, EQ2 and EQ3 is reported. Since the LVDTs placed at the top of the walls registers a displacement value constantly below the value of the displacement registered by the LVDTs placed at the bottom of the walls, it is evident that the walls are rotating around the prop toward the excavated side. In Figure 3.97 the time trend of the symmetrical displacements is reported and again it can be seen that the displacement at the bottom of the walls is constantly higher than the displacement at the top and that, moreover, the difference between those displacements increases from EQ1 to EQ3. In this test the influence of the laminar box displacement on the measure executed with the LVDTs is less important than in CWU2; in fact in Figure 3.96 for both the left wall and the right wall the top LVDT show a displacement lower than for the top LVDT during all the earthquakes.

In Figure 3.98, Figure 3.99 and in Figure 3.100 the rotation of the walls computed from the symmetrical displacements are reported and it is compared with the rotation given by the MEMS accelerometer placed at the top of the left wall. In all of these figures the rotation is negative, which again shows that the walls are rotating approaching the toes, and it increases passing from EQ1 to EQ2 and to EQ3. Similarly as for CWU2, the comparison between the rotation computed from the signals of the LVDTs and the ro-

tation computed from the signal of the MEMS accelerometer is satisfactory in terms of the time trend, which is similar in all the earthquakes, while the absolute value of the rotation cannot be compared because, as explained above for the test CWU2, the rotation obtained from the symmetrical displacements cannot be reliable. As regards the value of the rotation at the end of the swing up instead, for this test, on the contrary of test CWU2, there is not a good comparison of the rotation computed with the MEMS accelerometer and the rotation computed with the LVDTs; this can be related to a not correct measurement of the distance of the LVDTs.

In Figure 3.101 the space distribution of the walls displacements is plotted. The plots with the symmetrical displacements (Figure 3.101(b), Figure 3.101(d) and Figure 3.101(f)) clearly show the progressive accumulation of the rotation around the props of the walls during the earthquakes and the dissipation of the pore pressures after the earthquakes. At the end of the swing up the displacement at the top Is 2mm and the displacement at the bottom is 16mm, while, at the maximum time instant of EQ1 they are 3mm and 43mm, at the short term residual they are 1mm and 64mm and at the long term residual 1mm and 65mm. Similarly as for EQ1, the walls continue to accumulate displacements at the bottom, indeed the displacement at the top of the walls is 0.86mm, 1.28mm, 0.18mm and -0.06mm at the pre-earthquake time instant, the maximum time instant, the short term residual time instant and at the long term residual time instant, so it remains practically constant due to the constraint imposed by the prop, while for the same time instants the displacement at the bottom progressively increases passing from 64mm to 89mm, 112mm and 111mm. During EQ3 the displacement at the top is constantly around -2 and 3mm while the displacement at the bottom is 115mm, 158mm, 185mm and 184mm respectively for the pre-earthquake time instant, the maximum time instant, the short term residual time instant and the long term residual time instant.

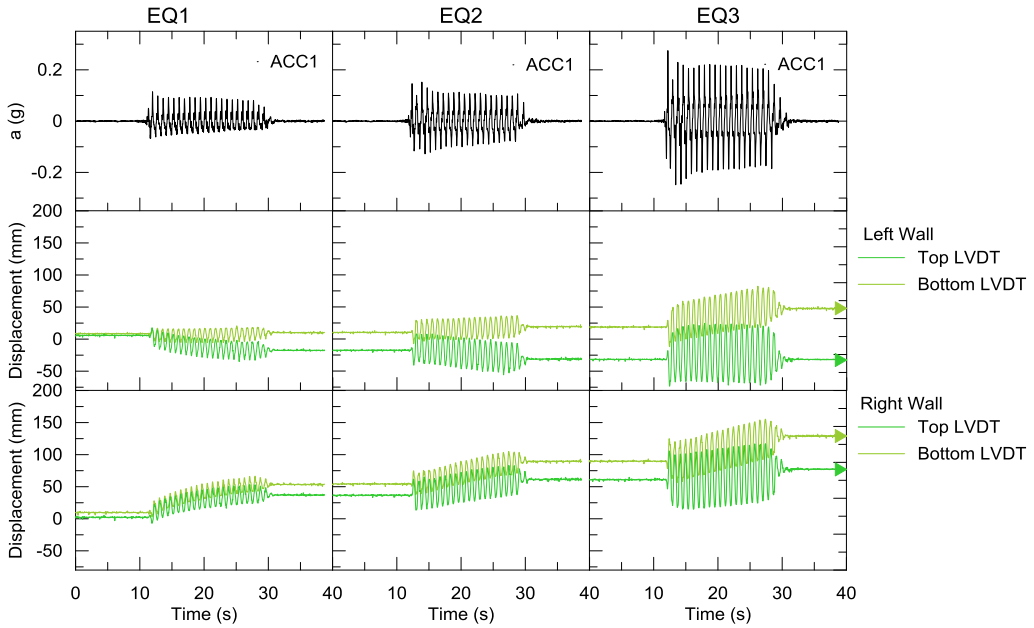

Figure 3.96: Test PWU2: walls horizontal displacement time histories during EQ1, EQ2 and EQ3.

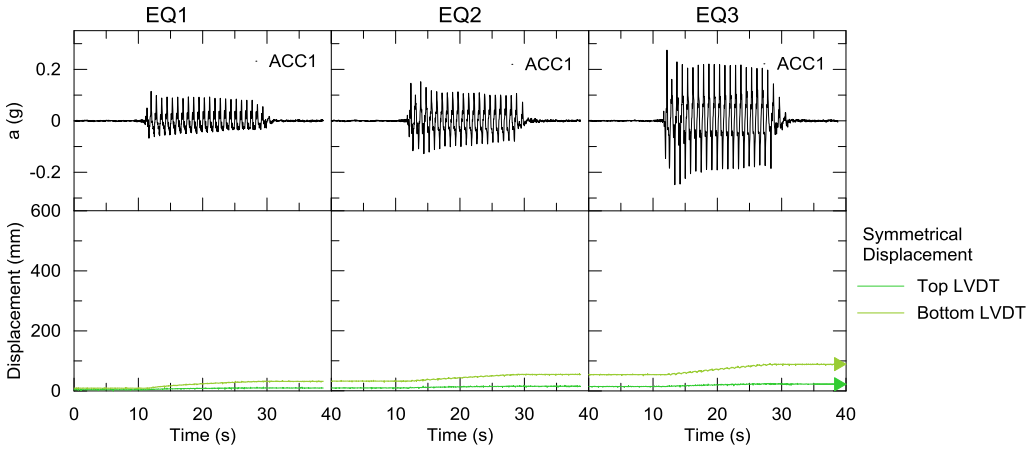

Figure 3.97: Test PWU2: walls horizontal symmetrical displacement time histories during EQ1 and EQ2.

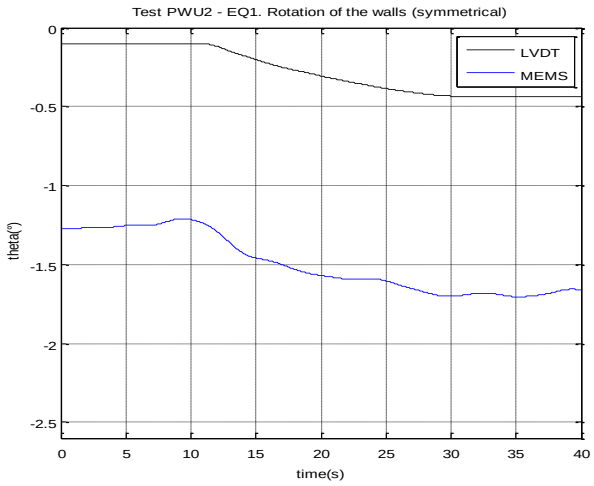

Figure 3.98: Test PWU2 EQ1: Rotation of the walls computed from the signals of the LVDTs (symmetrical)

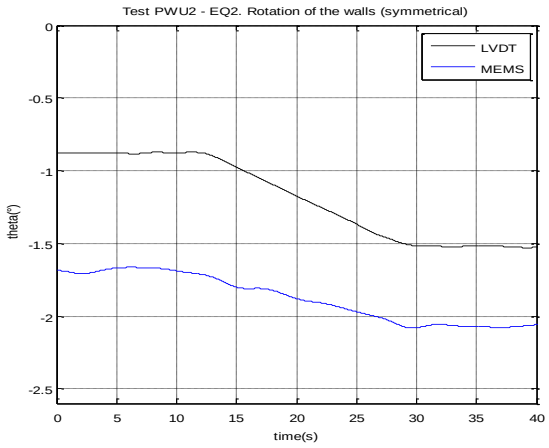

Figure 3.99: Test PWU2 EQ2: Rotation of the walls computed from the signals of the LVDTs (symmetrical)

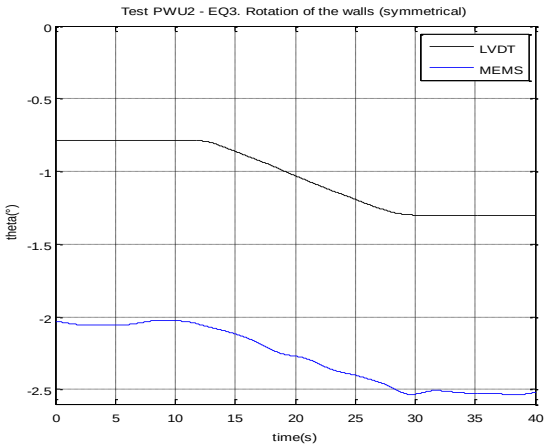

Figure 3.100: Test PWU2 EQ3: Rotation of the walls computed from the signals of the LVDTs (symmetrical).

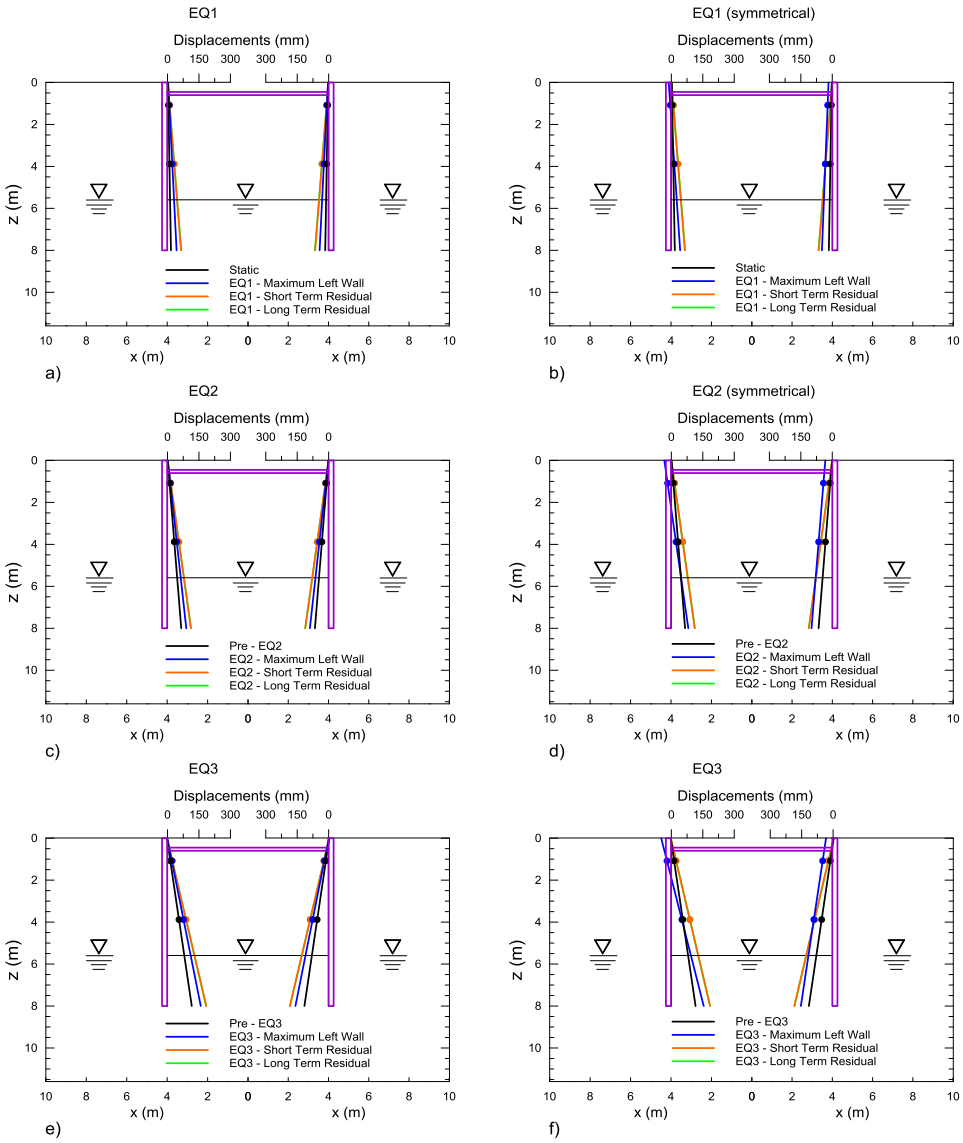

Figure 3.101: Test PWU2: displacement space distribution. (a) EQ1 and PS1 non-symmetrical, (b) EQ1 and PS1 symmetrical , (c) EQ2 and PS2 non-symmetrical, (d) EQ2 and PS2 symmetrical, (e) EQ3 and PS3 non-symmetrical, (f) EQ3 and PS3 symmetrical.

In Figure 3.102 the pore pressure time histories are reported. Unfortu-

nately only PPT3, PPT4, PPT6 and PPT7 worked during the test. Among them PPT4, PPT6 and PPT7 are placed at 1.2m below the head of the porous fluid and PPT3 at 2.0m. PPT4, PPT6 and PPT7 give very similar information: their static pore pressure, the pore pressure trend and the final value reached by the pore pressure at the end of the earthquakes are very similar.

In Figure 3.103 the time trend of the values of the ru coefficient rely not far from the horizontal line relative to $r_u = 1$ which corresponds to the occurrence of liquefaction, this is contrary to what is expected to happen for this test since it has been realized in dense sand; on the other hand sand boils have not been observed on the soil surface at the excavated side, differently with respect to test PWU1.

In Figure 3.104 the space distribution of the measured pore pressures is reported. Since only PPT3, PPT4, PPT6 and PPT7 worked during this test the space distribution of the pore pressures does not allow to widely investigate the pore pressures all over the domain occupied by the saturated soil layer.

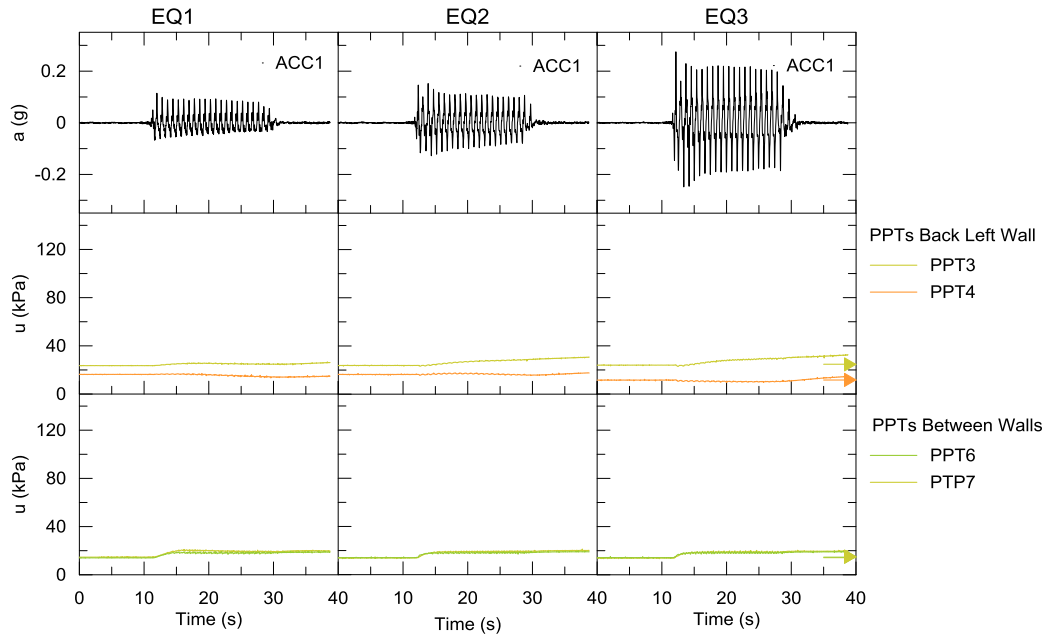

Figure 3.102: Test PWU2: pore pressure time histories during EQ1, EQ2 and EQ3.

Test PWU2: values of r_u at the end of the earthquakes			
	EQ1	EQ2	EQ3
PPT3	0.10	0.11	0.14
PPT4	0.06	0.10	0.11
PPT6	0.78	0.75	0.82
PPT7	0.93	0.91	0.96

Table 3.20: PWU2: values of r_u coefficient at the end of the earthquakes.

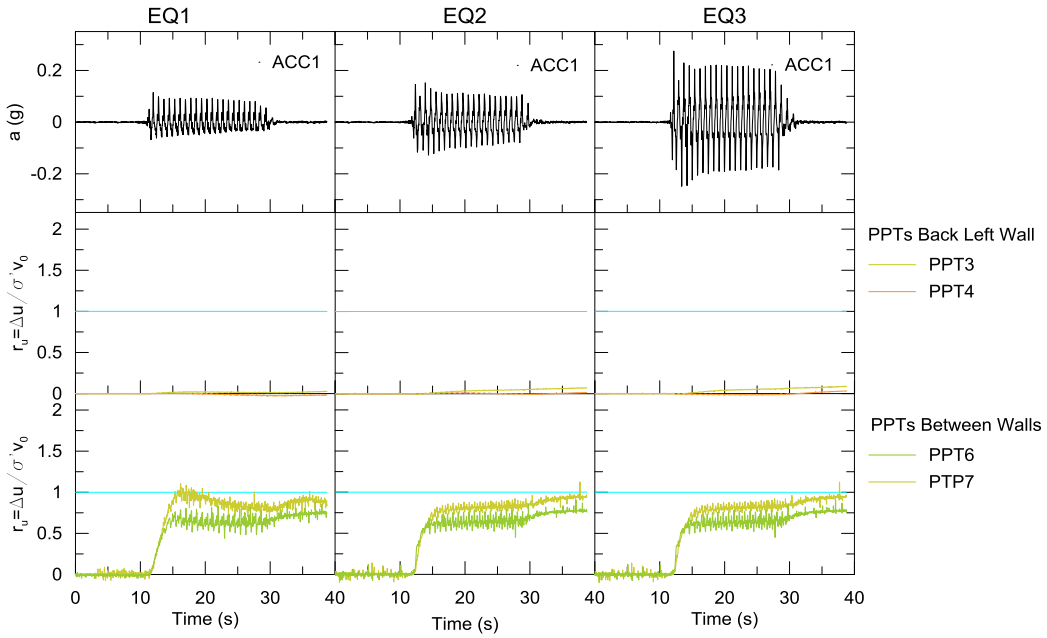

Figure 3.103: Test PWU2: r_u time history during EQ1, EQ2 and EQ3.

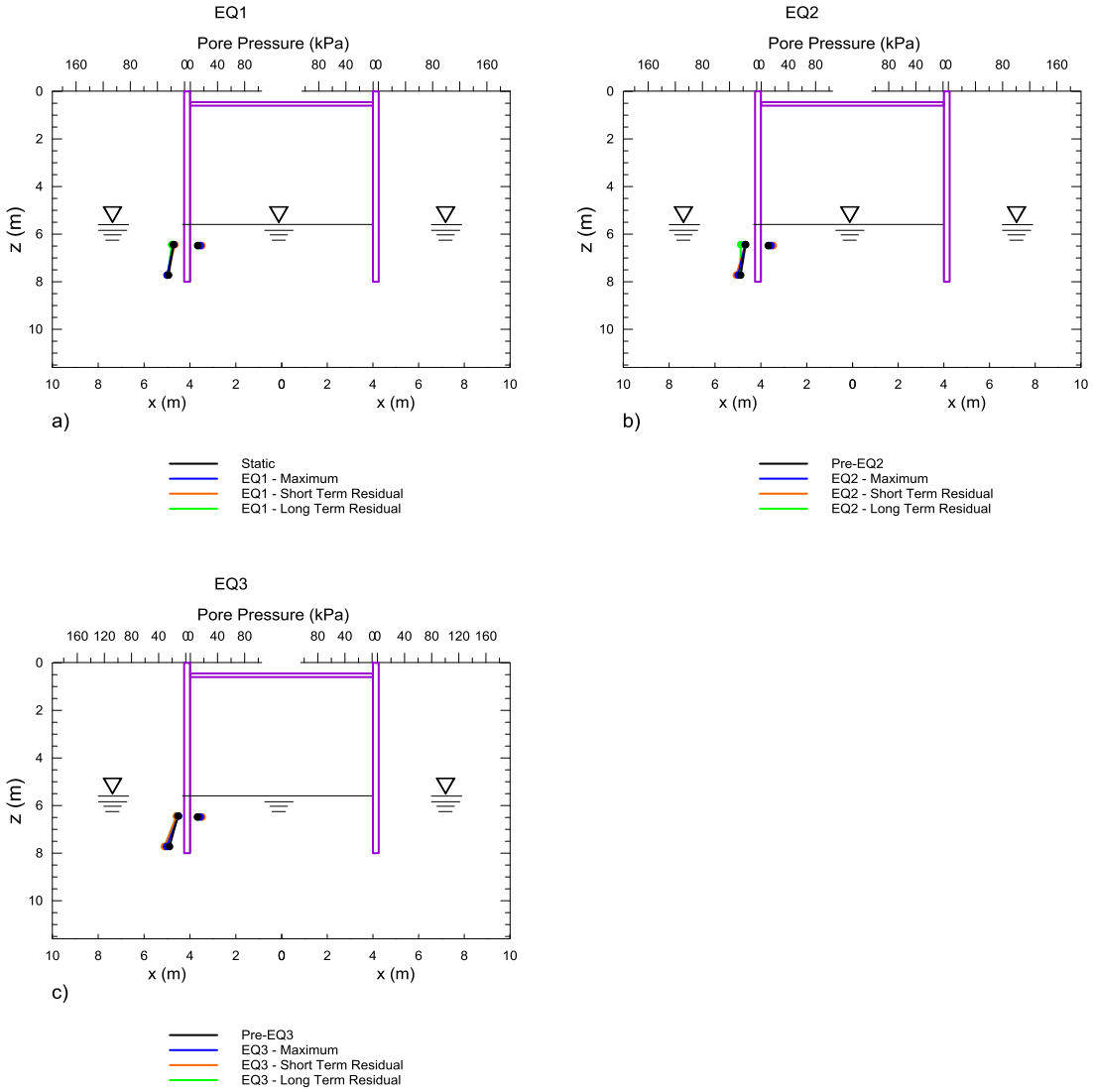

Figure 3.104: Test PWU2: pore pressure space distribution during EQ1, EQ2 and EQ3.

In Figure 3.105 the bending moment time histories are reported. The corresponding signals oscillate around an average value which continuously increases during shaking and the dynamic increments are proportional to the applied accelerations, consistently with other experimental work on embedded retaining walls in saturated sand (e.g. Zeng Steedman, 1993; Mad-

abhushi Zeng, 2007).

In Figure 3.106 the bending moment space distribution is represented. The static bending moment relative to the strain gauge 5, which is the maximum bending moment, is 42 kNm/m. At the same strain gauge, during EQ1, the bending moment reaches its maximum value that is 86 kNm/m; at the short term residual it is 71 kNm/m and at the long term residual it is 66 kNm/m. So an accumulation of the bending moment is observed at the end of EQ1. The accumulation of the bending moment is observed during EQ2 and EQ3 as well. Indeed at pre-EQ2 it is 64 kNm/m, then it reaches its maximum value 107 kNm/m and it becomes 79 kNm/m at the short term residual and finally 77 kNm/m at the long term residual while, as regards EQ3, at pre-EQ3 its value is 75 kNm/m, it is 130 kNm/m at the maximum time instant, and it reaches 89 kNm/m for both the short term residual and the long term residual. The response of the load cells is not symmetrical, and the axial force relative to the front cell passes from 120 kN to 170 kN during EQ1, then from 162 kN to 197 kN during EQ2 and from 190 kN to 224 kN during EQ3; as regards the back load cell, during EQ1 the relative axial force passes from 96 kN to 118 kN, then from 112 kN to 132 kN during EQ2 and from 125 kN to 123 kN during EQ3.

In Figure 3.107 the load cells response during the earthquakes is plotted. They show the progressive increment of the axial force within the props at the end of the earthquakes and the oscillations of the axial force during the earthquakes.

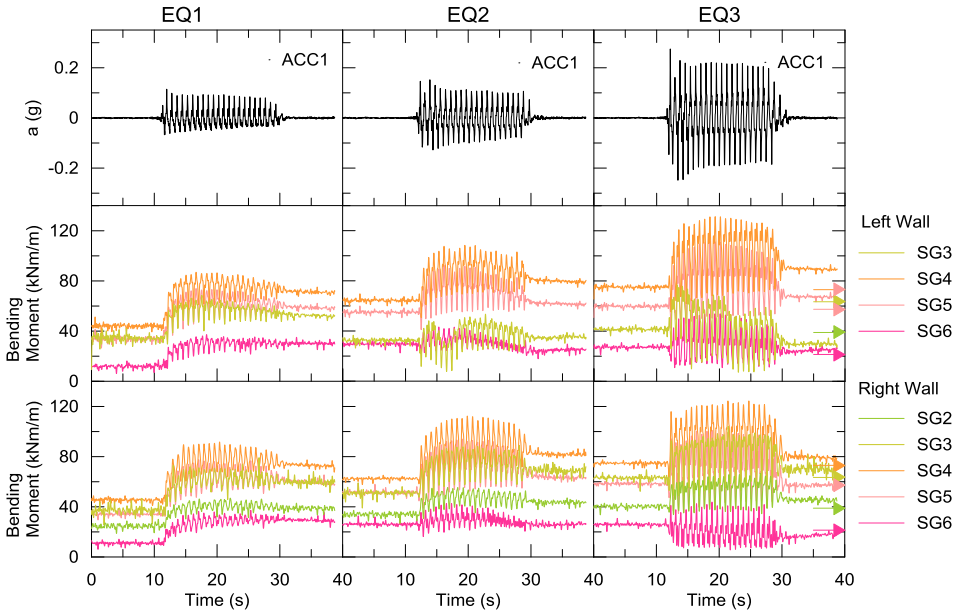

Figure 3.105: Test PWU2: bending moment displacement time histories during EQ1, EQ2 and EQ3.

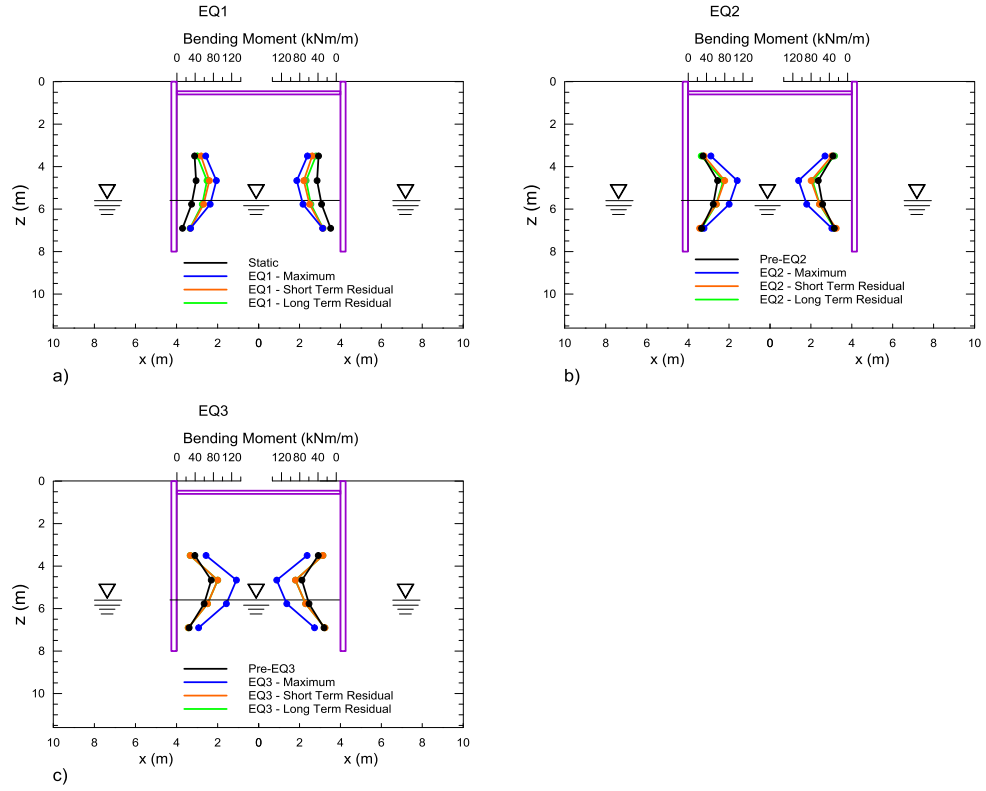

Figure 3.106: Test PWU2: bending moment space distribution: (a) EQ1 and PS1, (b) EQ2 and PS2, (c) EQ3 and PS3.

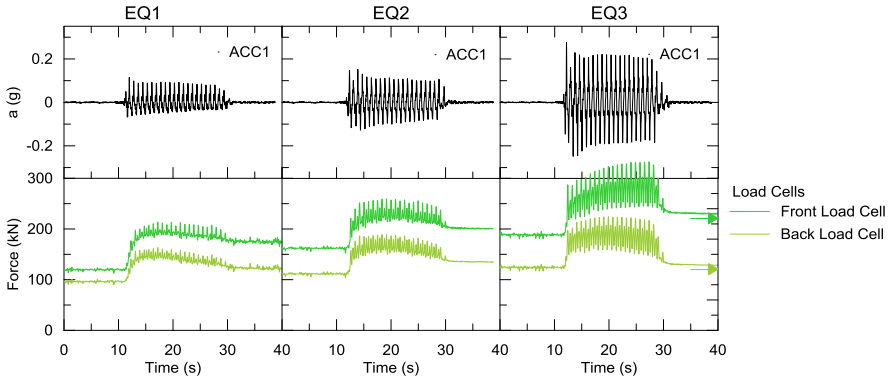

Figure 3.107: Test PWU2: axial force in the props time histories during EQ1, EQ2 and EQ3.

3.7 Tests CWU3 and PWU3 Data

These two tests have been performed in order to:

1. obtain additional data on models with the same geometrical configuration of the previous tests;

2. check the repeatability of the centrifuge tests with respect the specific geometry;

3. obtain a measure of the total pressure acting on the walls.

The data of CWU3 and test PWU3 are not entirely reported since these tests are geometrically identical to CWU2 and test PWU2. The comparison in terms of acceleration, amplification of the acceleration, horizontal displacements of the walls, pore pressures and bending moment between the pairs of identical tests is presented in Chapter 4, and it is shown that a satisfactory repeatability of the results has been obtained. Since the repeatability of the tests is proved in this chapter the attention is focused only on the data obtained by the Tekscan ultra-thin tactile pressure sensor, since it is the additional information with respect the homologous tests.

In Chapter 2 the technical information regarding the operating principle of the Tekscan have been reported as well as the modality of placement. Anyway, in order to facilitate the reading, the schematic showing the placement of the Tekscan from a lateral and frontal viewpoint are reported in

Figure 3.108 and in Figure 3.109 for test CWU3 and test PWU3 respectively.

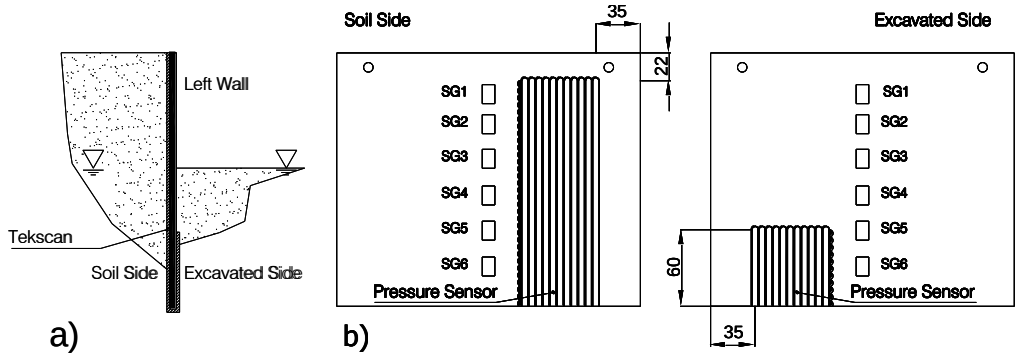

Figure 3.108: Test CWU3: modality of placement of the Tekscan pressure film, a) lateral view and b) frontal view

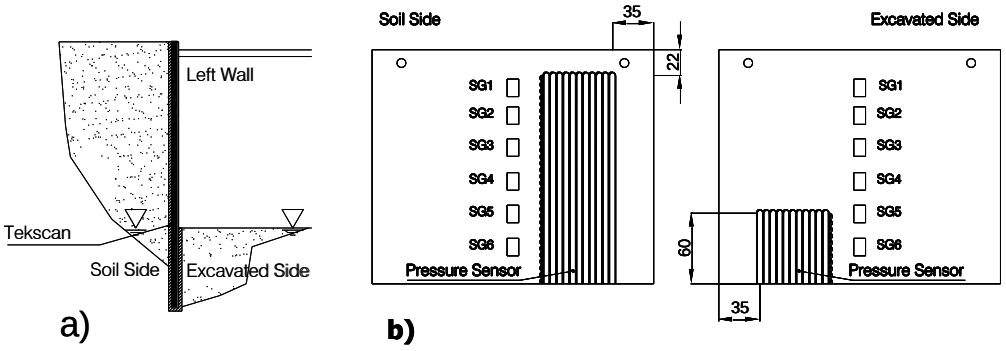

Figure 3.109: Test PWU3: modality of placement of the Tekscan pressure film, a) lateral view and b) frontal view.

The data acquisition with the Tekscan has been performed at a sample frequency of about 700 frames per second and for a duration of 10 seconds at the model scale, that correspond to 400 seconds at the prototype scale. During the performing of the tests CWU3 and PWU3 the data acquisition of Tekscan, which has a separated data acquisition system from the CDAQS one, has been launched about 3 seconds before the starting of the earthquakes (model scale) covering the duration of the earthquakes which last no more than 0.8 seconds at the model scale.

An example of the 2D visualization of the Tekscan data is reported in Figure 3.110. The figure represents the total horizontal pressure acting on the left wall of the test PWU3 before EQ3 (which has been taken as example). The first row of the data corresponds to the edge of the Tekscan film close to the top of the wall at the soil side (Figure 3.109(b). The rows of Tekscan film included between 1 and 30 measure the total horizontal pressure at the active side and the rows included between 36 and 44 measure the total horizontal pressure at the passive side. The rows included between 30 and 35 measure the total vertical pressure acting underneath the bottom of the wall; this is why the pressure attains the maximum measurable pressure by the Tekscan indicated by the colorbar at the right side of the figure.

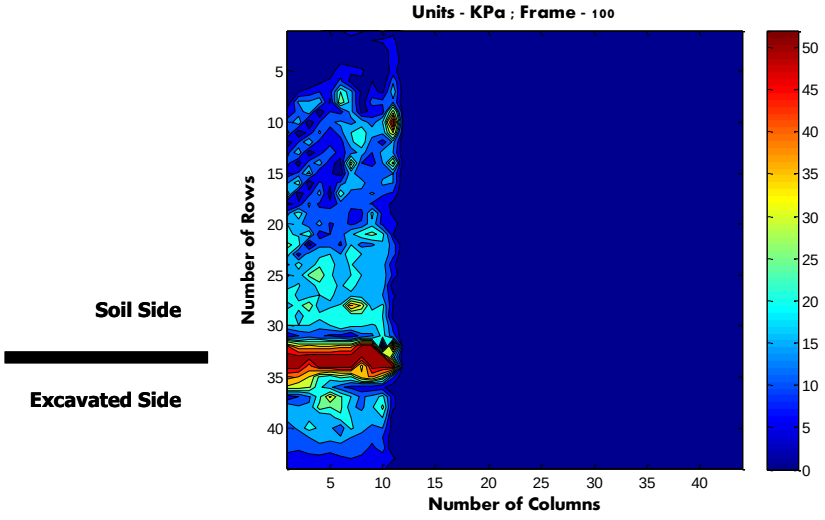

Figure 3.110: 2D Tekscan data from Test PWU3 before EQ3.

The data have been elaborated as described in the following steps:

1. visualization of the data in three dimensions;
2. subdivision of the total horizontal pressure acting at the active side from those acting at the passive side;
3. computation of the average of the pressures along the depth of the wall (that is along the columns of the Tekscan sheet;
4. computation of the resulting force acting on the wall from the active and form the passive side.

3.8 Tests CWU3 and PWU3 Tekscan Data

In this paragraph the resulting plots obtained from the sequence of operations detailed above are reported. In particular for both the tests CWU3 and PWU3 the three-dimensional plots and the distribution along the depth of the average horizontal pressure before all the earthquakes are reported. From Figure 3.111 to Figure 3.113 the three-dimensional plots for CWU3 and before EQ1 are reported; specifically in Figure 3.111 there is the 3D representation of the measured horizontal pressure obtained as direct 3D plot of the original 2D Tekscan data (see th above Figure 3.110, while in Figure 3.112 and in Figure 3.113 there is the subdivision of the previous 3D representation in the distribution at the back of the wall and in the distribution down the wall respectively; finally in Figure 3.114 there is the vertical distribution of the horizontal pressure along the wall obtained, at a given depth, as the average of the measured horizontal pressures. As well as for EQ1, in the following figures included between Figure 3.116 and Figure 3.122 there are the 3D and 2D plots relative to EQ2 and EQ3 and the vertical distribution of the horizontal pressure along the depth of the wall. Then, in Figure 3.123, the vertical distribution of the horizontal pressure is compared between the three earthquakes. With the same sequence as for test CWU3, the Tekscan data of test PWU3 are included between Figure 3.124 and Figure 3.136, where in the last one there is the comparison of the vertical distribution of the horizontal pressure between the three earthquakes.

From the observation of the Tekscan data it can be concluded that:

1. the 3D visualization shows that there is not a uniform distribution of the pressure acting on the wall at a given depth;

2. from the figures where the vertical distributions of the pressure of all the earthquake are reported, that are Figure 3.123 and Figure 3.136, an accumulation of the horizontal pressure both on active and passive side during the tests has emerged;

3. besides the accumulation of the horizontal pressure observed in Figure 3.123 and in Figure 3.136 an other important characteristic of the vertical plot can be highlighted, that is a remarkable low value of the horizontal pressure acting on the wall above the water table, especially for test CWU3, while it is less evident for test PWU3. Such observation seems to indicate that the horizontal pressure acting on the wall is less than it can be expected; this can be attributed to the effect of the capillary rise above the water table. This aspect it treated in Chapter

4 where the effect of the capillary rise is taken into account for the prediction of the bending moment;

4. The visualization of the vertical distribution along the wall during the entire duration of the earthquake base on a Matlab code has helped to visualize the dynamic response of the soil during the earthquake and to confirm what has been concluded computing the phase shift in the time domain, that is that a significant phase shift is present between the soil below the water table and the soil above the water table;

5. the value of the slope of the vertical distribution of the horizontal pressure is less than 10 kPa/m below the water table in both the tests on cantilever wall and on propped wall. In fact, considering the values of the horizontal pressure relative to tests CWU3 below the water table in Figure 3.123, that for instance refers to EQ3, at 4m and 7m from the top of the wall, which are about 10 kPa and 30 kPa, an average slope of 6.66 kPa/m is obtained; considering also the values of the horizontal pressure relative to EQ3 of PWU3 in Figure 3.136, at 5.6m and 7m from the top of the wall, which are about 17 kPa and 23 kPa, a slope of 4.28 kPa/m is obtained. This seems to indicate that there is an issue with the measurement of the total horizontal pressure with the use of the Tekscan pressure film.

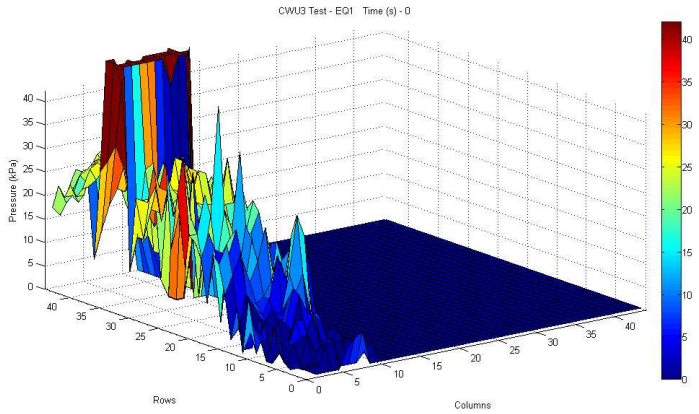

Figure 3.111: 3D visualization of the Tekscan data for test CWU3 before EQ1.

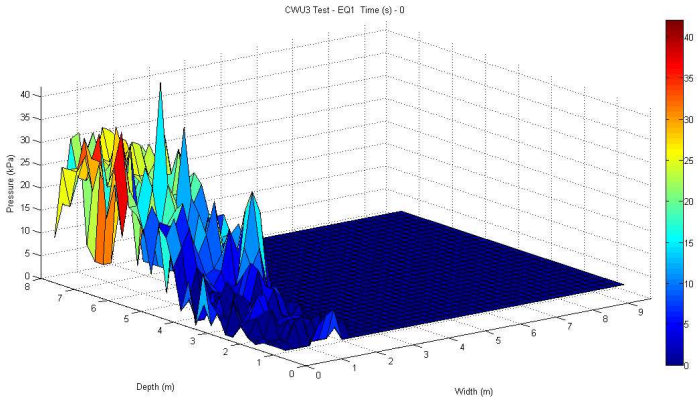

Figure 3.112: 3D visualization of the Tekscan data for test CWU3 before EQ1: pressures acting at the active side.

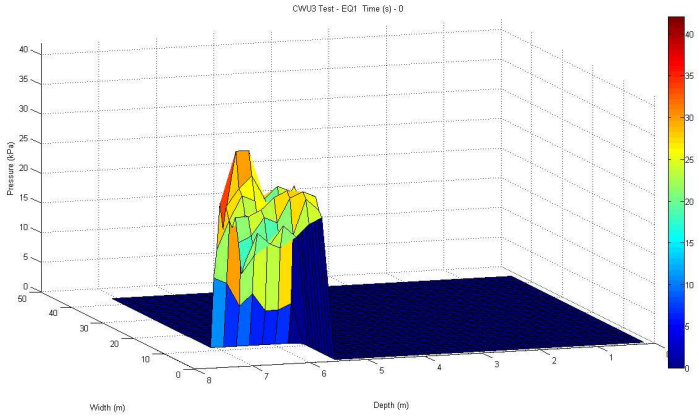

Figure 3.113: 3D visualization of the Tekscan data for test CWU3 before EQ1: pressure acting at the passive side.

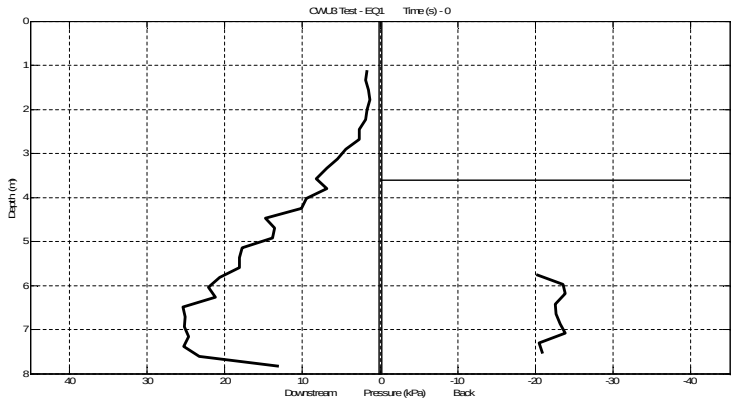

Figure 3.114: Test CWU3: vertical distribution of the total horizontal pressure before EQ1 computed as the average of the Tekscan measured pressure along the depth of the wall.

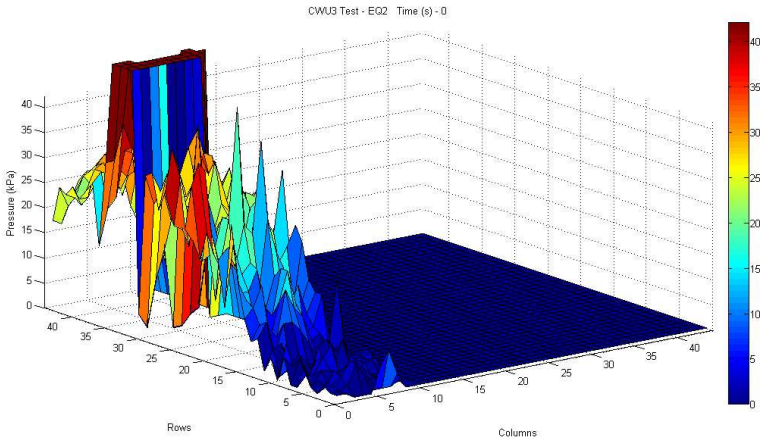

Figure 3.115: 3D visualization of the Tekscan data for test CWU3 before EQ2.

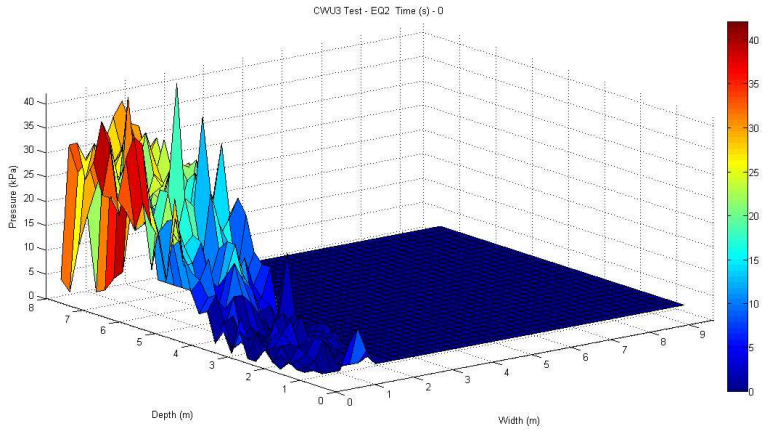

Figure 3.116: 3D visualization of the Tekscan data for test CWU3 before EQ2: pressures acting at the active side.

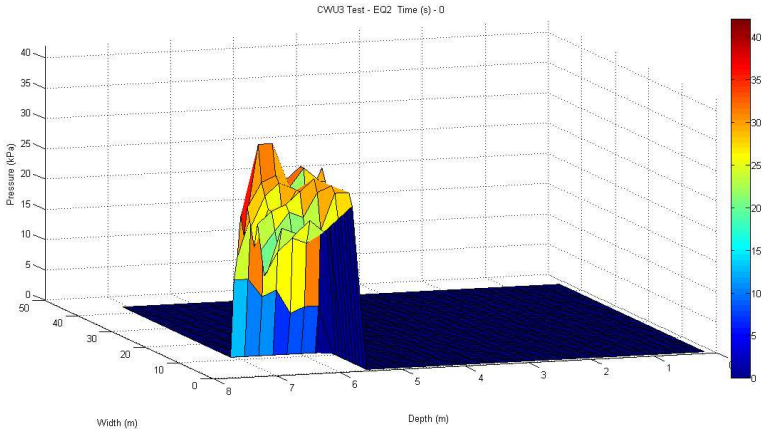

Figure 3.117: 3D visualization of the Tekscan data for Test CWU3 before EQ2: pressure acting at the passive side.

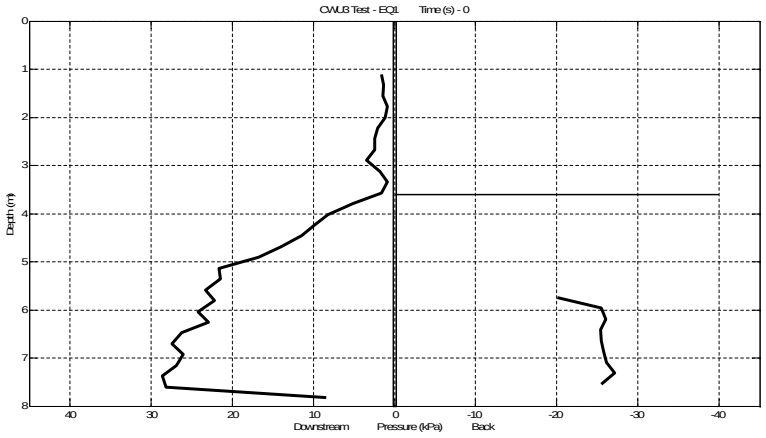

Figure 3.118: Test CWU3: vertical distribution of the total horizontal pressure before EQ2 computed as the average of the Tekscan measured pressure along the depth of the wall.

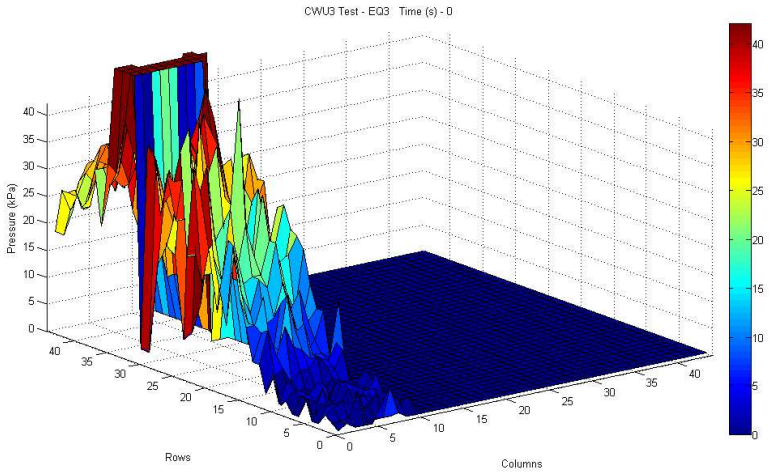

Figure 3.119: 3D visualization of the Tekscan data for test CWU3 before EQ3.

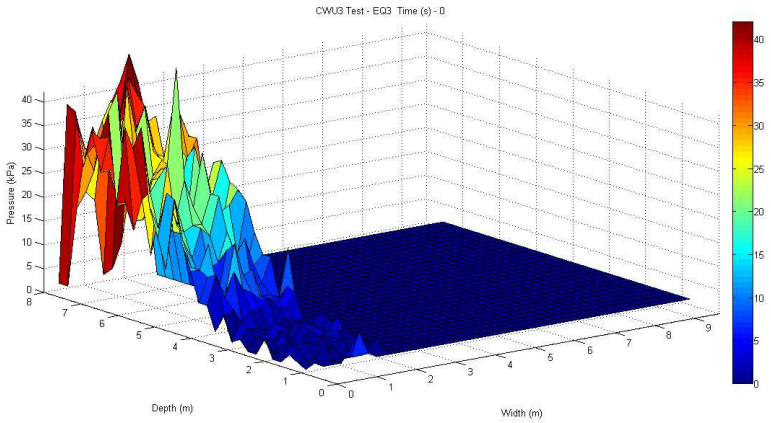

Figure 3.120: 3D visualization of the Tekscan data for test CWU3 before EQ3: pressures acting at the active side.

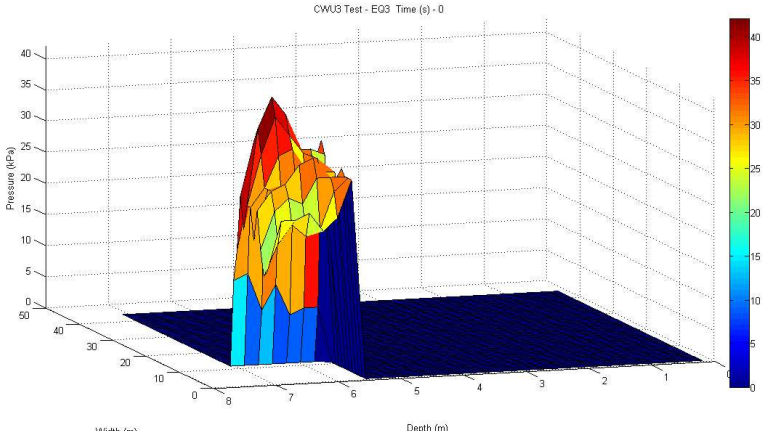

Figure 3.121: 3D visualization of the Tekscan data for test CWU3 before EQ3: pressure acting at the passive side.

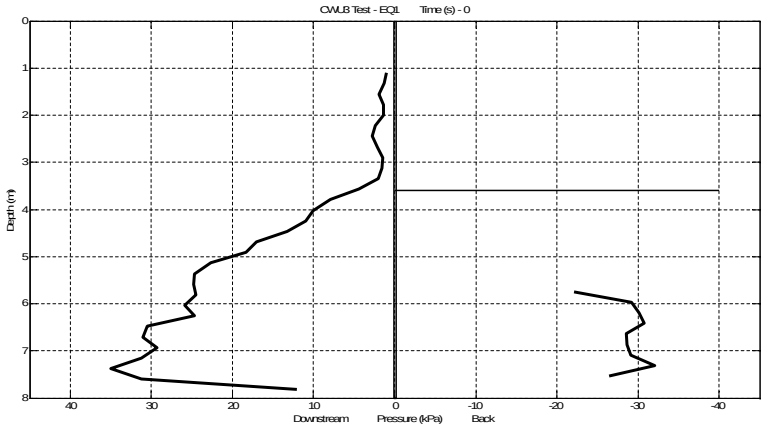

Figure 3.122: Test CWU3: vertical distribution of the total horizontal pressure before EQ3 computed as the average of the Tekscan measured pressure along the depth of the wall.

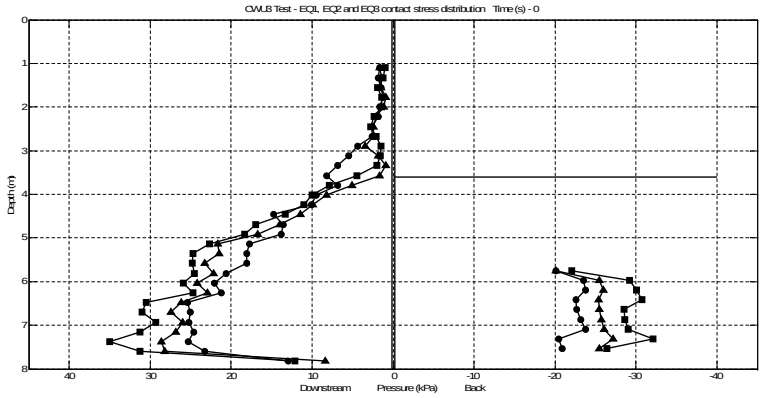

Figure 3.123: Test CWU3: comparison between the vertical distribution of the horizontal pressure in EQ1, EQ2 and EQ3; EQ1-circled marker, EQ2-tricangular marker, EQ3-squared marker.

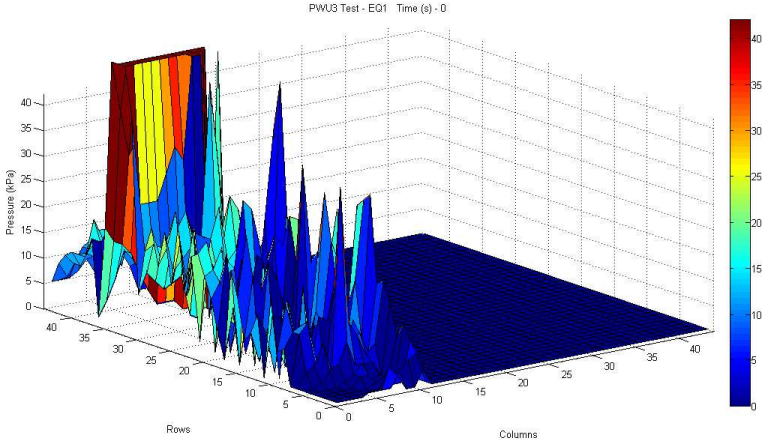

Figure 3.124: 3D visualization of the Tekscan data for test PWU3 before EQ1.

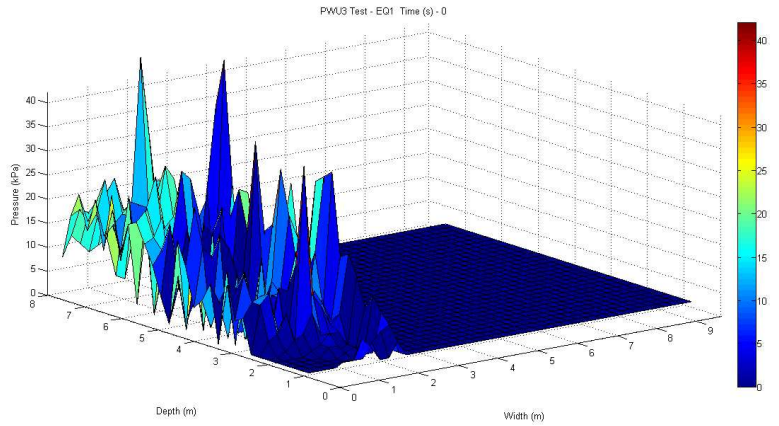

Figure 3.125: 3D visualization of the Tekscan data for test PWU3 before EQ1: pressures acting at the active side.

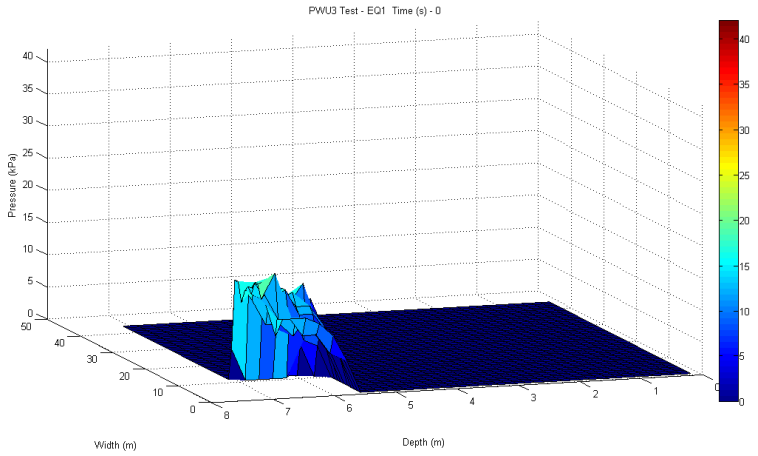

Figure 3.126: 3D visualization of the Tekscan data for test PWU3 before EQ1: pressure acting at the passive side.

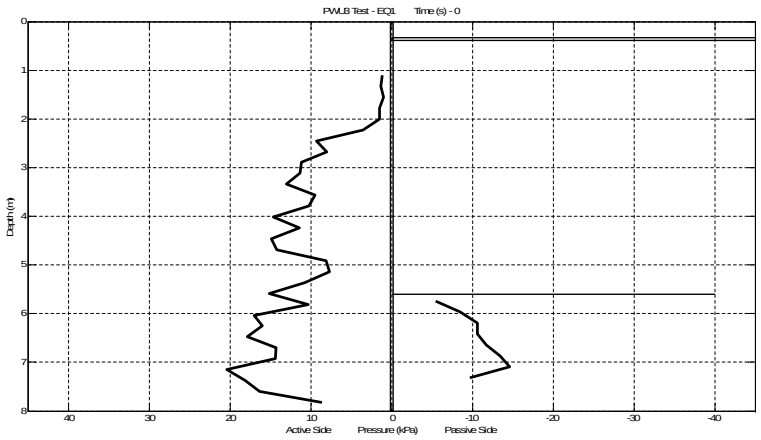

Figure 3.127: Test PWU3: vertical distribution of the total horizontal pressure before EQ1 computed as the average of the Tekscan measured pressure along the depth of the wall.

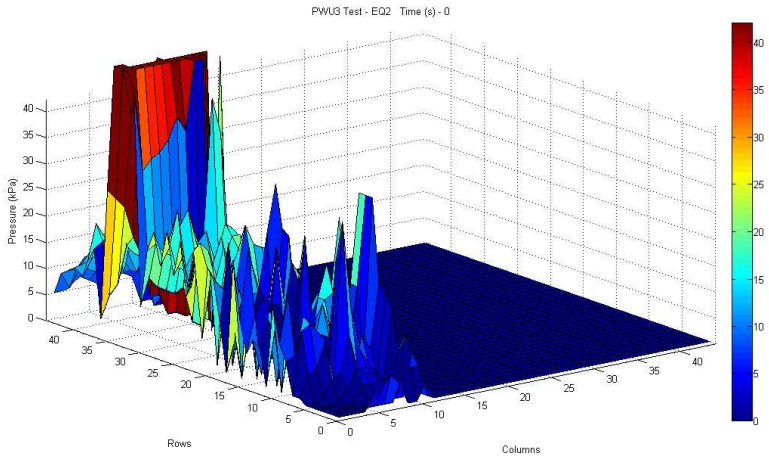

Figure 3.128: 3D visualization of the Tekscan data for test PWU3 before EQ2.

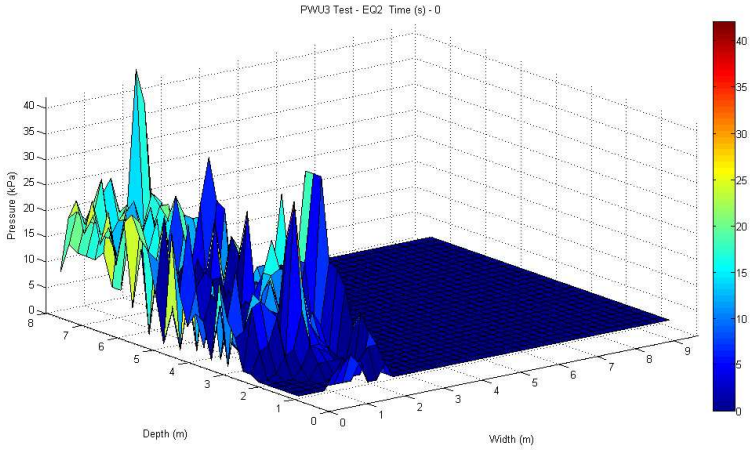

Figure 3.129: 3D visualization of the Tekscan data for Test PWU3 before EQ3: pressures acting at the active side.

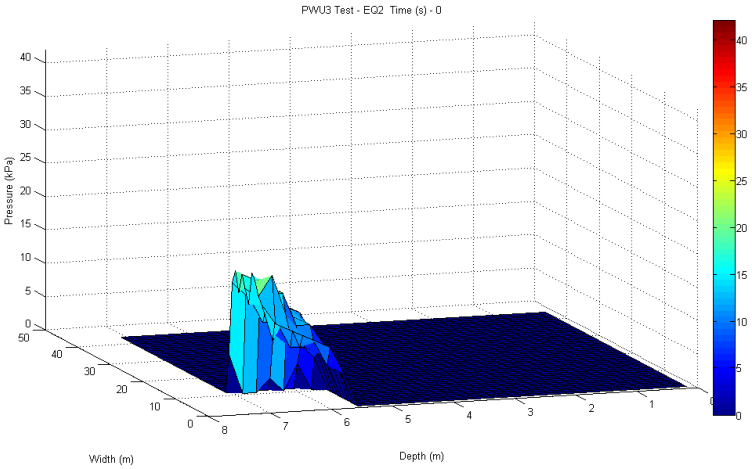

Figure 3.130: 3D visualization of the Tekscan data for Test PWU3 before EQ3: pressure acting at the passive side.

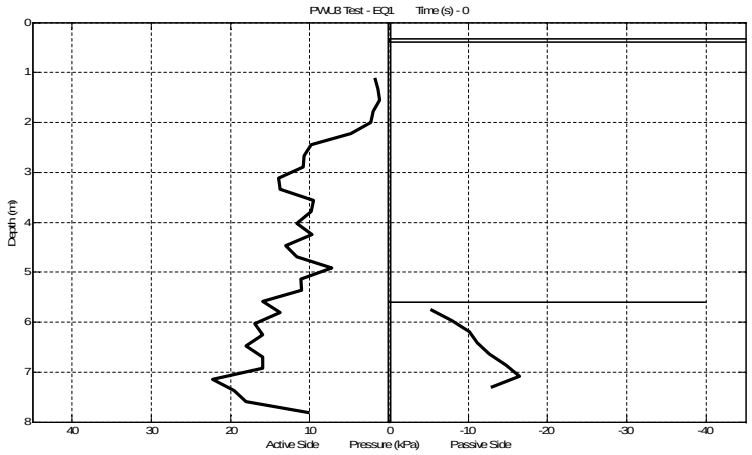

Figure 3.131: Test PWU3: vertical distribution of the total horizontal pressure before EQ3 computed as the average of the Tekscan measured pressure along the depth of the wall.

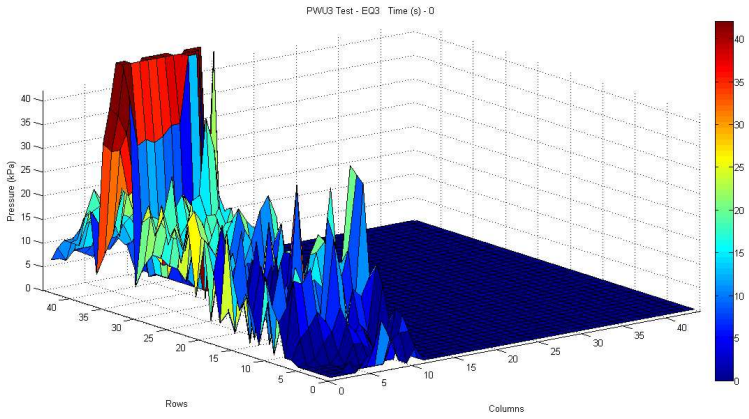

Figure 3.132: 3D visualization of the Tekscan data for Test PWU3 before EQ3.

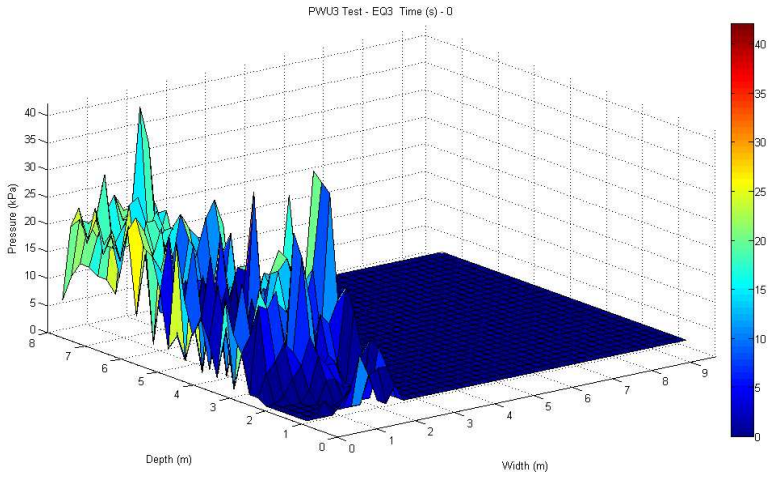

Figure 3.133: 3D visualization of the Tekscan data for Test PWU3 before EQ3: pressures acting at the active side.

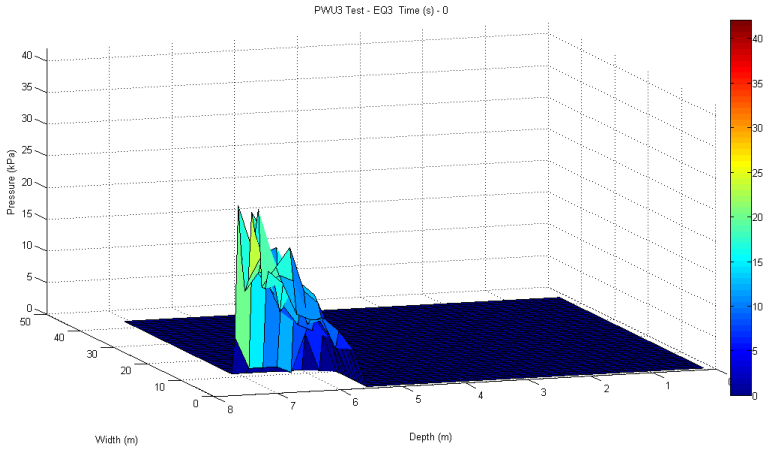

Figure 3.134: 3D visualization of the Tekscan data for Test PWU3 before EQ3: pressure acting at the passive side.

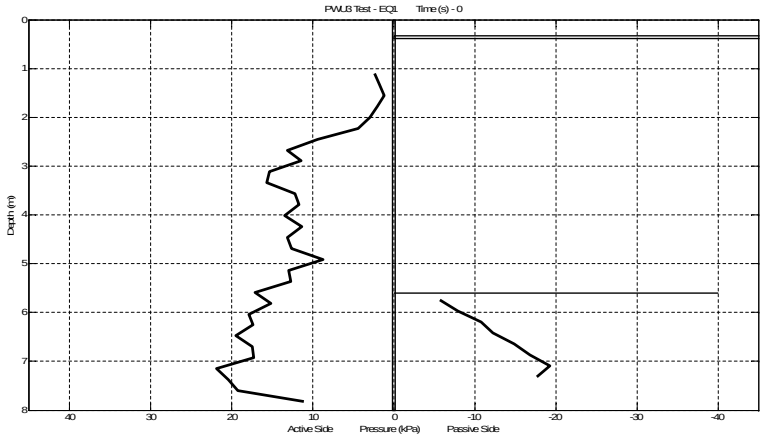

Figure 3.135: Test PWU3: vertical distribution of the total horizontal pressure before EQ3 computed as the average of the Tekscan measured pressure along the depth of the wall.

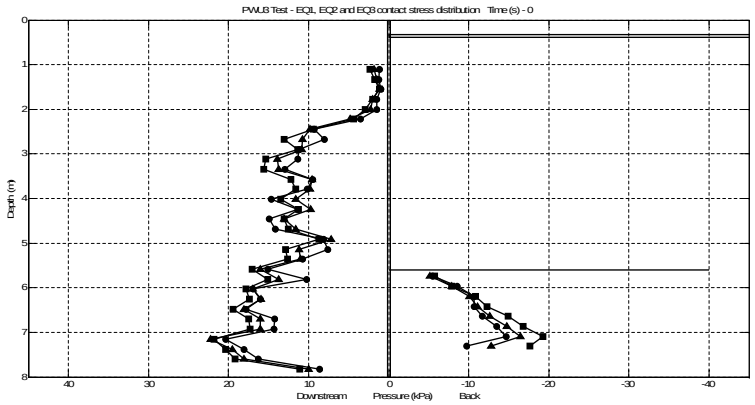

Figure 3.136: Test PWU3: comparison between the vertical distribution of the total horizontal pressure in EQ1, EQ2 and EQ3; EQ1 circles marker, EQ2 triangular marker, EQ3 squared marker.

3.9 CWU3 and PWU3 Laminar Box Displacements

In the introduction of 3.2 it has been highlighted the possible influence of the displacement of the laminar box on the displacements of the walls measured with the LVDTs. Also, the space distribution of the measured displacements and the symmetrical displacements have been plotted, which have allowed to focus on the collapse mechanism of the walls. The comparison of the measured displacements with the symmetrical displacements has allowed also to visualize the effect of the laminar box displacements on the displacements measured with the LVDTs. In Figure 3.137 the walls measured and symmetrical displacements in the space are have been proposed again for tests CWU1, PWU1, CWU2 and PWU2. For all the tests the influence of the laminar box displacements seems to be more significant as the number of earthquakes increases for a given test; moreover the strongest effect seems to have been observed for test CWU2. Anyway in general such influence seems no to be so important on the measured displacements of the walls

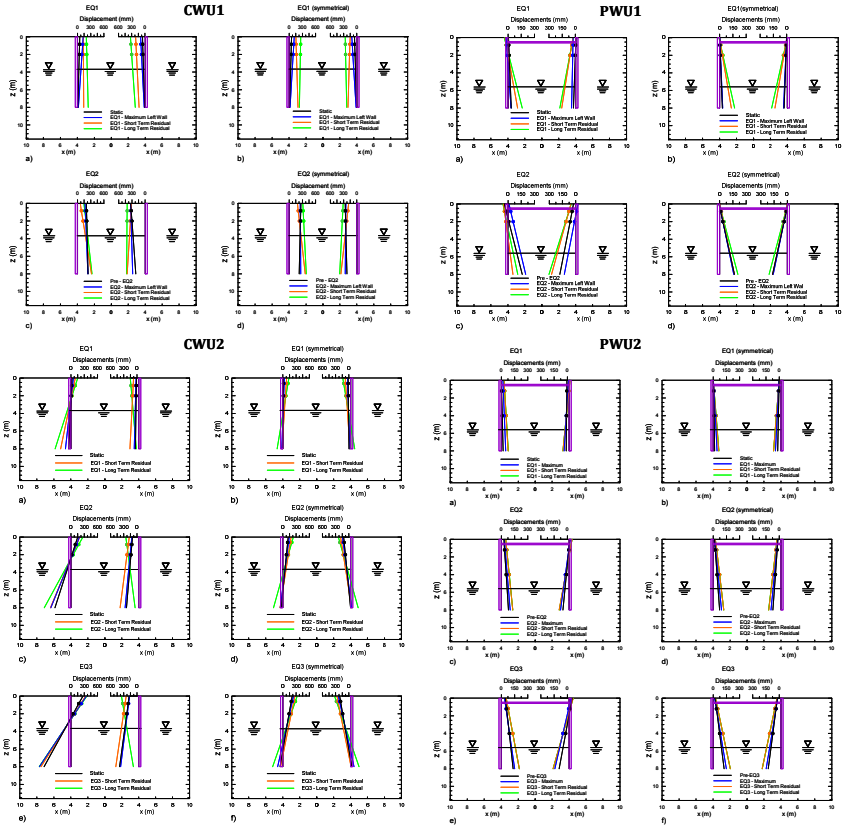

Figure 3.137: Test PWU3: comparison between the vertical distribution of the total horizontal pressure in EQ1, EQ2 and EQ3; EQ1 circles marker, EQ2 triangular marker, EQ3 squared marker.

For tests CWU3 and PWU3 two LVDTs measuring the displacements of the laminar box have been placed at the same depth of the LVDTs measuring the horizontal displacements of the walls. In Figure 3.138 the photography of the model of test PWU3 before the test can be seen and the LVDT measuring the laminar box displacements are visible on the left side. The displacements measured with the LVDTs outside the box have been used to compute the actual displacements of the walls so that the walls displacements computed as symmetrical displacements have been compared with the displacements computed as the difference between the measured displacements and the displacements of the laminar box rings; these last ones have been called corrected. In Figure 3.139 and in Figure 3.140 the measured, symmetrical and corrected displacements are reported for test CWU3 and

PWU3 respectively and with respect to EQ1, EQ2 and EQ3. As it can be observed from those images, there is not a significant difference between the measured displacements and the corrected displacements so that the symmetrical displacements can be considered a good approximation of the real displacements of the walls.

It can be concluded that there is not a strong influence of the laminar box rings displacements on the displacements of the walls measured with the LVDTs; only in test CWU2 the walls displacements have been apparently more affected from the laminar box displacements (Figure 3.137). The symmetrical displacements remain anyway a good approach for a direct representation of the collapse mechanism of the walls and for the computation of the rotation with respect to time of the walls.

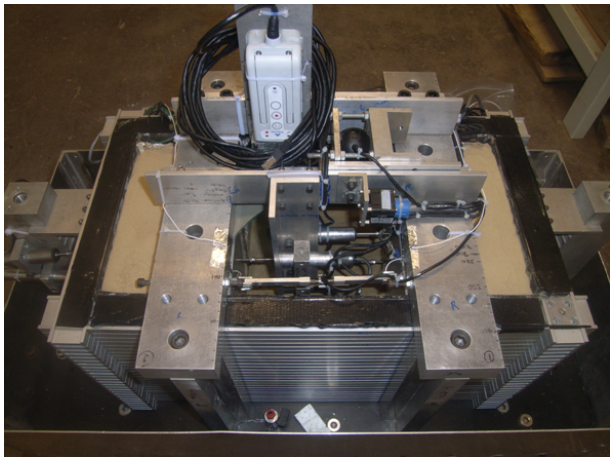

Figure 3.138: Test PWU3: model before the test.

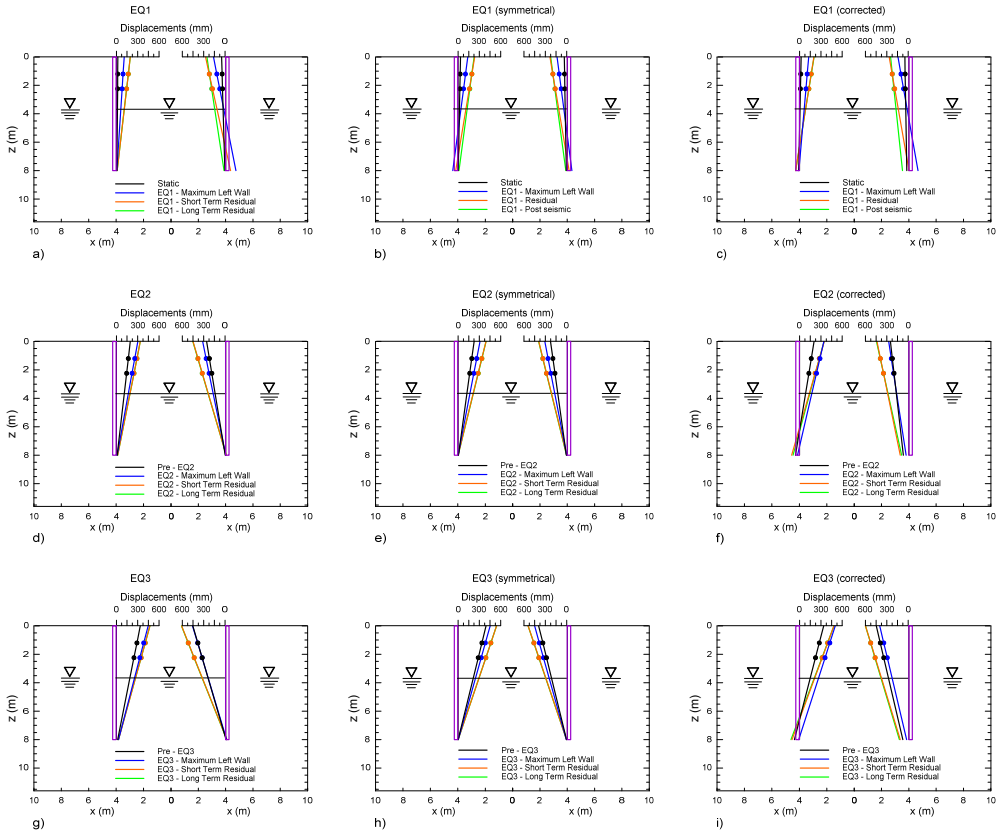

Figure 3.139: Test CWU3: walls measured displacements (a,d,g), symmetrical displacements (b,e,h) and corrected displacements (c,f,i).

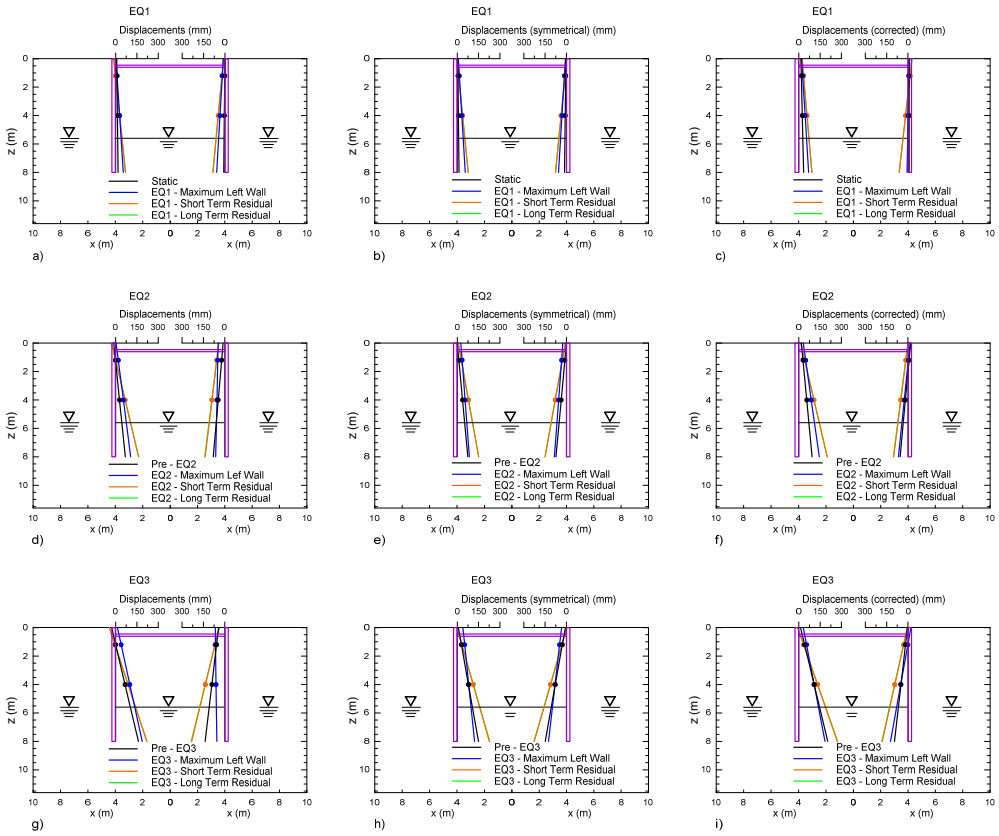

Figure 3.140: Test PWU3: walls measured displacements (a,d,g), symmetrical displacements (b,e,h) and corrected displacements (c,f,i).

3.10 Summary

From what has been seen from the data of the tests it can be concluded what follows:

1. Acceleration of the soil: the acceleration is significantly de-amplified in tests CWU1 and PWU1 carried out in loose sand; it is de-amplified in the tests CWU2 and PWU2 as well but less significantly than in tests CWU1 and PWU1. In fact the amplification factor is less than one in both tests in loose sand and in dense sand, but in the first ones it reaches even values lower than 0.5, while for the latter ones it is almost always above 0.5. As regards the phase difference of the acceleration

of the soil, in all the tests it has been observed that the portion of soil located below the excavated level presents a phase difference not higher than 50° while it reaches higher values, which are included between 100° and 150° or higher, approaching the top of the soil layer;

2. Displacement of the walls: the collapse mechanism of test CWU1 can be subdivided into two phases; the first one consists of a rotation around a point below the excavation level with a progressive approach of the tops of the walls while the second one consists in a counter-rotation of the walls, with an approach of the toes, due to a strong loss of resistance of the soil connected with an increase of the pore pressures in the excavated side. The collapse mechanism of the walls in test CWU2 on the contrary is equal to the typical collapse mechanism of a pair of walls embedded in dry soil, that is a rotation around a point located below the excavation level with a progressive approach of the tops of the walls. As regards the tests on propped walls, the collapse mechanism is represented by a rotation of the walls around the props, of course due to the constrain imposed by the props. In this latter case the accumulated displacement at the bottom at the end of the test is for 206mm for test PWU1 (long term residual of EQ2) and 184mm for test PWU2 (long term residual of EQ3). The fact that test PWU2 presents a displacement lower than in test PWU1 at the end of the test and after three earthquakes instead of two earthquakes as in test PWU1 indicates that in test PWU2 there is a less important accumulation of the displacement. As regards the entity of the accumulated displacement at the top of the walls for the tests on cantilever walls, it reaches about 300mm at the end of the tests for both CWU1 and CWU2, but such value of the displacement at the top is reached after two earthquakes, differently with respect to CWU2 where the same value of the displacement at the top is reached after three earthquakes. In the case of test CWU1 a marked translation of the walls is observed while in test CWU2 the collapse mechanism basically consists of a rotation. So also for the case of cantilever tests the loss of resistance in test with loose sand in the excavated side determines a proportionally higher accumulation of displacement with respect to the test in dense sand;

3. Pore pressures: the pore pressure coefficient at the back of the walls is significantly below the unity indicating that liquefaction does not occurs; this is due to the self weight of the partially saturated soil above

the excavation level that determines an increase of the effective stress state with respect to the case of absence of soil above the excavation level. The pore pressure coefficient is close to the unity in all the tests within the excavated side; this does not reflect the significant difference in the structural response between the tests in loose sand CWU1 and PWU1 and the tests in dense sand CWU2 and PWU2. There can be some accuracy errors in the measurement of the position of the PPTs that can be reflected in the value of the pore pressure coefficient; also it has been computed supposing a one-dimensional distribution of the effective stresses but probably the pore pressure coefficient cannot be the only indicator discriminating the occurrence or the non-occurrence of liquefaction in the excavated side;

4. Bending moment: for a given typology of structure the bending moment at the end of the swing up is higher for the test in loose sand than in the test in dense sand. For instance the maximum pre-EQ1 bending moment for test CWU1 is 35 kNm/m while for CWU2 it is 27 kNm/m while the maximum pre-EQ1 bending moment for test PWU1 is 76 kNm/m and for test PWU2 is 42 kNm/m. Clearly this is due to the difference in the relative density of the sand of the tests, because as the relative density of the sand decreases the angle of shearing resistance decreases and consequently the correspondent structural stress for a given equilibrated configuration is higher. Moreover, the residual bending moments for tests CWU1 and PWU1 decrease passing from the first earthquake to the following ones and this happens also for test CWU2 contrary to the fact that the test has been performed in dense sand, since it is expected to observe an accumulation of the bending moment as the earthquakes are executed. On the other hand the remaining test PWU2 shows a progressive accumulation of the bending moment coherently with the fact that the test has been performed in dry sand, and similarly as for the tests performed on dry cantilever walls (Conti, 2010) but with lower values. Thus in tests CWU1, PWU1 and CWU2 a progressive decrease of the bending moment as the earthquakes are executed has taken place. On the other hand, in test PWU2, as displacements are accumulated also the structural bending moment increases. So one difference between tests in loose sand and tests in dense sand is that for those in loose sand a decrease of the bending moment is observed while for PWU2, which has been performed in dense sand, an accumulation of the pre-earthquake bending moment is observed. These findings are confirmed consid-

ering the values of the bending moment at the short term residual and at the long term residual. Indeed for test CWU1 the short term residual values are 9 kNm/m and 10 kNm/m and the long term residual values are 23 kNm/m and 19 kNm/m respectively for EQ1 and EQ2; for test PWU1 the short term residual values are 33 kNm/m and -16 kNm/m and the long term residual values are 64 kNm7m and 56 kNm/m respectively for EQ1 and EQ2; for test CWU2 the short term residual values are 12 kNm/m, 8 kNm/m and 4 kNm/m and the long term residual values are 22 kNm/m, 15 kNm/m and 12 kNm/m respectively for EQ1, EQ2 and EQ3; for test PWU2 the short term residual values are 71 kNm/m, 79 kNm/m and 89 kNm/m and the long term residual values are 66 kNm/m, 77 kNm/m and 89 kNm/m respectively for EQ1, EQ2 and EQ3. Such behaviour in tests CWU1, PWU1 and CWU2 can be in principle explained considering that the pore pressure build up determines a drop in the bending moment due to a decrease of the total horizontal pressure acting on the wall; then, after the earthquake, the pore pressure dissipation takes place and the structure tends to recover a further equilibrated configuration increasing again the bending moment but not recovering it completely; this happens at every earthquake determining the above seen decrease of the short and long term residual values of the bending moment. On the other hand, for the structural behaviour in test PWU2 the increase of pore pressures, which in turn is related to the inhibited coupled distorsional-volumetric behaviour of the soil, does not determine a drop in the bending moment and, on the contrary, an accumulation is observed. It is important to underline that test CWU2 actually presents an intermediate response between that one corresponding to the tests in loose sand and that one corresponding in the tests in dense sand; indeed on one hand it presents a progressive accumulation of the displacements where the toes of the wall accumulate progressively and on the other hand the residual bending moments (short term residual and long term residual) decrease. Such intermediate response can be due to the relative density of the sand that likely has not achieved the value of 88% as consequence of the pouring of the sand during the model preparation. As regards the maximum bending moment, for tests on cantilever walls it is slightly higher for test CWU2, where it passes from 39 kNm/m to 39 kNm/m to 49 kNm/m, with respect to CWU1, where it passes from 44 kNm/m to 34 kNm/m; similarly, for the propped tests the maximum bending moment is slightly higher for the test in dense sand PWU2 than for the test PWU1 in loose sand,

where respectively it assumes the values 86 kNm/m and 94 kNm/m, and 86 kNm/m, 107 kNm/m and 130 kNm/m. Considering only the tests in loose sand, the maximum bending moment decreases passing from EQ1 to EQ2 for the test CWU1, while it increases for test PWU1; this happens even if a strong loss of shear resistance occurs in both tests. This is attributable to the different structural scheme and the consequent different way the structures have to react to external loads. The values of the bending moment are summarized in Table 3.21;

Test		Pre-EQ1	Maximum	Short Term Res.	Long Term Res.
CWU1	EQ1	35	38	9	23
	EQ2	23	24	10	19
PWU1	EQ1	76	86	33	64
	EQ2	65	94	-16	56
CWU2	EQ1	27	39	12	22
	EQ2	22	39	8	15
	EQ3	15	49	4	-12
PWU2	EQ1	42	86	71	66
	EQ2	64	107	79	77
	EQ3	75	130	89	89

Table 3.21: Bending moment at pre-earthquakes, maximum, short term residual and long term residual for the tests CWU1, PWU1, CWU2 and PWU2.

5. Axial force in the load cells: a significant drop of the axial force in the props is observed in test PWU1. This is again attributable to the loss of shearing resistance in the excavated side; due to such drop in the passive resistance of the soil the load on the structure decreases and consequently the axial force required to maintain the equilibrium decreases as well. On the contrary, in test PWU2 an accumulation of the axial force is observed, and this is probably attributable to a progressive mobilization of the passive resistance;

6. Displacements of laminar box rings: there seems not to be a significant influence of the laminar box rings displacements on the displacements of the walls measured with the LVDTs. This has been seen through the comparison of the displacements of the walls represented in the space domain as direct representation of the walls displacements measured with the LVDTs (measured displacements) and the representation in the space domain of the symmetrical displacements, that is the dis-

placements obtained attributing the average of the measured displacement to the left and right wall. Moreover in tests CWU3 and PWU3 two LVDTs placed outside the model and measuring the laminar box displacements have allowed to deduct from the measured displacements those of the laminar box. The comparison between the measured, symmetrical and corrected displacements has led to the same conclusion as above, that is that the laminar box displacement do not significantly affect the measurement of the walls displacement. The symmetrical representation anyway has represented a good approach for the visualization of the collapse mechanism;

7. The profile along the wall of the horizontal pressure determined computing the average, at a given depth, of the horizontal pressure with respect the rows of the Tekscan seems not to be credible since the slope of the diagram is less than 10 kPa/m below the water table; at the same time the Tekscan data allow to visualize some characteristic of the distribution of the horizontal pressure, that are the non uniform distribution of the pressure over the measuring area of the Tekscan, the accumulation of the horizontal pressure passing from EQ1 to EQ3 on both active side and passive side, the possible influence of the capillary rise above the water table on the horizontal pressure and the dynamic response of the soil during the earthquake in terms of phase shift through the visualization of the vertical distribution of the horizontal pressure during the shaking.

Chapter 4

Test Data - Part II

Chapter 3 has been dedicated to a detailed description of the data concerning each single test and a brief comparison of the results between the tests has been made at the summary of the chapter. In this chapter a further in-depth analysis of the results has been conducted in terms of:

(a) comparison between similar tests in terms of geometry and relative density in order to check the repeatability of the centrifuge tests;

(b) comparison of the amplification phenomenon with that observed in tests in dry sand;

(c) comparison of the phase difference computed in time domain with that obtained in the frequency domain and comparison with the phase difference of tests in dry sand;

(d) comparison of the accumulated displacements with those in tests in dry sand;

(e) prevision of the bending moment on the walls through limit equilibrium analyses with different horizontal stress distribution in order to take into account different possible influencing factors on the bending moment.

4.1 Comparison between similar Tests

The pairs of tests CWU2 and CWU3, PWU2 and PWU3, CWU2 and CWU4, CWU3 and CWU4 are similar both with respect the geometry and the relative density of the sand. Thus they give the possibility to check the repeatability of the results of the tests. For those pairs of tests the space distribution of bending moments, displacements and pore pressures has been compared for twelve different time instants: pre-EQ1, pre-EQ2, pre-EQ3, maximum EQ1, maximum EQ2, maximum EQ3, short term residual EQ1, short term residual EQ2, short term residual EQ3, long term residual EQ1, long term residual EQ2 and long term residual EQ3. As it has been done in Chapter 3 the maximum time instant is the time instant when the bending moment reaches its maximum value on the left wall. In order not to report too many figures only the comparisons relative to the pairs CWU2 and CWU3, and PWU2 and PWU3 are illustrated. The conclusions relative to the comparison between CWU2 and CWU3 are the same as for the pairs of tests CWU2 and CWU4, and CWU3 and CWU4.

4.1.1 Comparison between CWU2 and CWU3

The comparison between CWU2 and CWU3 reported in Figure 4.1, Figure 4.2 and Figure 4.3 highlights a good agreement between the two tests, especially for pore pressure distribution at the different time instants; the agreement is less good for the bending moment distribution and the displacement space distribution.

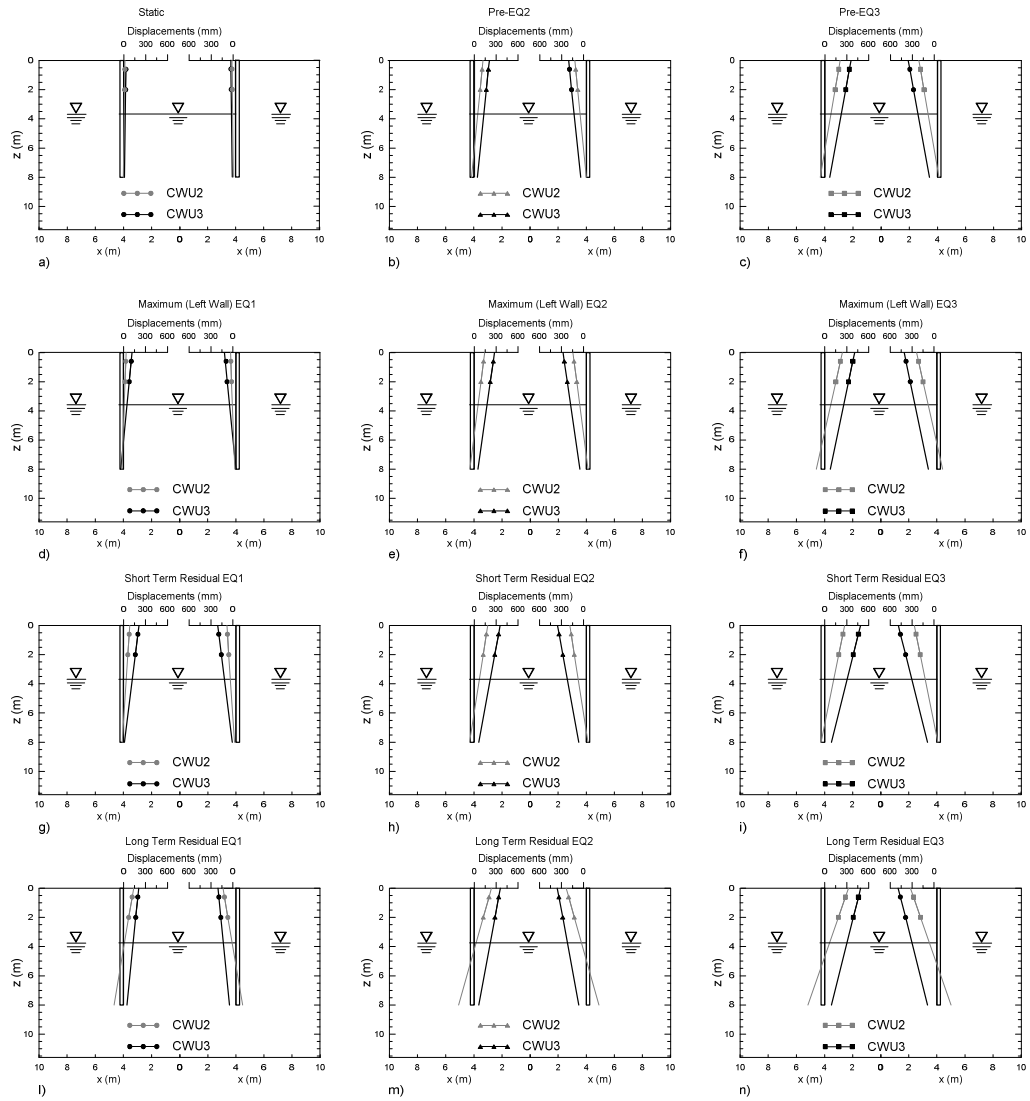

Figure 4.1: Displacement space distribution, comparison between CWU2 and CWU3. Time instants: a) static, b) Pre-EQ3, c) Pre-EQ3, d) Maximum EQ1 (left wall), e) Maximum EQ2 (left wall) , f) Maximum EQ3 (left wall), g) Short term residual EQ1, h) Short term residual EQ2, i) Short term residual EQ3, l) Long term residual EQ1, m) Long term residual EQ2, n) Long term residual EQ3.

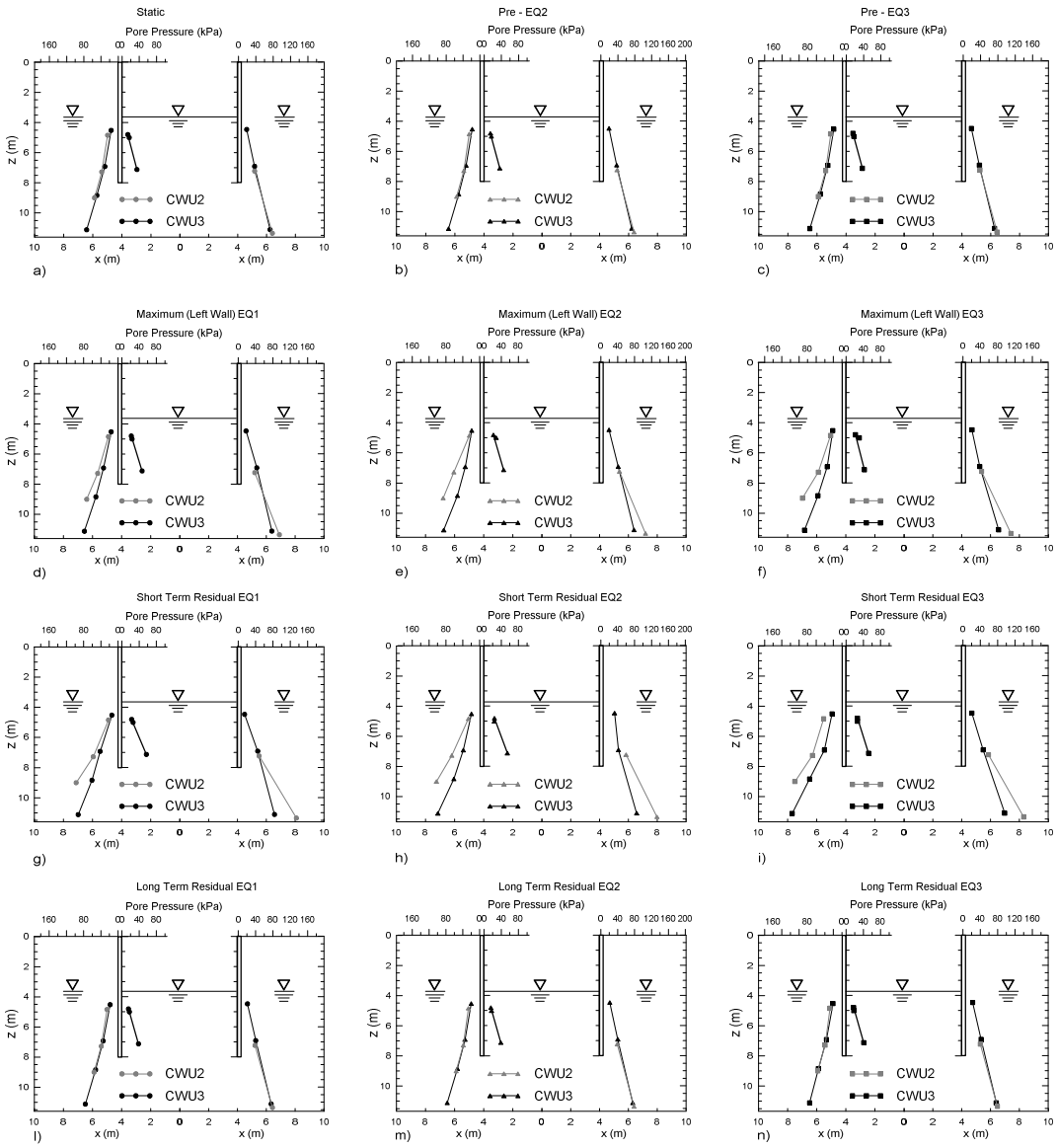

Figure 4.2: Pore pressure space distribution, comparison between CWU2 and CWU3. Time instants: a) static, b) Pre-EQ3, c) Pre-EQ3, d) Maximum EQ1 (left wall), e) Maximum EQ2 (left wall) , f) Maximum EQ3 (left wall), g) Short term residual EQ1, h) Short term residual EQ2, i) Short term residual EQ3, l) Long term residual EQ1, m) Long term residual EQ2, n) Long term residual EQ3.

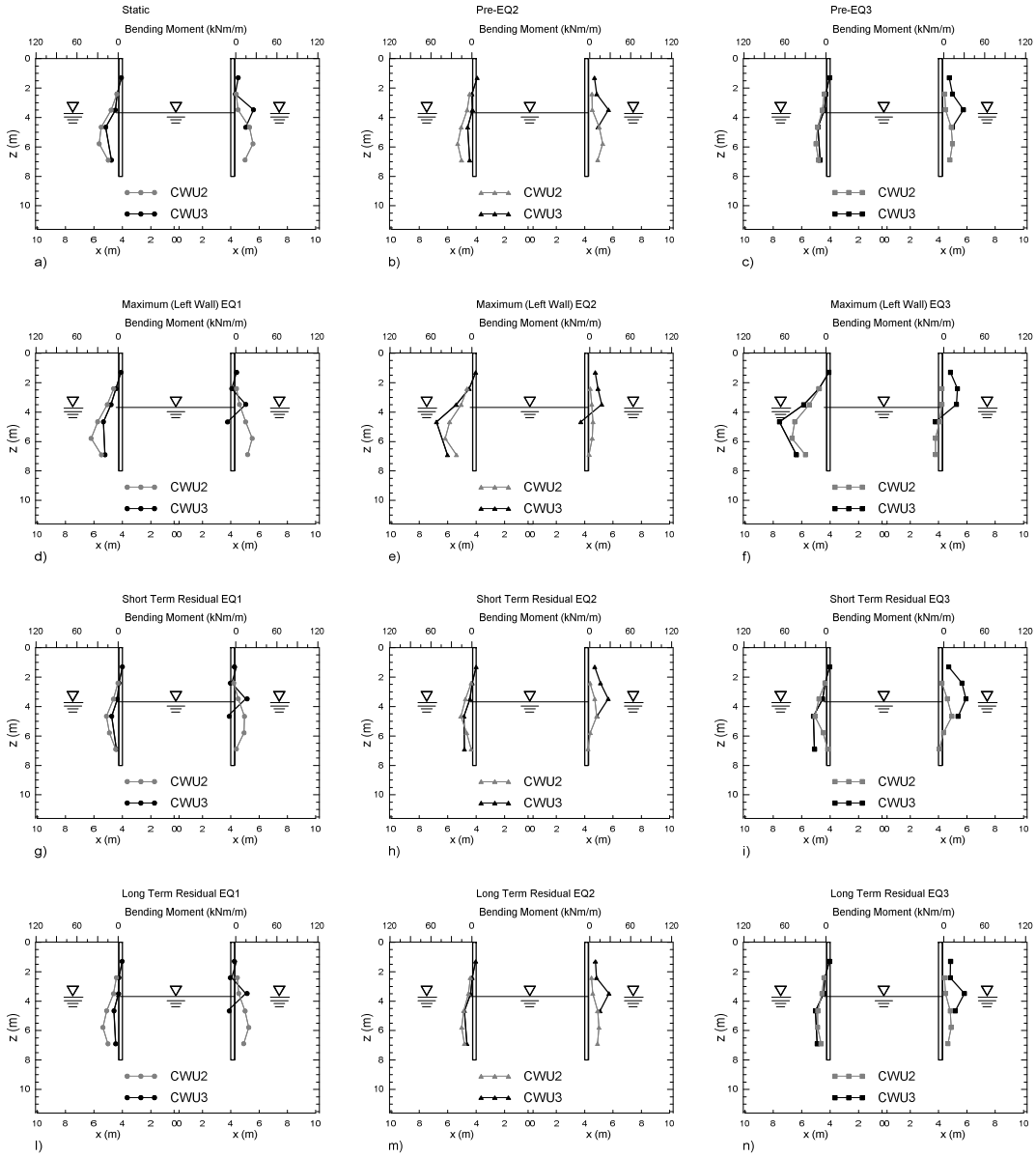

Figure 4.3: Bending moment space distribution, comparison between CWU2 and CWU3. Time instants: a) static, b) Pre-EQ3, c) Pre-EQ3, d) Maximum EQ1 (left wall), e) Maximum EQ2 (left wall) , f) Maximum EQ3 (left wall), g) Short term residual EQ1, h) Short term residual EQ2, i) Short term residual EQ3, l) Long term residual EQ1, m) Long term residual EQ2, n) Long term residual EQ3.

4.1.2 Comparison between PWU2 and PWU3

The results of the comparison between the tests PWU2 and PWU3 are reported in Figure 4.4, Figure 4.5 and Figure 4.6. Also here there is a good agreement between the results of the two tests considering the space distribution at the different time instants of the displacements, the pore pressures and the bending moment.

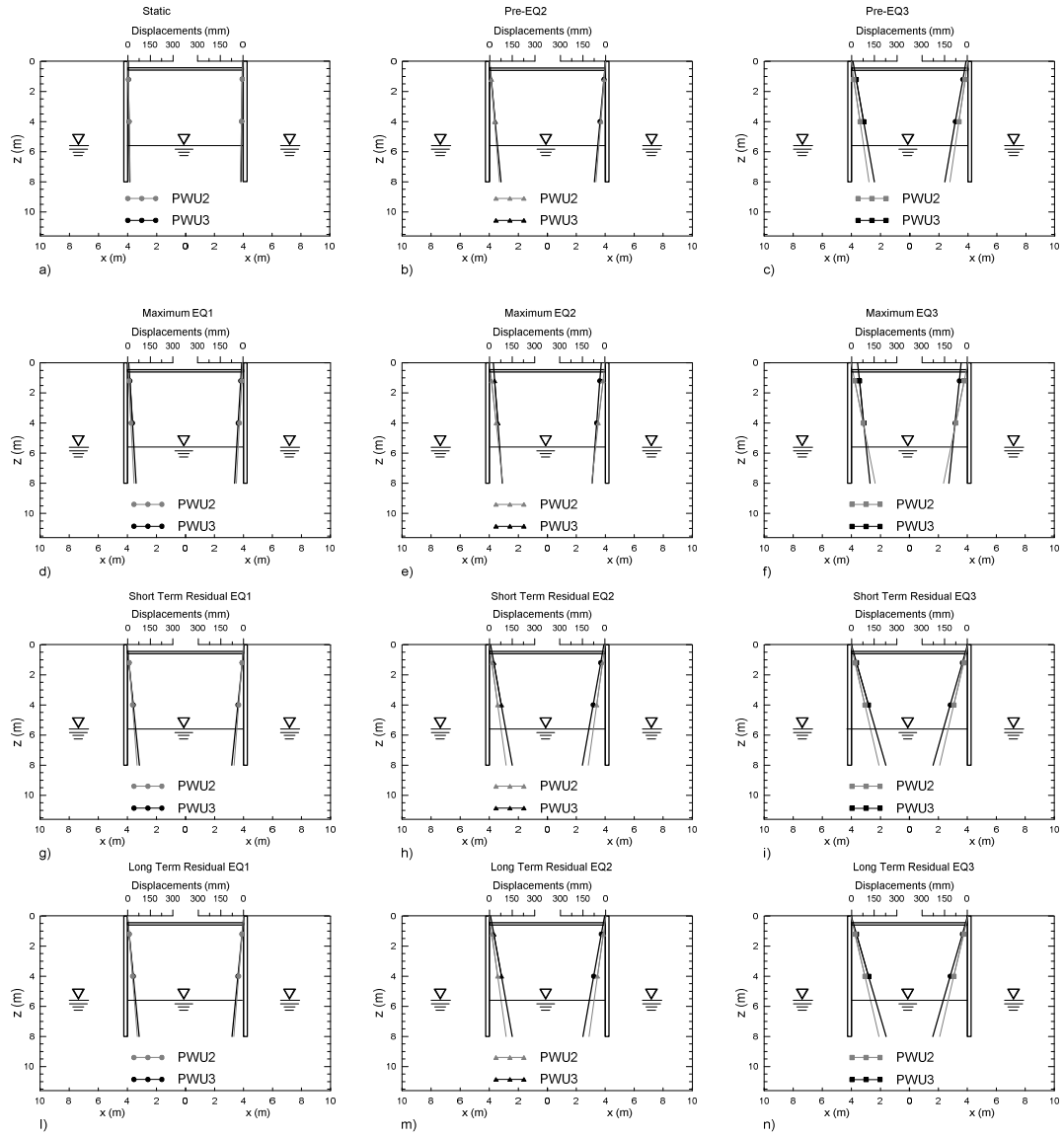

Figure 4.4: Displacement space distribution, comparison between PWU2 and PWU3. Time instants: a) static, b) Pre-EQ3, c) Pre-EQ3, d) Maximum EQ1 (left wall), e) Maximum EQ2 (left wall) , f) Maximum EQ3 (left wall), g) Short term residual EQ1, h) Short term residual EQ2, i) Short term residual EQ3, l) Long term residual EQ1, m) Long term residual EQ2, n) Long term residual EQ3.

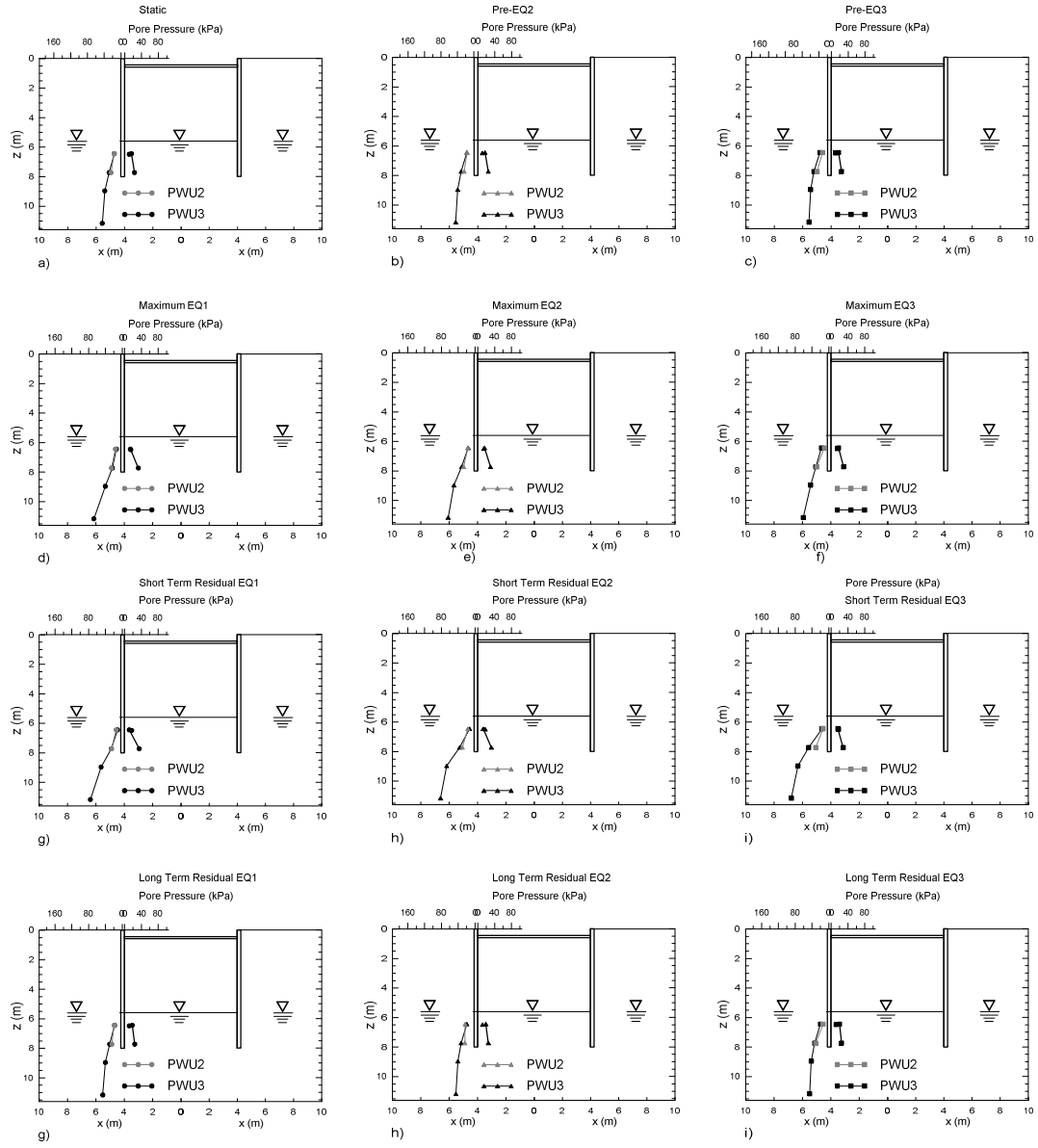

Figure 4.5: Pore pressure space distribution, comparison between PWU2 and PWU3. Time instants: a) static, b) Pre-EQ3, c) Pre-EQ3, d) Maximum EQ1 (left wall), e) Maximum EQ2 (left wall) , f) Maximum EQ3 (left wall), g) Short term residual EQ1, h) Short term residual EQ2, i) Short term residual EQ3, l) Long term residual EQ1, m) Long term residual EQ2, n) Long term residual EQ3.

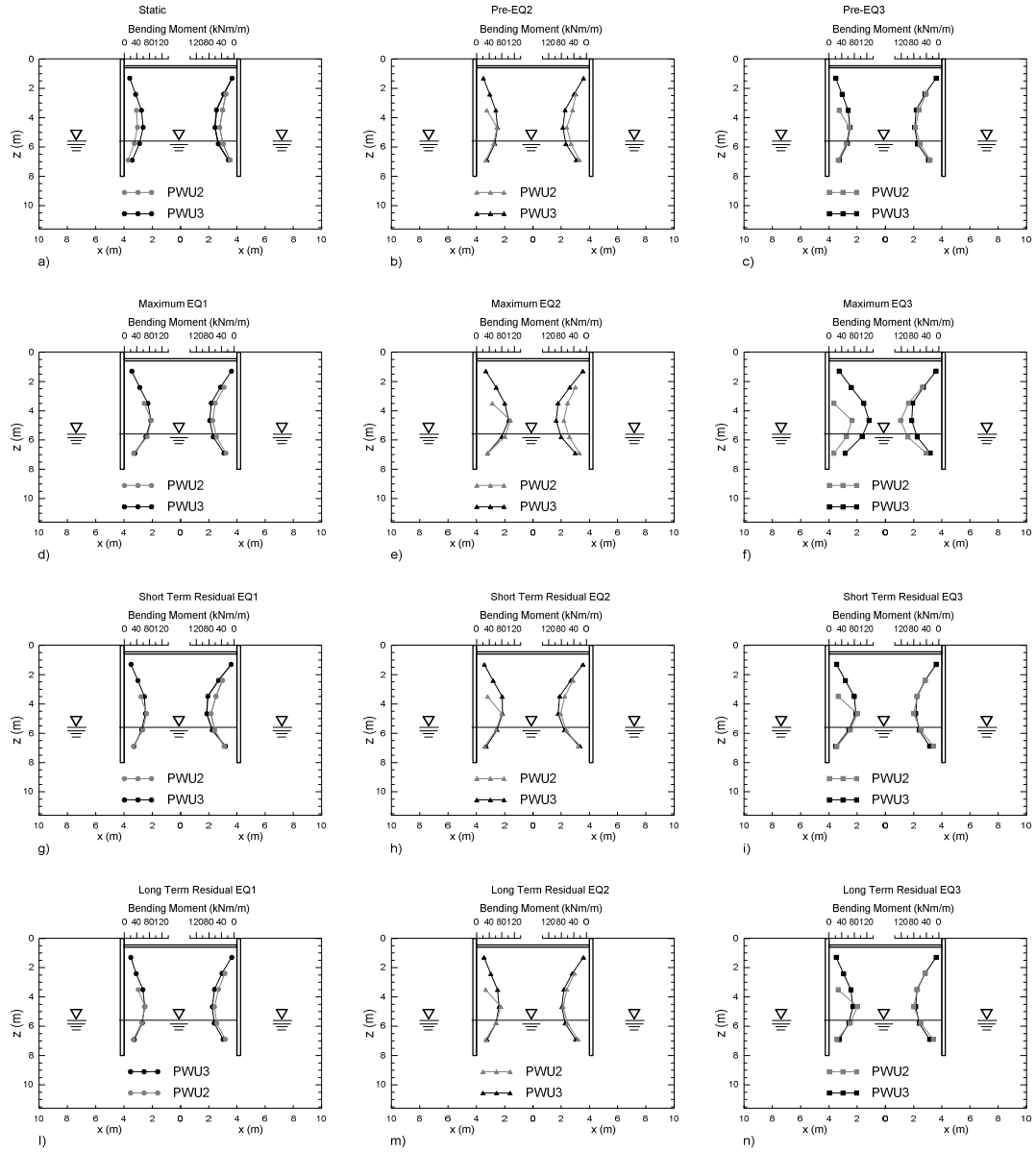

Figure 4.6: Bending moment space distribution, comparison between PWU2 and PWU3. Time instants: a) static, b) Pre-EQ3, c) Pre-EQ3, d) Maximum EQ1 (left wall), e) Maximum EQ2 (left wall) , f) Maximum EQ3 (left wall), g) Short term residual EQ1, h) Short term residual EQ2, i) Short term residual EQ3, l) Long term residual EQ1, m) Long term residual EQ2, n) Long term residual EQ3.

4.2 Amplification

It has been seen that in every model test two vertical alignments of accelerometers at the back of the left wall and at the excavated side are present. In this paragraph a more extended study of the amplification of the acceleration within the soil is presented.

In Figure 4.7 the comparison between the maximum input acceleration and the maximum top acceleration for the earthquakes of all the tests is reported. It can be observed that for the tests in loose sand (Figure 4.7(a) and (b)) the maximum top acceleration is lower than the maximum input acceleration, and that the difference increases passing from EQ1 to EQ2. For tests in dense sand, the top acceleration is about equal to the input acceleration or slightly amplified as long as the input acceleration remains lower than 0.2g a part for EQ1 of PWU2 where it is slightly less than one. If the maximum input acceleration is higher than 0.2g generally a de-amplification is observed; this does not happen for test CWU2, where for EQ3 the input acceleration reaches a maximum value higher than 0.2g and the top acceleration is about equal to 0.2g, and for test CWU4 for earthquakes EQ6 and EQ7, where the top acceleration is higher than the input acceleration when this is higher than 0.2g. These observations on the amplification of the acceleration reflect what it has already been seen in Chapter 3 through the plot of the amplification factor along the vertical. For test CWU4 a different amplification response between the earthquakes of the first flight (EQ1, EQ2 and EQ3) and the earthquakes of the second flight (EQ4, EQ5, EQ6 and EQ7) is observed. In the earthquakes of the second flight, differently with respect to the earthquakes of the first flight, a more marked amplification of the input acceleration is observed even if the entity of the maximum input acceleration is about the same and the model is the same; this is probably due to the fact that during the first flight, that is after the earthquakes EQ1, EQ2 and EQ3, the model could have experimented an increment of the relative density.

In Figure 4.8(a) the comparison between the maximum input acceleration and the maximum top acceleration is proposed again for all the tests in saturated sand and, in Figure 4.8(b), besides the data of Figure 4.8(a) also the same data relative to the tests in dry sand (Conti, 2010) are reported. It is worth noting that since the accelerometers within the models are placed close to the wall, also the acceleration

time histories relative to the tests is dry sand and considered for the comparison in Figure 4.8 are relative to accelerometers close to the wall. The acceleration in the tests in dry sand is clearly amplified. This difference in terms of amplification between the tests in saturated sand with respect the tests in dry sand is attributable to the filtering effect of the saturated layer. For the saturated tests in loose sand this effect is certainly more evident due to the strong increase of the pore pressures and correspondently the decrease of the shearing modulus.

The figures 4.7 and 4.8 are proposed again in terms of Arias intensity in Figure 4.9 and in Figure 4.10, which has been computed as follows:

$$I_a = \frac{\pi}{2g} \int_0^{\infty} [a(t)]^2 \, dt \tag{4.1}$$

where $a(t)$ represents the acceleration time history relative to the generic accelerometer of the vertical alignment.

With this representation the strong de-amplification in loose tests CWU1 and PWU1 becomes more evident, while for tests in dense sand, for a value less than 2 m/s of the Arias intensity of the input acceleration the top acceleration Arias intensity is about equal or lightly amplified while for a value higher than 2 m/s the Arias intensity is amplified (tests PWU2, CWU3, PWU3) or de-amplified (tests CWU2 and CWU4 for earthquakes EQ6 and EQ7).

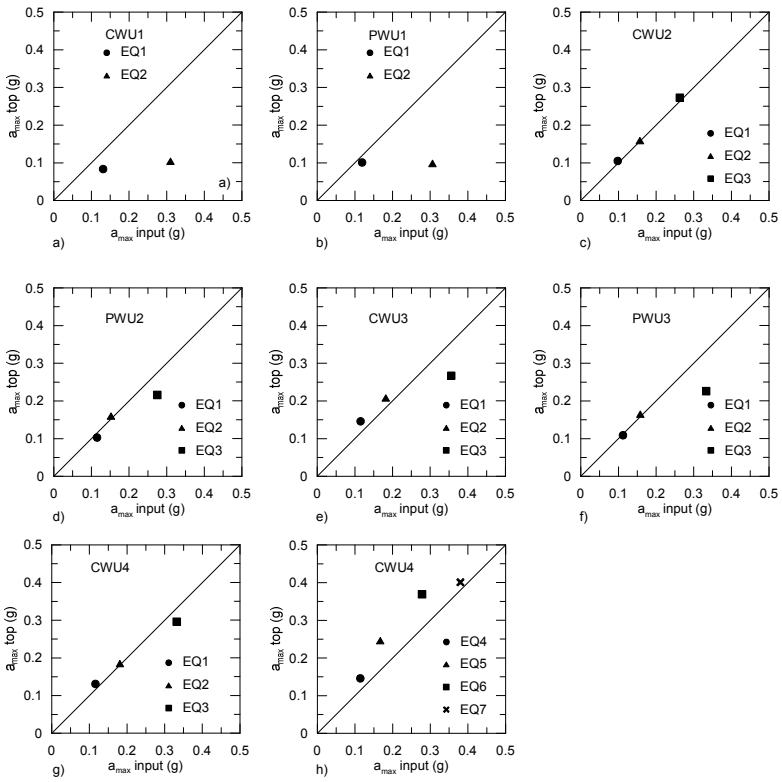

Figure 4.7: Comparison between the maximum input acceleration and the maximum top acceleration during the applied earthquakes of all the tests: a) test CWU1, b) PWU1 test, c) CWU2 test, d) PWU2 test, e) CWU3 test, f)PWU3 test, CWU4 test (EQ1, EQ2 and EQ3), h) CWU4 test (EQ4, EQ5, EQ6 and EQ7).

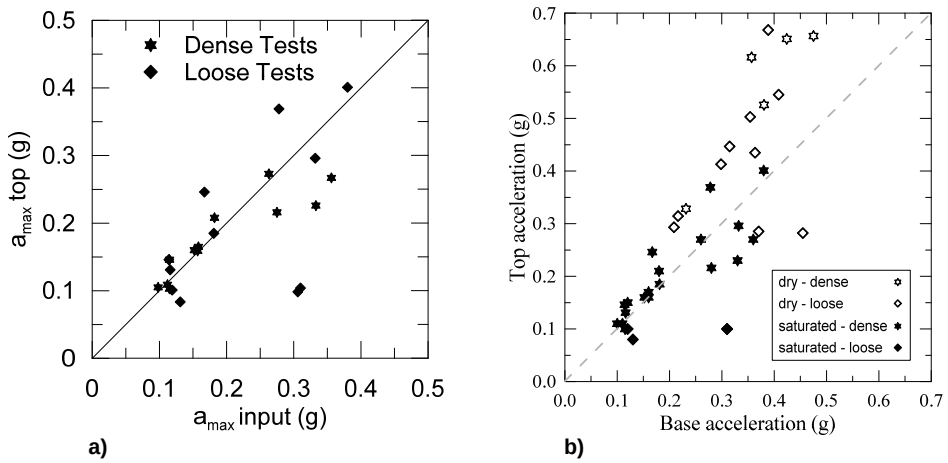

Figure 4.8: Comparison between the maximum input acceleration ad the maximum top acceleration a) for all the saturated tests and b) for the tests in saturated sand and those in dry sand (Conti, 2010).

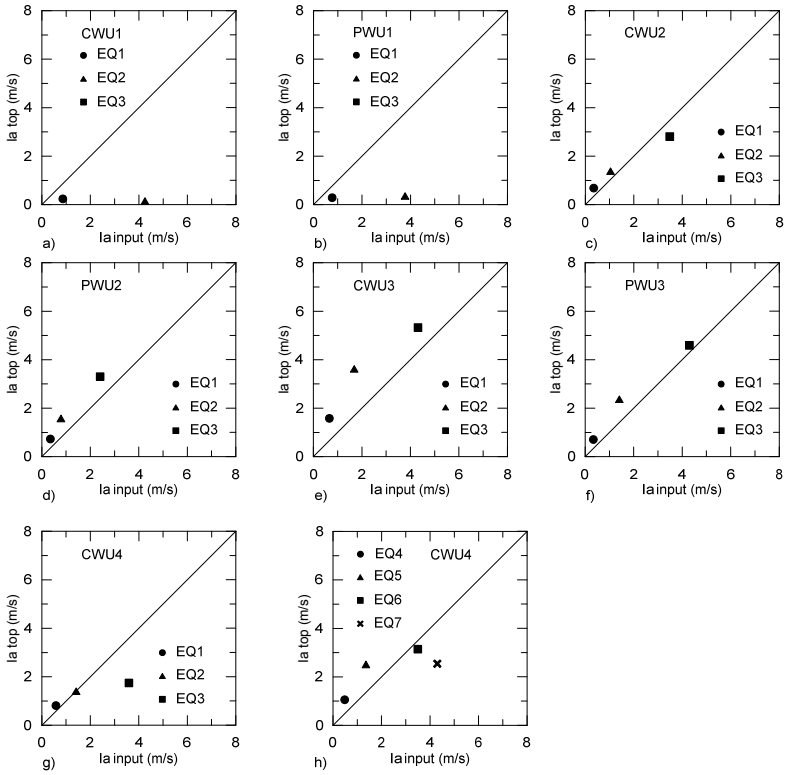

Figure 4.9: Comparison between the Arias intensity of the input acceleration and the Arias intensity of the maximum top acceleration during the applied earthquakes of all the tests: a) test CWU1, b) PWU1 test, c) CWU2 test, d) PWU2 test, e) CWU3 test, f)PWU3 test, CWU4 test (EQ1, EQ2 and EQ3), h) CWU4 test (EQ4, EQ5, EQ6 and EQ7).

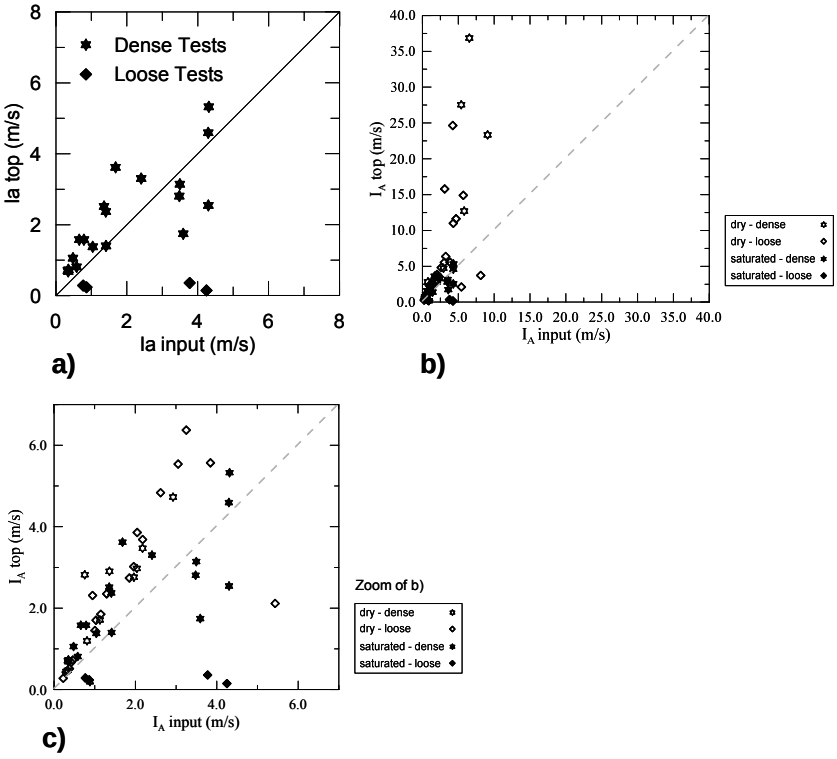

Figure 4.10: Comparison between the Arias intensity of the input acceleration and the Arias intensity for a) all the saturated tests and b) for the tests in saturated sand and those in dry sand (Conti, 2010); in c) an enlarged view of the figure in b) is proposed.

4.3 Soil Acceleration Phase Difference

In Chapter 3 the study of the phase difference of the acceleration of the soil with respect the input acceleration has been presented in the perspective of the single test and considering only one way to compute the phase difference, that is in the time domain. In Chapter 3 the exposition of all the results of the tests in terms of the different physical measured quantities for sake of completeness has been preferred. This has made the treatise of computation of the phase difference not complete, since the methodologies for such computation have not been

illustrated. In this Chapter both the methodologies to compute the phase difference during the shaking are presented, the issues regarding the application of such methodologies are illustrated and the comparison between the respective results is carried out. Moreover the comparison between all the tests will be made in order to achieve a more general conclusion about the phase difference.

4.3.1 Computation of Phase Difference in Time Domain

Considered two signals whose phase difference has to be computed, the computation of their phase difference in time domain can be performed considering one cycle of the first acceleration time history (that can be called reference acceleration time history) and selecting the time instants when the peaks of the reference acceleration take place and the time instants when the peaks of the second acceleration time history take place (see for instance Figure 4.11, where Figure 3.11 is proposed again from Chapter 3). Measuring the time lag between the first peak of the reference acceleration and the peak of the second acceleration time history and then comparing this to the time lag between two consecutive peaks of the first acceleration time history the phase difference can be finally computed. Practically the phase difference $\Delta\phi$ can be computed using the following formula:

$$\Delta\phi = 2\pi f_{inp}\Delta t \tag{4.2}$$

where δt is the time lag between the first peak of the second acceleration time history and the first peak of the reference acceleration time history and f_{inp} is the frequency of the reference acceleration time history referred to the considered cycle, that can be computed as $1/T$ (Figure 4.11).

An algorithm that performs this computation iteratively for each cycle of the reference acceleration has been implemented. In case of the tests of the present work this algorithm has been applied for all the tests considering as reference acceleration the input acceleration of the given earthquake and as second acceleration the acceleration time history recorded by the generic piezoelectric accelerometer placed within the soil. The reason of the use of the algorithm is the possibility to

computed the phase difference along the whole duration of the earthquake and also for the possibility to use it for all the tests and for all the relative earthquakes in order to perform such computation quickly.

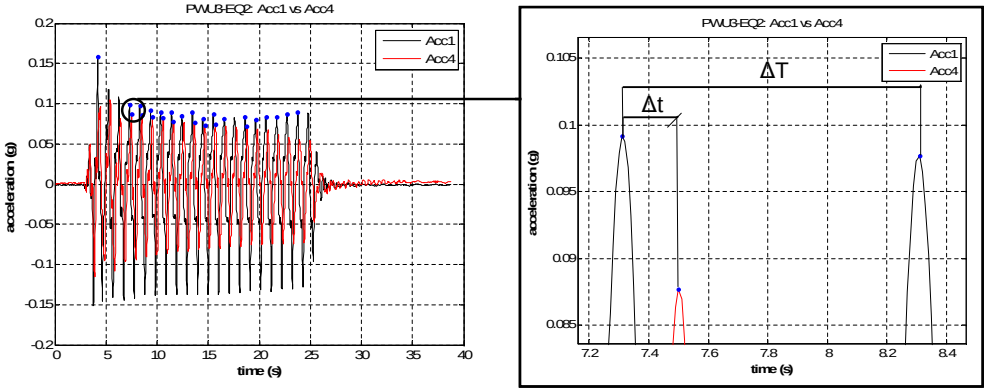

Figure 4.11: Example of the computation of the phase difference of two accelerometers during the shaking. PWU2 test, a) superposition of the accelerometers Acc1 (reference acceleration) and Acc4, b) zoom between 7.2s and 8.4s: individuation of the peaks of the reference acceleration and of the peak of the second acceleration time history.

The algorithm is described hereinafter:

(a) selection of all the peaks of the two acceleration time histories and individuation of the time instants where the peaks take place. In Fig. 4.12 the black line is the input acceleration (Acc1) while the red line is the second acceleration (Acc2) and the blue markers are the selected peaks of both the acceleration time histories;

(b) selection of one acceleration cycle of the reference acceleration;

(c) assuming that the peak of the second acceleration occurs before the occurring of the second peak of the reference acceleration (a phase difference higher than 360° is presumably hardly possible to observe in the case of the present tests) and selecting a threshold for the individuation of the peak of the second acceleration, that is that the algorithm has to select all the peaks of the acceleration that is higher than the threshold, the three consecutive peaks useful for the computation of the phase difference are individuated (Figure 4.11);

(d) the phase difference is computed through the use of the expression 4.1.

The application of this algorithm is not straightforward because the acceleration time histories could present two following problems:

(a) the peaks are not selectable (Figure 4.12 and 4.13) due to the presence of a plateau in the acceleration time history of either the input acceleration or the second acceleration;

(b) the second acceleration time history can present a double peak (or triple peak) response. This implies that the algorithm would select two intermediate (or three or even more) peaks relative to the second acceleration time history. This fact finally obligates the user to verify and eventually correct the results of the algorithm. This makes the algorithm, at this stage, non automatically applicable.

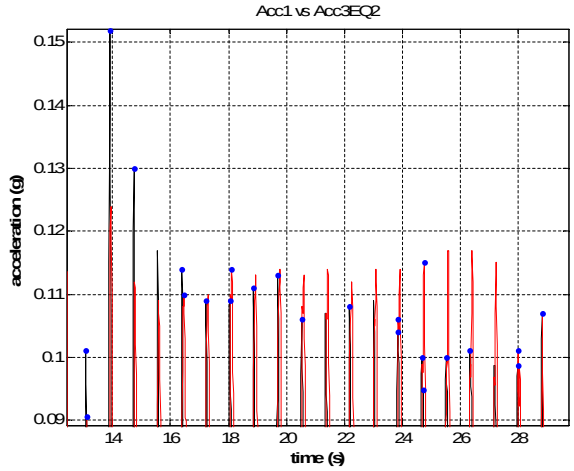

Figure 4.12: Peaks relative to Acc1 and Acc3 of test PWU2.

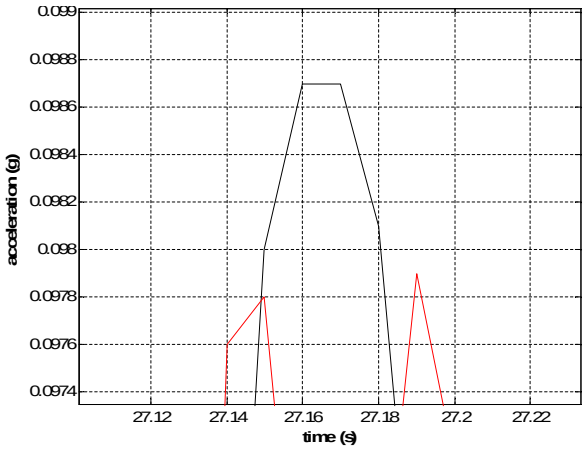

Figure 4.13: Example of non selectable peaks in the above presented acceleration time histories.

4.3.2 Computation of the phase difference in the frequency domain

The phase difference could be also computed in the frequency domain transforming the acceleration time histories in their equivalent in the frequency domain. This can be done in Matlab using the Fast Fourier Transform (FFT) algorithm which computes the Discrete Fourier Transform relative to the vector that represents the acceleration time history to be transformed in the frequency domain. More specifically the phase difference can be expressed as the imaginary part of the Cross Power Spectrum of the signals. The Cross Power spectrum of the signals can be expressed as follows:

If x and y are the signals whose Cross Power Spectrum has to be computed and $F(x)$ and $F(y)$ are the associated Fourier transforms, their Cross Power Spectrum Cxy can be computed as:

$$C(xy) = F(x) \cdot \overline{F(y)} \tag{4.3}$$

where $\overline{F(y)}$ is the complex conjugated of $F(y)$. The algorithm used in this case is described in the following points:

(a) computation of the Cross Power Spectrum of the signals, that is the product of the reference acceleration times the conjugated of the second acceleration time history. The real part of the Cross Power Spectrum is the product of the amplitudes of each frequency of the signal while the imaginary part is the searched phase difference;

(b) computation of the normalized Cross Power Spectrum by its maximum value (see for instance Figure 4.14;

(c) following Conti (2010), selection of the relevant frequencies where the phase difference is computed operating on the normalized Cross Power Spectrum. Specifically the relevant frequencies are those that correspond to a value normalized Cross Power Spectrum that is higher than a user defined threshold (0.01, 0.1, 0.5, 0.7 for instance);

(d) computation of the phase difference as the imaginary part of the Cross Power Spectrum for the selected frequencies.

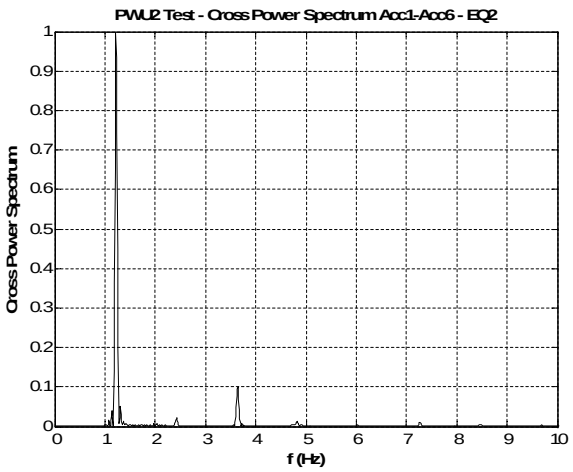

Figure 4.14: Example of normalized Cross Power Spectrum.

4.3.3 Comments on the computation of the phase difference in the time domain

(a) it has been seen that the computation of the phase difference in the time domain following the algorithm described in the paragraph 4.3.1 could present some difficulties due to the peculiar time response of the second acceleration time history. So it is worth illustrate some cases where a correction of the results has been made by the user and, once the correction has been applied, what is the effect of a double peak response of an acceleration time history on the phase difference time trend and finally if it affects the interpretation of the results. Among all the tests, PWU1 has been the test more heavily affected by this kind of response of the accelerometers. So the response of the accelerometers Acc3 during EQ2 and Acc5 during EQ1 is used in the following to show how the correction of the result of the algorithm has been made by the user and what is the final phase difference time trend. As an example, in Figure 4.15 the threshold for the individuation of the peaks of the second acceleration time history Acc3 during EQ2 of the test PWU1 has been fixed at 0.02g, and, among the selected peaks of a given cycle, the first one has been considered meaningful. For this couple of acceleration time histories only the

peak of about 0.03g and occurring at about 8s has been deleted from the final plot, that is reported in Figure 4.16. A jump in the phase difference can be observed at about 14s where it passes from 140° to about 70°. In the case of Acc5 of test PWU1, the higher peak occurs as first during the first part of the earthquake (Figure 4.17) and it occurs as second during the second part of the earthquake (Figure 4.18), this determines a jump in the phase difference for Acc5 as illustrated in Figure 4.19, where differently from Acc3 during EQ2 in Figure 4.16, the phase difference passes from about 30° to about 120°.

(b)

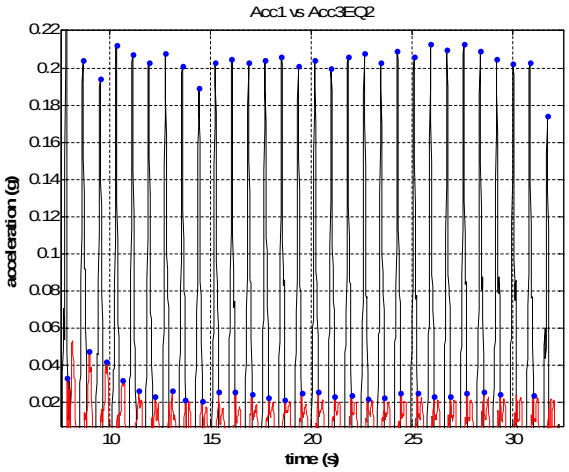

Figure 4.15: PWU1 test EQ2: example of double peak response of the second acceleration time history (Acc3), with the blue marker the selected peaks of the reference acceleration and of the second acceleration time history are highlighted with the blue marker.

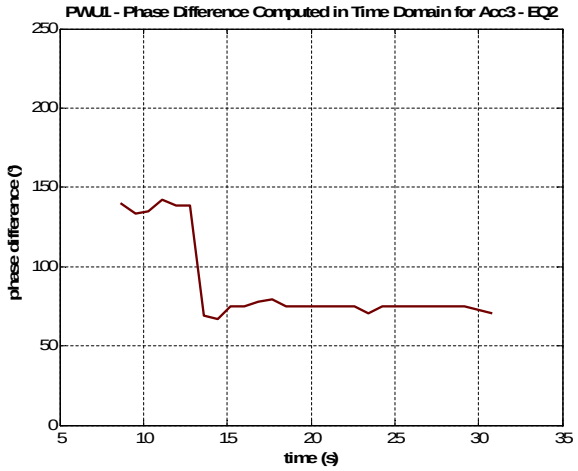

Figure 4.16: PWU1 test EQ2: resulting plot of the phase difference of Acc3 during the earthquake.

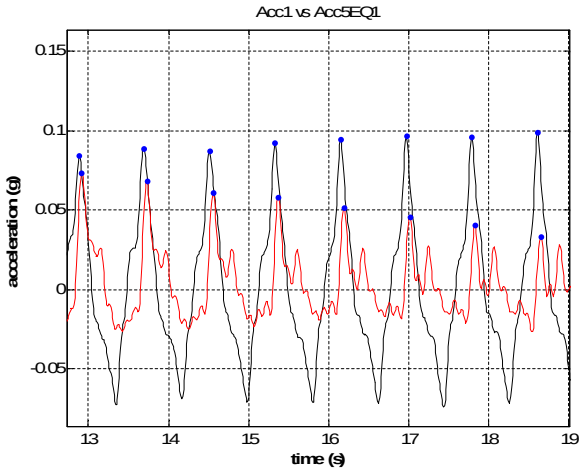

Figure 4.17: PWU1 test EQ1: double peak response of Acc5, highlight on the first part of the earthquake.

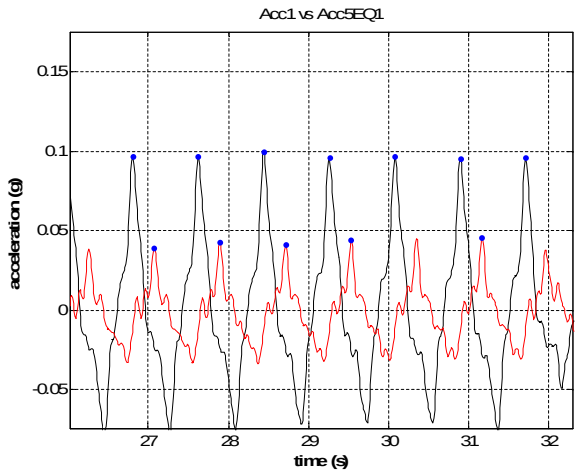

Figure 4.18: PWU1 test EQ1: double peak response of Acc5, highlight on the second part of the earthquake.

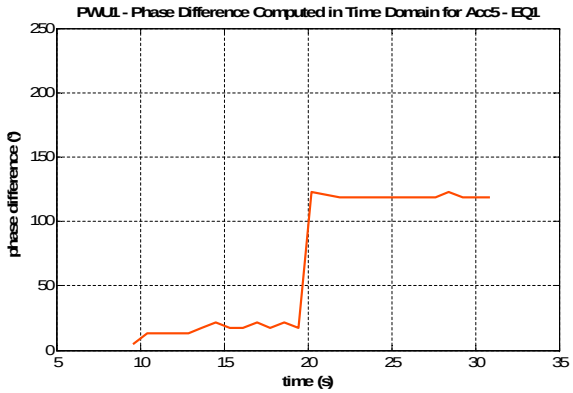

Figure 4.19: PWU1 test - EQ1: phase difference of Acc5 computed in time domain, jump on the computed phase difference due to the double peak response of Acc5.

However, as it has been seen in Chapter 3, the most significant and

problematic feature of the phase difference of the accelerometers of test PWU1 is that the accelerometers placed below the water table present a phase difference that is higher than the phase difference of the accelerometers placed above the water table, which of course is non acceptable from a physical viewpoint. This can be actually related not only to the effect of the liquefaction on the signals of the accelerometers, but also to the displacement of the bottom of the wall that determines a delay on the signal of the accelerometers Acc3, Acc6 and Acc7.

Also in test CWU2, for the earthquakes EQ1 and EQ3 the influence of the double peak response can be observed in the phase difference of Acc6 (Figure 4.20 and Figure 4.21), but it is not so important as in PWU1.

A part from test CWU2, which has been discussed above, for all the other tests there is not a significant influence of the double peak response on the time trend of the phase difference; while on test PWU1 the influence of the double peak response and the displacement of the wall is such that computation of the phase difference and its comparison among all the accelerometers conducts non significant results from the physical viewpoint.

Concluding this small paragraph, it can be said that, among all the tests performed, only for test PWU1 the modification on the signals is such that the phase difference cannot be computed with sufficient accuracy in order to extract a general conclusion about the dynamic behaviour of the models, but all the accelerometers of all the remaining tests have been found not to be significantly affected by the response of the soil and the movement of the wall so that the computation of the phase difference has brought to results that are acceptable from the physical viewpoint and that can be compared between the tests in order to obtain a general conclusion on the behaviour of the models during the tests in terms of the amplification phenomenon and the phase difference between the accelerometers.

8. In Chapter 3 it has been stated that, for tests CWU1, CWU2 and PWU2 the phase difference of the soil below the excavation level is not significant (about or less than 50°), while the phase difference of the soil above the excavation level is significant (from 80° to 150° or higher). Here also the phase difference relative to tests CWU3 and PWU3 are presented in order to confirm what has been concluded for

the tests CWU1, CWU2 and PWU2. In the Figure 4.22, Figure 4.23 and Figure 4.24 the phase difference computed in time domain for the test CWU3 and for EQ1, EQ2 and EQ3 is reported. In EQ1 it can be observed that Acc6, which is placed at the top of the model, present a phase difference about 100° for all the duration of the earthquake a part from the beginning where it is lower than 50°; all the others acceleration time histories present a phase difference lower or about 50° confirming what has been found for the tests CWU1, CWU2 and PWU2. The results relative to EQ2 and EQ3 reported in Figure 4.23 and in Figure 4.24 are affected by the significant presence of the plateau illustrated in Figure 4.13 in the acceleration time histories, so that only Acc5, Acc6 and Acc8 have been plotted in EQ2 and Acc4, Acc5 and Acc6 have been plotted in EQ3 as results of the application of the described algorithm. Anyway again Acc6 presents phase difference higher than 100° in EQ2 and about 130° in EQ3. As regards Acc5, which is placed below and close to the excavation level, presents a phase difference lower than 50° in EQ2 while it is about 100° in EQ3. In this case a phase difference significantly higher than 50° is observed even if the accelerometer is placed below the excavation level; this is likely due to the double effect of the increment of the relative density of the soil subsequent the previous earthquakes and to the higher peak input acceleration, which of for EQ3 is 0.22g. Acc4 and Acc8, which belong to the portion of soil below the excavation level as well, present always a phase difference lower than 60°.

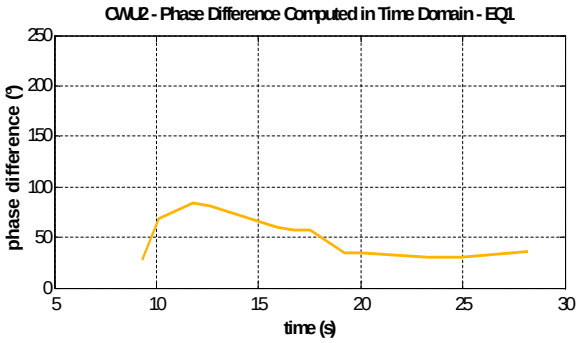

Figure 4.20: Test CWU2 EQ1: phase difference of Acc5 during EQ3, jump of the time trend.

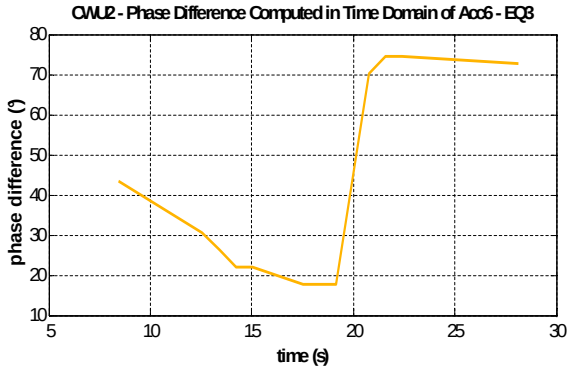

Figure 4.21: Test CWU2 EQ3: phase difference of Acc5 during EQ3, jump of the time trend.

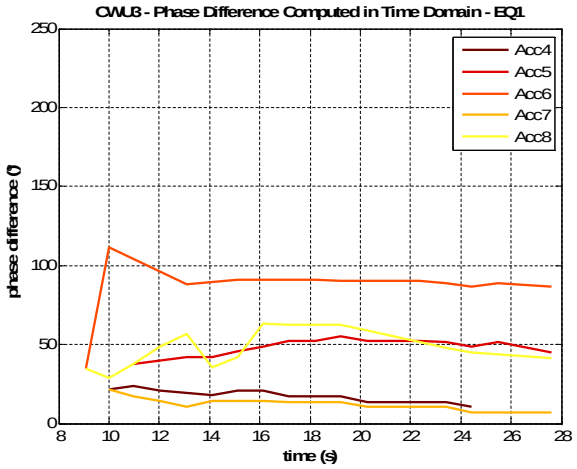

Figure 4.22: Test CWU3 EQ1: phase difference in the time domain.

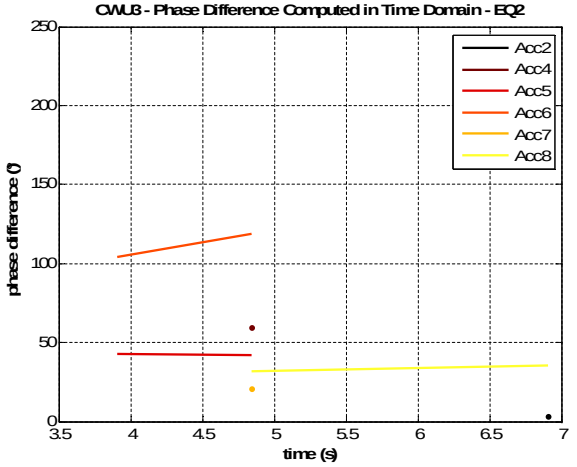

Figure 4.23: Test CWU3 EQ2: phase difference in the time domain.

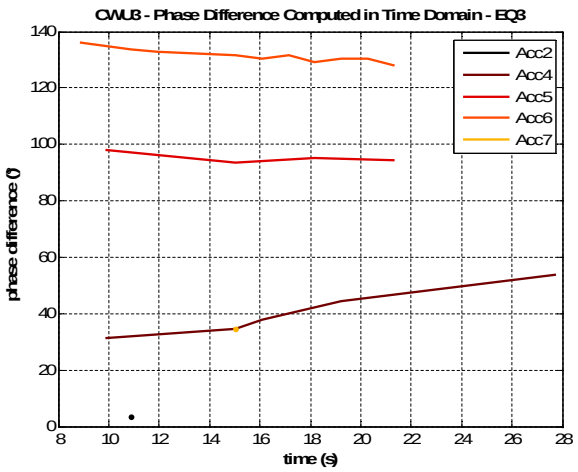

Figure 4.24: Test CWU3 EQ3: phase difference in the time domain.

In Figure 4.25, Figure 4.26 and in Figure 4.27 the phase difference for the test PWU3 computed in the time domain is reported. It is easy to realize that the accelerometers Acc3, Acc4, Acc7 and Acc8, which are placed below the excavation level present a phase difference always below 50°, while the phase difference of the accelerometers Acc5 and Acc6, which are placed above the excavation level, is included between 70° and 100° for EQ1 and it increases passing to EQ2 and EQ3 where it reaches values included between 120° and 150° approximately.

With these last considerations on the tests CWU3 and PWU3, besides the results presented in the Chapter 3 it can be concluded that for all the tests, excepted for PWU1, the soil below the excavation level present phase not significantly far from the input acceleration, while the soil above the excavation level is considerably out of sync with respect the input acceleration.

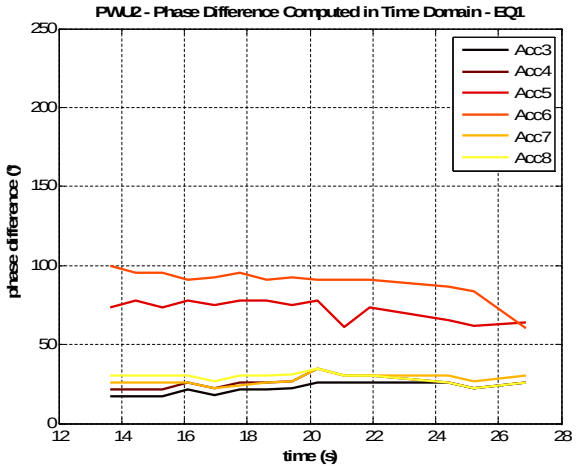

Figure 4.25: Test PWU2 EQ1: phase difference computed in time domain.

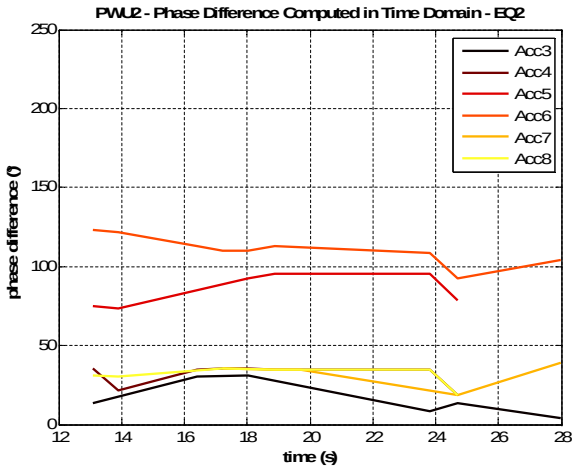

Figure 4.26: Test PWU2 EQ2: phase difference computed in time domain.

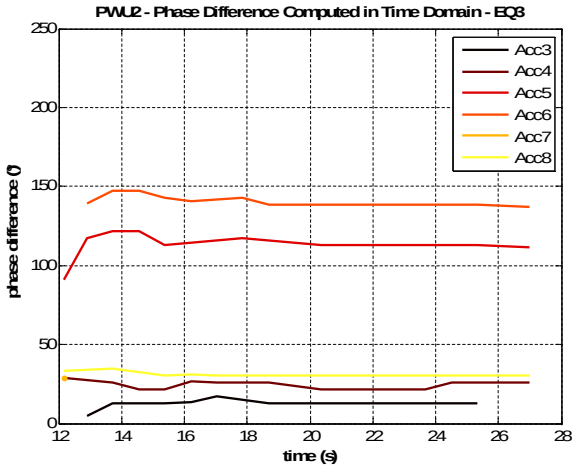

Figure 4.27: Test PWU2 EQ3: phase difference computed in time domain.

4.3.4 Comparison between the computation of the phase difference in the time domain and in the frequency domain

In the previous paragraphs it has been concluded that:

1. the phase difference in the test PWU1 is strongly influenced by the increase of the pore pressure of the soil and consequently by the decrease of the shear stiffness and of the shear resistance;

2. for all the other tests the soil below the excavation level is in sync with respect to the input acceleration and the soil above the excavation level is out of sync the input acceleration.

In this paragraph it is briefly discussed the comparison between the results obtained in the time domain with the results obtained in the frequency domain.

The computation of the phase difference in the frequency domain gives good agreement with the computation of the phase difference in the time domain for tests where the signals are more simple, that is for the dense tests, excepted for CWU2.

The results regarding the phase difference computed in the frequency domain are presented as plots where on the y-axis there is the phase difference

expressed in degrees and on the x-axis there is the frequency. The x-axis has been cut up to a frequency of 4 Hz and all the comments refer to the values of the phase difference corresponding to frequencies close to 1,25 Hz, which is for all the tests the dominant frequency of the input signal. Also the results are, for a given test, reported distinguishing the accelerometers at the active side and the accelerometers at the passive side since it would have been more complicated to present all the data on a single plot.

For instance in Figure 4.28 and in Figure 4.29 the phase difference computed in frequency domain for the test CWU1 is reported. Acc5 (Figure 4.28) has a phase difference of about 150°, which is in agreement with its computation in the time domain (Figure 4.30), while the phase difference of all the others (Acc2, Acc3, Acc4 and Acc6) is collocated at about 50°, excepted for Acc4 that presents also values of the phase difference between 50° and 100°. This is not in agreement with the fact that Acc3, Acc4, Acc6 and Acc7 present in the time domain (Figure 4.30) a phase difference that is less than 50°. As said before, this disagreement can be attributed to the fact that the acceleration time histories, for a test like CWU1, which is performed in saturated loose sand, present a complicated trend. Also for Acc7, whose phase difference computation is reported in Figure 4.29, it can be seen that the phase difference computed in the frequency domain gives values included between 50° and 100° while the computation in the time domain gives values lower than 50°.

Differently with respect to CWU1, for CWU3 the phase difference computed in the frequency domain (Figure 4.31 and Figure 4.32) is close to the phase difference computed in time domain (Figure 4.33). In fact Acc6 in Figure 4.31 has a phase difference of about 100°, as well as in Figure 4.33; Acc5 phase difference is about 50° (Figure 4.31), as well as in Figure 4.33, and Acc3 and Acc4 (Figure 4.31) has a phase difference of about 30° as in Figure 4.33; Acc7 and Acc8 have a phase difference in Figure 4.32 of about 50° and 30° as well as in Figure 4.33.

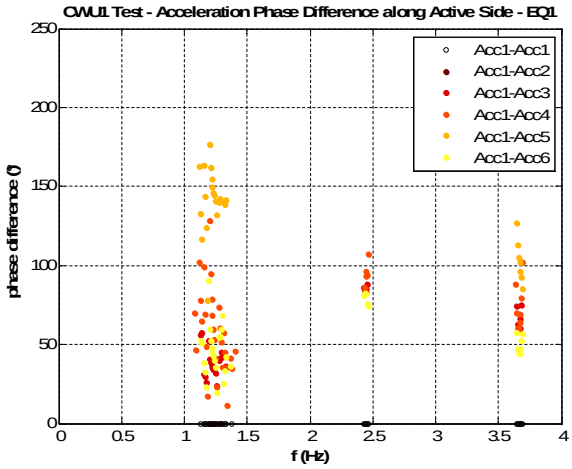

Figure 4.28: Test CWU1 EQ1 active side: phase difference computed in the frequency domain.

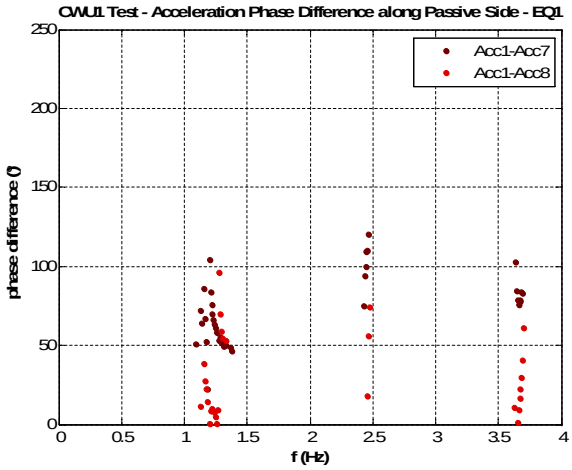

Figure 4.29: Test CWU1 EQ1 passive side: phase difference computed in the frequency domain.

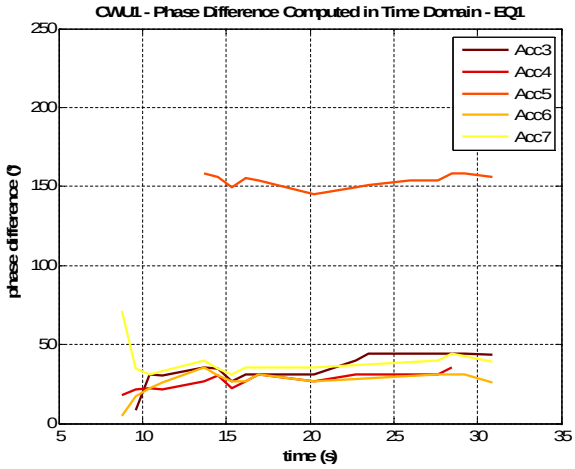

Figure 4.30: Test CWU1 - EQ1: phase difference computed in time domain.

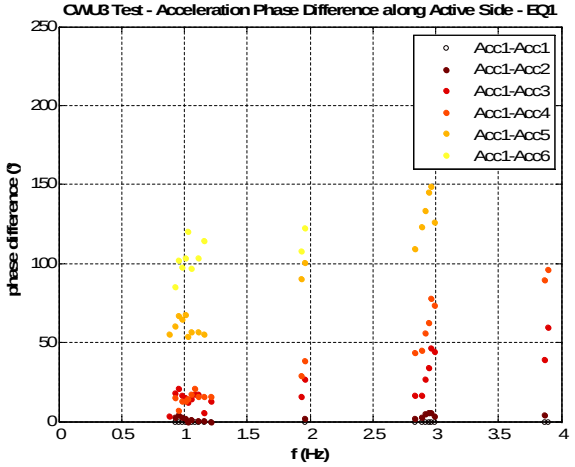

Figure 4.31: Test CWU3 - EQ1 active side: phase difference computed in frequency domain.

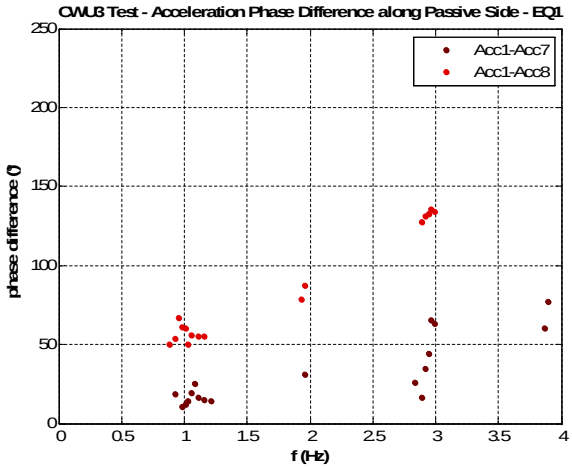

Figure 4.32: Test CWU3 - EQ1 passive side: phase difference computed in frequency domain.

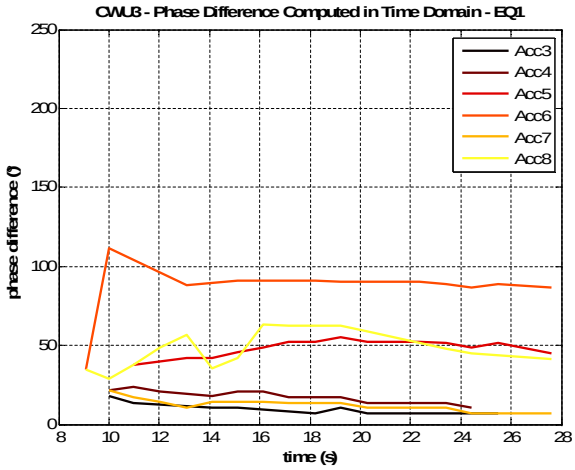

Figure 4.33: Test CWU3 - EQ1: phase difference computed in time domain.

4.3.5 Comparison of phase difference with test in dry sand (Conti, 2010).

The tests performed in dry sand (Conti, 2010) have shown that in both the geometries with cantilever walls and propped walls the soil is in sync with the input acceleration. This is visible in Figure 4.34 and in Figure 4.35 , where there are the layout of test CW1 and the acceleration time histories of the accelerometers A4, A5 and A6, as well as in Figure 4.36 and in Figure 4.37, where there are the layout of test PW1 and the acceleration time histories of the accelerometers A4, A5 and A6. In the perspective of the phase difference of the acceleration within the soil a relevant conclusion can be reached that is that the saturated soil determines a significant increase of the phase difference between the input acceleration and the acceleration at the top of the soil.

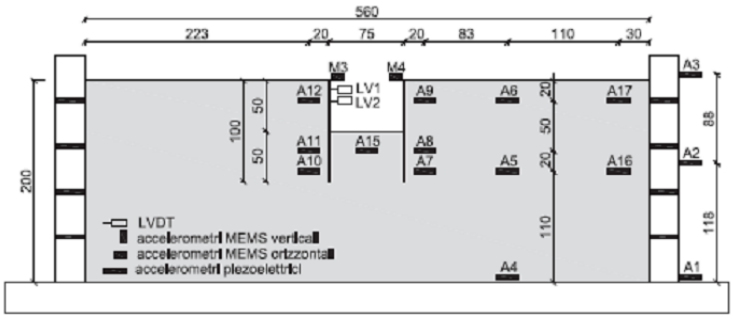

Figure 4.34: Layout of test CW1 relative to the tests performed in dry sand (Conti, 2010).

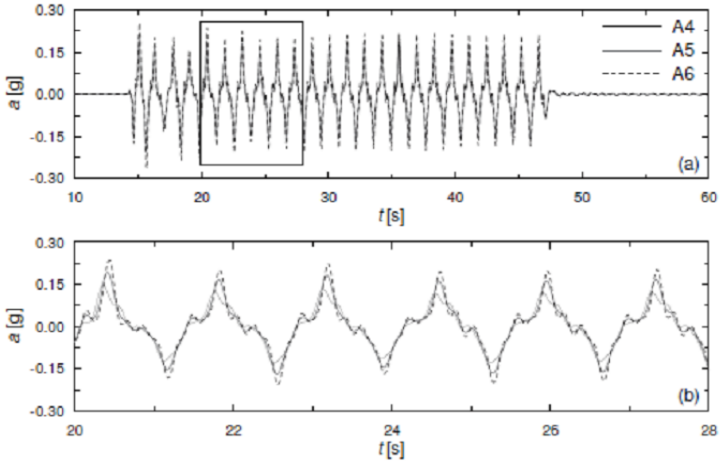

Figure 4.35: Acceleration time histories of accelerometers A4, A5 and A6 of test CW1 (Conti, 2010).

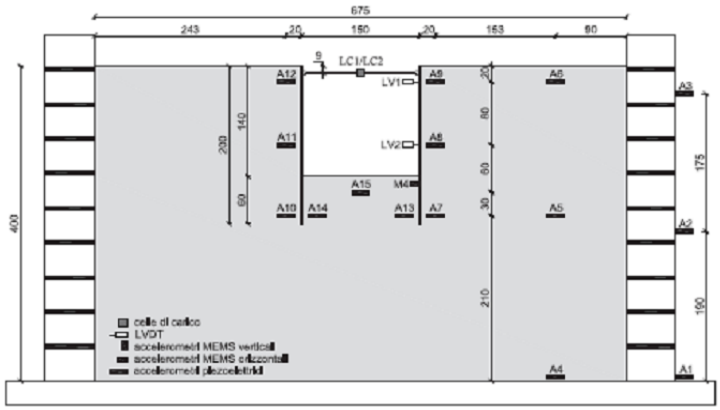

Figure 4.36: Layout of test PW1 relative to the tests in dry sand (Conti, 2010).

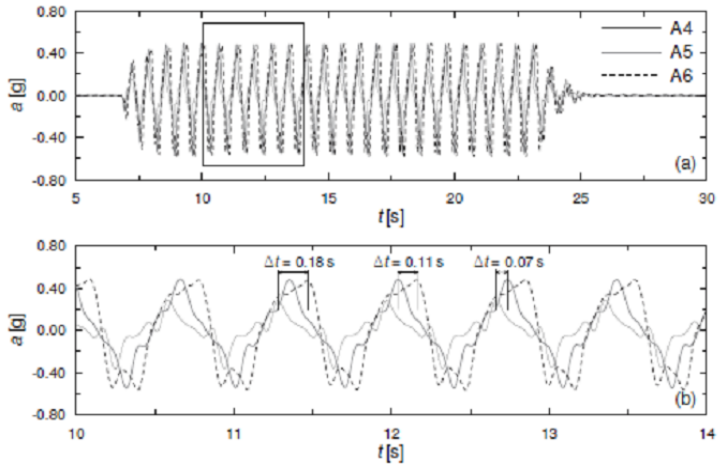

Figure 4.37: Acceleration time histories relative to the accelerometers A4, A5 and A6 of test PW1.

4.4 Displacements: Comparison with Tests in Dry Sand

In Chapter 3 the collapse mechanisms of the walls have been highlighted and the entity of the accumulated displacements at the top, for cantilever tests, has been compared, as well as the entity of the accumulated displacements at the bottom of the propped walls has been compared; it has been shown that the accumulated displacements are higher for tests in loose sand with respect the tests in dense sand and moreover that, in case of test CWU1 the collapse mechanism is no longer only a rotation with an approach of the tops of the walls but a counter-rotation occurs when the equilibrium of the structure in not guaranteed by the resistance of the soil at the passive side due the increase of pore pressures.

In this paragraph the entity of the accumulated displacements in compared with the accumulated displacements in dry tests (Conti, 2010). As reference for tests on cantilever walls the test CW1 among the tests performed in dry sand as been chosen, while test PW2 has been chosen as dry test reference. It has been seen in Chapter 3 that the final accumulated displacement at the top of the cantilever walls is 300 mm for both tests CWU1 and CWU2, while for the dry test CW1 it is 90 mm (Figure 4.38) which has been performed with the sand reconstituted at high relative density (D_r = 84%); while the final accumulated displacement at the bottom

of the propped tests PWU1 and PWU2 is 206 mm and 184 mm and the correspondent accumulated displacement at the bottom of the right wall if test PW2 is 100 mm, which has been performed with sand reconstituted at low relative density ($D_r = 42\%$). So in both the comparisons it is clear that the accumulated displacement in saturated tests, for a given typology of structure, is higher than the accumulated displacement in dry tests. Also the number of earthquakes in the case of dry tests is higher than the number of earthquakes of saturated tests, that are respectively 5 for dry tests and 3 or 2 in saturated tests, which further indicates that there is less accumulation of displacement for tests in dry sand with respect tests in saturated sand. In Table 4.1 there are the reported accumulated displacement at the top of the cantilever walls, for both tests in saturated sand and tests in dry sand.

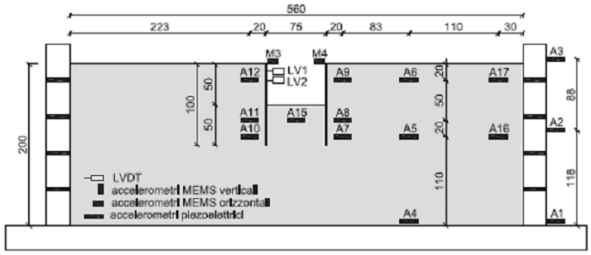

Figure 4.38: Layout of test dry CW1 (Conti. 2010).

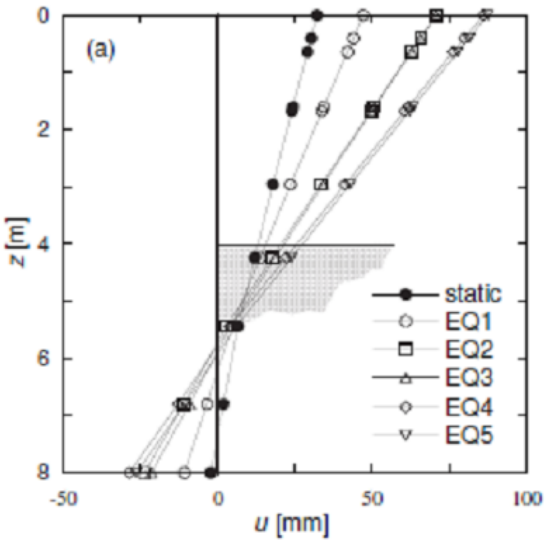

Figure 4.39: Test CW1: horizontal displacements of the left wall from the end of the swing up to EQ5 (Conti, 2010).

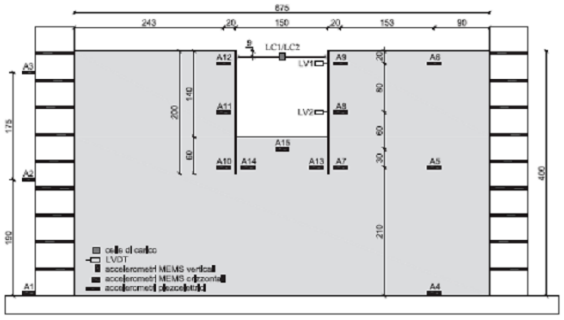

Figure 4.40: Layout of dry test PW2 (Conti, 2010).

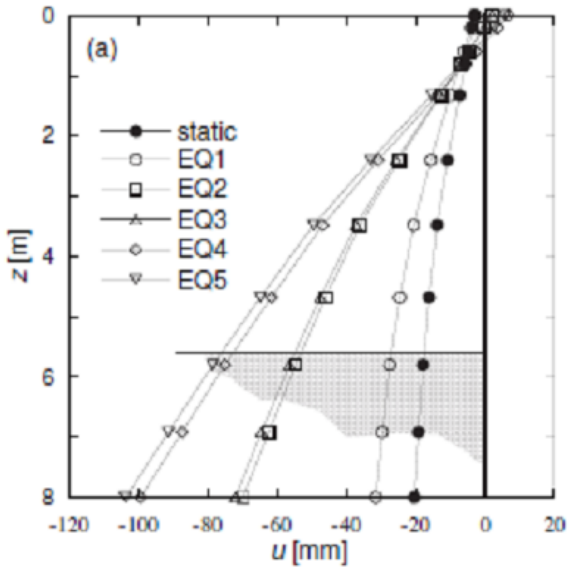

Figure 4.41: Test PW2: horizontal displacements of the right wall from the end of the swing up to EQ5 (Conti, 2010).

		Top Displ. (mm)	Bottom Displ. (mm)
Cantilever walls - saturated sand	CWU1	300	/
	CWU2	300	/
Cantilever walls - dry sand (Conti, 2010)	CW1	90	/
Propped walls - saturated sand	PWU1	/	206
	PWU2	/	184
Propped walls - dry sand (Conti, 2010)	PW2	/	100
		/	100

Table 4.1: Comparison between the tests in saturated sand and the tests in dry sand (Conti, 2010) of the accumulated displacement at the top of the cantilever walls and at the bottom of the propped walls.

4.5 Bending Moments: Comparison with Limit Equilibrium Analysis

The static and pre-earthquake bending moment distributions for all the tests have been compared with the previsions given by a pseudostatic analysis realized with different contact stress distributions. The contact stress has been computed using the Mononobe-Okabe expression (Okabe, 1926; Mononobe and Matsuo, 1929) for the active side and the Lancellotta (2007) expression for the passive side; the horizontal acceleration that appears within the expressions of the seismic coefficient has been considered equal to zero.

The reason why different contact stress distributions have been used is that the possible influencing factors on the measured bending moment distribution are i) the dependency of the angle of shearing resistance on the relative density and on the mean effective stress, ii) the arise of the capillary suction above the head of the porous fluid that tends to decrease the contact stress at the active side, iii) the progressive mobilization of passive resistance. Consequently, in the following the computation of the bending moment with four possible contact stress distributions is illustrated in its equilibrium equations at the limit equilibrium of the soil-structure system where the first one is a limit equilibrium analysis with linear vertical distribution of the horizontal pressure and the three following ones introduce the dependency of the angle of shearing resistance on the relative density and on the mean effective stress, the influence of the capillary suction and influence of the progressive mobilization of the passive resistance as said above.

As regards the influence of the capillary suction on the bending moment, for all the centrifuge tests performed, during the saturation of the model, the arise of the capillary suction within the soil and above the water table has been observed, as confirmed by the presence of water at the sand surface immediately after the saturation (Figure 4.41). The study of the influence of the capillary suction on the bending moment has been suggested by the values of the bending moment along the walls that have been seen to be lower than what a limit equilibrium analysis with the active coefficient for the horizontal pressure from the Okabe (1926) and Mononobe and Matsuo (1929) theory and with the passive coefficient for the horizontal pressure from the solution of Lancellotta (2007) has suggested. Specifically the bending moment predicted with the limit equilibrium analysis at the walls section correspondent to the excavation level is higher than the measured one, even if the value of the bending moment at the considered section of

the wall depends only on the horizontal pressure acting on the wall whose value is generally well predicted using the active coefficient for the horizontal pressure.

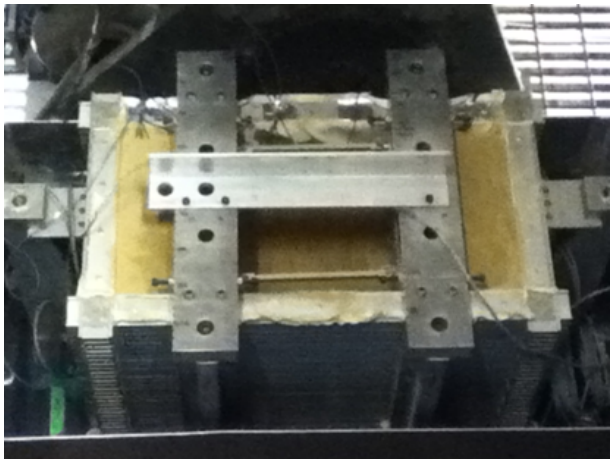

Figure 4.42: CWU1 test: the rise of the capillary suction up to the soil surface can be observed from the top view of the model before the beginning of the test.

During the swing up of the model instead, the increasing of the centrifuge acceleration causes a decrease of the capillary rise. So, the soil present above the water table is partially saturated during the centrifuge test and it is subjected to a wetting cycle during the saturation and to a drying cycle during the swing up. In order to take into account the behaviour of the soil in partially saturated conditions, the water retention curve of the soil has been determined. The water retention curve of the Leighton Buzzard Sand is reported in Figure 4.43 and in Figure 4.44 with respect two different values of the relative density. The water retention curve has been determined through the use of the Tempe Cells applying increasing suction values and calculating the corresponding degree of saturation. The details of the experimental procedure and equipment for the determination of the water retention curve are reported in Appendix B.

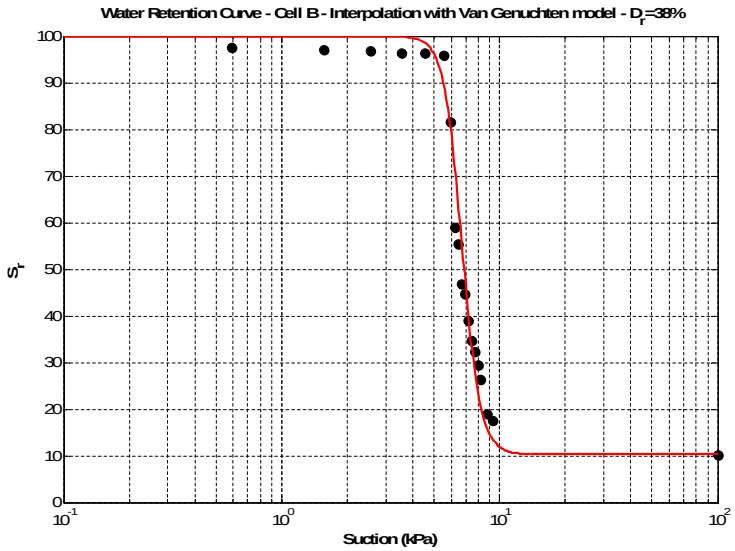

Figure 4.43: Leighton Buzzard sand water retention curve for loose sample and interpolation with the Van Genuchten model.

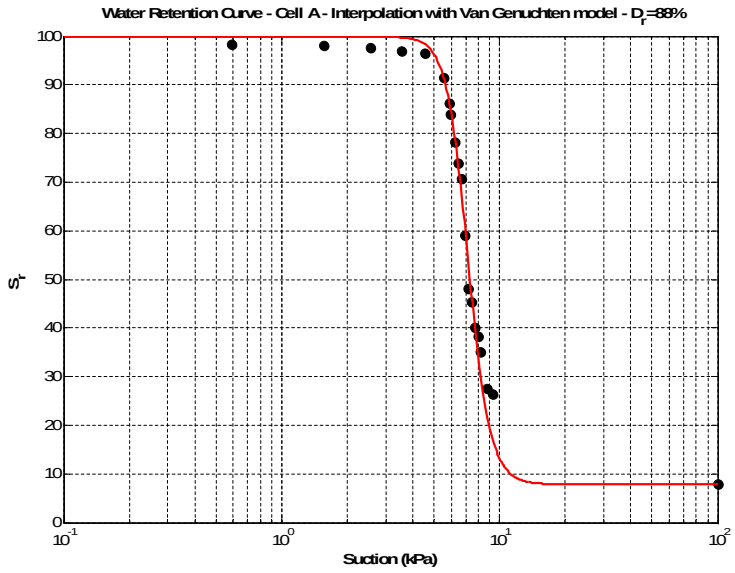

Figure 4.44: Leighton Buzzard sand water retention curve for dense sample and interpolation with the Van Genuchten model.

The possible contact stress distributions with the corresponding forces and equilibrium equations at the limit equilibrium condition are described below in four cases:

1. limit equilibrium analysis with linear distribution of the active and passive earth pressure (Figure 4.45). In the case of test in loose sand the considered angle of shearing resistance is the angle at the critical state, while the angle of shearing resistance in dense test is the peak angle of shearing resistance. The safety factor and the position of the center of rotation represent the unknowns of the equilibrium equations that are the translational equilibrium and the rotational equilibrium around the center of rotation. The forces that are considered into the equilibrium equations are represented in Figure 4.45. S_{a1}, S_{a2} and S_{a3} are the active forces above the center of rotation; S_{p1} is the passive force above the center of rotation; S_{p2} and S_{p3} are the passive force below the center of rotation; S_{a4} and S_{a5} are the active forces below the center of rotation. The equilibrium equations and the expressions of the forces at the limit equilibrium condition are reported hereinafter:

   (a) translational equilibrium: $S_{a1} + S_{a2} + S_{a3} + S_{p2} + S_{p3} - S_{p1} - S_{a4} - S_{a5)=0}$;

   (b) rotational equilibrium around the center of rotation: $S_{a1} \cdot y_{a1} + S_{a2} \cdot y_{a2} + S_{a3} \cdot y_{a3} + S_{p2} \cdot y_{p2} + S_{p3} \cdot y_{p3} - S_{p1} \cdot y_{p1} - S_{a4} \cdot y_{a4} - S_{a5} \cdot y_{a5}) = 0$ where $ya1$, $ya2$, $ya3$, $ya4$, $ya5$, $yp1$, $yp2$ and $yp3$ are the distance of the point of application of the forces $Sa1$, $Sa2$, $Sa3$, $Sa4$, $Sa5$, $Sp1$, $Sp2$ and $Sp3$ respectively from the center of rotation of the wall (Figure 4.45).;

   The expression of the forces considered in the equilibrium equations are:

   (a) $S_{a1} = \frac{1}{2} \cdot \gamma_d \cdot K_{ae} \cdot H^2$

   (b) $S_{a2} = \gamma_d \cdot H \cdot (x - H) \cdot K_{ae}$

   (c) $S_{a3} = \frac{1}{2} \cdot \gamma' \cdot K_{ae} \cdot (x - H)^2$

   (d) $S_{a4} = \gamma' \cdot K_{ae} \cdot (x - H) \cdot (L - x)$

   (e) $S_{a1} = \frac{1}{2} \cdot \gamma' \cdot K_{ae} \cdot (L - x)^2$

   (f) $S_{p1} = \frac{1}{2} \cdot \gamma' \cdot K_{pe} \cdot \frac{(x-H)^2}{SF}$

   (g) $S_{p2} = (\gamma_d \cdot H + \gamma' \cdot (x - H)) \cdot K_{pe} \cdot \frac{(L-x)}{SF}$

(h) $S_{p3} = \frac{1}{2} \cdot \gamma'(L-x) \cdot K_{pe} \cdot \frac{(L-x)}{SF}$

where γ_d is the dry unit weight of the soil, γ' is the effective weight of the soil, K_{ae} is the seismic active coefficient, K_{pe} is the seismic passive coefficient, H is the retained height, L is the height of the wall, SF is the safety factor.

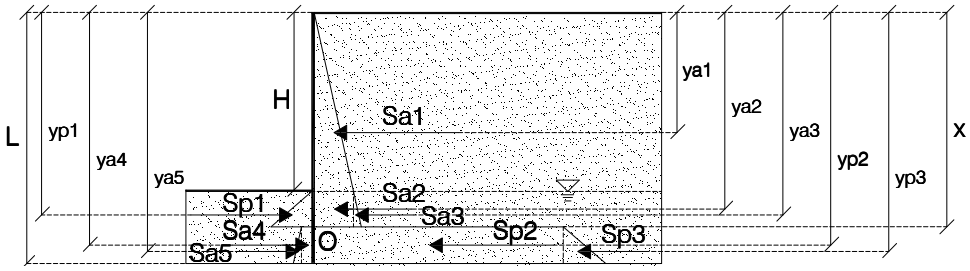

Figure 4.45: Earth pressure distribution used in the first method with linear distribution of active and passive side to predict the bending moment distribution for the cantilevered tests.

2. limit equilibrium analysis with the angle of shearing resistance depending on the effective mean stress p' and on the relative density D_r through the relation proposed by Bolton (1986): $\varphi' = \varphi'_{cv} + 5 \cdot D_r \cdot (10 - \ln p') - 1$ where φ_{cv} is 32° (angle of shearing resistance at critical state, Visone, Santucci de Magistris, 2009). The computation of the bending moment in this case is similar to the case at point 1. (Figure 4.45) but the distribution of the horizontal earth pressure is no more linear because it depends on the value of the angle of shear-

ing resistance through the seismic coefficients K_{ae} and K_{pe}. More specifically, at each depth, the mean effective stress p' is calculated as $\frac{1}{3} \cdot \gamma_d z \cdot (1 + 2K_0)$, where $k_0 = 1 - \sin(\varphi'_{cv})$.

3. limit equilibrium analyses taking into account the influence of the capillary suction above the water table. The reference scheme in this case is equal to that one reported in Figure 4.46 but the active force S_{a1} is computed differently. Considered the capillary suction arising up to the soil surface, the unit weight of the soil is computed considering the dependence on the degree of saturation Sr which in turn depends on the depth through the water retention curve of the material. The expression used to compute the unit weight of the material above the water table is the following: $\gamma(z) = (1 - n) \cdot \gamma_w \cdot G_s + \gamma_w \cdot S_r(z) \cdot n$, where n is the porosity of the material, G_s is the specific weight of the soil and the degree of saturation S_r depends on the depth z through the water retention curve represented by a function S_r of the suction. For a given depth $0 < z* < H$ the effective vertical stress σ'_v is computed as $\sigma'_v(z) = \int_0^z *\gamma(z)dz$ and the effective horizontal stress σ'_h is computed as $\sigma'_h(z) =_{ae} \cdot\sigma'_v(z) + S_r(z) \cdot (-\gamma_w \cdot (H - z)) \cdot (1 - K_{ae})$.

4. limit equilibrium analysis with linear distribution of the active earth pressure and bilinear distribution of the passive earth pressure (Figure 4.46). The unknowns of the equilibrium equation are the depth $x1$ where the slope of the passive earth distribution changes and $x2$ that is the depth of the center of rotation of the wall. The forces that are considered into the equilibrium equations are represented in Figure 4.47. S_{a1}, S_{a2} and S_{a3} are the active forces above the center of rotation; S_{p1}, S_{p2} and S_{p3} are the passive forces acting above the center of rotation; S_{a4} and S_{a5} are the active forces below the center or rotation; S_{p4} and S_{p5} are the passive forces below the center of rotation. The equilibrium equations are:

   (a) translational equilibrium: S_{a1}+S_{a2}+S_{a3}+S_{p2}+S_{p3}-S_{p1}-S_{a4}-S_{a5}

   (b) rotational equilibrium around the center of rotation: $S_{a1} \cdot \mathrm{y}_{a1}$+$\mathrm{S}_{a2}$· y_{a2}+$S_{a3} \cdot y_{a3}$+$S_{p2} \cdot y_{p2}$+$S_{p3} \cdot y_{p3}$-$S_{p1} \cdot y_{p1}$-S_{a4} ·y_{a4}−$\mathrm{S}_{a5} \cdot y_{a5}$

   where y_{a1}, y_{a2}, y_{a3}, y_{a4}, y_{a5}, y_{p1}, y_{p2}, y_{p3}, y_{p4} and y_{p5} are the distances of the point of application of the forces S_{a1}, S_{a2}, S_{a3}, S_{a4}, S_{a5}, S_{p1}, S_{p2}, S_{p3}, S_{p4} and S_{P5} respectively from the center of rotation of the wall (Figure 4.46).

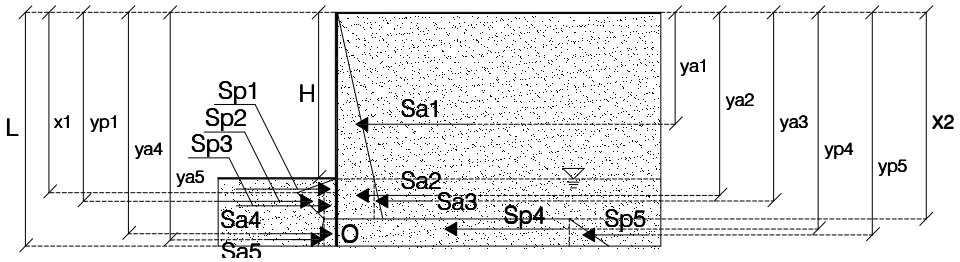

Figure 4.46: Earth pressure distribution used in the second method to compute the bending moment distribution along the wall. At the active side a linear distribution of the contact stress in considered. At the passive side a bilinear distribution of the passive resistance is supposed.

The expression of the forces considered in the equilibrium equations are:

1. $S_{a1} = \frac{1}{2} \cdot \gamma_d \cdot K_{ae} \cdot H^2$
2. $S_{a2} = \gamma_d \cdot H \cdot (x_2 - H) \cdot K_{ae}$
3. $S_{a3} = \frac{1}{2} \cdot \gamma' \cdot K_{ae} \cdot (x_2 - H^2)$
4. $S_{a4} = \gamma' \cdot K_{ae} \cdot (x_2 - H) \cdot (L - x_2)$
5. $S_{a5} = \frac{1}{2} \cdot \gamma' \cdot K_{ae} \cdot (L - x_2)^2$
6. $S_{p1} = \frac{1}{2} \cdot \gamma' \cdot K_{pe} \cdot \frac{(x_1 - H)^2}{SF}$
7. $S_{p2} = \gamma' \cdot K_{ae} \cdot (x_2 - H) \cdot (x_2 - x_1)$
8. $S_{p3} = \frac{1}{2} \cdot \gamma' \cdot K_{pe} \cdot (x1 - H) \cdot (x_2 - x_1) \cdot -\frac{1}{2} \cdot \gamma' k_{ae} \cdot (x_1 - H)$

9. $S_{p4} = (\gamma_d \cdot H + \gamma' \cdot (x_2 - H)) \cdot K_{pe} \cdot (L - x_2)$
10. $S_{p5} = \frac{1}{2} \cdot (\gamma_d \cdot H + \gamma' \cdot (L - H)) \cdot K_{pe} \cdot (L - x_2)$

    where γ_d is the dry unit weight of the soil, γ' is the effective weight of the soil, K_{ae} is the seismic active coefficient, K_{pe} is the seismic passive coefficient, H is the retained height, L is the height of the wall and SF is the safety factor.

In all the cases, γ_d has been considered equal to 15.00 kN/m^3 and γ' has been calculated as:

$$\gamma' = \gamma_{sat} - \gamma_w \tag{4.4}$$

where γ_{sat} is the saturated unit weight of the soil depending on the porosity as in the following expression:

$$\gamma_{sat} = (1 - n) \cdot \gamma_w \cdot G_s + \gamma_w \cdot S_r \cdot n. \tag{4.5}$$

In the tests with loose sand γ_{sat} is 18.90 kN/m^3, while in the tests with dense sand γ_{sat} is 19.74 kN/m^3.

The relative density used to compute the contact stress distribution is not the relative density that comes from the calibration of the sand hopper (38% for the tests in loose sand and 88% for the tests in dense sand), but that one that results from the knowing the mass pured into the model and the volume that it occupies (see introduction to data in paragraph 3.2).

The comparison between the prevision of the bending moment using the limit equilibrium methods with the different possible horizontal pressure distributions and the measured static bending moment, the pre-EQ2 bending moment and the pre-EQ3 bending moment for tests CWU1, PWU1, CWU2, PWU2, CWU3 and PWU3 are reported in Figure 4.47, Figure 4.48, Figure 4.49, Figure 4.50, Figure 4.51, Figure 4.52.

For the cantilever tests all of the contact stress distributions have been used, while for the propped tests the case n°4 (bilinear distribution of the passive resistance) has not been considered. Indeed the bilinear distribution of the passive resistance can be useful to describe the partial mobilization of the passive resistance in the excavated side.

The prevision of the bending moment given by the limit equilibrium analysis with linear distribution of the horizontal effective pressure is higher than the experimental measurements for the cantilever test in loose sand (CWU1 in Figure 4.47) while the prevision considering the angle of shearing resistance variable along the vertical (case 2) and considering the presence

of the suction above the water table (case 3) improves for the same test CWU1 and also for the tests CWU2 and CWU3, which present the same geometry as CWU1 but have a higher relative density (Figure 4.48 and Figure 4.49). Moreover the section where the maximum bending moment takes place is well predicted by the horizontal pressure distribution of the case 2 and case 3, while the horizontal pressure distribution of case 4 predicts a position of the maximum bending moment that is higher than that one of the measured bending moment distribution. These findings indicate that the pre-earthquake bending moment distributions are influenced by the capillary suction that arises above the excavation level and, at the same time, by the relative density of the sand which in turn modifies the angle of shearing resistance. On the other hand the bilinear distribution of the passive resistance is useless for these tests.

The prevision of the bending moment for the propped tests in loose sand (PWU1 in Figure 4.50) is in agreement with the experimental data in case 2 (angle of shearing resistance variable along the vertical) and in case 3 (suction present above the dredge level) as for tests on cantilever walls. For test PWU2 (Figure 4.51) the prevision with case 2 and case 3 is in agreement with the experimental data for pre-EQ1, while for pre-EQ2 and pre-EQ3 the closer to the data is relative to case 1 (linear distribution of active and passive pressures). For test PWU3 (Figure 4.52) the experimental data are well fitted with the case 1 for all the pre-earthquakes distributions. It can be seen that, for the tests on propped walls, there is a less marked difference in the prevision of the bending moment through the limit equilibrium analysis between the three possible contact stress distribution with respect to the prevision of the bending moment for cantilever tests and consequently the measured bending moment is not clearly predictable with a specific contact stress distribution.

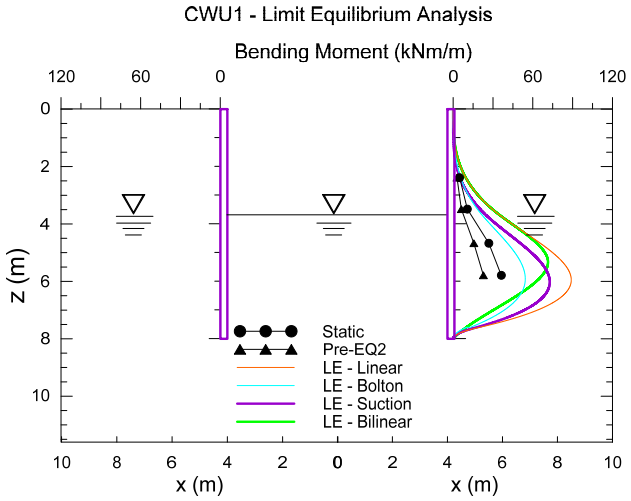

Figure 4.47: Test CWU1: comparison between the measured bending moment before EQ1 (static) and EQ2 and its prevision through limit equilibrium analysis (LE) with different horizontal earth pressure distributions.

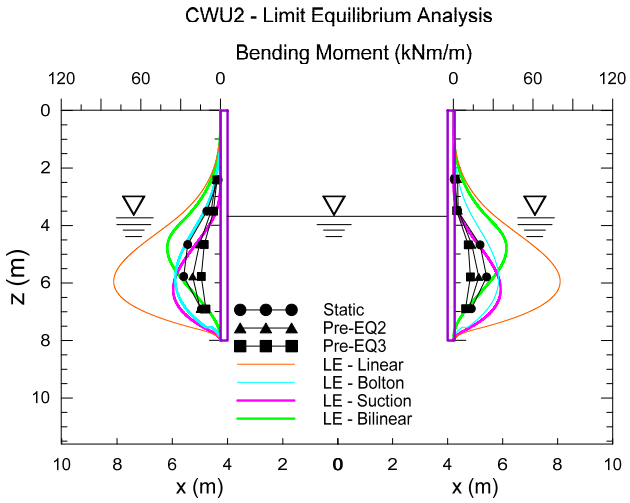

Figure 4.48: Test CWU2: comparison between the measured bending moment before EQ1 (static), EQ2 and EQ3 and prevision through limit equilibrium analysis with different horizontal earth pressure distributions.

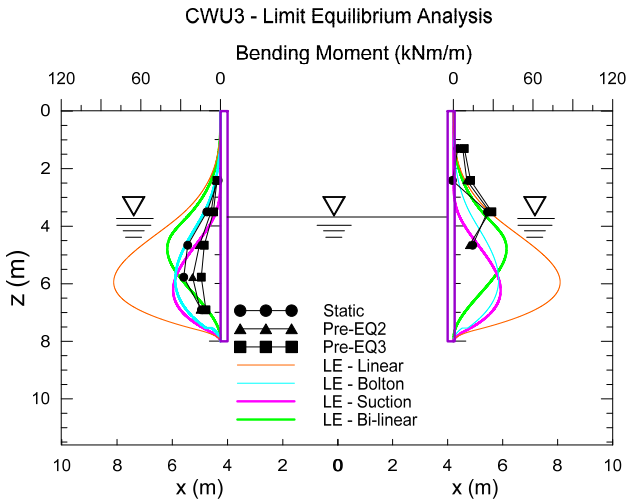

Figure 4.49: Test CWU3: comparison between the measured bending moment before EQ1 (static), EQ2 and EQ3 and its prevision through limit equilibrium analysis with different horizontal earth pressure distributions.

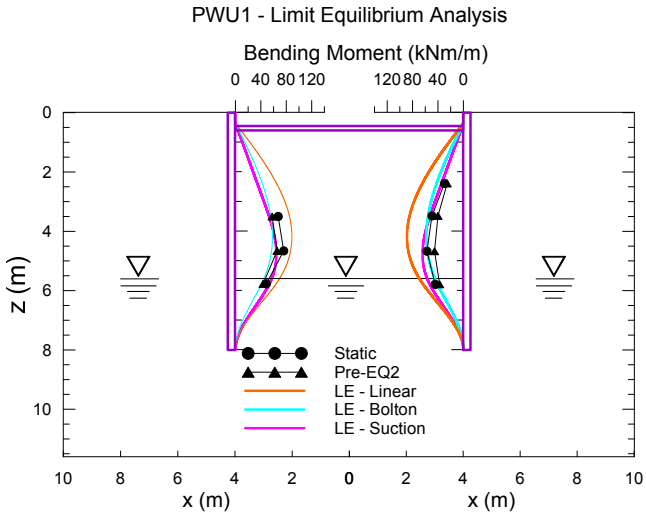

Figure 4.50: Test PWU1: comparison between the measured bending moment before EQ1 (static) and EQ2 and its prevision through limit equilibrium analysis (LE) with different horizontal earth pressure distributions.

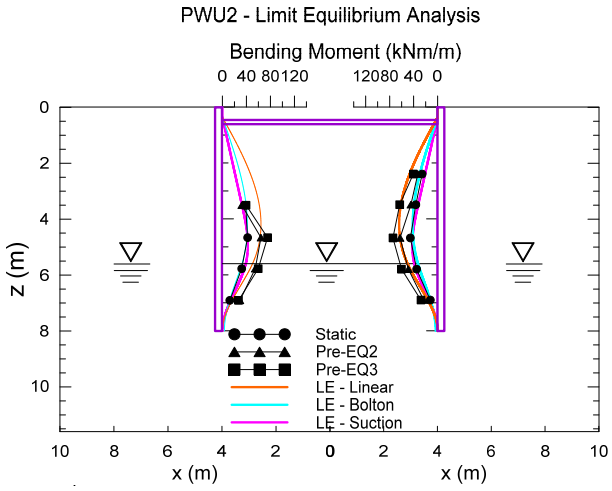

Figure 4.51: Test PWU2: comparison between the measure bending moment before EQ1 (static), EQ2 and EQ3 and the prevision through limit equilibrium analysis with different horizontal earth pressure distributions.

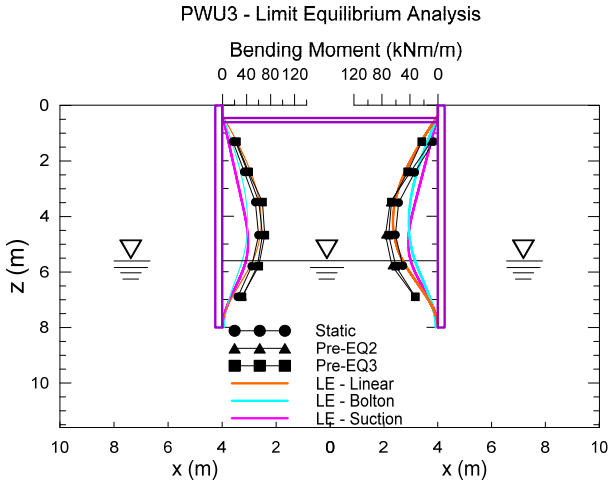

Figure 4.52: Test PWU3: comparison between the measured bending moment before EQ1 (static), EQ2 and EQ3 and its prevision through limit equilibrium analysis with different horizontal earth pressure distributions.

It has been seen that the static bending moment distribution is well

predicted mainly with two different contact stress distributions where i) the angle of shearing resistance depends on the relative density and the mean effective stress through the relation of Bolton (1986) and ii) the presence of suction due to the capillary rise above the water table is taken into account.

Considering these two contact stress distributions also the maximum bending moment distribution for the different earthquakes applied for a single test has been predicted supposing a constant value of the inertial acceleration a at the back of the wall and at the excavated side.

For tests CWU1 and PWU1 (Figure 4.53 and Figure 4.54) a value of a=0.08g has been seen to well predict the maximum bending moment distribution for EQ1 and EQ2 in both tests for the case where the angle of shearing resistance depends on the relation of Bolton (1986). The measured distributions do not significantly different passing from EQ1 to EQ2 and the value of 0.08g can be seen for both tests as representative of the acceleration of Acc4 which is collocated about at the middle of the height of the left wall.

For tests in dense sand the measured maximum bending moment can present a more significant variation passing from EQ1 to EQ3; this is evident in PWU2 and in CWU3 where the maximum bending moment respectively varies passing from 83 kNm/m, to 106 kNm/m and to 130 kNm/m and from 39kNm/m, to 39kNm/m and to 48kNm/m while the similar tests PWU3 and CWU2 present a less important variation of the bending moment. This means that for tests in dense sand it is less indicated to use only one value of the inertial acceleration to back-analyze the measured bending moment, differently as it has been done for the tests in loose sand. To this stage of analysis only one value of inertial acceleration has been considered.

For tests in dense sand the acceleration considered to back-analyze the measure maximum bending moment has been 0.15g, again considering the case of angle of shearing resistance depending on the relation of Bolton. It is important to underline that the relative density considered for the dense tests it is not the nominal density given from the calibration of the sand hopper (88%) but the relative density computed from the mass poured within the model and the volume that it occupies which has been deducted from the hand-made measurements before and after the tests (see in introduction to data in paragraph 3.2) which is about 65%.

The value of 0.15g and the relative density of 65% give a good approximation of the maximum bending moment distribution for tests CWU2 and PWU3 where there is not an important variation of the maximum bending moment passing from EQ1 to EQ3, while for tests CWU3 and PWU2 it well fits the maximum bending moment distribution of the first earthquake where the value of the acceleration equal to 0.15g is never attained within

the soil. This detailed aspect of the maximum bending moment prediction requires further investigations.

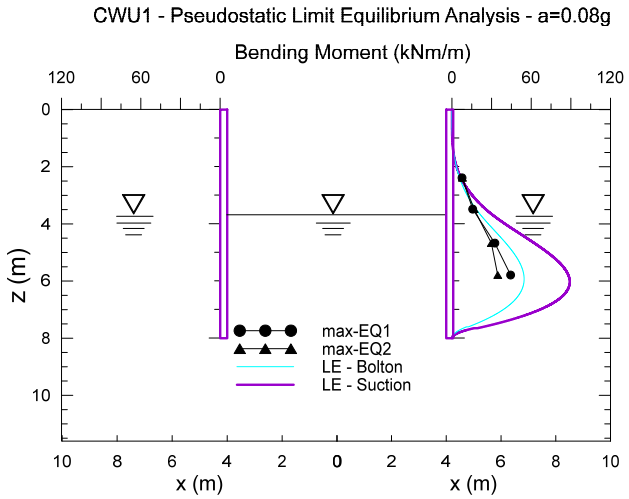

Figure 4.53: Test CWU1: comparison between the maximum measured bending moment during EQ1 and EQ2 and its prevision through limit equilibrium analysis with two different contact stress distribution.

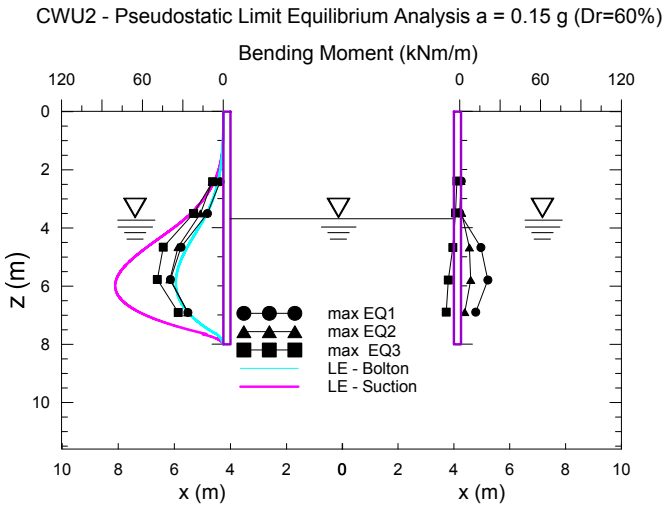

Figure 4.54: Test PWU1: comparison between the maximum measured bending moment during EQ1 and EQ2 and its prevision through limit equilibrium analysis with two different horizontal earth pressure distributions.

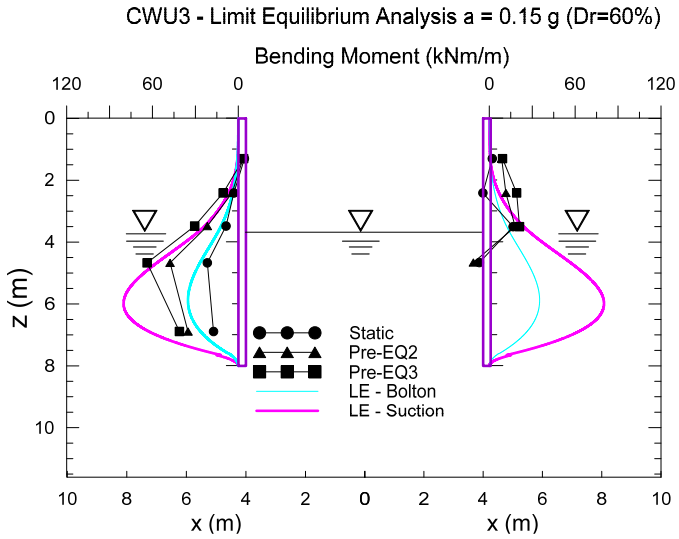

Figure 4.55: Test CWU2: comparison between the maximum measured bending moment during EQ1, EQ2 and EQ3 and prevision through limit equilibrium analysis with two different horizontal earth pressure distributions.

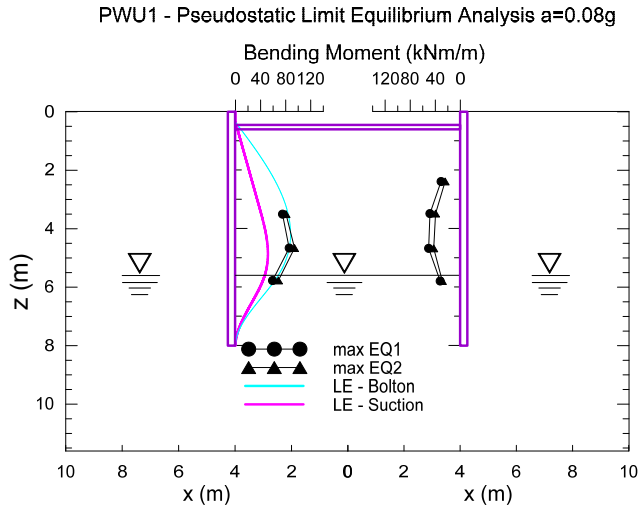

Figure 4.56: Test CWU3: comparison between the maximum measured bending moment during EQ1, EQ2 and EQ3 and its prevision through limit equilibrium analysis with two different horizontal earth pressure distributions.

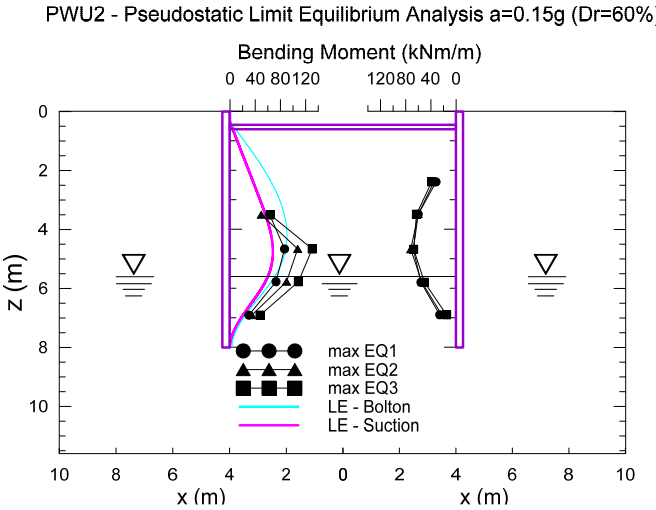

Figure 4.57: Test PWU2: comparison between the measure bending moment before EQ1 (static), EQ2 and EQ3 and the prevision through limit equilibrium analysis with different horizontal earth pressure distributions.

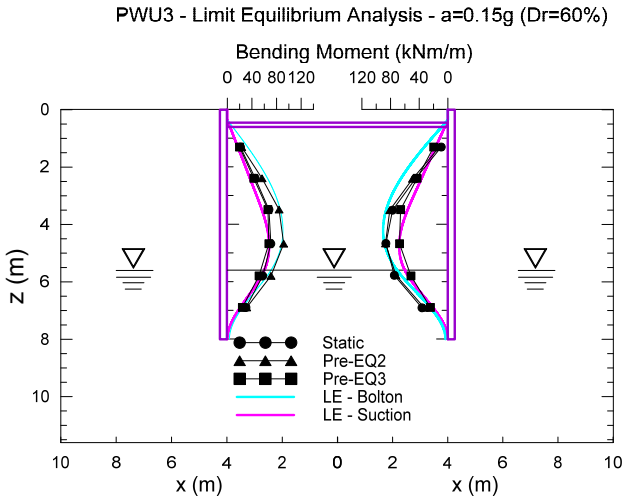

Figure 4.58: Test PWU3: comparison between the maximum measured bending moment during EQ1, EQ2 and EQ3 and its prevision through limit equilibrium analysis with two different horizontal earth pressure distributions.

4.6 Bending Moment - Comparison with Tests in Dry Sand

It relevant also for the bending moment the comparison with the results of the tests in dry sand. As regards the tests on cantilever walls it has been found in Chapter 3 that for test CWU1 the static bending moment is 35 kNm/m, the maximum bending moment is 38 kNm/m and 24 kNm/m for EQ1 and EQ2 respectively and the short term residual bending moment is 9 kNm/m and 10 kNm/m; while for test CWU2 the static bending moment is 27 kNm/m, the maximum bending moment is 39 kNm/m, 39 kNm/m and 49 kNm/m for EQ1, EQ2 and EQ3 respectively and the short term residual bending moment is 27 kNm/m, 22 kNm/m and 15 kNm/m. At the same time in test CW1 ($D_r = 84\%$) the static bending moment, chosen considering the maximum between the maximum static bending moment on the left wall and on he right wall, is 35 kNm/m, the maximum bending moment is 88 kNm/m and the residual bending moment (in tests in dry sand there is no distinction between the short term residual and the long term residual as it has been done for the tests in saturated sand) is 69 kNm/m. As regards the tests on propped walls it has been seen in Chapter 3 that the static bending moment for tests PWU1 is 76 kNm/m, its maximum

values are 86 kNm/m and 94 kNm/m respectively for EQ1 and EQ2, and the short term residual values are 33 kNm/m and -16 kNm/m; while the static bending moment for test PWU2 is 42 kNm/m, the maximum values are 86 kNm/m, 107 kNm/m and 130 kNm/m and the short term residual values are 71 kNm/m, 79 kNm/m and 89 kNm/m. The correspondent tests in dry sand on propped walls are PW1, whose relative density of the sand is 78%, and PW2, which presents a relative density of the sand equal to 42%. Considering both tests, the maximum static bending moment is 45 kNm/m, the maximum bending moment reaches values included between 120 kNm/m and 140 kNm/m and the residual values are included between 90 kNm/m and 110 kNm/m.

From the comparison between the bending moment of tests in saturated sand and bending moment of tests in dry sand it emerges, as it can be expected, that the structure is more stressed in tests in dry sand than in tests in saturated sand. Clearly this is a beneficial effect of the increase of the pore pressures during the earthquakes on both active and passive side.

4.7 Summary

In this Chapter it has been concluded that:

1. Repeatability of the centrifuge tests: the comparison in terms of space distribution of displacements, bending moments and pore pressures of similar tests with respect geometry and relative density has shown that there is a good agreement of the response of the models and thus that the repeatability of the tests is satisfactory;

2. Amplification: seven plots containing the maximum input acceleration compared with the maximum top acceleration for a given earthquake and its earthquakes have shown that for a maximum input acceleration lower than 0.2g the acceleration is about the same as the input acceleration or it is slightly amplified while if the maximum input acceleration is higher than 0.2g a de-amplification is observed for tests PWU2, CWU3, PWU3 and CWU4 relative to the first flight and a slight amplification is observed for tests CWU2 and CWU4 relative to the second flight. The same conclusion is reached if instead of the maximum acceleration the Arias intensity is used to quantify the intensity of the input acceleration or the top acceleration and 2m/s is considered as threshold. The comparison of the amplification study with that one relative to the tests performed in dry sand (Conti, 2010)

has shown that a more marked amplification occurs in tests in dry sand with respect the tests in saturated sand of the present work, such difference is attributable to the decrease of the tangential stiffness within the saturated soil layer correlated with the pore pressure increase that occurs during the shaking;

3. Acceleration phase difference within the soil: the comparison of the results of the phase difference computed in time domain with the phase difference computed in the frequency domain has brought to a good agreement of the results relative to the methodologies especially for dense tests. It has been confirmed that the phase difference relative to the soil collocated below the excavation level is close to the input acceleration while the phase difference of the soil collocate above the excavation level is out of sync with respect the input acceleration. Also, the issues regarding the application of such methodologies have been illustrated and it has been seen that they do not affect significantly the interpretation of the results. The acceleration phase difference of the present tests has been compared with that one of the tests performed in dry sand (Conti, 2010) where, differently with respect to tests of the present work, the soil is essentially in sync with respect the input acceleration;

4. The comparison of the entity of the accumulated displacements of the present tests with respect to the entity of the accumulated displacements of the tests in dry sand has shown that in tests in saturated sand there is a more significant displacement accumulation with respect the tests in saturated sand;

5. Bending moment: the static and pre-earthquake bending moment has been compared with a bending moment distribution obtained with a limit equilibrium analysis carried out with different contact stress distributions that take into account the influence on the bending moment of the dependency of the angle of shearing resistance on the mean effective stress and the relative density, the influence of the capillary rise above the water table and the influence of progressive mobilization of the passive resistance. For tests on cantilever walls there is a better approximation of the experimental bending moment introducing the dependency of the angle of shearing resistance on the mean effective stress and on the relative density and introducing the presence of the capillary rise above the water table; the prevision improves passing from test CWU1 realized in loose sand to tests CWU2 and CWU3

realized in dense sand. For tests on propped walls the prevision of the bending moment is in agreement with the stress distribution that considers the dependency of the dependency of the angle of shearing resistance on the mean effective stress and the relative density (case 2) and the presence of the capillary suction (case 1) for test PWU1 realized in loose sand, while it improves passing to PWU2 realized in dense sand, considering case 2 and case 3 relatively to pre-EQ1 and pre-EQ2 and considering case 1 relatively to pre-EQ3, and passing to PWU3 where the prevision is in agreement with the experimental data considering case 1 as contact stress distribution for pre-EQ1, pre-EQ2 and pre-EQ3. As regards the maximum bending moment, a good prevision of the measured bending moment has been obtained using the contact stress distributions that considers the influence of the suction above the water table and the angle of shearing resistance depending on the relation of Bolton (1986). For tests in loose sand there is not a marked difference in the maximum bending moment distribution during EQ1 and EQ2 and a single value of the inertial acceleration, 0.08g, has been sufficient to well interpolate the measured bending moment. For tests in dense sand a single value of the inertial acceleration, equal to 0.15g, has conducted to good results for tests PWU3 and CWU2 where, as for tests in loose sand, there is not a marked variation in terms of the maximum bending moment passing from EQ1 to EQ3. The same the value acceleration, 0.15g, has been used also to predict the maximum bending moment distribution for tests CWU3 and PWU2 where the maximum bending moment increases more significantly passing from EQ1 to EQ3 and it has given a good approximation for EQ1 where the maximum acceleration attained within the soil is less than 0.15g. It is relevant also to underline that the relative density used to predict bending moment is not the nominal one, coming from the calibration of the sand hopper, but that one computed on the basis of the mass poured within the model and the volume that is occupied estimated on the basis of the hand-made measurements of the height of the soil deposit. This indirectly appear to confirm the fact that the pouring of the sand within the model realizes a value of the relative density lower than that one expected from the calibration of the sand pouring.

Chapter 5

Calibration of Constitutive Model

This Chapter is dedicated to the numerical analyses carried out for the interpretation of the centrifuge tests. Numerical analyses require the choice of a proper model for the prevision of the mechanical response of the sand under cyclic and dynamic loading and the choice of a code for the numerical solution of the differential equations, which also include the constitutive equations, that describe the response of the whole soil-structure system.

5.1 Numerical Model for the mechanical Behaviour of the Sand: Dafalias and Manzari Model.

A model for the behaviour of the sand suitable for the interpretation of the centrifuge tests of the present work must be able to reproduce the response of the sand, which includes i) non linearity with respect to total and incremental deformations, ii) irreversible deformations, iii) hysteretic behaviour under cyclic loading and iv) developing pore pressures during the earthquakes when the soil is saturated and it has to be reproduced both at small deformation and at large deformations because not only the behaviour under cyclic and dynamic loading is relevant for the correct interpretation of the result of the tests, but also because the sand can reach the failure condition, which occurs at large deformations.

In general, this is a difficult task to achieve because the complexity of the model required to accomplish the purposes described above tends to

increase. A possible solution to this aim is represented by the model realized by Dafalias and Manzari, whose first development has been made in 1997 and it has been followed by a further improvement in 2004; the model is described in the following. The model of Manzari and Dafalias is based on the framework of bounding surface plasticity, which has been used for modelling different kinds of materials, such as metals, soils and concrete (Dafalias, 1984). The basic principle of the bounding surface plasticity is to associate to each stress state an image stress state laying on a bounding surface, which contains the stress state, and on the basis of the distance existing between the actual stress state and its image on the bounding surface the plastic modulus is individuated.

Maintaining this basic principle of the bounding surface plasticity, the authors have then developed their model setting the basic equations, individuating the yield surfaces and the bounding surface, setting the expression for the plastic modulus and incorporating the behaviour of the sand through the introduction of the Rowes (1962) dilatancy theory and the Critical State theory (Schofield and Wroth, 1968; Wood, 1990). Moreover, in the version of 2004, the effect of the fabric change on the dilatancy and consequently on the macroscopic behaviour of the material has been introduced. In the following the equations of the model in the triaxial space are briefly introduced, firstly in the simpler version in the case of axial symmetry and then with respect of the multiaxial generalization. Besides this, the basic assumption of the model is that the plastic deviatoric and volume changes occur only if a change in the stress ratio occurs.

The increments of the elastic and plastic strain are introduced through the following expressions:

$$d_{\epsilon_q}^{e} = \frac{dq}{3G} \tag{5.1}$$

$$d_{\epsilon_v}^{e} = \frac{dp'}{K} \tag{5.2}$$

$$d_{\epsilon_q}^{p} = \frac{d\eta}{h} \tag{5.3}$$

$$d_{\epsilon_v}^{p} = d d_{\epsilon_q}^{p} \tag{5.4}$$

where $d_{\epsilon_q}^{e}$ and $d_{\epsilon_v}^{e}$ are the increments of the elastic deviatoric and volumetric strain, $d_{\epsilon_q}^{p}$ and $d_{\epsilon_v}^{p}$ are the increments of the plastic deviatoric and volumetric strain, dp' and dq are the increment of the effective mean stress

and of the deviator and $d\eta = \frac{dq}{dp'}$ is the increment of the stress ratio, G and K are the elastic shear and bulk incremental moduli, H is the plastic hardening moduli associated with the the increment stress ratio $d\eta$ and finally d in equation 5.4 is the dilatancy. As it can be seen in equation 5.3, the increment of the plastic deviatoric deformation $d_{\epsilon_q}^p$ occurs only when a change in the stress ratio occurs; given $d_{\epsilon_q}^p$ a change in the plastic volumetric deformation is obtained from equation 5.4 as the product of $d_{\epsilon_q}^p$ and the dilatancy d. The elastic moduli are correlated with the void index and the mean effective stress p' through the following equations:

$$G = G_0 \cdot p_{at} \frac{(2.97 - e)^2}{1 + e} \left(\frac{p'}{p_{at}} \right)^2 \tag{5.5}$$

$$K = \frac{2(1 + \nu)^2}{3(1 - 2\nu)} G \tag{5.6}$$

where e is the void index, p_{at} is the atmospheric pressure and ν is the Poisson ratio.

The yield surface is represented in the triaxial space $p' - q$ by a wedge whose equation is:

$$f = |\eta - \alpha| - m = 0 \tag{5.7}$$

where α is the orientation of the bisecting line of the wedge in the triaxial space and m is a stress ratio quantity such that $2mp$ is the opening of the yield surface (Figure 5.1). The orientation of the yield surface is set so that the initial stress state is located on the bisecting line of the wedge and only elastic deformations occur up to when the stress is inside the wedge. The plastic deformations occur when the wedge is crossed and it can occur both when the increment of the stress ratio is positive or negative.

In Figure 5.1, besides the yield surface other surfaces are visible, and they are present on both the compression side, where the deviator is positive and the extension side, where the deviator is negative. In general their slope in the compression side and in the extension side is different due to the different mechanical response if the stress path is in the compressive side or in the extension side. Considering the compression side, the first surface met is the dilatancy surface, whose slope is M^d, then the critical state surface of slope M is encountered and finally there is the bounding surface of slope M^b .

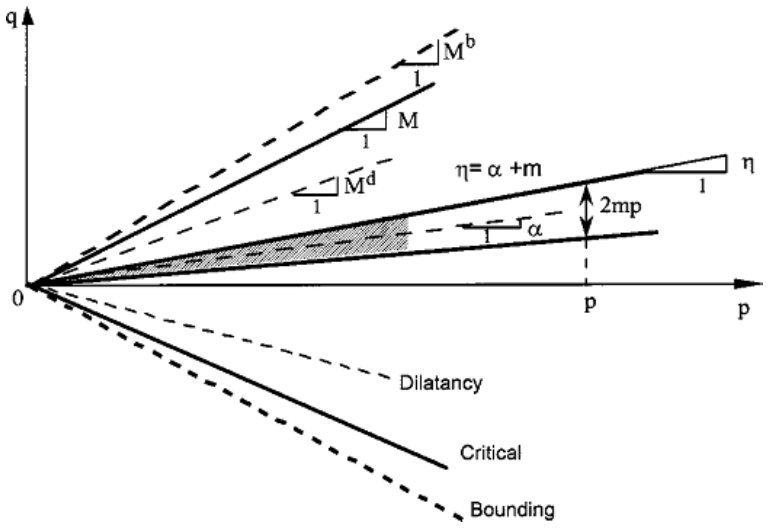

Figure 5.1: Yield surface and bounding surfaces of the model of Manzari and Dafalias model (from Manzari and Dafalias, 2004).

The plastic modulus H is defined on the basis of the distance $M^b\eta$ of the current stress state represented by the stress ratio η from the bounding surface of slope M^b:

$$H = h(M^b - \eta) \tag{5.8}$$

with

$$h = \frac{b_0}{|\eta - \eta_{in}|} \tag{5.9}$$

and

$$b_0 = G_0 h_0 (1 - c_h e)(\frac{p'}{p_{at}})^{-\frac{1}{2}} \tag{5.10}$$

where b_0 and c_h are scalar parameters and η_{in} is the initial stress state. The dilatancy d is computed as:

$$d = A_d(M^d - \eta) \tag{5.11}$$

The critical state behavior is also included in the model through the introduction of a relation that links the void index with the mean effective stress:

$$e_c = e_0 - \lambda_c(\frac{p'}{p_{at}})^{\xi} \tag{5.12}$$

where e_c is the void index at the critical state, e_0 is the void ratio at $p_c = 0$ and λ_c and ξ are constants, and a quantity that represents the distance of the current state of the material from the critical state:

$$\Psi = e - e_c \tag{5.13}$$

that is the state parameter introduced by Been and Jeffries (1985).

The state parameter is important to establish the rules for the evolution of the slope of the dilatancy surface and of the bounding surface. The evolution of the position of these surfaces is important because otherwise the model would predict a physically impossible infinite change of volume at the critical state and moreover it would not be able to reproduce the softening response of the dense sand because the bounding surface could not be overcome and thus the plastic modulus H would remain constantly positive. Since the evolution of the dilatancy surface and of the bounding surface is required in order to overcome these problems the following relations that link the slopes M^d and M^b with the state parameter Ψ:

$$M^d = Mexp(n^d\Psi) \tag{5.14}$$

$$M^b = Mexp(-n^b\Psi) \tag{5.15}$$

where n_d and n_b are material constants. The relations 5.12 and 5.13 imply that, when $\Psi < 0$, which happens when the sand is dense, $M^b < M < M^d$ while when $\Psi > 0$ $M^d < M < M^b$. At the critical state, where $\Psi = 0$, $M^d = M = M^b$ and the evolution of the surfaces stops.

As first step it is possible to understand how the model performs under a simple stress path represented by a monotonic evolution of the stress ratio at the compressive side. Later it will be shown how the model has been improved by the authors for a proper response under cyclic loading. As an example of the model response at a monotonic stress path a result from the calibration of the model is reported in the following. The calibration of the model has been based on the experiments performed on the Leighton Buzzard sand by Visone (2008). The attention is focused on the results of the calibration of a Drained Triaxial Compression test with an initial mean effective stress of 100kPa (DTC100).

In the case of a DTC100 the stress state at the beginning of the test is represented by a point laying on the p' axis and with a deviator equal

to zero. The initial stress state is inside the wedge representing the yield surface. Once the loading occurs an increment of the stress ratio is applied. Since the stress state remains inside the wedge only elastic deformations occur, following the equations 5.1, 5.2, 5.5 and 5.6. When the equation 5.7 holds, also plastic deformation occur, and they are quantified by the relations 5.3 and 5.4. The plastic deviatoric and volumetric strain increments depend on the plastic modulus H and on the dilatancy d respectively present in the equations 5.3 and 5.4.

The plastic modulus H is computed from equation 5.8 and depends on the actual distance of the stress state represented by the stress ratio η and the slope of the bounding surface M^b; the multiplier h in the same equation in computed through the equations 5.9 and 5.10, where it respectively depends from b_0 and the distance of the actual stress ratio from the initial stress ratio $\eta - \eta_{in}$. b_0 depends on the void ratio and the actual mean effective stress from the equation 5.10. The dilatancy d is computed through the equation 5.11 and it depends on the distance of the actual stress ratio η and the slope of the dilatancy surface.

Given $d\epsilon_v$ the change in the void index can be computed and consequently it is possible to compute Ψ and the new orientations of the dilatancy surface and the bounding surface. Then, given a new increment of the stress ratio, it is possible to update the plastic modulus and the the dilatancy to compute the new strain increments.

In Figure 5.2 there is the result of the calibration of the model of Manzari and Dafalias for the Drained Triaxial test performed by Visone. The figure presents four subplots where the calibration is seen from different perspectives. In position North-West there is the $p' - q$ plane where the dilatancy surface, the critical state surface and the bounding surface are visible and the stress state is represented by a dot. In Figure 5.2 the beginning of the numerical test is reported, in fact the position of the stress state lies on the p' axis. In position North-East there is the plane (ϵ_a,$_v$) where the curves obtained from the experiments and from the numerical test are compared and again the dot represents the state of the numerical test at the start. In position South-West there is $\epsilon_a - q$ plane, and here again the comparison between the curve predict by the model and the experimental curve can be found while the dot collocated at position (0, 0) represents the initial state of the numerical test. Finally in position South-East the $p' - e$ plane is reported where again the curves obtained from the numerical test and from the experiment are compared and also the Critical State line can be found. In Figure 5.3, Figure 5.4, Figure 5.5 and in Figure 5.6 there is the same picture as in Figure 5.1 but at different time instants that respectively are

at the beginning of the numerical test, before the peak of the $\epsilon_a - q$ plane, at the peak of the $\epsilon_a - q$ plane, at ϵ_a equal to 0.1 and at $\epsilon_a = 0.2$. It is possible to visualize the evolution of the dilatancy surface and of the bounding surface as the test goes on.

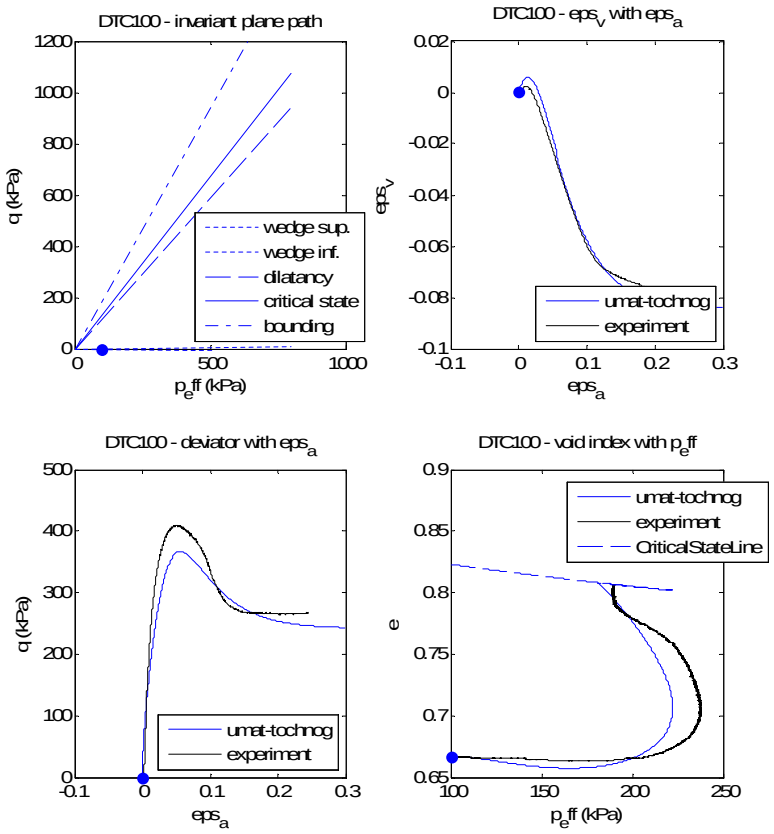

Figure 5.2: Initial state of Manzari and Dafalias model. Calibration of the model for a Drained Triaxial Test at 100kPa of pressure of consolidation. Example used to show how the model performs in the case of a simple calculation. In position N-W there is the $p' - q$ plane, in position N-E there is the $\epsilon_{a,v}$ plane, in position S-W there is the $\epsilon_a q$ plane, in position S-E there is the $p' - e$ plane.

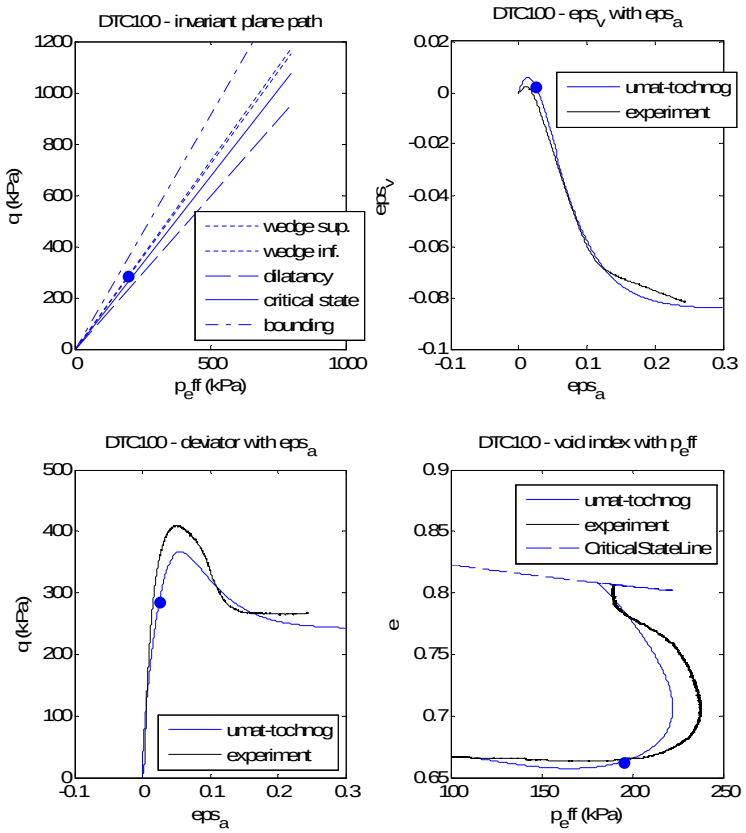

Figure 5.3: Example from the calibration of the Manzari and Dafalias model - state of the model before the peak of the $\epsilon_a - q$ plane.

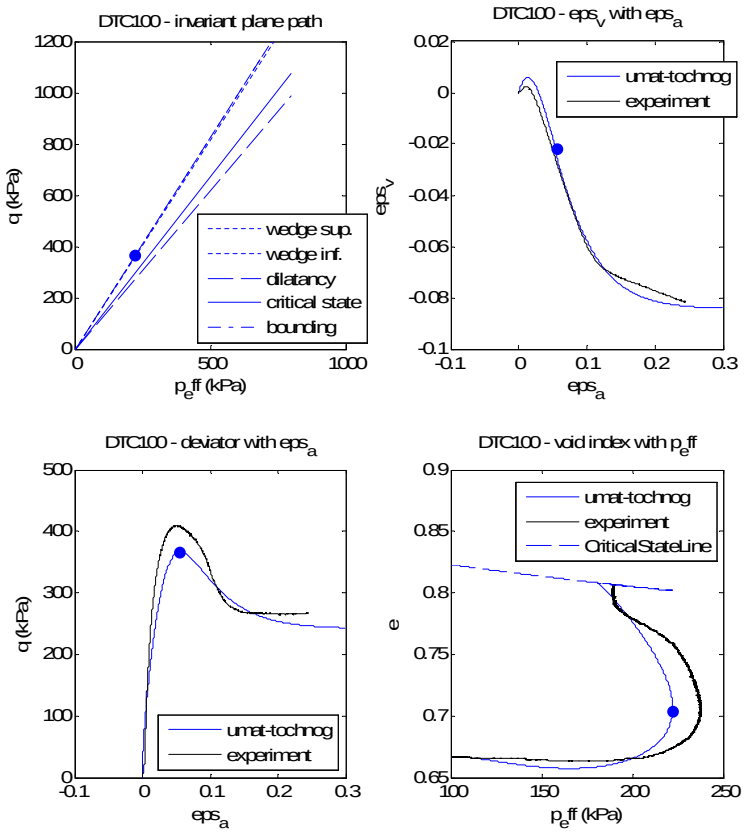

Figure 5.4: Example from the calibration of the Manzari and Dafalias model - state of the model at the peak of the $\epsilon_a - q$ plane.

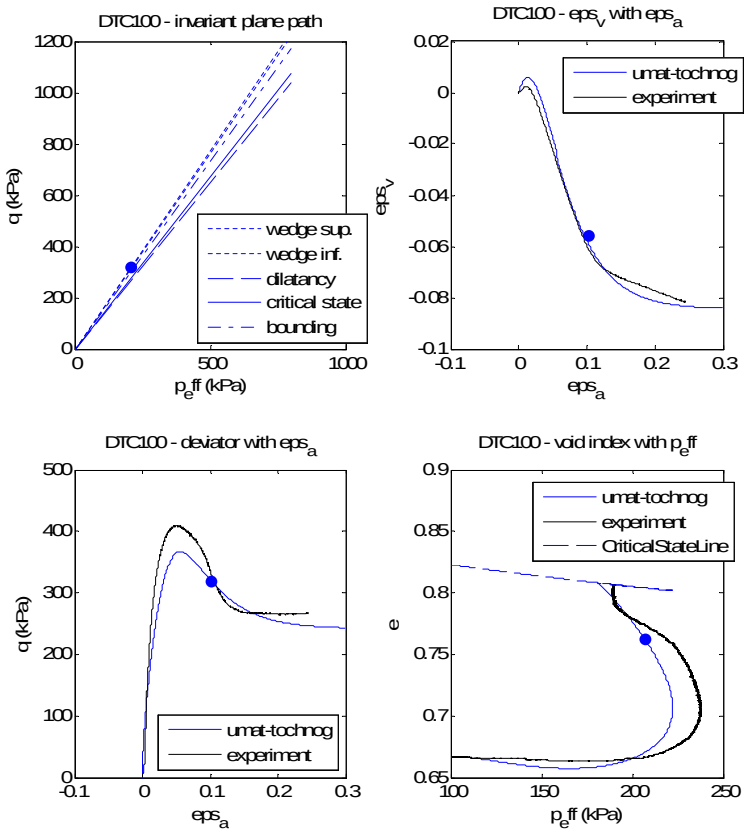

Figure 5.5: Example from the calibration of the Manzari and Dafalias model - state of the model at $\epsilon_a = 0.1$.

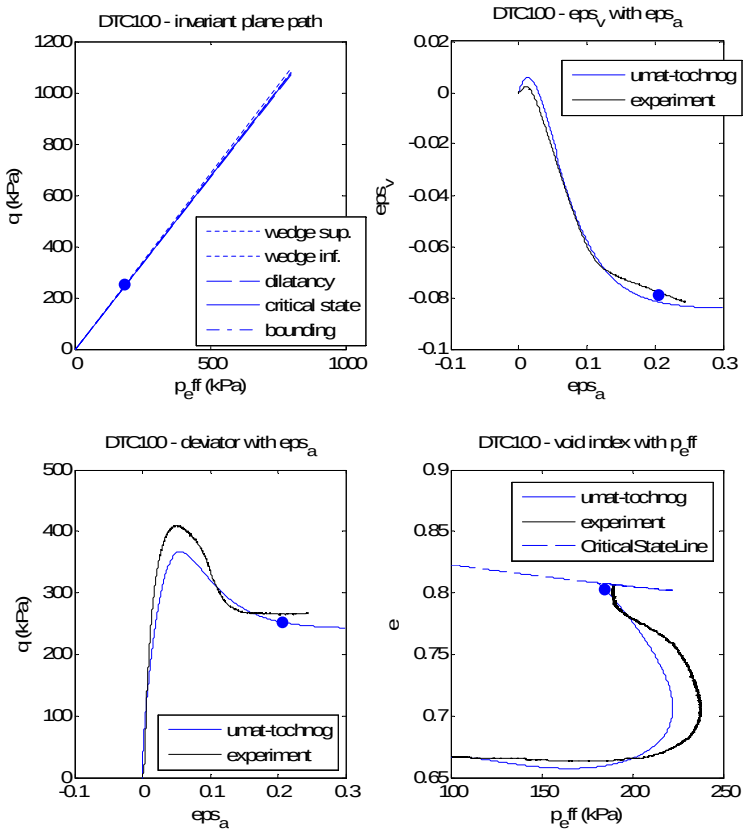

Figure 5.6: Example from the calibration of the Manzari and Dafalias model, state of the model at $\epsilon_a = 0.2$.

Then the authors have further developed the model to take into account the effect of the fabric change on the macroscopic behavior of the sand. It has been recognized by many authors (like Nemat Nasser, 1980 and Nemat-Nasser and Tobita 1982) that when volume increment occurs during the dilation phase of deformation a strong change in the sand particle orientation is observed. Once the fabric change has occurred and then the direction of shear is reversed, then a contraction of the volume takes place due to a rearrangement of the particle orientation.

If the effect of the fabric change on the macroscopic behavior is not taken into account then the undrained behavior of the sand under cyclic loading is not correctly predicted. In fact, as it can be seen in Figure 5.7(a) and in Figure 5.7(b), the effective mean stress is too high with respect to reality

because the model does not predict the increase of the pore pressure at the change of the shearing direction. In the case of a correct prevision of the mechanical behavior of the sand the stress path would have moved toward the point of lower values of p'.

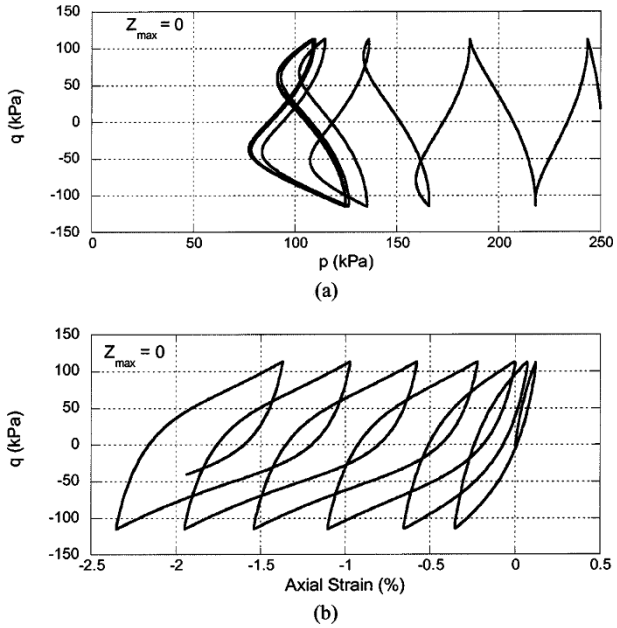

Figure 5.7: Dafalias and Manzari model in predicting the undrained response of the sand under cyclic loading without taking into account the fabric change in the macroscopic behavior (from Dafalias and Manzari, 2004).

The authors have then introduced the effect of the fabric change modifying the expression of the dilatancy d and introducing the fabric-dilatancy variable z as follows:

$$d = A_d(M^d - \eta) = A_0(1 + \langle sz \rangle) \tag{5.16}$$

$$d = A_d(M^d - \eta) = A_0(1 + \langle sz \rangle) \tag{5.17}$$

and

$$dz = -c_z - \langle d\epsilon_v^p \rangle (sz_{max} + z) \tag{5.18}$$

Where $\langle x \rangle = x$ if $x > 0$ and $\langle x \rangle = 0$ if $x0$, and $s = \pm 1$ correspondently to $\eta = \alpha \pm m$. z_{max} is another model constant and it is the maximum value that z can reach; c_z is a parametrer as well.

So, for instance, when the stress state is such that $\eta = 0$ and $z = 0$ it follows that $\langle sz \rangle = 0$ and the expression 5.11 is recovered, moreover $dz = 0$ because $d\epsilon_v^p$ up to when the stress ratio is less than $M^d \langle d\epsilon_v^p \rangle = 0$ in equation 5.18. Then, when $\eta > M^d$ and $\eta = \alpha + m$, so $s = +1$ and it follows that $d\epsilon_v^p < 0$ and z starts to decrease due to equation 5.18 that yields $dz < 0$. Since the initial value of z is zero, z becomes negative and $A_d = A_0$ due to equation 5.17. The condition $A_d = A_0$ holds up to when $d\eta > 0$ and $\eta = \alpha + m$ because successive negative plastic volumetric increments are accumulated and z continues to decrease. The limit for the decrease of z is z_{max}. When the stress ratio changes direction $d\eta < 0$ and $\eta = \alpha - m$ it follows that $s = -1$ and $\langle sz \rangle = \langle -z \rangle = |z|$ so that $A_d = A_0(1 + |z|)$ and thus determining the decrease of p' at the shear reversal in undrained conditions because the dilatancy d is increased as well. After that the shear reversal has taken place, z maintains its negative value because $d\epsilon_v^p$ and 5.18 yields $dz = 0$. The equation 5.18 is activated again when dilation occurs in triaxial extension yielding $dz > 0$. The model constants are reported in Table 5.1. The constants can be subdivided into the categories Elasticity, Critical State, Yield Surface, Plastic Modulus, Dilatancy and Fabric-dilatancy tensor. The elasticity constants are the elastic shear modulus G_0 and the Poisson ratio ν, the Crtitical State parameters are the slope of the critical state lines in the p', q plane M_c and M_e in compression and in extension respectively and the parameters of the power expression of the critical state line in the p', e plane 5.12, the yield surface parameter is the opening of the wedge that represents the yield surface in the p', q plane, the plastic modulus constants are :

subsubsectionMultiaxial Generalization

In the following the multiaxial generalization of the model is briefly presented. The tensorial quantities will be indicated with a line above the letter that indicates the name of the tensorial quantity.

The elasticity equation 5.1 is generalized as:

$$d\overline{e^e} = \frac{d\overline{s}}{2G} \tag{5.19}$$

where $\overline{e^e}$ and $\overline{s}$ are the deviatoric elastic strain and stress tensors respectively, while the equation 5.2 remains the same.

The increments of the plastic deviatoric and volumetric strain in equations 5.3 and 5.4 are modified as follows:

$$d\overline{e}^p = \langle L \rangle \, \overline{R'} \tag{5.20}$$

Elasticity	G_0 ν
Critical State	M_c M_e c e_0 ξ
Yield Surface	m
Plastic Modulus	h_0 c_h n^b
Dilatancy	A_0 n^d
Fabric-dilatancy tensor	z_{max} c_z

Table 5.1: Parameters of Dafalias and Manzari model.

$$d\overline{e}_v^p = \langle L \rangle \, D \tag{5.21}$$

where $\overline{e}^p$ is the deviatoric plastic strain, L is the plastic multiplier, $\overline{R'}$ is the direction of $d\overline{e}^p$ and D is the dilatancy in the multiaxial formulation.

The equations 5.5 and 5.6 remain the same as in the triaxial formulation.

The yield surface in equation 5.7 is generalized as follows:

$$f = [(\overline{s} - p\overline{\alpha}) : (\overline{s} - p\overline{\alpha})]^{\frac{1}{2}} - \sqrt{\frac{2}{3}} pm = 0 \tag{5.22}$$

where $\overline{\alpha}$ is the generalization in the multiaxial space of the orientation of the bisecting line of the yield surface in the triaxial space and $\overline{a} : \overline{b} = tr(\overline{a}\overline{b})$. The generalized yield surface is reported in 5.8 where there is its projection on the deviatoric plane π. The yield surface assumes a circular shape on the deviatoric plane.

In 5.8 can be found the definition of the quantities α^b, α^d and α^c that are defined respectively as $\alpha^b = M^b - m$, $\alpha^d = M^d - m$ and $\alpha^c = M - m$. These quantities allow to re-define the distances $M^b - \eta$, $M^d - \eta$ and M_η as $\alpha^b - \eta$, $\alpha^d - \eta$ and $\alpha^c - \eta$. Moreover, the introduction by the authors of the Lode angle Θdefined through the equation $\cos 3\Theta = \sqrt{6} tr\overline{n}^3$, where $\overline{n}$ is the normal to the yield surface, allows to interpolate the value of a generic quantity Q_Θ between its values at $\Theta = 0$ and $\Theta = \pi/3$ that correspond

to compression and extension respectively. The interpolation function is $Q_\Theta = g(\Theta, c)Q_c$, with $g(\Theta, c) = \frac{2c}{(1+c)-(1-c)\cos 3\Theta}$ and $c = \frac{Q_e}{Q_c}$.

The equation 5.8 that expresses the plastic modulus is transformed in:

$$K_p = (2/3)ph(\overline{\alpha}^b_\Theta - \overline{\alpha}) : n \tag{5.23}$$

where

$$h = \frac{b_0}{|\overline{\alpha} - \overline{\alpha}_{in}| : \overline{n}} \tag{5.24}$$

that replaces equation 5.9.

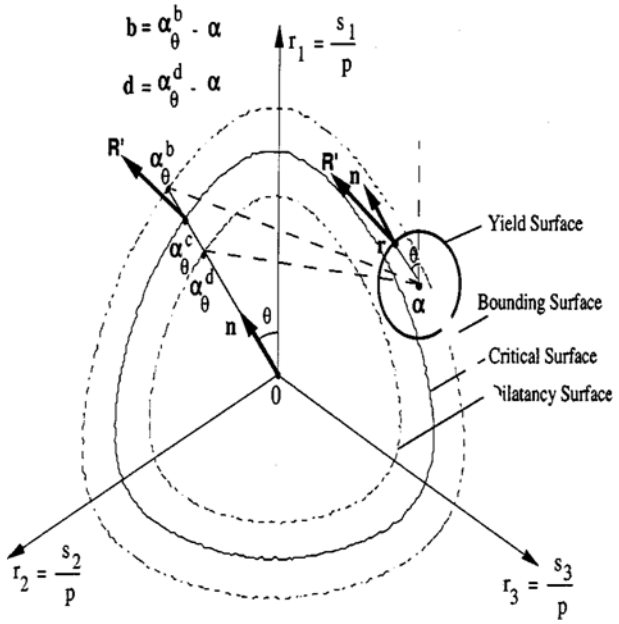

Figure 5.8: Multiaxial generalization of the Yielp surface, the Bounding surface, the Critical surface and the Dilatancy surface: projection on the π plane (from Dafalias and Manzari (2004).

The equation 5.10 remains the same. The equation 5.11 that expresses the dilatancy in terms of the distance of the current stress state from the dilatancy surface becomes:

$$D = A_d(\overline{\alpha}^d_\Theta) - \overline{\alpha}) : \overline{n} \tag{5.25}$$

The expression of the critical state line in equation 5.12(***) remains the same in the multiaxial formulation, while the expressions 5.14 and 5.16 change as follows:

$$\overline{\alpha}_{\Theta}^{b} = \sqrt{2/3}[2g(\Theta, c)Mexp(-n^{b}\Psi) - m]\overline{n} \tag{5.26}$$

$$\overline{\alpha}_{\Theta}^{b} = \sqrt{2/3}[2g(\Theta, c)Mexp(n^{d}\Psi) - m]\overline{n} \tag{5.27}$$

As regards the equations that regulate the effect of the fabric change on the macroscopic behaviour of the soil 5.17, 5.18 and 5.19 are respectively transformed into:

$$A_d = A_0(1 + \langle z : \overline{n} \rangle) \tag{5.28}$$

$$d\overline{z} = -c_z \left\langle -de_v^p \right\rangle (z_m ax\overline{n} + \overline{z}) \tag{5.29}$$

$$d\overline{\alpha} = \langle L \rangle (2/3)h(\overline{\alpha}_{\Theta}^{b} - \overline{\alpha}) \tag{5.30}$$

5.2 Tochnog Finite Element Code.

The Finite Element Code Tochnog has been used to solve the boundary value problem relative to the simulation of the centrifuge tests and to the simulation of the experiments performed on the Leighton Buzzard Sand for the calibration of the Dafalis and Manzari model.

The code Tochnog has been developed by Roddeman (2001) and it is well suited to solve geotechnical problems and mechanical problems in general since it contains various types of costitutive models, which also include the more recent incrementally non linear models, and gives the possibility to use costitutive models external to the code written for the Finit Element Code ABAQUS. This is the case of the model of Dafalias and Manzari that has been implemented as a User defined Material (UMAT) code in Fortran for the Finite Element Code ABAQUS by Tamagnini and Miriano (2008) and it has been further developed by Tamagnini, Martinelli and Miriano (2013). This last development of the implementation of the model can be found on the web site www.soilmodels.info.

Tochnog has been linked with the UMAT that has been used as material law for the behavior of the soil in the numerical simulations. In the following the calibration factors are reported and their calibration procedure is described.

5.3 Calibration of Dafalias and Manzari model.

The experimental program carried out by Visone (2008) has consisted of two Drained Triaxial tests in Compression (DTC), two Drained Triaxial tests in Extension (DTE), two Drained Triaxial tests in Compression at constant p' (DTCp'), two Drained Triaxial tests in Extension at constant p' (DTEp'), two Undrained Triaxial tests in Compression (UTC), two Undrained Triaxial tests in Extension (UTE), and four alternated Resonant Column tests and Torsional Shear tests (RCTS). For the tests with the same stress path, i.e. for two DTC tests, the consolidation pressure changes. The summary of the tests is reported in Table 5.2.

Test	Initial Relative Density	Consolidation Pressure (kPa)
DTC100	80.7	100
DTC200	70.2	200
DTE100	53.9	100
DTE200	52.7	200
DTCp'100	76.0	100
DTCp'200	77.1	200
DTEp'100	79.2	100
DTEp'200	63.3	200
UTC200	29.0	200
UTC400	51.4	400
UTE200	28.1	200
UTE400	29.5	400
RCTS100	47.1	100
RCTS200	52.4	200
RCTS400	71.3	400
RCTS400B	57.8	400

Table 5.2: List of the tests performed by Visone (2008).

The calibration of the parameters of Dafalias and Manzari model has been carried out both from the data of the experiments performed by Visone and performing single element tests through numerical analyses. In fact, some of those parameters can be directly calculated from the results of the experiments on the Leighton Buzzard Sand (Visone, 2008) and they are the Critical State parameters M_c, M_e, λ_c, e_0, ξ, the parameter G_0, which belongs to the elasticity parameters, the parameter n^b , which belongs to the Plastic Modulus parameters and n^d , which belongs to the Dilatancy parameters,

while the parameters h_0, c_h and A_0 have been calculated iteratively through the Tochnog finite element calculation performed with a single element. The remaining parameters $\nu$and m have been set directly by the user.

The slope of the critical state lines M_c and M_e in p',q plane are already present in the paper from Visone and they are 1.34 in compression and 0.88 in extension. The three parameters c, e0 and ξ have been determined from the data of the drained tests DTC,DTE, DTCp' and DTEp' for a total of eight tests. For each of them the values of the mean effective stress p' and the void ratio e_c at the end of the shear phase have been selected. Then, starting from those values, a second value for each test of e_c called e_c^* has been calculated from the equation 5.12 with an initial guess of the parameters e_0, λ_c and ξ . If an index i indicates one of the eight tests and $e_c(i)$ and $e_c^*(i)$ the correspondent values of e_c and e_c* then the error $err = \sum_{i=1}^{8}(e_c(i) - e_c^*(i))^2$ has been computed and minimized by varying the values e_0, λ_c and ξ through the use of the solver add-in of excel. With this procedure the resulting values of the three parameters have been $e_0 = 0.855$, $\lambda_c = 0.032$ and $\xi = 0.64$.

The values of n^d and n^b have been determined using the expressions 5.14 and 5.16. M^d and M^b can be seen as the value of the stress ratio η at the phase transformation point, which is the point where the derivative of the experimental curve ϵ_a, ϵ_v changes sign, and at the peak of the experimental curve $_a, q$. So from the experimental curves ϵ_a, ϵ_v and ϵ_a, q the values of the deviator q, the mean effective stress p' and of the void ratio e have been selected and the correspondent values of η is computable and Ψ from equation 5.13 as well, since the previously computed e_0, $_c$ and ξ allow to use equation 5.12 and compute e_c . The resulting values of n^b and n^d have been respectively 2.18 and 0.82.

The constant G_0 has been determined from the sequence of values of p', v, e, G of the tests RCTS100, RCTS200, RCTS400, where G represents the maximum shear modulus measured during the test. Then two arrays of values have been isolated, where the first one is the maximum shear modulus G and the other one is computed as $p_{at}\frac{(2.97-e)^2}{1+e}(\frac{p}{p_{at}})^{\frac{1}{2}}$. The parameter G_0 has been computed as the slope of the linear interpolation function of the two arrays of data.

Besides these model parameters directly individuated from the experimental data there are the Poisson ratio ν which has been set equal to 0.3 and the opening f the yield surface m that has been set equal to 0.01.

The remaining parameters h_0, A_0, c_h, have been determined iteratively through numerical analyses with single element tests. This has been built

considering four nodes forming a square of edge equal to one and the four corresponding edges that link them; in this way the domain where the calculation have been performed has been built. The four nodes and the edges are the corners and the edges of a single element of type quad. The edges have been used to impose the boundary condition of the problem (Figure 5.9), that are represented by the fixing of the velocity on one of the vertical lateral boundaries (the left one in Figure 5.9), the imposition of a lateral force on the remaining lateral boundary, the fixing of the velocity at the base boundary and the imposition of a vertical displacement at the top boundary.

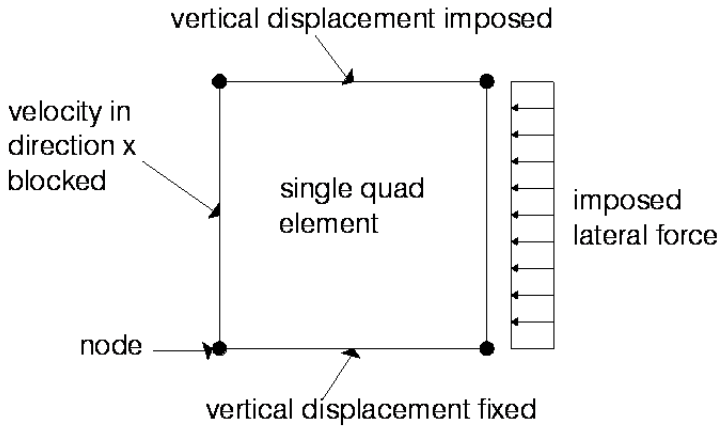

Figure 5.9: Multiaxial generalization of the Yield surface, the Bounding surface, the Critical surface and the Dilatancy surface: projection on the π plane (from Dafalias and Manzari (2004).

Besides the choice of the parameters of the model, the numerical simulations require the initialization of the state variables of the model that are the six components of the tensor α that sets the orientation of the yield surface and the initial void ratio. In the case of the drained tests, the initial void ratio has been set equal to the initial void ratio of the experiments, while in the case of the undrained tests, the initial void ratio has been chosen to be lower than the initial void ratio of the tests. The latter were about 0.850 in all the undrained tests, while the correct reproduction of the results required a value of the initial void ratio of 0.725, which has been used for all the undrained tests.

The resulting values of the parameters h_0, A_0, c_h are 0.4, 1.7, 0.65 and

0.4, 0.05, 0.65 respectively for the drained tests and for the undrained tests. In the following the results of the calibration are reported. The results of the numerical simulations have been compared with the experiments with reference to the curves $\epsilon a, q$ and $\epsilon a, \epsilon v$ for the drained tests, and $\epsilon a, q$ and $a, \Delta u$ for the undrained tests.

There is a very good match between the numerical simulation and experiment for the tests in compression, both drained and undrained. For the drained tests in extension there is a good approximation of the $\epsilon a, q$ curve while the $\epsilon a, \epsilon v$ curve is not well catched. For the undrained tests in extension both the $\epsilon a, q$ and $\epsilon a, \epsilon v$ curves are not well predicted from by the numerical simulation.

5.3.1 Calibration of Dafalias and Manzari model. Test DTC100 .

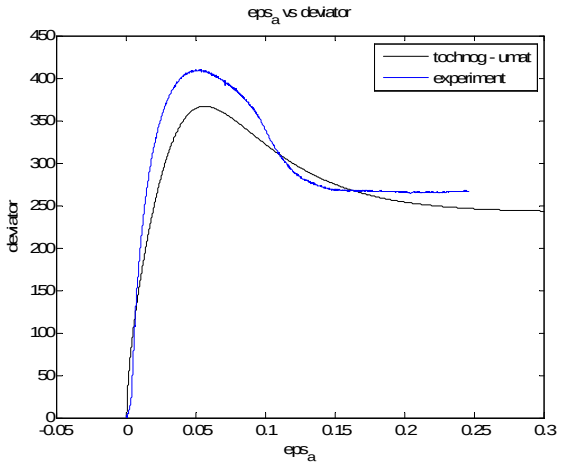

Figure 5.10: DTC100: axial deformation vs deviator comparison between numerical simulation and experiment.

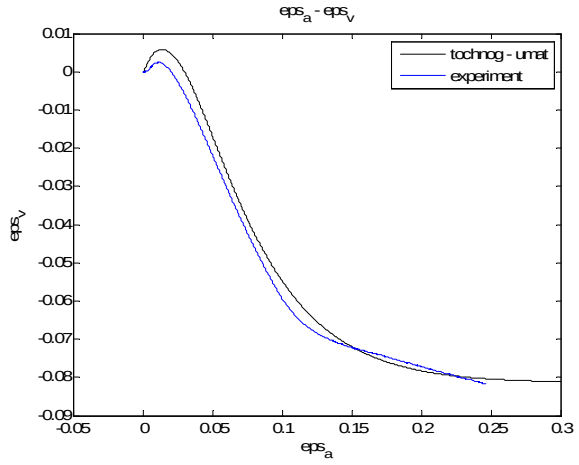

Figure 5.11: DTC100: axial strain vs volumetric strain comparison between numerical simulations and experiment.

5.3.2 Calibration of Dafalias and Manzari model. Test DTC200.

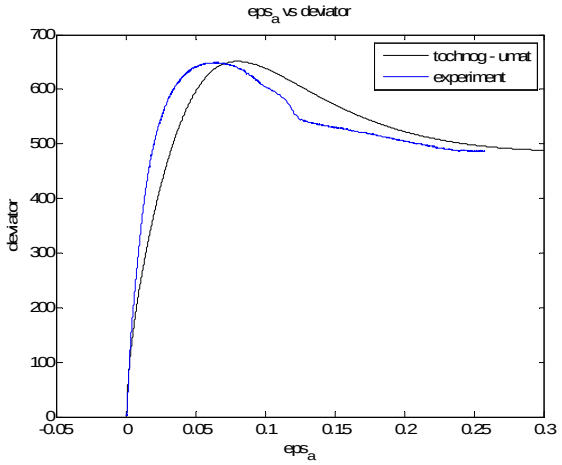

Figure 5.12: DTC200: axial strain vs deviator comparison between numerical simulation and experiments.

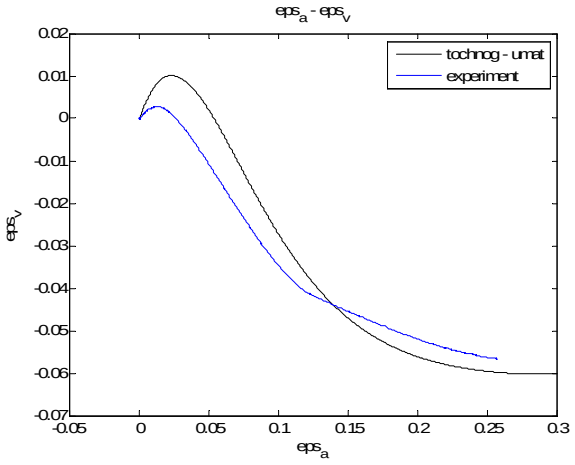

Figure 5.13: DTC200: axial strain vs volumetric strain comparison between numerical simulation and experiment.

5.3.3 Calibration of Dafalias and Manzari model. Test DTE100.

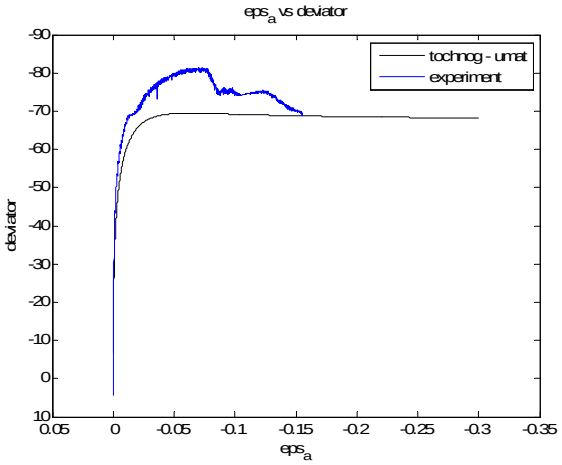

Figure 5.14: DTE100: axial strain vs deviator comparison between numerical simulation and experiment.

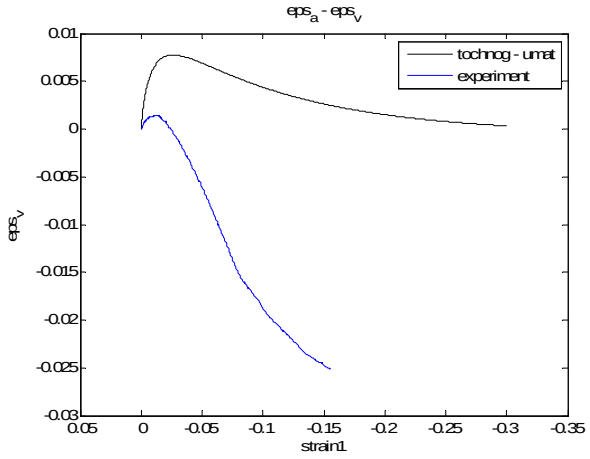

Figure 5.15: DTE100: axial strain vs volumetric strain comparison between numerical simulation and experiment.

5.3.4 Calibration of Dafalias and Manzari model. Test DTE200.

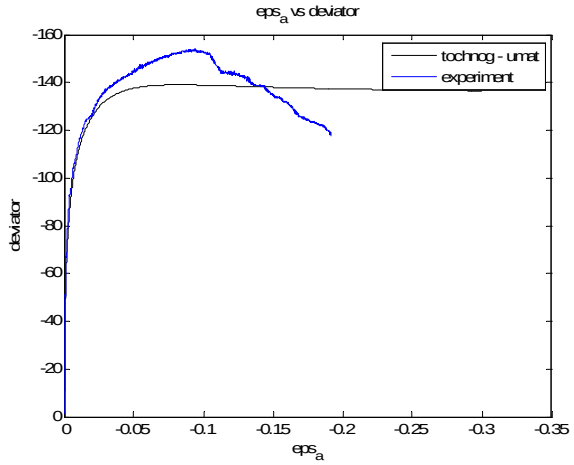

Figure 5.16: DTE200: axial strain vs volumetric strain comparison between numerical simulation and experiment.

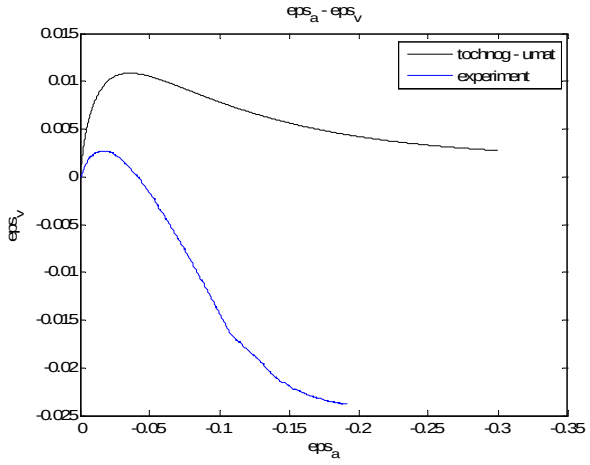

Figure 5.17: DTE200: axial strain vs volumetric strain comparison between numerical simulation and experiment.

5.3.5 Calibration of Dafalias and Manzari model. Test UTC 200.

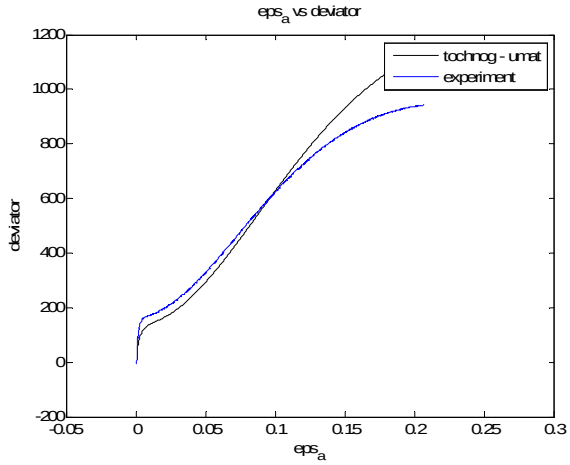

Figure 5.18: Axial strain vs deviator: comparison between numerical simulation and experiment.

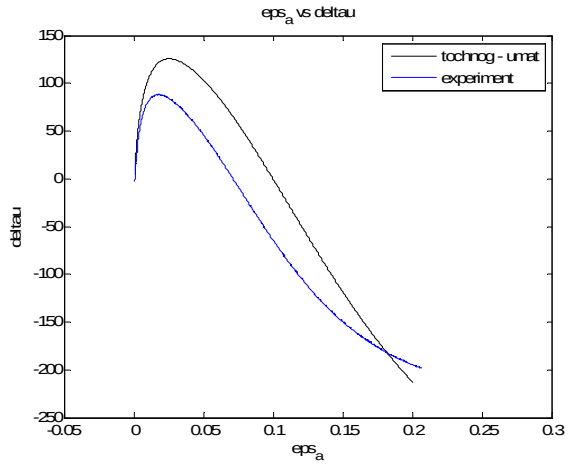

Figure 5.19: UTC200: axial deformation vs excess pore pressure comparison between numerical simulation and experiment.

5.3.6 Calibration of Dafalias and Manzari model.Test UTC400.

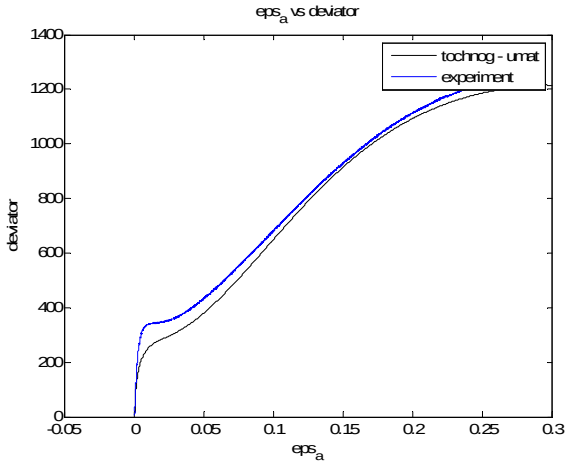

Figure 5.20: UTC400: axial strain vs deviator comparison between numerical simulation and experiment.

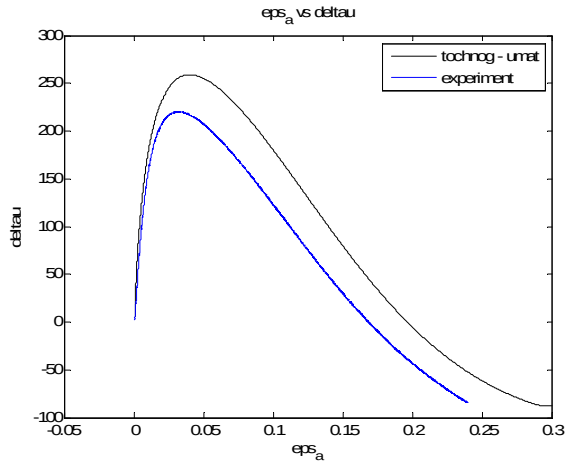

Figure 5.21: UTC400: axial strain vs excess pore pressure comparison between numerical simulation and experiment.

5.3.7 Calibration of Dafalias and Manzari model. Test UTE200.

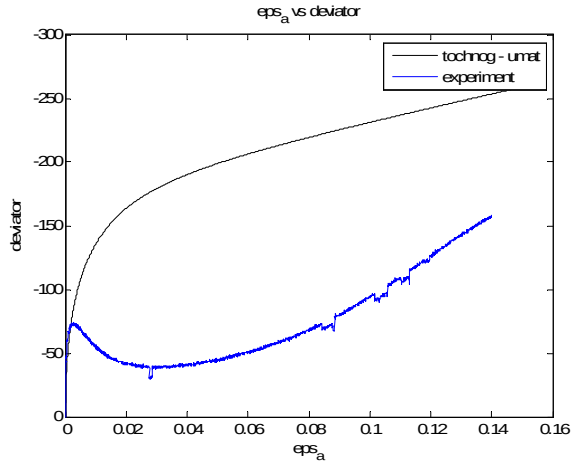

Figure 5.22: UTE200: axial deformation vs deviator comparison between numerical simulation and experiment.

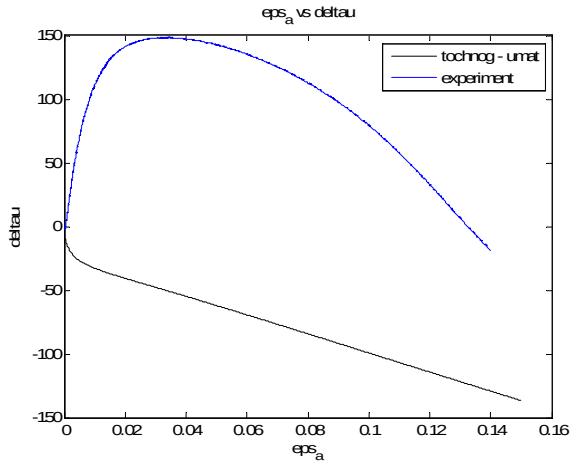

Figure 5.23: UTE200: axial deformation vs excess pore pressure comparison between numerical simulation and experiment.

5.3.8 Calibration of Dafalias and Manzari model. Test UTE400.

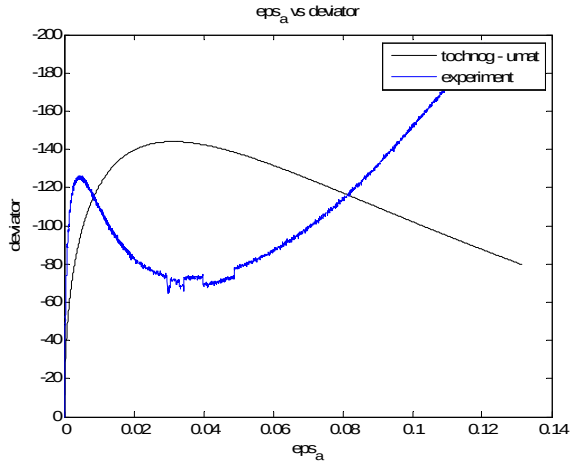

Figure 5.24: UTE400: axial strain vs deviator comparison between numerical simulation and experiment.

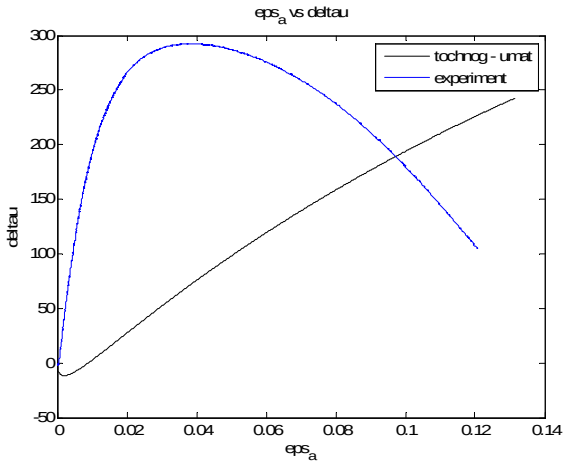

Figure 5.25: UTE400: axial strain vs excess pore pressure comparison between numerical simulation and experiment.

5.4 Summary

In this chapter the Dafalias and Manzari model has been illustrated. It is a model well suited to predict the behaviour of the sand under dynamic conditions and, through the incorporation of the fabric change effect on the macroscopic behaviour it gives the possibility to well predict the dynamic behaviour under dynamic undrained conditions. The model has been calibrated with respect to the experiments results on the Leighton Buzzard Sand. A very good approximation of the results has been obtained for the tests in compression. Still analyses at the finite volume need to be performed.

Chapter 6

Conclusions

The dynamic centrifuge tests performed have allowed to study the behaviour of flexible retaining walls embedded in saturated sand with fluid table localized at the excavated level. Two different kind of structures have been studied: cantilever retaining walls and walls with one level of props at the top; two different values of relative density have been considered. The details of preparation of the models and the instrumentation used have been illustrated in Chapter 2.

In Chapter 3 the response of the soil-structure system of each test has been described. It has emerged that the acceleration in the soil is significantly de-amplified in all the models up to the excavated side, where there is the top of the water table. In the soil portion localized above the excavation level the acceleration is again amplified remaining significantly below the input acceleration for the tests in loose sand, while for tests in dense sand the amplification above the fluid table determines a value of the acceleration at the top about equal to the input acceleration. On the other hand, in tests performed in dry sand (Conti, 2010), the acceleration at the top is generally higher than the input acceleration. Thus a first difference with respect the tests in dry sand is in terms of the amplification of the acceleration, which is more marked for the tests in dry sand with respect those in dry sand.

The acceleration within the soil presents also a marked phase difference. In particular the acceleration below the water table is close to that one of the input acceleration, being the phase difference lower than 50-60°, while the acceleration at the top of the soil deposit reaches values included between 100° and even 200°. In the tests in dry sand, the soil deposit has been seen to be non significantly out of phase with respect to the input acceleration.

As regards the accumulated displacements of the walls, a more rele-

vant entity of the displacements has been observed for tests in saturated sand on both types of structures. The collapse mechanism of the propped walls is a rotation of the walls around the point of constrain imposed by the props, while for tests on cantilever walls, a different response has been observed depending on the relative density of the sand. For tests in loose sand, the cantilever walls have undergone a counter-rotation and a subsequent counter-rotation during the earthquakes; this has not happened for the cantilever walls in dense sand where the typical collapse mechanism represented by the approaching of the tops of the walls has been observed as the shaking has been applied. With respect to tests in dry sand, a general more relevant accumulation of displacement has been observed.

The pore pressure coefficient has been seen to be far from the unity at the back of the walls for all the tests while it approaches the unity in the excavated side for all the tests indicating that the the condition of liquefaction has occurred. Probably a non perfect computation of the pore pressure coefficient, related to the position of the pore pressure transducers and the fact that it has been computed assuming a one-dimensional distribution of the effective stress state, has led to a non clear distinction in the values attained by the pore pressure coefficient in the excavated side from the tests in loose sand to the tests in dense sand.

The increase of the pore pressures has determined a drop of the bending moment during the earthquake. Indeed, especially for tests in loose sand, the short term residual bending moment is significantly low and, during the phase of dissipation of the excess pore pressures the bending moment tends to recover its configuration before the shaking. For instance, test PWU1 the bending moment at the short term residual has reached even negative values. Also in test CWU2, even if it has been performed in dense sand, a drop of the bending moment during the shaking has been observed as well. For test PWU2 instead a progressive accumulation of the bending moment has been observed. To this regard, in test PWU1, as the bending moment decreases during the earthquakes a drop of the axial force in the props has been observed while, in test PWU2, a progressive increase of the axial force in the prop has been seen as the bending moment progressively increases. The static values of the bending moment are higher for tests in loose sand with respect to those in dense sand due to the difference in the relative density of the sand. On the other hand the maximum bending moment is higher in tests in dense sand with respect to tests in loose sand. In this sense, the test CWU2 presents an intermediate behaviour since, as for tests in loose sand, a drop of the bending moment at the and of the earthquakes has been observed due to the increase of the pore pressures, and, on the other hand,

the maximum bending moment is higher with respect to that one of test CWU1, which presents the same geometry and has been performed in loose sand. With respect to tests in dry sand the bending moments have been seen to be lower due to the isolation effect of the increase of pore pressures.

In Chapter 4 the static and dynamic bending moment distributions have been calculated through the use of Limit Equilibrium analyses with different contact stress distributions that take into account i) the influence of suction related to the capillary rice above the water table, ii) the dependency of the angle of shearing resistance from the mean effective stress and from the relative density iii) the progressive mobilization of the passive resistance. The relative density used in the computation has been computed on the basis of the mass poured within the model and on the volume that it occupies, which has been computed on the basis of direct measurements on the models before and after the tests. The prevision of the static bending moment has been satisfactory considering the influence of the suction and the influence on the angle of shearing resistance of the mean effective stress and the relative density. Good approximation of the maximum bending moment profile has been obtained considering only the contact stress distribution that takes into account the dependency of the angle of shearing resistance on the relative density and on the mean effective stress. Particularly, for tests in loose sand an inertial acceleration of 0.08g has been found to well predict the EQ1 and EQ2 maximum bending moment, which present close experimental distributions passing from EQ1 to EQ2. For tests in dense sand the inertial acceleration of 0.15g has been chosen and it has led to a good prevision of the experimental results for tests PWU3 and CWU2, where there is not a significant variation in the value of the maximum bending moment for the earthquakes applied while for tests PWU2 and CWU3, the value of 0.15g produces an underestimation of the bending moment since the obtained profile approaches that one relative to EQ1 where the acceleration in the soil are lower than 0.15g. Further work regarding the pseudostatic analysis is needed to this aim.

These tests have represented also a possibility to check the repeatability of the tests and to measure the contact stress acting on the walls. In fact tests in dense sand have been repeated with the same geometry and relative density (CWU2 has the same geometry and relative density of tests CWU3 and CWU4 and PWU2 has the same geometry and relative density of PWU3). The repeatability has been satisfactory in terms of the various physical quantity monitored.

The measurement of the contact stress on the wall with Tekscan tactile pressure sensor still presents some issues from the experimental point of

view to be clarified since the slope of the diagram of the horizontal pressure acting on the wall is lower than the slope given by the water below the water table (10kPa/m).

The most important aspect regulating the response of the entire soil-structure system is the increase of the pore pressures in undrained conditions has been determined by the inhibited compaction of the soil during the earthquake. The pore pressure increase, which in turn is related to the relative density of the sand, has determined a reduction of the bending moment with respect to tests performed in dry sand (Conti,2010) and higher values of accumulated displacements. This finding is more relevant if liquefaction conditions are reached at the excavated side, which in turn likely happens as the relative density of the sand decreases. In case of cantilever walls the reaching of liquefaction conditions determines a counter-rotation of the walls while for tests on propped walls can even determine a change in sign of the bending moment, as it has been observed in test PWU1.

This is why the numerical analyses represent an important way to understand the basic mechanical phenomena at that regulate the response of the soil-structure system, since proper numerical model can take into account the dynamic and undrained soil behaviour. At this stage of the research only the calibration of the numerical model of Dafalias and Manzari (2004) is available and more work is needed to obtain results at finite domain.

Appendix A

Calibration Factors

In chapter 2 the procedure used for the calibration of the instruments has been shown and for each instrument the calibration factor relative to the test PWU3 has been considered as an example. In this appendix the calibration factors of all the tests are reported.

Test CWU1

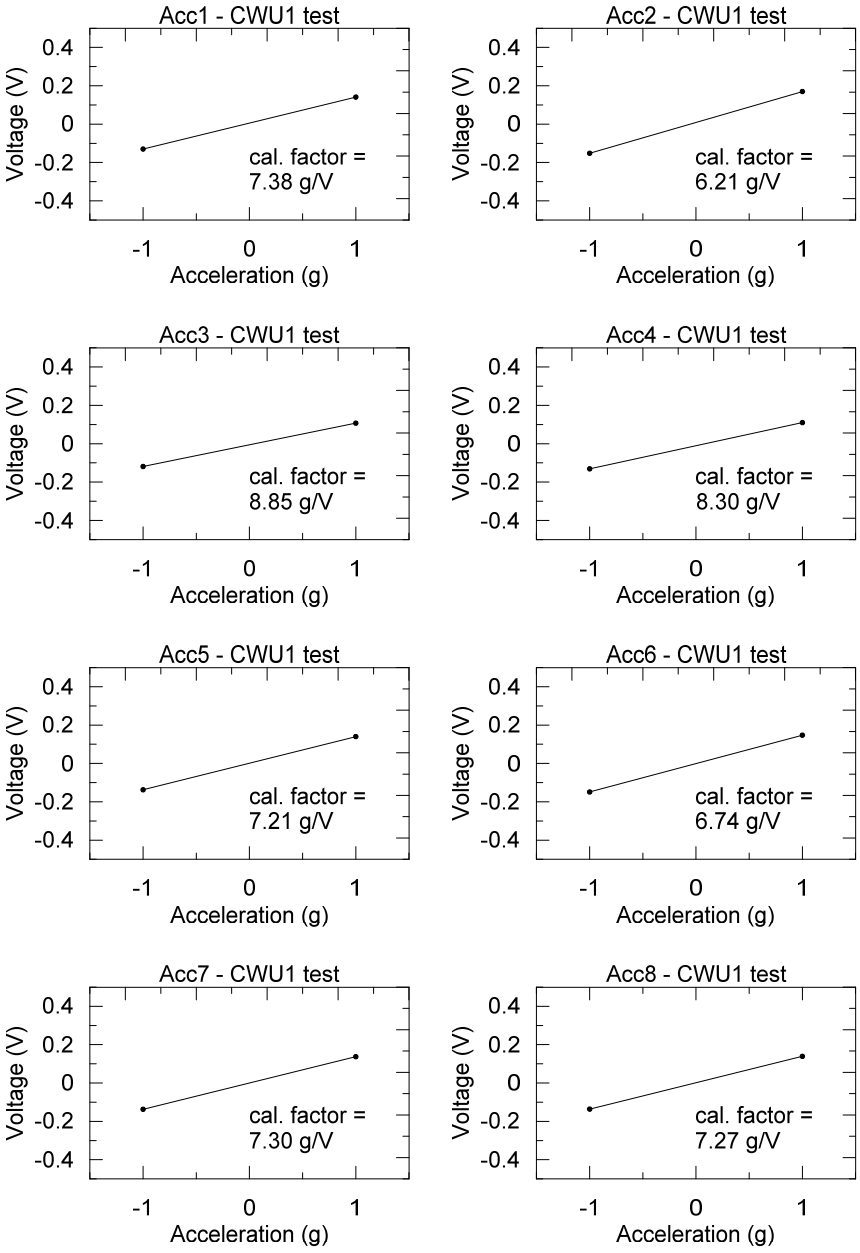

Figure A.1: Piezoelectric accelerometers calibration for test CWU1.

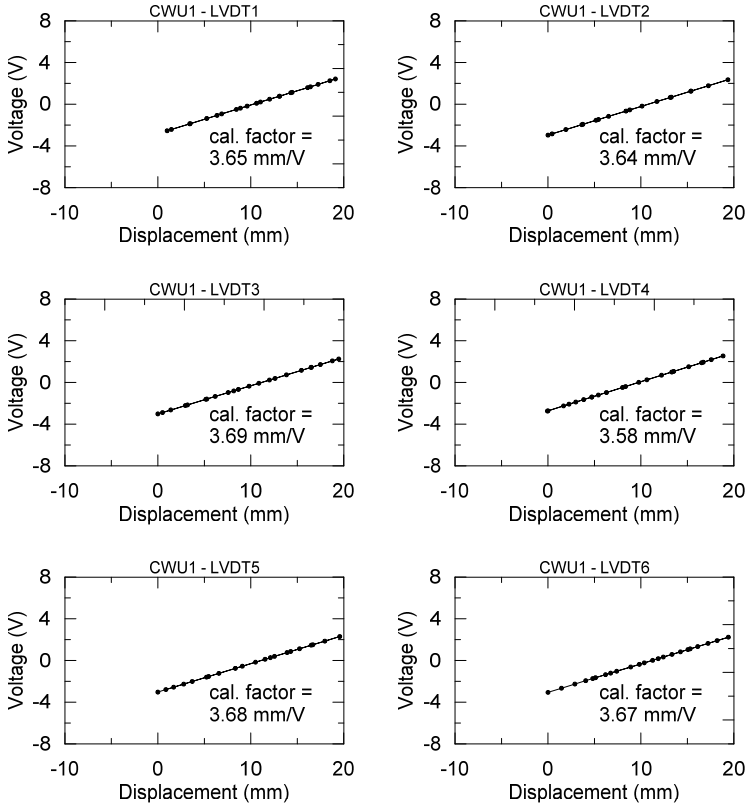

Figure A.2: LVDTs calibration for test CWU1.

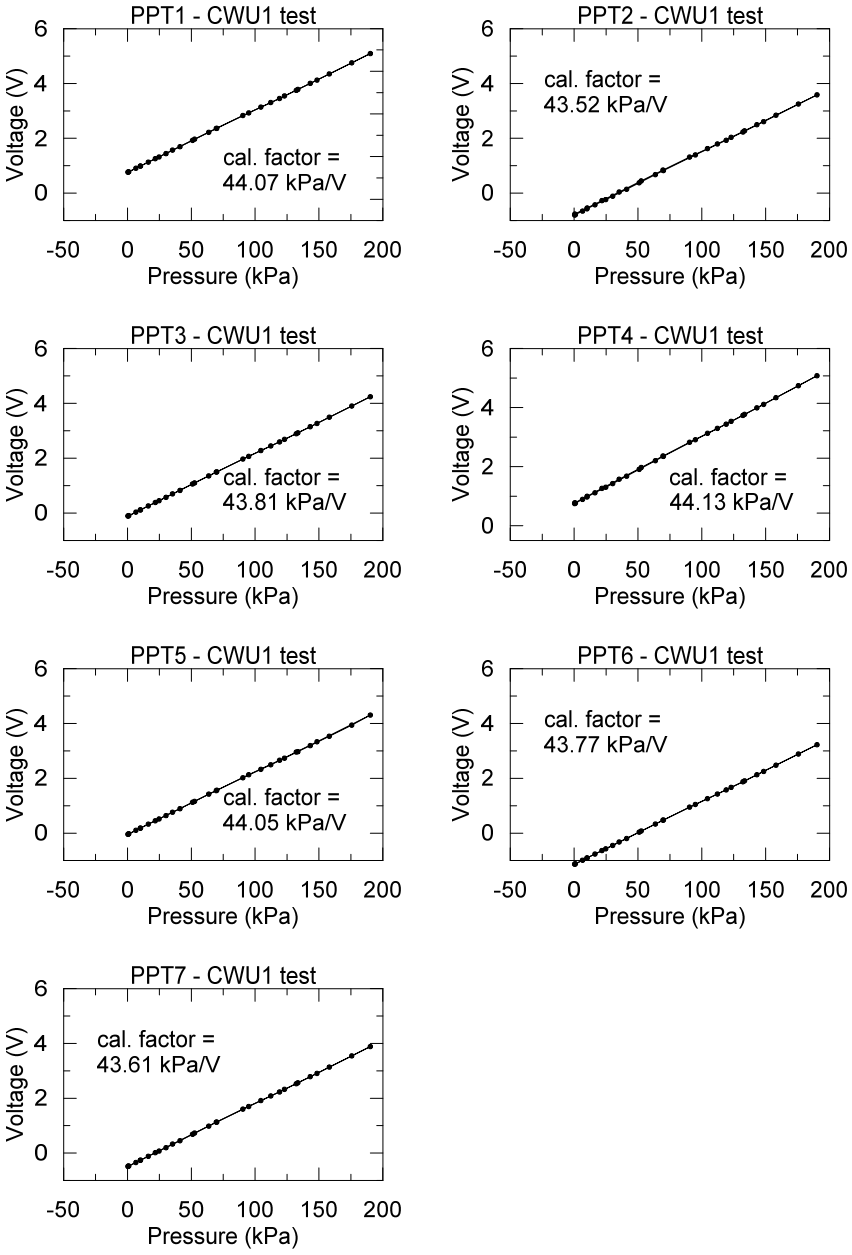

Figure A.3: Pore pressure transducers calibration for test CWU1.

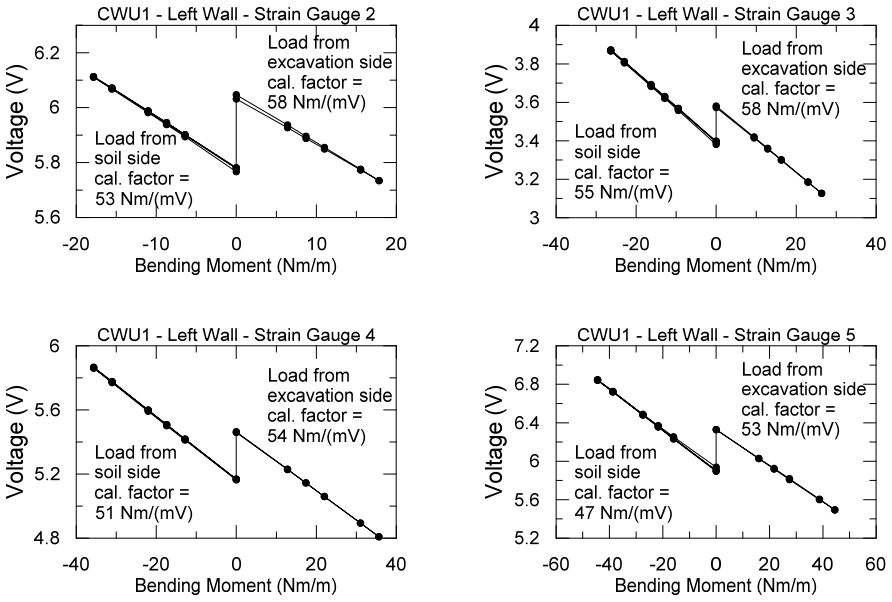

Figure A.4: Left wall strain gauges calibration for test CWU1.

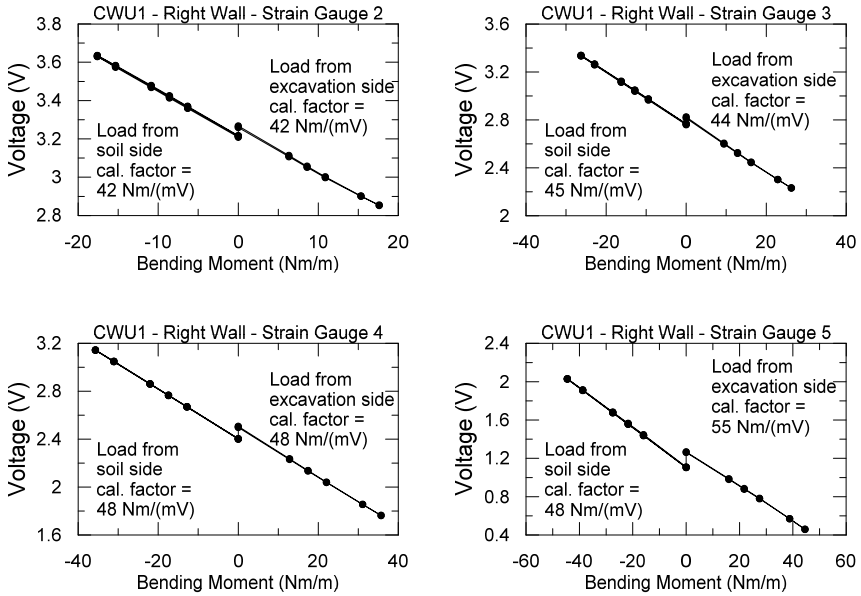

Figure A.5: Right wall strain gauges calibration for test CWU1.

Test PWU1

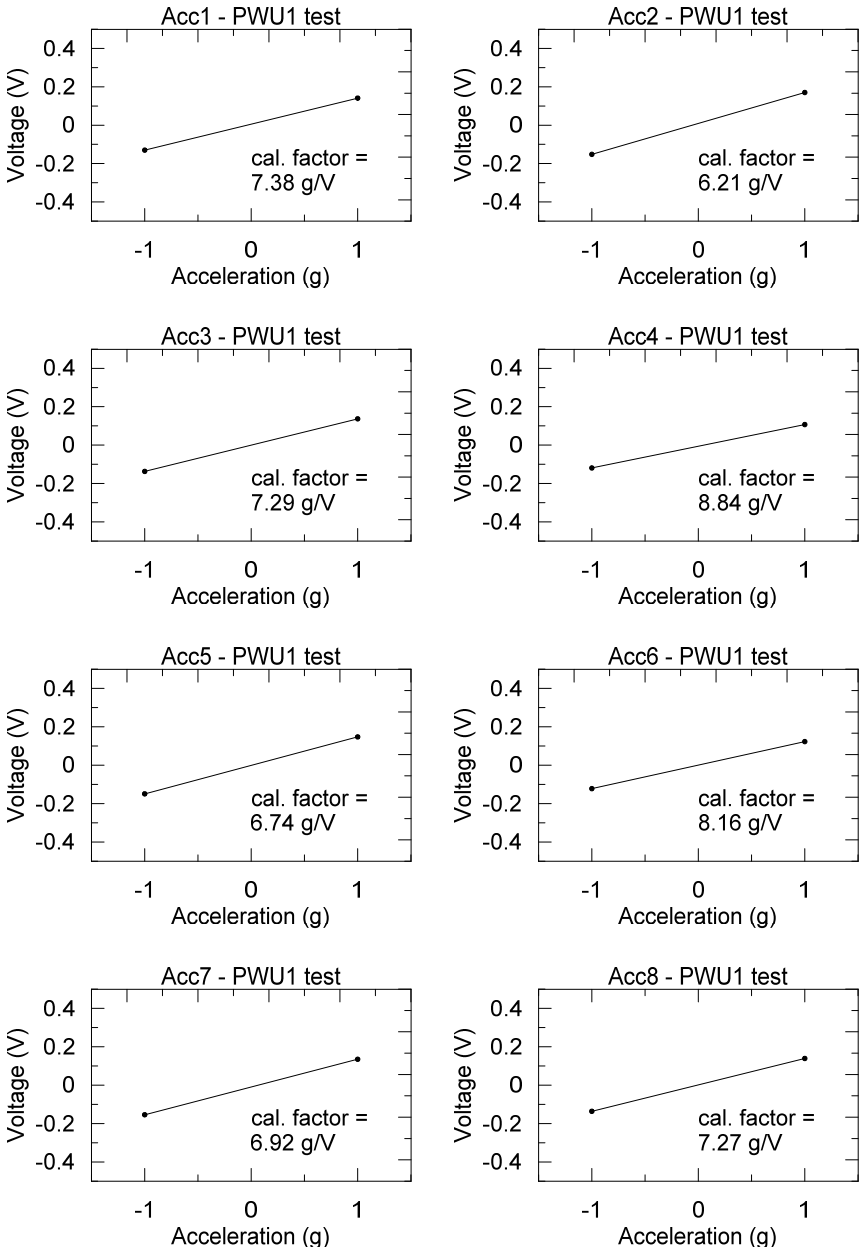

Figure A.6: Piezoelectric accelerometers calibration for test PWU1.

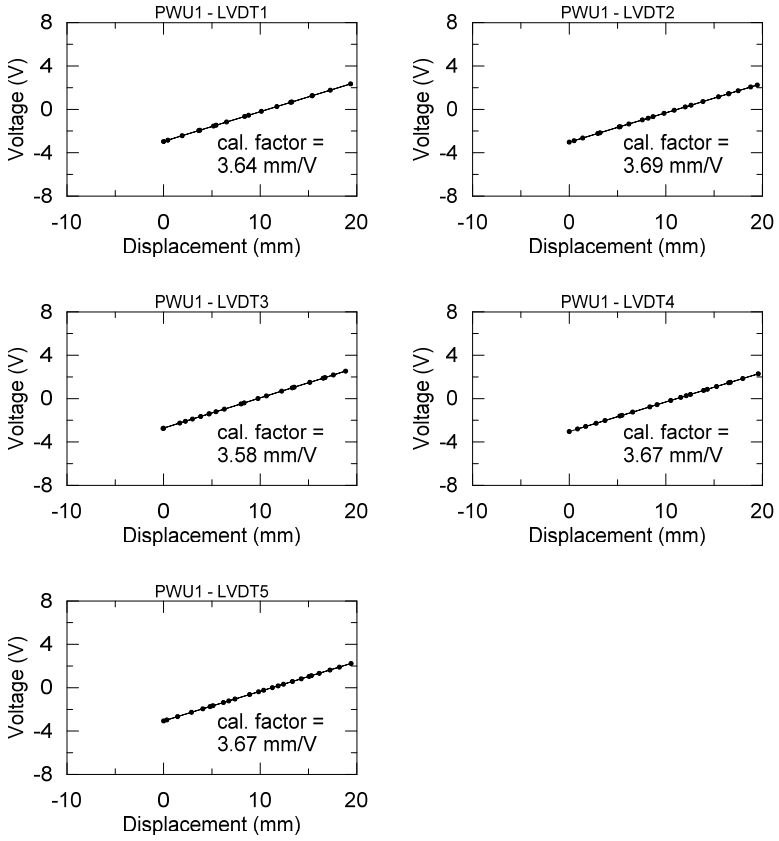

Figure A.7: LVDT calibration for test PWU1.

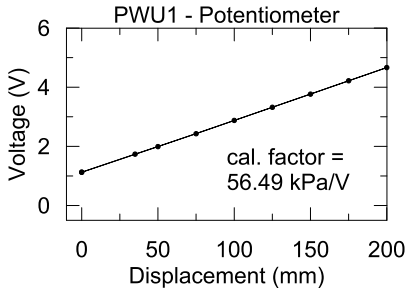

Figure A.8: Potentiometer calibration for test PWU1.

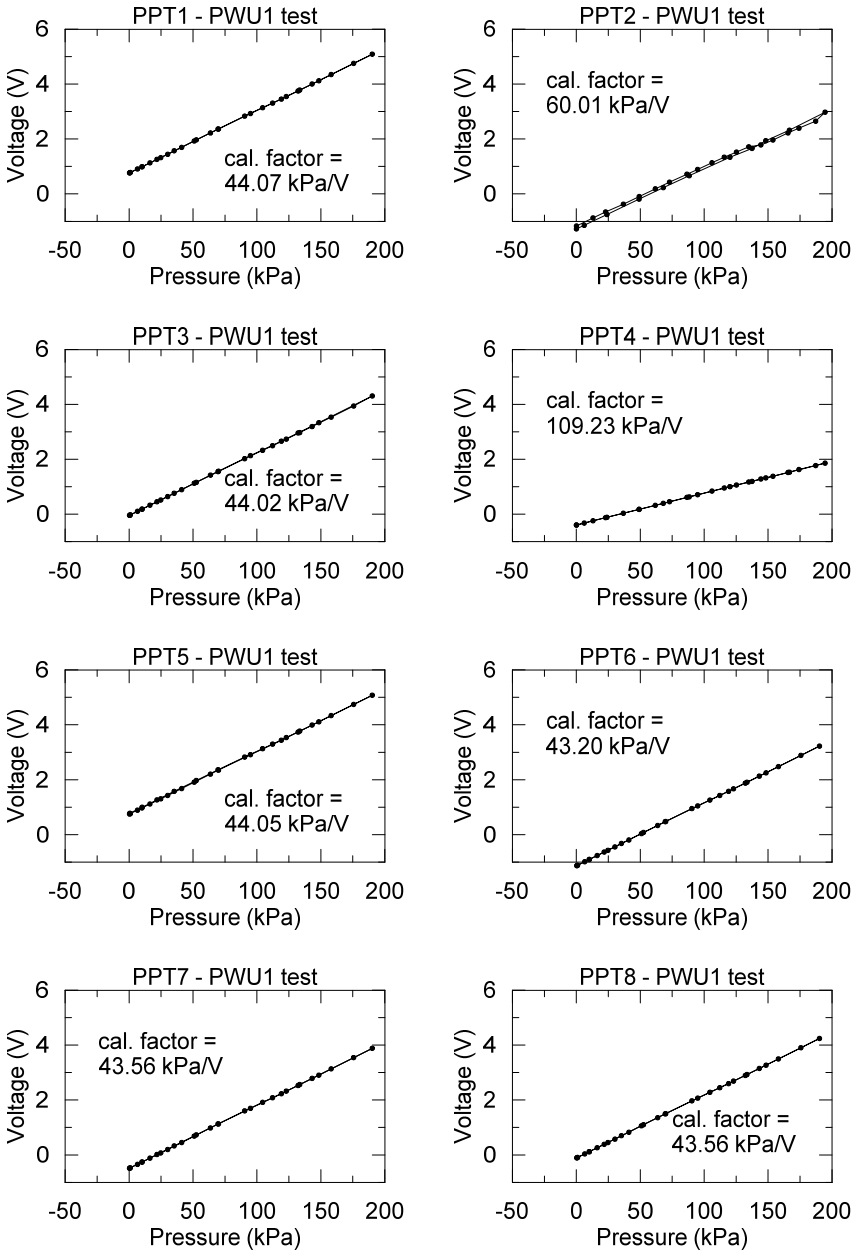

Figure A.9: Pore pressure transducers calibration for test PWU1.

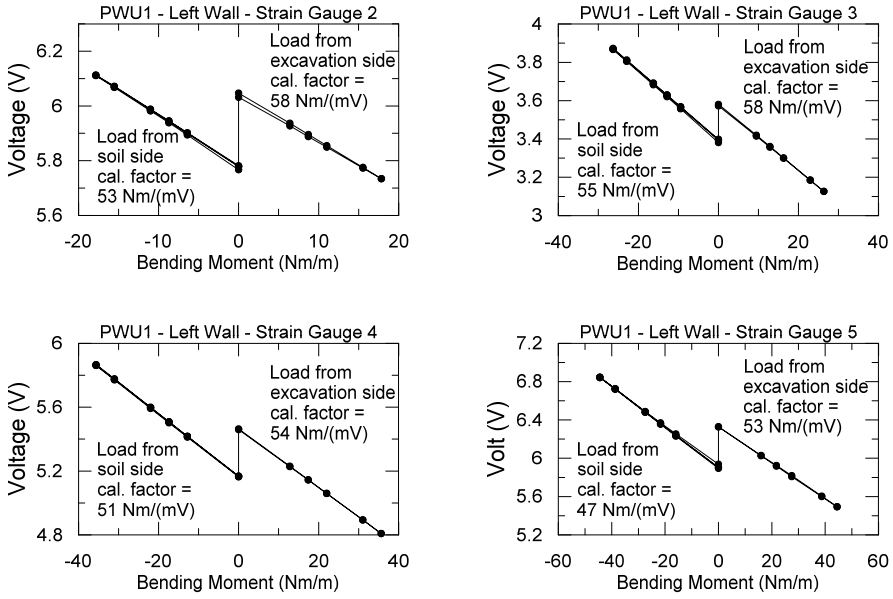

Figure A.10: Left wall strain gauges calibration for test PWU1.

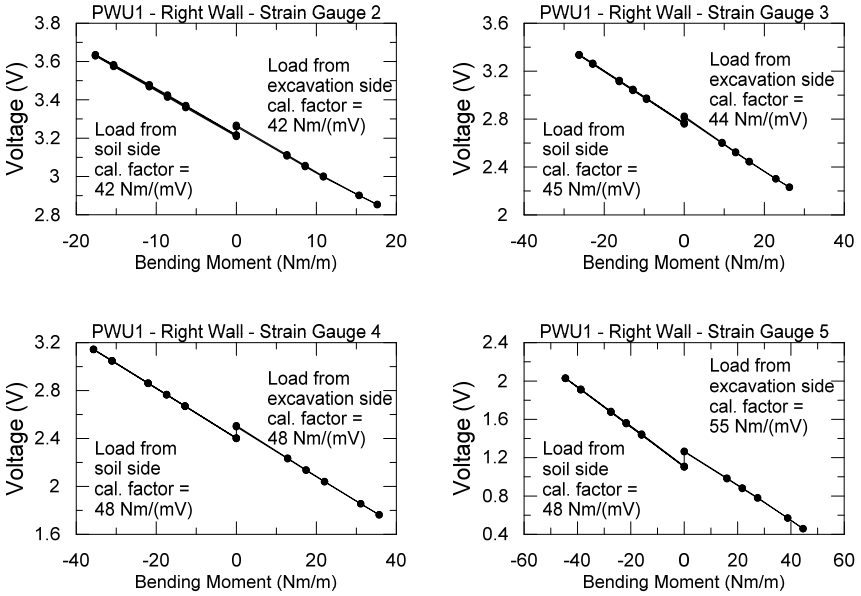

Figure A.11: Right wall strain gauges calibration for test PWU1.

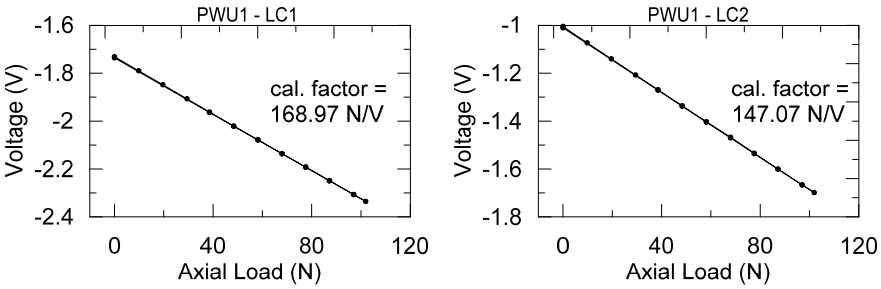

Figure A.12: Load cells calibration for test PWU1.

Test CWU2

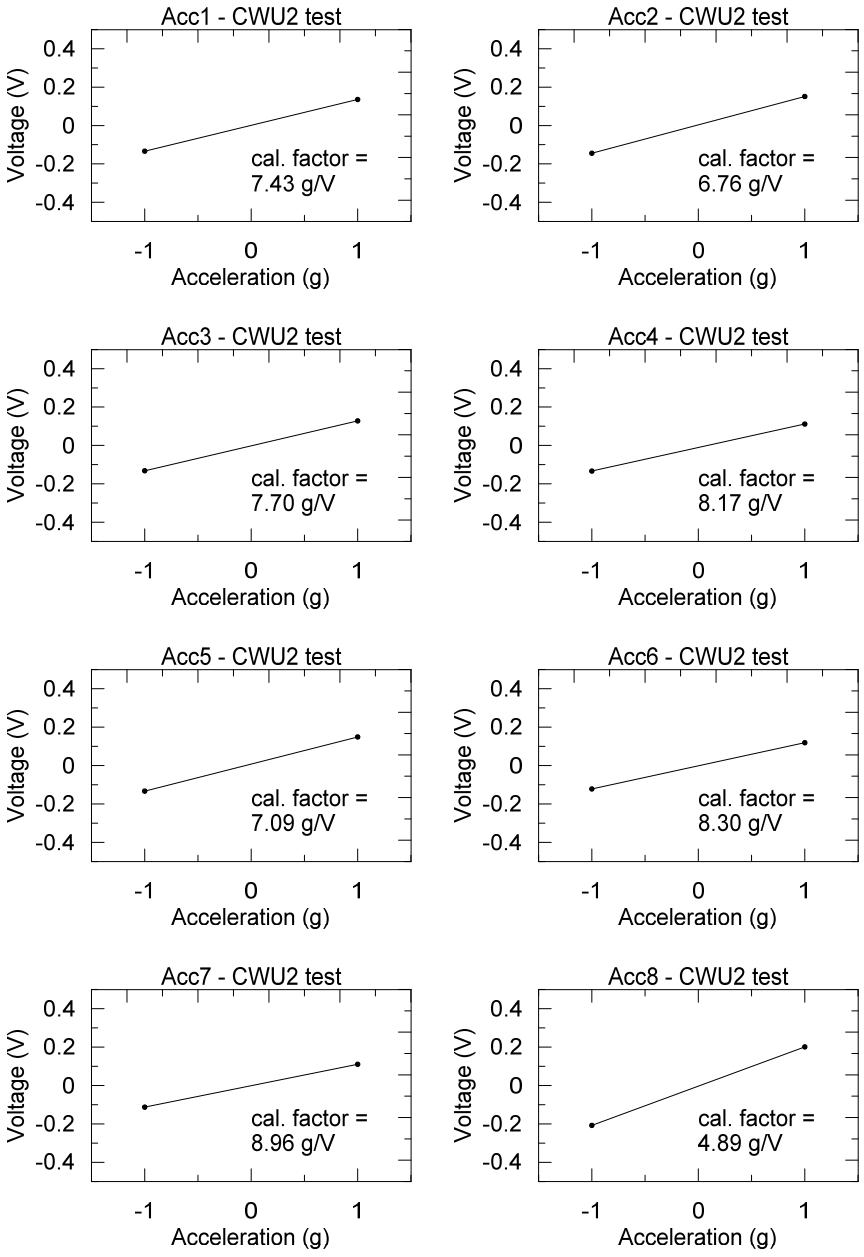

Figure A.13: Piezoelectric accelerometers calibration for test CWU2.

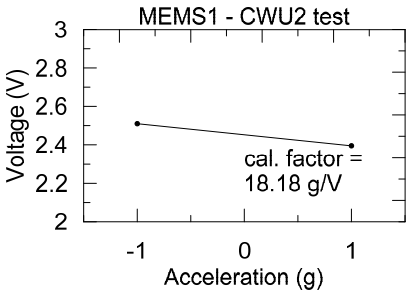

Figure A.14: MEMS accelerometers calibration for test CWU2.

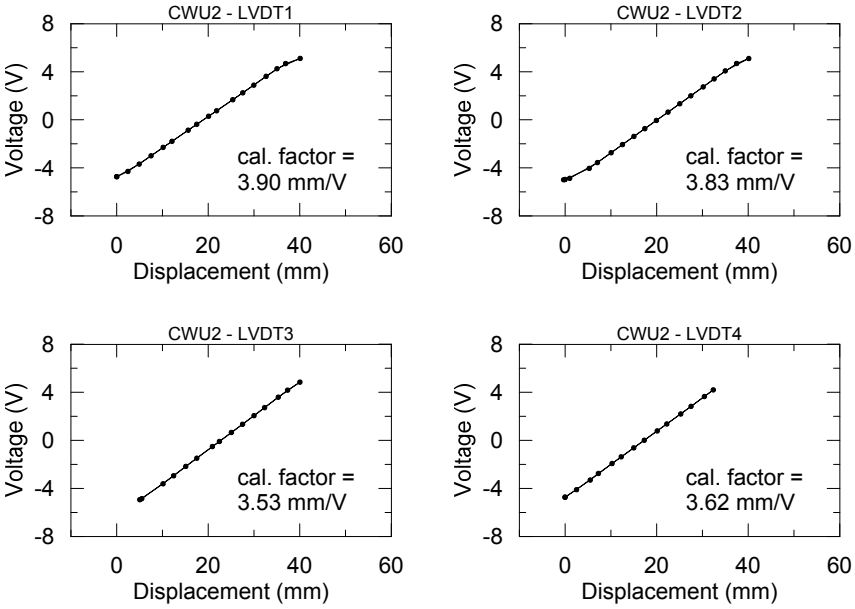

Figure A.15: LVDT calibration for test CWU2.

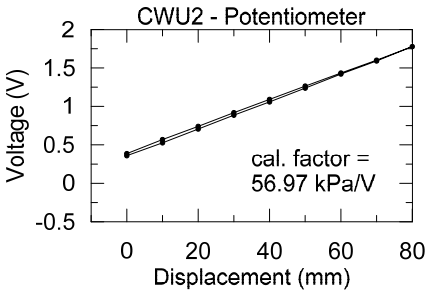

Figure A.16: Potentiometer calibration for test CWU2.

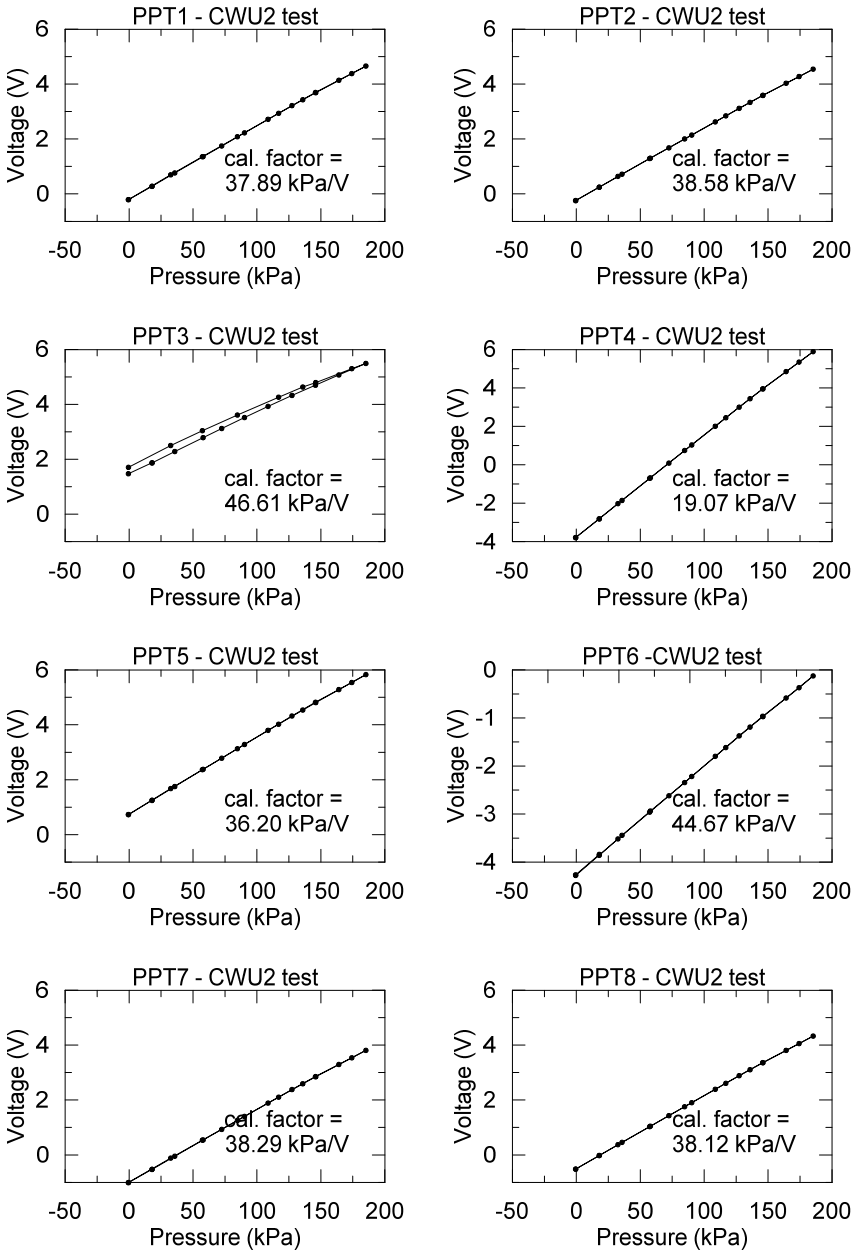

Figure A.17: Pore pressure transducers calibration for test CWU2.

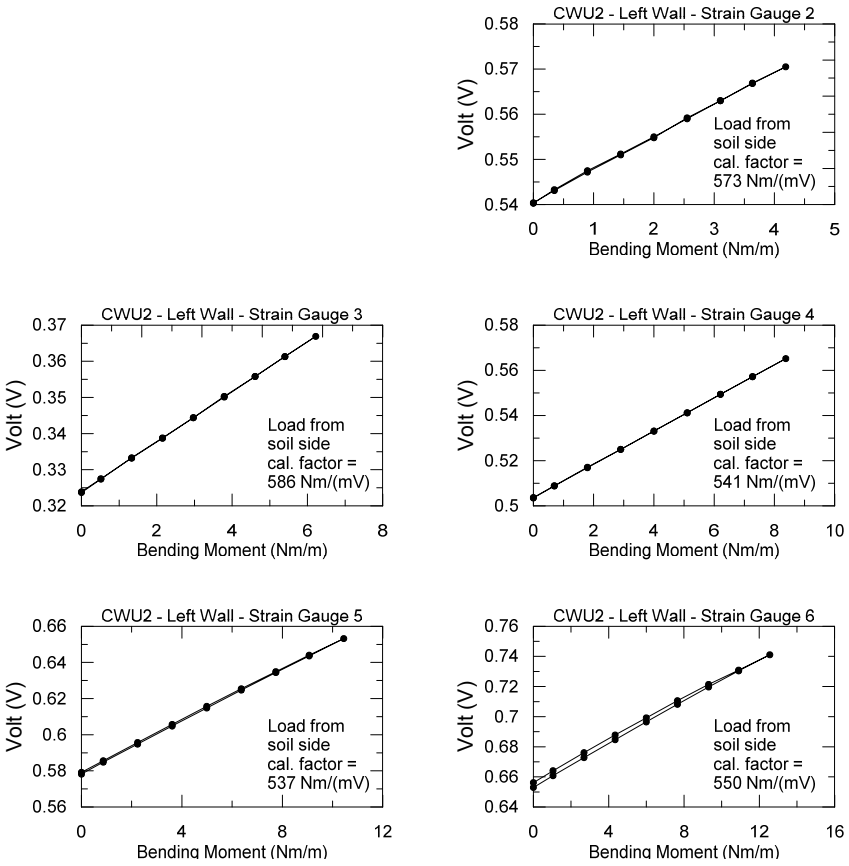

Figure A.18: Left wall strain gauges calibration for test CWU2.

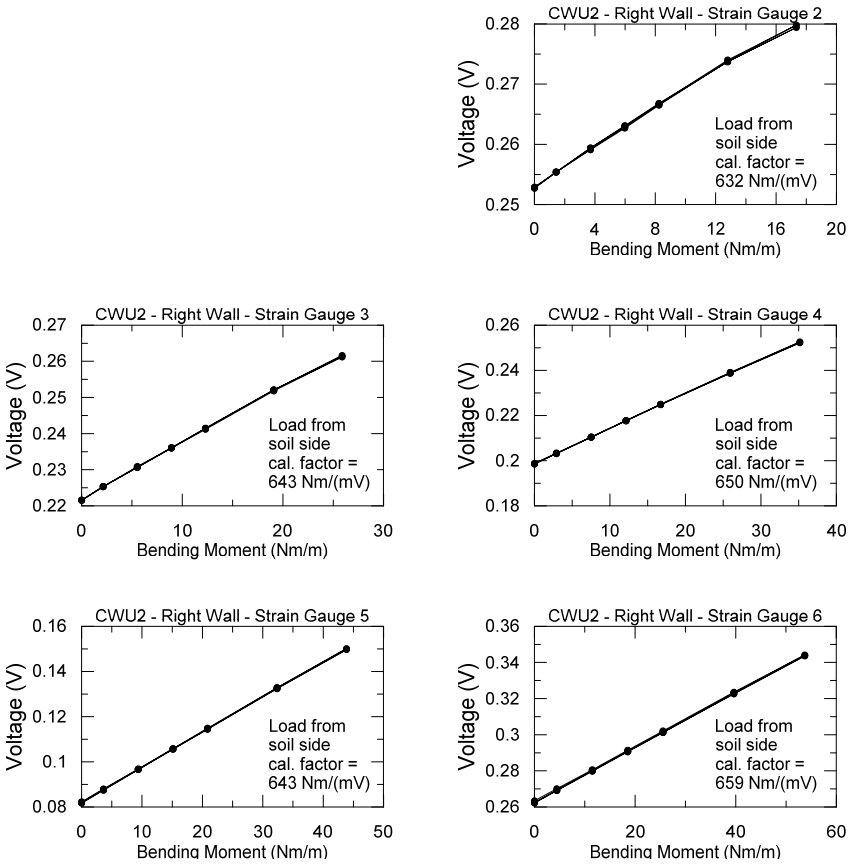

Figure A.19: Right wall strain gauges calibration for test CWU2.

Test PWU2

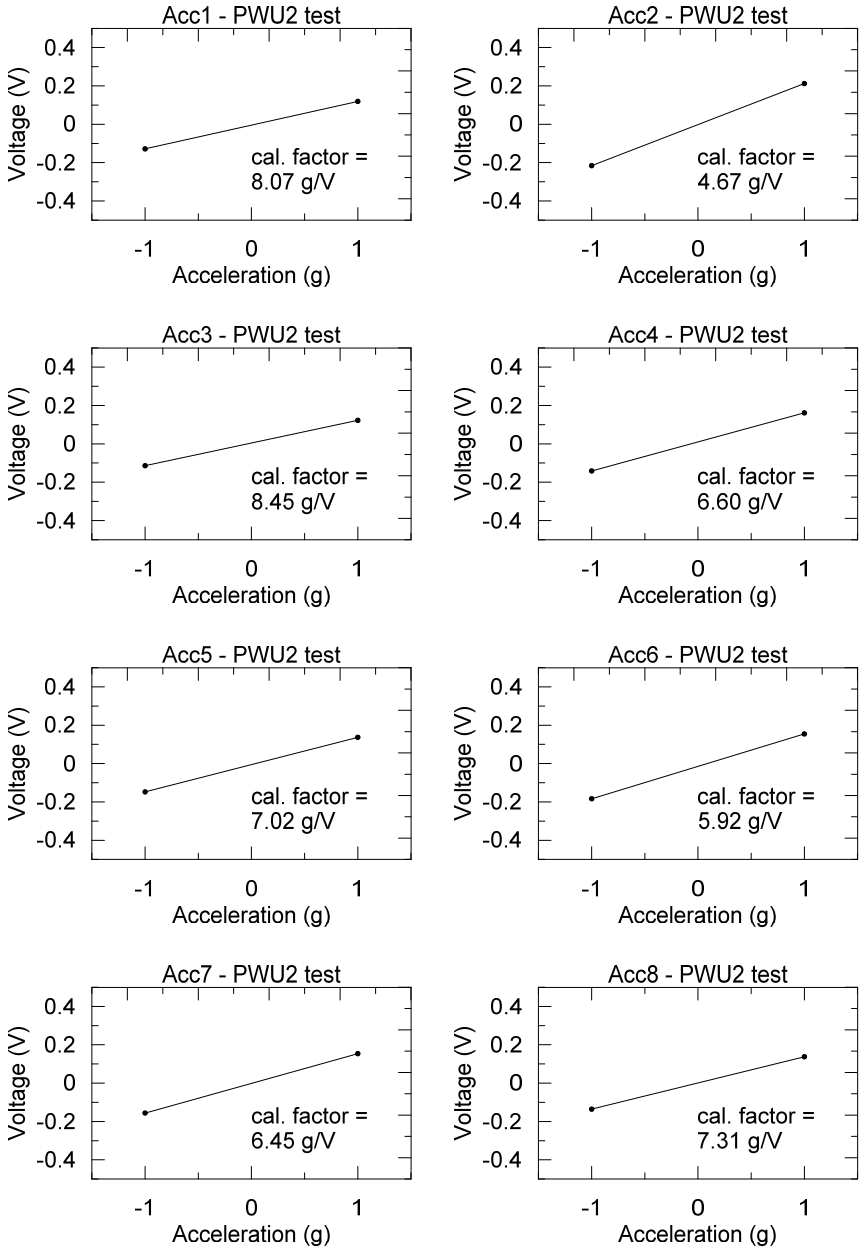

Figure A.20: Piezoelectric accelerometers calibration for test PWU2.

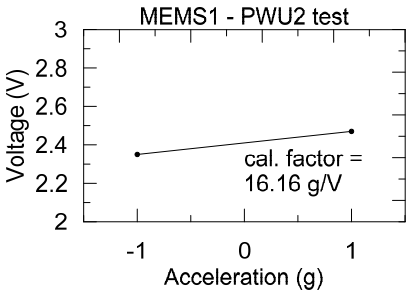

Figure A.21: MEMS accelerometer calibration for test PWU2.

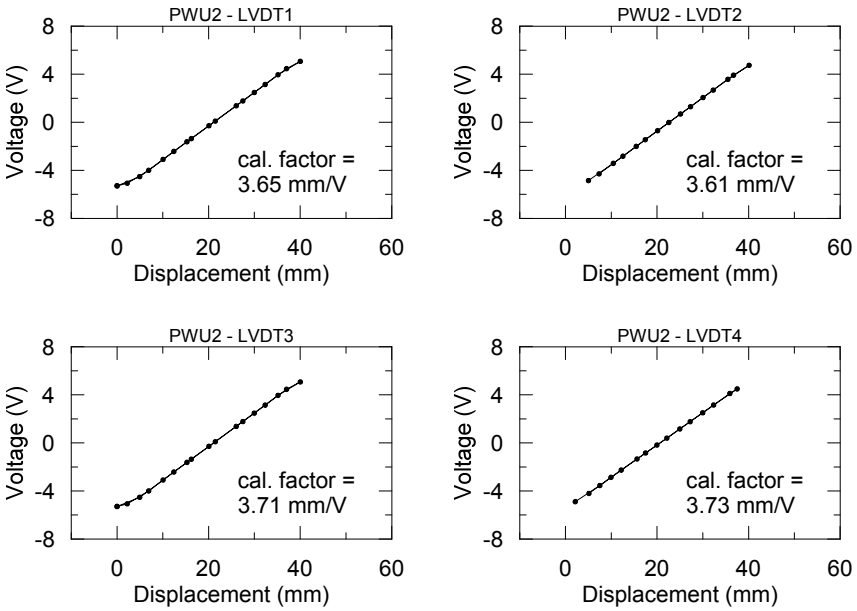

Figure A.22: LVDT calibration for test PWU2.

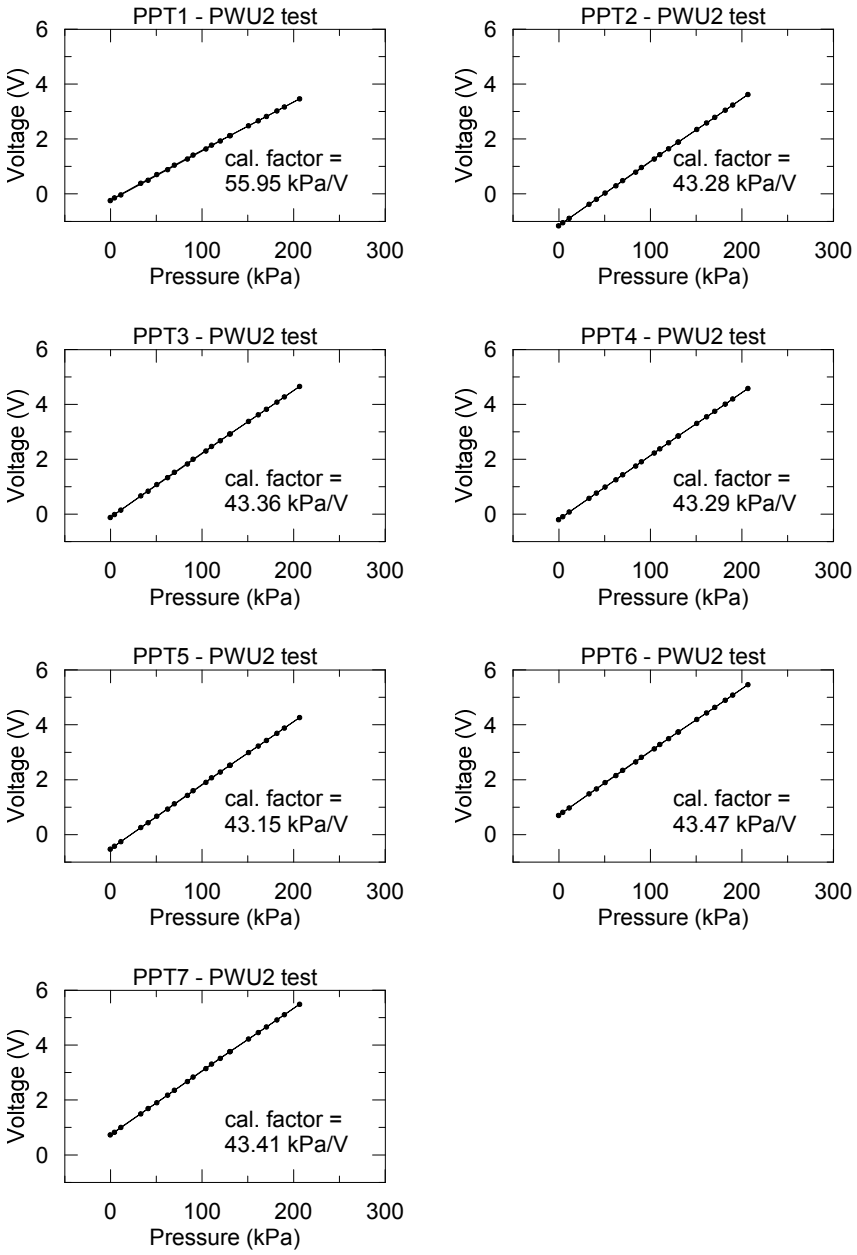

Figure A.23: Pore pressure transducers calibration for test PWU2.

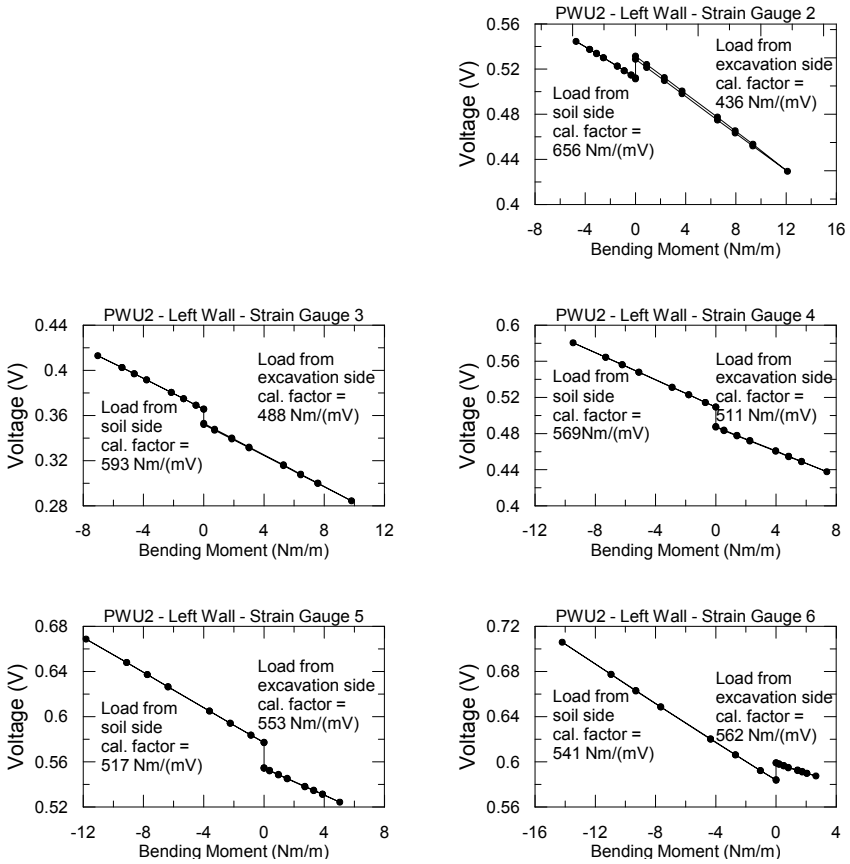

Figure A.24: Left wall strain gauges calibration for test PWU2.

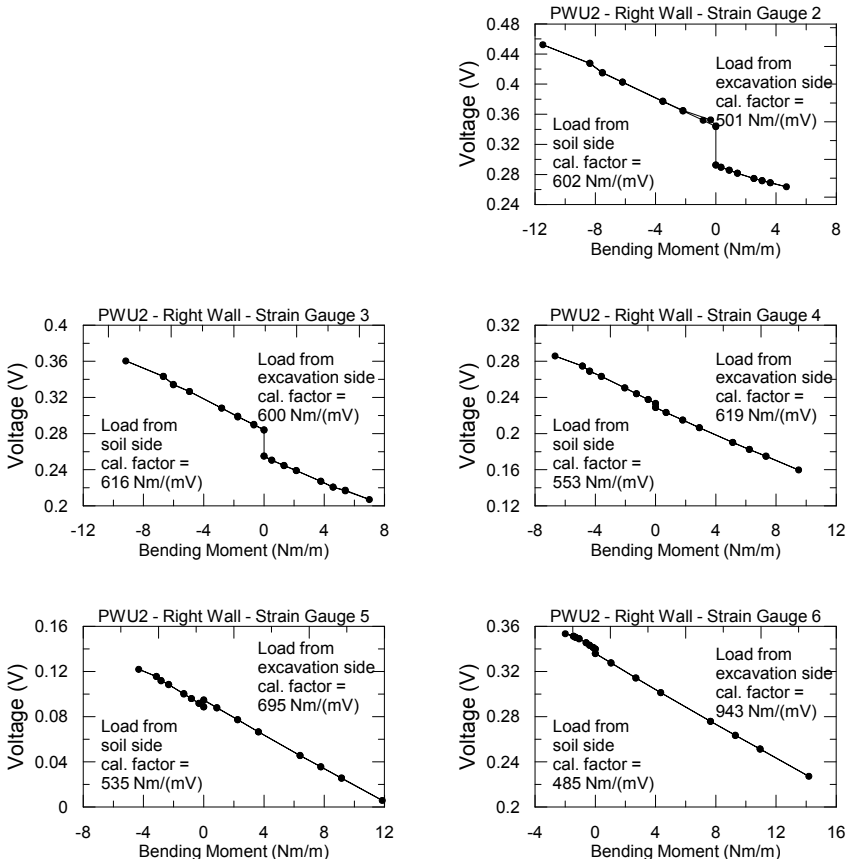

Figure A.25: Right wall strain gauges calibration for test PWU2.

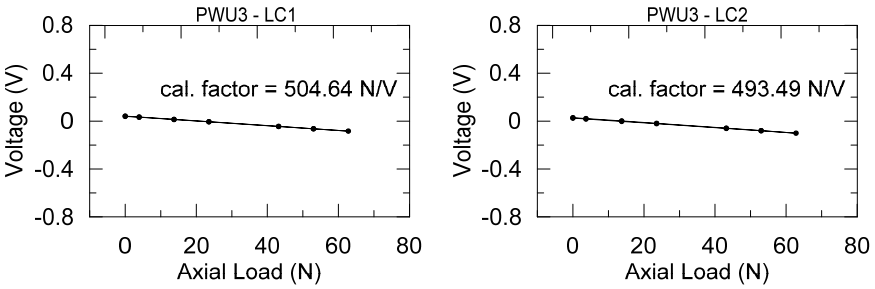

Figure A.26: Load cells calibration for test PWU2.

Test CWU3

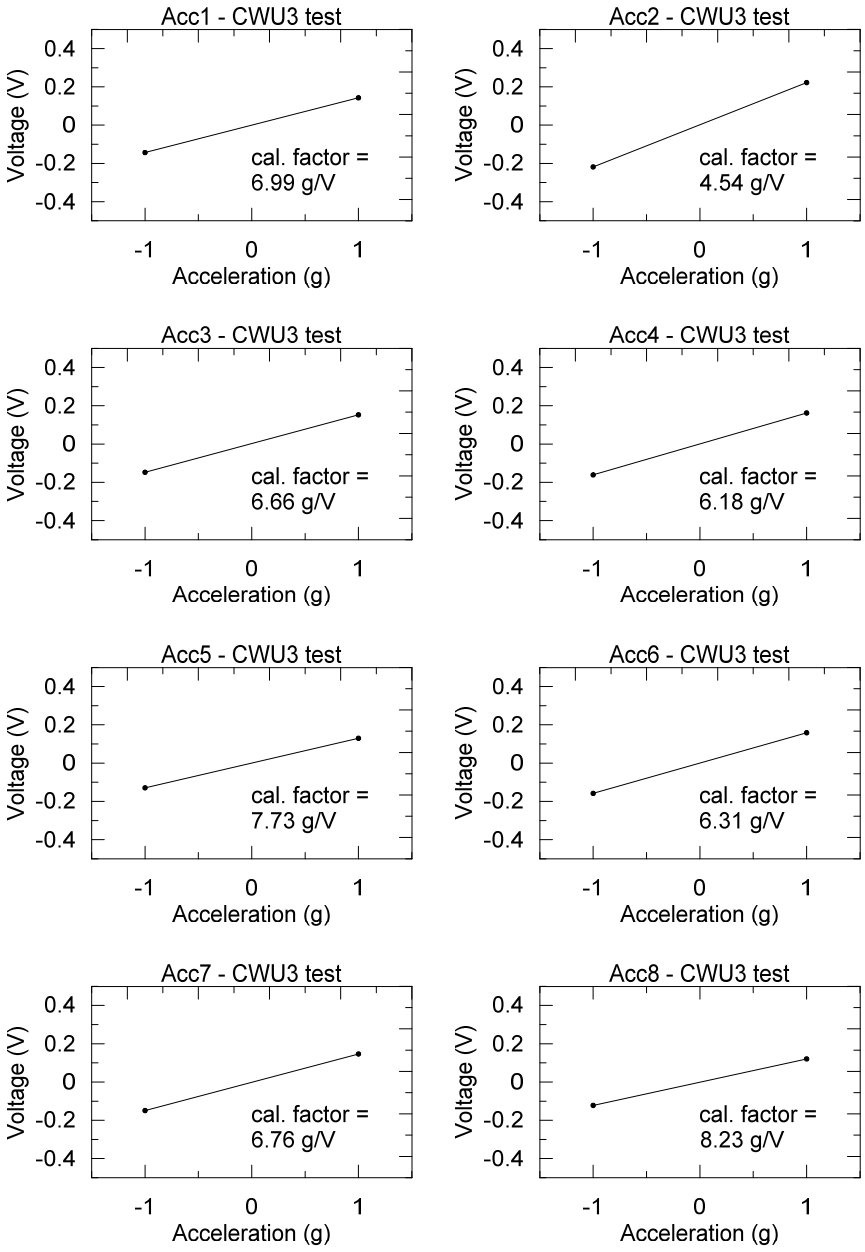

Figure A.27: Piezoelectric accelerometers calibration for test CWU3.

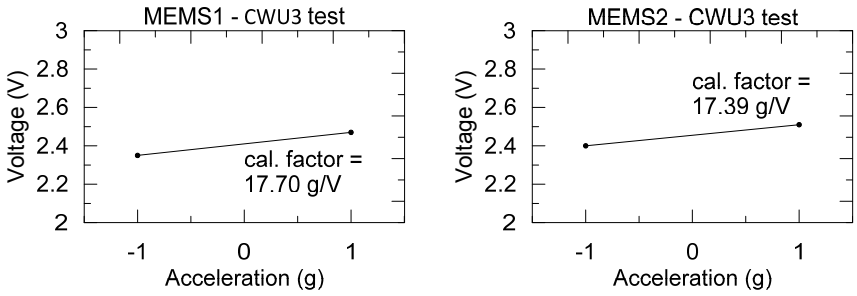

Figure A.28: MEMS accelerometer calibration for test CWU3.

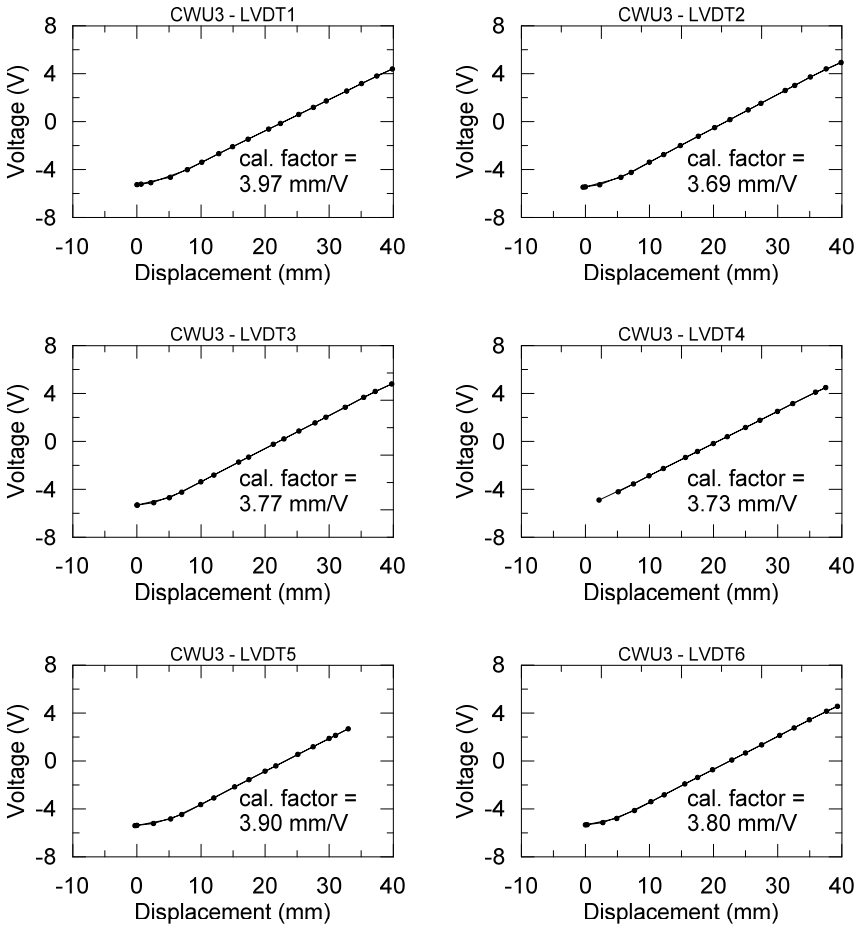

Figure A.29: LVDT calibration for test CWU3.

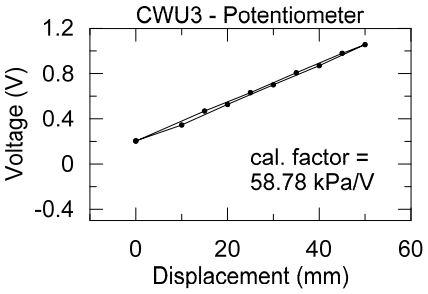

Figure A.30: Potentiometer calibration for test CWU3.

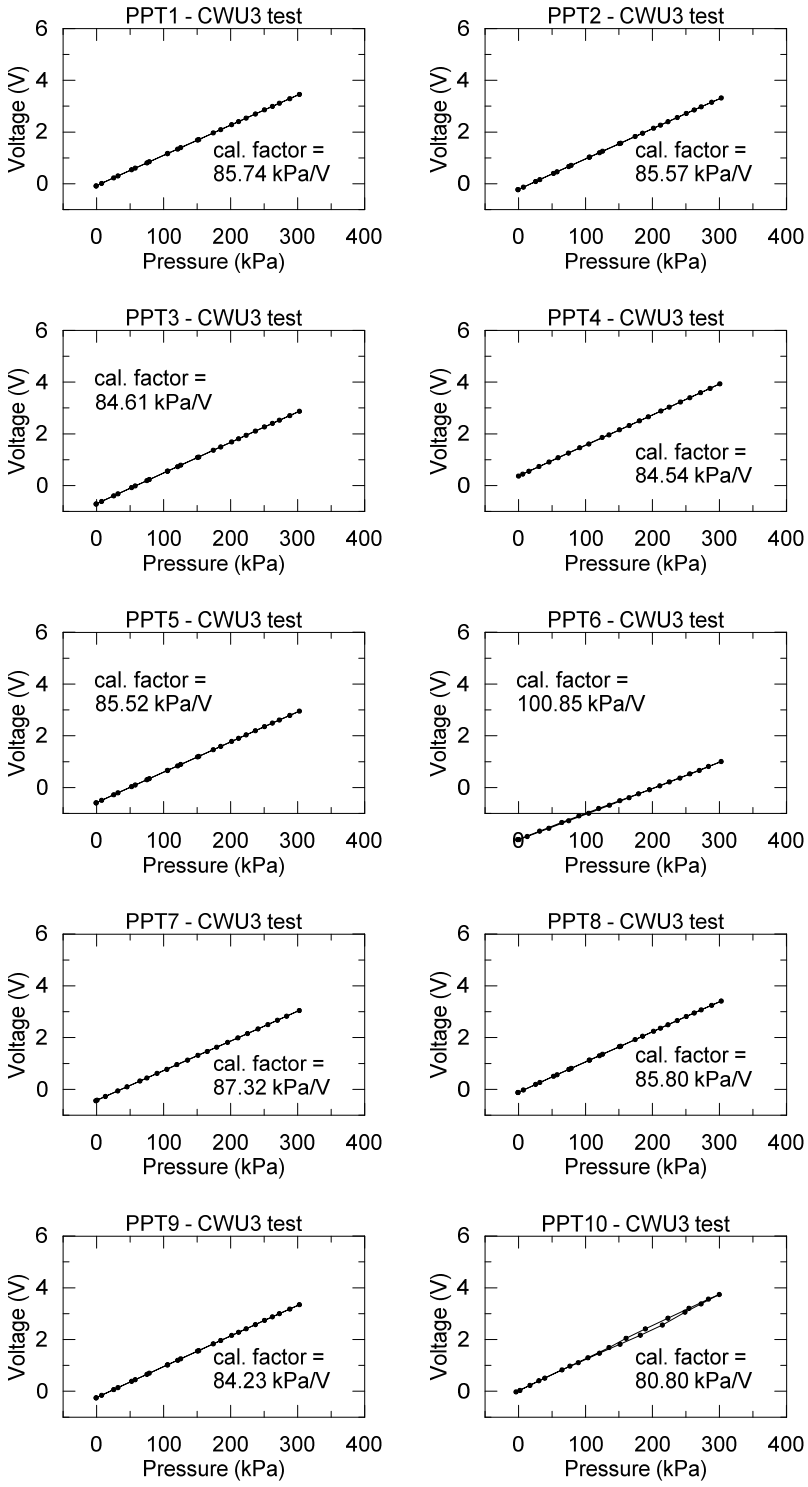

Figure A.31: Pore pressure transducers calibration for test CWU3.

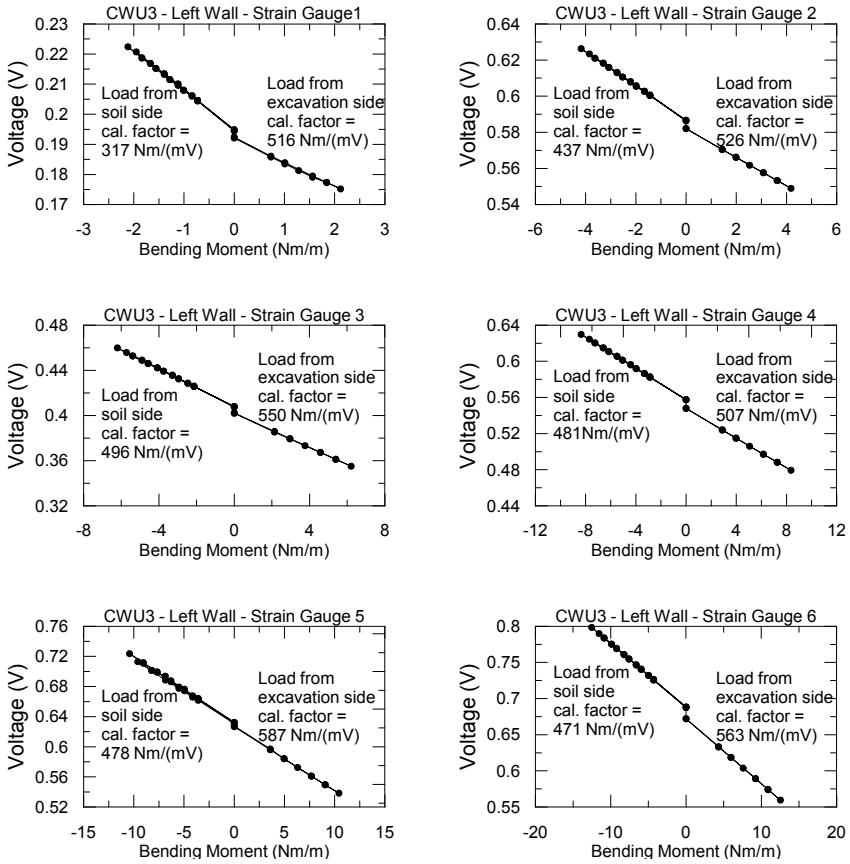

Figure A.32: Left wall strain gauges calibration for test CWU3.

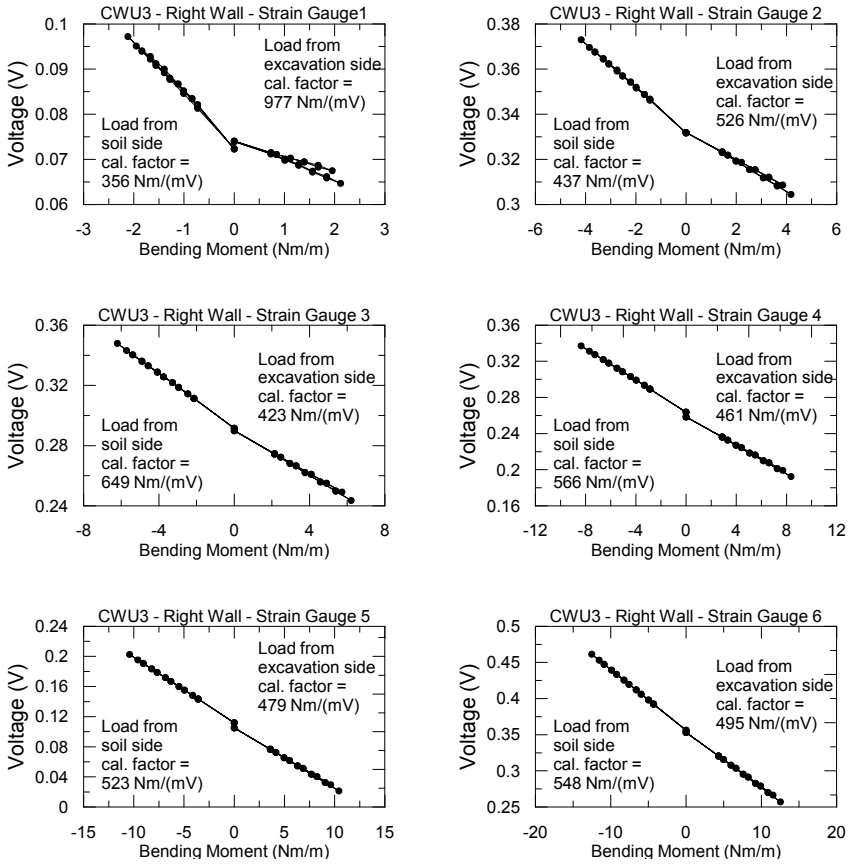

Figure A.33: Right wall strain gauges calibration for test CWU3.

Test PWU3

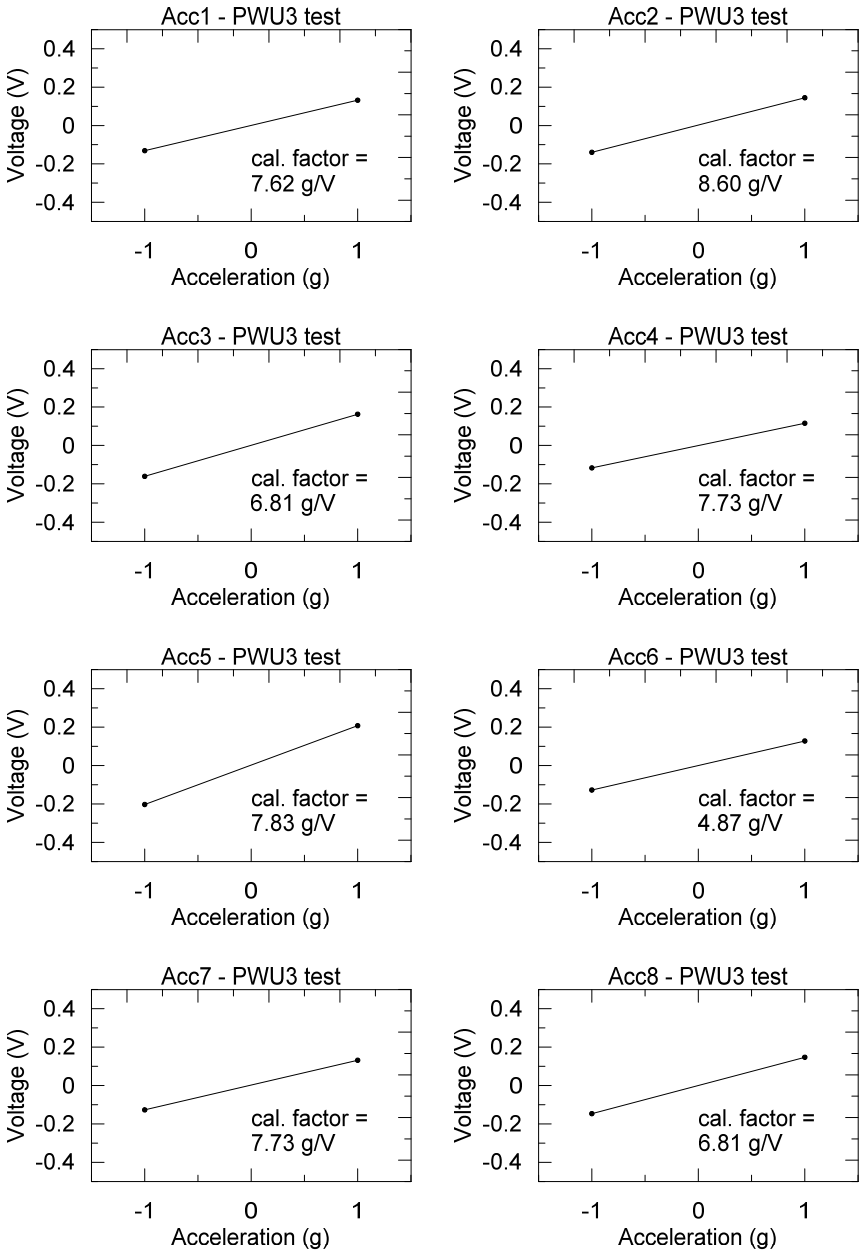

Figure A.34: Piezoelectric accelerometers calibration for test PWU3.

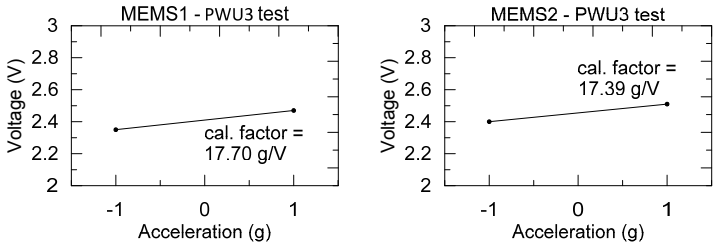

Figure A.35: MEMS accelerometers calibration for test PWU3.

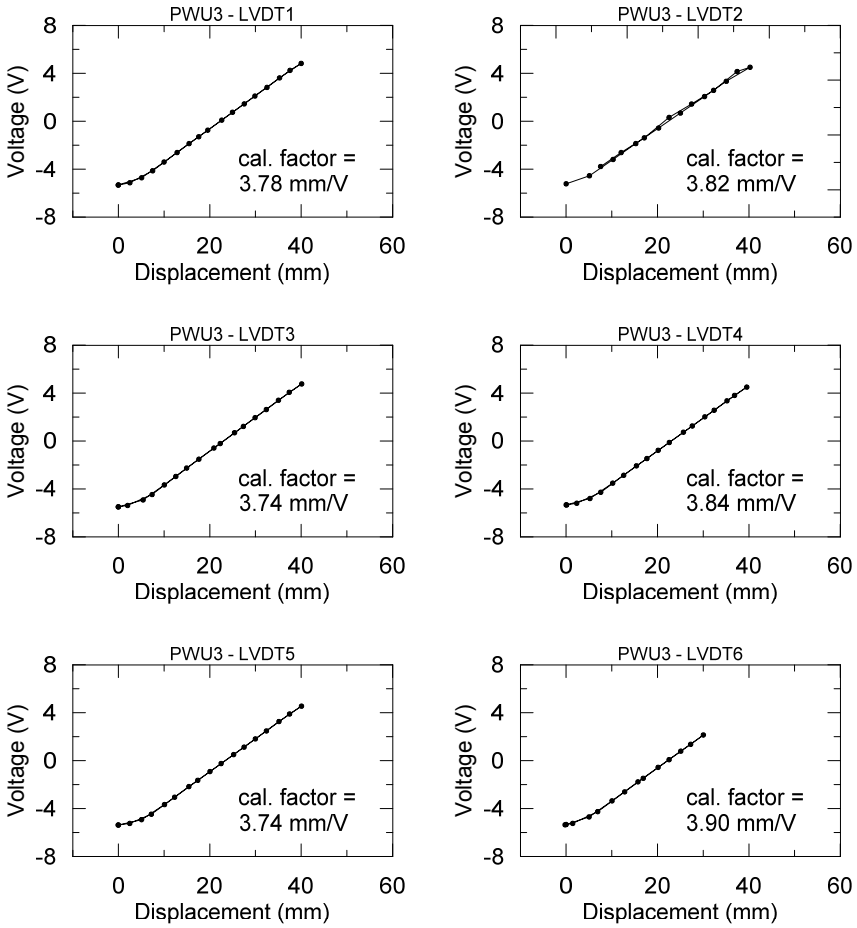

Figure A.36: LVDTs calibration for test PWU3.

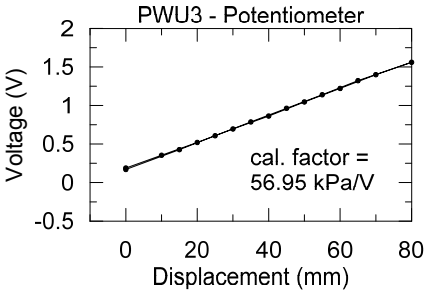

Figure A.37: Potentiometer calibration for the test PWU3.

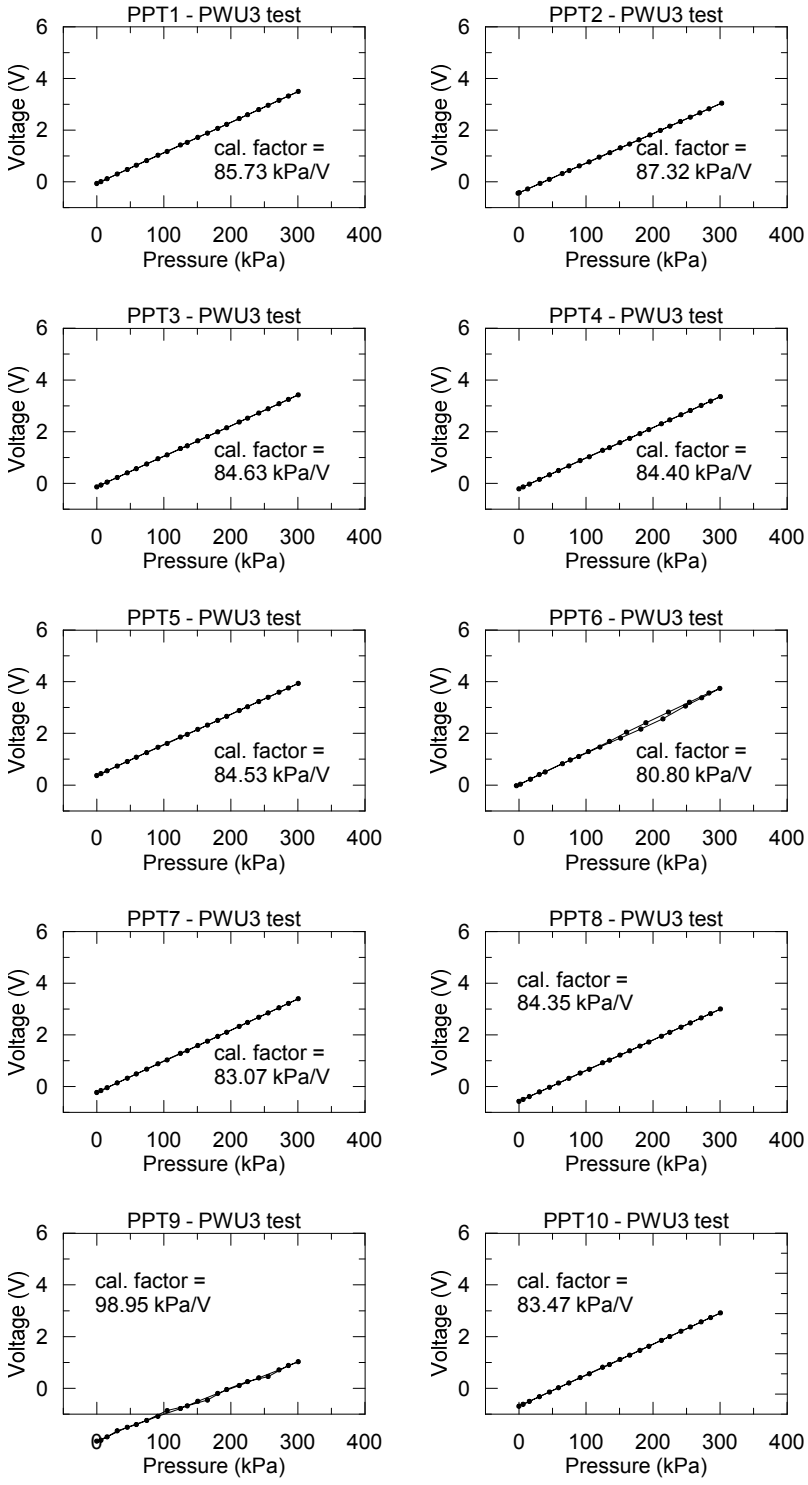

Figure A.38: Pore pressure transducers calibration for test PWU3.

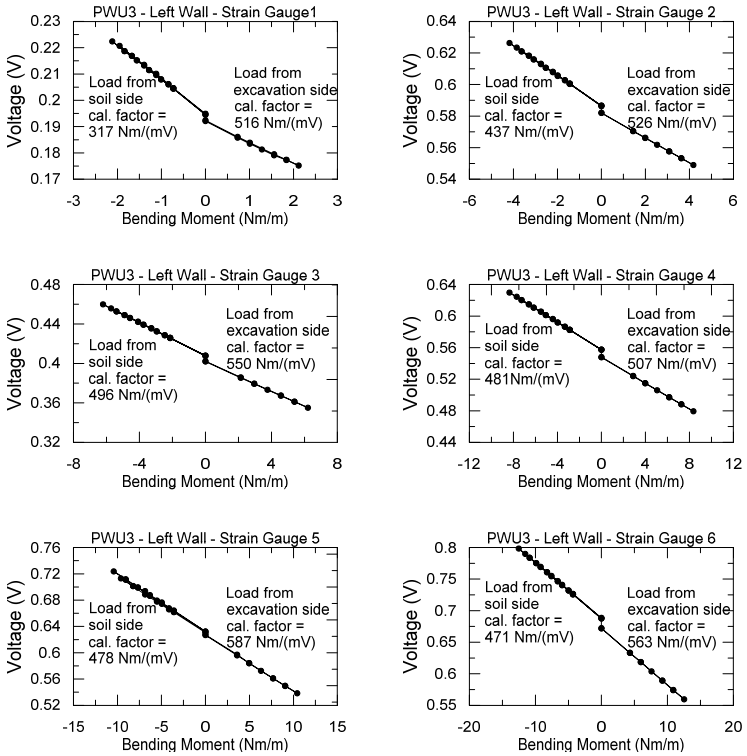

Figure A.39: Left wall strain gauges calibration for the test PWU3.

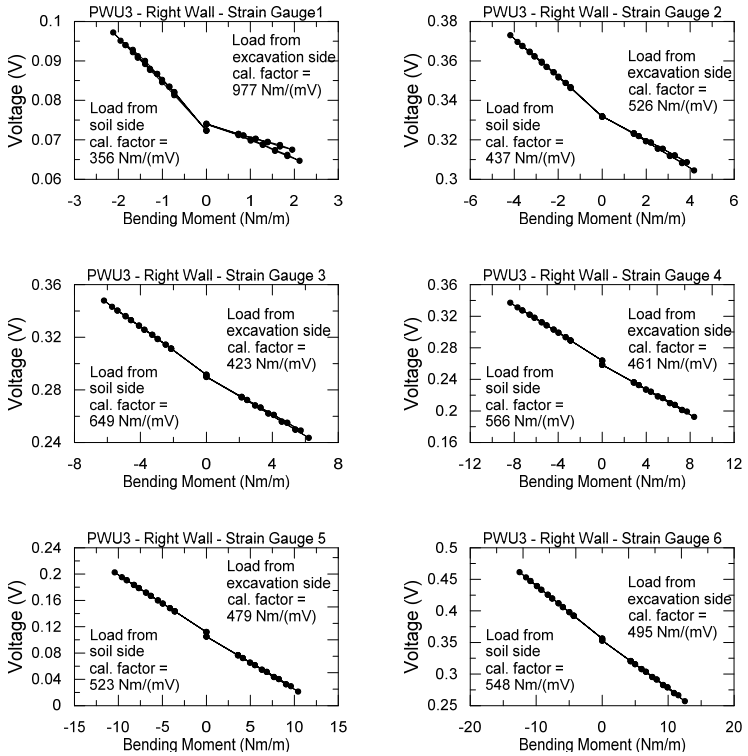

Figure A.40: Right wall strain gauges calibration for test PWU3.

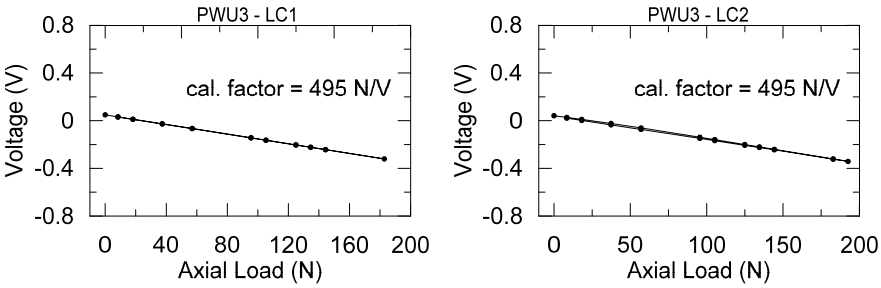

Figure A.41: Load cells calibration for test PWU3.

Test CWU4

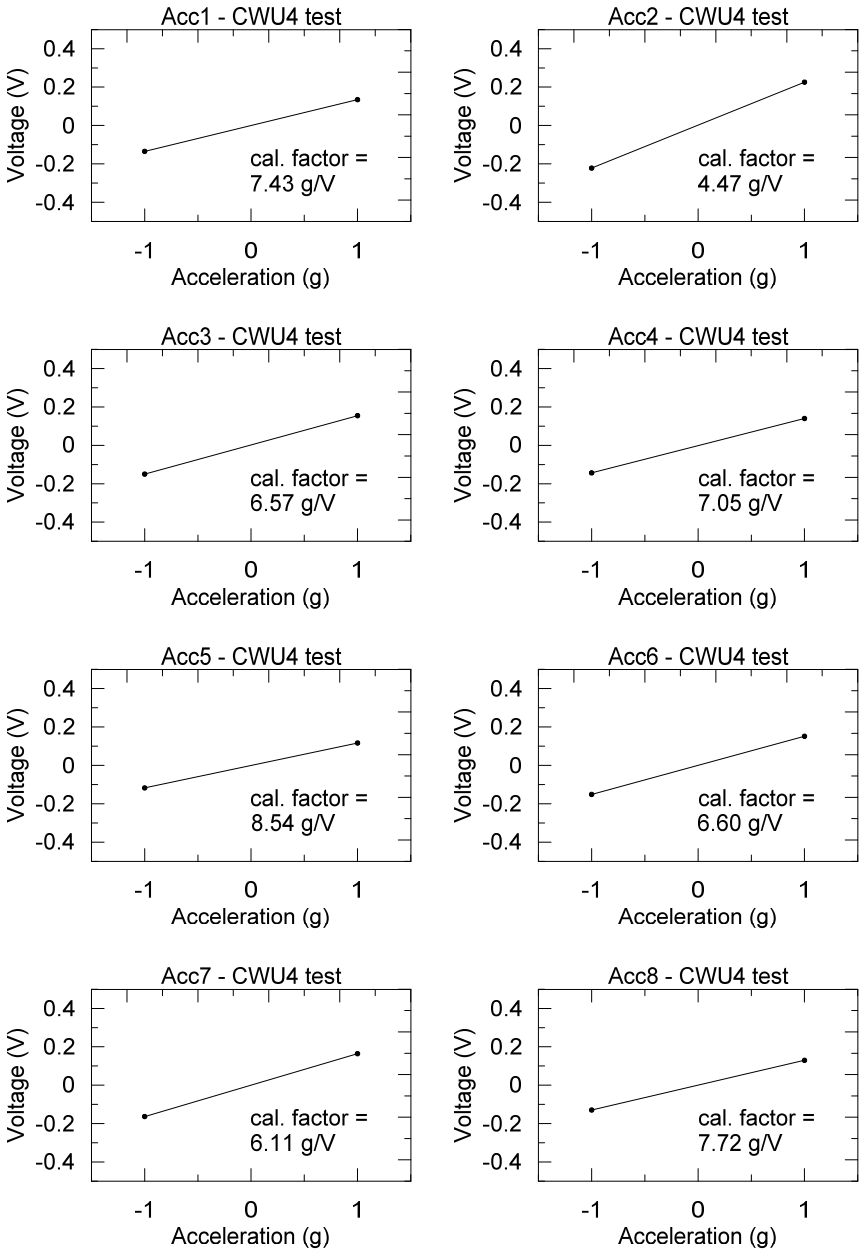

Figure A.42: Piezoelectric accelerometers transducers calibration for test CWU4.

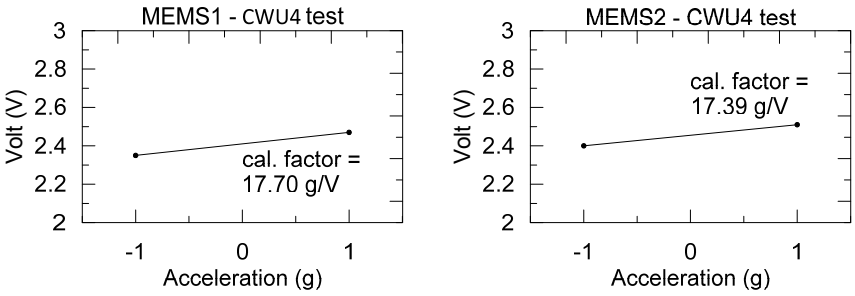

Figure A.43: MEMS accelerometers transducers calibration for test CWU4.

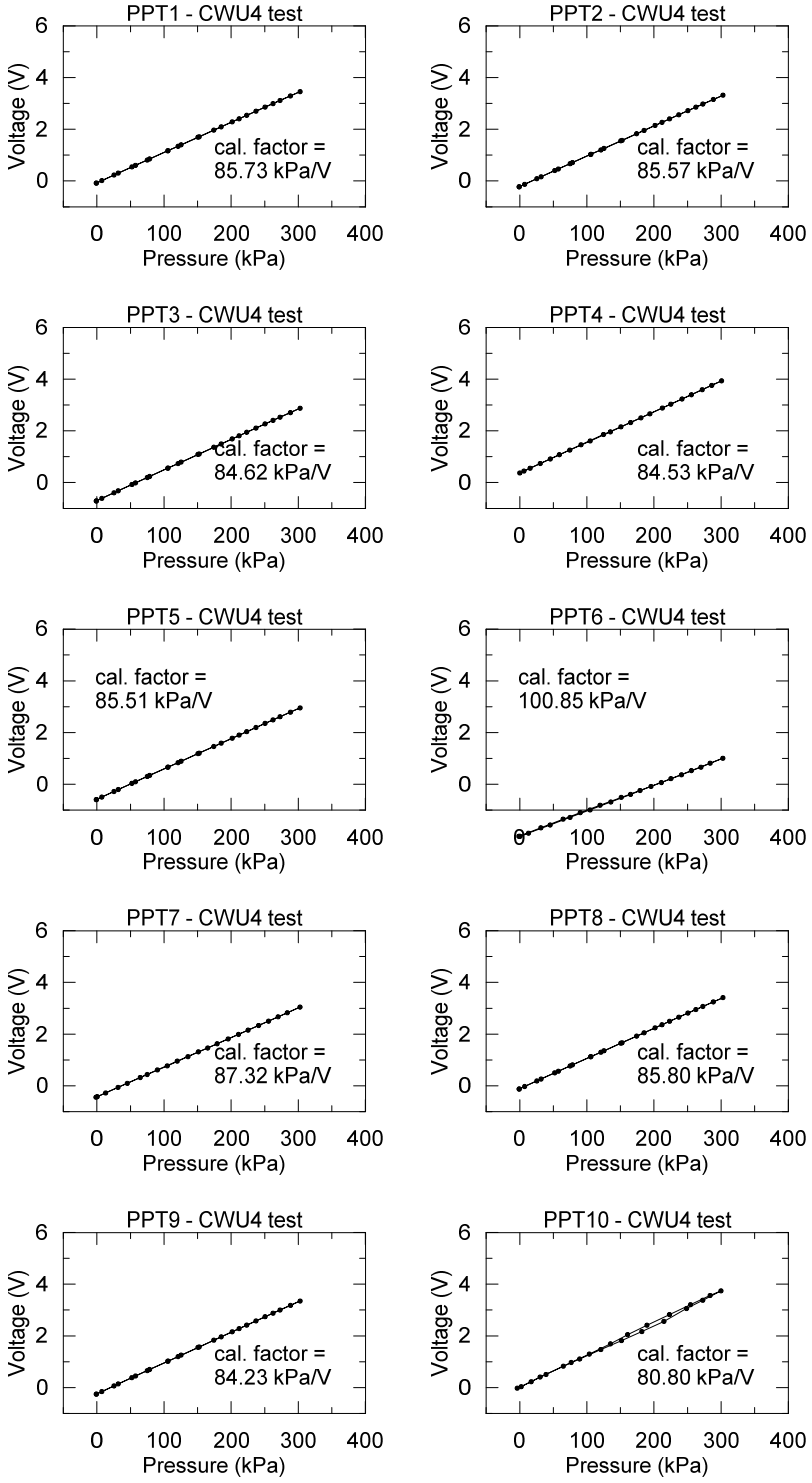

Figure A.44: Pore pressure transducers calibration for test CWU4.

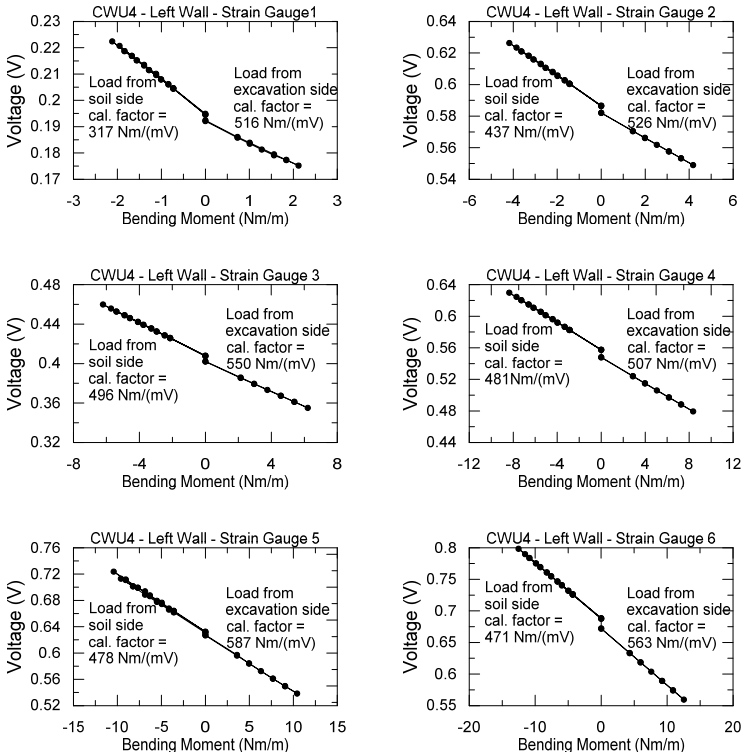

Figure A.45: Left wall strain gauges calibration for the test CWU4.

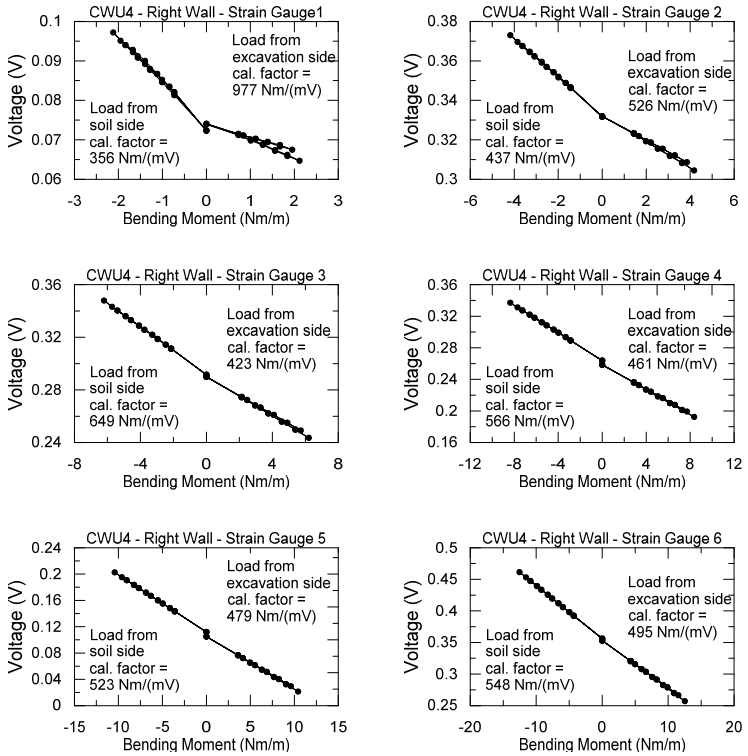

Figure A.46: Right wall strain gauges calibration for the test CWU4.

Appendix B

Position of Instruments

In this appendix the position of the piezoelectric accelerometers, the pore pressure transducers and the LVDTs for all the tests at the model scale is reported in Table B.2, Table B.3, Table B.4, Table B.5, Table B.6, Table B.7 and in Table B.8 in terms of three coordinates x, y and z relative to a reference system located at the left-bottom corner of all the model layouts reported in Figure B.1, Figure B.2, Figure B.3, Figure B.4, Figure B.5, Figure B.6 and in Figure B.7. The position of the instruments is reported both before and after the test execution. Besides those instruments also the position of the walls is reported since they rotate and sink during the tests. In all the tests a piezoelectric accelerometer is placed onto the baseplate of the laminar box in order to obtain a measure of the input acceleration; for this accelerometer the coordinates x,y and z are absent and they are substituted with a symbol /. The coordinates are also not available when a piezoelectric accelerometer is placed onto the support of the LVDTs and when an accelerometer or a pore pressure transducer is moved during the digging phase, thus sometimes the measure of the position after the test is not reported as well.

While the position of these instruments and of the walls after the tests depends on the model preparation, the strain gauges present a constant position from the top of the wall, as well as the MEMS accelerometers, and the potentiometers, when are used, because they are attached onto the top of the walls. So the position of the strain gauges in terms of vertical distance from the top of the walls is illustrated in Figure B.1 and summarized in Table B.1.

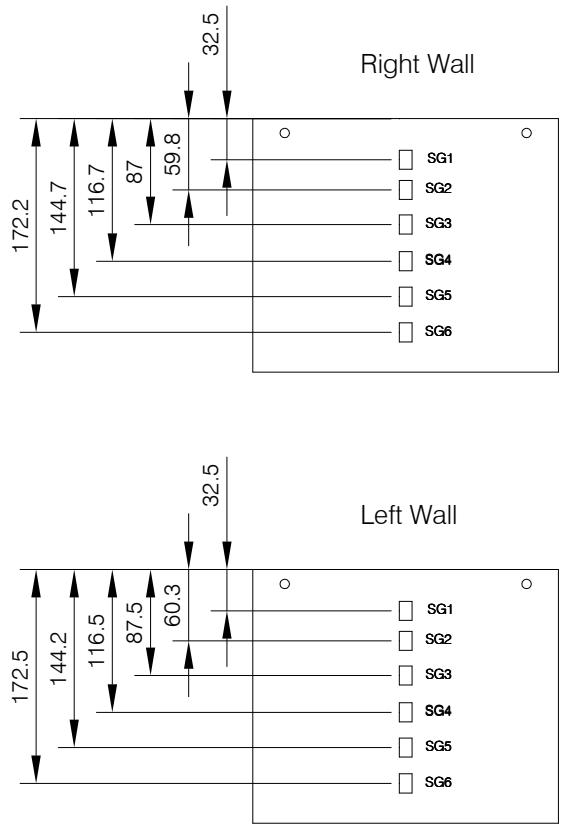

Figure B.1: Right wall strain gauges calibration for the test CWU4.

	Strain Gauge Position from the Top of the Walls at the Model Scale (mm)	
	Left Wall	Right Wall
Strain Gauge 1	32.5	32.5
Strain Gauge 2	60.3	59.8
Strain Gauge 3	87.5	87.0
Strain Gauge 4	116.5	116.7
Strain Gauge 5	144.2	144.7
Strain Gauge 6	172.5	172.2

Table B.1: Strain gauges positions from the top of the walls at the model scale.

Test CWU1

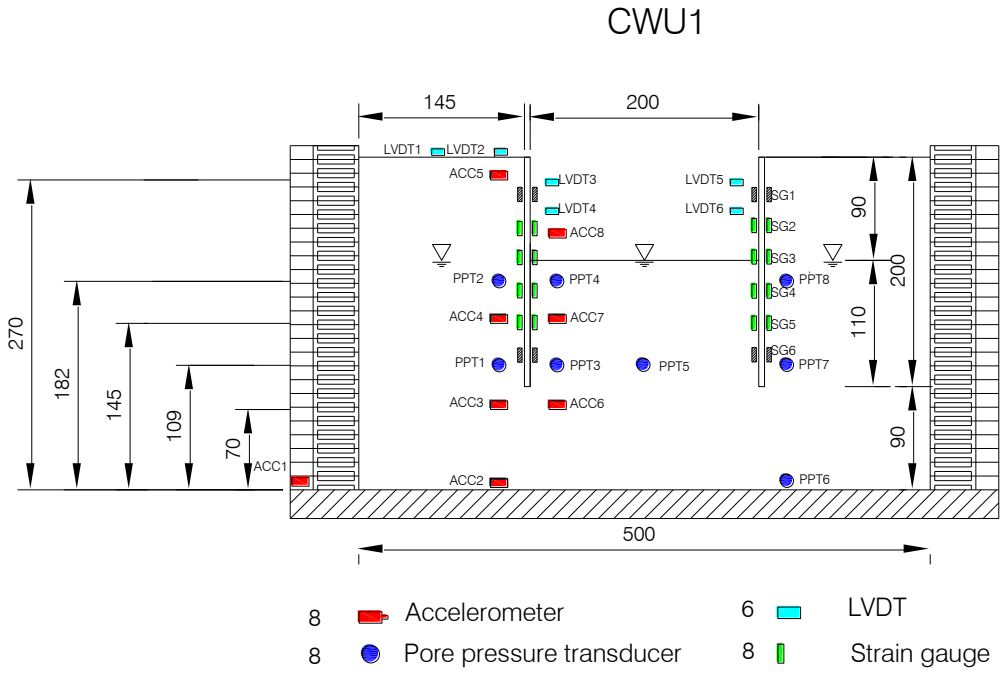

Figure B.2: CWU1: layout and coordinate reference system for the position of the instruments.

Instrument	Position before the Test			Position after the Test		
	x	y	z	x	y	z
Acc1 (base plate)	/	/	/	/	/	/
Acc2	120	1	123	120	3	123
Acc3	119	65	120	125	59	120
Acc4	120	140	123	125	130	128
Acc5	176	65	128	188	67	128
Acc6	176	143	130	180	148	128
Acc7	/	/	/	/	/	/
Acc8 (support of the LVDTs)	/	/	/	/	/	/
PPT1	118	117	126	/	/	/
PPT2	118	186	125	/	/	/
PPT3	175	119	126	180	125	128
PPT4	175	119	126	180	125	128
PPT5	254	119	122	250	141	122
PPT6	377	4 6 120	371	4	120	
PPT7	380	118	114	373	108	115
PPT8	383	186	132	369	170	115
LVDT1	62	289	128	62	268	128
LVDT2	111	289	128	111	266	128
LVDT3	/	269	/	/	269	/
LVDT4	/	239	/	/	239	/
LVDT5	/	269	/	/	269	/
LVDT6	/	241	/	/	241	/
Top Left Wall	145	290	/	153	130	/
Top Right Wall	/	269	/	/	269	/

Table B.2: Instrument position before and after test CWU1.

Test PWU1

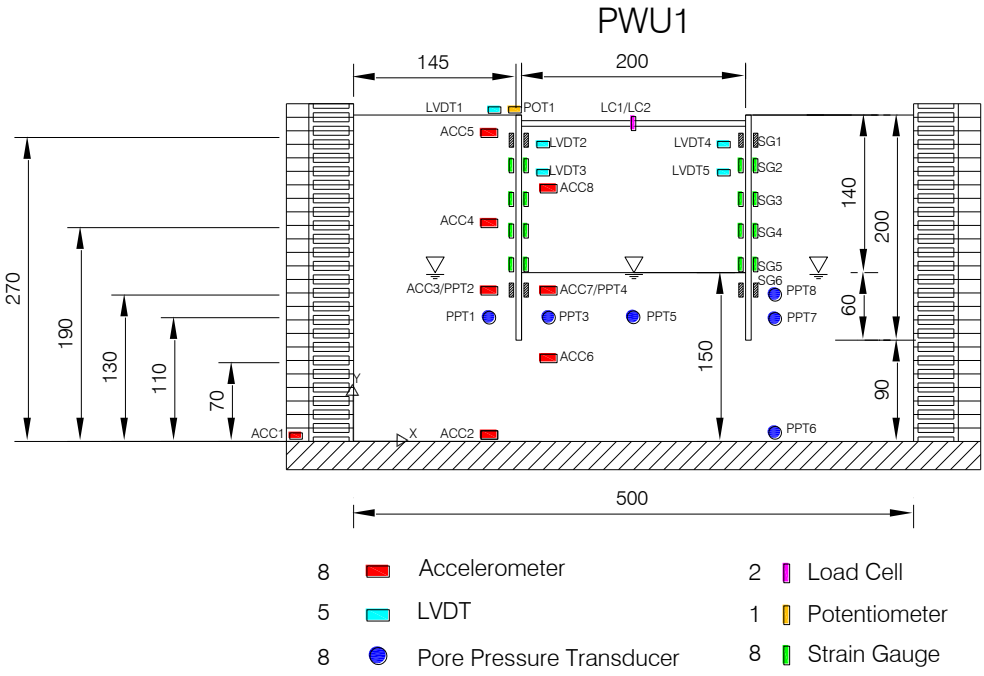

Figure B.3: PWU1: layout and coordinate reference system for the position of the instruments.

Instrument	Position before the Test			Position after the Test		
	x	y	z	x	y	z
Acc1 (base plate)	/	/	/	/	/	/
Acc2	119	9	122	123	/	/
Acc3	115	135	165	123	115	168
Acc4	114	192	129	117	173	128
Acc5	118	268	136	117	247	135
Acc6	174	71	140	184	73	142
Acc7	180	140	100	176	134	90
Acc8	/	/	/	/	/	/
PPT1	117	112	131	127	100	130
PPT2	115	134	105	127	120	101
PPT3	175	112	122	125	99	123
PPT4	172	133	90	/	/	/
PPT5	247	111	128	242	130	126
PPT6	380	2	131	380	3	131
PPT7	122	110	122	125	99	123
PPT8	379	128	119	372	117	119
LVDT1	111	286	128	111	286	128
LVDT2	/	269	/	/	269	/
LVDT3	/	239	/	/	239	/
LVDT4	/	269	/	/	269	/
LVDT5	/	241	/	/	241	/
Top Left Wall	145	291	/	/	279	/
Top Right Wall	355	291	/	/	279	/

Table B.3: Instrument position before and after test PWU1.

Test CWU3

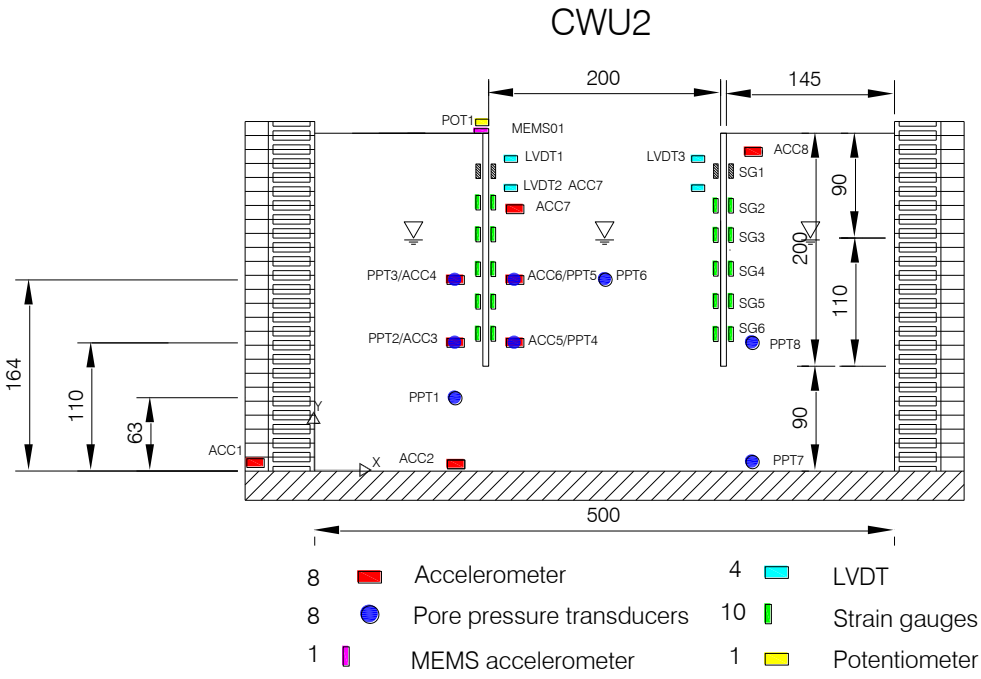

Figure B.4: CWU2: layout and coordinate reference system for the position of the instruments.

Instrument	Position before the Test			Position after the Test		
	x	y	z	x	y	z
Acc1 (base plate)	/	/	/	/	/	/
Acc2	115	8	130	115	8	130
Acc3	170	100	155	/	103	/
Acc4	120	172	156	/	103	/
Acc5	120	172	156	/	103	/
Acc6	127	101	155	/	161	160
Acc7	/	/	/	/	/	/
Acc8	380	273	130	380	268	120
PPT1	115	65	123	/	/	/
PPT2	127	108	95	/	104	/
PPT3	125	169	92	127	161	92
PPT4	170	109	100	/	112	/
PPT5	173	165	83	/	163	83
PPT6	250	165	83	/	163	/
PPT7	119	6	122	/	/	/
PPT8	380	109	115	120	105	115
LVDT1	/	269	/	/	269	/
LVDT2	/	237	/	/	237	/
LVDT3	/	269	/	/	269	/
LVDT4	/	237	/	/	237	/
Top Left Wall	/	290	/	/	289	/
Top Right Wall	/	290	/	/	289	/

Table B.4: Instrument position before and after test CWU2.

Test PWU2

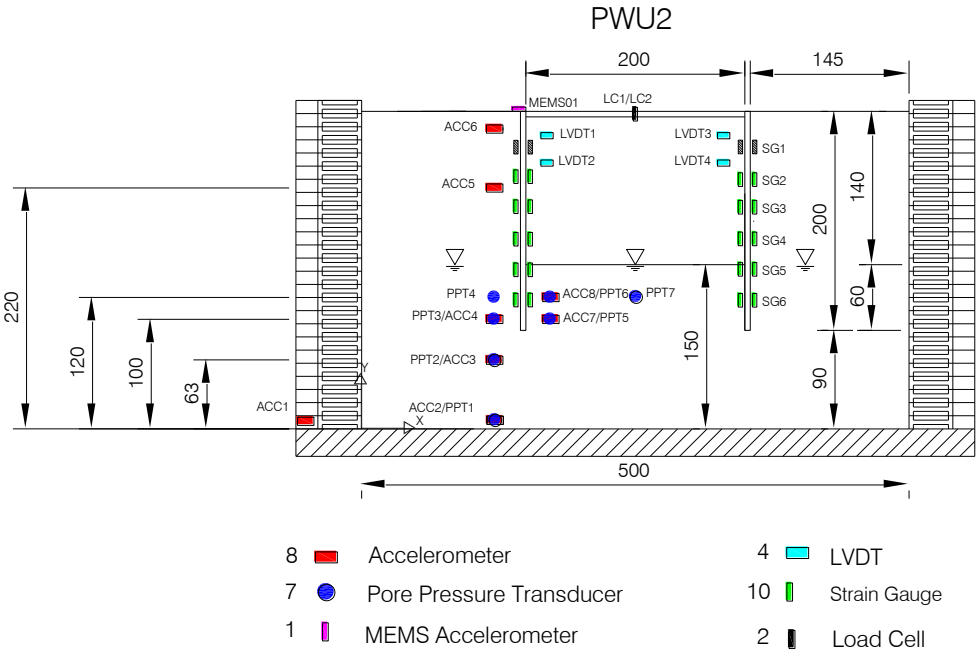

Figure B.5: PWU2: layout and coordinate reference system for the position of the instruments.

Instrument	Position before the Test			Position after the Test		
	x	y	z	x	y	z
Acc1 (base plate)	/	/	/	/	/	/
Acc2	110	6	162	110	6	162
Acc3	117	64	163	/	/	/
Acc4	117	101	170	115	96	165
Acc5	113	222	167	115	215	165
Acc6	/	/	/	123	249	177
Acc7	186	106	167	184	101	165
Acc8	186	122	167	115	215	165
PPT1	117	33	77	117	3	77
PPT2	120	67	90	120	72	/
PPT3	113	102	80	115	100	78
PPT4	120	122	83	125	115	83
PPT5	186	104	75	190	104	77
PPT6	181	123	85	/	/	/
PPT7	246	123	83	/	128	83
LVDT1	/	267	/	/	267	/
LVDT2	/	197	/	/	197	/
LVDT3	/	267	/	/	267	/
LVDT4	/	193	/	/	193	/
Top Left Wall	145	290	/	/	267	/
Top Right Wall	355	290	/	/	267	/

Table B.5: Instrument position before and after test PWU2.

Test CWU3

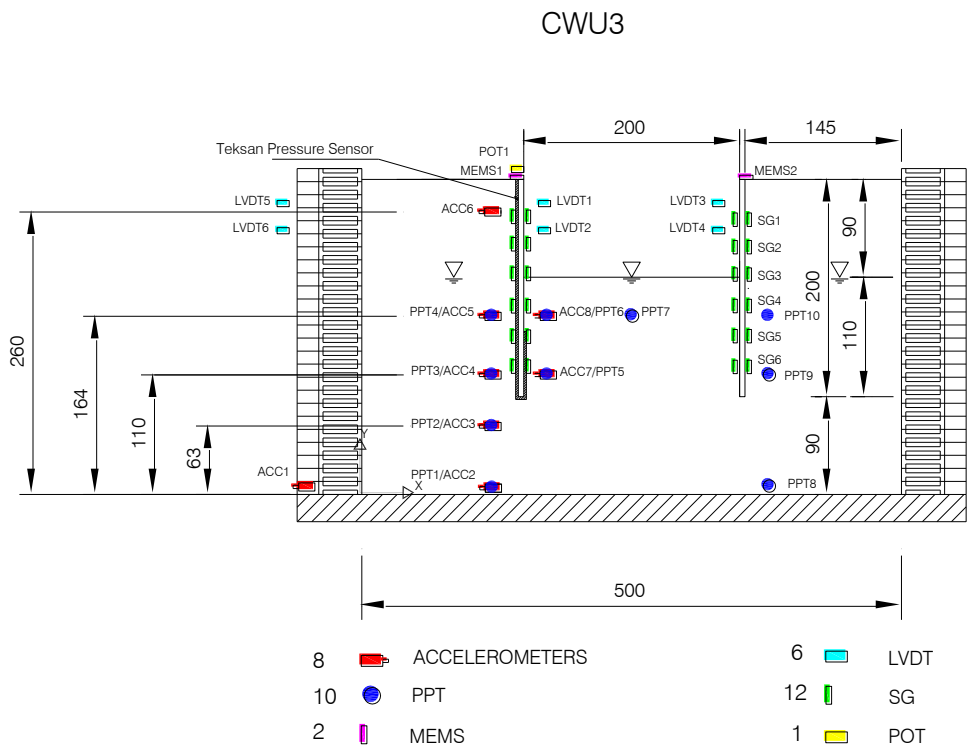

Figure B.6: CWU3: layout and coordinate reference system for the position of the instruments.

Instrument	Position before the Test			Position after the Test		
	x	y	z	x	y	z
Acc1 (base plate)	/	/	/	/	/	/
Acc2	110	6	60			
Acc3	125	66	58			
Acc4	100	116	53			
Acc5	110	170	60			
Acc6	110	256	61			
Acc7	186	117	50			
Acc8	186	169	60			
PPT1	117	6	180			
PPT2	120	63	172			
PPT3	110	114	155			
PPT4	110	165	170			
PPT5	191	114	87			
PPT6	181	164	173			
PPT7	251	164	115			
PPT8	379	4	68			
PPT9	122	114	110			
PPT10	125	168	110			
LVDT1	/	260	/		260	/
LVDT2	/	234	/	/	234	/
LVDT3	/	260 /	/	260	/	
LVDT4	/	234 /	/	234	/	
Top Left Wall	/	290	/	/	290	/
Top Right Wall	/	290	/	/	290	/

Table B.6: Instrument position before and after test CWU3.

Test PWU3

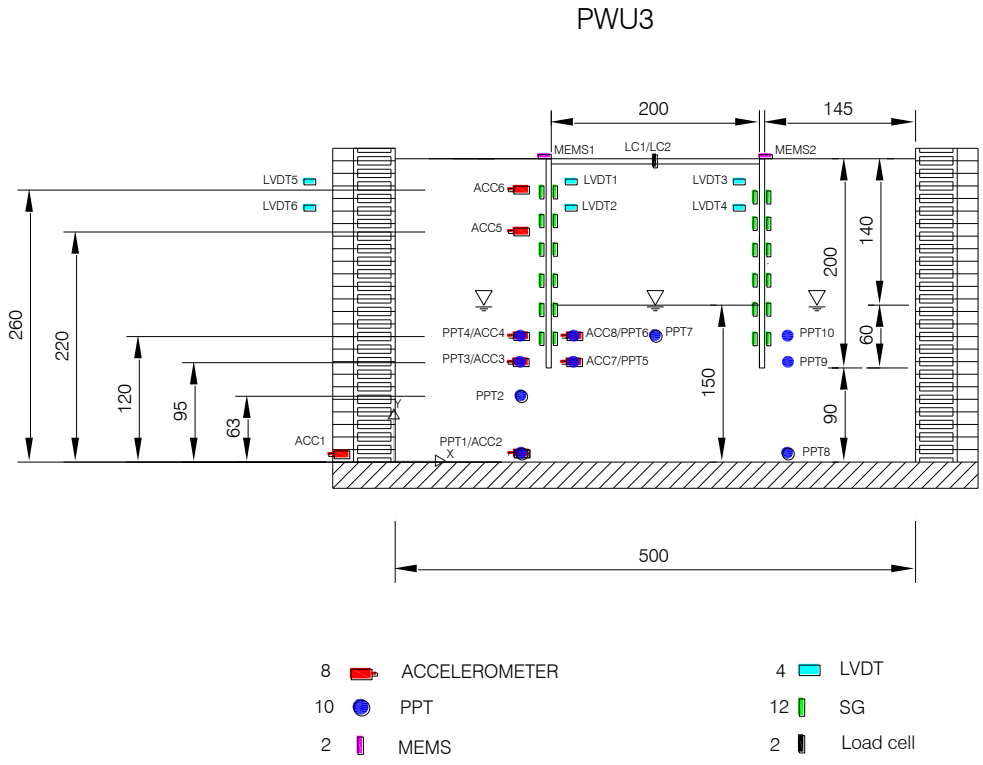

Figure B.7: PWU3: layout and coordinate reference system for the position of the instruments.

Instrument	Position before the Test			Position after the Test		
	x	y	z	x	y	z
Acc1 (base plate)	/	/	/	/	/	/
Acc2	117	8	68	117	7	75
Acc3	110	95	61	109	93	58
Acc4	112	131	75	113	126	67
Acc5	110	233	57	113	221	50
Acc6	107	258	58	112	212	63
Acc7	186	95	68	117	129	75
Acc8	186	169	60			
PPT1	117	8	181	117	10	180
PPT2	125	62	78	/	/	/
PPT3	105	94	172	107	96	168
PPT4	115	126	173	120	96	168
PPT5	183	94	172	107	96	168
PPT6	178	125	153	/	/	/
PPT7	246	126	94	241	132	92
PPT8	383	7	119	/	/	/
PPT9	385	94	140	390	93	145
PPT10	387	125	115	390	123	115
LVDT1	/	260	/		260	/
LVDT2	/	190	/	/	190	/
LVDT3	/	260	/	/	260	/
LVDT4	/	190	/	/	190	/
Top Left Wall	/	290	/	/	288	/
Top Right Wall	/	290	/	/	288	/

Table B.7: Instrument position before and after test PWU3.

Test CWU4

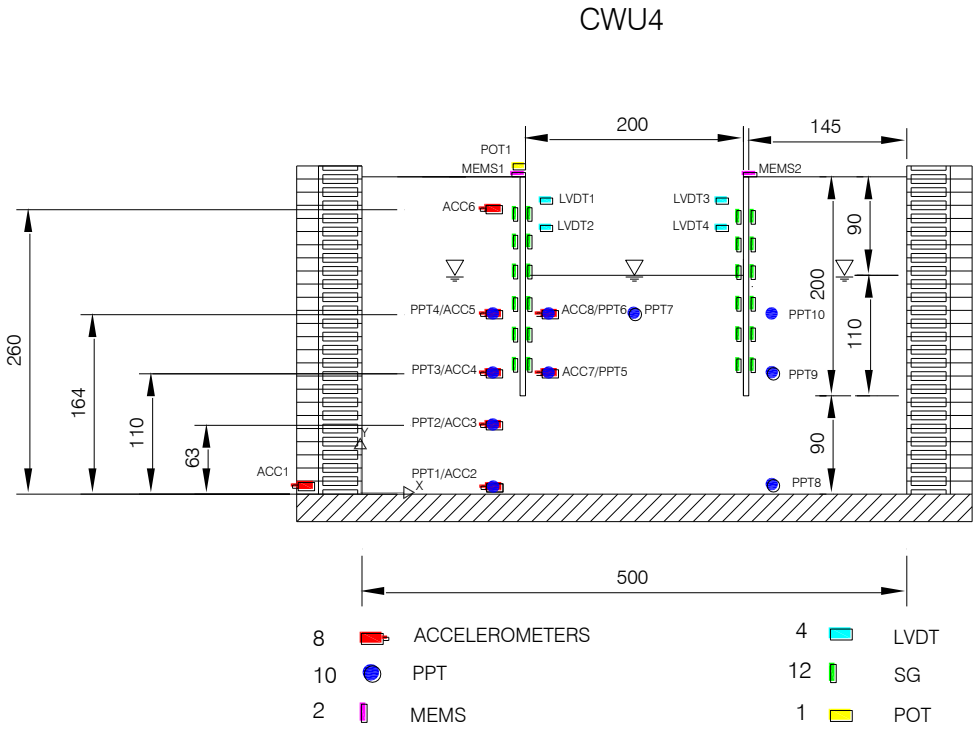

Figure B.8: CWU4: layout and coordinate reference system for the position of the instruments.

Instrument	Position before the Test			Position after the Test		
	x	y	z	x	y	z
Acc1 (base plate)	/	/	/	/	/	/
Acc2	112	5	77	113	2	75
Acc3	128	66	57	128	71	55
Acc4	113	113	73	99	/	108
Acc5	114	171	63	120	169	60
Acc6	115	259	85	101	252	/
Acc7	179	113	70	176	113	67
Acc8	186	172	62	177	173	60
PPT1	115	9	178	119	6	175
PPT2	128	66	162	125	68	162
PPT3	120	114	140	110	111	141
PPT4	112	174	140	110	111	141
PPT5	186	109	145	170	109	148
PPT6	176	167	110	175	167	100
PPT7	251	171	120	248	174	122
PPT8	385	9	115	385	5	115
PPT9	380	114	97	383	115	93
PPT10	383	175	135	322	172	132
LVDT1	/	275	/	/	275	/
LVDT2	/	240	/	/	240	/
LVDT3	/	275	/	/	275	/
LVDT4	/	240	/	/	240	/
Top Left Wall	145	290	/	162	288	/
Top Right Wall	355	290	/	338	288	/

Table B.8: Instrument position before and after test CWU4.

Appendix C

Soil Water Retention Curve

It has been shown in Chapter 4 that for all the centrifuge tests performed, during the saturation of the model, the arise of the capillary suction within the soil above the water table has taken place, as confirmed by the observed presence of water at the sand surface immediately after the saturation.

After the saturation, during the swing up of the model, the arise of the centrifuge acceleration causes a decrease of the capillary rise.

So, the soil present above the water table is partially saturated during the centrifuge test and it is subjected to a wetting cycle during the saturation and to a drying cycle during the swing up.

The bending moment distribution has been seen to be probably affected by the presence of the capillary suction within the soil above the water table and, a modified expression for the computation of the effective horizontal earth pressure σ_h at the active side and above the water table has been proposed between the possible limit equilibrium analyses (indicated as case 3 in chapter 4):

$$\sigma'_h(z) = K_{ae} \cdot \sigma'_v(z) + S_r(z) + \cdot(\gamma_w \cdot (H - z)) \cdot (1 - K_{ae}) \qquad \text{(C.1)}$$

Where the dependency from the water retention curve appears through the function Sr(z). The water retention curve of the Leighton Buzzard sand at low and high relative density has been determined at the laboratory of the University of Naples Federico II. Hereinafter the experimental setup and the test procedure for the determination of the water retention curve is reported.

Theoretical introduction Basic Concepts

In a partially saturated soil the pore water pressure is lower than the atmospheric pressure. The soil matrix suction is defined as the difference $u_a - u_w$ between the atmospheric pressure u_a and the pore water pressure u_w.

The soil water retention curve (SWRC) represents the relation between the soil matrix suction and an index of the degree of saturation of the soil. Three possible indices can be individuated:

1. the degree of saturation S_r defined as the ratio between the volume occupied by the water V_w and the volume of the voids V_v: $S_r = \frac{V_w}{V_v} \cdot 100$
2. the water content expressed as the ratio of the weight of water W_w to the weight of solids W_s: $w = \frac{W_w}{W_z} \cdot 100$;
3. the volumetric water content expressed as the ratio between V_w and the volume occupied by the soil V: $\Theta = \frac{V_w}{V} = S_r \cdot n$.

Typically the SWRC is represented with a semi-logaritmic diagram with the soil matrix suction on the x-axis and S_r (or one of the other indexes) on the y-axis, an example is reported in Figure C.1. The SWRC can be subdivided into three zones. The first one is the *boundary effect zone*, where the suction increases while the degree of saturation does not decrease significantly. The boundary effect zone finishes when the first air bubbles appear in the pores of the soil. The second zone is called *transition zone* and it is characterized by a strong decrease of S_r with the soil matrix suction. The third zone is the *residual zone of unsaturation* where as the suction increases very little reductions of S_r take place. The value of the suction correspondent to the passage between the first and the second zone is called *air-entry value*.

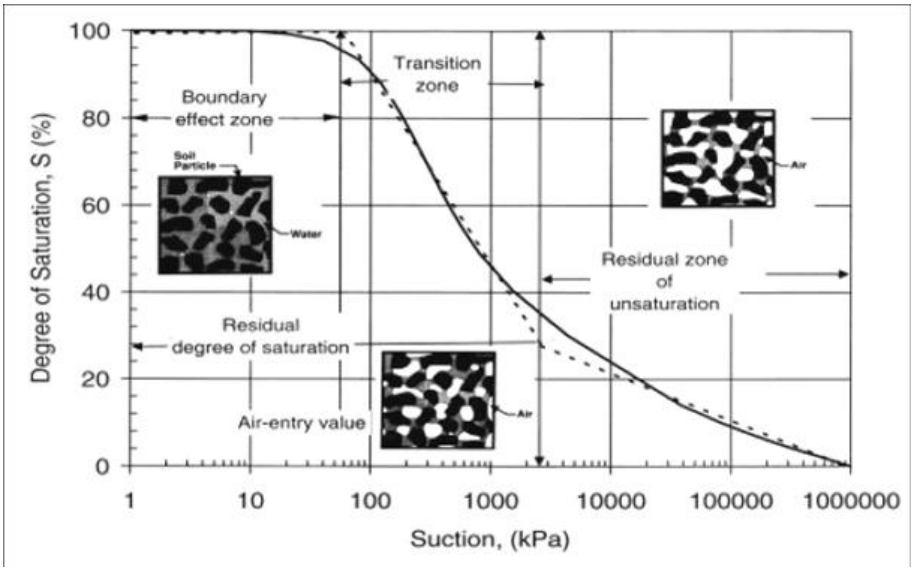

Figure C.1: Example of soil water retention curve (Vanapalli et al., 1996).

Gravel and sand present usually a low air-entry value and a steep transition zone since they present big and interconnected pores, while silt and clay present a high air-entry value a moderate slope of the transition zone.

The unsaturated soil also present an hysteretic behaviour when subjected to a drying-wetting cycle. The main drying is the curve representing the response during the first drying of the soil. If the soil the undergoes a wetting cycle the full saturation is not achieved.

The Van Genuchten model (1980) one of the model used to interpolate the SWRC. It expresses the volumetric water content as follows:

$$\Theta = \Theta_r + \frac{\Theta_s - \Theta_r}{(1 + (\alpha s)^n)^m} \tag{C.2}$$

where Θ_s is the water content for $S_r = 1$, s is the soil matrix suction, Θ_r is the residual volumetric water content, α, n and m are the model parameters.

In this work the water retention curve of the Leighton Buzzard sand has been determined through the use of the Tempe Cell apparatus. Its description and the test procedure is described hereinafter.

Test Equipment

The purpose of the Tempe Cells is to build a recipient for the soil where the value of the suction can be controlled. They are basically constituted of a brass cylinder where the soil sample is placed and a porous stone with a high air entry value placed below the brass cylinder (Figure C.2. The brass cylinder is placed within Plexiglas plates and is sealed through a combined action of screws that tend to approach the Plexiglas plates and of rubber o-rings that avoid the water flow through the top and the bottom of the cylinder. The Plexiglas plates present two brass pieces that are finally collocated at the top and at the bottom of the Tempe Cell; they allow a system of external pipes to be connected to the Tempe Cell that can be used to control the suction. The cylinder is used to contain the soil sample and the porous stone with a high air entry value allows to maintain the hydraulic continuity between the soil and a system of pipes through which the water pressure within the porous stone is controlled (Figure C.3). The system of pipes is connected to a water tank whose position regulates the pressure of the water within the pipes: the more the vertical distance between the bottom of the Temp Cell increases the more the pressure within the pipes decreases below the atmospheric pressure. The air entry value of the porous stone has to high enough such that the porous stone remains fully saturated while the pressure within the pipes decreases, in this way a change of water pressure within the system of pipes is transmitted at the water that fills the voids of the porous stone. Due to the realized hydraulic continuity of the system of pipes, the porous stone and the water within the soil sample the value of the water pressure is controlled also within the soil and consequently the suction is controlled.

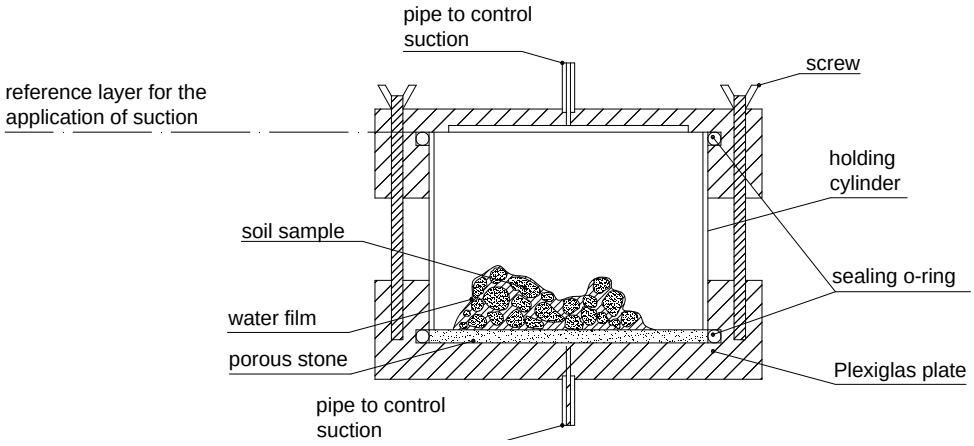

Figure C.2: Tempe Cell schematic.

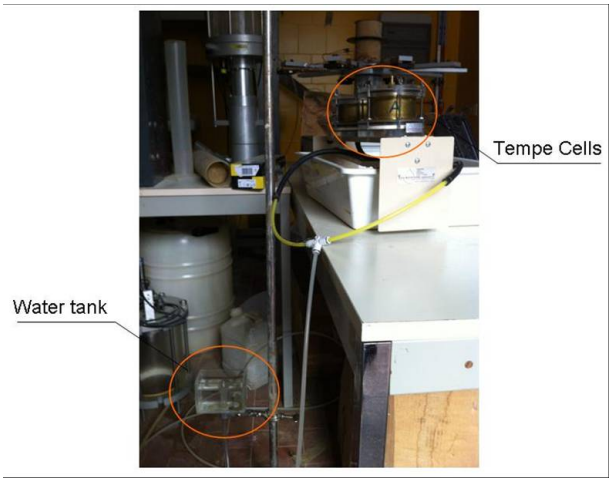

Figure C.3: System to apply the suction decreasing the water pressure. At the left bottom there is the water tank used to impose the suction. At the right top the Tempe Cells can be seen.

While the brass piece at the bottom has been used to control the water pressure within the soil, the top brass piece has been used to increase the air pressure within the soil, a consequently the suction, through the use of compressed air.

So two different methods of changing the suction within the soil have been used. With the first one the suction is changed through a modification of the soil water pressure u_w changing the position of the water tank that controls the water pressure within the pipes attached at the bottom of the Tempe Cell. With the second one the suction is changed increasing the air pressure u_a within the soil sample using compressed air.

The first method has been used for the determination of the water retention curve of the Leighton Buzzard Sand up to suction values of about 10 kPa. This method allows to obtain very low and accurate steps of water pressure decrement (for instance 0.1 kPa) but the maximum suction that can be applied is conditioned from the maximum achievable vertical distance between the water tank and the Tempe Cells, which is related with the length of the pipes of the drainage system and the height of the bar where the water tank is attached. This method has been used for the execution of the test because the water retention curve of the Leighton Buzzard Sand is mostly concentrated at low suction values, for example 0 10 kPa. Particularly, the air entry value is about at 3-5 kPa and the transition zone of the curve is about 10 kPa. So the applying of the suction through the decrement of the water pressure allows to accurately determine the water retention curve up to the end of the transition zone. The residual part of the curve has been determined using compressed air imposed from the top of the Tempe Cell.

Test Procedure and Results

The sand has been reconstituted at two different relative densities through the air pluviation technique. Within the Cell B the loose sand sample has been placed ($D_r = 57\%$), whilst the dense sand sample has been placed within the Cell A ($D_r = 80\%$). After that, the Tempe Cells have been saturated by imposing a water flux from the bottom to the top of the samples. The vertical water flux has been obtained moving the water tank represented in Figure C.3 up to about 0.4m above the top of the Tempe Cells. After the saturation the test has been started imposing increasing values of suction and, for a given value of the suction, measuring the total mass of the cells (constituted of the sum of sample mass and the tare) with time. For the given value of the suction an exponentially decrease of the total mass is

typically observed due the water content decrease within the sample. This process corresponds to the equalization of the pore water pressure with respect the suction imposed at the boundary of the sample. When the total mass reaches a stable value this transient process of equalization is concluded and the following suction value can be applied. The reference layer for the suction is the upper surface of the porous stone at the base of the Tempe Cell (Figure C.1). The suction 0 kPa corresponds to the water level coinciding with the top surface of the Tempe Cells while the suction 0.59 kPa is achieved for the water level coinciding with the bottom of the Tempe Cell. Hereinafter (Table C.1) the sequence of the suction values imposed for the determination of the water retention curve is reported.

Suction (kPa)	Suction Increment (kPa)
0.59	0.59
1.57	0.98
2.55	0.98
3.55	1
4.53	0.98
5.53	1
5.98	0.34
6.23	0.25
6.47	0.24
6.72	0.25
6.96	0.24
7.21	0.25
7.45	0.24
7.7	0.25
7.95	0.25
8.19	0.24
8.78	0.59
9.31	0.53
100	90.69

Table C.1: Applied suction and suction increments for the determination of the water retention curve of the Leighton Buzzard sand.

The asymptotic value of the measured total mass for the given suction value, the sand mass within the Tempe Cell and its tare are used for the calculation of the degree of saturation S_r corresponding to that suction value, thus a point of the water retention curve is obtained. In Table C.2

the basic physical properties of the Leighton Buzzard sand useful for the determination of the water retention curve and the sample mass, the volume occupied by the sand and the relative density are reported.

Basic physical properties of the sand	Maximum void index (e_{max})	1.014
	Minimum void index (e_{min})	0.613
	Specific gravity of the solid G_s	2.65
Cell A	Sand Mass M_s	535.0 g
	Total Volume V_{tot}	$3.41 \cdot 10^{-4} m^3$
	Relative Density D_r	80.7
Cell B	Sand Mass M_s	486.0 g
	Total Volume V_{tot}	$3.27 \cdot 10^{-4} m^3$
	Relative Density D_r	57.4%

Table C.2: Basic physical properties of the Leighton Buzzard sand.

The water retention curves are reported in Figure C.4 and in Figure C.5 interpolated with the Van Genuchten model whose parameters have been reported in Table C.3.

The first Cell that has shown the air entry has been the Cell A, which contains dense sand, at a suction of 5.49 kPa. After this point the suction has been increased by steps of about 0.5 kPa and then of about 0.25 kPa in order to get a more refined description of the water retention curve along its more steep part.

At the following step, reaching 5.98 kPa, the sand of the Cell B has passed the air entry value. This is not intuitive, since the dense sand is expected to show the air entry after the loose cell. Probably the air entry of the loose sample has been observed after the air entry of the dense sample due to the different velocity of equalization of the porous stone. After the air entry value, the time needed to equalize the system is significantly larger that the equalization time before the air entry. In the latter case 4-5 days are needed, while in the first case, 24 hours are usually enough to observe the measured total mass of the Cell becoming stable with time.

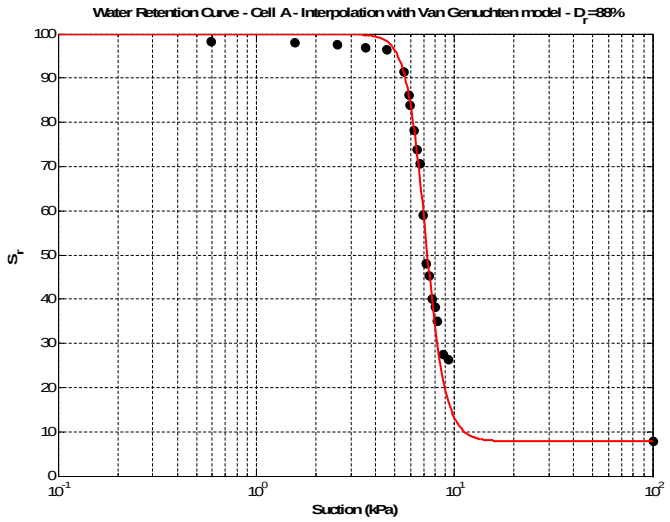

Figure C.4: Leighton Buzzard Sand;: water retention curve for dense sand and interpolation with the van Genuchten model.

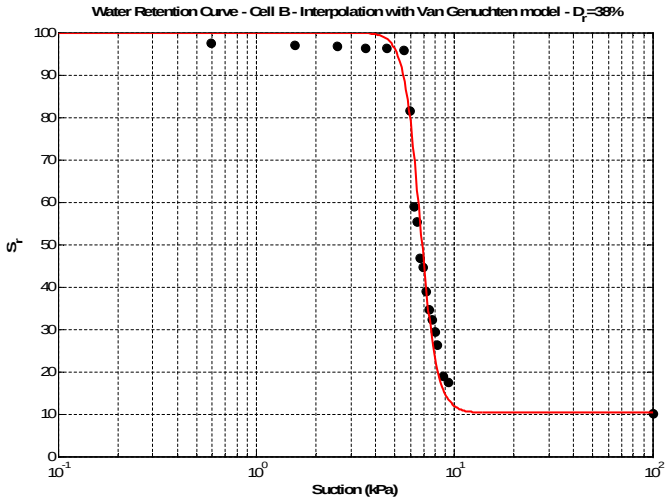

Figure C.5: Leighton Buzzard Sand: water retention curve for loose sand and interpolation with the van Genuchten model.

Van Genuchten Parameters	Loose Sample	Dense Sample
Θ_s	1.000	1.000
Θ_r	0.526	0.499
a	0.165	0.156
n	40.639	10.017
m	0.975	0.900

Table C.3: Van Genuchten parameters for Loose Sample and Dense Sample.

Bibliography

[1] Bureau of Ports and Harbors.,: *Earthquake resistant design for quay walls and piers in Japan* 1989: Ministry of Transport, Tokyo, Japan.

[2] Bilotta E., Taylor N., *Modellazione Geotecnica in Centrifuga* 2005.

[3] Bolton M., *The strength and dilatancy of sands* 1986: Geotechnique 36(1), 6578.

[4] Bridgman P.W., *Dimensional analysis* 1931: Yale University Press, New Haven.

[5] Buckingam E., *On physically similar systems; illustrations of the use of dimensional equations* 1914 Physical Review : (4): 345-376.

[6] Callisto L., Soccodato F. M., *Seismic Design of Flexible Cantilevered Walls. Journal of Geotechnical and Geoenvironmental Engineering*: ASCE, 136(2), 344354.

[7] Caquot A, Kerisel J., for Calculation of Passive Pressure, Active Pressure and Bearing Capacity of Foundations 1948: Gauthier-Villars, Paris.

[8] Conti R., Viggiani G. M. B., Cavallo S., *Un modello per lanalisi di muri di sostegno a gravità sotto azioni sismiche* 2013: IARG Conference Document.

[9] Dewoolkar, M. M., Ko, H. Y., and Pak, R. Y. S., *Seismic behaviour of cantilever retaining walls with liquefiable backfills* 2001: J. Geotech. Geoenviron. Eng., $127_{5,}424435$.

[10] Kamon, M., Wako, T., Isemura, K., Sawa, K., Mimura, M., Tateyama, K., and Kobayashi, S., *Geotechnical disasters on the waterfront.* 1996: Soils Found., Special issue, Japanese Geotechnical Society, January, 137147.

[11] Kerisel J., Absi E., *Tables de pousée et de butée des terres* 1990: 3rd ed., Presses delEcole Nationale des Pontset Chaussées, Paris, 1990..

[12] Kutter, B.L. & Balakrishnan, A., *Dynamic model test data from electronics to knowledge* 1998: In T. Kimura, O. Kusakabe & Takemura, eds., Centrifuge 98, vol. 2, 931-943, Balkema, Tokyo.

[13] Iai, S., and Kameoko, T., *Finite-element analysis of earthquake induced damage to anchored sheet pile quay walls.* 1993: Soils Found., $33_{1,}7191$.

[14] Lancellotta R., : *Lower-bound approach for seismic passive earth resistance* 2007: Geotechnique, 57(3), 319321.

[15] Newmark N. M., *Effects of earthquakes on dams and embankments* 1965: J. Geotech. Eng. Div., ASCE, 105(4), 449-464.

[16] Madabhushi, S.P.G., Houghton, N.E. & Haigh, S. K., *A new automatic sand pourer for mode preparation at University of Cambridge. International conference on physical modelling in geotechnics* ICPMG 2006: The Hong Kong University of Science and Technology, Hong Kong.

[17] Madabhushi, S. P. G., Schofield, A.N. & Lesley, S., *A new Stored Angular Momentum (SAM) based Earthquake Actuator* 1998: Proc. Centrifuge98, Int. Conf. on Centrifuge Modelling, Tokyo, Japan: 111-116.

[18] Madabhushi S.P.G., Stringer M.E., *Novel Computer Controlled Saturation of Dynamic Centrifuge Models Using High Viscosity Fluids* Geotechnical Testing Journal, Vol. 32, N° 6, GTJ102435.

[19] Madabhushi S. P. G., Zeng X., *Simulating Seismic Response of Cantilever Retaining Walls* 2007: J. Geotech. and Geonvir. Engng., ASCE, pp, 539-549.

[20] Matsusawa H., Ishibashi I.; Kawamura M., *Dynamic soil and water pressures of submerged soils* 1984: Journal of Geotechnical Engineering, 111 (10), 1161 1176.

[21] Mononobe N.; Matsuo H., *On the determination of earth pressure during earthquake* 1929: In Proc. 2nd World Engineering Conference, volume 9, pp. 177185.

[22] Okabe S., *General theory of earth pressure* 1926: Journal of Japanese Society of Civil Engineering, 12(1).

[23] Richards R., Elms D. G., *Seismic behavior of gravity retaining walls* 1979: J. Geotech. Eng. Div., ASCE, 105(4), 449-464.

[24] Schofield, A.N., *Cambridge geotechnical centrifuge operations* 1980: Geotechnique 30 (3): 227-268.

[25] Stewart D.P., Chen Y-R and Kutter B.L., *Experience with the Use of Methylcellulose as Viscous Pore Fluid in Centrifuge Models* 1998: Geotechnical testing Journal, GTJODJ, Vol. 21, pp. 365-369.

[26] Teymur, B. & Madabhushi, S.P.G., *Experimental study of boundary effects in dynamic centrifuge modelling* 2003: Geotechnique 53(7): 655-663.

[27] Van Diest, *On dimensional analysis and the presentation of data in fluid flow problems* 1946: J. Appl. Mech. Trans. ASME 13, A34.

[28] van Genuchten, M. Th., *A closed-form equation for predicting the hydraulic conductivity of unsaturated soils* 1980: Soil Sci. Soc. Am. J. 44: 892898.

[29] Visone, C., Santucci de Magistris, F., *Mechanical behaviour of the Leighton Buzzard Sand 100/170 under monotonic, cyclic and dynamic loading conditions* 2009: ANIDIS, Bologna.

[30] Westergaard, H. M., *Water Pressures on Dams During Earthquake* Transactions of ASCE, Vol. 98 1933, pp. 93-102.

[31] Zarrabi-Kashani K., *Sliding of gravity retaining wall during earthquakes considering vertical acceleration and changing inclination of failure surface* 1979: MS thesis, Department of Civil Engineering, Massachusetts Institute of Technology, Cambridge, Massachusetts.

[32] Zeng, X., *Seismic response of gravity quay walls. I: Centrifuge modeling* 1998: J. Geotech. Geoenviron. Eng., $124_{5,}$406417.

[33] Zeng, X., and Steedman, R. S., *On the behavior of quay walls in earthquakes* 1993: Geotechnique, $43_{3,}$417431.

[34] Zienckiewicz, O.C., Bicanic, N., and Shen F.Q., *Earthquake input definition and the transmitting boundary conditions* 1988: Conference on Advances in Computational Non-Linear Mechanics: 109130. Editor St. Doltnis I.

[35] Zhao Y., Gafar K., Elshafie M. Z. E. B., Deeks A. D.; Knappet J. A., Madabhushi S. P. G., *Calibration and use of a new automatic sand pourer* 2006: In Proc. 6th Int. Conf. on Physical Modelling in Geotechnics, pp. 265-270.